Micromechatronics

Kenji Uchino
Jayne R. Giniewicz

DEKKER MEDIA
software included

VISIT…

LANZAROTE
Caliente.COM

Micromechatronics

Kenji Uchino
International Center for Actuators and Transducers (ICAT)
The Pennsylvania State University
University Park, Pennsylvania, U.S.A.

Jayne R. Giniewicz
Indiana University of Pennsylvania
Indiana, Pennsylvania, U.S.A.

MARCEL DEKKER, INC. NEW YORK • BASEL

Marcel Dekker, Inc., and the author make no warranty with regard to the accompanying software, its accuracy, or its suitability for any purpose other than as described in the preface. This software is licensed solely on an "as is" basis. The only warranty made with respect to the accompanying software is that the CD-ROM medium on which the software is recorded is free of defects. Marcel Dekker, Inc., will replace a CD-ROM found to be defective if such defect is not attributable to misuse by the purchaser or his agent. The defective CD-ROM must be returned within 10 days to: Customer Service, Marcel Dekker, Inc., P.O. Box 5005, Cimarron Road, Monticello, NY 12701, (914) 796-1919.

Comments regarding the software may be addressed to the author, Kenji Uchino, 134 Mat. Res. Lab., Penn State University, University Park, PA 16802 or kenjiuchino@psu.edu.

Library of Congress Cataloging-in-Publication Data
A catalog record for this book is available from the Library of Congress.

ISBN: 0-8247-4109-9

This book is printed on acid-free paper.

Headquarters
Marcel Dekker, Inc.
270 Madison Avenue, New York, NY 10016, U.S.A.
tel: 212-696-9000; fax: 212-685-4540

Eastern Hemisphere Distribution
Marcel Dekker AG
Hutgasse 4, Postfach 812, CH-4001 Basel, Switzerland
tel: 41-61-260-6300; fax: 41-61-260-6333

World Wide Web
http://www.dekker.com

The publisher offers discounts on this book when ordered in bulk quantities. For more information, write to Special Sales/Professional Marketing at the headquarters address above.

Copyright © 2003 by Marcel Dekker, Inc. All Rights Reserved.

Neither this book nor any part may be reproduced or transmitted in any form or by any means, electronic or mechanical, including photocopying, microfilming, and recording, or by any information storage and retrieval system, without permission in writing from the publisher.

Current printing (last digit):

10 9 8 7 6 5 4 3 2 1

PRINTED IN THE UNITED STATES OF AMERICA

MATERIALS ENGINEERING

1. Modern Ceramic Engineering: Properties, Processing, and Use in Design: Second Edition, Revised and Expanded, *David W. Richerson*
2. Introduction to Engineering Materials: Behavior, Properties, and Selection, *G. T. Murray*
3. Rapidly Solidified Alloys: Processes • Structures • Applications, *edited by Howard H. Liebermann*
4. Fiber and Whisker Reinforced Ceramics for Structural Applications, *David Belitskus*
5. Thermal Analysis of Materials, *Robert F. Speyer*
6. Friction and Wear of Ceramics, *edited by Said Jahanmir*
7. Mechanical Properties of Metallic Composites, *edited by Shojiro Ochiai*
8. Chemical Processing of Ceramics, *edited by Burtrand I. Lee and Edward J. A. Pope*
9. Handbook of Advanced Materials Testing, *edited by Nicholas P. Cheremisinoff and Paul N. Cheremisinoff*
10. Ceramic Processing and Sintering, *M. N. Rahaman*
11. Composites Engineering Handbook, *edited by P. K. Mallick*
12. Porosity of Ceramics, *Roy W. Rice*
13. Intermetallic and Ceramic Coatings, *edited by Narendra B. Dahotre and T. S. Sudarshan*
14. Adhesion Promotion Techniques: Technological Applications, *edited by K. L. Mittal and A. Pizzi*
15. Impurities in Engineering Materials: Impact, Reliability, and Control, *edited by Clyde L. Briant*
16. Ferroelectric Devices, *Kenji Uchino*
17. Mechanical Properties of Ceramics and Composites: Grain and Particle Effects, *Roy W. Rice*
18. Solid Lubrication Fundamentals and Applications, *Kazuhisa Miyoshi*
19. Modeling for Casting and Solidification Processing, *edited by Kuang-O (Oscar) Yu*
20. Ceramic Fabrication Technology, *Roy W. Rice*
21. Coatings of Polymers and Plastics, *edited by Rose A. Ryntz and Philip V. Yaneff*
22. Micromechatronics, *Kenji Uchino and Jayne R. Giniewicz*
23. Ceramic Processing and Sintering: Second Edition, *Mohamed N. Rahaman*

Additional Volumes in Preparation

Handbook of Metallurgical Process Design, *edited by George E. Totten, Kiyoshi Funatani, and Lin Xie*

PREFACE

Remarkable developments have taken place in the field of mechatronics in recent years. As reflected in the "Janglish" (Japanese-English) word *mechatronics*, the concept of integrating electronic and mechanical devices in a single structure is one that is already well accepted in Japan. Currently, robots are employed to manufacture many products in Japanese factories, and automated systems for sample displays and sales are utilized routinely in the supermarkets of Japan. Further, the rapid advances in semiconductor chip technology have led to the need for microdisplacement positioning devices. Actuators that function through the piezoelectric, magnetostriction, and shape memory effects are expected to be important components in this new age of micromechatronic technology. In this sense, the term *micromechatronics* has a much broader context than just a single class of devices (such as the silicon-based MEMS devices) and is meant to include not only the other types of devices, but also the manner in which they are applied in a particular micromechatronic system.

This book is the latest in a series of texts concerned with ceramic actuators written by Kenji Uchino. The first, entitled *Essentials for Development and Applications of Piezoelectric Actuators,* was published in 1984 through the Japan Industrial Technology Center. The second, *Piezoelectric/Electrostrictive Actuators*, published in Japanese by the Morikita Publishing Company (Tokyo) in 1986, became one of the bestsellers of that company, and was subsequently translated into Korean. The problem-based text *Piezoelectric Actuators: Problem Solving*, was also published through Morikita and was sold with a 60-minute instructive videotape. The English translation of that text was completed and published in 1996 through Kluwer Academic Publishers. This sixth text, written in collaboration with Jayne Giniewicz, offers updated chapters on topics presented in the earlier texts as well as new material on current and future applications of actuator devices in micromechatronic systems. The emphasis is largely on electromechanical actuators, which are and will continue to be of primary importance in this area.

We present in the text a theoretical description of solid-state actuators, give an overview of practical materials, device designs, drive/control techniques, and typical applications, and consider current and future trends in the field of micromechatronics. An overview of the field and recent developments in micropositioning technology are presented in Chapter 1 along with an overview of the materials to be presented in the text. Theoretical basics and practical materials, design and manufacturing considerations are covered in Chapters 2 through 4 and drive/control techniques are described in Chapter 5. The unique challenges of modeling and practically regulating electromechanical losses and heat generation in actuator devices are addressed in Chapter 6. Chapter 7 is dedicated entirely to the modeling of these effects by means of finite element analysis and a demonstration of these methods is included on the CD-ROM that accompanies the text. Three distinct classes of applications are presented in Chapters 8 through 10. Servo displacement transducer applications are presented in Chapter 8, while pulse drive motor and ultrasonic motor applications are described in Chapter 9 and Chapter 10, respectively. Finally, in Chapter 11 we consider the future of micromechatronics in terms of the technological and economic impact these new systems will have on industry and society.

This textbook is intended for graduate students and industrial engineers studying or working in the fields of electronic materials, control system engineering, optical communications, precision machinery, and robotics. The text is designed primarily for a graduate course with the equivalent of thirty 75-minute lectures; however, it is also suitable for self-study by individuals wishing to extend their knowledge in the field. The CD-ROM supplement includes a 57-minute video in which some commercially produced actuators are presented and some examples of finite-element modeling are demonstrated. We are indebted to Dr. Philippe Bouchilloux, of Magsoft Corporation, Troy, NY, for creating this supplement and for writing the introduction to the finite element method presented in Chapter 7 of the text. Because the development of actuator devices and their use for micropositioning is a new, dynamic, and highly interdisciplinary field, it would be impossible to cover the full range of related material in a single text. Hence, we have selected what we feel are the most important and fundamental topics to provide an adequate understanding of the design and application of actuator devices for micromechatronic systems.

We would like to acknowledge in particular the following individuals for permitting the citation of their studies in the application chapters of the text:

Takuso Sato, Tokyo Institute of Technology
Katsunori Yokoyama and **Chiaki Tanuma**, Toshiba R&D Laboratory
Shigeo Moriyama and **Fumihiko Uchida**, Hitachi Central Research Laboratory
Teru Hayashi and **Iwao Hayashi**, Tokyo Institute of Technology, Precision Engineering Laboratory
K. Nakano and **H. Ohuchi**, Tokyo Institute of Technology, Precision Engineering Laboratory
Sadayuki Takahashi, NEC Central Research Laboratory
Ken Yano, NEC Communication Transfer Division
Michihisa Suga, NEC Microelectronics Laboratory
Toshiiku Sashida, Shinsei Industry
E. Mori, S. Ueha, and **M. Kuribayashi,** Tokyo Institute of Technology, Precision Engineering Laboratory
Akio Kumada, Hitachi Maxel
Kazumasa Onishi, ALPS Electric
Yoshiro Tomikawa and **Seiji Hirose**, Yamagata University
Kazuhiro Otsuka, Smart Structure Center, MISc
Yasubumi Furuya, Hirosaki University
Toshiro Higuchi, University of Tokyo
Ben K. Wada, Jet Propulsion Laboratory
J. L. Fanson and **M. A. Ealey**, Jet Propulsion Laboratory and Xinξtics
H. B. Strock, Strock Technology Associates
A. B. Flatau, Iowa State University

A. E. Clark, Clark Associates
Nesbit Hagood, Massachusetts Institute of Technology
Mark R. Jolly and **J. David Carlson**, Lord Corporation

For the reader who seeks current information on state-of-the-art actuator technology we recommend *The Handbook on New Actuators for Precision Control* edited by the Solid State Actuator Study Committee, JTTAS (editor-in-chief, K. Uchino), and published by Fuji Technosystem, Tokyo in 1995. A thorough and timely introduction to ferroelectric materials and applications is presented in *Ferroelectric Devices* by Kenji Uchino (published by Marcel Dekker, Inc., in 2000) and it is strongly recommended to readers interested in learning more about ferroelectric materials.

Finally, we express our gratitude to our colleagues at The Pennsylvania State University and the Indiana University of Pennsylvania. A special expression of gratitude is extended to Dr. Robert E. Newnham and Dr. L. Eric Cross of The Pennsylvania State University for their continuous encouragement and support during the preparation of this text. Kenji Uchino expresses his appreciation of his wife, Michiko, and her kind daily support throughout the project. Jayne Giniewicz wishes to thank her colleagues and friends in the Department of Physics and Dean John Eck of the Indiana University of Pennsylvania for their enthusiastic support of her participation in this project. Any good that she might produce in this or any task at hand is, as always, dedicated with the fullest heart to John and Theo Giniewicz.

Kenji Uchino
Jayne R. Giniewicz

CONTENTS

PREFACE *iii*
PREREQUISITE KNOWLEDGE *xi*
SUGGESTED TEACHING SCHEDULE *xiii*
SYMBOLS *xiv*

1 CURRENT TRENDS FOR ACTUATORS AND MICROMECHATRONICS
1.1 The Need for New Actuators 1
1.2 Conventional Methods for Micropositioning 3
1.3 An Overview of Solid-State Actuators 7
1.4 Critical Design Concepts and the Structure of the Text 32

2 A THEORETICAL DESCRIPTION OF FIELD-INDUCED STRAINS
2.1 Ferroelectricity 37
2.2 Microscopic Origins of Electric Field Induced Strains 48
2.3 Tensor/Matrix Description of Piezoelectricity 50
2.4 Theoretical Description of Ferroelectric and Antiferroelectric Phenomena 62
2.5 Phenomenology of Magnetostriction 80
2.6 Ferroelectric Domain Reorientation 82
2.7 Grain Size and Electric Field-Induced Strain in Ferroelectrics 92

3 ACTUATOR MATERIALS
3.1 Practical Actuator Materials 103
3.2 Figures of Merit for Piezoelectric Transducers 129
3.3 The Temperature Dependence of the Electrostrictive Strain 138
3.4 Response Speed 143
3.5 Mechanical Properties of Actuators 145

4 CERAMIC ACTUATOR STRUCTURES AND FABRICATION METHODS
4.1 Fabrication of Ceramics and Single Crystals 169
4.2 Device Design 176
4.3 Electrode Materials 208
4.4 Commercially Available Piezoelectric and Electrostrictive Actuators 213

5 DRIVE / CONTROL TECHNIQUES FOR PIEZOELECTRIC ACTUATORS
5.1 Classification of Piezoelectric Actuators 219
5.2 Feedback Control 221

5.3 Pulse Drive 241
5.4 Resonance Drive 256
5.5 Sensors and Specialized Components for Micromechatronic Systems 265

6 LOSS MECHANISMS AND HEAT GENERATION

6.1 Hysteresis and Loss in Piezoelectrics 285
6.2 Heat Generation in Piezoelectrics 310
6.3 Hard and Soft Piezoelectrics 319

7 INTRODUCTION TO THE FINITE ELEMENT METHOD FOR PIEZOELECTRIC STRUCTURES

7.1 Background Information 329
7.2 Defining the Equations for the Problem 330
7.3 Application of the Finite Element Method 334

8 SERVO DISPLACEMENT TRANSDUCER APPLICATIONS

8.1 Deformable Mirrors 347
8.2 Microscope Stages 353
8.3 High Precision Linear Displacement Devices 356
8.4 Servo Systems 360
8.5 VCR Head Tracking Actuators 368
8.6 Vibration Suppression and Noise Elimination Systems 371

9 PULSE DRIVE MOTOR APPLICATIONS

9.1 Imaging System Applications 375
9.2 Inchworm Devices 379
9.3 Dot Matrix Printer Heads 384
9.4 Inkjet Printers 390
9.5 Piezoelectric Relays 396
9.6 Adaptive Suspension Systems 399

10 ULTRASONIC MOTOR APPLICATIONS

10.1 General Description and Classification of Ultrasonic Motors 403
10.2 Standing Wave Motors 410
10.3 Mixed-Mode Motors 414
10.4 Traveling Wave Motors 417
10.5 Mode Rotation Motors 430
10.6 Performance Comparison Among Various Ultrasonic Motors 433
10.7 Microscale Walking Machines 434
10.8 Calculations for the Speed and Thrust of Ultrasonic Motors 436
10.9 Elements of Designing an Ultrasonic Motor 442
10.10 Other Ultrasonic Motor Applications 449
10.11 Magnetic Motors 453

10.12 Reliability of Ultrasonic Motors 454

11 THE FUTURE OF CERAMIC ACTUATORS IN MICROMECHATRONIC SYSTEMS

11.1 Development Trends as Viewed from Patent Statistics 463
11.2 The Piezoelectric Actuator/Ultrasonic Motor Market 465
11.3 Future Trends in Actuator Design 468

INDEX *483*

PREREQUISITE KNOWLEDGE

This study of micromechatronics assumes certain preliminary knowledge. Answer the following questions before referring to the answers on the next page.

Q1 Provide definitions for the *elastic stiffness, c*, and *elastic compliance, s*, using stress (X)-strain (x) equations.

Q2 Sketch a *shear stress* (X_4) and the corresponding *shear strain* (x_4) on the square material depicted below.

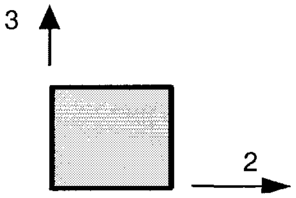

Q3 Write an equation for the *velocity of sound, v,* in a material with mass density, ρ, and elastic compliance, s^E.

Q4 Given a rod of length, l, made of a material through which sound travels with a velocity, v, write an equation for the *fundamental extensional resonance frequency,* f_o.

Q5 Provide the argument for the cosine function on the right-hand side of the following equation: $\cos(kx)\cos(\omega t) + \cos(kx-\pi/2)\cos(\omega t-\pi/2) = \cos[?]$

Q6 Calculate the capacitance, C, of a capacitor with area, A, and electrode gap, t, filled with a material of *relative permittivity, K.*

Q7 Write an equation for the *resonance frequency* of the circuit pictured below:

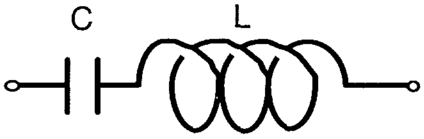

Q8 Write the *Laplace transform* for the impulse function [$\delta(t)$].

Q9 Given a power supply with an internal impedance, Z_o, what is the optimum circuit impedance, Z_l, required for maximum power transfer?

Q10 Write an equation for the polarization, P, induced in a *piezoelectric* with a piezoelectric strain coefficient, d, when it is subjected to an external stress, X.

Answers (A good score is 60% or better.)

Q1 $X = c\,x, \; x = s\,X$

Q2 $x_4 = 2 \quad x_{23} = 2\,\phi$
[Notes: Radian measure is generally preferred. This shear stress is not equivalent to the diagonal extensional stress.]

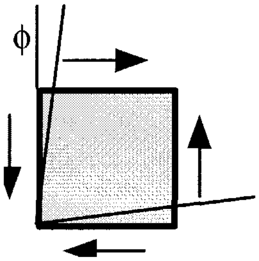

Q3 $$v = \frac{1}{\sqrt{\rho\, s^E}}$$

Q4 $f_o = v / 2l$Q5 $(kx - \omega t)$
[A traveling wave is obtained by superimposing two standing waves.]

Q6 $C = \varepsilon_o K\,(A / t)$

Q7 $$f = \frac{1}{2\pi\sqrt{LC}}$$

Q8 1
Note: The impulse function is occasionally used to obtain the transfer function of the system.

Q9 $Z_l = Z_o$
Note: The current and voltage associated with Z_l are $V/(Z_o+Z_l)$ and $[Z_l/(Z_o+Z_l)]V$, respectively, the product of which yields the power. Maximum power transfer occurs when: $Z_o / \sqrt{Z_l} = \sqrt{Z_l}$.

Q10 $P = d\,X$ (refer to $x = d\,E$)
(This is called the *direct piezoelectric effect.*)

SUGGESTED TEACHING SCHEDULE

(Thirty 75-minute sessions per semester)

0.	Course Overview and Prerequisite Knowledge Check	1 Time
1.	Current Trends for Actuators and Micromechatronics	3 Times
2.	Theoretical Description of Electric Field-Induced Strains	3 Times
3.	Actuator Materials	2 Times
4.	Actuator Structures and Fabrication Processes	2 Times
5.	Drive / Control Techniques	4 Times
6.	Loss Mechanisms and Heat Generation	1 Time
7.	Finite Element Analysis	2 Times
	Laboratory Demonstrations	1 Time
8.	Servo Displacement Transducer Applications	3 Times
9.	Pulse Drive Motor Applications	2 Times
10.	Ultrasonic Motor Applications	4 Times
11.	Future of Micromechatronics	1 Time
	Review/Q&A	1 Time

SYMBOLS

D	Electric Displacement
E	Electric Field
P	Dielectric Polarization
P_s	Spontaneous Polarization
α	Ionic Polarizability
γ	Lorentz Factor
μ	Dipole Moment
ε_o	Dielectric Permittivity of Free Space
ε	Dielectric Permittivity
K	Relative Permittivity or Dielectric Constant (assumed for ferroelectrics: $K \approx \chi = K-1$)
κ	Inverse Dielectric Constant
χ	Dielectric Susceptibility
C	Curie-Weiss Constant
T_o	Curie-Weiss Temperature
T_C	Curie Temperature (Phase Transition Temperature)
G	Gibbs Free Energy
A	Helmholtz Free Energy
F	Landau Free Energy Density
x	Strain
x_s	Spontaneous Strain
X	Stress
s	Elastic Compliance
c	Elastic Stiffness
v	Sound Velocity
d	Piezoelectric Charge Coefficient
h	Inverse Piezoelectric Charge Coefficient
g	Piezoelectric Voltage Coefficient
M,Q	Electrostrictive Coefficients
k	Electromechanical Coupling Factor
η	Energy Transmission Coefficient
Y	Young's Modulus
$\tan\delta$ ($\tan\delta'$)	Extensive (intensive) Dielectric Loss
$\tan\phi$ ($\tan\phi'$)	Extensive (intensive) Elastic Loss
$\tan\theta$ ($\tan\theta'$)	Extensive (intensive) Piezoelectric Loss

Micromechatronics

1

CURRENT TRENDS FOR ACTUATORS AND MICROMECHATRONICS

1.1 THE NEED FOR NEW ACTUATORS

An *actuator* is a transducer that transforms drive energy into a mechanical displacement or force. The demand for new actuators has increased significantly in recent years especially for *positioner*, *mechanical damper*, and *miniature motor* applications. These devices are used in a variety of fields such as optics, astronomy, fluid control, and precision machining.

Submicrometer fabrication, common in the production of electronic chip elements, is also becoming important in mechanical engineering. The trends depicted in Figure 1.1 show how machining accuracy has improved over the years.[1] One of the primary reasons for the improved accuracy is the development of more precise position sensors. Sensors utilizing lasers can easily detect nanometer scale displacements. This could be regarded as another instance of "the chicken or the egg" issue, however, as the fabrication of such precise optical instruments can only be achieved with the submicrometer machining equipment the sensors are designed to monitor.

In an actual machining apparatus comprised of translational components (the joints) and rotating components (the gears and motor) error due to backlash will occur. Machine vibration will also lead to unavoidable position fluctuations. Furthermore, the deformations due to machining stress and thermal expansion also cannot be ignored. The need for submicron displacement positioners to improve cutting accuracy is apparent. One example is a prototype for a lathe machine that uses a ceramic multilayer actuator and can achieve cutting accuracy of 0.01 μm.[2]

The concept of *"adaptive optics"* has been applied in the development of sophisticated new optical systems. Earlier systems were generally designed such that parameters like position, angle, or the focal lengths of mirror and lens components remained essentially fixed during operation. Newer systems incorporating adaptive optical elements respond to a variety of conditions to essentially adjust the system parameters to maintain optimum operation. The original "lidar" system (a radar system utilizing light waves) was designed to be used on the NASA space shuttle for monitoring the surface of the Earth.[3] A laser beam is projected towards the Earth's surface, and the reflected light is received by a reflection telescope, amplified by a photomultiplier, and the resulting signal is processed to produce an image. The vibration noise and temperature fluctuations of the shuttle make it difficult for a sharp image to be obtained, however, and the use of a responsive positioner was considered to compensate for the detrimental effects.

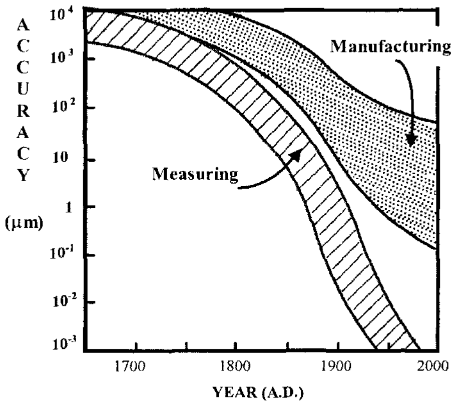

Figure 1.1 Obtainable accuracies in manufacturing and measurement over time. Note that current accuracies tend to be on the micrometer and nanometer scales, respectively.

Active and passive vibration suppression by means of piezoelectric devices is also promising technology for use in space structures and military and commercial vehicles. Mechanical vibration in a structure traveling through the vacuum of space is not readily damped and a 10 m long array of solar panels can be severely damaged simply by the repeated impact of space dust with the structure. Active dampers using shape memory alloys or piezoelectric ceramics are currently under investigation to remedy this type of problem. A variety of *smart skins* designed for military tanks or submarines are illustrated in Figure 1.2. A signal is generated in the sensitive skin with perhaps the impact of a missile on the tank or the complex forces applied to a submarine through turbulent flow, which is fed back to an actuator. The actuator responds by changing its shape to effectively minimize the impact damage on the tank (*structure protection*) or the drag force on the submarine.

The demand for other applications in the field of mechanical engineering is also increasing rapidly. One important class of devices that meets these demands is the "*solid-state motor*." Market research focused on just office equipment needs, such as printers and floppy disk drives, indicates that tiny motors smaller than 1 cm will be in increasing demand over the next ten years. Conventional electromagnetic motor designs, however, do not provide sufficient energy efficiency for these applications. Piezoelectric *ultrasonic motors*, whose efficiency is insensitive to size, are superior to the conventional devices when motors of millimeter size are required.

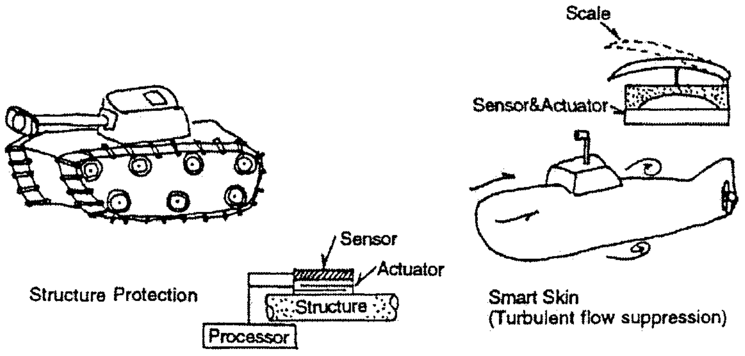

Figure 1.2 Smart skin structures for military tanks and submarines.

1.2 CONVENTIONAL METHODS FOR MICROPOSITIONING

A classification of actuators is presented in Table 1.1. This classification is based on the features of the actuator that relate to micropositioning controllability. Electrically controlled types are generally preferred for applications where miniature devices are needed. A few of the relevant specifications for the solid-state actuators included in this classification also appear in the table. Compared with conventional devices, the new principle actuators provide much quicker response, smaller size, higher resolution, and a higher power-to-weight ratio.

Conventional methods for micropositioning usually include displacement reduction mechanisms to suppress mechanical backlash, which are categorized into three general groups: (1) oil/air pressure displacement reduction, (2) the electromagnetic rotary motor with a gear, and (3) the voice coil motor.[4] A brief description of each follows.

(1) Oil Pressure Type Displacement Reduction Mechanism

Changing the diameter of an oil-filled cylinder as illustrated in Figure 1.3 effectively reduces the resulting displacement at the output. Devices utilizing this oil pressure mechanism are generally large and have slow responses. Transducers of this type are sometimes used in the reverse mode for amplifying the displacement produced by a solid-state actuator.

(2) Combination of a Motor and a Displacement Reduction Mechanism

Screw transfer mechanisms are typically used when the moving distance is long (see Figure 1.4). Using very precise ball screws, positioning accuracy of less than 5 μm can be obtained for a 100 mm motion. When higher accuracies are required, additional displacement reduction mechanisms are necessary.

Table 1.1 Displacement characteristics of various types of actuators.

Drive	Device	Displacement	Accuracy	Torque/ Generative Force	Response Time
Air pressure	Motor	Rotation	degrees	50 Nm	10 sec
	Cylinder	100 mm	100 μm	10^{-1} N/mm^2	10 sec
Oil pressure	Motor	Rotation	degrees	100 Nm	1 sec
	Cylinder	1000 mm	10 μm	100 N/mm^2	1 sec
Electricity	AC Servo Motor	Rotation	minutes	30 Nm	100 msec
	DC Servo Motor	Rotation	minutes	200 Nm	10 msec
	Stepper Motor	1000 mm	10 μm	300 N	100 msec
	Voice Coil Motor	1 mm	0.1 μm	300 N	1 msec
	New Piezoelectric	100 μm	0.01 μm	30 N/mm^2	0.1 msec
	Magnetostrictor	100 μm	0.01 μm	100 N/mm^2	0.1 msec
	Ultrasonic Motor (piezoelectric)	Rotation	minutes	1 Nm	1 msec

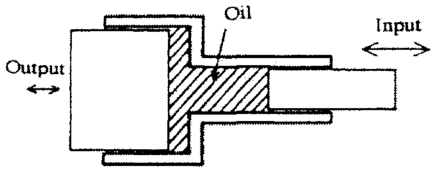

Figure 1.3 Schematic representation of an oil pressure displacement reduction mechanism.

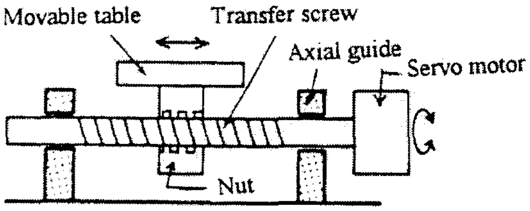

Figure 1.4 Illustration of a screw positioning mechanism.

There are several other commonly used displacement reduction mechanisms. The mechanisms highlighted in Figure 1.5 illustrate the action of a spring constant difference, a hinge lever, and a wedge. The combination of a motor with a ball screw or a displacement reduction mechanism has the advantages of quick response, a substantial generative force, and good controllability, but is generally difficult to fabricate in miniature form due to its structural complexity. In addition, the manufacturing tolerances of a typical transfer screw tend to promote backlash in positioning even when displacement reduction mechanisms are implemented.

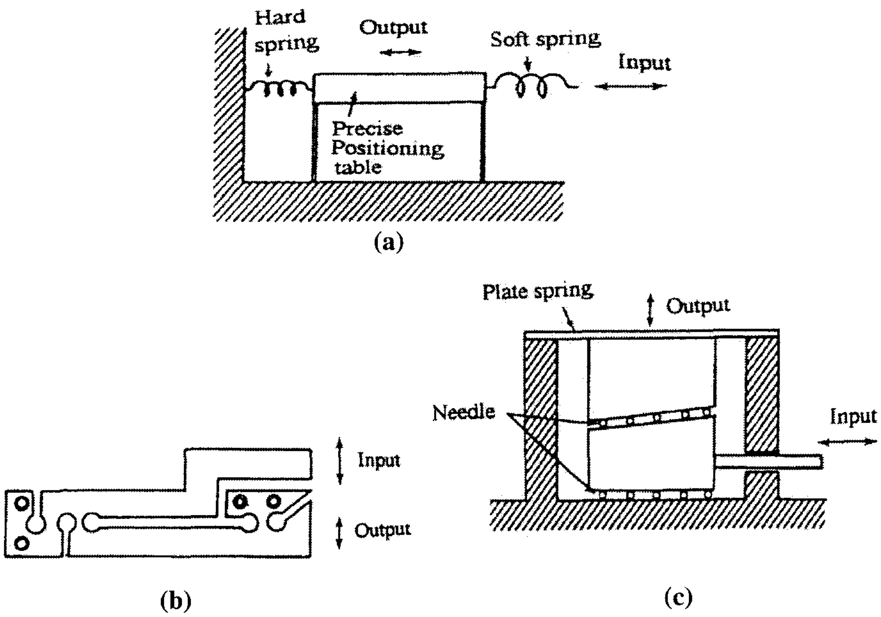

Figure 1.5 Illustrations of several displacement reduction mechanisms utilizing the action of: (a) a spring constant difference, (b) a hinge lever, and (c) a wedge.

The minimum size of an electromagnetic motor is generally limited to about 1 cm, as motors smaller than this will not provide adequate torque and efficiency. One of the smallest electromagnetic motors to be fabricated is shown in Figure 1.6.[5] A micromotor with a diameter of 1.9 mm typically generates a torque of only 7.5 μNm and rotational speeds of 100,000 rpm. An optional microgearbox with a reduction ratio of 47 can be used with this motor so that the drive can deliver an enhanced torque of up to 300 μNm. Use of this gearbox, however, reduces the efficiency of the motor significantly. Further, as the size of electromagnetic motor is reduced the winding wire thickness must also be reduced, which leads to a significant increase in the electrical resistance and Joule heating.

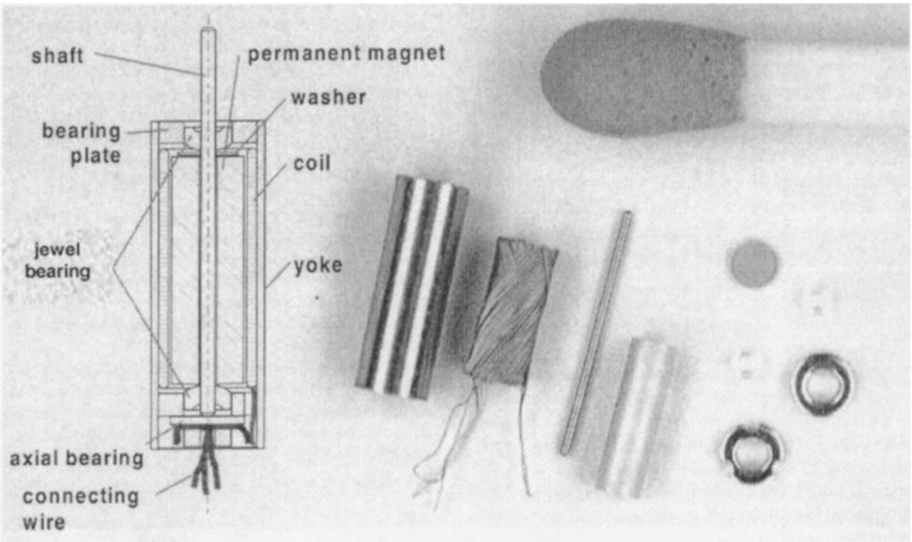
shaft
permanent magnet
washer
bearing plate
coil
jewel bearing
yoke
axial bearing
connecting wire

Figure 1.6 An electromagnetic micromotor with a diameter of 1.9 mm, developed by the Institute of Microtechnique GmbH, Mainz.[5]

(3) Voice Coil Motors

The structure of a voice coil motor is shown schematically in Figure 1.7. Among the three displacement control devices described here, this motor achieves the most precise positioning. It requires relatively large input electrical energy, however, has a slow response, and produces rather low generative forces.

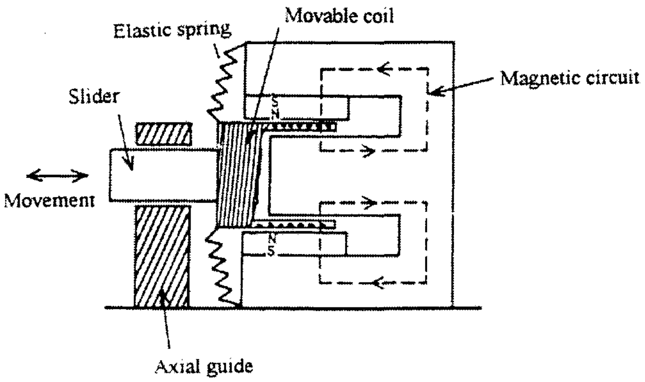
Elastic spring
Movable coil
Magnetic circuit
Slider
Movement
S
N
N
S
Axial guide

Figure 1.7 Schematic representation of a voice coil motor.

The search for new solid-state actuators that do not use springs or gear mechanisms has thus developed in recent years to more effectively and reliably provide the displacements required for micropositioning applications. A review of the current technology related to state-of-the-art solid-state actuators is presented in the next section.

1.3 AN OVERVIEW OF SOLID-STATE ACTUATORS

(1) Smart Actuators

Let us now consider the "smartness" of a material. The various properties relating the input parameters of electric field, magnetic field, stress, heat and light with the output parameters charge/current, magnetization, strain, temperature and light are listed in Table 1.2. Conducting and elastic materials, which generate current and strain outputs, respectively, with input, voltage or stress (diagonal couplings), are sometimes referred to as *"trivial" materials*. High temperature superconducting ceramics are also considered trivial materials in this sense, but the figure of merit (electrical conductivity) exhibited by some new compositions has been exceptionally high in recent years making them especially newsworthy.

On the other hand, pyroelectric and piezoelectric materials, which generate an electric field with the input of heat and stress, respectively, are called *smart materials*. These off-diagonal couplings have corresponding converse effects, the electrocaloric and converse piezoelectric effects, so that both "sensing" and "actuating" functions can be realized in the same material. One example is a tooth brace made of a shape memory (superelastic) alloy. A temperature dependent phase transition in the material responds to variations in the oral temperature, thereby generating a constant stress on the tooth.

"Intelligent" materials must possess a "drive/control" or "processing" function, which is adaptive to changes in environmental conditions in addition to their actuator and sensing functions. Photostrictive actuators belong to this category. Some ferroelectrics generate a high voltage when illuminated (the *photovoltaic effect*). Since the ferroelectric is also piezoelectric, the photovoltage produced will induce a strain in the crystal. Hence, this type of material generates a drive voltage dependent on the intensity of the incident light, which actuates a mechanical response. The self-repairing nature of partially stabilized zirconia can also be considered an intelligent response. Here, the material responds to the stress concentrations produced with the initial development of the microcrack (sensing) by undergoing a local phase transformation in order to reduce the concentrated stress (control) and stop the propagation of the crack (actuation).

If one could incorporate a somewhat more sophisticated mechanism for making complex decisions to its "intelligence," a *wise material* might be created. Such a material might be designed to determine that "this response may cause harm" or "this action will lead to environmental destruction," and respond accordingly. It would be desirable to incorporate such fail-safe mechanisms in actuator devices and systems. A system so equipped would be able to monitor for and detect the symptoms of wear or damage so as to shut itself down safely before serious damage or an accident occurred.

Table 1.2 Various basic and cross-coupled properties of materials.

OUTPUT INPUT	CHARGE/ CURRENT	MAGNETI-ZATION	STRAIN	TEMPERATURE	LIGHT
ELECTRIC FIELD	Permittivity Conductivity	Electromagnetic Effect	Converse Piezoelectric Effect	Electrocaloric Effect	Electrooptic Effect
MAGNETIC FIELD	Magnetoelectric Effect	Permeability	Magnetostriction	Magnetocaloric Effect	Magnetooptic Effect
STRESS	Piezoelectric Effect	Piezomagnetic Effect	Elastic Constants	****	Photoelastic Effect
HEAT	Pyroelectric Effect	****	Thermal Expansion	Specific Heat	****
LIGHT	Photovoltaic Effect	****	Photostriction	****	Refractive Index

Diagonal Coupling: ▨ Sensor: ▭

Off-Diagonal Coupling: Smart Material Actuator: ▭

(2) New Actuators

Actuators that operate by means of a mechanism different from those found in the conventional AC/DC electromagnetic motors and oil/air pressure actuators are generally classified as "*new actuators*." Some recently developed new actuators are classified in Table 1.3 in terms of input parameter. Note that most of the new actuators are made from some type of solid material with properties specifically tailored to optimize the desired actuating function. That is why these actuators are sometimes referred to as just *solid-state actuators*. We will examine in this section some of the most popular and useful types of materials utilized for this class of actuators and their associated properties.

The displacement of an actuator element must be controllable by changes in an external parameter such as temperature, magnetic field or electric field. Actuators activated by changes in temperature generally operate through the *thermal expansion* or dilatation associated with a phase transition, such as the ferroelectric and martensitic transformations. *Shape memory alloys*, such as Nitinol, are of this type. Magnetostrictive materials, such as Terfenol-D, respond to changes in an applied magnetic field. *Piezoelectric* and *electrostrictive* materials are typically used in electric field-controlled actuators. In addition to these, we will consider silicon-based microelectromechanical systems (MEMS), polymer artificial muscles, light activated actuators (for which the displacements occur through the photostrictive effect or a photoinduced phase transformation), and electro/magnetorheological fluids.

Table 1.3 New actuators classified in terms of input parameter.

Input Parameter	Actuator Type/Device
Electric Field	Piezoelectric/Electrostrictive Electrostatic (Silicon MEMS) Electrorheological Fluid
Magnetic Field	Magnetostrictive Magnetorheological Fluid
Stress	Rubbertuator
Heat	Shape Memory Alloy Bubble Jet
Light	Photostrictive Laser Light Manipulator
Chemical	Mechanochemical Metal-Hydrite

The desired general features for an actuator element include:

1) large displacement (sensitivity = displacement/ driving power),
2) good positioning reproducibility (low hysteresis),
3) quick response,
4) stable temperature characteristics,
5) low driving energy,
6) large generative force and failure strength,
7) small size and light weight,
8) low degradation/aging in usage,
9) minimal detrimental environmental effects (mechanical noise, electromagnetic noise, heat generation, etc.).

(3) MEMS: Microelectromechanical Systems

Silicon has become almost synonymous with integrated electronic circuitry. Due to its favorable mechanical properties, silicon can also be micromachined to create microelectromechanical systems (MEMS).[6] The techniques for micromachining silicon have developed over the past ten years in a variety of industries for a wide range of applications. Pressure and acceleration sensors are produced for application in medical instrumentation and automobiles. One important example is the acceleration sensor used to trigger an air bag in an automobile crash. The generative force/displacement levels produced by MEMS devices are, however, generally too small to be useful for many actuator applications.

In *bulk micromachining*, mechanical structures are fabricated directly on a silicon wafer by selectively removing wafer material. Etching is the primary technique for bulk micromachining, and is either isotropic, anisotropic, or a combination of the two states. The etch rate for anisotropic etching depends on the crystallographic orientation; for example, an anisotropy ratio of 100:1 is possible in the <100> directions relative to the <111> directions. Etch processes can be made selective by using dopants (heavily doped regions etch slowly), or may be halted electrochemically (etching stops in a region of different polarity in a biased p-n junction). After the etching process is complete, the silicon wafer is anodically bonded to Pyrex and finally diced into individual devices. This has been a standard technique for fabricating silicon pressure sensors and micropumps for many years.

Recently, however, *surface micromachining*, *silicon fusion bonding*, and a process called *LIGA* (Lithographie, Galvanoformung, Abformung) have also emerged as major fabrication techniques. Surface micromachining of a wafer involves selectively applying or removing thin film layers. Thin film deposition and wet and dry etching techniques are the primary tools for this. Thin films of polysilicon, silicon oxide, and silicon nitride are used to produce sensing elements, electrical interconnections, and the structural, mask, and sacrificial layers. Silicon epitaxial layers, grown and deposited silicon oxide layers and photoresist are used as sacrificial materials.

A typical surface micromachining process is depicted in Figure 1.8.[6] A sacrificial layer is applied (grown or deposited) in an appropriate pattern on the wafer and then removed from the areas where a mechanical structure will be attached to the substrate. Then, the mechanical layer is applied and patterned. Finally, the underlying sacrificial layer is etched away to release the mechanical structure. This process can produce structures on a scale of a few hundred micrometers, such as the microgripper appearing in Figure 1.9. This microgripper was fabricated by Berkeley Sensor and Actuator Center, CA, using released-polysilicon surface micromachining and is activated by electrostatic forces.[6]

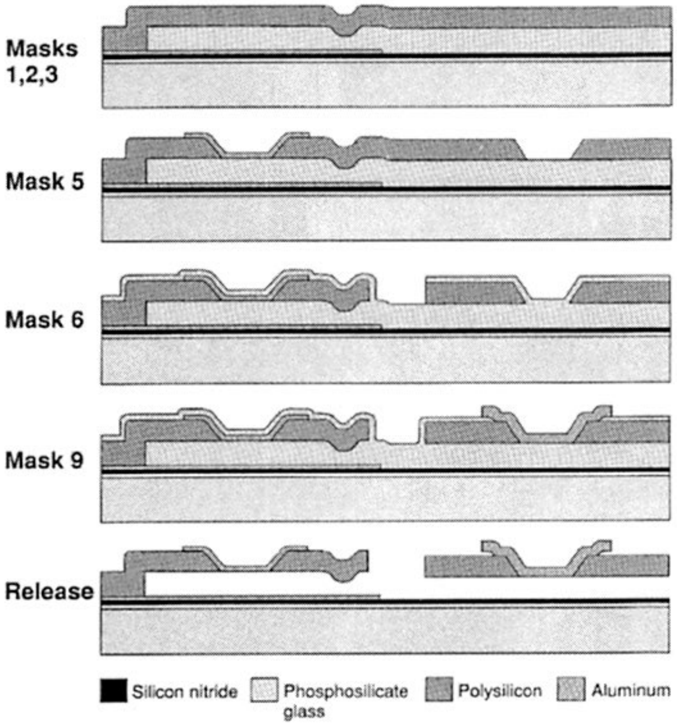

(© 1994 IEEE)

Figure 1.8 A typical surface micromachining process. The phosphosilicate glass layer is sacrificial in this process.[6]

The first step of the LIGA process involves generating a photoresist pattern on a conductive substrate using deep x-ray lithography. The gaps between the resist patterns can be fully electroplated, yielding a highly accurate negative replica of the original resist pattern. This can be used as a mold for plastic resins such as polyimide and polymethyl methacrylate or for ceramic slurries. Once the material has been cured, the mold is removed, leaving behind microreplicas of the original pattern. An epicyclic microgearbox appears in Figure 1.10 that is to be fitted onto the micromotor pictured in Figure 1.6. It contains seventeen microinjection-molded components made from the polymer POM.[5] Note that the chief disadvantage of this process is the need for a short-wavelength, highly collimated x-ray source, ideally a synchrotron. Few MEMS manufacturers can afford their own synchrotron.

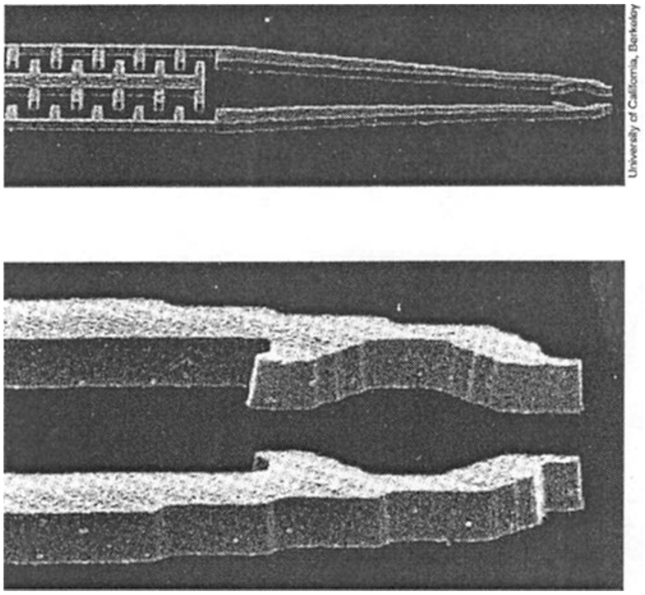
University of California, Berkeley

(© 1994 IEEE)

Figure 1.9 A microgripper fabricated by Berkeley Sensor and Actuator Center, CA using released-polysilicon suface micromachining.[6]

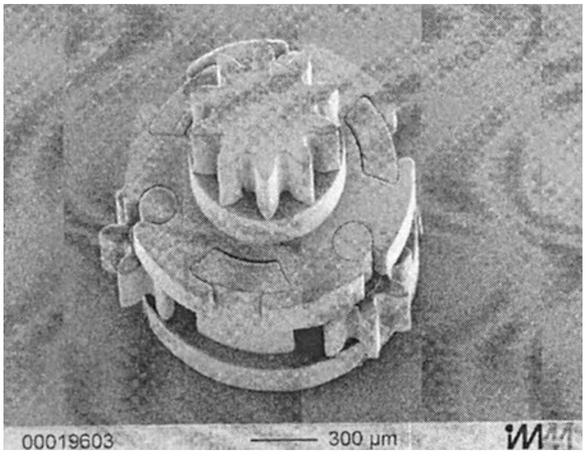
00019603
300 µm
IMM

Figure 1.10 A microgearbox made of polymer POM using a LIGA technique. It will be fitted onto the micromotor pictured in Figure 1.6.[5]

(4) Artificial Muscle

In a manner similar to the silicon MEMS devices, the operation of polymer film actuators is based on electrostatic principles. The artificial muscle described here, developed at the University of Tokyo, makes use of this type of actuator.[7]

The basic design and operation of the polymer film actuator is depicted in Figure 1.11. Two polymer films with embedded electrodes are placed adjacent to each other. When three-phase voltages (+V, –V, 0) are applied in succession to every three embedded electrodes in the stator film [Figure 1.11(a)], charges of –Q, +Q and 0 are induced on the opposing slider film [Figure 1.11(b)]. Then, when the three voltages are switched to –V, +V and –V [Figure 1.11(c)], a repulsive force is generated between the stator and slider films, and an attractive force is generated between the adjacent electrodes on the two films. This produces an electrode pitch displacement (in this case a shift of the slider to the right) [Figure 1.11(d)]. The electrostatic force generated increases significantly as the electrode gap is reduced.

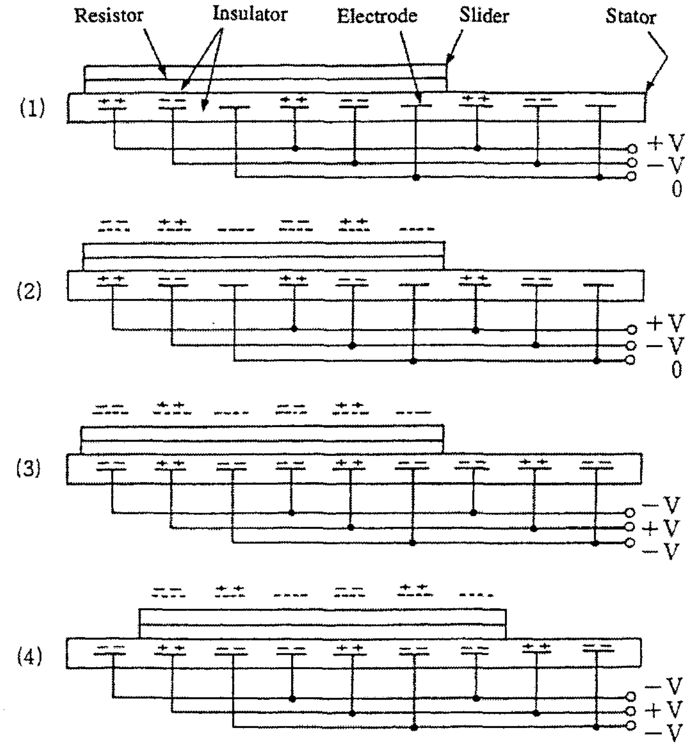

Figure 1.11 The basic design and operation of a polymer film actuator.[7]

The construction of the electrostatic polymer artificial muscle is illustrated in Figure 1.12. A thin film of PET, 12 μm in thickness, is used for the slider, to which a polyimide film with surface line electrodes is laminated which serves as the stator. Spacers are included in the structure as shown to maintain the proper separation between electroded surfaces. Five stator/slider pairs, 34 mm in width and 80 mm in length, are stacked together with a 0.35 mm gap between them. The prototype structure, which weighs 43 g is then dipped into "Fluorinat" (3M). When three-phase voltage at 10 Hz is applied with a pitch range of 0.1-1.0 mm, a speed of 1 m/sec is achieved without load. A propulsive force (thrust) of 1-3 N is possible with an applied root-mean-square voltage of 2.5 kV. The relatively high voltage required for operation is a major drawback of this artificial muscle.

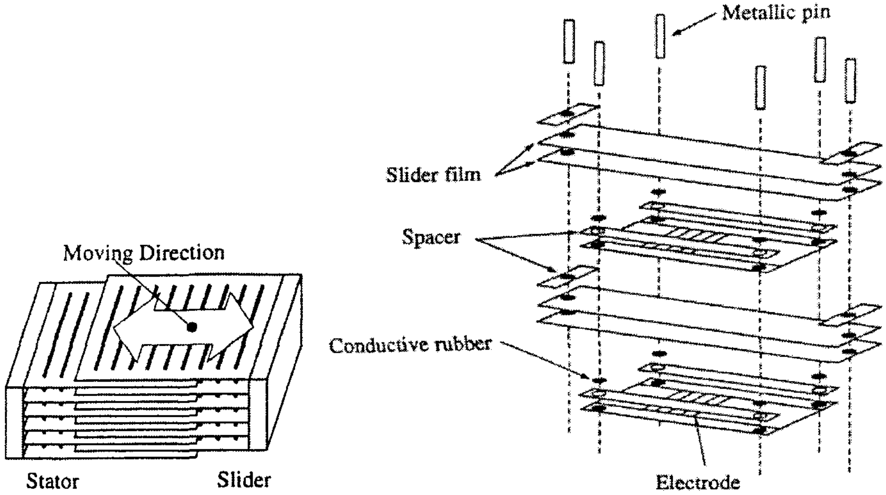

Figure 1.12 Construction of the electrostatic polymer artificial muscle.[7]

A robot arm driven by the electrostatic artificial muscles is shown in Figure 1.13. A 40-layer electrostatic actuator (generating 320 N) works in conjunction with a 20-layer actuator (generating 160 N) via a pulley mechanism.[8]

(5) Shape Memory Alloys

Many materials exhibit large mechanical deformations when undergoing a structural phase transition. This phase transition may be induced by temperature, stress, or electric field. In some materials, once the mechanical deformation is induced, some deformation may be retained with the release of the load and applied stress, but the original form may be restored with the application of heat. This type of action is called *shape memory*.

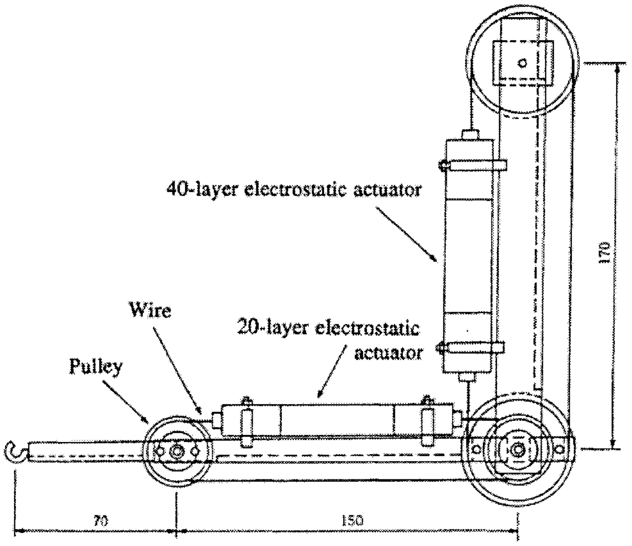
40-layer electrostatic actuator
Wire
20-layer electrostatic actuator
Pulley
170
70
150

Figure 1.13 Schematic representation of a robot arm incorporating two artificial muscles.[8]

The stress versus strain curves for typical shape memory and superelastic alloys and a normal metal are shown in Figure 1.14.[9] When the stress applied to a normal metal exceeds the elastic limit, irreversible (non-recoverable) plastic deformation results. A superelastic alloy subjected to the same level of stress, on the other hand, will become elastically soft at a level beyond the elastic deformation limit, due to a stress-induced phase transformation. The deformation that occurs in this case, however, is reversible and the original form is recovered as the load is removed and the stress is released. Finally, we see in the case of the shape memory alloy, a response quite similar to the normal metal except that for these materials the original form may be recovered after the load has been removed by heating the alloy at the appropriate temperature.

Depending on the temperature at which it is deformed, a shape memory alloy may exhibit one of two different types of mechanical behavior: *superelastic* or *pseudoplastic*. When Nitinol (a Ni-Ti alloy) is behaving as a *superelastic* material, reversible deformation of up to 10% may be obtained with a very small effective modulus, which is several orders of magnitude smaller than the modulus of the parent phase. When the material is *pseudoplastic*, the deformation occurs with some slight hardening accompanied by very large strains. The pseudoplastically deformed alloy can then be restored to its initial shape by heating. The generative force may be as high as 10^8 N/m^2 during the recovery process.

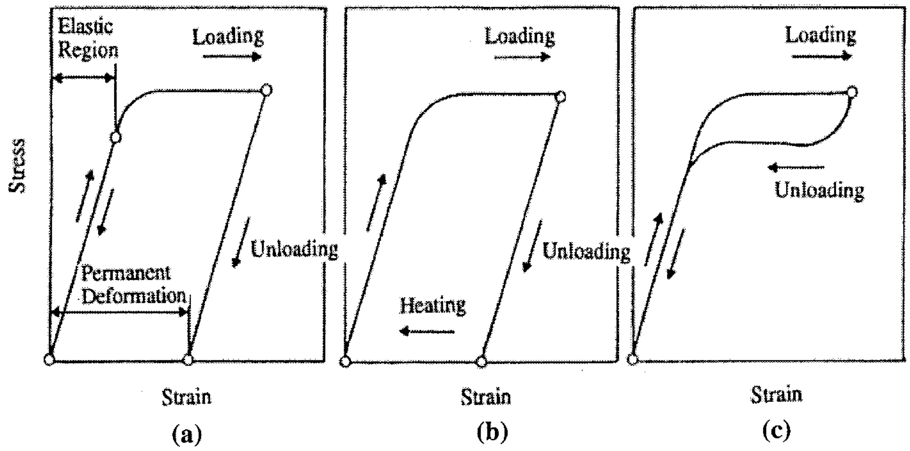

Figure 1.14 Typical stress versus strain curves for: (a) normal, (b) shape memory, and (c) superelastic materials.[9]

The *shape memory* and *superelastic* mechanisms are considered from a crystallographic viewpoint in Figure 1.15.[10] In a normal metal, atomic shifts occur above a certain critical stress, leading to a shear strain, which remains as a permanent residual strain even after the stress is removed [Figure 1.15(a)]. In a shape memory alloy, a *martensitic phase transformation* occurs under these conditions; if the parent phase (austenite) is below the transition temperature, the martensite phase will be induced. Macroscopically the material will retain the same shape, but on a microscopic level many twin structures will have been generated. Since the twin planes are easily moved, the martensite material is readily deformed by the external stress [Figure 1.15(b)]. However, when the deformed material is heated to a temperature higher than the reverse phase transition temperature, A_f, the parent phase (*austenite*) is induced and the initial shape is recovered. This is the *shape memory effect.* If stress is applied to a shape memory alloy above the transition temperature, A_f (that is, in the austenite phase), above a certain stress level the martensite phase is induced gradually, leading to a pseudoplastic response. The material is very compliant under these conditions. As the applied stress is decreased, the reverse phase transformation (martensite to austenite) occurs and the material returns to its original elastically stiff state. This elastic phenomenon, which is similar to what is observed for rubber, is called *superelasticity.*

Interestingly, one of the first commercial successes involving the shape memory alloy was in women's lingerie. One brassiere design incorporating the alloy exploited the material's superelastic properties to help maintain a comfortable fit while providing adequate support. Another big market has been for pipe couplers and electrical connectors.[11] The couplings are made by machining a cylinder of the alloy while it is in the austenite phase, usually with circumferential sealing bands on the inner diameter. A second, slightly wider cylinder is then inserted into the shape memory cylinder as it cools in order to force it to expand as the material transforms to the martensite phase. When the coupling is brought back to room temperature, the outer cylinder contracts as it reverts to the austenite phase, tightly clamping the inner cylinder.

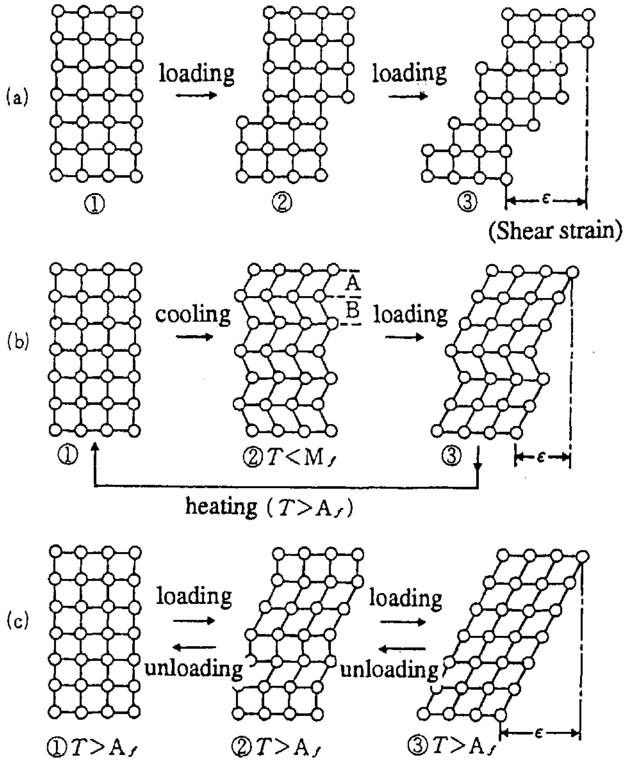
(a)
loading
loading
①
②
③
ε
(Shear strain)
(b)
cooling
A
B
loading
①
②T<M_f
③
ε
heating (T>A_f)
(c)
loading
unloading
loading
unloading
①T>A_f
②T>A_f
③T>A_f
ε

Figure 1.15 Microscopic lattice distortions for: (a) normal, (b) shape memory, and (c) superelastic metals.[10]

An actuator incorporating a shape memory spring is shown in Figure 1.16. A normal steel spring and a shape memory alloy (Ni-Ti, or Nitinol) spring, which will "remember" its fully extended form, are included in the design. At low operating temperatures, the shaft will be pushed to the right as the shape memory spring becomes soft. When the temperature is raised (for example, by means of an electric current), the spring constant of the shape memory actuator will increase significantly, causing the shaft to be pushed to the left.

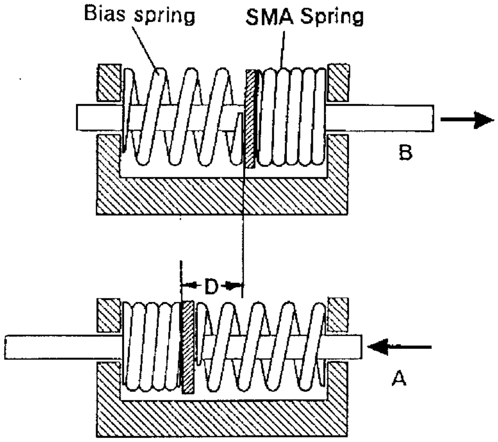

Figure 1.16 A two-way actuator incorporating shape memory alloy (SMA) and normal metal (bias) springs.

A similar mechanism is utilized in the flapper control unit for an air conditioning system. The temperature of the air passing from the air conditioner is constantly changing and can sometimes become uncomfortably cold. One solution to this problem is to adjust the air flow direction using a flap mounted on the front of the air conditioner that is actuated by a shape memory alloy as shown in Figure 1.17.[12] When the flowing air is cold, the flap will move so as to direct the air upward, and when the air temperature exceeds body temperature, it will move so as to direct the air downward. The link mechanism and the rocking motion of the flap are illustrated in Figure 1.17(a). The shape memory spring and bias spring act on the ends of the flapper to swing it like a seesaw about the pivot, thus redirecting the air flow as the temperature changes.

(6) Magnetostrictive Actuators

Magnetostrictive materials convert magnetic energy into mechanical energy and vice versa. A magnetostrictive material becomes strained when it is magnetized. Conversely, when either an applied force or torque produces a strain in a magnetostrictive material, the material's magnetic state (magnetization and permeability) will change.

Magnetostriction is an inherent material property that depends on electron spin, the orientation and interaction of spin orbitals, and the molecular lattice configuration. It is also affected by domain wall motion and rotation of the magnetization under the influence of an applied magnetic field or stress.[13]

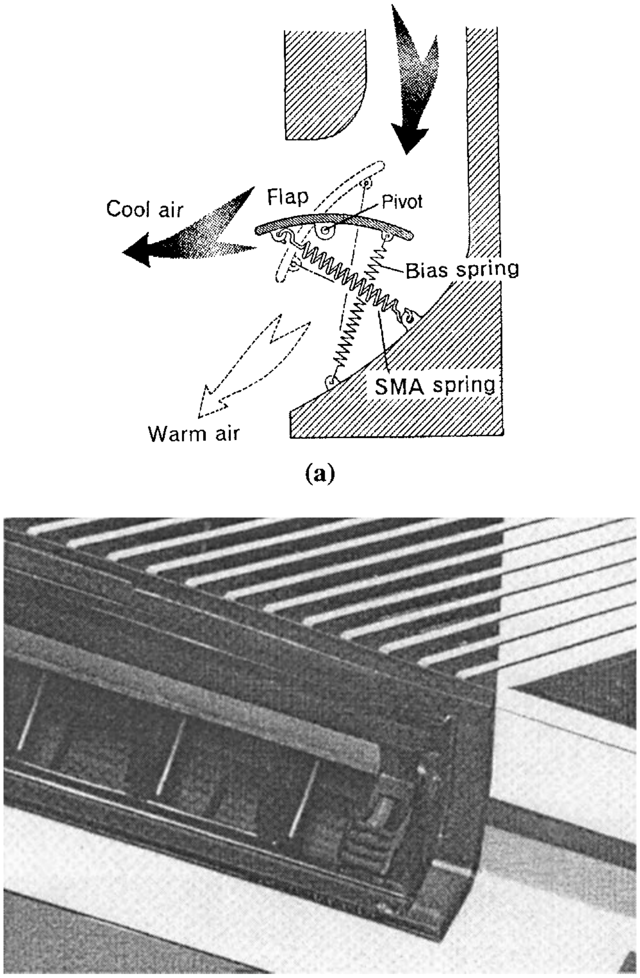

(a)

(b)

Figure 1.17 An air conditioning system with a shape memory flapper control mechanism: (a) schematic representation of the flapper control mechanism and (b) the flapper control unit as it appears in an actual air conditioner.[12]

Research on giant magnetostriction began with studies on Terfenol-D (a Tb-Dy-Fe alloy) conducted by Clark et al.[14] Longitudinally and transversely induced strain curves at various temperatures for Terfenol-D appear in Figure 1.18. The domain wall motion induced with the application of a small magnetic field occurs due to the growth of domains having magnetization aligned with the applied field, at the expense of domains with magnetization opposing the field. At moderate field strengths, the magnetic moments within unfavorably oriented domains overcome the anisotropy energy and suddenly rotate such that one of their crystallographic easy axes is more closely aligned with the external field direction. This sudden rotation is generally accompanied by a large change in strain. As the field is increased further, the magnetic moments undergo coherent rotation until they are completely aligned with the applied field. At this point the material is single-domain and the strain curve becomes saturated.

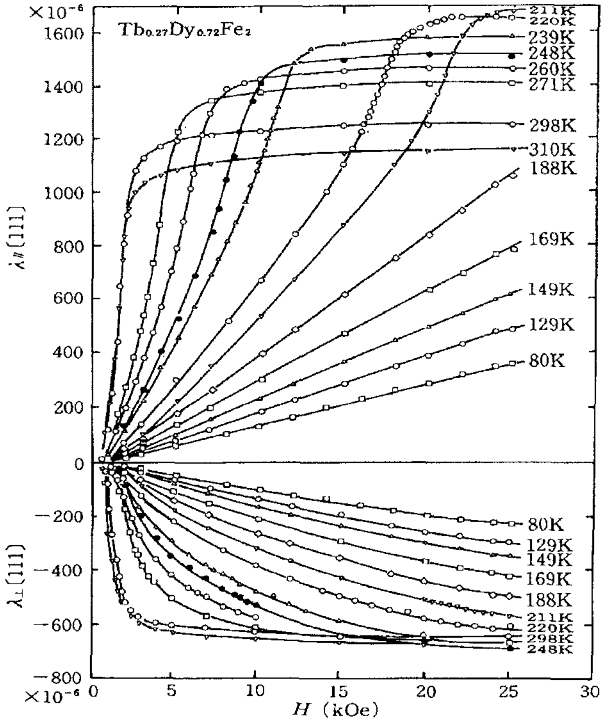

Figure 1.18 Longitudinally and transversely induced strains in Terfenol-D at various temperatures.[14]

Although one can attain strains exceeding 0.17% and sufficiently large generative stresses with magnetostrictive materials of this type, problems similar to those encountered with electromagnetic motors arise. These are related to the need for a magnetic coil and high field strengths to drive the devices. A typical design for a giant magnetostrictive actuator is depicted in Figure 1.19.[15] Two noteworthy features of this actuator are the pre-stressing mechanism and the magnetic coil and shield, which significantly increase the overall volume and weight of the system. The extensional pre-stress is important for optimum performance of the magnetostrictive alloy, and in some cases, a bias magnetic field must be maintained because the induced strain tends to be rather insensitive to the external field at low field strengths.

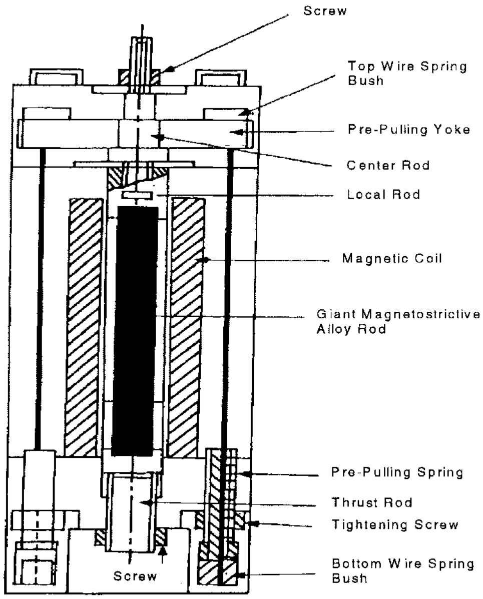
Screw
Top Wire Spring Bush
Pre-Pulling Yoke
Center Rod
Local Rod
Magnetic Coil
Giant Magnetostrictive Alloy Rod
Pre-Pulling Spring
Thrust Rod
Tightening Screw
Bottom Wire Spring Bush
Screw

Figure 1.19 A typical design for a giant magnetostrictive actuator.[15]

The sonar device depicted in Figure 1.20 includes a square array of four magnetostrictive (Terfenol-D) rods mounted in a metal ring.[16] The magnetostrictive rods are 6 mm in diameter and 50 mm in length, and have a free resonance frequency of 7.4 kHz. The resonance frequency of the entire ring device is 2.0 kHz.

In general, magnetostrictive actuators such as these are bulky due to the magnetic coil and shield required for their operation, and, hence, are difficult to miniaturize. On the other hand, since they can generate relatively large forces and their efficiency increases with increasing size, they tend to be especially suitable for applications often reserved for electromagnetic motors, such as in construction/demolition machines and for vibration control in large structures. Another intriguing application can be found in surgery, where miniature magnetostrictive actuators, controlled with external magnetic fields provided by means of technology similar to what is currently used in MRI machines, can be used for specialized procedures.

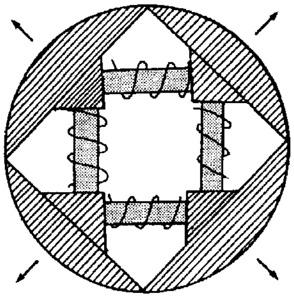

Figure 1.20 A high power acoustic transducer incorporating four magnetostrictive actuators.[16]

(7) Piezoelectric/Electrostrictive Actuators

When an electric field is applied to an insulating material, strain will be induced in the material either through the piezoelectric effect, electrostriction, or a combination of the two effects. The *converse piezoelectric effect* is a primary electromechanical effect, where the induced strain is proportional to the applied electric field, while the electrostrictive effect is a secondary phenomenon, whereby the induced strain is proportional to the square of the applied field. A brief introduction to this class of devices is given here. A more thorough description of the piezoelectric effect and electrostriction will be presented in the next chapter.

Electric field-induced strain curves are shown for piezoelectric lanthanum-doped lead zirconate titanate (PLZT) and electrostrictive lead magnesium niobate (PMN)-based ceramics in Figure 1.21.[17] The piezoelectric response shows the characteristic linear strain versus field relation with a noticeable hysteresis, while the electrostrictive response exhibits no hysteresis and a non-linear relation between the induced strain and the applied electric field is apparent. Due to this non-linear behavior, a sophisticated drive circuit is generally needed for electrostrictive actuators. Note that the maximum strain and stress levels for the piezoelectric ceramics are around 0.1% and 4×10^7 N/m^2, respectively.

Among all the solid-state varieties, piezoelectric actuators have undergone the most advanced development and remain the most commonly employed type for many applications at this time. The dot matrix printer head pictured in Figure 1.22, which operates by means of a multilayer piezoelectric actuator with sophisticated displacement amplification mechanisms, is one earlier application that was commercialized by NEC of Japan in 1987.[18]

Piezoelectric ultrasonic motors have also been developed intensively. Electronic component industries have currently focused their attention on the development of these devices, mainly because the piezoelectric motors offer distinct advantages of superior efficiency, miniature size (5-8 mm), and ease of manufacturing over conventional electromagnetic motors. Microultrasonic motors, developed and commercialized by Seiko Instruments, Japan, for wristwatch applications appear in Figure 1.23.[19] The 8 mm diameter motor is used as a silent alarm, and the 4 mm diameter motor is part of a date change mechanism.

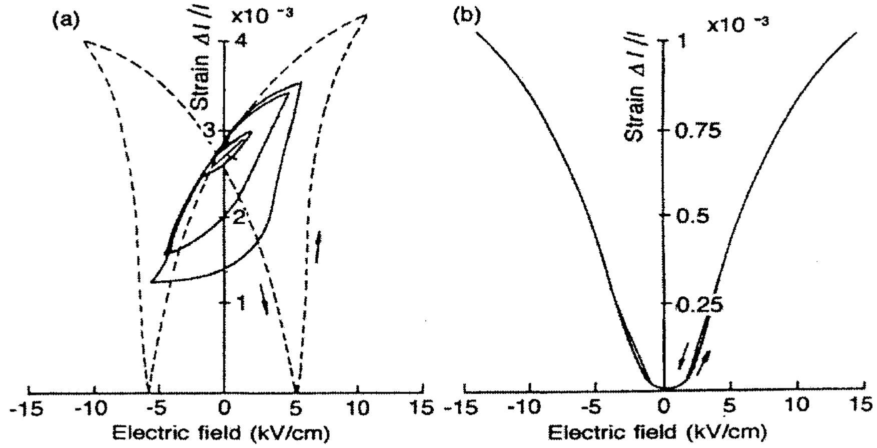

Figure 1.21 Electric field-induced strains in (a) piezoelectric lanthanum-doped lead zirconate titanate, and (b) electrostrictive lead magnesium niobate-based ceramics.[17]

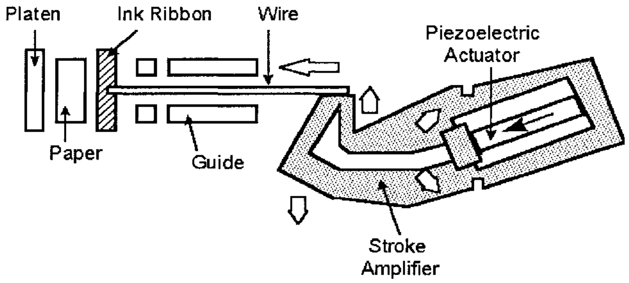

Figure 1.22 A dot matrix printer head incorporating a multilayer piezoelectric actuator and a hinge-lever type displacement amplification mechanism (NEC, Japan).[18]

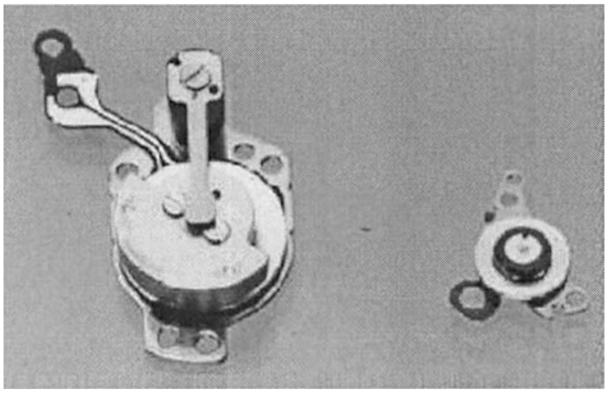

Figure 1.23 Microultrasonic motors utilized for silent alarm (8 mm diameter, left side) and date change (4 mm diameter, right side) mechanisms in a wristwatch (Seiko, Japan).[19]

(8) Polymer/Elastomer Actuators

Large strains can be generated in polymer materials without causing mechanical damage because of their high elastic compliance. Polymer actuator materials can be classified according to two general types: *polyvinylidene difluoride (PVDF)-based piezoelectric polymers* and *electret/elastomer* types.

Copolymers from the system polyvinylidene difluoride trifluoroethylene [P(VDF-TrFE)] are well known as piezoelectric materials. The strain induced in these materials is not very large, however, due to the very high coercive field. An electron irradiation treatment has been applied to materials from this system by Zhang et al. which significantly enhances the magnitude of the induced strain.[20] A 68/32 mole percent P(VDF-TrFE) copolymer film is irradiated by a 1.0 MeV electron beam at 105°C. The 70 Mrad exposure results in a diffuse phase transition and a decrease in the transition temperature as compared with the non-irradiated material. It is believed that the observed changes in the phase transition are due to the development of a microdomain state, similar to that associated with relaxor ferroelectrics, which effectively interrupts the long-range coupling of ferroelectric domains. The strain curve pictured in Figure 1.24 for an irradiated P(VDF-TrFE) specimen demonstrates that induced strains as high as 5% are possible with an applied field strength of 150 MV/m.

Elastomer actuators operate through the *Maxwell force* that occurs in an electrostatic capacitor. Considering a capacitor with an area, A, and electrode gap, t, filled with a dielectric material with a dielectric constant, K, the capacitance, C, and the stored energy, U, will be given by:

$$C = \varepsilon_0 K (A/t) \qquad (1.1)$$

$$U = (1/2)CV^2 \tag{1.2}$$

Note that an attractive force described by

$$F = (\partial U/\partial t) = -(1/2)\,\varepsilon_o K\, A(V/t)^2 \tag{1.3}$$

will be induced between the electrodes, which will lead to a decrease in the inter-electrode distance. Hence, we see that a larger displacement can be obtained by increasing the elastic compliance and the effective permittivity (and, therefore, the stored electric charge) of the material. A hybrid elastomer structure has been developed whereby a porous PTFE and a stiff PFCB phase are incorporated in the configuration depicted in Figure 1.25.[21] The stiffer PFCB phase serves to store the charge while the porous PTFE phase effectively increases the overall compliance of the structure. An effective piezoelectric d_{33} strain coefficient of around 600 pC/N, has been obtained for this composite structure, which is 20 times larger than that obtained for pure PVDF. In theory, one can reasonably predict a strain level as high as 100% (a twofold enhancement) for this material when a sufficiently soft polymer is used as the porous phase. It is important to note that even though one might feasibly anticipate large displacements for a polymer, they will be realized only at the expense of the generative force and responsivity of the device.

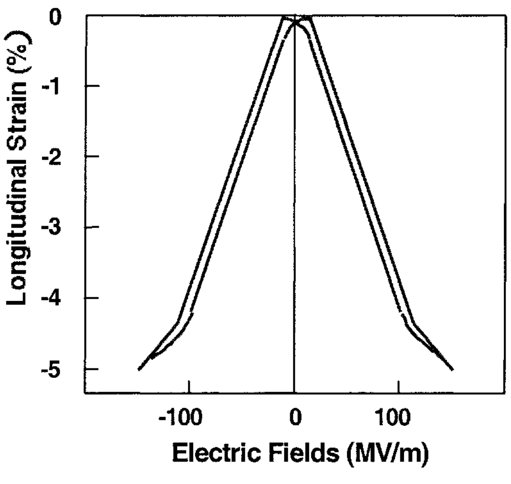

Figure 1.24 The electric field-induced strain curve for an irradiated polyvinylidene difluoride-based copolymer.[21]

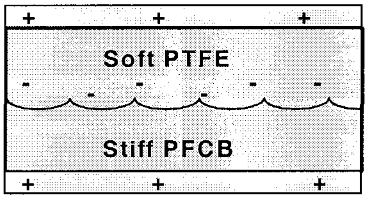

Figure 1.25 Schematic representation of a hybrid elastomer structure incorporating a porous PTFE and a stiff PFCB phase.[21]

(9) Photostriction

The ongoing emphasis on miniaturization and the integration of microrobotics and microelectronics has resulted in significant development of new ceramic actuators. Those utilizing wavelength-dependent optical actuation mechanisms are especially attractive at this time. *Photostrictive actuators*, which convert the photonic energy into mechanical motion, are of interest for their potential use in microactuation and microsensing applications. Optical actuators are also attractive for use as the driving component in optically controlled electromagnetic noise-free systems. The photostrictive effect has also been used recently for a photophonic device, in which light is transformed into sound through the mechanical vibration induced by intermittent illumination.

In principle, the *photostrictive effect* arises from a superposition of the photovoltaic effect (the generation of a potential difference in response to illumination), and the converse piezoelectric effect (strain induced by an applied electric field).[22] The photostrictive effect has been studied mainly in ferroelectric polycrystalline materials. Lanthanum-modified lead zirconate titanate (PLZT) ceramic is one of the most promising photostrictive materials due to its relatively high piezoelectric coefficient and ease of fabrication. The origin of the photovoltaic effect in PLZT is not yet clear, although several models for possible mechanisms have been proposed. Key issues in understanding the mechanisms behind the effect are both impurity doping and crystal asymmetry. One model has been proposed that describes the effect in terms of the electron energy band structure for PLZT ceramics.[23] According to this model, the donor impurity level associated with the lanthanum doping will occur slightly above the valence band as depicted in Figure 1.26. The asymmetric potential due to crystallographic anisotropy is expected to facilitate the transition of the electron between these levels by providing it with *preferred momentum*. An asymmetric crystal exhibiting a photovoltaic response should also be piezoelectric and, therefore, a photostrictive response is also expected through the coupling of the two effects.

Application of the photostriction effect has been demonstrated with the PLZT ceramic photo-driven relay and microwalking devices developed by Uchino et al.[24] These devices are activated entirely by the incident light and require no drive circuitry.

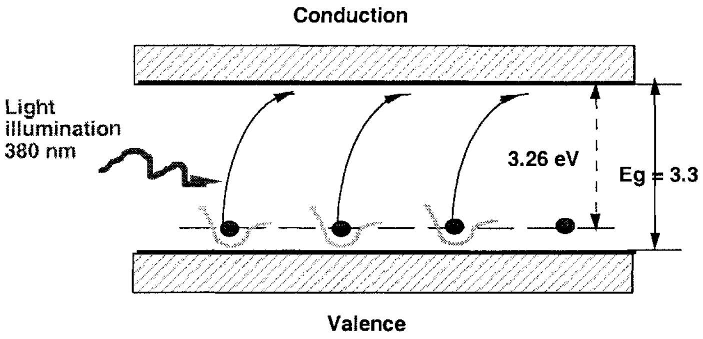

Figure 1.26 A current source model for the photovoltatic effect in PLZT.[23]

Recently, a new application for highly efficient photostrictive PLZT films on flexible substrates has been proposed for use in a new class of small exploratory land vehicles for future space missions.[25] The original π-shaped design of the micro-walking device can be modified to assume the arch shape pictured in Figure 1.27. It is comprised of a photoactuating composite film, similar to that conventionally used for unimorphs, fabricated in the form of an arch on which the triangular top piece is attached. The device executes the motion depicted in the figure when illuminated. Optimum photostrictive response has been observed for devices incorporating PLZT films approximately 30 μm in thickness. The device is driven at resonance with chopped illumination. Photomechanical resonance has been demonstrated in a PLZT bimorph.[26] Photoactuating films have been produced from PLZT solutions and applied to one side of a suitable flexible substrate designed to assume a curvature of 1 cm^{-1}. The walking device is designed to have a small difference in length between the right and left legs in order to establish a slight difference between their resonance frequencies. A chopped light source operating near these resonance frequencies is used to illuminate the device in order to induce the optimum vibration of the bimorph. Rotation of the walker in either the clockwise or counterclockwise directions is achieved by tuning the source to match the resonance frequency of one or the other leg.

(10) Electro/Magnetorheological Fluids

Composite materials whose rheological properties can be changed with the application of an electric or a magnetic field are referred to as *electrorheological* (ER) or *magnetorheological* (MR) materials, respectively. The ER and MR materials are generally in the liquid state. The rheological state of such fluids is affected when dipoles are induced in the suspension by the applied field. The dipoles interact to form columnar structures parallel to the applied field as depicted in Figure 1.28. These chain-like structures restrict the flow of the fluid, thereby increasing the viscosity of the suspension.

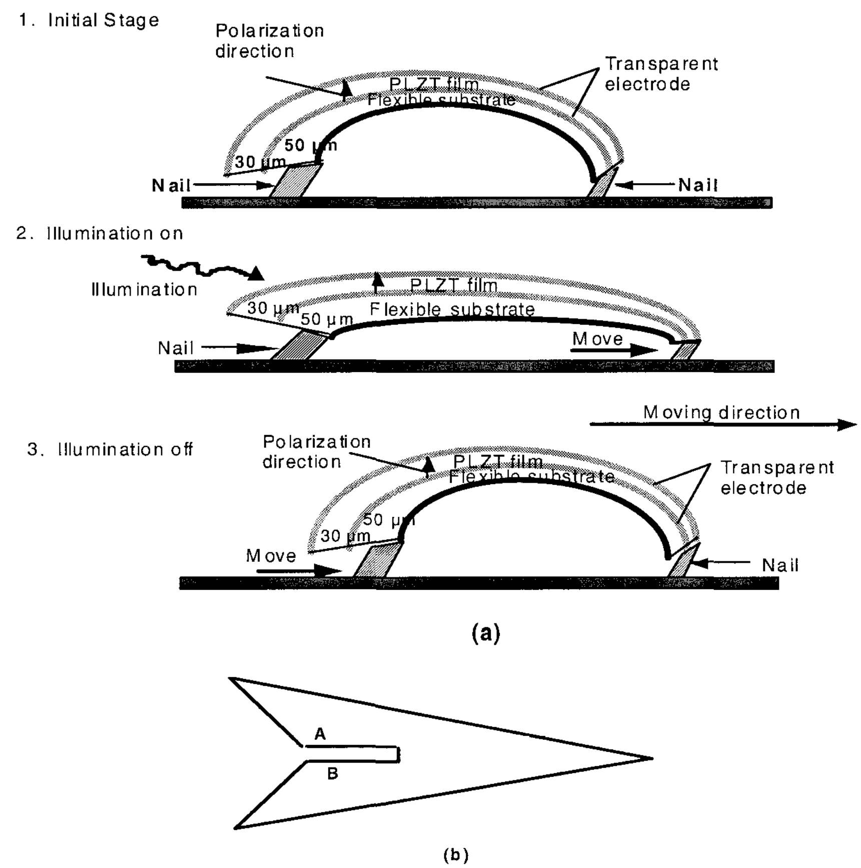
1. Initial Stage
Polarization direction
PLZT film
Flexible substrate
Transparent electrode
50 μm
30 μm
Nail
Nail
2. Illumination on
Illumination
PLZT film
30 μm
50 μm
Flexible substrate
Nail
Move
Moving direction
3. Illumination off
Polarization direction
PLZT film
Flexible substrate
Transparent electrode
50 μm
30 μm
Move
Nail
(a)
A
B
(b)

Figure 1.27 Schematic representation of an arch-shaped photoactuating film device: (a) action sequence and (b) the triangular top piece.[25]

Electrorheological (ER) fluids are composed of electrically polarizable particles suspended in an insulating medium. Ferroelectric particles, such as barium titanate and strontium titanate, are typically used in ER fluids because they have relatively high dielectric constants. On the other hand, magnetorheological (MR) fluids have a high concentration of magnetizable particles in a nonmagnetic medium. Spherical iron particles obtained from the thermal decomposition of iron pentacarbonyl are commonly used.[27]

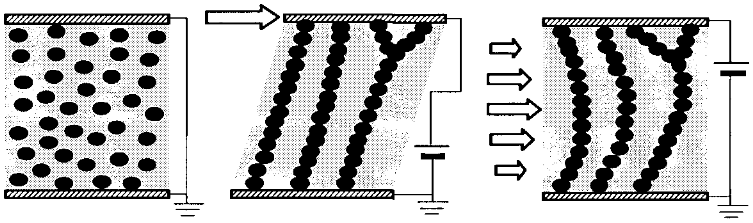

Figure 1.28 Schematic representation of the response of an electrorheological fluid to applied electric field and stress.

The properties of typical ER and MR fluids are summarized in Table 1.4. In general, ER and MR fluids are almost identical in terms of their rheological characteristics. However, from a production point of view, the MR fluid is preferred over the ER variety, because its properties are less affected by impurities.

Table 1.4 Properties of typical ER and MR fluids.

Property	ER Fluid	MR Fluid
Maximum Yield Strength	2-5 (kPa)	50-100 (kPa)
Maximum Field	4 (kV/mm)	250 (kN/Am)
Plastic Viscosity	0.1-1.0 (Pa-s)	0.1-1.0 (Pa-s)
Temperature Range	+10-90 (^{o}C) [DC] -10-125 (^{o}C) [AC]	-40-150 (^{o}C)
Response Time	ms	ms
Density	1-2 (g/cm^3)	3-4 (g/cm^3)
Maximum Energy Density	0.001 (J/cm^3)	0. 1 (J/cm^3)
Typical Power Supply	2-5 (kV)/1-10 (mA)	2-25 (kV)/1-2 (mA)
Impurity Sensitivity	intolerant	unaffected

The yield stress and apparent viscosity of the fluids increase with the applied field because the mechanical energy required to induce and to maintain these chain-like structures increases with increasing field strength. The storage modulus is plotted as a function of applied electric field for silicone elastomers containing 20-30% iron in Figure 1.29.[28] These elastomers exhibit significant variations in modulus with increasing electric field. The shear storage modulus was also found to be dependent on the alignment of the particles in the elastomer.

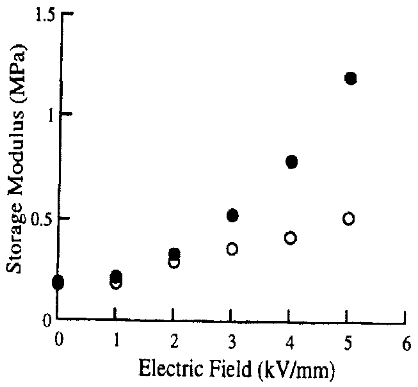

Figure 1.29 The storage modulus plotted as a function of applied electric field for silicone elastomers containing 20-30% iron.[28] [Random (o) and Aligned (●) particle orientation states]

The basic modes of operation for ER and MR fluids are illustrated in Figure 1.30. Magnetorheological fluid foam dampers are effective and exhibit long life. Little wear of the foam matrix occurs as the stresses are carried by the field-induced chain structure of iron particles in the MR fluid. A caliper type MR fluid brake design is depicted in Figure 1.31. Rather than a fully enclosed housing, the absorbent foam filled with MR fluid is attached to the pole faces of the steel yoke. These magnetorheological fluid-based devices have been successfully commercialized for use in exercise equipment[29] and in vehicle seat vibration control.[30]

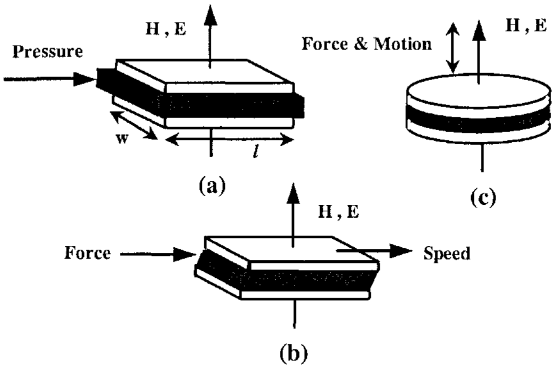

Figure 1.30 Basic modes of operation for ER and MR fluids: (a) valve mode, (b) direct shear mode, and (c) squeeze mode.

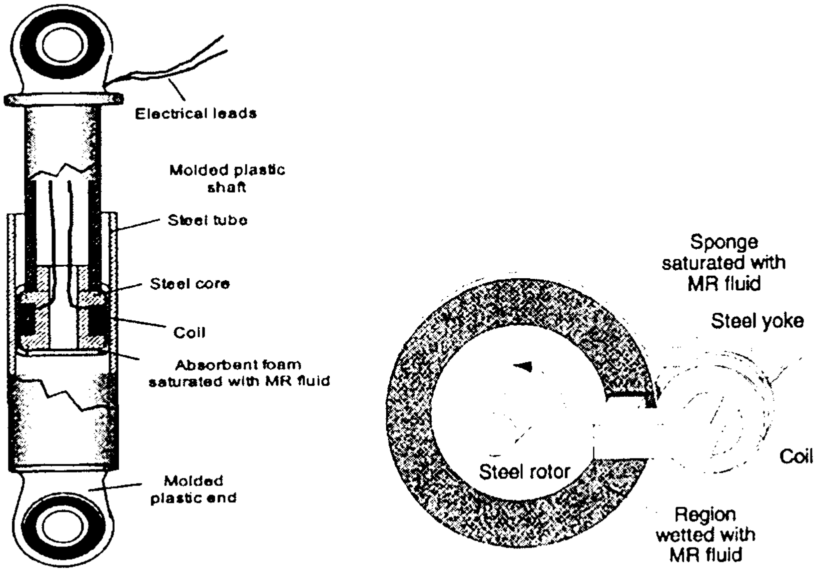
Electrical leads
Molded plastic shaft
Steel tube
Steel core
Coil
Absorbent foam saturated with MR fluid
Molded plastic end
Sponge saturated with MR fluid
Steel yoke
Coil
Steel rotor
Region wetted with MR fluid

Figure 1.31 Construction of two simple, low cost magnetorheological (MR) foam devices: (a) a vibration damper[30] and (b) a rotary caliper brake[29]. (Lord Corp.)

(11) Comparison among the Solid-State Actuators

The specifications for shape memory, magnetostrictive, piezoelectric and electrostrictive actuators are listed in Table 1.5. Certain characteristic features of each type become evident upon examining these data. The *shape memory actuators*, which operate in response to a temperature change, require a relatively large amount of input energy and typically have rather slow response speeds. A flat strip of Ni-Ti alloy, which alternates in form between an arc shape and an unbent strip to transfer energy to a spring, however, can be deformed repeatedly by heating and cooling via an electric current.

The magnetostrictive actuator likewise demonstrates some advantages and disadvantages. Although some magnetic alloys (such as Terfenol-D) may exhibit relatively large induced strains, more commonly the strain induced in this class of actuator is small. An additional drawback to this variety is the need for a driving coil, which in many applications can be troublesome; Joule heating is inevitable, and magnetic field leakage prevents it from being used adjacent to an operational amplifier or some other type of integrated circuit.

On the other hand, piezoelectric strain and electrostriction are induced by an electric field, and relatively large strains can be obtained in a variety of materials. Hence, the *piezoelectric* and *electrostrictive actuators* are considered the most promising. Lead zirconate titanate (PZT)-based piezoelectric ceramics are most commonly used due to their availability, linear characteristics, low driving energy (low permittivity), and temperature stability at room temperature, as compared to the electrostrictive devices. Electrostrictive actuators are preferred for applications where there may be significant temperature variations (such as experienced by components used on the space shuttle) or high stress conditions (as occur for cutting machine devices). In terms of their reliability, electrostrictive materials are considered better than piezoelectrics in these cases, because they exhibit significantly less degradation and aging under severe conditions.

Table 1.5 Specifications for shape memory, magnetostrictive, piezoelectric and electrostrictive actuators.

	Shape Memory	Magnetostrictive	Piezoelectric	Electrostrictive
Strain ($\Delta l/l$)	10^{-3}-10^{-2}	10^{-4}-10^{-3}	10^{-3}-10^{-2}	10^{-4}-10^{-3}
Hysteresis	Large	Large	Large	Small
Aging	Large	Small	Large	Small
Response	s	μs	ms	μs
Drive Source	Heat	Magnetic Coil	Electric Field	Electric Field

1.4 CRITICAL DESIGN CONCEPTS AND THE STRUCTURE OF THE TEXT

The framework for the themes presented in this text is based on certain design concepts and trends that are important in the development of new actuators and modern micromechatronic systems. Let's briefly consider these concepts and trends and some relevant examples in a general way before moving into the more detailed descriptions presented in the following chapters.

(1) Design Concepts Involving Smart Actuators

The performance of smart actuators is dependent on complex factors, which can be divided into three major categories: (1) the material properties, (2) the device design, and (3) the drive technique. The devices and systems to be presented in the following chapters will be described and characterized in terms of these primary factors.

In order to illustrate the significance of these factors with regard to the design of a device or system, let us focus for the moment just on piezoelectric devices. One material-related concern of primary importance will be the optimization of the piezoceramic or single crystal composition, which may involve the incorporation of dopants. The orientation of a single crystal material is also of importance. Control of material parameters such as these are necessary in order to optimize the strains induced under high stroke level drive and to stabilize temperature and external stress dependences. The design determines to a large extent the performance, durability, and lifetime of the device. The inclusion of some failure detection or "health" monitoring mechanism in the actuator is expected to increase its reliability significantly. When considering drive techniques, the pulse drive and AC drive modes require special attention. The vibration overshoot that occurs after applying an abrupt leading edge step/pulse voltage to the actuator will cause a large tensile force and a sustained applied AC voltage will generate considerable heat within the device. The product of such a design will be one for which all of these parameters have been optimized.

(2) Future Trends of Smart Actuators

Much of the current interest in ceramic actuators stems from the development of smart materials and structures. The evolution of this family of materials is gradually progressing through stages ranging from trivial functionality to *smart* to *intelligent* and finally to a more "*wise*" mode of operation. As already discussed, the off-diagonal couplings listed in Table 1.2 all have corresponding converse effects (such as the piezoelectric and converse-piezoelectric effects) so that both "sensing" and "actuating" functions can be realized in the same materials. One example of such a material is that employed in the electronic modulated automobile shock absorber developed by Toyota Motors, which is pictured in Figure 1.32.[31] The sensor used to detect the road roughness and the actuator used to modify the valve position to change the shock absorbing rate are both multilayer piezoelectric devices. The soft absorbing mode of operation provides the comfortable ride one expects in a vehicle such as a luxury limousine, while the hard absorbing mode provides the good steering control one might desire in a truck or sport utility vehicle. This smart suspension system can also provide both controllability and comfort simultaneously, depending on road conditions. We will consider the design and operation of this system in more detail in Chapter 9.

Mohandas Gandhi, a famous Indian leader, compiled the "The Seven Blunders of the World," in which we find very important principles that also apply in developing new devices. "Science without Humanity" is one of them. We have referred to the fact that in the future we may need to incorporate fail-safe mechanisms or some other "wise" function in our devices or systems to determine whether "this response may cause harm to humans" or "this action will lead to environmental destruction," and to respond accordingly.

In addition to the fail-safe mechanisms referred to earlier in this chapter, we can consider this idea of a "wise" system in a somewhat broader sense. Not long ago, one of the authors (K.U.) met an enthusiastic, middle-aged researcher in Tokyo. He was working on a piezoelectric actuator system for artificial insemination and proudly declared that their system could impregnate cows precisely and quickly, at the rate of some two hundred per hour. One question that might come to mind in considering such a system is: What are the moral/ethical implications of this sort of mass production of cows? While some may recognize that this system for artificial insemination has some utility in agriculture and might even potentially be of vital importance to humans who can conceive by no other means, others may regard it as morally or ethically unacceptable. Thus, in addition to the good, practical considerations that arise in designing and implementing a new system, moral and ethical concerns may also need to be considered for certain applications. Even if the appropriate "wise" function is not actually incorporated in a given device or system, one would hope that the wisdom of the designer(s) would ultimately prevail in situations where such issues apply.

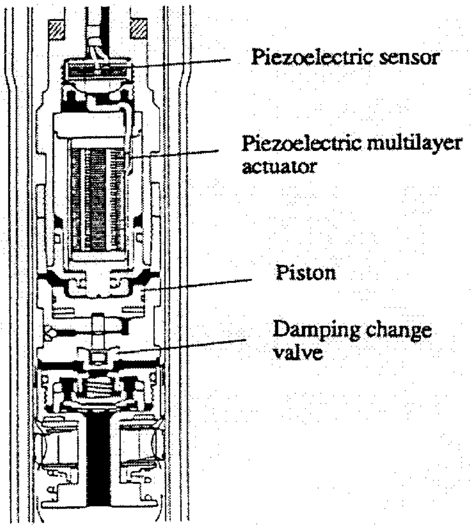

Figure 1.32 An electronic modulated automobile shock absorber developed by Toyota Motors using a both a multilayer piezoelectric sensor and actuator.[31]

CHAPTER ESSENTIALS

1. Applications for new actuators:
   a. positioners,
   b. micromotors,
   c. vibration suppressors.

2. Disadvantages of conventional positioning devices:
   a. oil/air pressure displacement reduction mechanism: slow response
   b. electromagnetic motor with transfer screw mechanism: backlash
   c. voice coil: slow response, small generative force.

3. Desired features for an actuator element:
   a. large displacement (sensitivity = displacement/driving power),
   b. good positioning reproducibility (low hysteresis),
   c. quick response,

   - d. stable temperature characteristics,
   - e. low driving energy,
   - f. large generative force and failure strength,
   - g. small size and light weight,
   - h. low degradation/aging in usage,
   - i. minimal detrimental environmental effects (such as mechanical noise, electromagnetic noise, heat generation).

4. Comparison among solid-state actuators:

	Shape Memory	Magnetostrictive	Piezoelectric	Electrostrictive
Strain ($\Delta l/l$)	10^{-3}-10^{-2}	10^{-4}-10^{-3}	10^{-3}-10^{-2}	10^{-4}-10^{-3}
Hysteresis	Large	Large	Large	Small
Aging	Large	Small	Large	Small
Response	s	μs	ms	μs
Drive Source	Heat	Magnetic Coil	Electric Field	Electric Field

5. Design considerations in the development of smart actuators:
   - a. materials designing,
   - b. device designing,
   - c. drive/control techniques, in terms of improved performance and reliability.

CHAPTER PROBLEMS

1.1 Compare the advantages and disadvantages of the various types of solid-state actuator materials (shape memory alloy, magnetostrictive, piezoelectric, electrostrictive) in terms of: a) displacement, b) response speed, c) generative force, d) efficiency, and e) environmental effects.

1.2 We wish to design a compact electromagnetic motor with a coil 1 cm in diameter. We will use 100 turns of a thin wire that is 100 μm in diameter. If the conductivity of Cu is $\sigma = 6.0 \times 10^7$ $(\Omega\ \text{m})^{-1}$, calculate the resistance of this coil. If a current of 0.5 A flows through this coil, calculate the Joule heat generated per second.

REFERENCES

1) I. Inazaki: Sensor Technology **2**, No. 2, 65 (1982).
2) K. Uchino: Ultrasonic Techno, No. 8, 19 (1993).
3) Optical Spectra, March, p.46 (1979).
4) S. Moriyama: Mechanical Design **27**, No. 1, 32 (1983).
5) U. Berg, M. Begemann, B. Hagemann, K.-P. Kamper, F. Michel, C. Thurigen, L. Weber and Th. Wittig: *Proc. 6th Int'l. Conf. New Actuators*, p.552 (1998).
6) J. Bryzek, K. Petersen and W. McCulley: IEEE Spectrum, No. 5, p.20 (1994).

7) S. Egawa, T. Niino and T. Higuchi: *Proc. 1991 IEEE Workshop on Micro Electro Mechanical Systems*, p.9 (1991).
8) T. Higuchi: *New Actuator Handbook for Precision Control*, p.182, Fuji Techno System, Tokyo (1994).
9) H. Horikawa and K. Otsuka: *New Actuator Handbook for Precision Control*, p.454, Fuji Techno System, Tokyo (1994).
10) K. Otsuka and C. M. Wayman: *Shape Memory Materials*, Chap.1, p.1, Cambridge University Press, UK (1998).
11) K.N. Nelton: *Shape Memory Materials*, Chap.10, Cambridge Univ. Press, UK (1998).
12) T. Todoroki, K. Fukuda and T. Hayakumo: Industrial Matcrials, **32**, No.7, 85 (1984).
13) A. B. Flatau, M. J. Dapino and F. T. Calkins: Magnetostrictive Composites, *Comprehensive Composite Materials*, Chapter 5.26, p.563 (2000).
14) A. E. Clark and H. S. Belson: US Patent 4,378,258 (1983).
15) H. Eda: Giant Magnetostrictive Actuators, *New Actuator Handbook for Precision Control*, p.90, Fuji Techno System, Tokyo (1994).
16) J. L. Butler: Edge Technologies, Ames, IA (1988).
17) K. Uchino: *Ferroelectric Devices*, p.11, Marcel Dekker, NY (2000).
18) K. Yano, T. Hamatsuki, I. Fukui and E. Sato: *Proc. Annual Mtg. EE Japan*, p.1-157 (Spring, 1984).
19) M. Kasuga, T. Satoh, N. Tsukada, T. Yamazaki, F. Ogawa, M. Suzuki, I. Horikoshi and T. Itoh: J. Soc. Precision Eng., **57**, 63 (1991).
20) V. Bharti, H. S. Xu, G. Shanti, Q. M. Zhang and K. Liang: J. Appl. Phys. **87**, 452 (2000).
21) S. Bauer: *Proc. Int'l. Symp. Smart Actuators*, ICAT/Penn State, PA (April, 1999).
22) K. Uchino: Mat. Res. Innovat., **1**, 163 (1997).
23) M. Tanimura and K. Uchino: Sensors and Mater., **1**, 47 (1988).
24) K. Uchino: J. Rob. Mech., **1**(2), 124 (1989).
25) S. Thakoor, J. M. Morookian and J. A. Cutts: *Conf. Proc. 10th IEEE Int'l. Symp. on Appl. Ferroelectrics*, **1**, 205 (1996).
26) P. Poosanaas, K. Tonooka, and K. Uchino, Mechatronics **10**, 467 (2000).
27) M. R. Jolly and J. D. Carlson: Composites with Field-Responsive Rheology, *Comprehensive Composite Materials*, Chapter 5.27, p.575 (2000).
28) T. Shiga, A. Okada and T. Kurauchi: Macromolecules, **26**, 6958 (1993).
29) V. D. Chase: Appliance Manufacturer, May, p.6 (1996).
30) J. D. Carlson and K. D. Weiss: US Patent 5,382,373 (1995).
31) Y. Yokoya: Electronic Ceramics **22**, No.111, 55 (1991).

The following review papers and books are recommended for further study:

32) K. Uchino: *Piezoelectric/Electrostrictive Actuators*, Morikita Publishing, Tokyo (1986).
33) K. Uchino: Ceramic Actuators: Principles & Applications, MRS Bull. **18**(4), 42 (1993).
34) S. Ueha, Y. Tomikawa, M. Kurosawa and N. Nakamura: *Ultrasonic Motors: Theory and Applications*, Oxford Science Publ., Monographs in EE. Eng. 29 (1993).
35) K. Uchino: *Ferroelectric Devices*, VCH, Materials Sci. and Tech. Vol.11, Chap.12 (1994).
36) K. Uchino: Proc. Electroceramics IV, Vol.1, p.179, RWTH, Aachen (1994).
37) K. Uchino: *Piezoelectric Actuators and Ultrasonic Motors*, Kluwer Academic Publishers, MA (1996).
38) K. Uchino: *Ferroelectric Devices*, Marcel Dekker, NY (2000).

2

A THEORETICAL DESCRIPTION OF FIELD-INDUCED STRAINS

Generally speaking, the word "*electrostriction*" is used to describe electric field-induced strain, and hence frequently also implies the "converse piezoelectric effect." According to solid-state theory, however, the converse piezoelectric effect is defined as a primary electromechanical coupling effect where the induced strain is directly proportional to the applied electric field, while electrostriction is a second order coupling in which the strain is proportional to the square of the electric field. Thus, strictly speaking, they should be distinguished. The piezoelectric effect for a ferroelectric with a centrosymmetric high temperature prototype phase, however, originates from the electrostrictive coupling, and hence the two effects are closely related. This is true assuming that the material is a single domain crystal and that its state does not change with the application of an electric field. In a piezoelectric ceramic, the additional strains that develop with the reorientation of ferroelectric domains are also important. A description of ferroelectricity in terms of crystal structure is presented first in this chapter followed by a phenomenological description of the piezoelectric effect and electrostriction.

2.1 FERROELECTRICITY

(1) Crystal Structure and Ferroelectricity

In the so-called *dielectric materials*, the constituent atoms are typically ionized to a certain degree. When an electric field is applied to such ionic crystals, centers of positive charge are drawn to the cathode and centers of negative charge to the anode due to electrostatic attraction, thus inducing electric dipoles within the material. This phenomenon is known as *electric polarization*, which is characterized by the number of electric dipoles induced per unit volume (C/m^2). The mechanisms of electric polarization are represented in Figure 2.1. There are three fundamental mechanisms that give rise to the net polarization of a dielectric: (1) *electronic polarization*, (2) *ionic polarization,* and (3) *dipole orientation polarization.*

A capacitor with a dielectric between its electrodes can store more electric charge than a device of similar dimensions filled with air due to polarization of the dielectric as depicted in Figure 2.2. The physical quantity corresponding to the stored electric charge per unit area is called the *electric displacement*, **D**, and is related to the electric field according to the equation:

$$\mathbf{D} = \varepsilon_0 \mathbf{E} + \mathbf{P} = K \varepsilon_0 \mathbf{E} \qquad (2.1)$$

Here, ε_0 is the permittivity of free space (8.854×10^{-12} F/m), and K is the *relative permittivity*, also referred to as the *dielectric constant*, which has a second-rank tensor property.

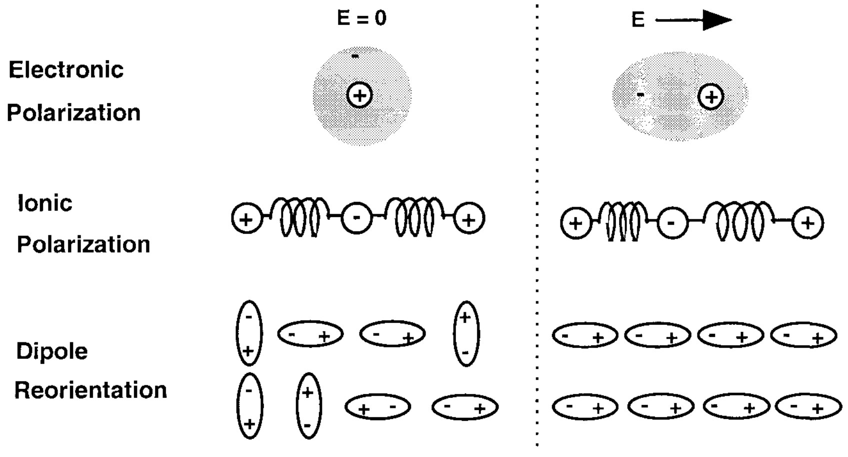
E = 0
E →
Electronic Polarization
Ionic Polarization
Dipole Reorientation

Figure 2.1 Microscopic origins of polarization.

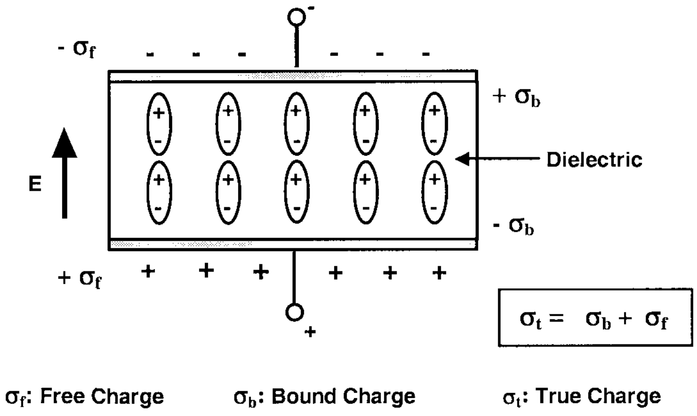
- σf
+ σb
Dielectric
- σb
E
+ σf
σt = σb + σf
σf: Free Charge
σb: Bound Charge
σt: True Charge

Figure 2.2 Charge accumulation in a dielectric capacitor.

There are certain crystal structures for which the centers of positive and negative charge do not coincide, even when no external electric field is applied. Such crystals are said to possess a *spontaneous polarization*. When the spontaneous polarization of the dielectric can be reversed by an applied electric field, the material is called a *ferroelectric*.

Not every dielectric is a ferroelectric. Crystals can be classified into 32 point groups according to their crystallographic symmetry, and these point groups can be divided into two classes, one with a center of symmetry and the other without one. This classification of the point groups is presented in Table 2.1. There are twenty-one point groups which do not have a center of symmetry. Among these, twenty point groups [point group (432) being the sole exception] are *piezoelectric*; that is, positive and negative charges are generated on their surfaces when stress is applied. *Pyroelectricity* is the phenomenon whereby, due to the temperature dependence of the spontaneous polarization, electric charges are generated on the surface of the crystal when the temperature of the crystal is changed. Among the pyroelectric crystals, those whose spontaneous polarization can be reversed by an electric field (not exceeding the breakdown limit of the crystal) are called *ferroelectrics*. One necessary test for ferroelectricity, therefore, is to experimentally observe the polarization reversal when an electric field of the appropriate magnitude is applied.

Table 2.1 Crystallographic classification scheme based on polarity and the presence of a center of symmetry. [Hex: Hexagonal, Tetra: Tetragonal, Rhomb: Rhombohedral, Ortho: Orthorhombic, Mono: Monoclinic, Tri: Triclinic]

Polar	Symm.	Crystal System										
		Cubic		Hex		Tetra		Rhomb		Ortho	Mono	Tri
Non-Polar (22)	Centro (11)	m3m	m3	6/mmm	6/m	4/mmm	4/m	$\bar{3}$m	$\bar{3}$	mmm	2/m	$\bar{1}$
	Non-Centro (21)	432 $\bar{4}$3m	23	622 $\bar{6}$m2	$\bar{6}$	422 $\bar{4}$2m	$\bar{4}$	32		222		
Polar (10)				6mm	6	4mm	4	3m	3	2mm	2 m	1

Piezoelectric point groups appear in shaded cells.

(2) Origin of the Spontaneous Polarization

Why is it that crystals, which on the basis of their elastic energy alone should be stable in a non-polar state, still experience a shifting of ions and become spontaneously polarized? For simplicity, let us assume that dipole moments result from the displacement of one kind of ion, A, (with an electric charge q) relative to the undistorted crystal lattice. We will consider the case in which the polarization is characterized by all the A ions being displaced in the same way.

This kind of ionic displacement could occur with the normal thermal vibration of the lattice. Some possible ion configurations are depicted for a perovskite crystal in

Figure 2.3. If a particular lattice vibration effectively lowers the crystal energy, the ions will shift accordingly, thereby stabilizing the crystal structure and minimizing the energy of the system. Starting with the original cubic structure pictured in Figure 2.3(a), if the configuration in Figure 2.3(b) is established, only the oxygen octahedra are distorted without generating dipole moments (acoustic mode). On the other hand, when the configurations in Figure 2.3(c) or (d) are established, dipole moments are generated (optical mode). The states depicted in Figures 2.3(c) and (d) correspond to ferroelectric and antiferroelectric states, respectively. If either of these modes exist, a decrease in the vibration frequency will occur with decreasing temperature (soft phonon mode), until finally, at a certain critical temperature corresponding to a phase transition, the vibration frequency becomes zero.

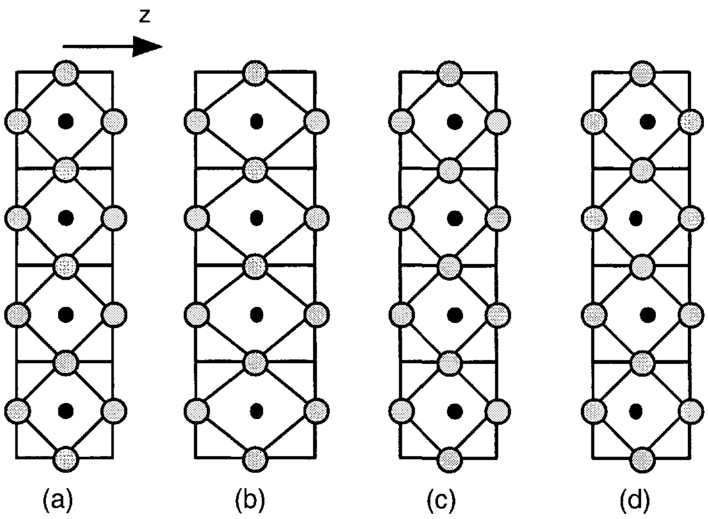

Figure 2.3 Some possible ion configurations in a perovskite crystal corresponding to: (a) the initial cubic structure, (b) a symmetrically elongated structure, (c) a structure with coherently shifted center cations, and (d) a structure with an anti-polar shift of the center cations. [Dark: center cations; Shaded: oxygen octahedra atoms]

It follows that, at any individual A ion site, there exists a local field associated with the surrounding polarization **P**, even if there is no external field, E_o, applied. It can be shown that:

$$\mathbf{E}_{loc} = \mathbf{E}_o + \sum_i \left[\frac{3(\mathbf{p}_i \cdot \mathbf{r}_i) - r_i^2 \mathbf{p}_i}{(4\pi \varepsilon_o) r_i^5} \right] = \left[\frac{\gamma}{3\varepsilon_o} \right] \mathbf{P} \qquad (2.2)$$

where, $\mathbf{r}_i$, is a position vector relating the location of a given dipole with dipole moment $\mathbf{p}_i$ to a particular location in space as depicted in Figure 2.4, and γ is called the *Lorentz factor*. In the case of an isotropic, cubic system, γ is considered to be unity.[1] The local field is the driving force for the ion shift.

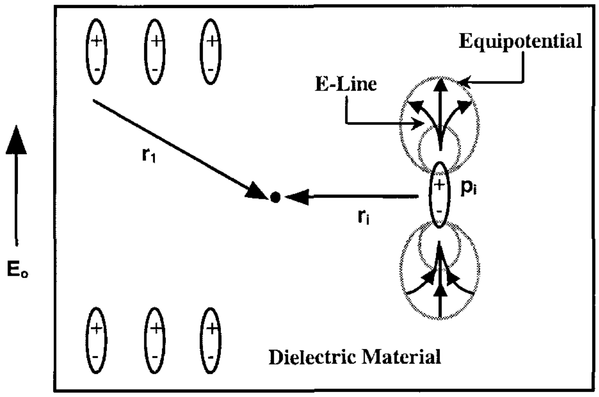

Figure 2.4 Schematic representation of the parameters used to define the local field, $\mathbf{E}_{loc}$.

If the *ionic polarizability* of ion A is α, then the dipole moment, μ, of a unit cell of this crystal is given by:

$$\mu = \left[\frac{\alpha\gamma}{3\varepsilon_o}\right]\mathbf{P} \qquad (2.3)$$

The energy of this dipole moment (dipole-dipole coupling) is defined as:

$$w_{dip} = -\mu\cdot\mathrm{E}_{loc} = -\left[\frac{\alpha\gamma^2}{9\varepsilon_o^2}\right]P^2 \qquad (2.4)$$

If there are N atoms per unit volume, the energy is expressed as:

$$w_{dip} = N\,w_{dip} = -\left[\frac{N\alpha\gamma^2}{9\varepsilon_o^2}\right]P^2 \qquad (2.5)$$

Furthermore, when the A ions are displaced from their nonpolar equilibrium positions, the elastic energy increases. The elastic energy per unit volume is expressed as:

$$w_{elast} = N\left[\left(\frac{k}{2}\right)u^2 + \left(\frac{k'}{4}\right)u^4\right] \tag{2.6}$$

where u is the magnitude of the displacement, and k and k' are force constants. The higher order force constant, k', plays an important role in determining the magnitude of the dipole moment in pyroelectric crystals. Making use of the relationship:

$$P = N\,q\,u \tag{2.7}$$

in Equation (2.5) and combining with Equation (2.6), we may express the total energy as:

$$w_{tot} = w_{dip} + w_{elast} = \left[\left(\frac{k}{2Nq^2}\right) - \left(\frac{N\alpha\gamma^2}{9\varepsilon_o^2}\right)\right]P^2 + \left[\frac{k'}{4N^3q^4}\right]P^4 \tag{2.8}$$

The shapes of the total energy and individual energy functions are depicted in Figure 2.5. It is apparent from this analysis that when the coefficient associated with the harmonic term of the elastic energy is equal to or greater than the coefficient associated with the dipole-dipole coupling, the polarization, **P**, will be zero; that is, the A ions are stable and will remain at their nonpolar equilibrium positions. Otherwise, a shift from the equilibrium positions will occur to establish a stable configuration and a net spontaneous polarization will result. Spontaneous polarization tends to develop more readily in perovskite crystal structures (such as barium titanate) because they generally have a higher value of the Lorentz factor (γ=10) than most other crystal structures.[2]

(3) Physical Properties of Ferroelectrics and Their Applications

An important ferroelectric material is barium titanate, $BaTiO_3$. It is often presented as a classic example of a ferroelectric that exhibits so-called first-order behavior. Barium titanate has the perovskite crystal structure depicted in Figure 2.6. In its high temperature, paraelectric (nonpolar) phase there is no spontaneous polarization and a cubic symmetry (O_h-m3m) exists. Below the transition temperature, which is designated by T_C and called the *Curie temperature* (about 130°C for $BaTiO_3$), spontaneous polarization develops, and the crystal structure becomes slightly elongated, assuming a tetragonal symmetry (C_{4v}-4mm). There are also two lower temperature phase transitions for $BaTiO_3$, one from a tetragonal to an orthorhombic phase and the other from an orthorhombic to a rhombohedral phase. We will focus for the moment on the higher temperature paraelectric to ferroelectric transition.

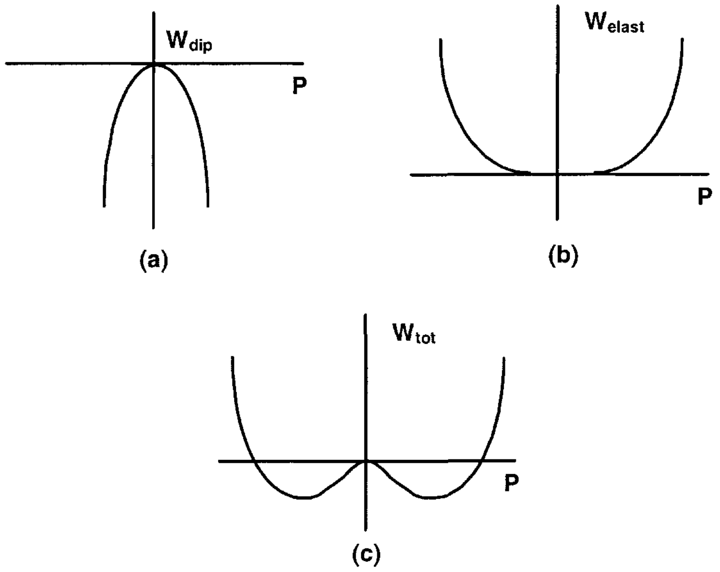

Figure 2.5 Representations of the energies considered in describing the microscopic mechanisms for spontaneous polarization. Shown as a function of polarization: (a) the dipole energy per unit volume, W_{dip}, (b) the elastic energy per unit volume, W_{elas}, and (c) the total energy per unit volume, W_{tot}, for a perovskite structure.

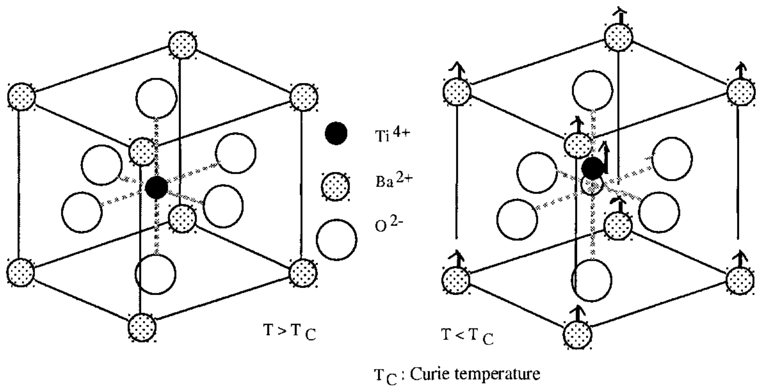

Figure 2.6 The crystal structure of $BaTiO_3$.

A general depiction of the temperature dependences of the spontaneous polarization, P_S, and the dielectric constant, K, for barium titanate is shown in Figure 2.7. The general trends depicted in the figure illustrate how the spontaneous polarization, P_S, decreases with increasing temperature and vanishes at the Curie point, while K tends to diverge near T_C. The inverse dielectric constant, 1/K, also shown in the figure, has a linear dependence on temperature over a broad range in the paraelectric region. This behavior is described by the so-called *Curie-Weiss law*,

$$K - 1 \approx \chi = \frac{C}{(T - T_o)} \tag{2.9}$$

where χ is the dielectric susceptibility, C is the *Curie constant* and T_o is the *Curie-Weiss temperature.* The inverse dielectric constant is also discontinuous at T_C for a first-order transition, as we shall see in Section 2.4(1), and when one extends the linear paraelectric portion of this curve back across the temperature axis it intersects at the Curie-Weiss temperature, T_o, as depicted in Figure 2.7. It is generally observed that T_o is slightly lower than the Curie temperature, T_C, which is the actual transition temperature for the material.

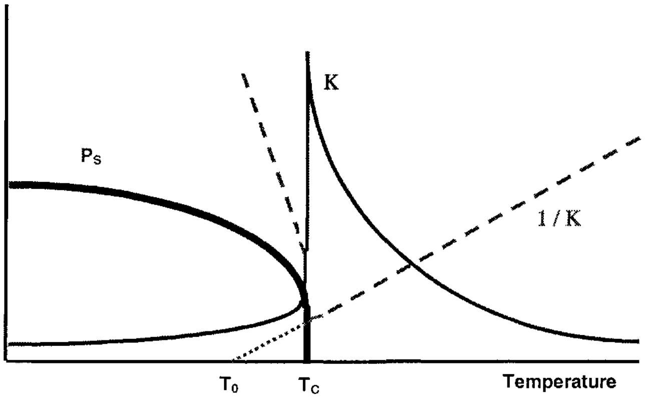

Figure 2.7 A general depiction of the temperature dependences of the spontaneous polarization, the dielectric constant, and the inverse dielectric constant for a ferroelectric material such as $BaTiO_3$.

The spontaneous polarization, P_S, and the spontaneous strain, x_S, are related as described by the following equation:

$$x_S = Q\,P_S^2 \tag{2.10}$$

The spontaneous strain, x_S, associated with barium titanate typically decreases with increasing temperature in an almost linear manner. Barium titanate is piezoelectric in its ferroelectric phase, but becomes nonpiezoelectic in its paraelectric phase. It exhibits only an electrostrictive response in this nonpolar phase. When the ferroelectric is to be used as a capacitor it is operated at a temperature near the Curie temperature where the peak dielectric constant occurs. The pronounced temperature variation of the polarization below the Curie temperature is exploited when the material is to be used for pyroelectric applications. Piezoelectric materials can be used as sensors and actuators. Piezoelectric pressure and acceleration sensors are now commercially available as well as a variety of piezo-vibrators. Precision positioners and pulse drive linear motors can be found in precision lathe machines, semiconductor manufacturing apparatus, and popular office equipment. The development of ultrasonic motors for a variety of new applications has been dramatic and widespread in recent years. Ferroelectric materials generally exhibit excellent electrooptic properties as well and are thus seen as promising candidates for application in displays and optical communication systems of the future.

Example Problem 2.1

$BaTiO_3$ exhibits the ionic displacements at room temperature illustrated in Figure 2.8. The lattice constants are c = 4.036 (Å) and a = 3.992 (Å). Calculate the magnitude of the spontaneous polarization for barium titanate in this tetragonal form.

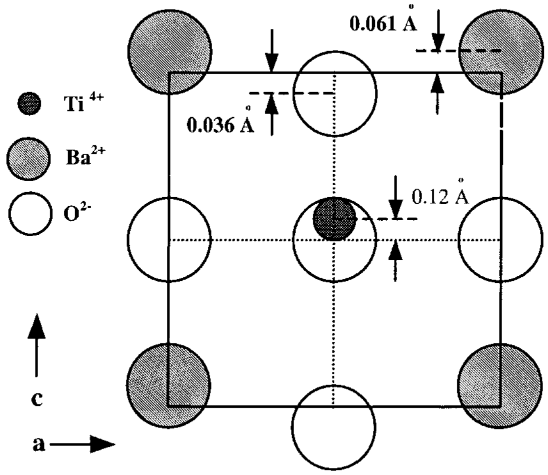

Figure 2.8 Ionic shifts in $BaTiO_3$ at room temperature.

Solution

The dipole moment is defined to be the product of the magnitude of the ion charge and its displacement. The total dipole moment in a unit cell is calculated by summing the contributions of all the Ba^{2+}, Ti^{4+}, O^{2-}-related dipoles.

$$\begin{aligned} p &= 8[2e/8][0.061\text{x}10^{-10}(\text{m})] + [4e][0.12\text{x}10^{-10}(\text{m})] + 2[-2e/2][\,-0.036\text{x}10^{-10}\,(\text{m})] \\ &= e\,[0.674\text{x}10^{-10}(\text{m})] \\ &= 1.08\text{x}10^{-29}\,(\text{C m}) \qquad \text{(P2.1.1)} \end{aligned}$$

where e is the fundamental charge: $1.602 \text{ x } 10^{-19}$ (C).

The unit cell volume is given by

$$\begin{aligned} v &= a^2 c = (3.992)^2 (4.036) \text{ x } 10^{-30}\,(\text{m}^3) \\ &= 64.3 \text{ x } 10^{-30}\,(\text{m}^3) \qquad \text{(P2.1.2)} \end{aligned}$$

The spontaneous polarization represents the number of (spontaneous) electric dipoles, p, per unit volume:

$$\begin{aligned} P_S &= P/v = 1.08 \text{ x } 10^{-29}\,(\text{Cm}) / 64.3 \text{ x } 10^{-30}\,(\text{m}^3) \\ &= 0.17\,(\text{C/m}^2) \qquad \text{(P2.1.3)} \end{aligned}$$

This theoretical value of P_S is in reasonable agreement with the experimental value of 0.25 (C/m^2).

---

(4) Antiferroelectrics

The previous section dealt with the configuration of spontaneous dipoles associated with a polar crystal where the dipoles are oriented parallel to each other. There are, however, cases in which antiparallel orientation of the dipoles lowers the dipole-dipole interaction energy. Crystals with such a dipole configuration are called antipolar crystals. The orientation of the spontaneous electric dipoles associated with this antipolar state is depicted schematically in Figure 2.9. The orientation of dipoles within a polar crystal is also pictured in the figure. In an antipolar crystal, where the free energy of an antipolar state does not differ appreciably from that of a polar state, the application of an external electric field or mechanical stress may cause a reorientation of the dipoles to a parallel configuration. Such antipolar crystals for which this type of a field- or stress-induced transition occurs are called *antiferroelectrics*.

Dielectric hysteresis curves characteristic of paraelectric, ferroelectric and antiferroelectric phases are shown in Figure 2.10. It is apparent from these curves that the P-E relationship for the paraelectric phase is linear while in the ferroelectric phase dielectric hysteresis occurs due to the reorientation of the spontaneous polarization. When a crystal is in an antiferroelectric state, the induced polarization is proportional to the applied electric field, E, at low field strengths, but when **E** exceeds a certain critical value, $\mathbf{E}_{crit}$, the crystal undergoes an electric field-induced phase transition and the hysteretic response depicted in Figure 2.10(c) is observed.

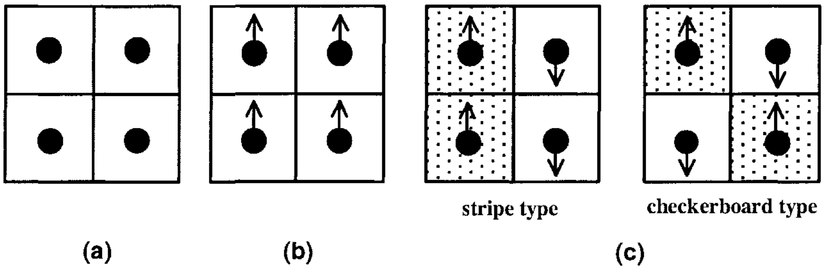

Figure 2.9 Schematic depiction of the spontaneous dipoles in: (a) nonpolar, (b) polar, and (c) antipolar materials.

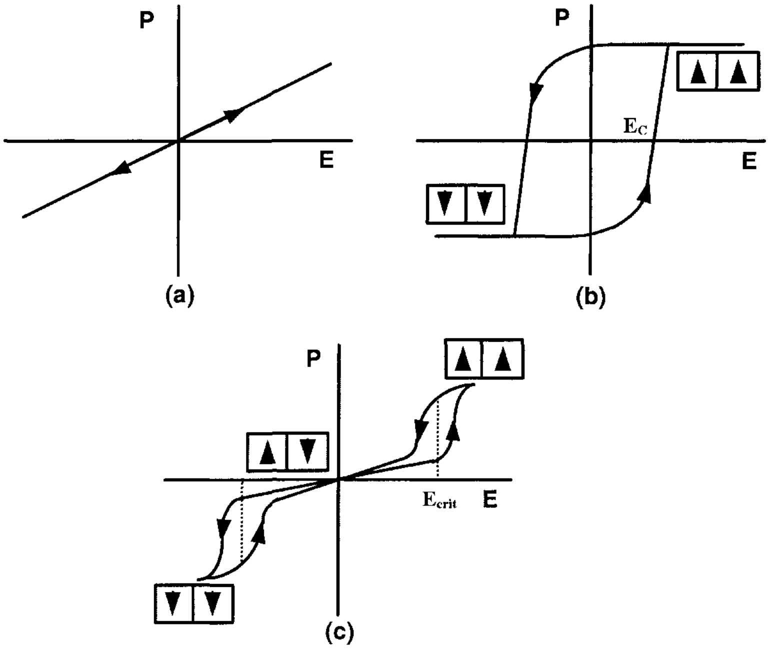

Figure 2.10 Dielectric (P-E) curves for materials in: (a) paraelectric, (b) ferroelectric, and (c) antiferroelectric states.

Once the electric field is removed, the crystal returns to its antipolar state, and no net spontaneous polarization remains. This characteristic antiferroelectric P-E response is called a *double hysteresis curve*

2.2 MICROSCOPIC ORIGINS OF ELECTRIC FIELD-INDUCED STRAINS

Solids, especially ceramics (inorganic polycrystalline materials), are relatively hard mechanically, but still expand or contract depending on the change of the state parameters. The strain is defined to be the ratio of the length extension, Δl, to the initial length, l, of the material. When the strain is induced by temperature change and stress, the effects are referred to as *thermal expansion* and *elastic deformation*, respectively. The application of an electric field can also cause deformation in insulating materials. This is called *electric field-induced strain.*

We will now consider the mechanisms for electric field-induced strains.[3] For the sake of simplicity let us consider an ionic crystal such as NaCl. A one-dimensional rigid-ion spring model of the crystal lattice is depicted in Figure 2.11. The springs represent the cohesive force resulting from the combined action of the electrostatic Coulomb interaction and quantum mechanical repulsion. The centrosymmetric case is shown in Figure 2.11(b) and the more general noncentrosymmetric case is pictured in Figure 2.11(a). The springs joining the ions are considered to be all identical for the centrosymmetric case of Figure 2.11(b). The springs joining the ions for the noncentrosymmetric case shown in Figure 2.11(a), however, are different for the longer and shorter ionic distances, where stiffer (higher k) springs are associated with the shorter distances. When the centrosymmetric crystal is subjected to an applied electric field, the cations are displaced in the direction of the electric field and the anions in the opposite direction, leading to a change in the interionic distance. Depending on the direction of the electric field, the soft springs in our model are displaced more than the stiff springs thus producing a strain, x, in the structure and a change in the unit cell length that is proportional to the applied electric field strength, E. This is the known as the *converse piezoelectric effect* and is expressed as:

$$x = d\ E \tag{2.11}$$

where the proportionality constant d is called the *piezoelectric strain coefficient.*

As for the centrosymmetric case represented in Figure 2.11(b), the displacements of the springs are nearly the same and, therefore, the interionic distances and the lattice constants remain practically the same; hence, there is no induced strain. In reality ions are not connected by such ideal springs. Ideal in this sense means harmonic springs, for which Hooke's law applies. In most cases, the springs are *anharmonic* ($F=k_1\Delta-k_2\Delta^2$), that is, they are easily extended, but resistant to compression. The subtle differences in ion displacement resulting from this anharmonicity, lead to a change in the lattice parameter and an associated strain, which is independent of the direction of the applied electric field, and hence is an even-function of the electric field. This is called the *electrostriction effect*, which is expressed as:

$$x = M E^2 \tag{2.12}$$

where M is the electrostriction coefficient.

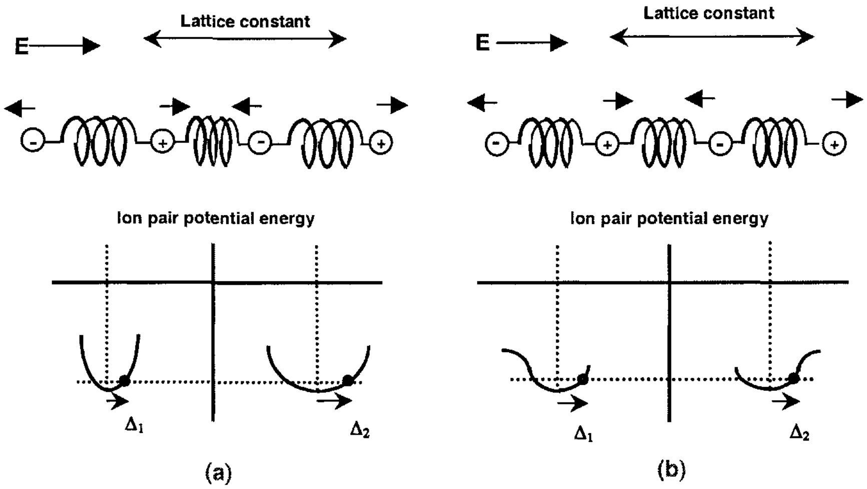

Figure 2.11 One-dimensional rigid-ion spring model of a simple NaCl-type crystalline lattice: (a) a noncentrosymmetric case (piezoelectric strain), and (b) a centrosymmetric case (electrostriction).

The one-dimensional crystal represented in Figure 2.11(a) also possesses a spontaneous dipole moment. The total dipole moment per unit volume is called the spontaneous polarization. When a large reverse bias electric field is applied to a crystal that has a spontaneous polarization in a particular polar direction, a transition "phase" is formed which is another stable crystal state in which the relative positions of the ions are reversed (in terms of an untwinned single crystal, this is equivalent to rotating the crystal 180° about an axis perpendicular to its polar axis). This transition, referred to as *polarization reversal*, also causes a significant change in strain and materials that undergo such a transition are referred to as *ferroelectrics*. Generally speaking, what is actually observed as a field-induced strain is a complicated combination of the three basic effects (piezoelectricity, electrostriction and polarization reversal) described in this section.

2.3 TENSOR / MATRIX DESCRIPTION OF PIEZOELECTRICITY

(1) Tensor Representation

In the solid-state theoretical treatment of the phenomenon of piezoelectricity or electrostriction, the strain x_{kl} is expressed in terms of the electric field, E_i, or electric polarization, P_i, as follows:

$$\begin{aligned} x_{kl} &= d_{ikl} E_i + M_{ijkl} E_i E_j \\ &= g_{ikl} P_i + Q_{ijkl} P_i P_j \end{aligned} \tag{2.13}$$

where d_{ikl} and g_{ikl} are the piezoelectric coefficients and M_{ijkl} and Q_{ijkl} are the electrostrictive coefficients. Represented in this way we regard the quantities E_i and x_{kl} as first-rank and second-rank tensors, respectively, while d_{ikl} and M_{ijkl} are considered third-rank and fourth-rank tensors, respectively. Generally speaking, if two physical properties are represented by tensors of p-rank and q-rank, *the quantity that combines the two properties in a linear relation is represented by a tensor of (p+q)-rank.*

The d_{ijk} tensor can be viewed as a three dimensional array of coefficients comprised of three "layers" of the following form:

$$\begin{array}{ll}
\text{1st layer } (i = 1) & \begin{matrix} d_{111} & d_{112} & d_{113} \\ d_{121} & d_{122} & d_{123} \\ d_{131} & d_{132} & d_{133} \end{matrix} \\[2ex]
\text{2nd layer } (i = 2) & \begin{matrix} d_{211} & d_{212} & d_{213} \\ d_{221} & d_{222} & d_{223} \\ d_{231} & d_{232} & d_{233} \end{matrix} \\[2ex]
\text{3rd layer } (i = 3) & \begin{matrix} d_{311} & d_{312} & d_{313} \\ d_{321} & d_{322} & d_{323} \\ d_{331} & d_{332} & d_{333} \end{matrix}
\end{array} \tag{2.14}$$

(2) Crystal Symmetry and Tensor Form

A physical property measured along two different directions must have the same value if these two directions are crystallographically equivalent. This consideration sometimes reduces the number of independent tensor coefficients representing a given physical property. Let us consider the third-rank piezoelectricity tensor as an example. The converse piezoelectric effect is expressed in tensor notation as:

$$x_{kl} = d_{ikl} E_i \tag{2.15}$$

An electric field, E, initially defined in terms of an (x, y, z) coordinate system, is redefined as E' in terms of another system rotated with respect to the first with coordinates (x', y', z') by means of a transformation matrix (a_{ij}) such that:

$$E'_i = a_{ij} E_j \tag{2.16}$$

or

$$\begin{bmatrix} E'_1 \\ E'_2 \\ E'_3 \end{bmatrix} = \begin{pmatrix} a_{11} & a_{12} & a_{13} \\ a_{21} & a_{22} & a_{23} \\ a_{31} & a_{32} & a_{33} \end{pmatrix} \begin{bmatrix} E_1 \\ E_2 \\ E_3 \end{bmatrix} \tag{2.17}$$

The matrix (a_{ij}) is thus seen to be simply the array of direction cosines that allows us to transform the components of vector E referred to the original coordinate axes to components referred to the axes of the new coordinate system. The second-rank strain tensor is thus transformed in the following manner:

$$x'_{ij} = a_{ik}\, a_{jl}\, x_{kl} \tag{2.18}$$

or

$$\begin{bmatrix} x'_{11} & x'_{12} & x'_{13} \\ x'_{21} & x'_{22} & x'_{23} \\ x'_{31} & x'_{32} & x'_{33} \end{bmatrix} = \begin{pmatrix} a_{11} & a_{12} & a_{13} \\ a_{21} & a_{22} & a_{23} \\ a_{31} & a_{32} & a_{33} \end{pmatrix} \begin{bmatrix} x_{11} & x_{12} & x_{13} \\ x_{21} & x_{22} & x_{23} \\ x_{31} & x_{32} & x_{33} \end{bmatrix} \begin{pmatrix} a_{11} & a_{21} & a_{31} \\ a_{12} & a_{22} & a_{32} \\ a_{13} & a_{23} & a_{33} \end{pmatrix} \tag{2.19}$$

while the transformation of the third-rank piezoelectric tensor is expressed as:

$$d'_{ijk} = a_{il} a_{jm} a_{kn}\, d_{lmn} \tag{2.20}$$

If the d_{lmn} tensor coefficients are symmetric with respect to m and n such that $d_{lmn}=d_{lnm}$, the following equivalences can be established:

$d_{112} = d_{121}$ $\quad$ $d_{113}= d_{131}$ $\quad$ $d_{123} = d_{132}$

$d_{221}= d_{212}$ $\quad$ $d_{213}= d_{231}$ $\quad$ $d_{223}= d_{232}$

$d_{221}= d_{212}$ $\quad$ $d_{213}= d_{231}$ $\quad$ $d_{223}= d_{232}$

The number of independent coefficients is thus reduced from an original 27 ($=3^3$) to only 18 and the d_{lmn} tensor may then be represented by layers of the following form:

$$\begin{array}{llll}
\text{1st layer} & d_{111} & d_{112} & d_{131} \\
 & d_{112} & d_{122} & d_{123} \\
 & d_{131} & d_{123} & d_{133} \\
 & & & \\
\text{2nd layer} & d_{211} & d_{212} & d_{231} \\
 & d_{212} & d_{222} & d_{223} \\
 & d_{231} & d_{223} & d_{233} \\
 & & & \\
\text{3rd layer} & d_{311} & d_{312} & d_{313} \\
 & d_{312} & d_{322} & d_{323} \\
 & d_{313} & d_{323} & d_{333}
\end{array} \tag{2.21}$$

(3) Matrix Notation

The reduction in tensor coefficients just carried out for the tensor quantity d_{ijk} makes it possible to render the three-dimensional array of coefficients in a more tractable two-dimensional matrix form. This is accomplished by abbreviating the suffix notation used to designate the tensor coefficients according to the following scheme:

Tensor notation	**11**	**22**	**33**	**23,32**	**31,13**	**12,21**
Matrix notation	**1**	**2**	**3**	**4**	**5**	**6**

The layers of tensor coefficients represented by Equation (2.21) may now be rewritten as:

$$\begin{array}{llll}
 & d_{11} & (1/2)d_{16} & (1/2)d_{15} \\
\text{1st layer} & (1/2)d_{16} & d_{12} & (1/2)d_{14} \\
 & (1/2)d_{15} & (1/2)d_{14} & d_{13} \\
 & & & \\
 & d_{21} & (1/2)d_{26} & (1/2)d_{25} \\
\text{2nd layer} & (1/2)d_{26} & d_{22} & (1/2)d_{24} \\
 & (1/2)d_{25} & (1/2)d_{24} & (1/2)d_{23} \\
 & & & \\
 & d_{31} & (1/2)d_{36} & (1/2)d_{35} \\
\text{3rd layer} & (1/2)d_{36} & d_{32} & (1/2)d_{34} \\
 & (1/2)d_{35} & (1/2)d_{34} & d_{33}
\end{array} \tag{2.22}$$

The last two suffixes in the tensor notation correspond to those of the strain components, therefore, for the sake of consistency, we will also make similar substitutions in the notation for the strain components.

$$\begin{bmatrix} x_{11} & x_{12} & x_{13} \\ x_{21} & x_{22} & x_{23} \\ x_{31} & x_{32} & x_{33} \end{bmatrix} \rightarrow \begin{bmatrix} x_1 & (\tfrac{1}{2})x_6 & (\tfrac{1}{2})x_5 \\ (\tfrac{1}{2})x_6 & x_2 & (\tfrac{1}{2})x_4 \\ (\tfrac{1}{2})x_5 & (\tfrac{1}{2})x_4 & x_3 \end{bmatrix} \qquad (2.23)$$

Note that here the number of independent coefficients for this second-rank tensor may also be reduced from 9 ($=3^2$) to 6 because it is a symmetric tensor and $x_{ij}=x_{ji}$. The factors of (1/2) in this and the piezoelectric layers of Equation (2.22) are included in order to retain the general form that, like the corresponding tensor equation expressed by Equation (2.15), includes no factors of 2 so that we may write:

$$x_j = d_{ij} E_i \qquad (i = 1, 2, 3 \; ; \; j = 1, 2, ..., 6) \qquad (2.24a)$$

or

$$\begin{bmatrix} x_1 \\ x_2 \\ x_3 \\ x_4 \\ x_5 \\ x_6 \end{bmatrix} = \begin{pmatrix} d_{11} & d_{21} & d_{31} \\ d_{12} & d_{22} & d_{32} \\ d_{13} & d_{23} & d_{33} \\ d_{14} & d_{24} & d_{34} \\ d_{15} & d_{25} & d_{35} \\ d_{16} & d_{26} & d_{36} \end{pmatrix} \begin{bmatrix} E_1 \\ E_2 \\ E_3 \end{bmatrix} \qquad (2.24b)$$

When deriving a matrix expression for the direct piezoelectric effect in terms of the matrix form of the stress X_{ij}, the factors of (1/2) are not necessary and the matrix may be represented as:

$$\begin{bmatrix} X_{11} & X_{12} & X_{13} \\ X_{21} & X_{22} & X_{23} \\ X_{31} & X_{32} & X_{33} \end{bmatrix} \rightarrow \begin{bmatrix} X_1 & X_6 & X_5 \\ X_6 & X_2 & X_4 \\ X_5 & X_4 & X_3 \end{bmatrix} \qquad (2.25)$$

so that:

$$P_j = d_{ij} X_j \qquad (i = 1, 2, 3 \; ; \; j = 1, 2, ..., 6) \qquad (2.26a)$$

or

$$\begin{bmatrix} P_1 \\ P_2 \\ P_3 \end{bmatrix} = \begin{bmatrix} d_{11} & d_{12} & d_{13} & d_{14} & d_{15} & d_{16} \\ d_{21} & d_{22} & d_{23} & d_{24} & d_{25} & d_{26} \\ d_{31} & d_{32} & d_{33} & d_{34} & d_{35} & d_{36} \end{bmatrix} \begin{bmatrix} X_1 \\ X_2 \\ X_3 \\ X_4 \\ X_5 \\ X_6 \end{bmatrix} \qquad (2.26b)$$

Although the matrix notation has the advantage of being more compact and tractable than the tensor notation, one must remember that the matrix coefficients, d_{ij}, do not transform like the tensor components, d_{ijk}. Applying the matrix notation in a similar manner to the electrostrictive coefficients M_{ijkl}, we obtain the following equation corresponding to Equation (2.13):

$$\begin{pmatrix} x_1 \\ x_2 \\ x_3 \\ x_4 \\ x_5 \\ x_6 \end{pmatrix} = \begin{pmatrix} d_{11} & d_{21} & d_{31} \\ d_{12} & d_{22} & d_{32} \\ d_{13} & d_{23} & d_{33} \\ d_{14} & d_{24} & d_{34} \\ d_{15} & d_{25} & d_{35} \\ d_{16} & d_{26} & d_{36} \end{pmatrix} \begin{bmatrix} E_1 \\ E_2 \\ E_3 \end{bmatrix} + \begin{pmatrix} M_{11} & M_{21} & M_{31} & M_{41} & M_{51} & M_{61} \\ M_{12} & M_{22} & M_{32} & M_{42} & M_{52} & M_{62} \\ M_{13} & M_{23} & M_{33} & M_{43} & M_{53} & M_{63} \\ M_{14} & M_{24} & M_{34} & M_{44} & M_{54} & M_{64} \\ M_{15} & M_{25} & M_{35} & M_{45} & M_{55} & M_{65} \\ M_{16} & M_{26} & M_{36} & M_{46} & M_{56} & M_{66} \end{pmatrix} \begin{pmatrix} E_1^2 \\ E_2^2 \\ E_3^2 \\ E_2E_3 \\ E_3E_1 \\ E_1E_2 \end{pmatrix} \tag{2.27}$$

Tables 2.2 and 2.3 summarize the matrices d_{ij} and M_{ij} for all crystallographic point groups.[4]

Example Problem 2.2

Suppose that a shear stress is applied on a crystal with a square cross-section such that it is deformed as illustrated in Figure 2.12. Calculate the induced strain x_5 ($=2x_{31}$).

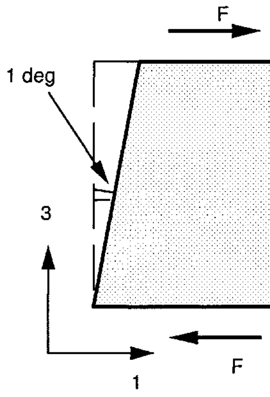

Figure 2.12 The induced strain for a crystal with a square cross-section subjected to a shear stress.

Solution

Since $x_5 = 2x_{31} = \tan\theta \approx \theta$ and $1^\circ = [\pi/180]$ (rad), $x_5 = 0.017$.

Example Problem 2.3

Barium titanate ($BaTiO_3$) has a tetragonal crystal symmetry (point group 4mm) at room temperature. The appropriate piezoelectric strain coefficient matrix is therefore of the form:

$$d_{ij} = \begin{pmatrix} 0 & 0 & 0 & 0 & d_{15} & 0 \\ 0 & 0 & 0 & d_{15} & 0 & 0 \\ d_{31} & d_{31} & d_{33} & 0 & 0 & 0 \end{pmatrix}$$

(a) Determine the nature of the strain induced in the material when an electric field is applied along the crystallographic **c** axis.

(b) Determine the nature of the strain induced in the material when an electric field is applied along the crystallographic **a** axis.

Solution

The matrix equation that applies in this case is:

$$\begin{bmatrix} x_1 \\ x_2 \\ x_3 \\ x_4 \\ x_5 \\ x_6 \end{bmatrix} = \begin{pmatrix} 0 & 0 & d_{31} \\ 0 & 0 & d_{31} \\ 0 & 0 & d_{33} \\ 0 & d_{15} & 0 \\ d_{15} & 0 & 0 \\ 0 & 0 & 0 \end{pmatrix} \begin{bmatrix} E_1 \\ E_2 \\ E_3 \end{bmatrix} \tag{P2.3.1}$$

from which we may derive expressions for the induced strains:

$x_1 = x_2 = d_{31}E_3$ $\quad x_3 = d_{33}E_3$ $\quad x_4 = d_{15}E_2$

$x_5 = d_{15}E_1$ $\quad x_6 = 0$

so that the following determinations can be made:

(a) When E_3 is applied, elongation in the c direction ($x_3 = d_{33}E_3$, $d_{33} > 0$) and contraction in the a and b directions ($x_1 = x_2 = d_{31}E_3$, $d_{31} < 0$) occur.

(b) When E_1 is applied, a shear strain x_5 ($= 2x_{31}$) $= d_{15}E_1$ is induced. The case where $d_{15} > 0$ and $x_5 > 0$ is illustrated in Figure 2.13(a) (after Example Problem 2.4).

Example Problem 2.4

Lead magnesium niobate has a cubic crystal symmetry (point group m3m) at room temperature and does not exhibit piezoelectricity; however, a large electrostrictive response is induced with the application of an electric field. The relationship between the induced strain and the applied electric field is given in matrix form by:

$$\begin{bmatrix} x_1 \\ x_2 \\ x_3 \\ x_4 \\ x_5 \\ x_6 \end{bmatrix} = \begin{pmatrix} M_{11} & M_{12} & M_{12} & 0 & 0 & 0 \\ M_{12} & M_{11} & M_{12} & 0 & 0 & 0 \\ M_{12} & M_{12} & M_{11} & 0 & 0 & 0 \\ 0 & 0 & 0 & M_{44} & 0 & 0 \\ 0 & 0 & 0 & 0 & M_{44} & 0 \\ 0 & 0 & 0 & 0 & 0 & M_{44} \end{pmatrix} \begin{bmatrix} E_1^2 \\ E_2^2 \\ E_3^2 \\ E_2E_3 \\ E_3E_1 \\ E_1E_2 \end{bmatrix} \qquad \text{(P2.4.1)}$$

Calculate the strain induced in the material when an electric field is applied along the [111] direction.

Solution

Substituting the electric field applied in this case:

$$E_1 = E_2 = E_3 = E_{[111]} / \sqrt{3}$$

into Equation (P2.4.1), we obtain:

$$x_1 = x_2 = x_3 = (M_{11} + 2M_{12}) \frac{E_{[111]}^2}{3} \quad (= x_{11} = x_{22} = x_{33}) \qquad \text{(P2.4.2a)}$$

$$x_4 = x_5 = x_6 = M_{44} \frac{E_{[111]}^2}{3} \quad (= 2x_{23} = 2x_{31} = 2x_{12}) \qquad \text{(P2.4.2b)}$$

The resulting distortion is illustrated in Figure 2.13(b). The strain, x, induced along an arbitrary direction is given by

$$x = \Sigma x_{ij} l_i l_j \qquad \text{(P2.4.3)}$$

where l_i is a direction cosine defined with respect to the i axis. The strain induced along the [111] direction, $x_{[111]\parallel}$, is therefore given by:

$$x_{[111]\parallel} = \sum x_{ij} (1/\sqrt{3})(1/\sqrt{3})$$

$$= x_1 + x_2 + x_3 + \frac{2[(x_4/2) + (x_5/2) + (x_6/2)]}{3}$$

$$= (M_{11} + 2M_{12} + M_{44})\frac{E^2_{[111]}}{3} \tag{P2.4.4}$$

The strain induced perpendicular to the [111] direction, $x_{[111]\perp}$, is calculated in a similar fashion.

$$x_{[111]\perp} = [M_{11} + 2M_{12} - (M_{44}/2)]\frac{E^2_{[111]}}{3} \tag{P2.4.5}$$

The distortion associated with this strain is depicted in Figure 2.13(b).

It is important to note here that the volumetric strain ($\Delta V/V$) will be given by:

$$\frac{\Delta V}{V} = x_{[111]\parallel} + 2x_{[111]\perp} = (M_{11} + 2M_{12})E^2_{[111]} \tag{P2.4.6}$$

and is independent of the applied field direction.

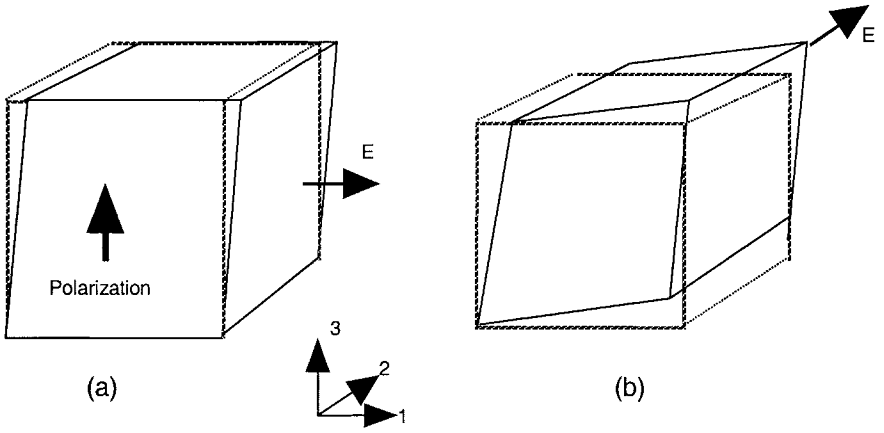

Figure 2.13 Induced strains considered for Problems 2.3 and 2.4: (a) the shear strain induced through the piezoelectric effect for a $BaTiO_3$ single crystal with *tetragonal* point group symmetry 4mm and (b) the electrostrictive strain induced along [111] in a PMN single crystal with *cubic* point group symmetry m3m.

Table 2.2 Piezoelectric strain coefficient (d) matrices.[4]

$$* \begin{cases} d_{mn} = d_{ijk} \ (n = 1,\ 2,\ 3) \\ d_{mn} = 2d_{ijk} \ (n = 4,\ 5,\ 6) \end{cases}$$

Symbol meanings	
·	Zero component
●	Non-zero component
●—●	Equal component
●—○	Equal with opposite signs
◎	-2 times of the ● connected point

I Centro symmetric point group

Point group $\bar{1}$, $2/m$, mmm, $4/m$, $4/mmm$, $m3$, $m3m$, $\bar{3}$, $\bar{3}m$, $6/m$, $6/mmm$ All components are zero

II Non- centro symmetric point group

Triclinic

Point group 1

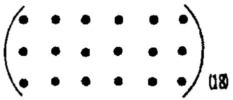

Monoclinic

Point group 2

2 ‖ x_2 (Standard) orientation

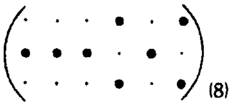

Point group 2

2 ‖ x_3

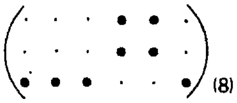

Point group m

$m \perp x_2$ (Standard) orientation

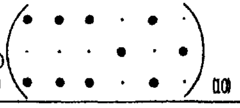

Point group m

$m \perp x_3$

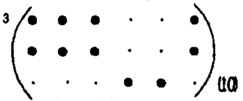

Orthorhombic

Point group 222

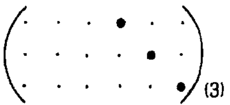

Point group mm2

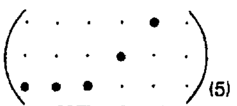

Tetragonal

Point group 4

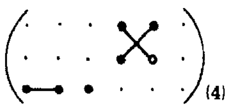

Point group $\bar{4}$

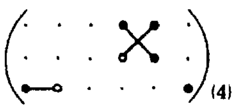

Table 2.2 Piezoelectric strain coefficient (d) matrices.[4] (continued)

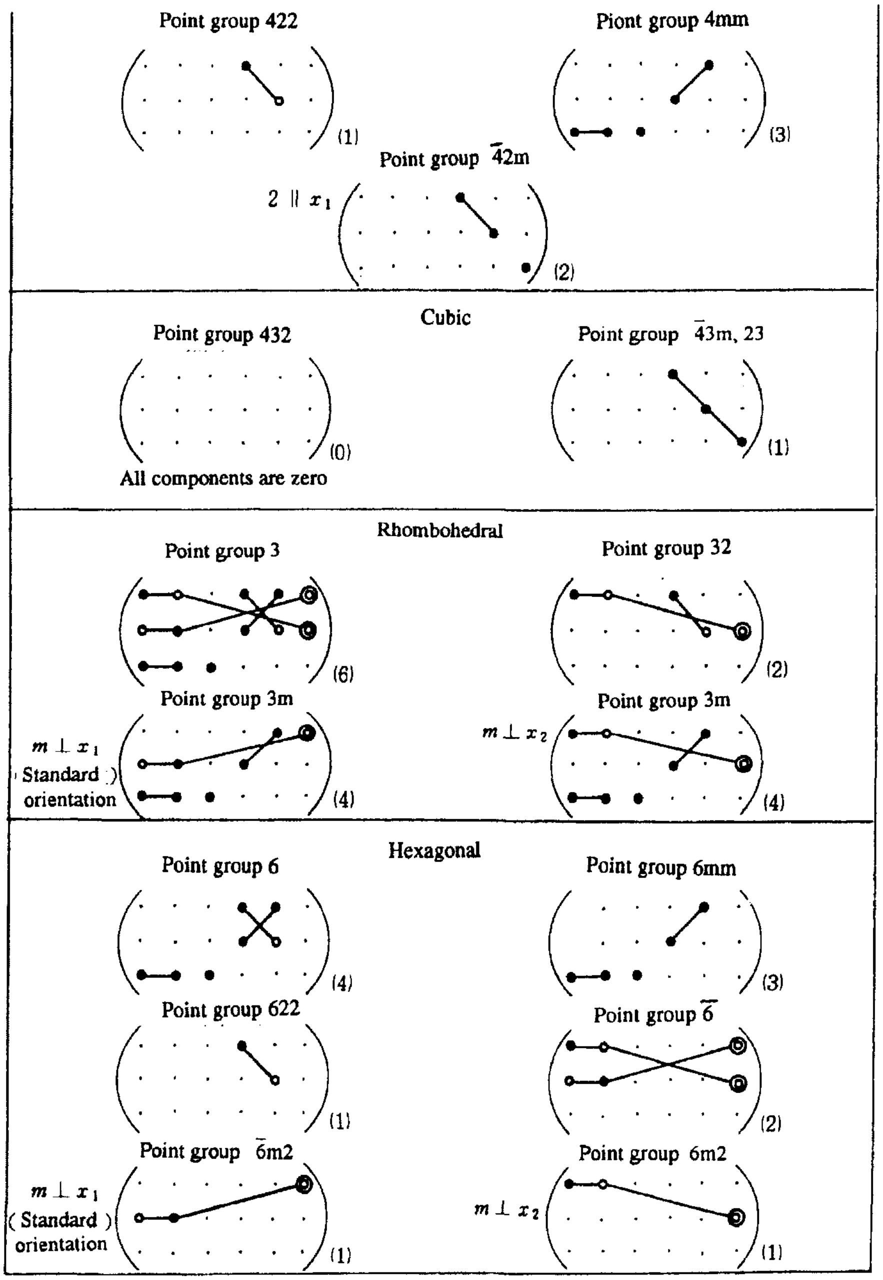
Point group 422
(1)
Piont group 4mm
(3)
Point group $\bar{4}2m$
$2 \parallel x_1$
(2)
Cubic
Point group 432
(0)
All components are zero
Point group $\bar{4}3m$, 23
(1)
Rhombohedral
Point group 3
(6)
Point group 32
(2)
Point group 3m
$m \perp x_1$
(Standard orientation)
(4)
Point group 3m
$m \perp x_2$
(4)
Hexagonal
Point group 6
(4)
Point group 6mm
(3)
Point group 622
(1)
Point group $\bar{6}$
(2)
Point group $\bar{6}m2$
$m \perp x_1$
(Standard orientation)
(1)
Point group 6m2
$m \perp x_2$
(1)

Table 2.3 Electrostriction Q coefficient matrices.[4]

$$
* \begin{cases} Q_{mn} = Q_{ijkl} & (m,\ n = 1,\ 2,\ 3) \\ Q_{mn} = 2\,Q_{ijkl} & (m \text{ か } n = 4,\ 5,\ 6) \\ Q_{mn} = 4\,Q_{ijkl} & (m,\ n = 4,\ 5,\ 6) \end{cases}
$$

Symbol meanings

•	Zero component
●	Non-zero component
●—●	Equal components
●—○	Equal with opposite signs
⊙	2 times of the ʒ ● connected component
◎	-2 times of the ● connected component
×	$2\ (Q_{11} - Q_{12})$

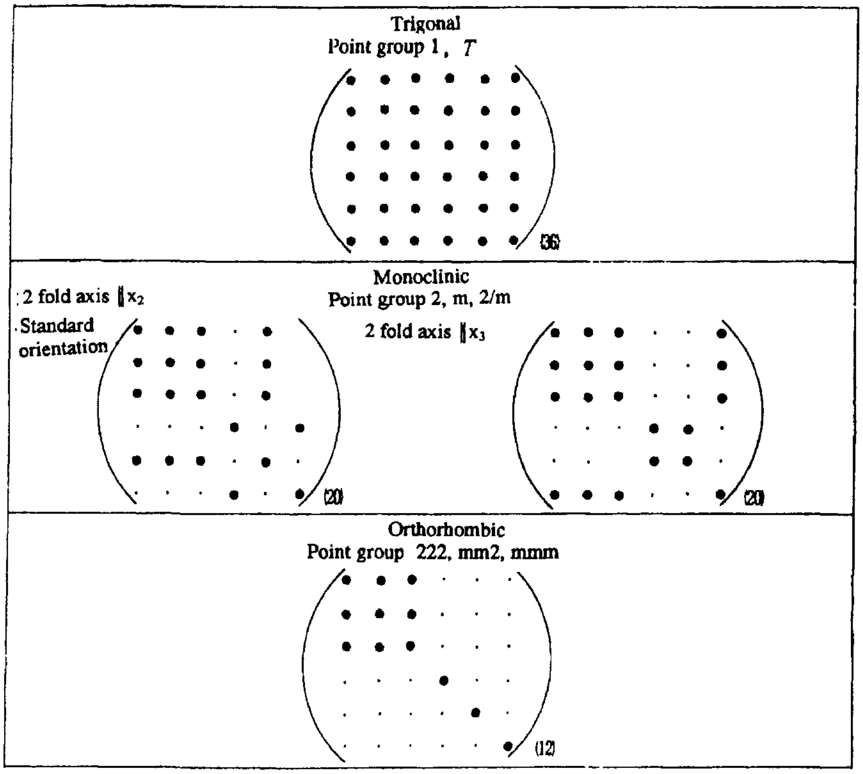
Trigonal
Point group 1, 1̅
(36)
Monoclinic
Point group 2, m, 2/m
; 2 fold axis ∥x₂
· Standard orientation
(20)
2 fold axis ∥x₃
(20)
Orthorhombic
Point group 222, mm2, mmm
(12)

Table 2.3 Electrostriction Q coefficient matrices.[4] (continued)

Point group 4, $\bar{4}$, 4 / m	Teragonal	Point group 4mm, 42m, 422, 4 / mmm
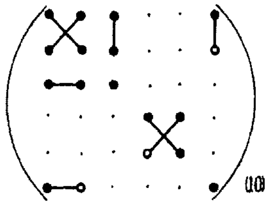		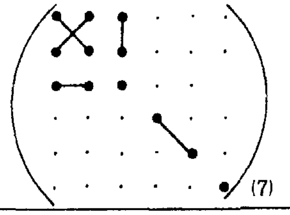
Point group 3, $\bar{3}$	Rhombohedral	Point group 3m, 32, $\bar{3}$m
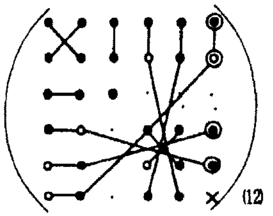		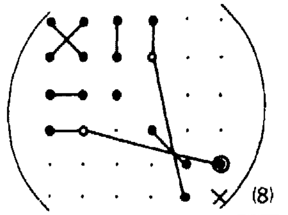
Point group 6, $\bar{6}$, 6 /m	Hexagonal	Point group 6m2, 6mm, 622, 6 / mmm
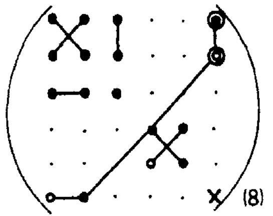		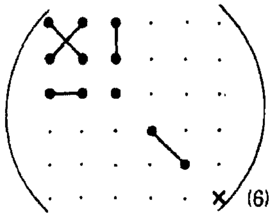
Point group 23, m3	Cubic	Point group 43m, 432, m3m
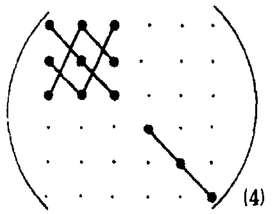		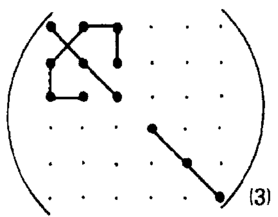
	Isotropic	
	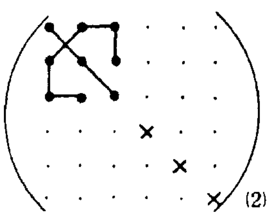	

2.4 THEORETICAL DESCRIPTION OF FERROELECTRIC AND ANTIFERROELECTRIC PHENOMENA

(1) Landau Theory of the Ferroelectric ←→Paraelectric Phase Transition

A thermodynamic description of ferroelectric phenomena is obtained by considering the expansion of the free energy function with respect to the polarization, P. The one-dimensional Landau free energy density function, F(P,T), is expressed as:

$$F(P,T) = (1/2)\alpha P^2 + (1/4)\beta P^4 + (1/6)\gamma P^6 + \cdots \qquad (2.28)$$

The coefficients α, β, γ are temperature dependent. The series does not contain odd powered terms of P because the free energy of the crystal is unaffected by polarization reversal $[P \rightarrow (-P)]$. The phenomenological formulation is applied for the entire temperature range over which the crystal is in its paraelectric and ferroelectric states.

The equilibrium polarization, P, established with the application of an electric field, E, satisfies the condition:

$$\partial F/\partial P = E = \alpha P + \beta P^3 + \gamma P^5 \qquad (2.29)$$

A ferroelectric state is described when the coefficient of the P^2 term, α, is negative, representative of a stable polarized state, and a paraelectric state is described when it is positive. The α coefficient passes through zero when the temperature is equal to the Curie-Weiss temperature, T_o, according to the following relationship:

$$\alpha = \frac{(T - T_o)}{C} \qquad (2.30)$$

where the Curie constant, C, is assumed to be positive and T_o may be equal to or lower than the actual transition temperature T_C (Curie temperature). The temperature dependence of α is associated with thermal expansion and higher order thermal effects.

The Second Order Transition

When β is positive, the γ term may be neglected. Incorporating the definition for α given by Equation (2.30) into Equation (2.29) and applying the condition of zero applied electric field, we may evaluate the spontaneous polarization, P_S, as a function of temperature.

$$\left[\frac{(T - T_o)}{C}\right] P_S \; + \; \beta P_S^3 \; = \; 0 \tag{2.31}$$

We see from this expression that either $P_S^2 = 0$ or $P_S^2 = (T_o - T)/\beta\, C$.

When the temperature is greater than the Curie-Weiss temperature ($T > T_o$), the unique solution $P_S = 0$ is obtained. When the temperature is less than the Curie-Weiss temperature ($T < T_o$), the minimum of the Landau free energy is obtained at:

$$P_S \; = \; \sqrt{\frac{(T_o - T)}{\beta\, C}} \tag{2.32}$$

The phase transition occurs at $T_C = T_o$ and the polarization decreases continuously from its low-temperature maximum to zero at the transition temperature; this is called a *second order transition*

The inverse relative permittivity, 1/K, is defined in terms of these parameters to be:

$$1/K = (\partial E/\partial P) = \; \alpha + 3\beta P^2 \tag{2.33}$$

and for temperatures greater than the Curie-Weiss temperature, where the polarization is zero, when there is no applied electric field:

$$K = C/(T - T_o) \tag{2.34a}$$

while at temperatures less than the Curie-Weiss temperature:

$$K = C/[2(T_o - T)] \tag{2.34b}$$

The temperature dependences of P_S and K are shown in Figure 2.14(a). It should be noted for the temperature dependence of the dielectric constant how it becomes infinite at the transition temperature. Triglycine sulphate is a classic example of a ferroelectric that exhibits the characteristics of a second order transition.

The First Order Transition

When β is negative in Equation (2.28) and γ is taken to be positive, a first order transition is described. The equilibrium condition for $E = 0$ in this case is expressed by:

$$[(T - T_o)/C]\, P_S + \beta\, P_S^3 + \gamma\, P_S^5 = 0 \tag{2.35}$$

and leads to either $P_S = 0$ or to a spontaneous polarization that is a root for:

$$[(T-T_o)/C]+\beta P_S^2+\gamma P_S^4=0 \qquad (2.36)$$

The transition temperature T_C is obtained when the condition that the free energies of the paraelectric and ferroelectric phases are equal is applied such that $F = 0$ and:

$$[(T-T_o)/C]+(1/2)\beta P_S^2+(1/3)\gamma P_S^4=0 \qquad (2.37)$$

which allows us to write:

$$T_C=T_o+(3/16)(\beta^2C/\gamma) \qquad (2.38)$$

Note how, according to this equation, the Curie temperature, T_C, is slightly higher than the Curie-Weiss temperature, T_o, and that a discontinuity in the spontaneous polarization, P_S, as a function of temperature occurs at T_C. This is represented in Figure 2.14(b) where we also see the dielectric constant as a function of temperature peak at T_C. The inverse dielectric constant is also discontinuous at T_C as depicted in the figure and when one extends the linear paraelectric portion of this curve back across the temperature axis it intersects at the Curie-Weiss temperature, T_o. These are characteristic behaviors for a *first order transition*. Barium titanate is a classic example of a ferroelectric that undergoes a first order transition of this type.

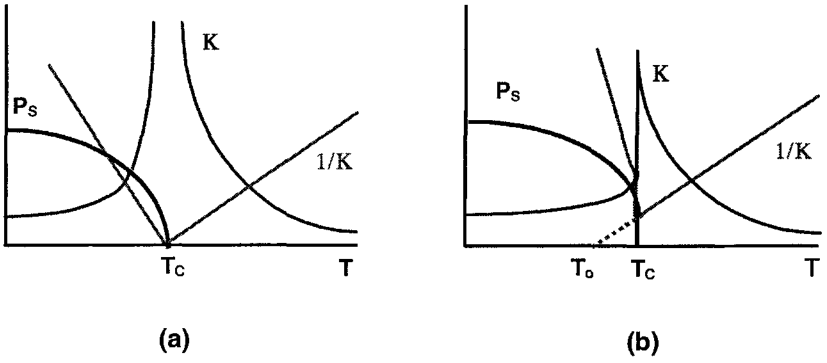

(a) (b)

Figure 2.14 Characteristic features of ferroelectric phase transitions: (a) second order and (b) first order.

(2) Phenomenological Description of Electrostriction

The theory describing the electrostriction effect, as it applies to ferroelectric materials, was formulated in the 1950's by Devonshire[5] and Kay.[6] We will begin with a series expansion of the elastic Gibbs energy function in one dimension:

$$G_1(P,X,T) = (1/2)\alpha P^2 + (1/4)\beta P^4 + (1/6)\gamma P^6 - (1/2)s X^2 - Q P^2 X \quad (2.39)$$

where the coefficient α is defined to be:

$$\alpha = (T - T_o)/C$$

and P is the polarization, X the applied stress, T the temperature, s the elastic compliance, and Q the electrostriction coefficient. This allows us to write the following expressions for the electric field, E, and the strain, x:

$$E = \frac{\partial G_1}{\partial P} = \alpha P + \beta P^3 + \gamma P^5 - 2QPX \quad (2.40)$$

$$x = -\frac{\partial G_1}{\partial X} = sX + QP^2 \quad (2.41)$$

We will consider two important cases in terms of these two equations.

Case I: Zero applied stress

When the applied stress is zero, Equations (2.41) and (2.42) become:

$$E = \alpha P + \beta P^3 + \gamma P^5 \quad (2.42)$$

$$x = QP^2 \quad (2.43)$$

and from Equation (2.42) we may express:

$$1/K = (\partial E/\partial P) = \alpha + 3\beta P^2 + 5\gamma P^4 \quad (2.44)$$

In the paraelectric phase the spontaneous polarization is zero ($P_S = 0$) and, if a small electric field is applied, a polarization will be induced with a magnitude given by:

$$P = \varepsilon_o K E \quad (2.45)$$

The dielectric constant will exhibit a temperature dependence in this state that obeys the Curie-Weiss law:

$$K = C/(T - T_o) \quad (2.46)$$

so that the electrostrictive effect for the paraelectric material is given by:

$$x = Q \varepsilon_o^2 K^2 E^2 \quad (2.47)$$

The electrostrictive coefficient, M, was previously described as the quantity that relates the induced strain to the square of the applied electric field as expressed by Equation (2.13). This electrostriction coefficient can thus be related to the Q coefficient according to the following expression:

$$M = Q\,\varepsilon_o^2 K^2 \tag{2.48}$$

In the ferroelectric phase the spontaneous polarization is nonzero and the polarization of the material, P, under a small applied field is given by:

$$P = P_S + \varepsilon_o K E \tag{2.49}$$

so that:

$$x = Q(P_S + \varepsilon_o K E)^2 = QP_S^2 + 2\varepsilon_o KQP_S E + Q\,\varepsilon_o^2 K^2 E^2 \tag{2.50a}$$

The spontaneous strain is given by:

$$x_S = QP_S^2 \tag{2.51}$$

so that the piezoelectric strain coefficient, d, may be expressed as:

$$d = 2\,\varepsilon_o K Q P_S \tag{2.52}$$

A general depiction of the temperature dependences of these quantities appears in Figure 2.15.

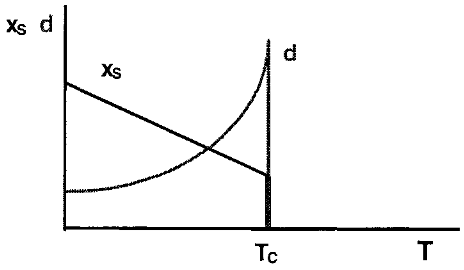

Figure 2.15 General depiction of the temperature dependences of the spontaneous strain, x_S, and the piezoelectric strain coefficient, d.

Incorporating these relationships for the spontaneous strain, x_S, and the piezoelectric strain coefficient, d, into Equation (2.50a) allows us to rewrite it in this alternative form:

$$x = x_S + d\,E + M\,E^2 \tag{2.50b}$$

It is apparent from this expression that we may regard the piezoelectric effect as essentially the electrostrictive effect biased by the spontaneous polarization.

Case II: Non-zero applied stress

When a hydrostatic pressure p is applied [$X = (-)p$], a new term that is proportional to the applied pressure is added to our series expression for the inverse permittivity [Equation (2.44)] such that:

$$1/K = \alpha + 3\,\beta\,P^2 + 5\,\gamma\,P^4 + 2Q_h(p) \tag{2.52}$$

where the hydrostatic electrostrictive coefficient, Q_h, is positive and the constant α is still assumed to be:

$$\alpha = \frac{(T - T_o)}{C}$$

Substituting for α in Equation (2.52), solving for T_o, and considering the first derivative of that function with respect to the applied hydrostatic pressure, p, yields:

$$\frac{\partial T_o}{\partial p} \approx \frac{\partial T_C}{\partial p} = -2\,Q_h C \tag{2.53}$$

It is seen from this equation that T_C and T_o will generally decrease with increasing applied hydrostatic pressure.

Example Problem 2.5

Barium titanate ($BaTiO_3$) has electromechanical properties at room temperature characterized by $d_{33}=320\text{x}10^{-12}$ (C/N), $K_3=800$ and $Q_{33}=0.11$ (m^4C^{-2}). Estimate the magnitude of the spontaneous polarization, P_S, for barium titanate at this temperature.

Solution

Let us use the relation:

$$d_{33} = 2\,\varepsilon_o\,K_3\,Q_{33}\,P_S \tag{P2.5.1}$$

Solving for P_S yields:

$$P_S = \frac{d_{33}}{2\varepsilon_o\,K_3\,Q_{33}}$$

$$= \frac{320 \times 10^{-12}\ (\mathrm{C/N})}{2[8.854 \times 10^{-12}\ (\mathrm{F/m})][800][0.11(\mathrm{m^4C^{-2}})]} \quad \text{(P2.5.2)}$$

→ $P_S = 0.21\ [\mathrm{C/m^2}]$

Example Problem 2.6

In the case of a second order phase transition, the elastic Gibbs energy is expanded in one-dimensional form as follows:

$$G_1(P,X,T) = (1/2)\alpha P^2 + (1/4)\beta P^4 - (1/2)s X^2 - Q P^2 X \quad \text{(P2.6.1)}$$

where only the coefficient α is dependent on temperature: $\alpha = (T-T_o)/C$. Determine the dielectric constant, K, the spontaneous polarization, P_S, the spontaneous strain, x_S, and the piezoelectric strain coefficient, d, as a function of temperature.

Solution

$$E = (\partial G_1/\partial P) = \alpha P + \beta P^3 - 2Q P X \quad \text{(P2.6.2)}$$

$$x = -(\partial G_1/\partial X) = sX + QP^2 \quad \text{(P2.6.3)}$$

When the external stress is zero, we obtain the three characteristic equations:

$$E = \alpha P + \beta P^3 \quad \text{(P2.6.4)}$$

$$x = QP^2 \quad \text{(P2.6.5)}$$

$$1/K = (\partial E/\partial P) = \alpha + 3\beta P^2 \quad \text{(P2.6.6)}$$

Initially setting E = 0, we obtain two stable states characterized by the following conditions: $P_S^2=0$ or $P_S^2=-(\alpha/\beta)$. In the paraelectric phase ($T>T_o$), the spontaneous polarization is zero ($P_S = 0$) so that $1/K=\alpha$ and:

$$K = C/(T - T_o) \quad \text{(P2.6.7)}$$

In the ferroelectric phase ($T<T_o$) and we may write:

$$P_S = \sqrt{\frac{(T_o - T)}{\beta C}} \quad \text{(P2.6.8)}$$

so that $[1/K = \alpha + 3\beta P^2 = -2\alpha]$ and:

$$K = C/2(T_o - T) \tag{P2.6.9}$$

Combining this result with Equation (P2.6.8) yields:

$$x_S = QP_S^2 = Q\left[\frac{(T_o - T)}{\beta C}\right] \tag{P2.6.10}$$

Combining Equations (P2.6.8) and (P2.6.9), we may rewrite our expression for the piezoelectric strain coefficient, d, in the following form:

$$d = 2\varepsilon_o K\, Q\, P_S = \varepsilon_o Q\sqrt{\frac{C}{(T_o - T)\beta}} \tag{P2.6.11}$$

---

(3) Direct and Converse Electromechanical Effects

So far we have discussed the electric field-induced strains produced by the *converse piezoelectric effect*, $x = d\,E$, and the *direct electrostriction effect*, $x = M\,E^2$. Let us consider here the corresponding effects related to the material's response to an applied stress, X, which is applicable to sensors. The *direct piezoelectric effect* is simply the change in the polarization induced by an applied stress, expressed by:

$$P = d\,X \tag{2.54}$$

When considering the electrostrictive effect, it is the change in the dielectric permittivity with applied stress that is the operative response. This is expressed by:

$$1/\varepsilon_o K = 2QX \tag{2.55}$$

which is representative of the *converse electrostriction effect.*

Example Problem 2.7

One of the lead zirconate titanate (PZT) ceramics has a piezoelectric coefficient, $d_{33}=590\times10^{-12}$(C/N), a dielectric constant, $K_3=3400$, and an elastic compliance, $s_{33}=20\times10^{-12}$ (m^2/N).

(a) Calculate the induced strain under an applied electric field of $E_3=10\times10^5$(V/m). Then, calculate the generative stress under a completely clamped (mechanically constrained) condition.

(b) Calculate the induced electric field under an applied stress of $X_3=3\times10^7$(N/m^2), which corresponds to the generative stress in (a). The magnitude of the induced electric field does not correspond to the magnitude of the applied electric field in (a) [that is, 10×10^5(V/m)]. Explain why.

Solution

Part (a):

$$x_3 = d_{33} E_3 = [590 \times 10^{-12} (\mathrm{C/N})][10 \times 10^5 \,(\mathrm{V/m})] \tag{P2.7.1}$$
$$\rightarrow \; x_3 = 5.9 \times 10^{-4}$$

Under completely clamped (mechanically constrained) conditions,

$$X_3 = x_3/ s_{33} = 5.9 \times 10^{-4}/20 \times 10^{-12} \,(\mathrm{m^2/N}) \tag{P2.7.2}$$
$$\rightarrow \; X_3 = 3.0 \times 10^7 \,(\mathrm{N/m^2})$$

Part (b):

$$P_3 = d_{33} X_3 = [590 \times 10^{-12} \,(\mathrm{C/N})][3 \times 10^7 \,(\mathrm{N/m^2})] \tag{P2.7.3}$$
$$\rightarrow \; P_3 = 1.77 \times 10^{-2} \,(\mathrm{C/m^2})$$

$$E_3 = P_3/\varepsilon_o K = [1.77 \times 10^{-2} \,(\mathrm{C/m^2})]/[3400][8.854 \times 10^{-12} \,(\mathrm{F/m})] \tag{P2.7.4}$$
$$\rightarrow \; E_3 = 5.9 \times 10^5 \,(\mathrm{V/m})$$

The induced field is only 59% of the electric field applied for the case given in Part (a). This is most readily explained in terms of the electromechanical coupling factor, k.

Considering the mechanical energy produced through the electromechanical response of the piezoelectric with respect to the electrical energy supplied to the material, the so-called *electromechanical coupling factor, k,* is defined according to the following:

$$k^2 = \frac{[\text{Stored Mechanical Energy}]}{[\text{Input Electrical Energy}]}$$

$$= \frac{(\tfrac{1}{2})[x^2/s]}{(\tfrac{1}{2})[\varepsilon_o K E^2]} = \frac{(\tfrac{1}{2})[(dE)^2/s]}{(\tfrac{1}{2})[\varepsilon_o K E^2]} = \frac{d^2}{s\varepsilon_o K} \tag{P2.7.5a}$$

An alternative way of defining the electromechanical coupling factor is by considering the electrical energy produced through the electromechanical response of the piezoelectric with respect to the mechanical energy supplied to the material, which leads to the same outcome:

$$k^2 = \frac{[\text{Stored Electrical Energy}]}{[\text{Input Mechanical Energy}]}$$

$$= \frac{(\frac{1}{2})[P^2/\varepsilon_o K]}{(\frac{1}{2})[s X^2]} = \frac{(\frac{1}{2})[(d X)^2/\varepsilon_o K]}{(\frac{1}{2})[s X^2]} = \frac{d^2}{s \varepsilon_o K} \qquad \text{(P2.7.5b)}$$

In this case, we may evaluate the electromechanical coupling factor associated with the piezoelectric response, taking place through d_{33}, and find that:

$$k_{33}^2 = \frac{d_{33}^2}{(s_{33}\,\varepsilon_o\,K_3)} = \frac{[590 \times 10^{-12}\,(C/N)]^2}{[20 \times 10^{-12}\,(m^2/N)][8.854 \times 10^{-12}\,(F/m)][3400]}$$

$$\rightarrow\ k_{33}^2 = 0.58$$

So we see why the induced electric field determined in Part (b) has a magnitude that is only a fraction of the field applied in Part (a) of 10×10^5 (V/m). Here we see that this fraction corresponds roughly to about k^2. In this sense we may regard the quantity k^2 to be the transduction ratio associated with a particular electrical-to-mechanical or mechanical-to-electrical piezoelectric event.

(4) The Temperature Dependence of Electrostriction

Several expressions for the electrostriction coefficient, Q, have been given in this chapter. Based on these relationships various experimental methods for determining the electrostriction coefficients of various classes of materials have been developed. Among the more commonly employed methods for determining the electrostrictive Q coefficients for ferroelectric materials are those that make use of the following data:

a) the electric field-induced strain of the material measured for the paraelectric phase,
b) the spontanteous polarization and spontaneous strain of the material measured for the ferroelectric phase,
c) the piezoelectric strain coefficients determined from electric field-induced strains measured for the ferroelectric phase either directly or by means of a resonance method,
d) the dielectric constant measured as a function of pressure for the paraelectric phase.

The electrostrictive coefficients Q_{33} and Q_{13} for the complex perovskite $Pb(Mg_{1/3}Nb_{2/3})O_3$ (Curie temperature about 0°C) are shown plotted as a function of temperature in Figure 2.16.[7] No anomalies in the magnitudes of the electrostrictive coefficients Q_{33} and Q_{13} are observed within this range of temperatures over which the paraelectric to ferroelectric transition would occur and the material becomes piezoelectric. Overall, the electrostrictive coefficients for this material are seen to be essentially temperature independent.

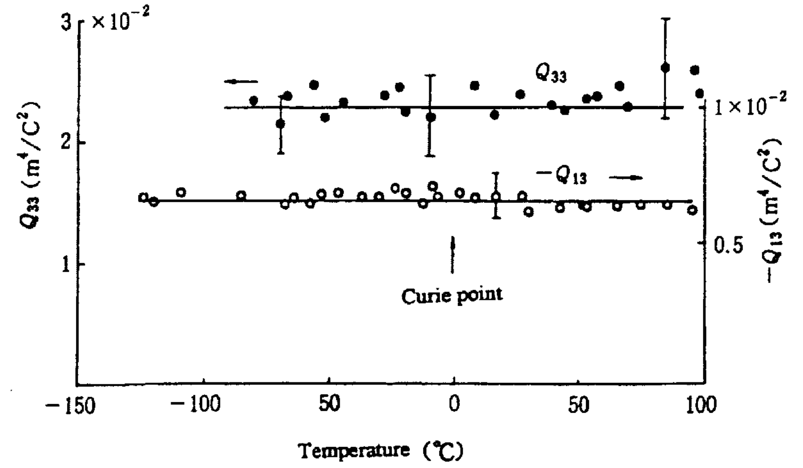

Figure 2.16 The electrostriction coefficients Q_{33} and Q_{13} for the complex perovskite $Pb(Mg_{1/3}Nb_{2/3})O_3$ plotted as a function of temperature.[7]

(5) The Piezoelectric Effect and Crystal Symmetry

Although some rather thorough studies of the piezoelectric effect for several piezoelectrics in single crystal form have been made in the past, the actual use of single crystal piezoelectrics has not been actively pursued. This is mainly due to the fact that the most popular lead zirconate titanate (PZT)-based materials are generally synthesized in polycrystalline form. There is currently renewed interest in the single crystal studies, however, spurred by recent developments in the production and application of epitaxially grown thin films (pseudo single crystals) and high quality single crystals of various compositions. Piezoelectric single crystals generally have higher strain coefficients, d, and generate larger strains than their polycrystalline counterparts and therefore are especially attractive for actuator applications at this time.

A series of theoretical calculations made on perovskite ferroelectric crystals suggests that large effective piezoelectric constants and electromechanical coupling factors can be obtained when the applied electric field direction is canted by 50-60 degrees from the spontaneous polarization direction. This principle is illustrated in

Figure 2.17. When the electric field is applied in this direction, the piezoelectric response is acting through the d_{15} strain coefficient. Maximum strain is thus induced since the shear coupling that occurs via this coefficient is highest in most piezoelectric crystals with perovskite structure.

The dependence of the piezoelectric properties on crystallographic orientation has been modeled phenomenologically for PZT compositions in the vicinity of the morphotropic phase boundary.[8,9] The results summarized here have been determined by simply transforming the dielectric stiffness, piezoelectric coefficients, and elastic compliances from one orientation to another via the transformation matrices, using original data collected for the compositions of interest.[10] A surface representing the variation of the dielectric constant with crystallographic orientation for the rhombohedral 60/40 PZT composition appears in Figure 2.18. The dielectric constant decreases monotonically as the sample cut direction is varied from the spontaneous polarization (P_S) direction along the z-axis (z-cut plate) to the y direction (y-cut plate). This trend is observed for both tetragonal and rhombohedral phases, as shown in Figure 2.19.

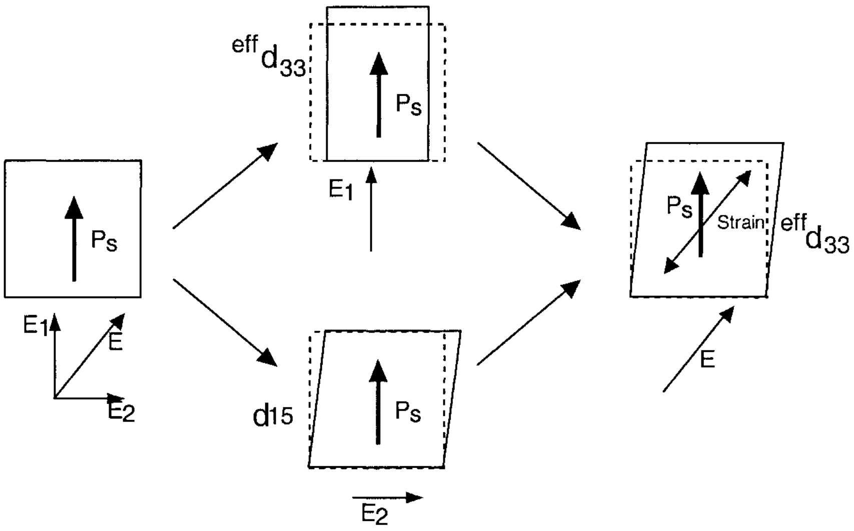

Figure 2.17 Schematic depiction of the deformation of a ferroelectric single cystal produced by an electric field, E, applied at different angles with respect to the spontaneous polarization, P_S, direction.

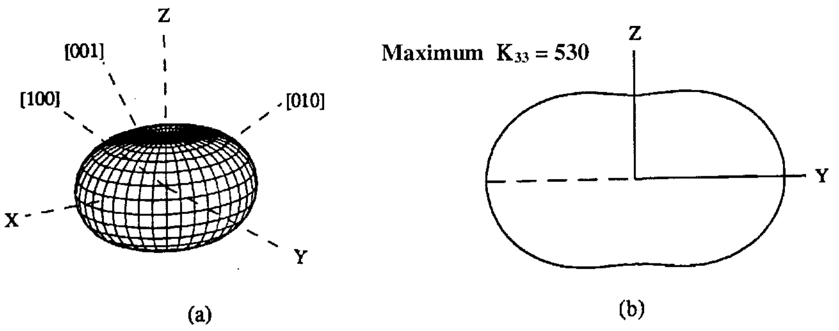

Figure 2.18 The dielectric constant of rhombohedral PZT 60/40: (a) the quadric surface and (b) the y-z cross-section of the surface.[8]

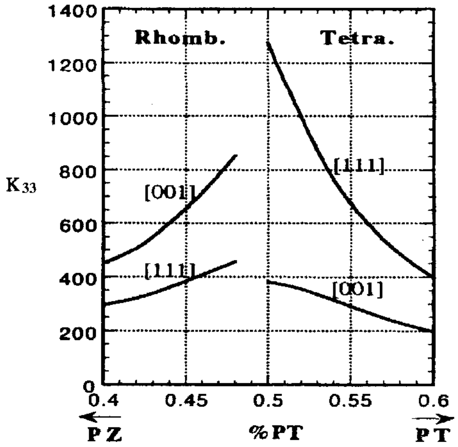

Figure 2.19 Effective dielectric constant of PZT as a function of composition.[9] (Note that the dielectric constant along P_S is the smallest for both the rhombohedral and tetragonal phases.)

In contrast, the electromechanical coupling exhibits an interesting crystal anisotropy. A pronounced variation in the coupling is observed with orientation as shown in Figure 2.20 in which the quadric surface representing the effective d_{33} for the tetragonal 48/52 PZT composition and the (010) cross-section of this surface are depicted. We see from this surface that the ${}^{eff}d_{33}$ attains its maximum in the direction of the spontaneous polarization, [001].

A quite different trend is observed for the rhombohedral 52/48 PZT composition, which is depicted in Figure 2.21. Here we see ${}^{eff}d_{33}$ reach its maximum in the y-z plane at an angle 59.4° from the z-axis. This is very close to the [001] directions of the paraelectric (cubic perovskite) phase. Theoretically determined effective piezoelectric strain coefficients, ${}^{eff}d_{33}$, along the [001] and [111] directions in PZT are plotted as a function of composition in Figure 2.22. A dramatic increase in the ${}^{eff}d_{33}$ along [001] is apparent on approaching the morphotropic phase boundary from the rhombohedral side. This suggests that the optimum response of actuators and sensors made from PZT epitaxial thin films will be attained for those with rhombohedral compositions in the vicinity of the morphotropic phase boundary that have a [001] orientation. These results also indicate that a ${}^{eff}d_{33}$ four times greater than what has been experimentally observed for PZT films so far is possible for specimens of this composition and orientation.

The exceptionally high electromechanical coupling observed for $Pb(Zn_{1/3}Nb_{2/3})O_3$-$PbTiO_3$ and $Pb(Mg_{1/3}Nb_{2/3})O_3$-$PbTiO_3$ single crystals at their morphotropic phase boundaries can be described in similar terms. We will look more closely at experimental data characterizing the response of these materials in Chapter 3.

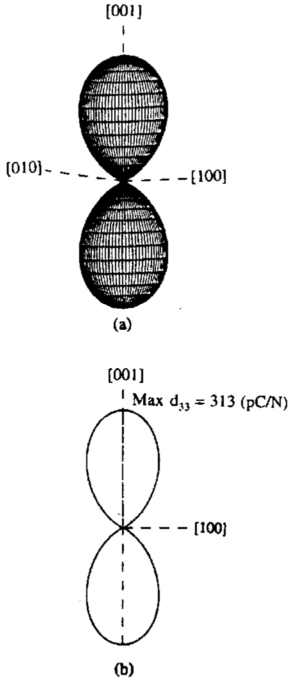

Figure 2.20: The effective d_{33} for (tetragonal) 48/52 PZT: (a) the quadric surface and (b) the (010) cross-section of the quadric surface.[9]

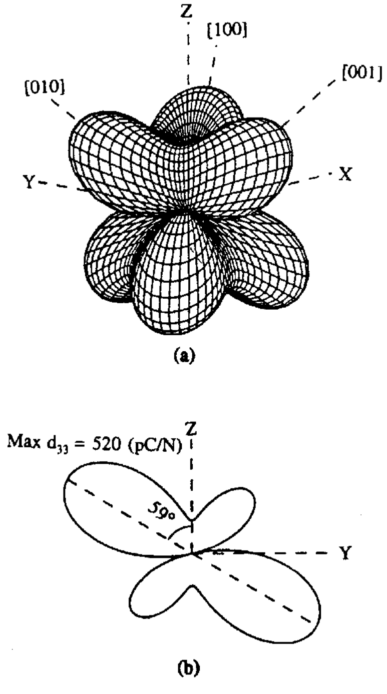

Figure 2.21: The effective d_{33} for (rhombohedral) 52/48 PZT: (a) the quadric surface and (b) the y-z cross-section of the quadric surface.[9]

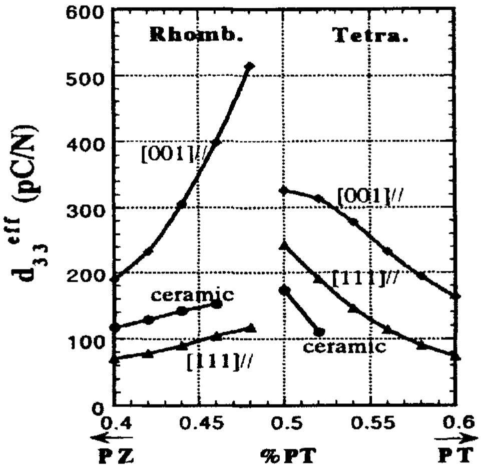

Figure 2.22 Effective d_{33} of PZT as a function of composition.[9]

Example Problem 2.8

The variations of the dielectric constant, K_{33}, and the piezoelectric strain coefficient, d_{33}, with crystallographic orientation for a tetragonal PZT are shown in Figure 2.23. Let us consider a uniformly oriented polycrystalline sample. Discuss the change in the K_{33} and d_{33} before and after poling.

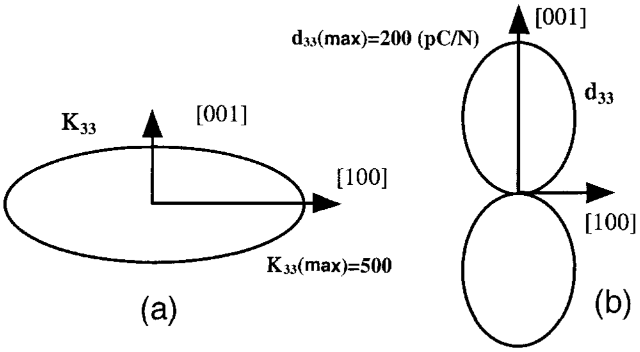

Figure 2.23 Quadric surfaces representing (a) the dielectric constant, K_{33}, and (b) the piezoelectric strain coefficient, d_{33}, for a tetragonal PZT.

Solution

Before the specimen is poled, the polarization directions of the individual crystallites are randomly oriented so that the dielectric constant has a value intermediate between K_{33}(min) and K_{33}(max), and the piezoelectric coefficient, d_{33}, is zero.

When the sample is poled, the polarization vectors of the crystallites become aligned in the poling direction (the "z" or [001] direction), resulting in an overall decrease in the dielectric constant. The piezoelectric coefficient, d_{33}, will increase monotonically with increasing poling field strength, saturating when the field reaches a level close to the coercive field.

(6) Phenomenology of Antiferroelectrics

The simplest model for antiferroelectric materials is the so-called "one-dimensional two-sublattice model," in which the electrostrictive coupling is described in terms of Kittel's free energy expression for antiferroelectrics.[7,8] As the name suggests, the model treats the lattice as a one-dimensional system, in which a superlattice (with dimensions twice that of the unit cell) is formed between two neighboring sublattices with sublattice polarizations, P_a and P_b. The state defined by $P_a=P_b$ represents the ferroelectric phase, while that defined by $P_a=(-P_b)$ represents the antiferroelectric phase. When considering the electrostriction effect, the coupling between the two sublattices is generally ignored and the strains from the two sublattices are QP_a^2 and QP_b^2, respectively (assuming equal electrostriction coefficients, Q, for both sublattices). The total strain induced in the crystal thus becomes:

$$x = Q\,(P_a^2 + P_b^2)\,/\,2 \qquad (2.56)$$

Where antiferroelectricity arises from a coupling between sublattices, however, it is more appropriate to also consider the sublattice coupling in our description of the electrostrictive effect. We will include the coupling term, Ω, in the antiferroelectric free energy equation in order to arrive at this more complete description of the electrostriction. The free energy may then be expressed in the following form:

$$\begin{aligned} G_1 &= (1/4)\,\alpha\,(P_a^2+P_b^2) + (1/8)\,\beta\,(P_a^4+P_b^4) + (1/12)\,\gamma\,(P_a^6+P_b^6) \\ &\quad + (1/2)\,\eta\,P_aP_b - (1/2)\,\chi_T\,p^2 + (1/2)\,Q_h\,(P_a^2+P_b^2+2\Omega\,P_aP_b)p \qquad (2.57) \end{aligned}$$

where p is the hydrostatic pressure, χ_T is the isothermal compressibility, and Q_h is the hydrostatic electrostriction coefficient. Making use of the transformations for the ferroelectric polarization, $P_F=(P_a+P_b)/2$, and the antiferroelectric polarization, $P_A=(P_a-P_b)/2$ in this equation yields:

$$\begin{aligned} G_1 = {} & (1/2)\alpha[P_F^2 + P_A^2] + (1/4)\beta[P_F^4 + P_A^4 + 6P_F^2P_F^2] \\ & + (1/6)\gamma[P_F^6+P_A^6+15P_F^4P_A^2+15P_F^2P_A^4] + (1/2)\eta[P_F^2 - P_A^2] \\ & - (1/2)\,\chi_T\,p^2 + Q_h\,[P_F^2 + P_A^2 + \Omega(P_F^2 - P_A^2)]p \qquad (2.58) \end{aligned}$$

The dielectric and elastic equations of state may then be written as follows:

$$E = \partial G_1/\partial P_F$$
$$= P_F[\alpha+\eta+2Q_h(1+\Omega)p+\beta P_F^2+3\beta P_A^2+\gamma P_F^4+10\gamma P_F^2P_A^2+ 5\gamma P_A^4] \quad (2.59)$$

$$0 = \partial G_1/\partial P_A$$
$$= P_A[\alpha-\eta+2Q_h(1-\Omega)p+\beta P_A^2+3\beta P_F^2+\gamma P_A^4+10\gamma P_F^2P_A^2+ 5\gamma P_F^4] \quad (2.60)$$

$$\Delta V/V = \partial G_1/\partial p$$
$$= -\chi_T p + Q_h(1+\Omega)P_F^2 + Q_h(1-\Omega)P_A^2 \quad (2.61)$$

We see from Equation (2.61) how the contribution to the volume change related to the ferroelectric polarization, P_F, is given by:

$$(\Delta V/V)_{ind} = Q_h(1+\Omega)P^2_{F(ind)} \quad (2.62)$$

Below the phase transition temperature, which is called the *Néel temperature* for an antiferroelectric, the spontaneous volume strain, $(\Delta V/V)_S$, and the spontaneous antiferroelectric polarization, $P_{A(S)}$, are related according to:

$$(\Delta V/V)_S = Q_h(1 - \Omega)\, P_{A(S)}^2 \quad (2.63)$$

We see from this relationship that even when a given perovskite crystal has a positive hydrostatic electrostriction coefficient, Q_h, the spontaneous volume strain can be positive or negative depending on the value of Ω ($\Omega<1$ or $\Omega>1$). If the intersublattice coupling is stronger than the intrasublattice coupling, a volume contraction is observed at the Néel temperature. This is in stark contrast to what is observed for ferroelectrics, which always undergo a volume expansion at the Curie point.

The spontaneous strain induced in a case where $\Omega>1$ is illustrated in Figure 2.24(a). When P_a and P_b are parallel, as occurs for the ferroelectric phase, the Ω term will act to effectively increase the spontaneous strain, x_S. When they are antiparallel, as occurs for the antiferroelctric phase [Figure 2.24(b)], the Ω term acts to decrease the strain. This phenomenological treatment accurately describes what is observed experimentally for the antiferroelectric perovskite $PbZrO_3$ among others.[9] The induced strain for an antiferroelectric $Pb_{0.99}Nb_{0.02}[(Zr_{0.6}Sn_{0.4})_{0.94}Ti_{0.06}]_{0.98}O_3$ ceramic is plotted as a function of applied electric field in Figure 2.25.[10] The volume change associated with the field-induced transition from the antiferroelectric to ferroelectric phase can be estimated by:

$$\Delta V/V = Q_h(1+\Omega)P_{F(S)}^2 - Q_h(1 - \Omega)P_{A(S)}^2 = 2\, Q_h\, \Omega\, P_{F(S)}^2 \quad (2.64)$$

Here, we assume that the magnitudes of P_a and P_b do not change drastically through the phase transition.

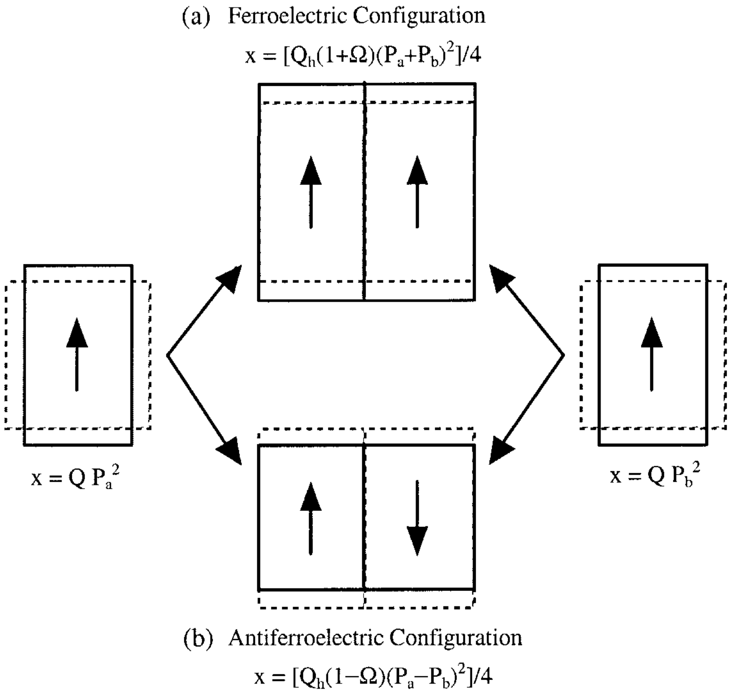
(a) Ferroelectric Configuration
$x = [Q_h(1+\Omega)(P_a+P_b)^2]/4$
$x = Q P_a^2$
$x = Q P_b^2$
(b) Antiferroelectric Configuration
$x = [Q_h(1-\Omega)(P_a-P_b)^2]/4$

Figure 2.24 Schematic representation of the sublattice coupling accompanying the electrostrictive strain response (for $\Omega > 0$).

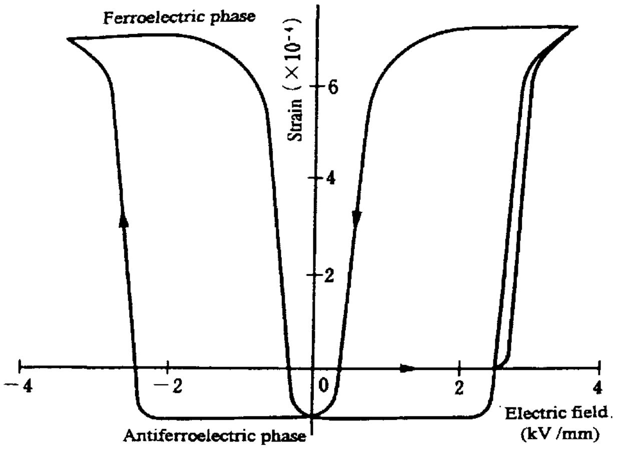

Figure 2.25 The electric field-induced strain in a Pb(Zr,Sn)O_3-based antiferroelectric.

The ferroelectric strain state is characterized by both the significant strain induced by the electric field, and the stability of the state, which can be optimized by carefully adjusting the Ti content. A given strain state, once induced, can be well maintained even when the applied field is removed, which is an important feature of a *shape memory function.*

2.5 PHENOMENOLOGY OF MAGNETOSTRICTION

Similar to piezoelectrics, certain magnetic materials can also exhibit spontaneous strains along the magnetization direction, and magnetostriction when a magnetic field is applied. Magnetostriction occurs in these materials due to the reorientation of the spontaneous magnetization in response to an applied magnetic field. Typical strain curves representing the strain, ($\Delta l/l$), developed in such a magnetic material parallel to the applied magnetic field ($\lambda_{//}$) and perpendicular to the field ($\lambda_{\perp}$) are shown in Figure 2.26. Depending on the material, the parallel strain may be positive (an extension) or negative (a contraction). The perpendicular strain will be positive or negative depending on the value of Poisson's ratio for the material.

A simple model representing the spontaneous strain associated with the magnetization in a ferromagnetic material is pictured in Figure 2.27. If we assume that each magnet depicted in this diagram corresponds to the spin associated with an iron (Fe) atom in a metallic crystal, the opposite poles of adjacent magnets will attract, resulting in contraction of the lattice in the b-direction. At the same time, adjacent atoms with parallel spins repel each other, resulting in expansion of the lattice in the a-direction. The magnetic energy associated with the resulting shift of lattice atoms is ultimately balanced by the elastic energy of the lattice, and an equilibrium level of spontaneous strain is established.

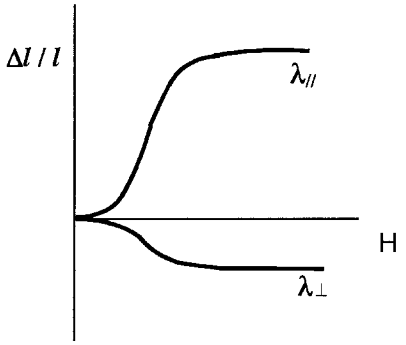

Figure 2.26 Typical strain curves representing the strain ($\Delta l/l$) developed in a magnetic material parallel to the applied magnetic field ($\lambda_{//}$) and perpendicular to the field ($\lambda_{\perp}$).

In magnetic crystals with a cubic structure, such as Fe and Ni, the magnitude of the induced strain, $\Delta l/l$, in the direction of the applied magnetic field can be expressed as:

$$\begin{aligned}\Delta l/l = \; & (3/2)\lambda_{100}[\alpha_1^2\beta_1^2+\alpha_2^2\beta_2^2+\alpha_3^2\beta_3^2-1/3] \\ & + (3)\lambda_{111}[\alpha_1\alpha_2\beta_1\beta_2+\alpha_2\alpha_3\beta_2\beta_3+\alpha_3\alpha_1\beta_3\beta_1] \qquad (2.65)\end{aligned}$$

Here, λ_{100} and λ_{111} are the magnitudes of the magnetostriction when the magnetization is completely saturated along [100] and [111], respectively. Higher order perturbation is neglected.[15]

When the magnetic material is in a polycrystalline or amorphous form with perfectly isotropic characteristics, $\lambda_{100} = \lambda_{111} = \lambda_s$, so that Equation (2.65) may be simplified to:

$$\Delta l/l = (3/2)\,\lambda_s(\cos^2\theta-1/3) \qquad (2.66)$$

where θ is the angle between the magnetization and the strain directions, and λ_s is the saturated magnetostriction. When the sample is polycrystalline, the following relationship is satisfied:

$$\lambda_s = 0.4\,\lambda_{100} + 0.6\,\lambda_{111} \qquad (2.67)$$

The quantities λ_{100} and λ_{111} are determined at the saturated strain levels in a single crystal, and λ_s can be determined from the saturated strain in a polycrystalline sample.

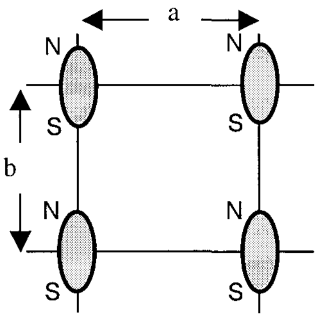

Figure 2.27 A simple model representing the spontaneous strain associated with the magnetization in a ferromagnetic material.

2.6 FERROELECTRIC DOMAIN REORIENTATION

(1) Strains Accompanying Ferroelectric Domain Rotation

It has been assumed in the phenomenological descriptions presented so far that the materials in question are *monodomain single crystals* and the application of the field does not change their state of polarization or magnetization. When considering piezoelectric ceramics, however, this assumption does not strictly hold. The material typically used in an actual device may have a multiple domain structure even in a single crystal form, and a much more complicated domain structure will exist in a polycrystalline ceramic.

The strains induced parallel ($\Delta l/l = x_3$) and perpendicular ($\Delta l/l = x_1$) to the applied electric field in a 7/62/38 (Pb,La)(Zr,Ti)O_3 (PLZT) ceramic are shown in Figure 2.28. For a cycle with a small maximum electric field (curve a in the figure), the field-induced strain curve appears nearly linear, and reflects primarily the "*converse piezoelectric effect.*" As the amplitude of the applied electric field is increased, however, the strain curve becomes more hysteretic, and finally transforms into the characteristic symmetric butterfly shape when the electric field exceeds a certain critical value known as the *coercive field.* This is caused by the switching of ferroelectric domains under the applied electric field, resulting in a different state of polarization. Strictly speaking, this composition of PLZT undergoes this change in polarization state in two stages:

1) individual domain reorientation in each grain, and

2) overall multidomain reorientation and domain wall movement within the entire polycrystalline structure (which may be regarded as just an assembly of randomly oriented tiny crystallites).

The reorientation of domains in a $BaTiO_3$ single crystal subjected to an applied electric field is apparent in the series of CCD images that appear in Figure 2.29. The 90° domain walls are eliminated with increasing electric field until the entire crystal finally attains a single domain state. In a polycrystalline specimen, however, domain wall motion tends to be suppressed by grain boundaries, and a purely monodomain state cannot be achieved.

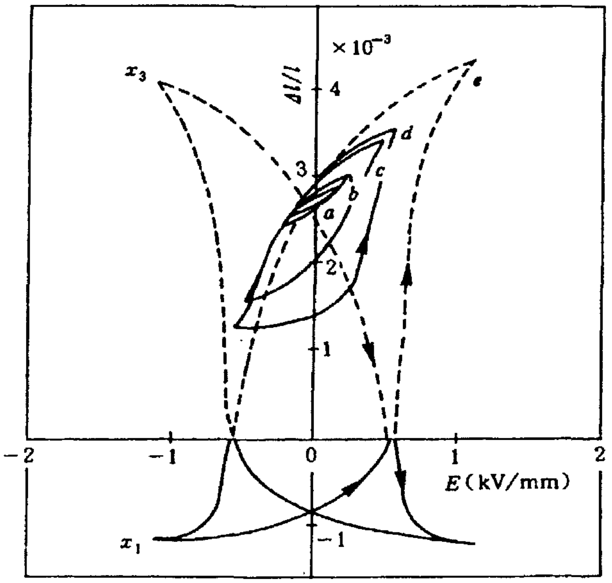

Figure 2.28 The electric field-induced strain in a piezoelectric PLZT 7/62/38 ceramic.

A schematic depiction of the domain reorientation that occurs in a polycrystalline body under an applied electric field appears in Figure 2.30. Suppose an electric field is applied to a sample that has been poled in the opposite direction. The crystal should shrink as the applied field is initially increased, because the field direction opposes that of the remanent polarization. The shrinkage will proceed until it reaches a certain minimum that corresponds to an applied field strength equal to the *coercive field*, E_c, when polarization reversal will begin to occur in each grain. Above E_c the crystal will start to expand and continue to deform in this manner until the applied field strength reaches a certain saturation level, E_{max}. At E_{max}, all the reversible polarization vectors associated with the individual domains have been reversed, and the crystal displays "piezoelectric" behavior once again with a small hysteresis. As the electric field is decreased from this level, no further reorientation of the polarization should occur except for a few unstable domains that might still remain. The strain decreases monotonically as the field is reduced to zero. The polarization state at E=0 is equivalent to the initial state but with all the polarization directions reversed. The crystal is now essentially poled in the positive direction. *Poisson's ratio*, σ, which is the ratio of the transverse strain (in this case, a contraction) to the longitudinal strain (here an expansion) is similar for all perovskite piezoelectric ceramics, about 0.3.

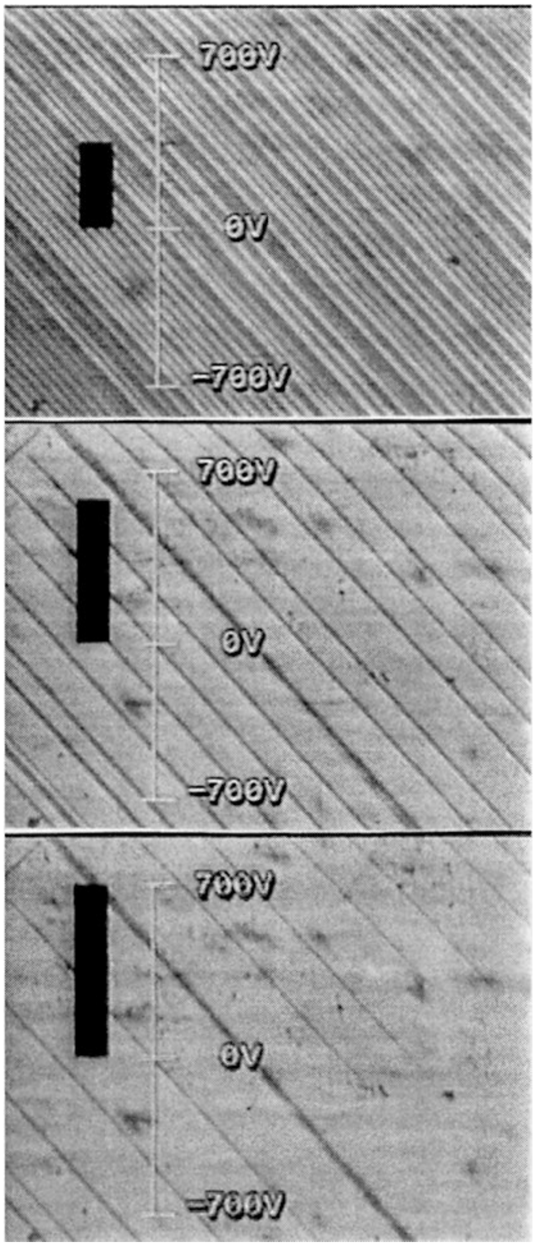
700V
0V
-700V
700V
0V
-700V
700V
0V
-700V

Figure 2.29 Domain reorientation in a $BaTiO_3$ single crystal. E direction: ↑.

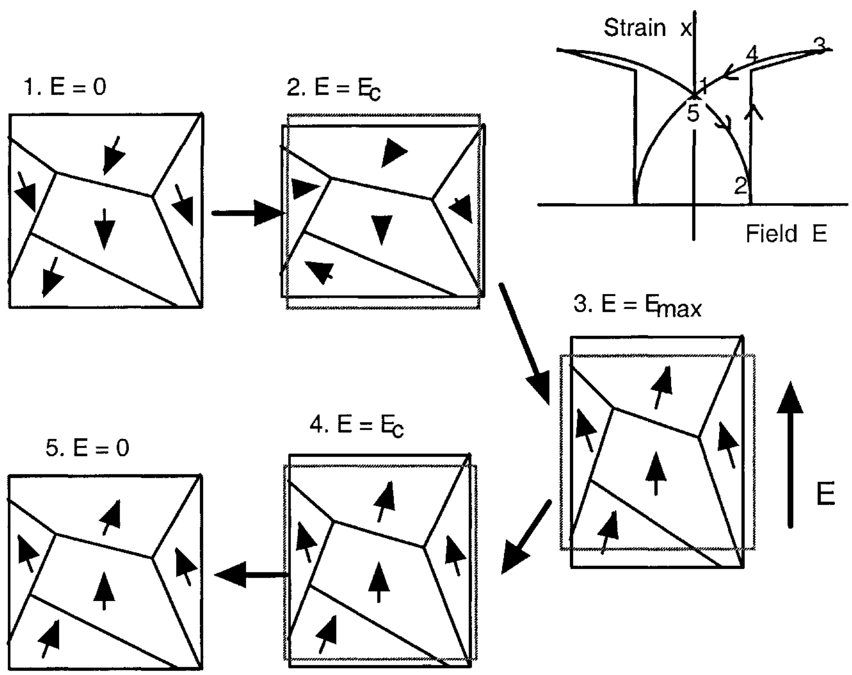

Figure 2.30 A schematic depiction of the reorientation of ferroelectric domains in a polycrystalline material under an applied electric field.

Example Problem 2.9

Barium titanate ($BaTiO_3$) has a rhombohedral crystal symmetry at liquid nitrogen temperature (−196°C) and the distortion from the cubic structure is not very large (=1°). Determine all possible angles between the two non-180° domain walls.

Solution

The polarization of barium titanate at this temperature is oriented along the <111> directions of the perovskite cell. Let's consider the three shown in Figure 2.31(a): $[111]$, $[11\bar{1}]$, and $[1\bar{1}\bar{1}]$. Assuming a head-to-tail alignment of the spontaneous polarization across the domain wall as depicted in Figure 2.31(b), we expect the plane of the domain wall plane to be normal to one of the following directions or their equivalent directions.

$$[111]+[11\bar{1}]=[220] \qquad \text{and} \qquad [111]+[1\bar{1}\bar{1}]=[200]$$

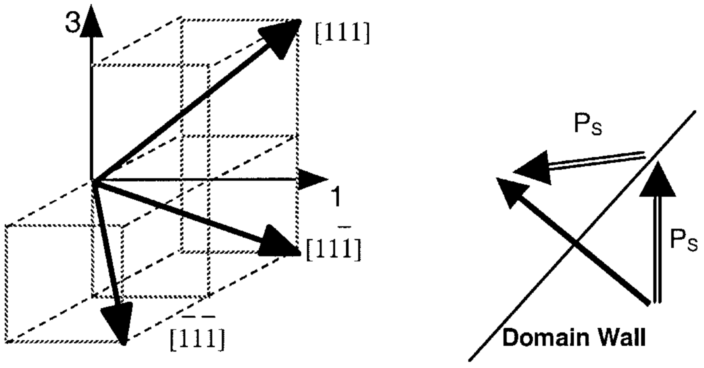

(a) (b)

Figure 2.31 Rhombohedral $BaTiO_3$: (a) polarization directions and (b) the orientation of the spontaneous polarization vectors across a domain wall.

The angle between two of the non-180° domain walls is thus calculated as follows:

1) $(002)/(200)\ ;\ (022)/(0\bar{2}2)\ ;\ (002)/(220)$

$(002)\cdot(200) = 2^2[\cos(90^\circ)] = 0$

2) $(022)/(220)\ ;\ (022)/(2\bar{2}0)$

$(022)\cdot(220) = (2\sqrt{2})^2[\cos\theta] = 4 \text{ or } -4 \quad \rightarrow\rightarrow\ \theta = 60^\circ \text{ or } 120^\circ$

3) $(002)/(022)\ ;\ (002)/(0\bar{2}2)$

$(022)\cdot(220) = 2(2\sqrt{2})[\cos\theta] = 4 \text{ or } -4 \quad \rightarrow\rightarrow\ \theta = 45^\circ \text{ or } 135^\circ$

In the following section, we will discuss the Uchida-Ikeda theory, by which the polarization and strain curves for piezoelectric polycrystalline specimens are described and predicted in terms of domain reorientation, the crystal structure, and the coercive field.

(2) The Uchida-Ikeda Model

Let us take as an example a barium titanate ($BaTiO_3$) single crystal, which has a tetragonal symmetry at room temperature. X-ray diffraction of the crystal reveals a slight elongation along the [001] direction of the perovskite unit cell with c/a=1.01. Therefore, if an electric field is applied on an "a" plane single crystal, a 90° domain reorientation from an "a" to a "c" domain is induced, resulting in a strain of 1% in the field direction. However, the situation is much more complicated in the case of a polycrystalline specimen. Uchida and Ikeda treated this problem statistically, assuming the grains (or small crystallites) are randomly oriented.[16,17]

There will be no remanent polarization in a homogeneous unpoled polycrystalline sample. Let this state be the basis for zero strain. If an electric field, E_3 is applied to this sample, a net polarization P_3 will be induced. The strains x_1, x_2 and x_3 will also be generated, where $x_1=x_2=x_3= -\sigma$ and σ is Poisson's ratio. Let the spontaneous polarization and the *principal strain* of the individual crystallites be designated by P_S and S_S, respectively. For uniaxial crystal symmetries, such as the tetragonal and rhombohedral, the principal strain, S_S, is in the direction of P_3 and is defined for each symmetry as follows:

$$S_S = [(c/a) - 1] \qquad \text{(tetragonal crystal)} \qquad (2.68)$$

$$S_S = (3/2)[\pi/2 - \alpha] = (3/2)\,\delta \qquad \text{(rhombohedral crystal)} \qquad (2.69)$$

It should be noted at this point in the discussion the distinction between the principal strain and the spontaneous strain. They are not interchangeable terms, but in fact define two very different strains. Using $BaTiO_3$ as an example, we see that the principal strain is $S_S=0.01$, but the spontaneous strains are defined as:

$$\begin{aligned} x_{3(S)} &= [(c/a_o) - 1] \\ x_{1(S)} = x_{2(S)} &= [(a/a_o) - 1] \end{aligned} \qquad (2.70)$$

where a_o is the lattice parameter of the paraelectric phase. When the appropriate lattice parameters are used in Equation (2.70), the spontaneous strains $x_{3(S)}$ and $x_{1(S)}$ are 0.0075 and −0.0025, respectively.

First, assuming an angle, θ, between the direction of the spontaneous polarization, P_S, of a microscopic volume, dv, in a ceramic and the direction of the electric field, E_3, then the polarization, P_3, is given by:

$$P_3 = \frac{\int P_S \cos\theta \, dv}{\int dv} = P_S \overline{\cos\theta} \qquad (2.71)$$

where $\overline{\cos\theta}$ is the average value of $\cos\theta$ in all the volume elements of the ceramic. The average strain is determined from the orientation of the strain ellipsoid:

$$x_3 = S_S \left[\frac{\int \cos^2\theta \, dv}{\int dv} - \frac{1}{3} \right] = S_S\,[\overline{\cos^2\theta} - (1/3)] \qquad (2.72)$$

It is assumed in this model that the spontaneous strains associated with the microscopic regions change only in their orientation with no change in volume, and hence $\sigma = 0.5$. This also implies that:

$$x_1 = x_2 = x_3/2 \tag{2.73}$$

This result, however, does not agree at all well with the experimental data.

In order to arrive at an expression for the induced strain as a function of the applied electric field, the relationship between θ and E_3 must be determined. This is accomplished in the context of this model by introducing a characteristic angle, θ_{90}, for non-180° domain reorientations. In tetragonal crystals this corresponds to a 90° reorientation and in rhombohedral crystals, 71° and 109° reorientations will occur, but in order to simplify the analysis, all reorientations are represented by the former. Suppose a 90° domain rotation occurs in a small volume element, dv, in a ceramic, and as a result the domain orientation within dv becomes θ. It is assumed that there exists a characteristic angle θ_{90}, such that if $\theta < \theta_{90}$, a 90° rotation will occur, whereas if $\theta > \theta_{90}$, no rotation will occur, and the region will remain in its initial state. Given a specific angle, θ_{90}, which corresponds to a certain applied field strength, E_3, Equation (2.71) can be integrated over the range of volume for which $\theta < \theta_{90}$ is satisfied to obtain the induced strains x_3, x_2, and x_1 as a function of θ_{90}. The quantity $(\overline{\cos^2\theta} - 1/3)$ is plotted as a function of the characteristic angle, θ_{90}, in Figure 2.32, and Figure 2.33(a) shows the measured values of induced strain for a rhombohedral PZT ceramic. When the equations defining these trends are combined, the curve representing the relationship between θ_{90} and E_3 depicted in Figure 2.33(b) is generated. A pronounced hysteresis is apparent in this curve.

Furthermore, by finding the polarization P_3 and field-induced strain x_3 (or x_1) as a function of the electric field, E_3, it is possible to estimate the volume in which a 180° reversal or a 90° rotation occurs. This is because only the 90° rotation contributes to the induced strain, whereas 180° domain reversal contributes mainly to the polarization. Curves representing the volume fraction of 180° domains that have undergone reversal and 90° domains that have rotated by 90° as a function of applied electric field are shown in Figure 2.34. We see from these curves that the 180° reversal occurs quite rapidly as compared to the slower process of 90° rotation.[18] It is notable that at G on the curve there remains some polarization and the induced strain is zero, while at H the strain is not at a minimum, but contributions to the polarization from the 180° and 90° reorientations cancel each other so that the net polarization becomes zero. A plot of the induced strain, x_3, as a function of polarization for a PLZT (6.25/50/50) ceramic, in which 180° reversal is dominant, is shown in Figure 2.35. We see that it is characterized by a rather large hysteresis.[19] In contrast, materials whose polarization is dominated by non-180° domain rotations, such as the low temperature phase of $Pb(Mg_{1/3}Nb_{2/3})O_3$, exhibit no significant hysteresis in their x-P curves [see Figure 2.36 (b)].[7]

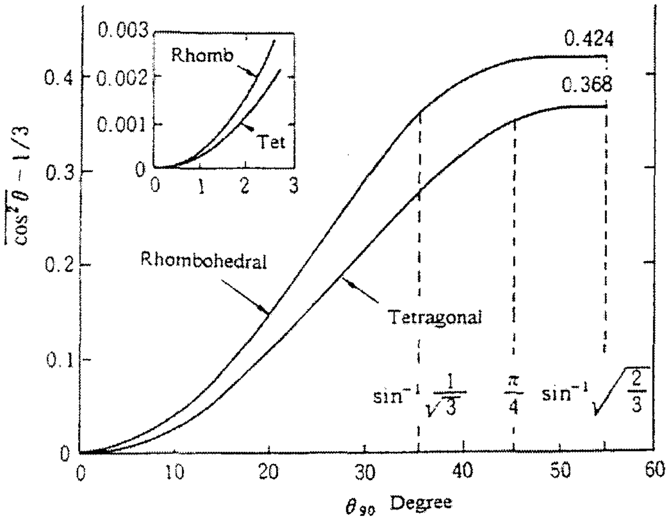

Figure 2.32 The quantity ($\overline{\cos^2\theta} - 1/3$) plotted as a function of the characteristic angle, θ_{90}, where θ_{90} is a critical angle related to the non-180° domain reorientation and ($\overline{\cos^2\theta} - 1/3$) is proportional to the field-induced strain.[16,17]

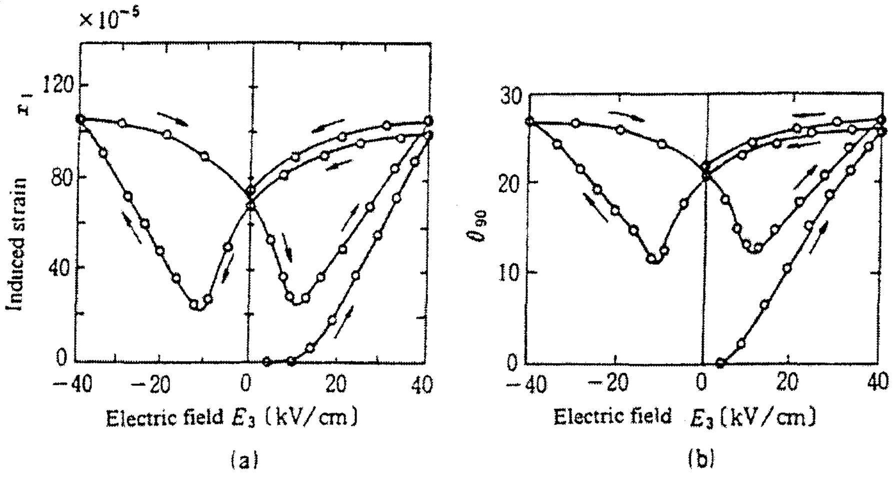

Figure 2.33 The field-induced transverse strain, x_1, in a $Pb(Zr_{0.57}Ti_{0.43})O_3$ ceramic sample: (a) x_1 as a function of applied electric field, E_3, and (b) calculated characteristic angle, θ_{90}, as a function of E_3. The measurement was done at 30°C.[16,17]

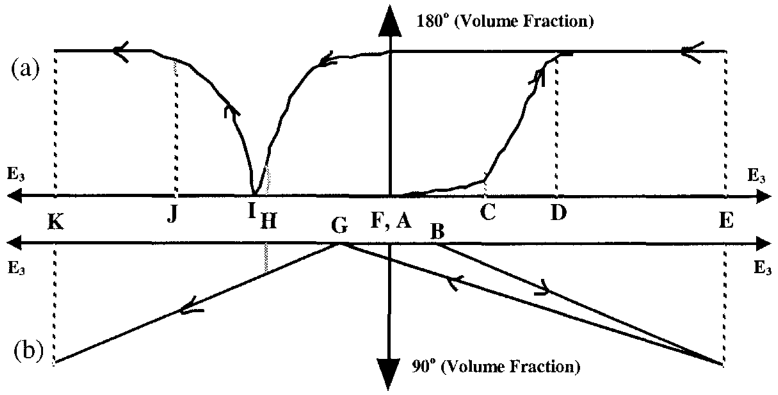

Figure 2.34 Electric field dependence of the volume fraction of domains that have undergone: (a) 180° reversal and (b) 90° reorientation. Notice the noncoincidence of the zero fraction points I and G, which correspond to the 180° and 90° cases, respectively.[18]

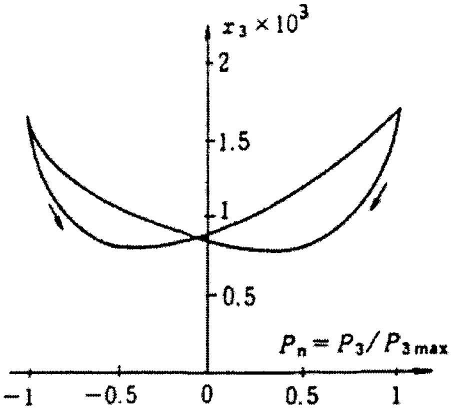

Figure 2.35 The induced strain, x_3, as a function of polarization for a tetragonal PLZT (6.25/50/50) ceramic.[19]

The saturation values of the polarization and the strain of a tetragonal and rhombohedral ceramic under high electric field are as follows:

Tetragonal:	$P_3 \rightarrow (0.831)P_S$	$x_3 \rightarrow (0.368)S_S$
Rhombohedral:	$P_3 \rightarrow (0.861)P_S$	$x_3 \rightarrow (0.424)S_S$

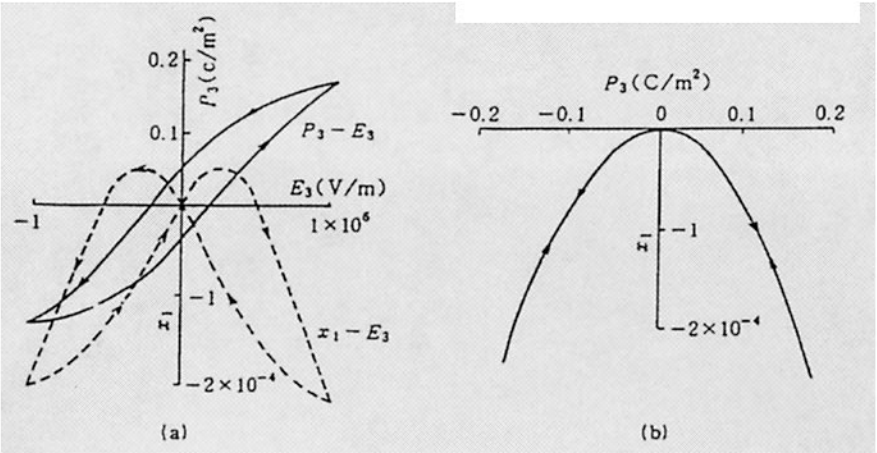

Figure 2.36 Rhombohedral $Pb(Mg_{1/3}Nb_{2/3})O_3$ at −110°C: (a) polarization, P_3, and transverse strain, x_1, as a function of applied electric field, E_3, and (b) transverse strain, x_1, as a function of polarization, P_3.[7]

(3) Crystal Structure and Coercive Field

In the previous section, a comparison was made between tetragonal and rhombohedral ceramic systems from the viewpoint of the saturation values, P_3 and S_S, under a sufficiently large electric field. In this section we will consider the difference between the two systems in terms of the more useful quantity, the coercive field, E_c. The principal strain, S_S, spontaneous polarization, P_S, volume percent of reoriented domains, γ_{90}, and coercive field, E_c, for a series of PLZT ceramics as reported by Schmidt[19] are summarized in Table 2.4. We see from the data presented in this table that the tetragonal compositions generally have smaller principal strains than the rhombohedral compositions. This implies that domain rotation is more readily achieved for the tetragonal compositions (larger γ_{90}), and the associated coercive fields are accordingly smaller. The following expression for the coercive field has been derived:

$$E_c = (\alpha\, Y\, S_S^2\, \gamma_{90}) / P_S \qquad (2.74)$$

where Y is Young's modulus. The quantity α is a factor which takes into account the difference in domain orientation between neighboring grains, and typically has values of 0.1 and 0.074 for tetragonal and rhombohedral compositions, respectively.[19,20]

Table 2.4 Principal strain, S_S, spontaneous polarization, P_S, reoriented volume fraction, and coercive field, E_c, for some tetragonal (T) and rhombohedral (R) PLZT ceramics.[19]

Symmetry	Composition (La/Zr/Ti)	S_S (%)	P_S ($\mu C/cm^2$)	Reoriented Domains (%)	E_c [measured] (kV/cm)	E_c [calculated] (kV/cm)
T	25/50/50	2.40	71.0	22.0	18.0	17.8
	25/52/48	2.20	72.0	28.0	14.7	18.8
	5//50/50	2.16	65.0	18.0	16.3	13.0
	5/52/48	1.96	64.5	23.0	14.8	13.7
	5/54/46	1.68	65.0	30.0	11.7	13.0
R	25/58/42	0.732	56.5	86.5	8.2	7.0
	25/60/40	0.740	58.5	78.5	7.6	5.4
	6/65/35	0.650	45.0	85.0	5.6	5.9
	6.25/60/40	0.610	49.0	85.0	5.7	4.8

2.7 GRAIN SIZE AND ELECTRIC FIELD-INDUCED STRAIN IN FERROELECTRICS

In recent years, ceramics that have controlled grain size (fine ceramics) or very fine grains (nanoparticles) have been manufactured and their properties, especially the electric field-induced strain, have been reported.[21-24] When characterizing the grain size dependence of the dielectric properties, we must consider two size regions: the micrometer range, in which a multiple domain state becomes a monodomain state, and the submicrometer range, in which ferroelectricity becomes destabilized.

The transverse field-induced strains of a 0.8 atomic percent Dy-doped fine grain ceramic $BaTiO_3$ (grain diameter around 1.5 μm) and of an undoped, coarse-grained ceramic (50 μm), as reported by Yamaji[21], are shown in Figure 2.37. As the grains become finer we see that the absolute value of the strain decreases and the hysteresis becomes smaller. This is because the coercive field for the 90° domain rotation increases with decreasing grain size. The grain boundaries "pin" the domain walls and do not allow them to move easily. Also the decreasing grain size seems to make the phase transition much more diffuse. The temperature dependence of the piezoelectric strain coefficient, d_{33}, is shown in Figure 2.38. Although the absolute value of d_{33} decreases for the Dy-doped sample, the temperature dependence is significantly flattened. It should be noted that it is not possible in Yamaji's experiment to separate the effect due to intrinsic grain size from that due to the dopants.

The effects of grain size on the induced strain in PLZT ceramic have been investigated with samples fabricated from PLZT (9/65/35) powders prepared by a co-precipitation method.[22] Samples with various grain sizes were fabricated by hot-pressing over a range of sintering periods. Samples with the PLZT (9/65/35) composition show significant *dielectric relaxation* (that is, a frequency dependence of the dielectric constant) below the Curie point (about 80°C), and the dielectric constant tends to be higher at lower frequency. The dependence of the peak dielectric constant on grain size is such that grain sizes larger than 1.7 μm, the dielectric constant decreases with decreasing grain size, but at grain sizes below 1.7 μm, the dielectric constant increases dramatically. The dependence of the longitudinal field-induced strain on the grain size is shown in Figure 2.39. We see that as the grain size becomes smaller, the maximum strain decreases monotonically. When the grain size becomes less than 1.7 μm, the hysteresis is significantly reduced. This behavior can be explained in terms of the multidomain-monodomain transition model as follows: with decreasing grain size, ferroelectric/antiferroelectric and ferroelastic domains are less readily formed so that in the grain, the domain rotation contribution to the strain becomes smaller. The critical grain size for this is about 1.7 μm. The domain size is not constant, however, and generally decreases with decreasing grain size.

A number of experiments have been conducted which examine the grain/particle size effects on the induced strain in finer grained ceramics.[23-25] The variation of the c/a tetragonality ratio with particle size in pure $BaTiO_3$ at room temperature is shown in Figure 2.40.[23] The c/a ratio is seen to decrease drastically for particle sizes below 0.2 μm and becomes 1 (that is, cubic!) for 0.12 μm particles. The particle size at which this structural transition occurs is called the *critical particle size, D_{crit}*. The temperature dependence of the c/a ratio for powders with various particle sizes is shown in Figure 2.41. It is clear from these data that the Curie temperature decreases with decreasing particle size.

A similar critical particle size has also been reported for $(Ba,Sr)TiO_3$,[24] $(Ba,Pb)TiO_3$[25] and for antiferroelectric $PbZrO_3$.[24] The relationship between the critical particle size, D_{crit}, and the Curie (or Néel) temperature, T_C (or T_N), for these materials is shown in Figure 2.42.[24] An important empirical rule is derived from these data:

$$D_{crit}\,[T_C - T_R] = \text{Constant} \qquad (2.75)$$

where T_R is room temperature.

Although various experiments have been reported so far, and the existence of the critical particle size has been repeatedly confirmed, the actual critical particle size reported varies significantly among sources and no satisfactory explanation has yet been presented. One possible explanation is based on a *hydrostatic pressure model.* In general, the ferroelectric transition temperature decreases sharply (50°C/MPa) with increasing hydrostatic pressure. The *effective surface tension*, γ, on a fine particle produces an intrinsic hydrostatic pressure, p:

$$p = 2\gamma / R \qquad (2.76)$$

where R is the radius of the particle.[27] The effective surface tensions listed in Table 2.5 were calculated from the critical particle size, D_{crit} (= $2R_{crit}$), and the critical hydrostatic pressure, p_{crit}, above which the cubic structure exists at room temperature. We see from these data that γ is practically contant for all perovskite ferroelectrics, and is about fifty times larger than that of nonpolar oxides. This may be due to the additional energy contributed by the surface charge and/or from a crystallographically different phase on the surface (*core-shell model*).

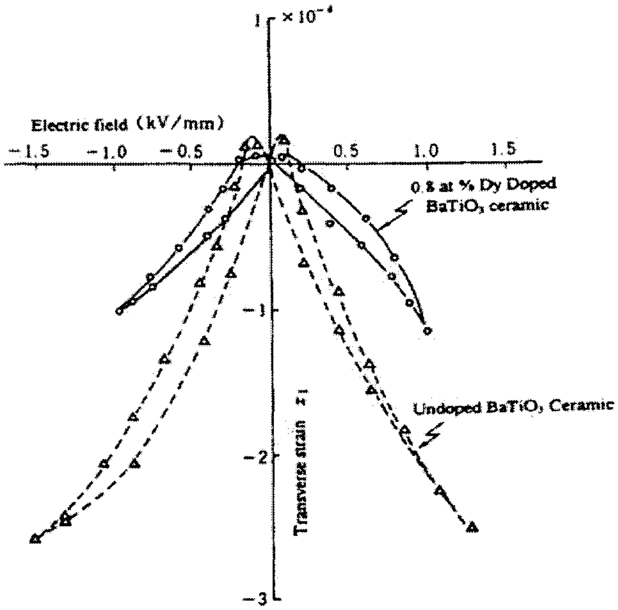

Figure 2.37 Strain curves for Dy-doped and undoped $BaTiO_3$ ceramics.[21]

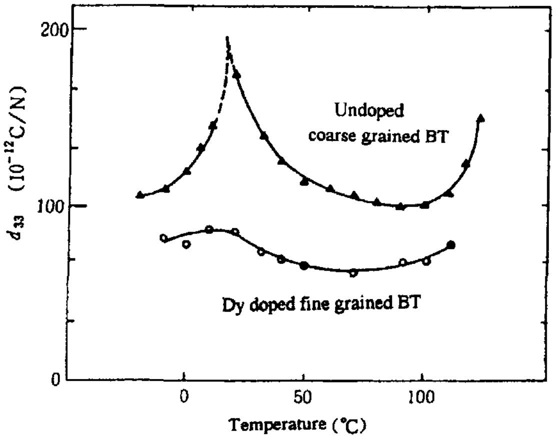

Figure 2.38 Temperature dependence of the piezoelectric strain coefficient, d_{33}, for Dy-doped and undoped $BaTiO_3$ ceramics.[21]

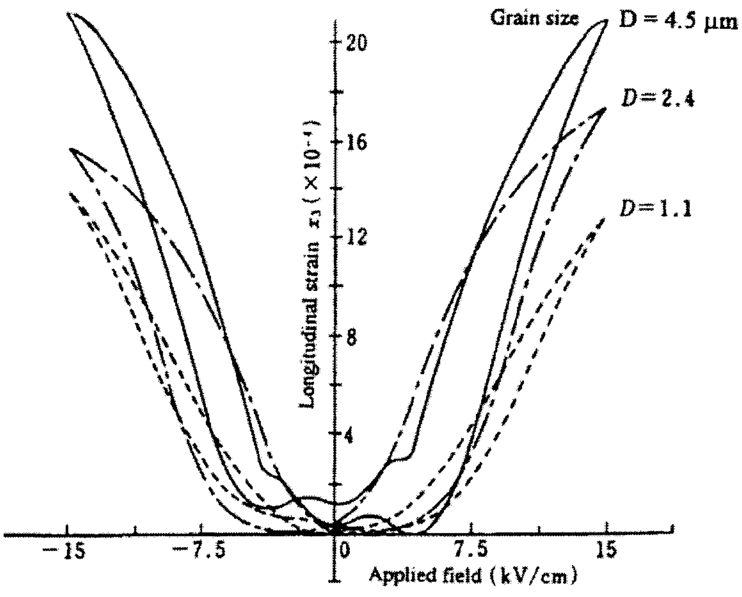

Figure 2.39 Field-induced strain for (9/65/35) PLZT ceramics with various grain sizes.[22]

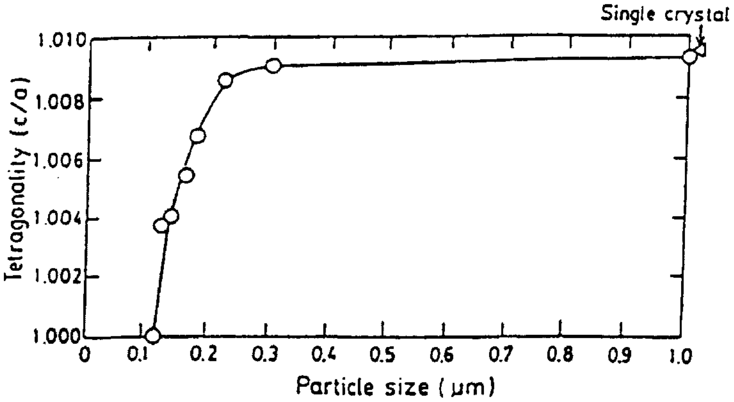

Figure 2.40 Particle size dependence of the c/a tetragonality ratio for $BaTiO_3$ at room temperature.[23]

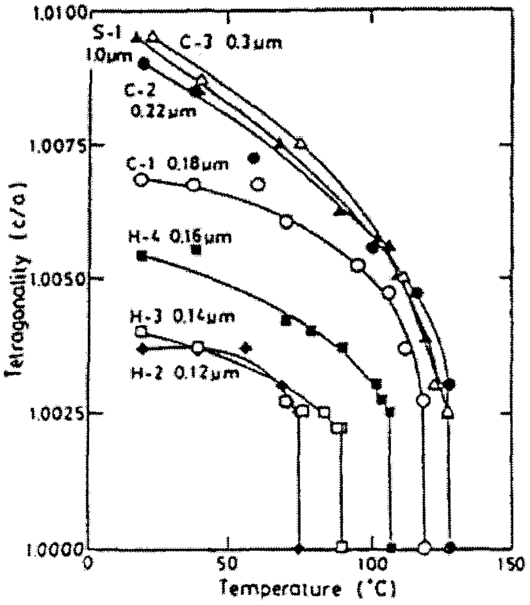

Figure 2.41 The temperature dependence of the c/a tetragonality ratio for a series of $BaTiO_3$ samples with various particle sizes.[23]

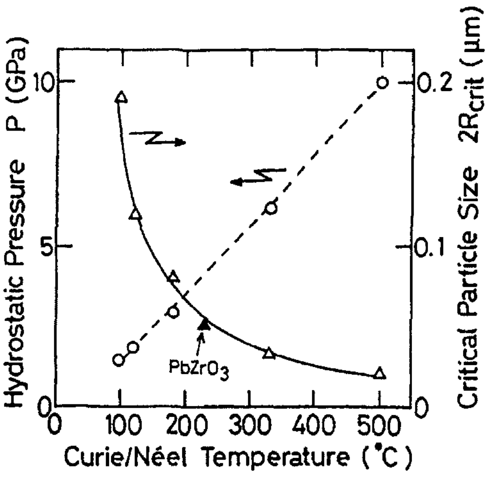

Figure 2.42 The critical particle size, D_{crit}, and the critical hydrostatic pressure, p_{crit}, as a function of the phase transition temperature.[24]

Table 2.5 Critical particle size, $D_{crit}(=2R_{crit})$, critical hydrostatic pressure, P_{crit} $(=2\gamma/R_{crit})$, and the effective surface tension, γ, for various perovskites.[26]

Material	T_C (°C)	$2R_{crit}$ (μm)	P_{crit} (GPa)	γ (N/m)
$Ba_{0.9}Sr_{0.1}TiO_3$	95	0.190	1.2	57
$BaTiO_3$	125	0.120	1.8	54
$Ba_{0.85}Pb_{0.15}TiO_3$	180	0.080	2.9	58
$Ba_{0.5}Pb_{0.5}TiO_3$	330	0.032	6.2	50
$PbTiO_3$	500	0.020	10.0	50

Example Problem 2.10

In order to better understand why ferroelectricity will diminish with decreasing particle size, we can examine the energy fluctuation of a nanosized ferroelectric particle in the following way. Consider a one-dimensional finite chain of two kinds of ions, +q and −q, arranged in an alternating configuration with an interionic distance of a as shown in Figure 2.43. Assume the nanosized crystal grows gradually, starting from a single pair of ions to which are progressively added pairs of negative or positive ions, so that the crystal size at any given time is 2na (n = 1, 2, 3, ...). As the crystal size increases, calculate the change in the crystal's Coulomb energy and determine the minimum number of ion pairs needed to stabilize the fluctuation to less than ±10%.

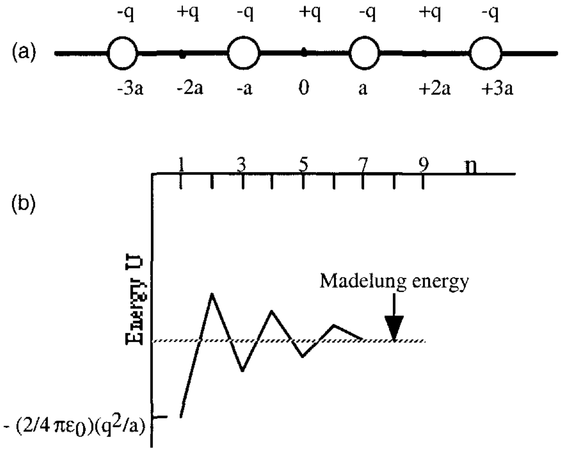

Figure 2.43 A one-dimensional finite chain of two kinds of ions, +q and −q, in an alternating configuration: (a) a schematic depiction of the configuration and (b) the energy fluctuation as a function of the number of ion pairs in the chain.

The Madelung energy as a function of lattice size, n, is calculated according to the following:

$$U_1 = (2/4\pi\varepsilon_o K)\,[-(q^2/a)]$$
$$U_2 = (2/4\pi\varepsilon_o K)\,[-(q^2/a) + (q^2/2a)]$$
$$U_3 = (2/4\pi\varepsilon_o K)\,[-(q^2/a) + (q^2/2a) - (q^2/3a)]$$
$$\ldots$$
$$U_n = (2/4\pi\varepsilon_o K)\,[-(q^2/a) + (q^2/2a) - (q^2/3a) + \cdots]$$

Thus, the minimum crystal size (2na) which maintains the crystal energy at a level that fluctuates less than ±10% will be around $n = 10$, because the additional energy term in the series is about $\pm(q^2/10a)$. If the Coulomb energy of the crystal is not stabilized to less than this degree of fluctuation, the long-range cooperative interaction of dipoles required of the ferroelectric phase will not occur. For a perovskite material, the minimum particle size for ferroelectricity to exist will be about 80 Å.

CHAPTER ESSENTIALS

1. Functional Classification: Dielectrics > Piezoelectrics > Pyroelectrics > Ferroelectrics.

2. Origin of the spontaneous polarization: the dipole coupling with the local field.

3. Piezoelectricity: can be modeled with ideal springs.
   Piezostriction: can be described in terms of the difference between the harmonic terms of the two equivalent springs.
   Electrostriction: can be modeled with anharmonic equivalent springs.

4. Origins of the field-induced strains:
   a. **The Inverse Piezoelectric Effect**: $x = d\,E$
   b. **Electrostriction:** $x = M\,E^2$
   c. **Domain reorientation**: strain hysteresis
   d. **Phase Transition (antiferroelectric←→ferroelectric):** strain "jump."

5. Polarization- and electric field-induced strain in polycrystalline materials:

Tetragonal:	$P_3 \rightarrow (0.831)\,P_S$	$x_3 \rightarrow (0.368)\,S_S$
Rhombohedral:	$P_3 \rightarrow (0.861)\,P_S$	$x_3 \rightarrow (0.424)\,S_S$
Coercive field:	Tetragonal > Rhombohedral (perovskite)	

6. Shear strain: $x_5 = 2\,x_{31} = 2\,\phi$, taken as positive for smaller angle.

7. The electrostriction equation:

$$x = \underset{\textbf{(spontaneous strain)}}{Q P_S^2} + \underset{\textbf{(piezostriction)}}{2 Q \varepsilon_o K P_S E} + \underset{\textbf{(electrostriction)}}{Q \varepsilon_o^2 K^2 E^2}$$

8. The piezoelectric equations:

$x = s^E X + d E$

$P = d X + \varepsilon_o K^X E$

9. Electromechanical coupling factor (k):

$k^2 = d^2 / s^E \varepsilon_o K^X$

10. Electromechanical properties of ceramics: grain size dependence
Smaller grain → reduced strain and smaller hysteresis → enhanced mechanical strength.

CHAPTER PROBLEMS

2.1 Consider a 2-dimensional infinite array of two kinds of ions, +q and −q, arranged in a rock salt configuration with an interionic distance of a. Calculate the Coulomb potential energy at a +q ion, and obtain the Madelung energy. Remember that:

$$U = -(1/4\pi_o K)\,(q^2/r)$$

2.2 The room temperature form of quartz belongs to class 32.

a. Show that the piezoelectric matrix (d_{ij}) is given by:

$$\begin{pmatrix} d_{11} & -d_{11} & 0 & d_{14} & 0 & 0 \\ 0 & 0 & 0 & 0 & -d_{14} & -2d_{11} \\ 0 & 0 & 0 & 0 & 0 & 0 \end{pmatrix}$$

Notice that the piezoelectric tensor must be invariant for a 120° rotation around the 3-axis and for a 180° rotation around the 1-axis. The transformation matrices are respectively:

$$\begin{pmatrix} -\frac{1}{2} & \frac{\sqrt{3}}{2} & 0 \\ -\frac{\sqrt{3}}{2} & -\frac{1}{2} & 0 \\ 0 & 0 & 1 \end{pmatrix} \quad \text{and} \quad \begin{pmatrix} 1 & 0 & 0 \\ 0 & -1 & 0 \\ 0 & 0 & -1 \end{pmatrix}$$

b. The measured values of the d_{ij} for right-handed quartz are:

$$\begin{pmatrix} -2.3 & 2.3 & 0 & -0.67 & 0 & 0 \\ 0 & 0 & 0 & 0 & 0.67 & 4.6 \\ 0 & 0 & 0 & 0 & 0 & 0 \end{pmatrix} \text{x } 10^{-12} \ (\text{C}/\text{N})$$

i. If a compressive stress of 1 kgf/cm^2 is applied along the 1-axis of the crystal, find the induced polarization. (kgf = kilogram force = 9.8 N)

ii. If an electric field of 100 V/cm is applied along the 1-axis, find the induced strains.

2.3 We have a cube-shaped specimen, to which a tensile stress, X, and a compressive stress, –X, are applied simultaneously from the corners along the (1 0 1) and $(\bar{1}\,0\,1)$ axes, respectively. If we refer to another coordinate system canted 45° from the original coordinate system, the stress tensor is represented by:

$$\begin{bmatrix} X & 0 & 0 \\ 0 & 0 & 0 \\ 0 & 0 & -X \end{bmatrix}$$

Using the transformation matrix A given by:

$$\begin{pmatrix} \cos\theta & 0 & \sin\theta \\ 0 & 1 & 0 \\ -\sin\theta & 0 & \cos\theta \end{pmatrix}$$

calculate AXA^{-1}, and verify that the stress is equivalent to a pure shear stress with respect to the original coordinates.

2.4 Verify that the Curie temperature, T_C, and the Curie-Weiss temperature, T_o, are related according to the following equation:

$$T_C = T_o + (3/16)[(\beta^2 \varepsilon_o C)/\gamma]$$

for a first-order phase transition, where the Landau free energy is expanded as:

$$F(P,T) = (1/2)\alpha P^2 + (1/4)\beta P^4 + (1/6)\gamma P^6$$

where $\alpha = (T-T_o)/C$.

2.5 In the case of a first-order phase transition, the Landau free energy is expanded as given in Problem 2.4. Calculate the inverse permittivity near the Curie temperature, and verify that the slope $\partial(1/\varepsilon)/\partial T$ just below T_C is 8 times larger than the slope just above T_C.

2.6 Barium titanate has a tetragonal crystal symmetry at room temperature and the distortion from the cubic structure is not very large ($c/a = 1.01$). Calculate all possible angles between the two non-180° domain walls.

2.7 In calculating Eqs. (2.71) and (2.72), the volume element dv is given by:

$$dv = (2\pi r^2\, dr)\,(\sin\theta\, d\theta)$$

Using this dv, calculate $\int dv$, $\int \cos\theta\, dv$, and $\int \cos^2\theta\, dv$, assuming the polarization is uniformly distributed with respect to θ.

REFERENCES

1) C. Kittel: *Introduction to Solid State Physics*, John Wiley & Sons, NY (1966).
2) W. Kinase, Y. Uemura and M. Kikuchi: J. Phys. Chem. Solids, **30**, 441 (1969).
3) K. Uchino and S. Nomura: Bull. Jpn. Appl. Phys. **52**, 575 (1983).
4) J. F. Nye: *Physical Properties of Crystals*, Oxford University Press, London, p.123, 140 (1972).
5) A. F. Devonshire: Adv. Phys. **3**, 85 (1954).
6) H. F. Kay: Rep. Prog. Phys. **43**, 230 (1955).
7) J. Kuwata, K. Uchino and S. Nomura: Jpn. J. Appl. Phys. **19**, 2099 (1980).
8) X.–H. Du, U. Belegundu and K. Uchino: Jpn. J. Appl. Phys. **36** (Part 1, 9A), 5580 (1997).
9) X.–H. Du, J. Zheng, U. Belegundu and K. Uchino: Appl. Phys. Lett. **72** (19), 2421 (1998).
10) M. J. Haun, E. Furman, S. J. Jang and L. E. Cross: Ferroelectrics **99**, 13 (1989).
11) C. Kittel: Phys. Rev. **82**, 729 (1951).
12) K. Uchino: Solid State Phys. **17**, 371 (1982).

13) K. Uchino, L. E. Cross, R. E. Newnham and S. Nomura: J. Appl. Phys. **52**, 1455 (1981).
14) K. Uchino: Jpn. J. Appl. Phys. **24**, Suppl. 24-2, 460 (1985).
15) K. Ohta: Fundamentals of Magnetic Engineering II, Kyoritsu Publ. Co., Tokyo (1985).
16) N. Uchida and T. Ikeda: Jpn. J. Appl. Phys. **6**, 1079 (1967).
17) N. Uchida: Rev. Elect. Commun. Lab. **16**, 403 (1968).
18) N. Uchida and T. Ikeda: Jpn. J. Appl. Phys. **4**, 867 (1965).
19) N. A. Schmidt: Ferroelectrics **31** , 105 (1981).
20) P. Gerthsen and G. Kruger: Ferroelectrics **11**, 489 (1976).
21) A. Yamaji, Y. Enomoto, K. Kinoshita and T. Tanaka: Proc. 1st Mtg. Ferroelectric Mater. & Appl., Kyoto, p.269 (1977).
22) K. Uchino and T. Takasu: Inspec. **10**, 29 (1986).
23) K. Uchino, E. Sadanaga and T. Hirose: J. Amer. Ceram. Soc. **72**, 1555 (1989).
24) T. Yamakawa and K. Uchino: Proc. Int'l. Symp. Appl. Ferroelectrics '90, p.610 (1991).
25) K. Saegusa et al.: Amer. Ceram. Soc., 91st Ann. Mtg. (1989).
26) K. Uchino, E. Sadanaga, K. Oonishi and H. Yamamura: Ceramic Trans. **8**, Ceramic Dielectrics, 107 (1990).

3

ACTUATOR MATERIALS

3.1 PRACTICAL ACTUATOR MATERIALS

(1) History of Piezoelectrics

The discovery of piezoelectricity is credited to the famous brothers Pierre and Jacques Curie, who first examined the effect in quartz crystals in 1880. The discovery of ferroelectricity in 1921 and the subsequent characterization of new ferroelectric materials further extended the number of useful piezoelectric materials available for study and application. The first ferroelectric material discovered was Rochelle salt. Prior to 1940 only two general types of ferroelectric were known, Rochelle salt and potassium dihydrogen phosphate (KDP) and its isomorphs. Extensive characterization of the new ferroelectric barium titanate ($BaTiO_3$) was independently undertaken by Wainer and Salmon, Ogawa, and Wul and Golman from 1940 to 1943. The new material exhibited unusual dielectric properties including an exceptionally high dielectric constant with distinctive temperature and frequency dependences. Compositional modifications of $BaTiO_3$ were made by the next generation of researchers to tailor the properties of the material for improved temperature stability and enhanced high voltage output. The first piezoelectric transducers based on $BaTiO_3$ ceramics were also developed at this time and implemented for a variety of applications.

In the 1950's Jaffe and co-workers examined the lead zirconate-lead titanate (PZT) solid solution system and found certain compositions exhibited an exceptionally strong piezoelectric response. In particular, the maximum piezoelectric response was found for compositions near the morphotropic phase boundary between the rhombohedral and tetragonal phases. Since then, modified PZT ceramics have become the dominant piezoelectric ceramics for various applications. More recently, the development of PZT-based ternary solid solution systems have allowed for the production of even more responsive materials whose properties can be very precisely tailored for a variety of applications.

Kawai et al. discovered in 1969 that certain polymers, most notably polyvinylidene difluoride (PVDF), are piezoelectric when stretched during fabrication. Piezoelectric polymers such as these are also useful for transducer applications. The development of piezoelectric composite materials systematically studied by Newnham et al. in 1978, allow for the further refinement of the electromechanical properties. The composite structures, incorporating a piezoelectric ceramic and a passive polymer phase, have been formed in a variety of configurations each precisely designed to meet specific requirements of a particular application.

The relaxor ferroelectric electrostrictors are another class of ceramic material, which has recently become important. Among the many useful compositions that have emerged is lead magnesium niobate (PMN), doped with 10% lead titanate (PT),[18] which has been used extensively for a variety of ceramic actuator applications. Recent advances in the growth of large, high quality single crystals[22] have made these materials even more attractive candidates for a variety of new applications, ranging from high strain actuators to high frequency transducers for medical ultrasound devices. More recently, thin film piezoelectrics such as zinc oxide (ZnO) and PZT have been developed for use in microelectromechanical (MEMS) devices.

(2) The Perovskite Structure

Among the practical piezoelectric/electrostrictive materials, many have the perovskite crystal structure ABO_3 pictured in Figure 3.1. These materials typically undergo a phase transition on cooling from a high symmetry high temperature phase (cubic paraelectric phase) to a noncentrosymmetric ferroelectric phase. Materials with a high ferroelectric transition temperature (Curie temperature) will be piezoelectric at room temperature, whereas those with a transition temperature near or below room temperature will exhibit the electrostriction. In the case of the latter, at a temperature just above the Curie temperature, the electrostriction is extraordinarily large because of the large anharmonicity of the ionic potential. Furthermore, simple compositions such as barium titanate ($BaTiO_3$) and lead zirconate ($PbZrO_3$), solid solutions such as $A(B,B')O_3$, and complex perovskites such as $A^{2+}(B^{3+}_{1/2}B'^{5+}_{1/2})O_3$ and $A^{2+}(B^{2+}_{1/3}\ B'^{5+}_{2/3})O_3$ are all readily formed. Supercells of the complex perovskite structures listed above, in which ordering of the B-site cations exists, are pictured in Figures 3.2(b) and 3.2(c). When the B and B' cations are randomly distributed the unit cell corresponds to the simple perovskite structure depicted in Figure 3.2(a).

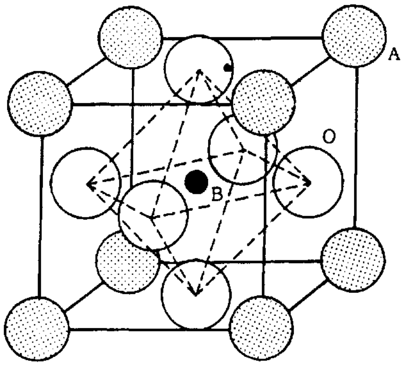

Figure 3.1 The perovskite crystal structure of ABO_3.

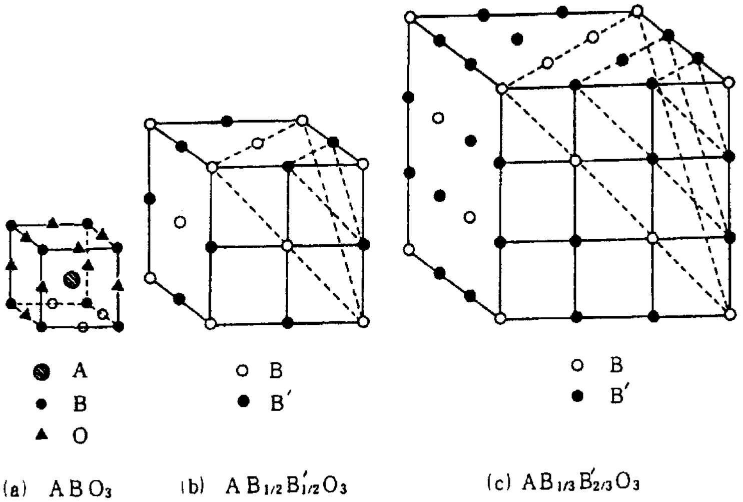

(a) ABO_3 (b) $AB_{1/2}B'_{1/2}O_3$ (c) $AB_{1/3}B'_{2/3}O_3$

Figure 3.2 Complex perovskite structures with various B ion arrangements: (a) ABO_3, simple structure, (b) $A(B_{1/2}B'_{1/2})O_3$, 1:1 ordering (long-range), double cell and (c) $A(B_{1/3}B'_{2/3})O_3$, 1:2 ordering (short-range), multiple cell.

(3) Piezoelectric Materials

An overview of the current status of piezoelectric materials is presented in this section. It includes crystalline materials, piezoceramics, electrostrictive materials, shape memory ceramics, piezopolymers, piezocomposites, and piezofilms. The electromechanical properties for some of the most popular piezoelectric materials are summarized in Table 2.1.[1,2]

Table 2.1 Piezoelectric properties of some popular piezoelectric materials.[1,2]

	Quartz	$BaTiO_3$	PZT4	PZT 5H	$(Pb,Sm)TiO_3$	PVDF-TrFE
d_{33} (pC/N)	2.3	190	289	593	65	33
g_{33} (mVm/N)	57.8	12.6	26.1	19.7	42	380
k_t	0.09	0.38	0.51	0.50	0.50	0.30
k_p		0.33	0.58	0.65	0.03	
K_{33}^T	5	1700	1300	3400	175	6
Q_m	$>10^5$		500	65	900	3-10
T_C (°C)		120	328	193	355	

Single Crystals

Although piezoelectric ceramics are used for a wide range of applications, single crystal materials are also used, especially for such applications as frequency stabilized oscillators and surface acoustic wave (SAW) devices. The most popular single crystal piezoelectric materials are quartz, lithium niobate ($LiNbO_3$), and lithium tantalate ($LiTaO_3$). Piezoelectric single crystals are anisotropic, exhibiting different material properties depending on the cut.

Quartz is a well-known piezoelectric material. Alpha (α) quartz belongs to the triclinic crystal system with point group 32 and undergoes a phase transition at 537°C to its beta (β) form, which is not piezoelectric. One particular cut of quartz, the AT-cut, has a zero temperature coefficient. Quartz oscillators, made from an AT-cut crystal and operated in the thickness shear mode, are used extensively for clock sources in computers, and frequency-stabilized devices are used in televisions and video recorders. An ST-cut quartz, when used as a substrate for surface acoustic waves propagating in the x direction will also have a zero temperature coefficient for such waves, thus making it suitable for frequency-stabilized surface acoustic wave (SAW) devices. Another distinctive characteristic of quartz is its exceptionally high mechanical quality factor, $Q_m > 10^5$.

Lithium niobate and lithium tantalate are isomorphs and have Curie temperatures of 1210°C and 660°C, respectively. The crystal symmetry of the ferroelectric phase of these single crystals is 3m and the polarization direction is along the c-axis. These materials have high electromechanical coupling coefficients for surface acoustic waves. Large single crystals can easily be obtained from the melt using the Czochralski technique. Thus both materials are important for SAW device applications.

Polycrystalline Materials

Barium titanate ($BaTiO_3$) is one of the most thoroughly studied and most widely used piezoelectric materials. Just below the Curie temperature (130°C), the material has a tetragonal symmetry and the spontaneous polarization is directed along [001]. Below 5°C, the material is orthorhombic and the polarization is oriented along [011]. At −90°C a transition to a rhombohedral phase occurs and the polarization direction is along [111]. The electromechanical properties of ceramic $BaTiO_3$ are affected by the stoichiometry and microstructure of the material, as well as the presence of dopants on both the A and B sites of the perovskite lattice. Ceramic $BaTiO_3$ has been modified with dopants such as Pb or Ca in order to stabilize the tetragonal phase over a wider temperature range. These compositions were originally designed for use in Langevin-type piezoelectric vibrators and are currently commercially available for this and a variety of other applications.

Piezoelectric ceramics from the Pb(Zr,Ti)O_3 (PZT) solid solution system have been widely used because of their superior piezoelectric properties. The phase diagram for the $Pb(Zr_xTi_{1-x})O_3$ system appears in Figure 3.3. The symmetry of a given composition is determined by the Zr content. Lead titanate also has a perovskite structure and a tetragonally distorted ferroelectric phase. With increasing Zr content, x, the tetragonal distortion decreases and at $x > 0.52$ the structure changes from tetragonal 4mm to another ferroelectric phase with rhombohedral 3m symmetry. The line dividing these two phases in Figure 3.3 is called the *morphotropic phase boundary (MPB)*. The composition at the morphotropic phase boundary is assumed to be a mixture of the tetragonal and rhombohedral phases. The dependence of several piezoelectric strain coefficients, (d), on composition over a narrow compositional range near the morphotropic phase boundary is shown in Figure 3.4. All the d coefficients are observed to peak at the morphotropic phase boundary. The enhancement in the piezoelectric effect at the morphotropic phase boundary has been attributed to the coexistence of the two phases, whose polarization vectors become more readily aligned by an applied electric field when mixed in this manner than may occur in either of the single phase regions.

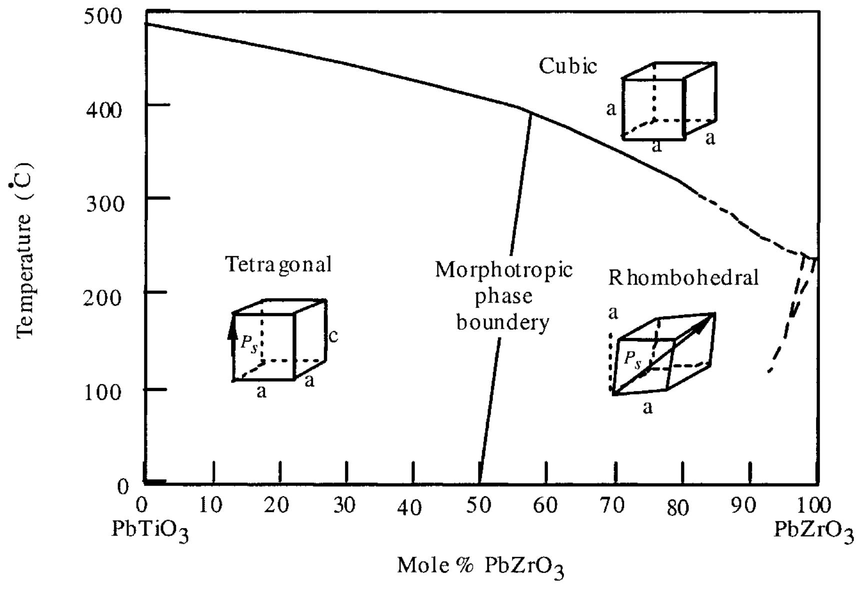

Figure 3.3 Phase diagram of the lead zirconate titanate $Pb(Zr_xTi_{1-x})O_3$ solid solution system.

Doping the PZT material with donor or acceptor ions changes its properties dramatically. Materials doped with donor ions such as Nb^{5+} or Ta^{5+} are soft piezoelectrics. A soft piezoelectric has a low coercive field. The material becomes soft with donor doping largely due to the presence of Pb vacancies, which effectively facilitate domain wall motion. Materials doped with acceptor ions such as Fe^{3+} or Sc^{3+}, on the other hand, are hard piezoelectrics. A hard piezoelectric has a high coercive field. The material becomes hard with acceptor doping due to the generation of oxygen vacancies, which pin domain wall motion. We will examine these mechanisms further in Section 6.3(1).

Various ternary solid solutions incorporating PZT and another ferroelectric perovskite have also been investigated. Some noteworthy examples utilize the following third phases: $Pb(Mg_{1/3}Nb_{2/3})O_3$, $Pb(Mn_{1/3}Sb_{2/3})O_3$, $Pb(Co_{1/3}Nb_{2/3})O_3$, $Pb(Mn_{1/3}Nb_{2/3})O_3$, $Pb(Ni_{1/3}Nb_{2/3})O_3$, $Pb(Sb_{1/2}Sn_{1/2})O_3$, $Pb(Co_{1/2}W_{1/2})O_3$, and $Pb(Mg_{1/2}W_{1/2})O_3$.[70]

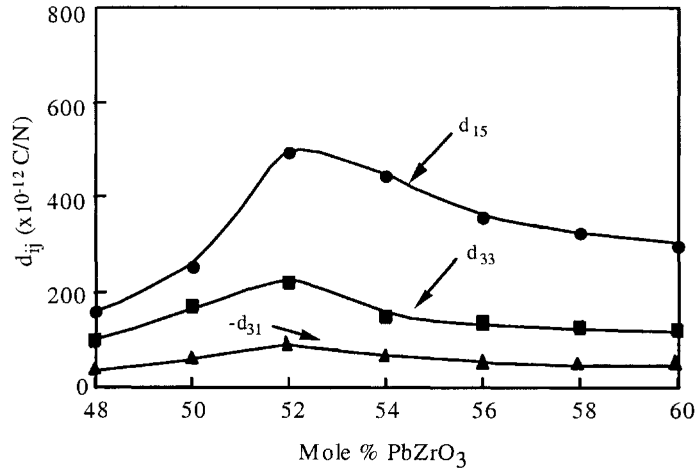

Figure 3.4 Dependence of several d constants on composition near the morphotropic phase boundary in the $Pb(Zr_xTi_{1-x})O_3$ solid solution system.

A new solid solution system, $BiScO_3$-$PbTiO_3$, has been proposed from which materials with improved temperature stability can be derived for high temperature applications.[3] The morphotropic phase boundary composition for this system has a Curie temperature of 450°C, which is about 100°C higher than that of the MPB composition in the PZT system.

Lead titanate, $PbTiO_3$, has an exceptionally large unit cell distortion. It is tetragonal at room temperature with a tetragonality ratio $c/a=1.063$ and its Curie temperature is 490°C. Dense sintered $PbTiO_3$ ceramics are not easily obtained, because they break up into a powder when cooled through the Curie temperature due to the large spontaneous strain. Modified lead titanate ceramics incorporating A-site dopants are mechanically stronger and exhibit a high piezoelectric anisotropy. The modified compositions $(Pb,Sm)TiO_3$[4] and $(Pb,Ca)TiO_3$[5] exhibit extremely low planar coupling, that is, they have a large k_t/k_p ratio. The quantities k_t and k_p are the thickness-extensional and the planar electromechanical coupling factors, respectively. Since medical imaging ultrasonic transducers made with these compositions can generate purely longitudinal waves through k_t, clear images are possible because the "ghost" image, generally associated with the transverse wave and generated through k_{31}, is not produced. Ceramics of another modified composition, $(Pb,Nd)(Ti,Mn,In)O_3$, have been developed which have a zero temperature coefficient of surface acoustic wave delay and, therefore, are superior substrate materials for SAW device applications.[6]

The physical properties of a solid solution with end members A and B [designated by (1−x)A-(x)B] can be from *phenomenological theory*.[7,8] The Gibbs elastic energy of a solid solution is assumed to be a linear combination of the Gibbs elastic energy of each component, so that:

$$\begin{aligned} G_1(P,X,T) = {} & (1/2)[(1-x)\alpha_A+(x)\alpha_B]P^2 + (1/4)[(1-x)\beta_A + x\beta_B]P^4 \\ & + (1/6)[(1-x)\gamma_A+ x\gamma_B]P^6 - (1/2)[(1-x)s_A+x_B]X^2 \\ & - [(1-x)Q_A+xQ_B]P^2 X \qquad (3.1) \end{aligned}$$

where $\alpha_A = (T - T_{o\,(A)})/\varepsilon_o C_A$ and $\alpha_B = (T - T_{o\,(B)})/\varepsilon_o C_B$.

Reasonable first-order estimates of the Curie temperature, spontaneous polarization, the spontaneous strain, the permittivity, the piezoelectric coefficients, and the electromechanical coupling factors can be derived from the energy equation.

The dielectric constant as a function of temperature for various compositions from the solid solution system $(x)Pb(Zn_{1/3}Nb_{2/3})O_3$ - $(1-x)PbTiO_3$ (PZN-PT) is shown in Figure 3.5.[8] The calculated and measured data are in reasonable agreement in terms of the Curie temperature, the magnitude of the dielectric constant, and the anomaly associated with the phase transition from the tetragonal to rhombohedral phase. The only significant difference appears in the breadth of the dielectric constant peaks, which will be examined in the next section.

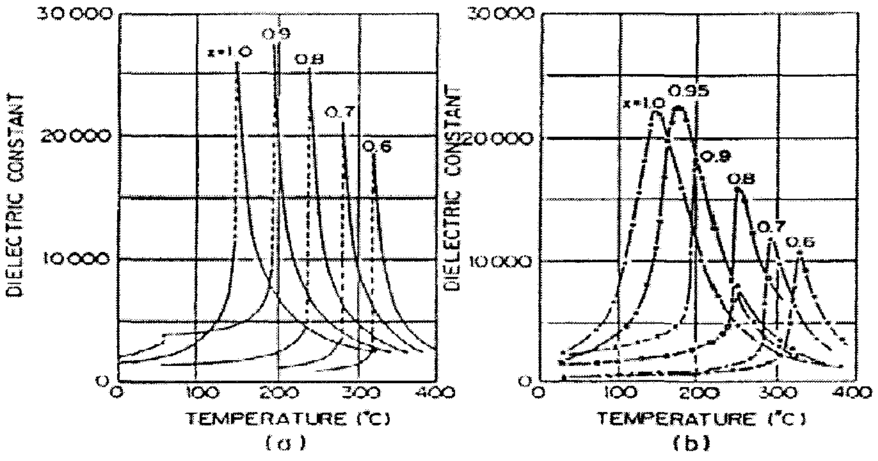

Figure 3.5 The dielectric constant as a function of temperature for various compositions from the solid solution system $(x)Pb(Zn_{1/3}Nb_{2/3})O_3$-$(1-x)PbTiO_3$: (a) phenomenological prediction (b) experimentally determined.[8]

A typical magnitude for the piezoelectric strain coefficient d_{33} of a ceramic piezoelectric is $1x10^{-10}$-$5x10^{-10}$ (m/V). If an electric field of 10^6 (V/m) is applied to a 10 (mm) sample, a strain $x_3 \approx 1x10^{-3}$ is induced, which translates to a 10 μm displacement. Under such a large electric field, domain reorientation will occur in most cases, leading to a strain much larger than predicted just from the product (dE). The discrepancy can range from 10 to 100 percent. It is for this reason that piezoelectric coefficient measurements obtained at low field strengths (< 10 V/mm), such as those taken at an electromechanical resonance with an impedance analyzer, are practically useless for accurately characterizing actuator response.

In as-fired samples of piezoelectric ceramics, the net polarizations of individual grains are randomly oriented so as to produce a net polarization of zero for the entire sample. The net strain is likewise negligibly small under an applied electric field. Hence, as a final treatment of all piezoelectric ceramics a relatively large electric field (>3 kV/mm) is applied in order to align the polarization directions of all grains as much as possible. This is called is called *electric poling*.

The strain induced along the electric field direction (the longitudinal effect) in a poled $(Pb,La)(Zr,Ti)O_3$ (7/62/38) sample is shown in Figure 3.6(a).[9] When the applied field is small, the induced strain is nearly proportional to the field; this is the converse piezoelectric effect ($x = dE$), and the piezoelectric strain coefficient d_{33} can be determined from the slope ($\partial x/\partial E$). As the field becomes larger (> 100 V/mm), the strain curve deviates from this linear trend and significant *hysteresis* occurs. This limits the usefulness of this material for actuator applications that require a nonhysteretic response. Once the applied field exceeds the coercive field strength, E_c, the hysteresis assumes the characteristic "butterfly-shaped" curve traced with the dotted line in Figure 3.6(a). This strain hysteresis is caused by the reorientation of ferroelectric domains.

An interesting new family of actuators with a small hysteresis has been produced using ceramics from the barium stannate titanate solid solution system, $Ba(Sn,Ti)O_3$.[10] The attractive feature of $Ba(Sn_{0.15}Ti_{0.85})O_3$ is its unusual strain curve. We see from Figure 3.6(b) that domain reorientation occurs only at low field strengths, and there is a broad linear range for higher applied fields. The coercive field is unusually small. This good linear response comes at the expense of the strain, however, with a maximum induced strain of only $x_3=0.5\times10^{-3}$.

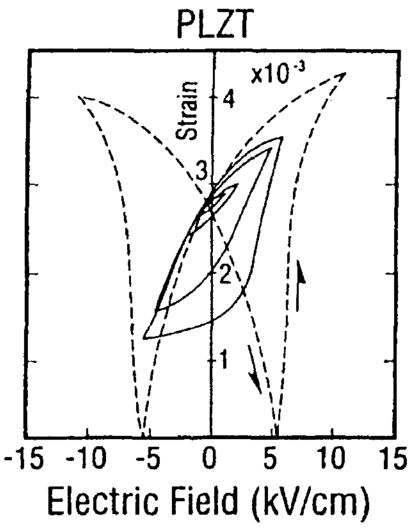

Figure 3.6 Field-induced strain curves for piezoelectric: (a) PLZT (7/62/38),[9] and (b) $Ba(Sn,Ti)O_3$.[10]

The induced strain curves for various PLZT compositions under *bipolar* [−20 (kV/cm) < E < +20 (kV/cm)] and *unipolar* [0 < E < +20 (kV/cm)] drives are shown in Figure 3.7.[9] Bipolar drive is generally not used, however, because cracks are readily initiated with repeated polarization reversal thus significantly shortening the lifetime of the device.

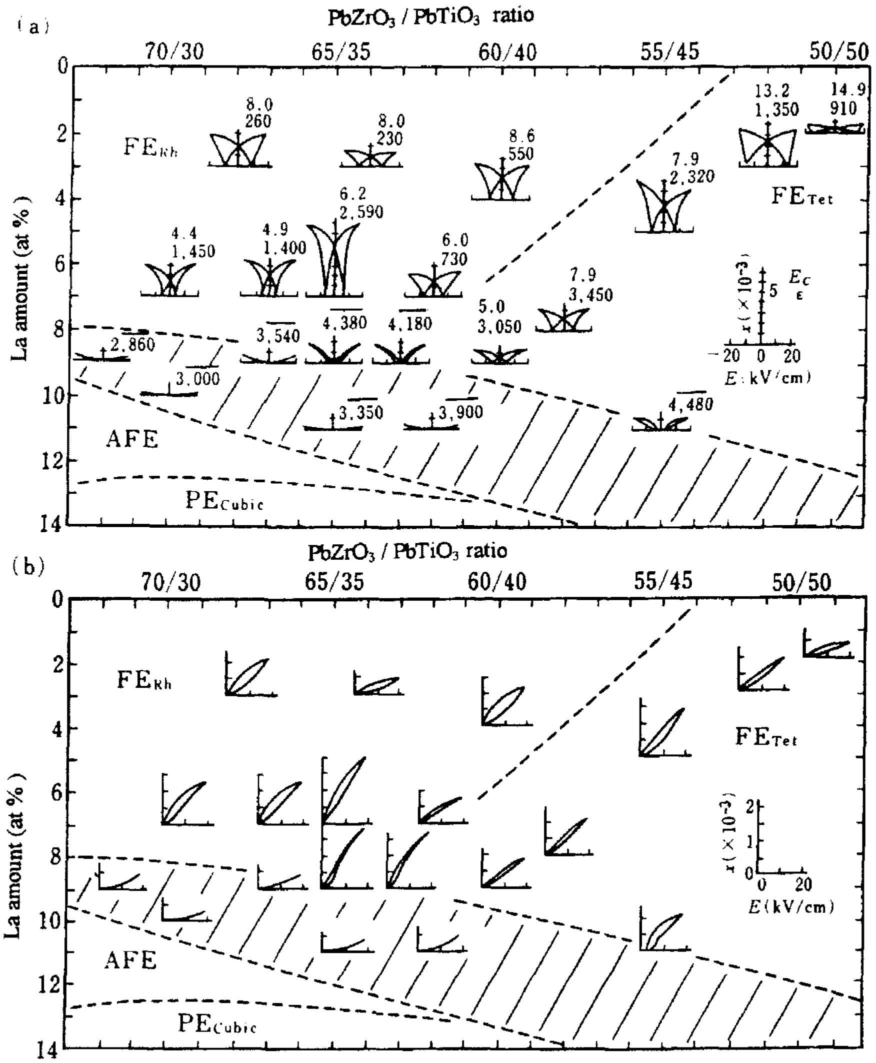

Figure 3.7 Field-induced strain curves for various PLZT compositions under: (a) bipolar, and (b) unipolar drive.[9] The magnitudes of the coercive field, E_c, and the dielectric constant are written above each curve in the top figure.

So far, we have considered mainly soft piezoelectrics suitable for off-resonance or nearly static operating conditions. Very hard, high power piezoelectrics are typically used for ultrasonic resonance applications under AC conditions. Since the resonance displacement is determined by $Q_m dE$, a material that retains a high mechanical quality factor, Q_m, and piezoelectric strain coefficient, d, at high vibration levels is essential. High power drive causes heat generation, which can lead to serious degradation of the electromechanical properties. One of the best high power piezoelectrics is a rare-earth doped PZT-$Pb(Mn_{1/3}Sb_{2/3})O_3$ ceramic, which can generate a maximum vibration velocity of 1 m/sec.[11] We will examine these materials and their properties in more detail in Chapter 6. Note that under these high power operating conditions, increasing the applied electric field does not increase the vibration energy. Any additional input energy is converted entirely into heat.

Relaxor Ferroelectrics

Relaxor ferroelectrics differ from the normal ferroelectrics described thus far in that they exhibit a broad phase transition from the paraelectric to ferroelectric state, a strong frequency dependence of the dielectric constant (i.e., dielectric relaxation) and a weak remanent polarization. Many of the lead-based relaxor materials have complex disordered perovskite structures. They can be prepared either in polycrystalline form or as single crystals.

Although several compelling theories exist to describe relaxor ferroelectric phenomena, the exact mechanisms for the diffuse phase transition exhibited by these materials are yet to be fully understood. We introduce here a widely accepted description referred to as the *microscopic composition fluctuation model*, which is applicable even to macroscopically disordered structures.[12-14] The model proposes the existence of the so-called *Kanzig region,* which is essentially the smallest region in which ferroelectricity can occur. The range of size for these regions is on the order of 100-1000 Å. It is assumed that there will be local fluctuations in the distribution of Mg^{2+} and Nb^{5+}, for example, on the B-site of the disordered perovskite cell for the relaxor composition $Pb(Mg_{1/3}Nb_{2/3})O_3$. A computer simulation of the composition fluctuations for a perovskite material with the general formula $A({}^{I}B_{1/2}{}^{II}B_{1/2})O_3$ and varying degrees of B-site ordering is shown in Figure 3.8.[14] The fluctuation of the ${}^{I}B/{}^{II}B$ ratio is well represented by a Gaussian distribution function. It has been proposed in the context of this theory that local variations in composition will produce local variations in Curie temperatures, thus leading to the diffuse phase transition that is observed in the dielectric data. Short-range B-site ordering in $Pb(Mg_{1/3}Nb_{2/3})O_3$ has been observed by electron microscopy.[15] The high resolution image revealed ordered regions with sizes in the range of 20-50 Å, as schematically depicted in the center diagram of Figure 3.8.

Another significant characteristic of a relaxor ferroelectric is its dielectric relaxation (the frequency dependence of the dielectric constant) from which their name is derived. The dielectric constant for $Pb(Mg_{1/3}Nb_{2/3})O_3$ is plotted as a function of temperature in Figure 3.9 at various measurement frequencies.[16] We see from these data that as the measurement frequency is increased, the low temperature dielectric constant decreases and the peak in the curve shifts to higher temperature. This is in contrast to the trends observed for a normal ferroelectric, such as $BaTiO_3$, where the temperature of the dielectric constant peak varies very little with frequency. The origin of this effect has been examined in studies focused on $Pb(Zn_{1/3}Nb_{2/3})O_3$ single crystals.[17] The dielectric constant and loss are plotted as a function of temperature for an unpoled and a poled PZN sample in Figure 3.10. Domain configurations corresponding to each are also shown on the right-hand side of the figure. We see from these data that macroscopic domains are not present in the unpoled sample even at room temperature, and large dielectric relaxation and loss are observed below the Curie range. Once macrodomains are induced by the external electric field, the dielectric dispersion disappears and the loss becomes very small (that is, the dielectric behavior becomes rather normal!) below 100°C. The dielectric relaxation is thus associated with the microdomains present in this material.

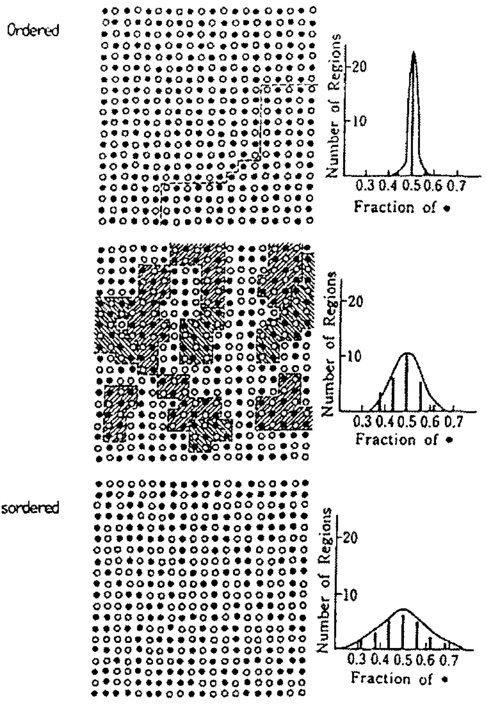

Figure 3.8 Computer simulation of the compositional fluctuations in a $A(^{I}B_{1/2}\ ^{II}B_{1/2})O_3$ perovskite calculated for varying degrees of B-site ordering.[14]

Ceramics of PMN are easily poled when the poling field is applied near the transition temperature, but they are depoled completely when the field is removed as the macrodomain structure reverts to microdomains (with sizes on the order of several hundred Å). This microdomain structure is believed to be the source of the exceptionally large electrostriction exhibited by these materials. The usefulness of the material is thus further enhanced when the transition temperature is adjusted to near room temperature.

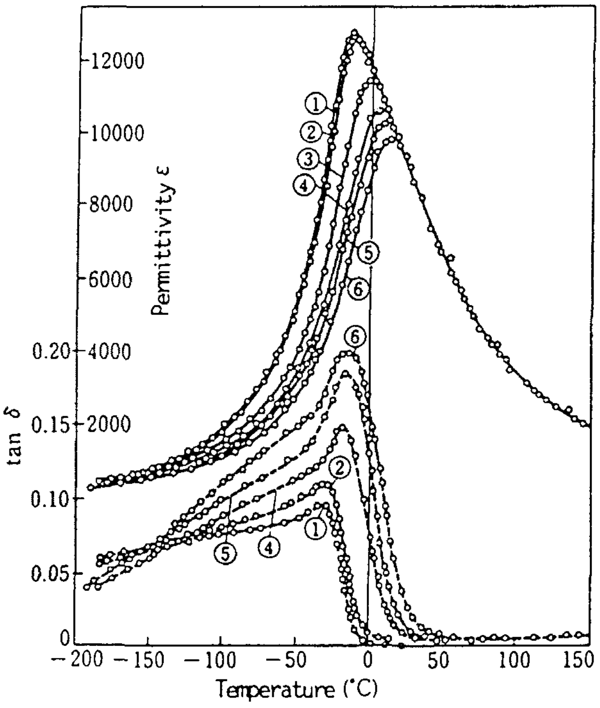

Figure 3.9 The temperature dependence of the dielectric permittivity for $Pb(Mg_{1/3}Nb_{2/3})O_3$ at various frequencies (kHz): (1) 0.4, (2) 1, (3) 45, (4) 450, (5) 1500, (6) 4500.[16]

The longitudinal induced strain at room temperature as a function of applied electric field for 0.9PMN-0.1PbTiO$_3$ ceramic is shown in Figure 3.11.[18] Notice that the order of magnitude of the electrostrictive strain (10^{-3}) is similar to that induced under unipolar drive in PLZT (7/62/38) through the piezoelectric effect [Figure 3.6(a)]. An attractive feature of this material is the near absence of hysteresis

Other electrostrictive materials include (Pb,Ba)(Zr,Ti)O$_3$[19] and various compositions from the PLZT system.[9,20] The large electrostriction effect in all these materials appears to be associated with the microdomain structure. In order to promote microscopic inhomogeneity throughout a given sample and the development of microdomain regions, dopant ions with a valence or ionic radius different than those of the ion they replace are introduced into the structure. We will examine this process further in Section 3.3.

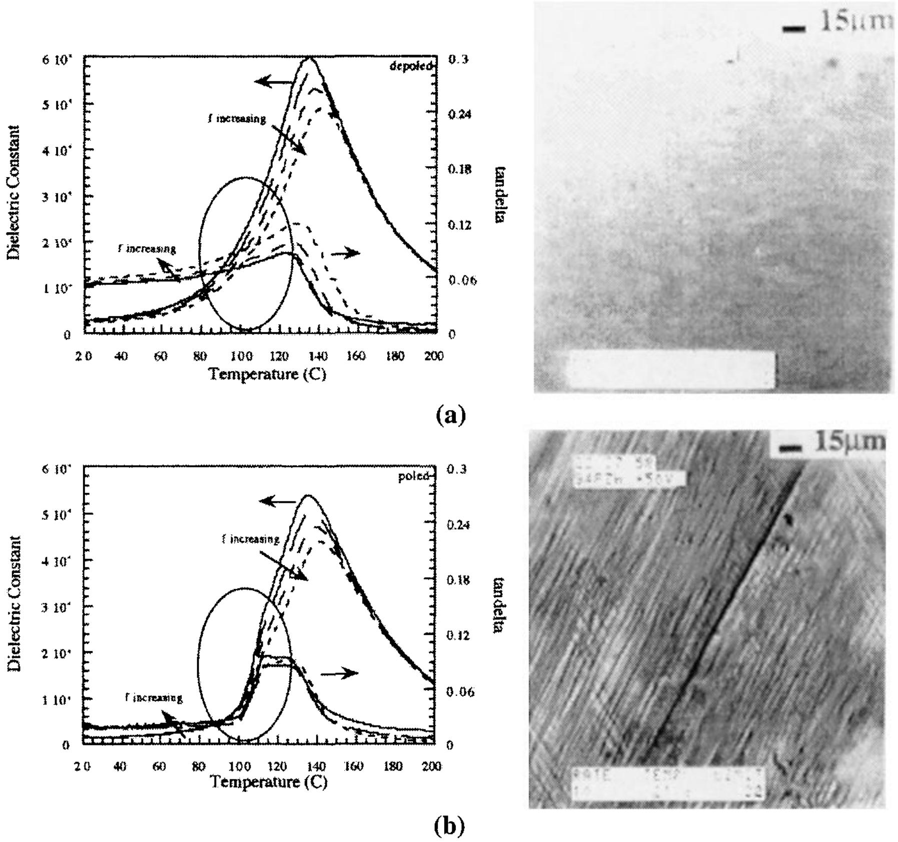

Figure 3.10 The dielectric constant and dielectric loss (tanδ) as a function of temperature measured along <111> (the P_S direction) of a $Pb(Zn_{1/3}Nb_{2/3})O_3$ single crystal: (a) a depoled sample (b) and a poled sample.[17] (Domain configurations corresponding to each are shown on the right-hand side of the figure.)

We can now summarize and compare the practical characteristics of piezoelectric and electrostrictive ceramics:

1. The electrostrictive strain is about the same order of magnitude as the piezoelectric (unipolar) strain (0.1%). There is practically no hysteresis in the electrostrictive strain.

2. Piezoelectric materials require an electrical poling process, which can lead to significant aging. Electrostrictive materials do not need such pretreatment, but require a DC bias field for some applications due to the nonlinear response.

3. Compared with piezoelectrics, the electromechanical response of electrostrictive ceramics tends not to deteriorate under severe operating conditions such as high temperature and large mechanical load (Section 3.5).

4. Piezoelectrics are superior to electrostrictive materials with regard to their temperature characteristics.

5. Piezoelectrics have smaller dielectric constants than electrostrictive materials, and thus exhibit a quicker response (see Section 3.4).

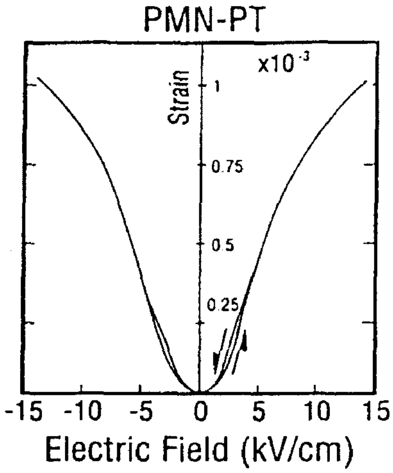

Figure 3.11 Field-induced strain curve for $0.9Pb(Mg_{1/3}Nb_{2/3})O_3$-$0.1PbTiO_3$ at room temperature.[18]

A relaxor ferroelectric does exhibit an induced piezoelectric effect and the electromechanical coupling factor, k_t, is observed to vary with the DC bias field strength. As the DC bias is increased, the coupling factor increases and eventually saturates. This behavior is highly reproducible and makes it possible to employ relaxor ferroelectrics as field-tunable ultrasonic transducers.[21]

Recently, highly responsive single crystal relaxor ferroelectrics from solid solution systems with a morphotropic phase boundary (MPB) have been grown and characterized for application as ultrasonic transducers and electromechanical actuators. Compositions very near the morphotropic phase boundary tend to show the most promise for these applications. Extremely high values for the electromechanical coupling factor (k_{33}=92-95%) and piezoelectric strain coefficient (d_{33}=1500 pC/N) were first reported for single crystals at the MPB of the $Pb(Zn_{1/3}Nb_{2/3})O_3$-$PbTiO_3$ (PZN-PT) system in 1981 by Kuwata, Uchino, and

Nomura.[22,23] Various electromechanical parameters (at room temperature) are plotted as a function of composition in Figure 3.12. Notice how two different values are plotted for the morphotropic phase boundary composition, $0.91Pb(Zn_{1/3}Nb_{2/3})O_3$-$0.09PbTiO_3$. The highest values for the piezoelectric coefficients and electromechanical coupling factors are observed for the rhombohedral composition only when the single crystal is poled along the perovskite [001] direction, not along [111], which is the direction of the spontaneous polarization.

Approximately 10 years later, Yamashita et al. (Toshiba)[24] and Shrout et al. (Penn State)[25] independently reproduced these findings, and refined data were collected in order to characterize the material for medical acoustic applications. Strains as large as 1.7% can be induced in single crystals from the morphotropic phase boundary composition of this system. The field-induced strain curve for a [001] oriented 0.92PZN-0.08PT crystal is shown in Figure 3.13.[25]

The mechanism for the enhanced electromechanical coupling in this case is the same as that for PZT, as described in Chapter 2. The shear coupling that occurs through d_{15} is dominant for perovskite piezoelectrics. The applied electric field should therefore be applied such that its direction is somewhat canted from the spontaneous polarization direction in order to produce the optimum piezoelectric response. The exceptionally high strain generated in materials with compositions near the morpotropic phase boundary (up to 1.7%) is associated with the field-induced phase transition from the rhombohedral to the tetragonal phase. The applied electric field is generally directed along the perovskite [001] direction so that the electrostrictive response occurs in conjunction with a piezoelectric one, thereby enhancing the magnitude of the field-induced strain.

It is convenient to classify electromechanical materials according to their coercive field. A material with a coercive field larger than 10 kV/cm is called a *hard piezoelectric*, and has a broad linear range, but exhibits relatively small induced strains. A material with a coercive field between 1-10 kV/cm is called a *soft piezoelectric*, and exhibits large induced strain, but also relatively large hysteresis. A material with a very small coercive field of less than 1 kV/cm is called an *electrostrictor*. It exhibits a strain that is approximately quadratic with respect to the applied electric field. Each type of material may also be characterized by its Curie point. The Curie point of the hard piezoelectric is generally much higher (> 250°C) than its usual operating temperature (room temperature), in contrast to an electrostrictive material, which has a transition temperature somewhat lower than room temperature. The Curie point of soft piezoelectrics ranges from 150°C to 250°C.

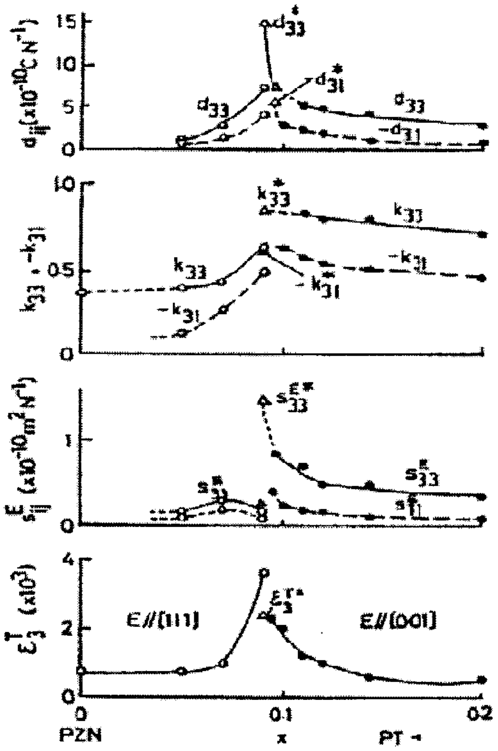

Figure 3.12 Various electromechanical parameters of materials from the (1−x)Pb($Zn_{1/3}Nb_{2/3}$)O_3-(x)$PbTiO_3$ (PZN-PT) system as a function of PT content, x. Note that all peak at the morphotropic phase boundary composition, x = 0.9.[22,23]

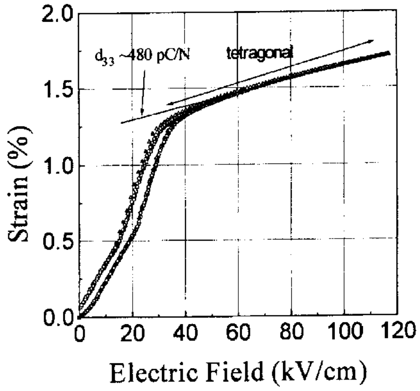

Figure 3.13 The field-induced strain for a [001] oriented 0.92PZN-0.08PT single crystal.[25]

Phase-Change Materials

The primary phase-change-induced strains employed for actuator applications typically involve a transition from an antiferroelectric to a ferroelectric phase, which is accompanied by an induced polarization.[26] The change in the spontaneous strain that occurs with this type of field-induced phase transition is theoretically much larger than that associated with a paraelectric to ferroelectric phase change or the non-180° domain reorientation that occurs for certain ferroelectrics under an applied field [see Section 2.2(3)]. The field-induced strain for an antiferroelectric lead zirconate stannate-based composition from the $Pb_{0.99}Nb_{0.02}[(Zr_xSn_{1-x})_{1-y}Ti_y]_{0.98}O_3$ (PZST) system is shown in Figure 3.14.[27] We see from these data that a maximum induced strain of about 0.4% is possible for this material, which is much larger than what is typically observed for conventional piezoelectrics or electrostrictors. A more rectangular-shaped hysteresis curve is observed for some compositions from this system [Figure 3.14(a)], because the change in strain occurring at the phase transition is much larger than the strain change induced in either the antiferroelectric or the ferroelectric phases. This mode of operation is referred to as *digital displacement* because the material effectively switches between "on" and "off" strain states.

A *shape memory effect* is observed for certain compositions [Figure 3.14(b)]. Once the ferroelectric phase has been induced, the material will retain or "memorize" its ferroelectric state, even if the field is completely removed. A relatively small reverse bias field restores the material to its original state as shown in the figure. One advantage to this type of shape memory ceramic is that it does not require a sustained applied electric field; instead only a pulse drive is required, thereby saving considerable energy. The transient tip deflection of a shape memory ceramic bimorph after a triangular pulse is applied is shown in Figure 3.15.[28] The response speed of the phase transition is quick enough to generate a resonant mechanical vibration.

Piezoelectric Polymers

Polyvinylidene difluoride, PVDF or PVF2, becomes piezoelectric when it is stretched during the curing process. The basic structure of this material is depicted in Figure 3.16. Thin sheets of the cast polymer are drawn and stretched in the plane of the sheet, in at least one direction, and frequently also in the perpendicular direction, to transform the material to its microscopically polar phase. Crystallization from the melt produces the nonpolar α-phase, which can be converted into the polar β-phase by this uniaxial or biaxial drawing operation. The resulting dipoles are then aligned by electrically poling the material. Large sheets can be manufactured and thermally formed into complex shapes.

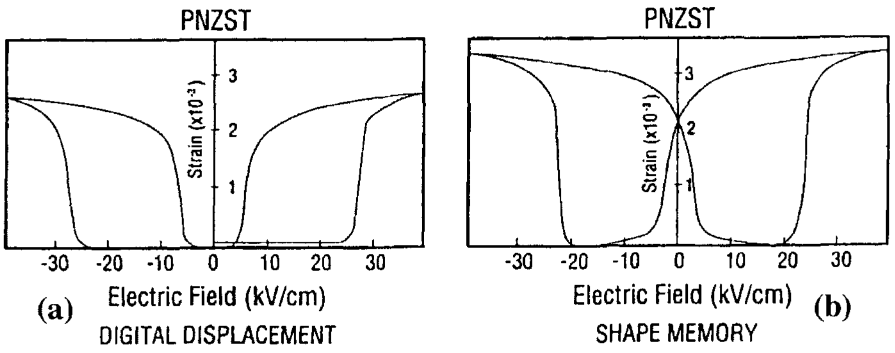

Figure 3.14 The field-induced strain for an antiferroelectric composition from the $Pb_{0.99}Nb_{0.02}[(Zr_xSn_{1-x})_{1-y}Ti_y]_{0.98}O_3$ (PZST) system (longitudinal effect): (a) digital displacement response and (b) shape memory response.[27]

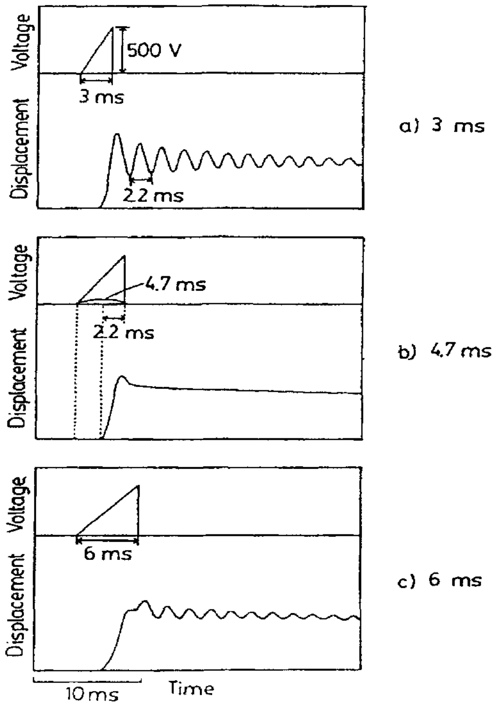

Figure 3.15 Transient tip deflection of a PZST shape memory ceramic bimorph.[28]

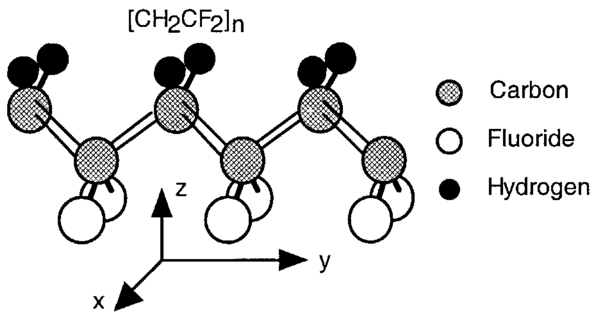

Figure 3.16 Structure of polyvinylidene difluoride (PVDF).

The copolymerization of polyvinylidene difluoride with trifluoroethylene (TrFE) results in a random copolymer (PVDF-TrFE) with a stable polar β-phase. This polymer need not be stretched; the microscopically polar regions are formed during the copolymerization process so that the as-formed material can be immediately poled. The poled material has a thickness-mode coupling coefficient, k_t, of 0.30.

Piezoelectric polymers have the following characteristics: (a) they have small piezoelectric strain coefficients, d (for actuators), and large g constants (for sensors), (b) they are light weight and elastically soft, allowing for good acoustic impedance matching with water and human tissue, (c) they have a low mechanical quality factor, Q_m, allowing for a broad resonance band width. Piezoelectric polymers are used for directional microphones and ultrasonic hydrophones. The major disadvantages of these materials for actuator applications are the relatively small generative stress and the considerable heat generation that is generally associated with a low mechanical quality factor.

Piezoelectric Composites

Piezoelectric composites, comprised of a piezoelectric ceramic and a polymer phase, are promising materials because of their excellent and readily tailored properties. The geometry for two-phase composites can be classified according to the dimensional connectivity of each phase into ten basic structures; 0-0, 0-1, 0-2, 0-3, 1-1, 1-2, 1-3, 2-2, 2-3 and 3-3.[29] A 1-3 piezoelectric composite, such as the PZT rod:polymer composite shown in Figure 3.17, is an interesting example. The advantages of this composite are its high electromechanical coupling factors, good acoustic impedance match to water or human tissue, mechanical flexibility, broad bandwidth, and low mechanical quality factor. The thickness mode electromechanical coupling, k_t, of the composite can exceed that of the ceramic phase (0.40-0.50), approaching the magnitude of the electromechanical coupling factor, k_{33} (0.70-0.80), of the ceramic.[30] Acoustic impedance is the square root of the product of the material's density and elastic stiffness. The acoustic match to tissue or water (1.5 Mrayls) of typical piezoelectric ceramics (20-30 Mrayls) is significantly improved when the ceramic is incorporated into a ceramic:polymer composite structure. Piezoelectric composite materials are especially useful for underwater sonar and medical diagnostic ultrasonic transducer applications.

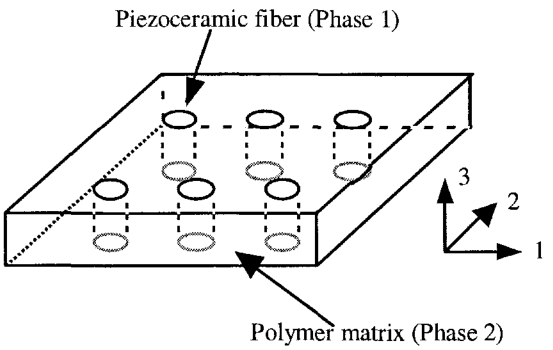

Figure 3.17 A schematic depiction of a 1-3 PZT rod:polymer composite. The top and bottom surfaces are rigid electrodes.

The piezoelectric response of a PZT ceramic, PVDF, and several PZT:polymer composites is presented in Table 3.2.[31] We see that the piezoelectric strain coefficient, d, of PVDF, which represents the strain per unit electric field (important for actuator applications), is smaller than that of the PZT ceramic by an order of magnitude, because of its small dielectric constant. The piezoelectric voltage coefficient, g, of PVDF, which represents the voltage per unit stress (important for sensor applications), is also larger than that of PZT by an order of magnitude. The highest figures of merit for sonar devices, $d_h g_h$ (where d_h and g_h are the hydrostatic piezoelectric coefficients), are achieved with composite materials, which tend to have magnitudes of d and g that lie between those values for the individual ceramic and polymer phases.

Similar to polymer piezoelectrics, a PZT:polymer composite actuator generates and retains significant heat during a single drive cycle. The heat produced by the PZT is not dissipated due to the low thermal conductivity of the polymer phase.

Table 3.2 Electromechanical properties of a PZT ceramic, PVDF, and several PZT:polymer composites.[31]

Material [connectivity]	ρ (10^3 kg/m^3)	c_{33} (GPa)	K_{33}	d_{33} (pC/N)	g_{33} (mVm/N)	g_h (mVm/N)
PZT(501A)	7.9	81	2000	400	20	3
Extended PVDF	1.8	3	13	20	160	80
PZT:Epoxy [3-1]	3.0	19	400	300	75	40
PZT:Silicone Rubber [3-3] (Replica-Type)	3.3	3	40	110	280	80
PZT:Silicone Rubber [3-3] (Ladder-Type)	4.5	19	400	250	60	--
PZT:PVDF [0-3]	5.5	2.6	120	90	85	--
PZT: Rubber [0-3]	6.2	0.08	73	52	140	30
PZT:Chloroprene [0-3]	--	--	40	--	--	90

Example Problem 3.1

A piezoelectric composite consists of two phases, 1 and 2, and is poled in the direction indicated by the arrow in Figure 3.18. Analogous to the terminology used in electronic circuit analysis, the structures pictured in Figures 3.18(a) and 3.18(b) are designated as "parallel" and "series" configurations, respectively. The volume fraction is ${}^1V:{}^2V$ (where ${}^1V + {}^2V = 1$). Assuming the top and bottom electrodes are rigid enough to prevent bending, and the transverse piezoelectric coupling between Phases 1 and 2 is negligibly small, calculate the following physical properties for the composite with the parallel configuration:

(a) the effective dielectric constant, K_{33}',
(b) the effective piezoelectric strain coefficient, d_{33}',
(c) the effective piezoelectric voltage coefficient g_{33}'.

Use the parameters D_3, E_3, X_3, x_3, s_{33}, which are the dielectric displacement, the electric field, the stress, the strain, and the elastic compliance, respectively.

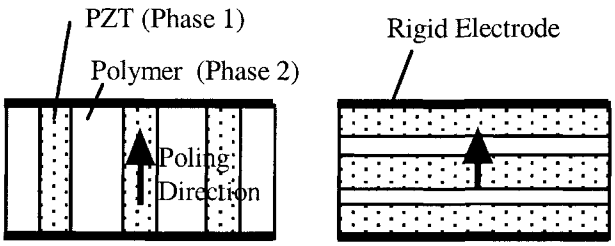

(a) (b)

Figure 3.18 Diphasic composites with (a) parallel and (b) series configurations.

Solution

(a) Since the electrodes are common to all elements in the parallel configuration, E_3 is common to Phases 1 and 2, so that:

$$D_3 = {}^1V\,{}^1K_{33}\,\varepsilon_o\,E_3 + {}^2V\,{}^2K_{33}\,\varepsilon_o E_3 \;=\; K_{33}'\,\varepsilon_o\,E_3 \qquad \text{(P3.1.1)}$$

Therefore,

$$K_{33}' = {}^1V\,{}^1K_{33} + {}^2V\,{}^2K_{33} \qquad \text{(P3.1.2)}$$

and when ${}^1K_{33} >> {}^2K_{33}$, $K_{33}' = {}^1V\,{}^1K_{33}$.

(b) If Phases 1 and 2 are independent and mechanically free, then:

$$ {}^1x_3 = {}^1d_{33}\,E_3 \qquad \text{and} \qquad {}^2x_3 = {}^2d_{33}\,E_3 \qquad \text{(P3.1.3)}$$

The strain x_3 must be common to both Phases 1 and 2 and the effective strain x_3' is given by the following equation:

$$\frac{{}^1V\,({}^1x_3 - {}^1x_3')}{{}^1s_{33}} = \frac{{}^2V\,({}^2x_3' - {}^2x_3)}{{}^2s_{33}} \qquad \text{(P3.1.4)}$$

Therefore,

$$x_3' = \left[\frac{({}^1V\,{}^2s_{33}\,{}^1d_{33} + {}^2V\,{}^1s_{33}\,{}^2d_{33})}{({}^1V\,{}^2s_{33} + {}^2V\,{}^1s_{33})}\right]E_3 \qquad \text{(P3.1.5)}$$

and, consequently, the effective piezoelectric constant is:

$$d_{33}' = \left[\frac{({}^1V\,{}^2s_{33}\,{}^1d_{33} + {}^2V\,{}^1s_{33}\,{}^2d_{33})}{({}^1V\,{}^2s_{33} + {}^2V\,{}^1s_{33})}\right] \qquad \text{(P3.1.6)}$$

and when ${}^1s_{33} << {}^2s_{33}$, $d_{33}' = {}^1d_{33}$.

(c) Since $g_{33}' = d_{33}' / \varepsilon_o K_{33}'$, we can express this quantity in the following form:

$$d_{33}' = \left[\frac{({}^1V\,{}^2s_{33}\,{}^1d_{33} + {}^2V\,{}^1s_{33}\,{}^2d_{33})}{({}^1V\,{}^2s_{33} + {}^2V\,{}^1s_{33})\varepsilon_o({}^1V\,{}^1K_{33} + {}^2V\,{}^2K_{33})}\right] \qquad \text{(P3.1.7)}$$

and when ${}^1s_{33} << {}^2s_{33}$ and ${}^1K_{33} >> {}^2K_{33}$, $g_{33}' = {}^1g_{33}/{}^1V$.

Piezoelectric Thin Films

Both zinc oxide (ZnO) and aluminum nitride (AlN) are simple binary compounds with the Wurtzite structure which can be sputter-deposited as a [001]-oriented thin film on a variety of substrates. Zinc oxide has large piezoelectric coupling and thin films of this material are widely used in bulk acoustic and surface acoustic wave devices. The fabrication of highly oriented [001] ZnO films have been studied and developed extensively. The performance of ZnO devices is limited, however, due to their low piezoelectric coupling (20-30%). Lead zirconate titanate (PZT) thin films are expected to exhibit better piezoelectric properties. At present PZT thin films are grown for use in microtransducers and microactuators. Relatively high power drive is possible for these thin film devices, because the heat generated in operation is readily dissipated through the substrate. These actuators cannot provide large mechanical output, however, because the power is determined by the total volume of the piezoelectric material present, which in this case is quite small.

(4) Shape Memory Alloys

Reversible martensitic transformations are observed in many alloys; however, an especially pronounced shape memory effect is observed in alloys based on NiTi and Cu. The former is known as Nitinol (the "nol" indicates the alloy was discovered by the Naval Ordinance Laboratory, now called the Navy Surface Warfare Center). The properties of some typical shape memory materials are summarized in Table 3.3.[32]

Table 3.3 Properties of typical shape memory alloys.[32]

Property	Ni-Ti	Cu-Al-Ni	Cu-Al-Zn
Induced ("Self") Strain, x_o	20%	20%	20%
Latent Heat of Transition, q (J/kg K)	470-620	400-480	390
Maximum Recovery Stress, X_{max} (MPa)	600-800	600	700
Macroscopic Strain Effect			
Polycrystalline	4%	2%	2%
Single Crystal	10%	10%	10%

The induced strain (sometimes called the self-strain) for a typical martensitic transition between close-packed structures, face centered cubic (fcc) and body centered cubic (bcc) or hexagonal close packed (hcp) for the NiTi alloys, is as high as 20%. The R-phase in NiTi-based alloys has a smaller induced strain of about 3%, which is still an order of magnitude larger than the strains produced in piezoelectrics.[33] The large strain effect and the structural reversibility of the martensitic transformation in these alloys make them effective for actuator applications. The induced strain leads to the development of stress when the transformation is impeded. The stress generated by the phase transition depends on the thermodynamics of the transformation and on the mechanical boundary conditions imposed on the specimen. The maximum value of the actuation stress, X_{max}, on cooling can be estimated according to:

$$X_{max} = q / x_o \tag{3.2}$$

where q is the latent heat of the phase transformation, and x_o is the induced (self) strain.

(5) Magnetostrictive and Giant Magnetostrictive Materials

Magnetostriction was discovered by James Joule in the 19th century. Since then the effect has been investigated in magnetic metals, such as Fe, Ni, and Co, and oxides such as the ferrites. Research on giant magnetostrictive materials including rare earth metals commenced in the 1960's. The magnetic structure and magnetic anisostropy of rare earth metals were under intensive study at this time. In particular, giant magnetostriction of more than 1% was reported for Tb and Dy metal single crystals at cryogenic temperatures.[34,35] This level of induced strain is two to three orders of magnitude higher than the strains typically observed in Ni and the ferrites.

The research of the 1970's was focused on compounds consisting of rare earth (R) and transition metal (T) elements. The RT_2 alloys, exemplified by RFe_2 (known as the cubic Laves phase), were of particular interest. Exceptionally large magnetostriction of up to 0.2% was reported for $TbFe_2$ at room temperature.[36,37] This triggered a boom in research on this enhanced effect now known as giant magnetostriction. In 1974, $Tb_{0.3}Dy_{0.7}Fe_2$, which exhibits enormous magnetostriction under relatively small magnetic field strengths at room temperature, was produced.[38]

In 1987, sophisticated crystal control technology was developed[39] and a magnetostriction jump phenomenon was discovered in [112]-oriented alloys.[40] (The mechanism for the jump is a sudden realignment of the spin with one of the crystallographic easy axes closer to the external field direction). These technologies helped to stabilize the magnetostriction. Strains of 0.15% can be consistently achieved under an applied magnetic field of 500 Oe and compressive stress of 1 kgf/mm^2. The materials in the compositional range $Tb_{0.27-0.3}Dy_{0.7-0.73}Fe_{1.9-2.0}$ are called Terfenol-D (dysprosium modified terbium iron produced at "nol"), and are currently commercially produced by several manufacturers.

The saturated magnetostrictive strain for some magnetic materials at 300K are summarized in Table 3.4.[41] Note that several materials in the table have a negative magnetostriction coefficient (that is, their length decreases under an applied magnetic field), while other materials, including Terfenol-D, have a positive magnetostriction coefficient.

Table 3.4 The saturated magnetostrictive strain for some magnetic materials at 300K.[41]

Material	Induced Strain ($\Delta l/l \times 10^{-6}$)
Fe	−9
Ni	−35
Co	−60
0.6Co-0.4Fe	68
0.6Ni-0.4Fe	25
$TbFe_2$	1753
Terfenol-D	1600
$SmFe_2$	−1560
Metglass 2605SC	40

There are three primary mechanical concerns in the design of Terfenol-D transducers: (a) optimization of the output strain, (2) mechanical impedance matching, and (3) strengthening against fracture.[42] A pre-stress in the range of 7-10 MPa is generally applied to the Terfenol-D actuator in order to enhance its magnetostrictive response. This level of stress is sufficient to align the magnetic moments parallel to an easy axis, which is almost perpendicular to an actual crystallographic axis. Actuator displacements are enhanced by a factor of three for samples subjected to the pre-stress treatment.[43] Mechanical impedance matching is required between a magnetostrictive actuator and its external load to ensure efficient energy transfer to the load. Terfenol-D has a low tensile strength, with a yield strength of 700 MPa in compression, but only 28 MPa in tension.[44]

Various composite structures have been investigated in recent years to more effectively address these mechanical problems and to optimize the magnetostrictive response. Terfenol-D:epoxy composites, for example, are automatically subject to the pre-stress treatment during the cure process.[45,46] Models of the system have been developed to investigate the effects of particulate volume fraction and thermal expansion of the polymer matrix on the strain-field-load characteristics of the composite. It was determined that a low-viscosity matrix facilitates the formation of particle chains and helps to inhibit the production of voids during the cure process. The models were verified with Terfenol-D:epoxy samples representing various particle loading conditions (10-40%), and polymer thermal expansion coefficients ($30\text{x}10^{-6}$-$50\ \text{x}10^{-6}$ degree^{-1}), Young's moduli (0.5-3 GPa), and viscosities (60-10,000 cps).

The magnetostrictive strain for Terfenol-D:epoxy composites is shown in Figure 3.19.[46] We see in this response the competing influences of the magnetostrictive force needed to overcome and strain the matrix and the pre-stress force, which increases with decreasing volume fraction of Terfenol-D. As the volume fraction increases from 10 to 20%, an overall increase in the force and strain occurs largely due to the higher concentration of magnetostrictive material in the composite. As the volume fraction increases beyond 20%, however, the decrease in the pre-stress that is applied to the magnetostrictive composite on curing ultimately limits the force and strain generated in the structure and the net response is reduced despite the higher concentration of magenetostrictive material.

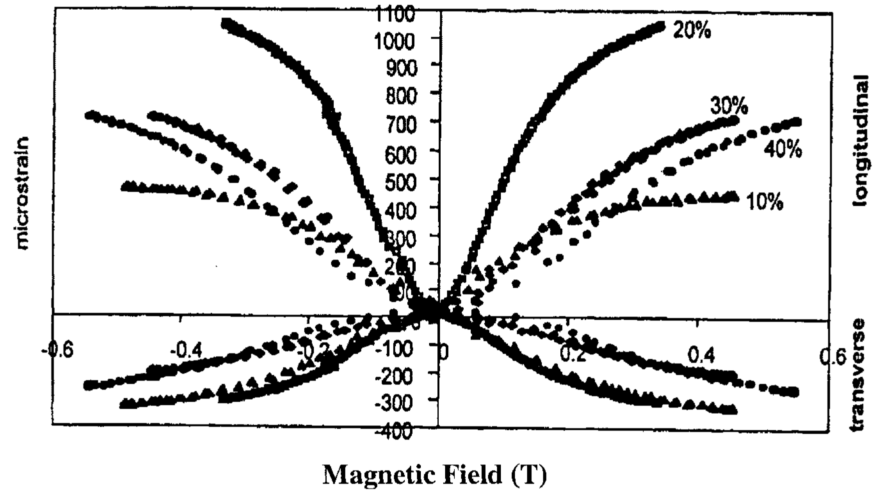

Figure 3.19 The longitudinal and transverse magnetostrictive strain as a function of applied magnetic field for Terfenol-D:epoxy composites with various volume fractions of Terfenol-D.[46]

3.2 FIGURES OF MERIT FOR PIEZOELECTRIC TRANSDUCERS

There are five important figures of merit for piezoelectrics: (1) the piezoelectric strain coefficient, d, (2) the piezoelectric voltage coefficient, g, (3) the electromechanical coupling factor, k, (4) the mechanical quality factor, Q_m, and (4) the acoustic impedance, Z. Each of these quantities will be defined in this section.

(1) The Piezoelectric Strain Coefficient, d

The magnitude of the strain, x, induced by an applied electric field, E, is characterized by the piezoelectric strain coefficient, d, according to:

$$x = dE \quad (3.3)$$

This quantity is an important figure of merit for actuators.

(2) The Piezoelectric Voltage Coefficient, g

The induced electric field, E, is related to the applied stress, X, through the piezoelectric voltage coefficient, g, according to:

$$E = gX \quad (3.4)$$

This quantity is an important figure of merit for sensors.

Recall that the direct piezoelectric effect is described by P=dX, where P is the induced polarization. When we combine this expression with Equation (3.4) we obtain an important relationship between g and d:

$$g = d / \varepsilon_o K \quad (3.5)$$

where K is the dielectric constant.

Example Problem 3.2

Obtain the relationship between the piezoelectric d and g coefficients which indicate the strain per unit electric field and the electric field per unit stress, respectively.

Solution

Starting with the fundamental piezoelectric equations:

$$x = s^E X + d E \quad (P3.2.1)$$

$$P = d X + \varepsilon_o K^X E \quad (P3.2.2)$$

The actuator figure of merit, d (defined for X = 0), is given by Equation (P3.2.1) to be x=dE, and the sensor figure of merit, g (defined for E = 0), is given by Equation (P3.2.2) to be P=dX. The polarization, P, induced in a material with a dielectric permittivity, $\varepsilon = \varepsilon_o K^X$, results in the development of an electric field, E, with a magnitude given by:

$$E = P / \varepsilon_o K^X = d X / \varepsilon_o K^X \quad (P3.2.3)$$

Combining this equation with the defining equation for the piezoelectric voltage coefficient, E = g X, yields:

$$\rightarrow\rightarrow g = d / \varepsilon_o K^X \quad (P3.2.4)$$

(3) The Electromechanical Coupling Factor, k, and Related Quantities

The terms electromechanical coupling factor, k, energy transmission coefficient, λ_{max}, and efficiency, η, are sometimes misrepresented. All are related to the conversion rate between electrical energy and mechanical energy, but they are defined differently.

The Electromechanical Coupling Factor

The electromechanical coupling factor is defined by either of the following expressions:

$$k^2 = \frac{\text{Stored Mechanical Energy}}{\text{Input Electrical Energy}} \tag{3.6a}$$

$$k^2 = \frac{\text{Stored Electrical Energy}}{\text{Input Mechanical Energy}} \tag{3.6b}$$

Let us work with Equation (3.6a) to determine the electromechanical coupling factor when an electric field, E, is applied to a piezoelectric material. The input electrical energy per unit volume is:

$$\text{Input Electrical Energy} = (1/2)\ \varepsilon_0 K\ E^2 \tag{3.7a}$$

and the stored mechanical energy per unit volume under zero external stress is given by:

$$\text{Stored Mechanical Energy} = (1/2)x^2/s = (1/2)\ (d\ E)^2/s \tag{3.7b}$$

where s is the elastic compliance of the material. Making these substitutions into Equation (3.6a) and simplifying allows us to now express k^2 as:

$$k^2 = \frac{(\frac{1}{2})(d\,E)^2/s}{(\frac{1}{2})\varepsilon_0 K\ E^2} = \frac{d^2}{\varepsilon_0 K s} \tag{3.8}$$

The Energy Transmission Coefficient

Not all the stored energy can actually be used, and the actual work done depends on the mechanical load. When there is no mechanical load or when the material is completely clamped (that is, it is not allowed to strain), the output work is zero and the maximum energy transmission coefficient is defined by either of the following expressions:

$$\lambda_{max} = \left[\frac{\text{Output Mechanical Energy}}{\text{Input Electrical Energy}}\right]_{max} \quad (3.9a)$$

$$\lambda_{max} = \left[\frac{\text{Output Electrical Energy}}{\text{Input Mechanical Energy}}\right]_{max} \quad (3.9b)$$

Let us consider the case where an electric field, E, is applied to a piezoelectric under constant external stress. Here a compressive stress ($X<0$) is required to produce the desired work and energy. The output mechanical work (energy), represented by the shaded area in the strain versus stress plot shown in Figure 3.20(b), is determined according to

$$\text{Output Mechanical Energy} = \int -X\,dx = -(dE + sX)X \quad (3.10a)$$

The corresponding input electrical energy, represented by the shaded area indicated in the polarization versus applied electric field plot shown in Figure 3.20(c), is likewise given by:

$$\text{Input Electrical Energy} = \int E\,dP = (\varepsilon_o KE + dX)E \quad (3.10b)$$

We need to choose a proper load to maximize the energy transmission coefficient. We begin by expressing the energy transmission coefficient in terms of the definitions of the output work and input electrical energy given by Equations (3.10a) and (3.10b):

$$\lambda = \frac{-(dE + sX)X}{(\varepsilon_o KE + dX)E} \quad (3.11)$$

The maximum energy transmission coefficient, λ_{max}, which is readily determined from this expression by the process carried out in Example Problem 3.3, is written in terms of the electromechanical coupling factor, k, as follows:

$$\lambda_{max} = \left[(1/k) - \sqrt{(1/k^2) - 1}\right]^2 = \left[(1/k) + \sqrt{(1/k^2) - 1}\right]^{-2} \quad (3.12)$$

Notice that the range of λ_{max} is just:

$k^2/4 < \lambda_{max} < k^2/2$

and, in general, when k is small, $\lambda_{max} = k^2/4$, while for larger values of k, $\lambda_{max} = k^2/2$.

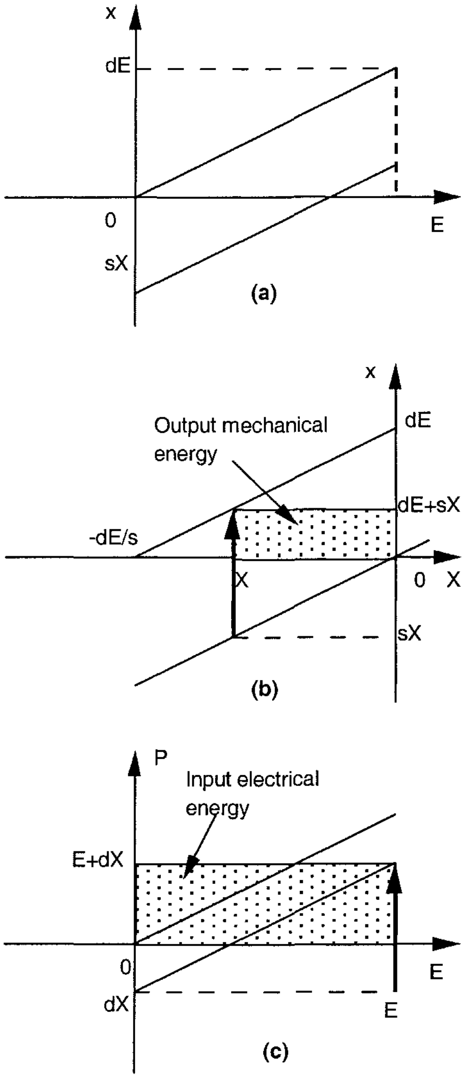
x
dE
0
E
sX
(a)
x
Output mechanical energy
dE
dE+sX
-dE/s
X
0 X
sX
(b)
P
Input electrical energy
E+dX
0
E
dX
E
(c)

Figure 3.20 Plots for determining the input electrical and the output mechanical energy of a piezoelectric actuator: (a) induced strain as a function of applied electric field, (b) induced strain as a function of applied stress, and (c) induced polarization as a function of applied electric field.

It should also be noted that the conditions for maximum energy transmission do not correspond to the conditions required for maximum output mechanical energy. The maximum output energy actually occurs when the load is equal to half of the maximum generative stress: $-[dE-s(dE/2s)](-dE/2s)=(dE)^2/4s$. In this case, since the input electrical energy is given by:

$$\text{Input Electrical Energy} = [\varepsilon_o K E + (-d^2E/2s)]\,E \tag{3.13}$$

The energy transmission coefficient under these conditions is given by:

$$\lambda = \frac{1}{2[(2/k^2)-1]} \tag{3.14}$$

This is close to, but not precisely equal to, the maximum value, λ_{max}.

The Efficiency

The efficiency, η, is defined by either of the following expressions:

$$\eta = \left[\frac{\text{Output Mechanical Energy}}{\text{Consumed Electrical Energy}}\right] \tag{3.15a}$$

$$\eta = \left[\frac{\text{Output Electrical Energy}}{\text{Consumed Mechanical Energy}}\right] \tag{3.15b}$$

In a single work cycle (that is, one complete cycle of the applied electric field), the input electrical energy to the actuator is transformed partially into mechanical energy and the remaining is stored as electrical energy (essentially as electrostatic energy in a capacitor). If the losses are small, nearly all the nonmechanical energy is returned to the power source, leading to near 100% efficiency. The dielectric loss in PZT is typically in the range of about 1-3% and increases significantly above a certain level of applied electric field. This is, of course, less than ideal and the actual efficiencies obtained for PZT-based devices will depend on a variety of material-related parameters as well as the experimental conditions. We will consider these issues in more detail in Chapter 6.

Example Problem 3.3

Show that the maximum energy transmission coefficient, λ_{max}, for a piezoelectric actuator may be expressed in terms of the electromechanical coupling coefficient, k, as follows:

$$\lambda_{max} = \left[(1/k) + \sqrt{(1/k^2) - 1}\right]^{-2} \qquad \text{(P3.3.1)}$$

Solution

The energy transmission coefficient is defined by:

$$\lambda = \left[\frac{\text{Output Mechanical Energy}}{\text{Input Electrical Energy}}\right]$$

Considering the case where an electric field, E, is applied to a piezoelectric under a constant external stress, X, the energy transmission coefficient, λ, can be expressed as:

$$\lambda = \frac{-xX}{PE} = \frac{-(dE + sX)X}{(\varepsilon_o KE + dX)E}$$

$$= \frac{-[d(X/E) + s(X/E)^2]}{[\varepsilon_o K + d(X/E)]} \qquad \text{(P3.3.2)}$$

We need to determine the appropriate applied stress and electric field, E, conditions required to produce the maximum energy transmission coefficient, λ_{max}. If we let $y = X / E$, then Equation (P3.3.2) becomes:

$$\lambda(y) = \frac{-(sy^2 + dy)}{(dy + \varepsilon_o K)} \qquad \text{(P3.3.3)}$$

The maximum energy transmission coefficient, λ_{max}, is obtained when the derivative of λ with respect to y is equal to zero:

$$\frac{d\lambda}{dy} = \left[\frac{-(2sy + d)(dy + \varepsilon_o K) + (sy^2 + dy)d}{(dy + \varepsilon_o K)^2}\right] = 0 \qquad \text{(P3.3.4)}$$

Simplifying and designating y as y_o produces:

$$y_o^2 + 2(\varepsilon_o K/d)\, y_o + (\varepsilon_o K/s) = 0$$

Solving for y_o yields:

$$y_o = (\varepsilon_o K/d)\left[-1+\sqrt{1-k^2)}\right] \tag{P3.3.5}$$

We may now substitute, $k^2=d^2/s\varepsilon_o K$ and by replacing y with y_o in Equation (P3.3.3), we can obtain an expression for the maximum energy transmission coefficient, λ_{max}, as follows:

$$\lambda_{max} = \frac{[2(s\varepsilon_o K/d)y_o + \varepsilon_o K - d\,y_o]}{(d\,y_o + \varepsilon_o K)}$$

$$= \frac{[d\,y_o(2/k^2-1) + \varepsilon_o K]}{(d\,y_o + \varepsilon_o K)}$$

$$= \frac{[(-1+\sqrt{1-k^2})(2/k^2-1)+1]}{(-1+\sqrt{1-k^2}+1)}$$

$$\rightarrow\rightarrow\ \lambda_{max} = [(1/k)-\sqrt{(1/k^2)-1}\,]^2 \tag{P3.3.6}$$

---

(4) The Mechanical Quality Factor

The mechanical quality factor, Q_m, is a parameter that characterizes the sharpness of the electromechanical resonance spectrum. Considering the motional admittance, Y_m, in the vicinity of the resonance frequency, ω_o, the mechanical quality factor is defined with respect to the bandwidth ($\Delta\omega$) as:

$$Q_m = \omega_o / 2\,\Delta\omega \tag{3.16}$$

It should be noted that the inverse of the mechanical quality factor, Q_m^{-1}, is equal to the intensive mechanical loss ($\tan\delta'$). The magnitude of Q_m is very important in evaluating the magnitude of the resonant strain. The vibration amplitude at an off-resonance frequency [given by (dEl), where l is the length of the sample] is amplified by a factor proportional to Q_m at the resonance frequency. A rectangular plate excited into a longitudinal vibration through d_{31}, for example, will undergo a maximum displacement of $[(8/\pi^2)\,Q_m d_{31} E\,l]$.[47]

(5) The Acoustic Impedance

The acoustic impedance, Z, is a parameter used for evaluating the acoustic energy transfer between two materials. It is defined, in general, by

$$Z^2 = \frac{\text{Pressure}}{\text{(Volume)(Sound Velocity)}} \tag{3.17}$$

A definition that applies specifically to a solid material is:

$$Z = \sqrt{\rho c} \tag{3.18}$$

where ρ is the mass density and c is the elastic stiffness of the material.

In more advanced discussions, there are three kinds of characteristic impedances: (1) the specific acoustic impedance (pressure/particle speed), (2) the acoustic impedance [pressure/(volume)(sound velocity)], and (3) the radiation impedance (force/sound velocity).[48]

Example Problem 3.4

Why is acoustic impedance (or mechanical impedance) matching necessary for the efficient transfer of mechanical energy from one material to another? Explain conceptually.

Solution

The mechanical work done by one material to drive another is characterized by the product of the magnitudes of the applied force, F, and the displacement, Δl (that is, the component of the displacement along the direction of the applied force):

$$W = F\,\Delta l \tag{P3.4.1}$$

A cartoon illustrating two extreme cases appears in Figure 3.21. If the material is very "soft," the force, F, required to produce a given displacement can be very small, and practically no work is done according to our basic definition. This case is depicted in the first cartoon appearing in Figure 3.21. A practical example of this extreme case is when an acoustic wave is generated in water by a hard PZT transducer. In this case, most of the acoustic energy generated in the PZT will be reflected at the interface, and only a small portion is transferred into the water. The other extreme case is illustrated in the second cartoon in Figure 3.21. Exerting a moderate force on a very hard material will generally result in very little displacement of that medium and again the work done is practically zero. A good practical example of this is the use of piezoelectric PVDF (polyvinylidene difluoride) to drive a material such as hard steel. In order to optimize the output mechanical power when employing a given material (medium 1) to drive another (medium 2), it is necessary to match the acoustic impedances of the two media:

$$\sqrt{\rho_1 c_1} = \sqrt{\rho_2 c_2} \tag{P3.4.2}$$

where ρ is the mass density and c is the elastic stiffness of the materials. In practice, acoustic impedance matching layers with elastic properties intermediate between the piezoelectric ceramic and the other medium are applied to a PZT device to optimize the transfer of mechanical energy from the transducer to water or human tissue.

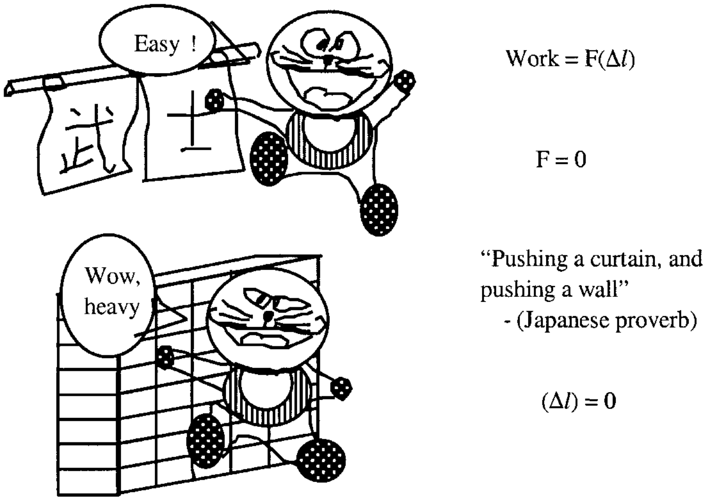
Easy !
武
士
Work = F(Δl)
F = 0
Wow, heavy
"Pushing a curtain, and pushing a wall" - (Japanese proverb)
(Δl) = 0

Figure 3.21 Cartoons illustrating the need for acoustic impedance matching between an actuator (cat) and a given medium (curtain and wall).

3.3 THE TEMPERATURE DEPENDENCE OF THE ELECTROSTRICTIVE STRAIN

The temperature dependence of the field-induced strain in an electrostrictive $0.9Pb(Mg_{1/3}Nb_{2/3})O_3$-$0.1PbTiO_3$ ceramic under an applied field of 3.3 (kV/cm) is shown in Figure 3.22. Researchers strive to significantly reduce or eliminate the temperature dependence of the strain response when developing new electrostrictive materials. Two methods in particular have been effective in improving the temperature stability of new materials. The first is a macroscopic composite approach, where two materials with different temperature characteristics are combined in a suitable configuration to mutually compensate for and effectively cancel their individual temperature dependences. The other method involves the design of new solid solutions with intermediate compositions that provide optimum temperature characteristics.

(1) Macroscopic Composite Method

A composite structure incorporating $Pb(Mg_{1/3}Nb_{2/3})O_3$ (PMN) and $Pb(Zr,Ti)O_3$ (PZT) calcined powders has been developed as a new material possessing dielectric and electromechanical properties that are very stable over a broad range of temperatures.[49] The dielectric permittivity is shown as a function of temperature for diphasic mixtures of PMN and PZT (molar ratio 0.9:0.1) sintered at various temperatures in Figure 3.23. The induced piezoelectric strain coefficient, d_{31}, is shown as a function of temperature for some diphasic PMN-PZ composites, 0.9PMN-0.1PT, and pure PMN under a bias of 1 kV/cm in Figure 3.24. We see from these data that the composite materials have electromechanical responses that are far more stable with temperature (over the temperature range of −10°C to 70°C) than those exhibited by the pure PMN and 0.9PMN-0.1PT ceramics.

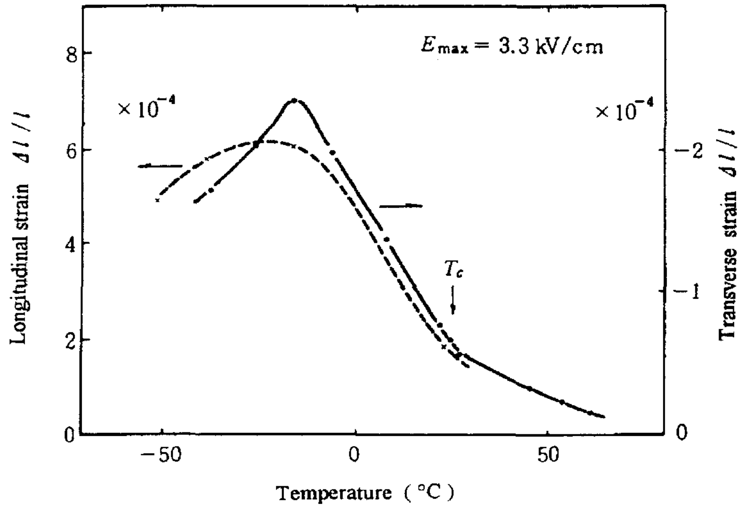

Figure 3.22 The temperature dependence of the electrostrictive strain for $0.9Pb(Mg_{1/3}Nb_{2/3})O_3$-$0.1PbTiO_3$ materials.

(2) Microscopic Approach

Another approach for improving the temperature dependence of electrostriction involves microscale modifications of the material. A simple relationship between the temperature coefficient of electrostriction (TCE) and the diffuseness of the phase transition has been discovered for the solid solution systems

$Pb(Mg_{1/3}Nb_{2/3})O_3$-$Pb(Mg_{1/2}W_{1/2})O_3$ (PMN-PMW) and $Pb(Mg_{1/3}Nb_{2/3})O_3$-$PbTiO_3$ (PMN-PT).[50] The diffuse phase transition (DPT) observed for these materials has been associated with the short-range ordering of cations on the B-site of the perovskite lattice. Long-range ordering of B-site cations tends to occur for certain annealed $Pb(^{I}B_{1/2}{}^{II}B_{1/2})O_3$ perovskites, while only limited short-range ordering has been observed for $Pb(^{I}B_{1/3}{}^{II}B_{2/3})O_3$-type compounds. A clear correlation between the degree of long-range ordering of B-site cations and the diffuseness of the phase transition has been observed for complex perovskites of this type. The difference between the temperatures of the dielectric constant maximum for measurements made at 1 MHz and 1 kHz, ΔT_{max}, is plotted as a function of composition for these systems in Figure 3.25(a). This quantity, ΔT_{max} [= T_{max}(1 MHz) − T_{max}(1 kHz)] is one measure of the diffuseness of the phase transition. The noteworthy feature of this plot is the maximum that occurs at the $0.4Pb(Mg_{1/3}Nb_{2/3})O_3$-$0.6Pb(Mg_{1/2}W_{1/2})O_3$ composition. This is an indication that the diffuseness of the phase transition is strongly affected by the degree of cation order on the B-site.

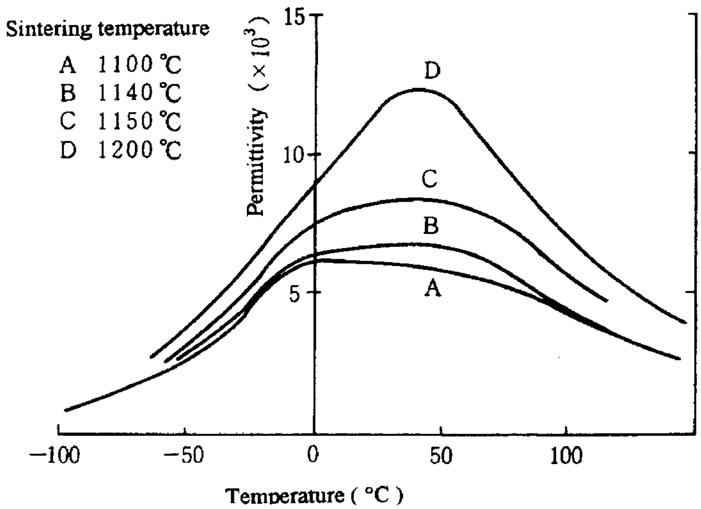

Figure 3.23 The dielectric permittivity as a function of temperature for diphasic mixtures of $Pb(Mg_{1/3}Nb_{2/3})O_3$ (PMN) and $Pb(Zr,Ti)O_3$ (PZT) powders (molar ratio 0.9:0.1) sintered at various temperatures.[49]

The temperature coefficient of electrostriction (TCE) is defined as follows:

$$\frac{\partial[\ln(x)]}{\partial T} = \frac{[x(0^{\circ}C) - x(50^{\circ}C)]}{50^{\circ}C[x(25^{\circ}C)]} \tag{3.19}$$

The TCE at room temperature for materials from the PMN-PMW and PMN-PT systems is plotted as a function of composition in Figure 3.25(b). We see from these data that the TCE decreases to values as low as 0.8% ($^{o}C^{-1}$) (at the 0.4PMN-0.6PMW composition) as ordering at the B-site increases (which occurs with increasing PMW content). These data were collected under low bias fields (1 to 3 kV/cm). A simple empirical equation that relates the ΔT_{max} for a given material with its TCE has been derived from the results depicted in Figures 3.25(a) and 3.25(b):

$$\Delta T_{max}(TCE) = \Delta T_{max}\left[\frac{\Delta x}{x(\Delta T)}\right] = 0.22 \pm 0.03 \tag{3.20}$$

We see from this expression that the product of these parameters should be nearly constant for diffuse phase transition materials.

The electrostrictive materials developed for practical transducers can be classified into three categories based on the structural features giving rise to the DPT:

Category I: Perovskite structures with disordered B-site cations:

Type I(a): Materials produced from the combination of ferroelectric and non-ferroelectric compounds [such as the solid solution system $(Pb,Ba)(Zr,Ti)O_3$ in which $BaZrO_3$ is the non-ferroelectric component].

Type I(b): Materials in which A-site lattice vacancies also occur, which further promote the diffuse phase transition [such as the solid solution system $(Pb,La,\square)(Zr,Ti)O_3$].

Category II: Perovskite structures with some degree of short-range ordering of B-site cations [such as the solid solution systems $Pb(Mg_{1/3}Nb_{2/3},Ti)O_3$ and $Pb(Mg_{1/2}W_{1/2},Ti)O_3$].

This classification also represents general techniques for improving the TCE. Improvement by means of the mechanism identified with Case II has been demonstrated with materials from solid solutions of PMN-PT with PMW or $Ba(Zn_{1/3}Nb_{2/3})O_3$ (BZN). The addition of PMW tends to generate microregions with 1:1 B-cation ordering, while incorporation of PZN tends to promote the formation of microregions with 1:2 ordering. Unfortunately, these modifications also tend to cause a decrease in the electrostrictive coefficient, M. The search continues for new solid solution systems such as these with compositions for which the TCE is optimized and acceptably high electrostriction coefficients are maintained.

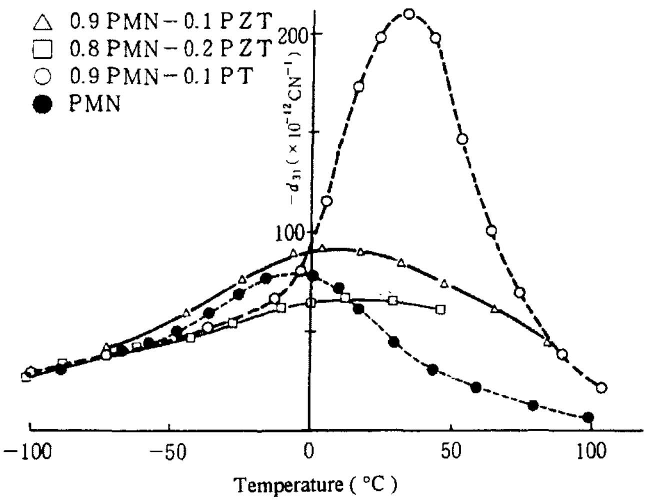

Figure 3.24 The induced piezoelectric strain coefficient, d_{31}, as a function of temperature for some diphasic PMN-PZ composites, 0.9PMN-0.1PT, and pure PMN under a bias of 1 kV/cm.[49]

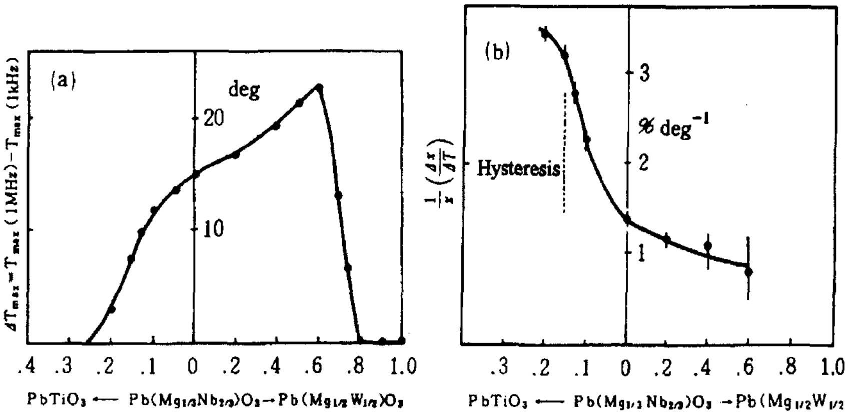

Figure 3.25 Dielectric and electrostriction data for materials from the $Pb(Mg_{1/3}Nb_{2/3})O_3$-$Pb(Mg_{1/2}W_{1/2})O_3$ and $Pb(Mg_{1/3}Nb_{2/3})O_3$-$PbTiO_3$ systems: (a) the difference in the temperatures of the dielectric constant maximum for measurements made at 1 MHz and at 1 kHz, and (b) the temperature coefficient of electrostriction (TCE), both as a function of composition.[50]

3.4 RESPONSE SPEED

The response speed of piezoelectric/electrostrictive actuators depends not only on the material properties, but also on the mechanical resonance frequency of the device and on the specifications of the drive power supply.

(1) Material Limitations

Since the speed of domain wall motion is limited and very much dependent on the magnitude of the applied electric field, the polarization and induced strain will also exhibit pronounced frequency dependences. This is the source of the observed *hysteresis* in the polarization and induced strain with respect to the applied electric field. It is also the cause of the *zero point drift* (that is, the gradual shift in the strain level at zero field following the application of the unipolar drive voltage), *creep* and *aging* (that is, long-term strain degradation due to *depoling*). The creep characteristic of PZT-4 is shown in Figure 3.26, where we see the transverse strain as measured after an electric field pulse of 1 kV/cm is applied to the sample.[51] The induced strain, x, can be represented as the superposition of a fast-response part (x_o) and a slow-response part (Δx). The time dependence of Δx is approximated by an exponential function. The ratio of $\Delta x_\infty : x_0$ (where Δx_∞ represents Δx at saturation, or t equal to infinity) depends not only on temperature, but also on the applied electric field. When the field is small, as is the case for the data appearing in Figure 3.26, this ratio can be as high as 20 or 30 percent.

The frequency dependence of the field-induced strain in simple disk samples of PLZT is shown in Figure 3.27.[9] We see from these data that at low frequencies the coercive field and the hysteresis generally increase with increasing drive frequency. This has been attributed to a decrease in the slow-response domain contribution at higher frequencies.

(2) Device Limitations

At frequencies in the vicinity of the mechanical resonance frequency of the piezoelectric device, the amplitude of the induced strain is enhanced considerably. Well above the resonance frequency, however, the strain is completely suppressed. The quickest response is thus achieved for operation frequencies near resonance. The resonance frequency of a bimorph bending actuator is not high (around 100 Hz-10 kHz), which ultimately limits the response speed of actuators of this type to this range. (We will consider the operation of these devices further in Chapters 4 and 5.) On the other hand, multilayer thickness extensional actuators have a resonance frequency as high as 100 kHz and therefore are quite a bit quicker. The limiting factor for the speed of these devices is related to the power supply.

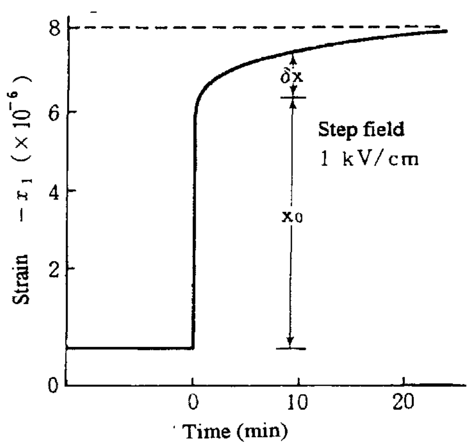

Figure 3.26 The creep characteristic of PZT-4.[51]

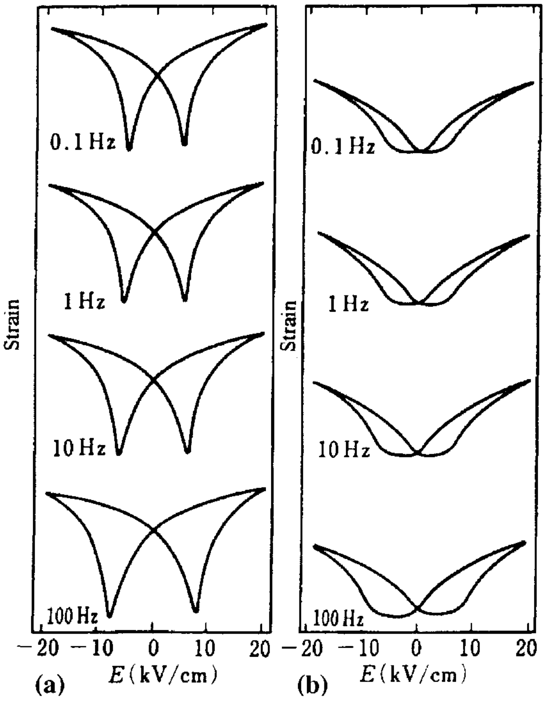

Figure 3.27 The frequency dependence of the field-induced strain in simple disk samples of PLZT: (a) PLZT 7/65/35 and (b) PLZT 9/63/37.[9]

(3) Drive Circuit Limitation

Driving a ceramic actuator is essentially a process of charging a large capacitor. Assuming a conventional power supply is used with an output impedance of 100 Ω, the *time constant*, which is determined by the product of the resistance and the capacitance (RC), is just 10^{-4} s. This corresponds to a response speed of 10 kHz, which is the practical limit for a multilayer device with a capacitance of 1 μF. If we used a power supply with an output impedance of 10 Ω, the response speed would be increased to 100 kHz. Another consideration is the maximum current of the power supply, which must be sufficient to charge the actuator. When 100 V is applied to the 1 μF actuator for 10^{-5} s (corresponding to 100 kHz), the transient current attained is 10 A. In order to reduce the current drawn from the power supply, the capacitance of the device, or more specifically the dielectric constant of the material, must be reduced. This is the primary reason why a soft piezoelectric is preferred over an electrostrictive ceramic for pulse drive applications. We will examine this condition further in Example Problem 5.6.

3.5 MECHANICAL PROPERTIES OF ACTUATORS

Solid-state actuators are used in mechanical systems, occasionally under certain pre-stress conditions in order to optimize efficiency as well as to improve mechanical reliability. We will consider in this section the stress dependence of piezoelectricity and the mechanical strength of materials. The use of acoustic emission (AE) from piezoelectrics as a means of monitoring for device failure will also be discussed.

(1) The Uniaxial Stress Dependence of Piezoelectricity and Electrostriction

Even elastically stiff ceramic actuators will deform under an applied stress. The electric field-induced strain is affected by a bias stress. The uniaxial compressive stress dependence of the longitudinal field-induced strain in $BaTiO_3$ (BT)-, PZT-, and lead magnesium niobate-lead titanate (0.65PMN-0.35PT)-based ceramics is shown in Figure 3.28.[68] The PZT- and PMN-based ceramics exhibit *maximum field-induced strains* (which is indicated on the plot where the individual lines intersect with the strain axis) much larger than the BT-based material. The *maximum generative stress* (indicated where the lines intersect the stress axis and is sometimes referred to as the *blocking force*), on the other hand, is very nearly the same (about 3.5×10^7 N/m^2) for all the samples. This is because the elastic compliance of lead-based ceramics tends to be relatively large (that is, they are elastically soft).

The strain as a function of stress is plotted for electrostrictive PMN-PT actuators in Figure 3.29.[52] We see from these data that the 0.9PMN-0.1PT devices exhibit the larger maximum field-induced strains of the two compositions, but the maximum generative forces for each composition at similar field strengths are nearly the same (≈ 46 MPa). It is worth noting here that the elastic compliance of the 0.9PMN-

0.1PT electrostrictor decreases abruptly with increasing bias stress, while the piezoelectric 0.65PMN-0.35PT specimens exhibit practically straight and parallel lines at each applied electric field strength.

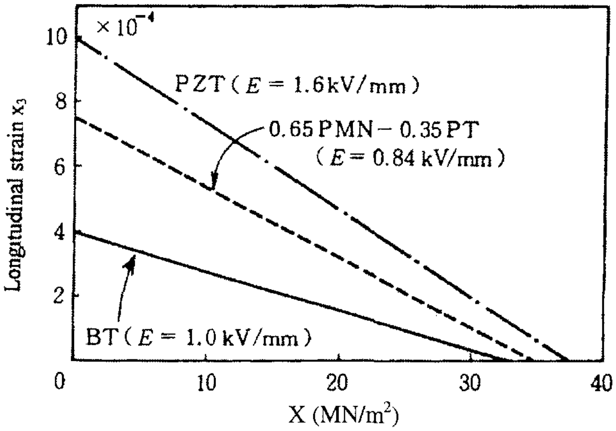

Figure 3.28 The uniaxial stress dependence of the electric field-induced strain in $BaTiO_3$ (BT)-, $Pb(Mg_{1/3}Nb_{2/3})O_3$ (PMN)-, and $Pb(Zr,Ti)O_3$ (PZT)-based piezoelectric ceramics.[68]

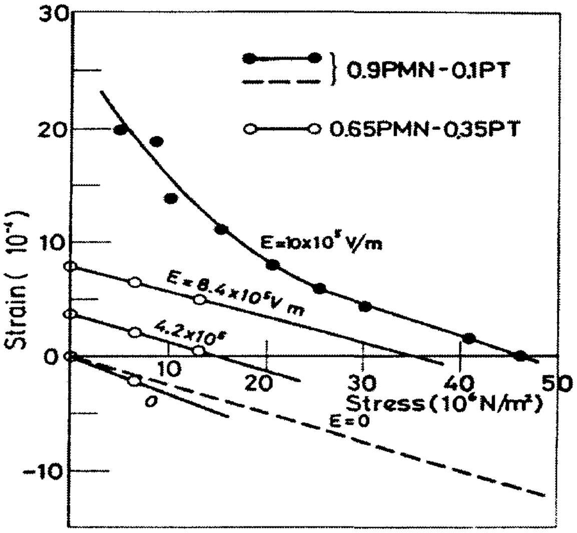

Figure 3.29 Uniaxial pressure dependence of the longitudinal strain for PMN-PT actuators.[52] [0.9PMN-0.1PT: electrostrictive, 0.65PMN-0.35PT: piezoelectric]

The variation of the large field effective piezoelectric strain coefficient, d_{33} (which corresponds to the maximum value of $(\partial x/\partial E)$ for the electrostrictive materials), with applied compressive stress for various electrostrictive, soft piezoelectric, and hard piezoelectric ceramics is shown in Figure 3.30.[53] All the samples show a dramatic decrease in the piezoelectric coefficient above a certain critical level of applied stress. This change is reversible later in the stress cycle for electrostrictive materials, but in hard piezoelectric ceramics it is not, and the lower d_{33} is retained even after the compressive stress is removed. This degradation has been related to the reorientation of domains induced by the applied stress.[54] Note that this critical level of stress tends to be highest for the hard piezoelectrics, somewhat less for soft piezoelectrics, and lowest for electrostrictors. We can deduce from these data that for conditions where the maximum stress is less than 10^8 N/m^2 (1 ton/cm^2), piezoelectric ceramics will be the most useful, while under larger stresses electrostrictive ceramics will prove to be the most responsive.

The variation of the weak field effective piezoelectric coefficient with applied compressive stress is quite different from the large field response. The piezoelectric strain coefficients, d_{33} and d_{31}, for various PZT compositions [from soft (PZT-5H) to hard (PZT-8)] are plotted as a function of applied compressive stress in Figure 3.31.[69] We see in all cases the piezoelectric coefficients increase up to a certain critical stress, and then dramatically decrease beyond this level of applied stress. The degradation in this case is associated with a stress-induced depoling effect. It is irreversible for soft piezoelectric materials.

The most interesting feature of the data plotted in Figure 3.31 is the increase in the piezoelectric coefficients when subjected to the lower applied stresses. This is related to the poling direction with respect to the applied stress direction. The dependence of the piezoelectric d_{33} coefficient on specimen orientation with respect to the poling direction is shown in Figure 3.32.[55] After the ceramic PZT specimens were poled, they were cut as illustrated in Figure 3.32(a), and the effective d_{33} coefficient (normalized by $d_{33//Ps}$, the value of d_{33} along the poling direction) was measured for each. The effective d_{33} for the specimens from this series are plotted as a function of orientation with respect to the poling direction in Figure 3.32(b). The actual magnitudes of the effective strain coefficients of specimens oriented parallel to the poling direction, $d_{33//}$, for the tetragonal PZT (48/52) and rhombohedral PZT (54/46) compositions are 98 pC/N and 148 pC/N, respectively. Note that for rhombohedral PZT, d_{33} increases as the cutting angle increases from 0° to 45°, attaining at 45° an enhancement of 1.25 times the response observed for the specimen with the parallel alignment. This is directly related to the crystal orientation effects, d_{33}, discussed in Section 2.4(5). Similar to what occurs for the samples previously described, the spontaneous (or remanent) polarization for these ceramic specimens subjected to a large compressive uniaxial stress (greater than the critical stress) will be somewhat canted and the samples will become partially depoled. Thus, for applied stresses below the critical stress the piezoelectric coefficient increases, but beyond this permanent degradation occurs. It is due to this stress-enhanced piezoelectric response that the so-called "bolt-clamped design," through which the appropriate level of stress is maintained on the device during operation, was developed and commonly applied to hard PZT Langevin tansducers.

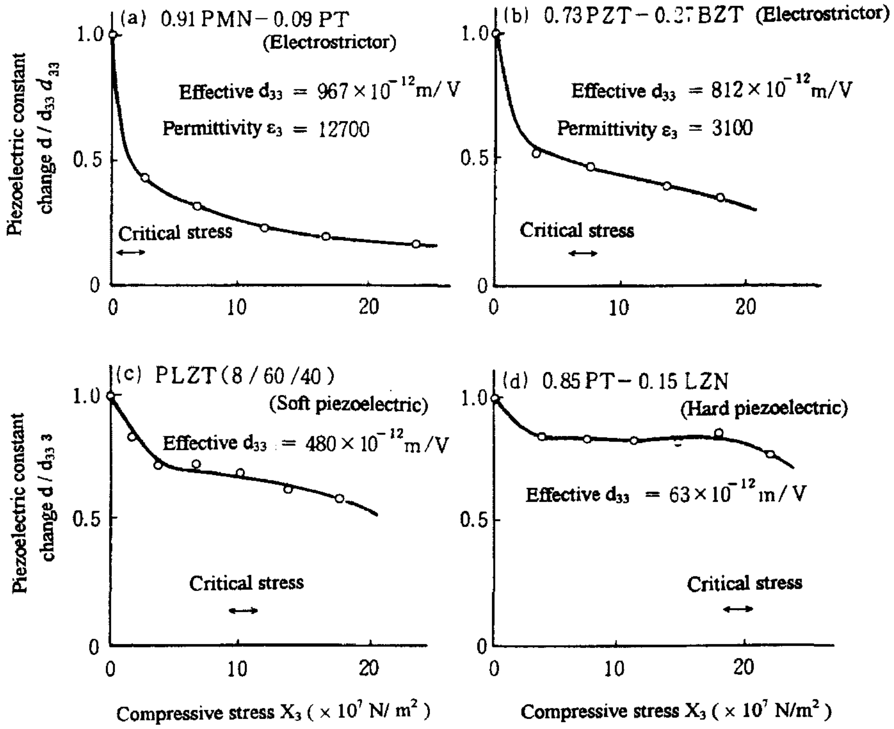

Figure 3.30 The variation of the large field effective piezoelectric strain coefficient, d_{33}, with applied compressive stress for various electrostrictive, soft piezoelectric and hard piezoelectric ceramics.[53] [The effective d_{33} corresponds to the maximum value of $(\partial x/\partial E)$ for the electrostrictive materials.]

(2) Mechanical Strength

The mechanical properties and the mechanical strength of the ferroelectric ceramics used in actuator devices are as important as the electrical and electromechanical properties. We will now consider some general principles of fracture mechanics, the fracture toughness of the ceramic as it relates to grain size, and the mechanical strength of the material as it is affected by field-induced strains. The use of acoustic emission (AE) from piezoelectrics as a means of monitoring for device failure will also be presented.

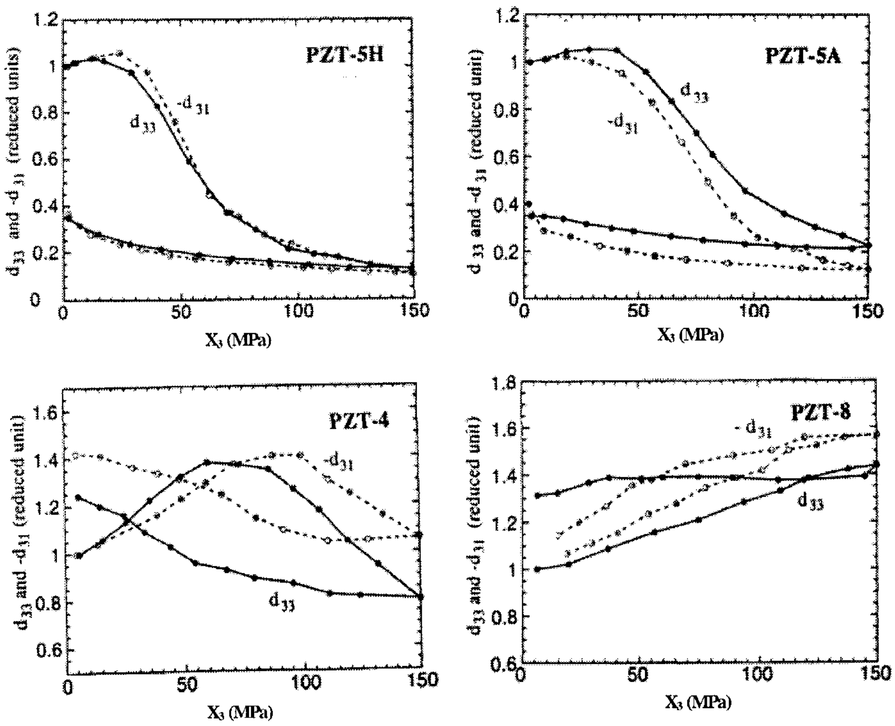

Figure 3.31 The weak field piezoelectric strain coefficients, d_{33} (solid line) and d_{31} (dashed line), for various PZT compositions [from soft (PZT-5H] to hard (PZT-8)) plotted as a function of applied compressive stress.[69] (Reduced units are defined with respect to the actual d values measured at X_3=0.)

Fracture Mechanics

Ceramics are generally *brittle*, and fracture of these bodies tends to occur suddenly and catastrophically.[56] Improvement of the *fracture toughness* (which is essentially the material's resistance to the development and propagation of cracks within it) is thus a key issue in the design of new ceramics for actuator applications. The brittle nature of ceramic materials is directly related to their crystal structure. The atoms in the ceramic crystallites are typically *ionically or covalently bonded* and their displacement under external influences, such as an applied stress, is limited. The mechanisms for relieving stress in such structures are few and, therefore, even a small stress can cause fracture. In polycrystalline samples, there are two types of crack propagation: (1) *transgranular*, in which the cracks pass through grains, and (2) *intergranular*, in which the cracks propagate along grain boundaries.

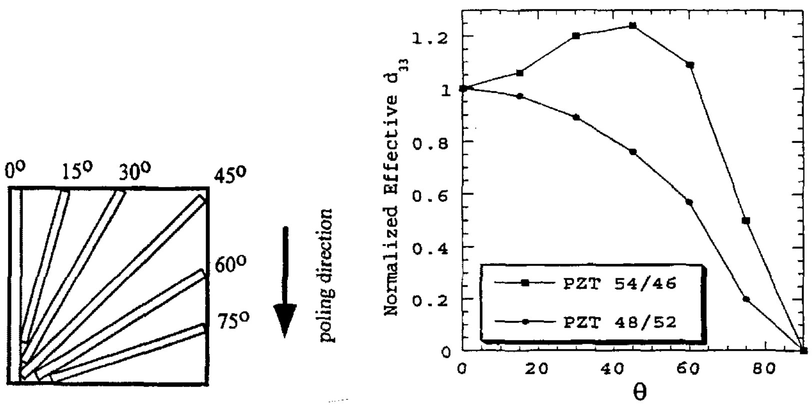

(a) (b)

Figure 3.32 The dependence of the effective piezoelectric d_{33} coefficient on specimen orientation: (a) sample orientation with respect to the poling direction, and (b) the effective d_{33} plotted as a function of orientation with respect to the poling direction, θ.[55] (Data are normalized by $d_{33//Ps}$, the value of d_{33} along the poling direction.)

Three fundamental stress modes which may act on a propagating crack are depicted in Figure 3.33. Mode I involves a tensile stress as shown in Figure 3.33(a). Mode II leads to a sliding displacement of the material on either side of the crack in opposite directions as shown in Figure 3.33(b). The stress distribution associated with Mode III-type produces a tearing of the medium. The fracture of most brittle ceramics corresponds primarily to Mode I, and, thus, this is the mode of principal concern to designers of new ceramic materials for actuator devices.[57]

Theoretically, the fracture strength of a material can be evaluated in terms of the cohesive strength between its constituent atoms, and is approximately one-tenth of Young's modulus, Y. The experimentally determined values do not support this premise, however, as they are typically three orders of magnitude smaller than the theoretically predicted values. This discrepancy has been associated with the presence of microscopic cracks in the material before any stress is applied to it, which are sometimes called *stress raisers*.[58] It has been shown that for a crack with an elliptical shape, oriented with its major axis perpendicular to the applied stress, σ_o (Mode I), the local stress concentration, σ_m, at the crack tip increases significantly as the ellipticity of the defect increases. The relationship between the applied and local stresses is given by:

$$\sigma_m = K_t \, \sigma_o \tag{3.21}$$

where K_t is the stress concentration factor.

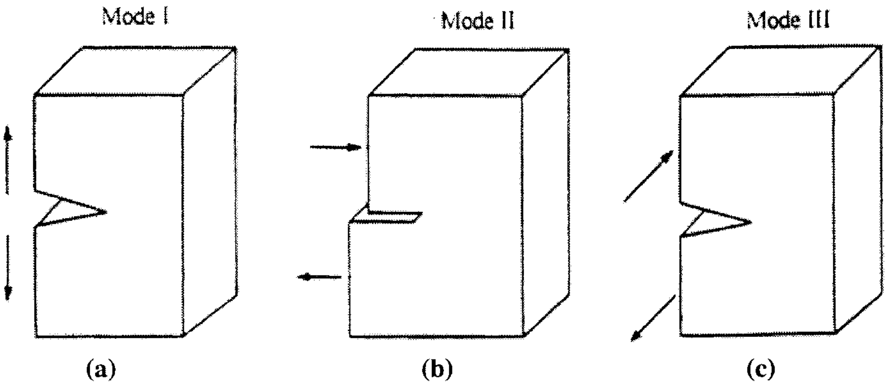

Figure 3.33 Three fundamental stress modes which may act on a propagating crack: (a) Mode I: tensile mode in which a tensile stress acts normal to the crack plane, (b) Mode II: sliding mode in which a shear stress acts normal to the crack edge plane, (c) Mode III: tearing mode in which a shear stress acts parallel to crack edge plane.

Fracture is expected to occur when the applied stress level exceeds some critical value, σ_c. The *fracture toughness*, K_{Ic}, is defined as follows:

$$K_{Ic} = F\sigma_c\sqrt{\pi a} \tag{3.22}$$

where F is a dimensionless parameter that depends on both the sample and crack geometries, σ_c is the critical stress, and a is the microcrack size. The fracture toughness is a fundamental material property that depends on temperature, strain rate, and microstructure.

Measurement of Fracture Toughness

There are four common methods for measuring the fracture toughness of a ceramic: (1) Indentation Microfracture (IM), (2) Controlled Surface Flow (CSF), (3) Chevron Notch (CN), and (4) Single Edge Notched Beam (SENB). We will focus most of our attention on the first of these methods as it is of the four perhaps one of the most commonly employed.

The test is initiated by artificially generating cracks on a polished surface of the sample with a Vickers pyramidal diamond indenter. The fracture toughness, K_{Ic}, is then determined from the indentation size and the crack length.

Three types of cracks are produced by indentation: (1) the Palmqvist crack, (2) the median crack, and (3) the lateral crack as illustrated in Figure 3.34. A *Palmqvist crack* is generated at the initial stage of loading. It has the shape of a half ellipse, and occurs around the very shallow region of plastic deformation near the surface. As the load is increased, a crack in the shape of a half circle starts to form at the boundary between the plastic and elastic deformation regions. This is called a *median crack.* Above a certain critical indenter load the median crack will reach the surface. The indentation also produces a residual stress around the indented portion of the sample, in which are generated more Palmqvist and median cracks, as well as *lateral cracks* in the plastic deformation region which will not reach the surface.

The indentation microfracture method is used to characterize Palmqvist and/or median cracks in order to determine K_{Ic}. A theoretical equation descriptive of median cracks has been derived, which has the following form:

$$\left[\frac{K_{Ic}\,\phi}{H\sqrt{a}}\right]\left(\frac{Y\phi}{H}\right)^{2/5} = (0.055)\,\log\left(\frac{8.4\,a}{c}\right) \qquad (3.23)$$

where ϕ is a restriction constant, H is the hardness, Y is Young's modulus, and a and c are half of the indentation diagonal and the crack length, respectively.[59] The theory that produced this equation was further refined and modified expressions[60] which individually characterize the Palmqvist and median cracks were derived as follows:

$$\left[\frac{K_{Ic}\,\phi}{H\sqrt{a}}\right]\left[\frac{H}{Y}\right]^{2/5} = 0.018\left[\frac{(c-a)}{a}\right]^{-1/2} \qquad \text{[Palmqvist crack]} \qquad (3.24)$$

$$\left[\frac{K_{Ic}\,\phi}{H\sqrt{a}}\right] = 0.203\left[\frac{c}{a}\right]^{-3/2} \qquad \text{[Median crack]} \qquad (3.25)$$

The fracture toughness, K_{Ic}, can be calculated using the crack length determined from the IM method. Other methods require precracking a sample prior to failure testing, and then K_{Ic} is calculated using the fracture stress determined from the test. The controlled surface flow method, for example, uses the median crack generated by a Vickers indenter as a precrack to determine the relationship between the fracture stress, σ_f, and the crack length, 2c, under three- or four-point bending tests. The fracture toughness, K_{Ic}, is then calculated from:

$$K_{Ic} = 1.03\,\sigma_f\sqrt{\frac{\pi b}{q}} \qquad (3.26)$$

The parameter q is defined to be:

$$q = \Phi^2 - 0.212\left[\frac{\sigma_f}{\sigma_y}\right]^2 \qquad (3.27)$$

where σ_y is the tensile yield stress and Φ is the second perfect elliptic integration given by:

$$\Phi = \int_0^{\pi/2}[\cos^2\theta + (b/c)^2\sin^2\theta]^{1/2}\,d\theta \qquad (3.28)$$

Here, b is half of the minor axis of the elliptically shaped crack (referred to as the crack depth) and c is half of the major axis of the elliptical crack (referred to as the crack length).

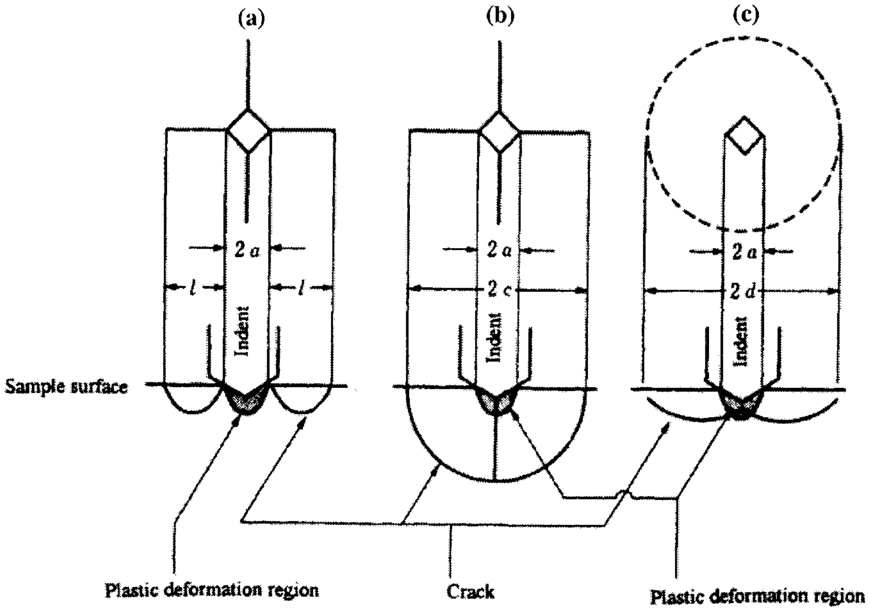
(a)
(b)
(c)
2a
l
l
Indent
2a
2c
Indent
2a
2d
Indent
Sample surface
Plastic deformation region
Crack
Plastic deformation region

Figure 3.34 Crack shapes generated by the Vickers indentation: (a) the Palmqvist crack, (b) the median crack and (c) the lateral crack. [Top and sectional views are shown.]

The probability of fracture, $p(\sigma_f)$, for a sample subjected to a stress, σ_f, in a three- or four-point bend test is described by the following equation:

$$1 - p(\sigma_f) = \exp[-(\sigma_f/\sigma_o)^m] \qquad (3.29)$$

where σ_o is the average bending strength and m is referred to as the *Weibull coefficient*. When this relationship is rendered in terms of the natural logarithm (see Example Problem 3.5), we should find that the quantity $\ln(\ln[1/(1-p)])$ is linearly related to $\ln(\sigma_f)$. A graph of this function is called a *Weibull plot*.

Example Problem 3.5

Three-point bend tests were carried out on a series of barium titanate-based multilayer actuators. The sample configuration is illustrated in Figure 3.35. The results of the tests are summarized in the following table:

Sample	Length, *l* (cm)	Width, b (cm)	Height, h (cm)	Load, M (kg)
1	0.38	0.420	0.106	4.60
2	0.48	0.415	0.121	4.00
3	0.49	0.420	0.093	2.00
4	0.40	0.420	0.112	5.50
5	0.31	0.415	0.102	2.90
6	0.55	0.420	0.099	2.34

Calculate the average bending strength, σ_o, and the Weibull coefficient, m.

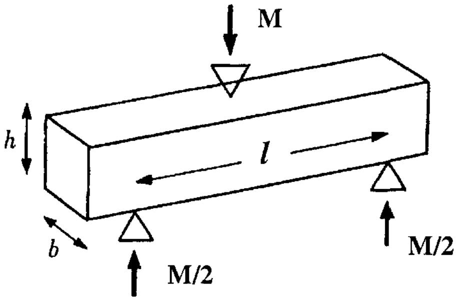

Figure 3.35 Configuration for the three-point bend test.

Solution

The fracture stress, σ_f, can be obtained from:

$$\sigma_f = 3\,M\,l\,/\,2\,b\,h^2 \qquad \text{(P3.5.1)}$$

which yields for each of the samples tested the following:

Sample	**1**	**2**	**3**	**4**	**5**	**6**
σ_f [MN/m^2]	54.4	46.5	40.1	61.7	30.3	46.0

The nonfracture probability, $1-p(\sigma_f)$, of the sample under the applied stress, σ_f, of a three-point bend test is described by:

$$1-p(\sigma_f) = \exp[-(\sigma_f/\sigma_o)^m] \quad \text{(P3.5.2)}$$

where $p(\sigma_f)$ is the fracture probability, σ_o is the average bending strength, and m is the Weibull coefficient. This equation can be rewritten in the following form:

$$\ln[\ln(1/[1-p(\sigma_f)])] = m(\ln\sigma_o-\ln\sigma_f) \quad \text{(P3.5.3)}$$

Designating the total number of samples as N, the nonfracture probability is given by:

$$1-p(\sigma) = (1-n)/(N+1) \quad \text{(P3.5.4)}$$

where $(\sigma_n < \sigma < \sigma_{n+1})$.

The Weibull plot for this set of fracture tests appears in Figure 3.36. We are able to determine the Weibull coefficient to be m=4.8 and the average bending strength to be σ_o=49 [MN/m^2] from this plot.

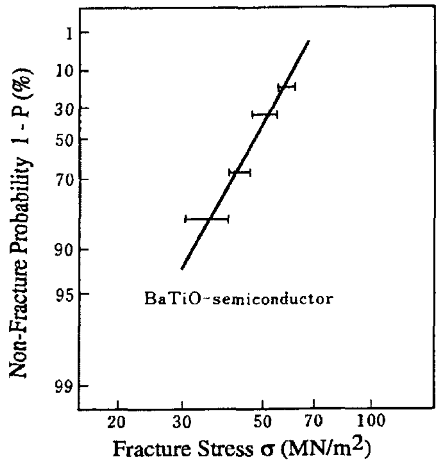

Figure 3.36 Weibull plot for the data collected from the three-point bend tests conducted on a series of barium titanate-based multilayer actuators.

Grain Size and Fracture Toughness

The mechanical strength of ceramics is strongly dependent on the grain size. Micrographs of indentations made on two PLZT 9/65/35 samples with different grain sizes are shown in Figure 3.37.[61] Notice that the crack length for the sample with the smaller grain size (1.1 μm) is much shorter than for the sample with the larger grain size (2.4 μm), while the center indentation size is almost the same. The grain size dependence of the hardness, H_v, and the fracture toughness, K_{Ic}, are shown in Figure 3.38. We see from these data that the hardness, H_v, is insensitive to the grain size, while the fracture toughness, K_{Ic}, increases dramatically for specimens with grain sizes below 1.7 μm. A multidomain grain model has been proposed to explain this increase in K_{Ic}. The ferroelastic domain structure in ferroelectric and antiferroelectric ceramics has a multidomain state if the grain size is large, and assumes a single-domain state with decreasing grain size. In general, the ceramic tends to retain a residual compressive stress, which is generated during sintering. This residual stress is relieved by a multi-domain structure. The residual stress is not relieved in a single domain state. It is this residual stress that increases the apparent fracture toughness, K_{Ic}, in a small grain sample.

Field-Induced Strains and Mechanical Strength

Mechanical strength is also dependent on the magnitude of the induced strain. An acoustic emission (AE) accompanies the reorientation of domains, a phase transformtion, or crack propagation in a ferroelectric ceramic. It is in general an inaudible, high frequency acoustic signal caused by mechanical vibration in the specimen.[65-67] The acoustic emission counts accumulated in a single drive cycle are plotted in Figure 3.39 as a function of the total number of drive cycles for three multilayer devices.[62] The field-induced strain generates a large stress concentration near the internal electrode edge, which can initiate a crack (see Section 4.4). All the samples exhibited a dramatic increase in the acoustic emission count while the cracks were propagating and leveled off after crack propagation had ceased. The significant differences in the durability (measured by the number of drive cycles before failure occurs) among the three samples are attributed mainly to the magnitude of the maximum strain attainable by each device: 0.1% for the electrostrictor, 0.2% for the piezoelectric, and 0.4% for the antiferroelectric sample. Assuming the grain-grain adhesion is similar among the samples, it is reasonable to expect that the larger strain will lead to larger stress, and therefore a greater likelihood of fracture.

Poling and Mechanical Strength

Piezoelectric ceramics require an electric poling process, which induces an anisotropy to the mechanical strength.[63] A schematic representation of the microindentation and cracks generated in a poled PLZT 2/50/50 (tetragonal) specimen appears in Figure 3.40. The results of this study confirmed that a crack that is oriented perpendicular to the poling direction propagates much faster than one oriented parallel to it. The sample geometry and the bending and poling directions are illustrated in Figure 3.41, and Weibull plots for samples bending perpendicular and parallel to the poling direction in a 3-point bending test are shown in Figure 3.42. These data indicate that cracks propagate more easily in the direction perpendicular to the poling direction. This has been attributed to the anisotropic internal stress caused by the strain induced during the poling process.

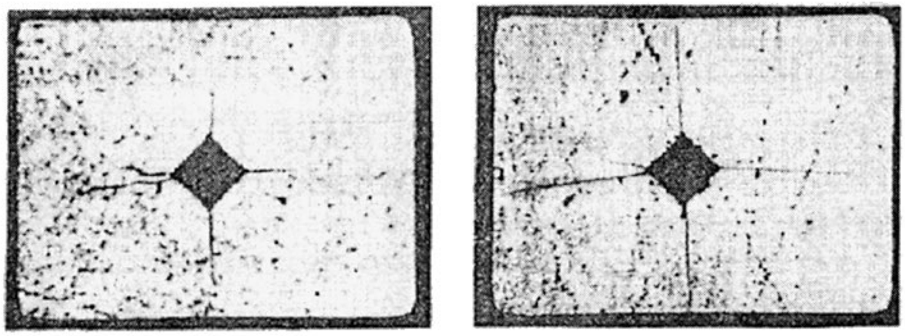

Figure 3.37 The indentation mark and cracks generated on a (9/65/35) PLZT surface: (a) grain size 1.1 μm, crack length c = 208 μm and (b) grain size 2.4 μm, crack length c = 275 μm.[61]

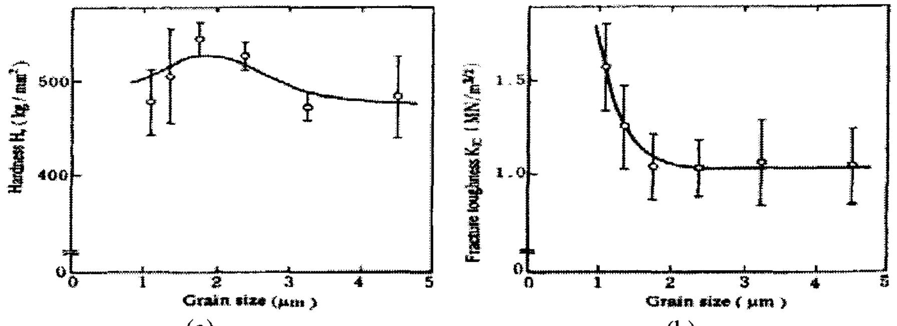

(a) (b)

Figure 3.38 Mechanical strength data for (9/65/35) PLZT ceramics showing the grain size dependence of: (a) the hardness, H_v, and (b) the fracture toughness K_{Ic}.[61]

Crack propagation in unpoled PZT and PMN ceramics subjected to an applied electric field has also been investigated.[64] In this investigation it was found that the applied electric field promotes crack propagation perpendicular to the electric field and inhibits it parallel to the field. It was also observed that no mechanical stress is generated in a mechanically constrained, defect-free electrostrictive ceramic subjected to a uniform electric field, even when an electrostrictive response is induced. This has been attributed to microstructural inhomogeneities. The microcrack is regarded as a source of the internal stress, which is concentrated at the crack tip. Calculations based on this model have accurately predicted these experimentally observed trends.

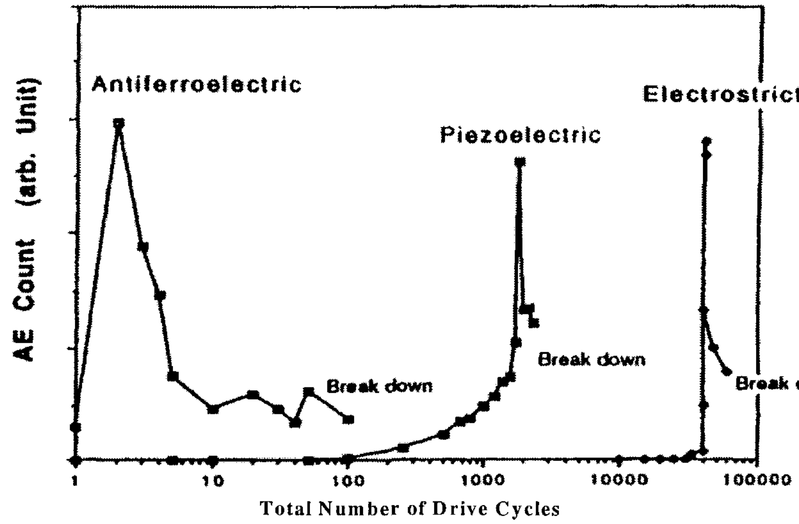

Figure 3.39 Acoustic emission (AE) counts as a function of total number of drive cycles for electrostrictive, piezoelectric, and phase-change materials.[62]

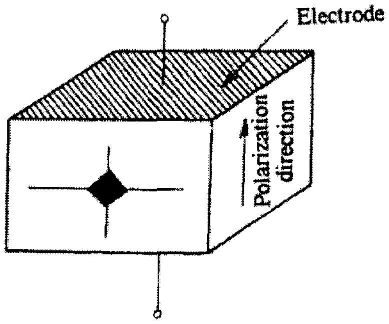

Figure 3.40 A schematic representation of the microindentation and the cracks generated in a poled piezoelectric ceramic.

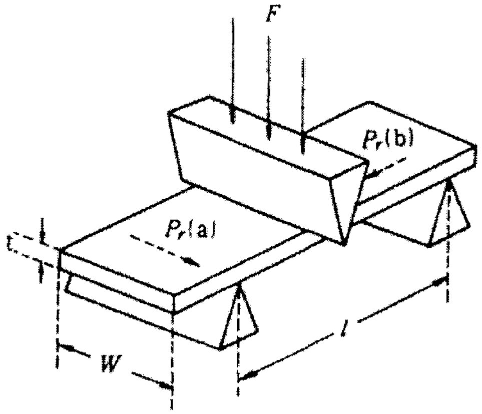

Figure 3.41 The three-point bend test configuration: (a) bending direction parallel to the polarization and (b) bending direction perpendicular to the polarization.

(3) Acoustic Emission in Piezoelectrics

An acoustic emission (AE) accompanies the reorientation of domains, a phase transformation, or crack propagation in a ferroelectric ceramic. It is in general an inaudible, high frequency acoustic signal caused by mechanical vibration in the specimen.[65-67]

The Kaiser Effect Associated with Field-Induced Acoustic Emission

The acoustic emission from, the induced displacement of, and the electric field applied to an unpoled soft PZT ceramic disk are shown as a function of time in Figure 3.43.[66] The threshold level of the acoustic emission signal was 400 mV at 100 dB. An electric field of 20 kV/cm was applied to the sample during the first cycle. It was increased to 25 kV/cm during the second cycle, and up to 30 kV/cm during the third cycle.

The sample was poled during the first cycle of the applied electric field. The induced displacement and total residual displacement (observed as a zero point shift) are observed to increase with increasing applied field. This is because the degree of poling becomes greater as the applied field strength is increased. During the first cycle, an acoustic emission occurs with the first displacement as the field is increased. No acoustic emission signal is generated as the field is decreased immediately following this first displacement. The next acoustic emission is observed during the second cycle as the applied field is increased above 20 kV/cm.

Another acoustic emission occurs during the third cycle, as the applied field is this time increased above 25 kV/cm. We see from these data that acoustic emission events subsequent to the first will occur only when the applied field exceeds the maximum value of the previous cycle. This characteristic electric field dependence of the acoustic emission, which is known as the Kaiser effect, involves a field-induced deformation of the PZT ceramic.

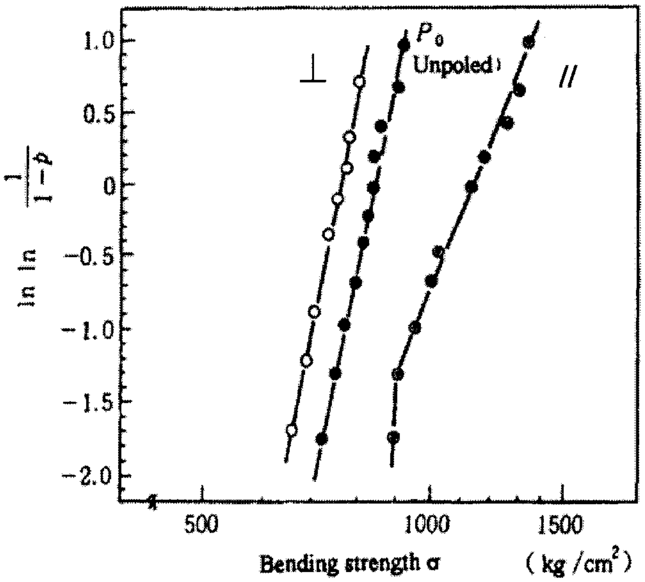

Figure 3.42 Weibull plots of samples for which the bending is perpendicular to [⊥] and parallel to [//] the poling direction.[63]

It has been proposed that domain motion is the cause of the field-induced acoustic emission.[66] It has been shown, however, that not all types of domain motion, but rather only certain domain reorientation processes can be identified with an acoustic emission event. Another possible cause of the acoustic emission is the mechanical stress generated in a highly strained sample.

Electric Field-Induced Acoustic Emission

The acoustic emission count rate and the induced displacement as a function of applied field for a specimen subjected to a ±35 kV/cm, $1.5\text{x}10^{-3}$ (Hz) driving field is shown in Figure 3.44.[66] The threshold level of the acoustic emission signal was 400 mV at 100 dB. The characteristic "butterfly-shaped" induced displacement is observed which occurs due to domain reorientation. At a critical level of the applied electric field, where the acoustic emission is first stimulated, we see a point of inflection in the curve for the displacement as a function of the applied field. A spike is apparent at this field strength in the corresponding *d(displacement)/dE* curve, which is also shown in Figure 3.44.

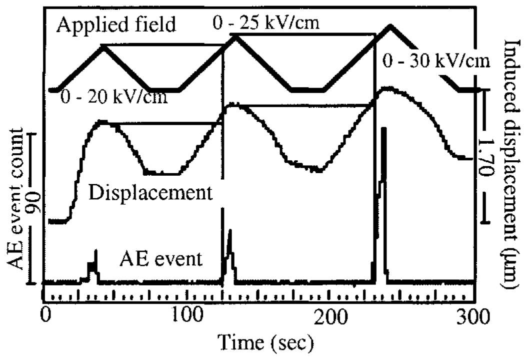

Figure 3.43 The acoustic emission from AE event, the induced displacement of, and the electric field applied to an unpoled soft PZT ceramic disk as a function of time.[66]

It should be noted that the maximum in the acoustic emission count rate does not occur at the maximum applied field strength. It actually occurs at about 27 kV/cm. Where it is known that the internal stress in a ferroelectric increases with the applied field, this decrease in the acoustic emission indicates that a mechanism other than internal stress could also be the source of an acoustic emission. The induced displacement in the ferroelectric ceramics is associated with two types of deformation, one due to domain reorientation and the other a piezoelectric deformation that involves no domain reorientation. It has been proposed that initially the field-induced acoustic emission in PZT ceramics subjected to a bipolar electric field is stimulated in conjunction with the deformation related to domain reorientation. Once the domain reorientation is complete, subsequent AE events are believed to occur in conjunction with the piezoelectric deformation and the internal stresses that are induced at high field strengths. The decrease in the acoustic emission count rate observed in these studies may, therefore, correspond to the completion of domain reorientation in the specimen and its associated deformation.

The Fractal Dimension of the Electric Field-Induced Acoustic Emission

The acoustic emission count rate can be described by the following function:

$$f(x) = c\,x^{-m} \qquad (3.30)$$

where **x** is the acoustic emission signal amplitude, c is a constant, and m is a number representing a fractal dimension. The fractal dimension, m, is used to estimate the degree of damage in the materials. The integrated acoustic emission function:

$$F(x)=\int_x^{\infty}f(x)\cdot dx=\frac{1}{m-1}cx^{-m+1}\quad(m>1)\tag{3.31}$$

is obtained experimentally by monitoring the change in the acoustic emission signal as the signal threshold level is varied.

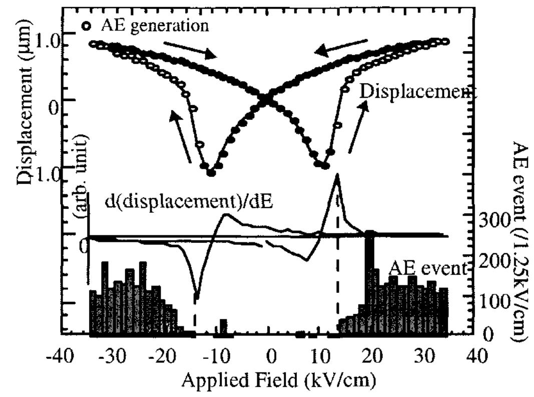

Figure 3.44 The acoustic emission count rate and the induced displacement as a function of applied field for a specimen subjected to a ±35 kV/cm, 1.5×10^{-3} (Hz) driving field.[66]

The acoustic emission count rate per cycle is shown as a function of the signal threshold level in Figure 3.45.[66] The AE count rate is observed to decrease logarithmically with signal threshold level under an applied field of ± 25 kV/cm. A fractal dimension of m=1 was determined from these data. The fractal dimension corresponding to the acoustic emission signal associated with plastic deformation is typically found to be more than 2. This is regarded as a critical number for assessing the mechanical condition of a material. When the material is damaged, the fractal dimension is lower than 2. The experimentally determined fractal dimension of m=1 for the data shown in Figure 3.45 should then indicate that the sample has been damaged. In this case, however, it has been proposed that the fractal dimension is less than the critical value due more to the existence of ferroelectric domains and the deformation related to the reorientation of those domains than to damage. The reproducibility of the field-induced acoustic emission signal from samples of this type has been presented as justification for this interpretation.

At higher applied field strengths, the acoustic emission rate as a function of threshold level no longer follows a logarithmic trend. The critical electric field amplitude, above which a nonlogarithmic AE function is observed, was found to be around 27 kV/cm. These curves also followed a nearly logarithmic form at lower signal threshold levels. At higher AE signal threshold levels (typically $>10^{-4}$ mV) a linear decrease with threshold level is observed. When an electric field of ±35 kV/cm is applied, a fractal dimension of m=2.8 is obtained. Since the domain reorientation should be complete at electric fields greater than the critical electric field (27 kV/cm), it is assumed here that the acoustic emission characterized by fractal dimension of 2.8 is representative of piezoelectric deformation.

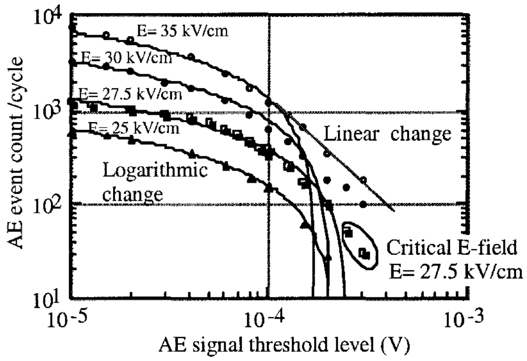

Figure 3.45 The acoustic emission count rate per cycle is shown as a function of the signal threshold level.[66]

In conclusion, the fractal dimension of the field-induced AE associated with deformation related to domain reorientation is characterized by a fractal dimension of (m=1), which is lower than that associated with piezoelectric deformation (m=2.8). A fractal dimension greater than 2 has been conventionally associated with plastic deformation. It is not appropriate to categorize the electrically induced deformation of ferroelectric ceramics as plastic deformation, however, because the induced displacement is restored to its initial state when the applied field is removed. This is an important distinction between the acoustic emission response as it occurs for ferroelectric ceramics and the documented characteristic acoustic emission response from metals and structural ceramics.

CHAPTER ESSENTIALS

1. Hard Piezoelectrics: $E_c > 10$ kV/cm
   Soft Piezoelectrics: 1 kV/cm $< E_c <$ 10 kV/cm
   Electrostrictors: $E_c < 1$ kV/cm

2. Comparison between **electrostriction** and **piezoelectricity**:
   a. Electrostriction produces strains of about the same order of magnitude as the piezoelectric (unipolar) strain (0.1%). An additional attractive feature of this effect is the absence of any significant hysteresis
   b. Piezoelectric materials require an electrical poling process, which makes these materials subject to significant aging as the sample depoles over

time. Electrostrictive materials do not need such a preliminary treatment, but do require a DC bias field for some applications because of their nonlinear response.

c. In contrast to piezoelectrics, electrostrictive ceramics are durable and reliable when operated under severe conditions, such as high temperature and large mechanical load.
d. The temperature characteristics (that is, the variation of electromechanical properties with temperature) of piezoelectrics are superior to electrostrictors.
e. Piezoelectrics have smaller dielectric constants than electrostrictors, thus allowing for a quicker response.

3. **Materials classification** for developing compositions with an optimum temperature coefficient of electrostriction (TCE):

Category I: Perovskite structures with disordered B-site cations:

Type I(a): Materials produced from the combination of ferroelectric and non-ferroelectric compounds (such as the solid solution system (Pb,Ba)(Zr,Ti)O_3 in which BaZrO_3 is the non-ferroelectric component).

Type I(b): Materials in which A-site lattice vacancies also occur, which further promote the diffuse phase transition (such as, the solid solution system (Pb,La,□)(Zr,Ti)O_3).

Category II: Perovskite structures with some degree of short-range ordering of B-site cations (such as the solid solution systems Pb($Mg_{1/3}Nb_{2/3}$,Ti)O_3 and Pb($Mg_{1/2}W_{1/2}$,Ti)O_3).

4. **Figures of Merit for Transducers**:

a. The Electromechanical Coupling Factor, k:

$$k^2 = \frac{\text{Stored (Mechanical or Electrical) Energy}}{\text{Input (Electrical or Mechanical) Energy}} = \frac{d}{\varepsilon_o K s}$$

where d is the piezoelectric strain coefficient, K is the dielectric constant, and s is the elastic compliance.

b. The Energy Transmission Coefficient, λ_{max}:

$$\lambda_{max} = \left[\frac{\text{Output (Mechanical or Electrical) Energy}}{\text{Input (Electrical or Mechanical) Energy}}\right]_{max}$$

and

$$\lambda_{\max} = \left[(1/k) - \sqrt{(1/k^2) - 1}\right]^2 = \left[(1/k) + \sqrt{(1/k^2) - 1}\right]^{-2}$$

where $k^2/4 < \lambda_{\max} < k^2/2$.

c. The Efficiency, η:

$$\eta = \frac{\text{Output (Mechanical or Electrical) Energy}}{\text{Consumed (Electrical or Mechanical) Energy}}$$

which for many actuator designs is practically 100%.

5. **Mechanical Strength**:
   a. The differences in durability among the electromechanical and phase-change transducers are attributed mainly to the magnitude of the maximum strain attainable by each device: 0.1% for the electrostrictor, 0.2% for the piezoelectric, and 0.4% for the antiferroelectric sample.
   b. The grain size dependence of the Vickers indentation is such that the crack length becomes shorter with decreasing grain size, while the center indentation size is virtually independent of grain size.
   c. The electric poling process for piezoelectric ceramics tends to induce a significant anisotropy in the mechanical strength of the material.

CHAPTER PROBLEMS

3.1 The piezoelectric strain matrix (d) for a tetragonal PZT is:

$$\begin{pmatrix} 0 & 0 & 0 & 0 & 200 & 0 \\ 0 & 0 & 0 & 200 & 0 & 0 \\ -60 & -60 & 180 & 0 & 0 & 0 \end{pmatrix} \quad [\text{pC/N}]$$

The sample has dimensions [10 mm x 10 mm x 10 mm]. The spontaneous polarization is along the c-axis, and an electric field of 10 kV/cm is applied along the a-axis. Calculate the deformation of the cubic specimen and make a drawing illustrating the deformation.

3.2 A monochromatic acoustic wave is initially propagating through a solid with mass density, ρ_1, and elastic stiffness, c_1. It encounters a planar boundary with another solid with mass density, ρ_2, and elastic stiffness, c_2, from which it is reflected normal to the boundary. Derive an equation for the reflection coefficient for this wave.

REFERENCES

1) Y. Ito and K. Uchino: Piezoelectricity, *Wiley Encyclopedia of Electrical and Electronics Engineering*, Vol. **16**, p. 479, John Wiley & Sons, NY (1999).
2) W. A. Smith: Proc. SPIE - The International Society for Optical Engineering 1733 (1992).
3) T. R. Shrout, R. Eitel, C. A. Randall, P. Rehrig,W. Hackenberger and S.–E. Park: Proc. 33rd Int'l. Smart Actuator Symp., State College, April (2001).
4) H. Takeuchi, S. Jyomura, E. Yamamoto and Y. Ito: J. Acoust. Soc. Am., **74**, 1114 (1982).
5) Y. Yamashita, K. Yokoyama, H. Honda and T. Takahashi: Jpn. J. Appl. Phys., **20**, Suppl. 20-4, 183 (1981).
6) Y. Ito, H. Takeuchi, S. Jyomura, K. Nagatsuma and S. Ashida: Appl. Phys. Lett., **35**, 595 (1979).
7) K. Uchino and S. Nomura: Jpn. J. Appl. Phys. **18**, 1493 (1979).
8) K. Abe, O. Furukawa and H. Inagawa: Ferroelectrics **87**, 55 (1988).
9) K. Furuta and K. Uchino: Adv. Ceram. Mater. **1**, 61 (1986).
10) J. von Cieminski and H. Beige: J. Phys. D **24**, 1182 (1991).
11) Y. Gao, Y. H. Chen, J. Ryu, K. Uchino and D. Viehland: Jpn. J. Appl. Phys. **40**, 79-85 (2001).
12) B. N. Rolov: Fiz. Tverdogo Tela, **6**, 2128 (1963).
13) V. A. Isupov: Izv. Akad. Nauk SSSR, Ser. Fiz., **28**, 653 (1964).
14) K. Uchino, J. Kuwata, S. Nomura, L. E. Cross and R. E. Newnham: Jpn. J. Appl. Phys. **20**, Suppl. 20-4, 171 (1981).
15) H. B. Krause, J. M. Cowley and J. Wheatley: Acta Cryst., **A35**, 1015 (1979).
16) G. A. Smolensky, V. A. Isupov, A. I. Agranovskaya and S. N. Popov: Soviet Phys.-Solid State **2**, 2584 (1961).
17) M. L. Mulvihill, L. E. Cross and K. Uchino: Proc. 8th European Mtg. Ferroelectricity, Nijmegen (1995).
18) L. E. Cross, S. J. Jang, R. E. Newnham, S. Nomura and K. Uchino: Ferroelectrics **23**, 187 (1980).
19) K. M. Leung, S. T. Liu and J. Kyonka: Ferroelectrics **27**, 41 (1980).
20) A. Varslavans: USSR Licenzintorg (Peter Stuchka Latvian State University) (1980).
21) H. Takeuchi, H. Masuzawa, C. Nakaya and Y. Ito: Proc. IEEE 1990 Ultrasonics Symposium, 697 (1990).
22) J. Kuwata, K. Uchino and S. Nomura: Ferroelectrics **37**, 579 (1981).
23) J. Kuwata, K. Uchino and S. Nomura: Jpn. J. Appl. Phys. **21**(9), 1298 (1982).
24) K. Yanagiwara, H. Kanai and Y. Yamashita: Jpn. J. Appl. Phys. **34**, 536 (1995)
25) S. E. Park and T. R. Shrout: Mat. Res. Innovt. **1**, 20 (1997).
26) K. Uchino and S. Nomura: Ferroelectrics **50**, 191 (1983).
27) K. Uchino: Proc. Int'l. Mtg. Adv. Mater. **9**, 489 (1989).
28) A. Furuta, K. Y. Oh and K. Uchino: Sensors and Mater. **3**, 205 (1992).

29) R. E. Newnham, D. P. Skinner and L. E. Cross: Materials Research Bulletin, **13**, 525 (1978).
30) W. A. Smith: Proc. 1989 IEEE Ultrasonic Symposium, 755 (1989).
30) K. A. Klicker, J. V. Biggers and R. E. Newnham: J. Amer. Ceram. Soc. **64**, 5 (1981).
31) K. Uchino, S. Nomura and R. E. Newnham: Sensor Tech. **2**, No. 7, 81 (1982).
32) K. Otsuka and S. M. Wayman: Chap. 1 in *Shape Memory Materials*, Cambridge University Press, Cambridge, UK (1998).
33) A. L. Roytburd, J. Slutsker and M. Wuttig: Chap. 5.23 Smart Composites with Shape Memory Alloys in *Comprehensive Composite Materials*, Elsevier Science, Oxford, UK (2000).
34) S. Legvold, J. Alstad and J. Rhyne: Phys. Rev. Lett. **10**, 509 (1963).
35) A. E. Clark, B. F. DeSavage and R. Bozorth: Phys. Rev. **138**, A216 (1965).
36) N. C. Koon, A. Schindler and F. Carter: Phys. Lett. **A37**, 413 (1971).
37) A. E. Clark, H. Belson: AIP Conf. Proc., No. 5, 1498 (1972).
38) A. E. Clark: *Ferroelectric Materials*, Vol. 1, p. 531, Eds. K. H. J. Buschow and E. P. Wohifarth, North-Holland, Amsterdam (1980).
39) J. D. Verhoven, E. D. Gibson, O. D. McMasters and H. H. Baker: Metal Trans. A, **18A**, No. 2, 223 (1987).
40) A. E. Clark, J. D. Verhoven, O. D. McMasters and E. D. Gibson: IEEE Trans. Mag. MAG-22, p.973 (1986).
41) J. B. Restorff: *Encyclopedia of Applied Physics*, Vol. 9, p.229, VCH Publ., New York (1994).
42) A. B. Flatau, M. J. Dapino and F. T. Calkins: Chap. 5.26 Magnetostrictive Composites in *Comprehensive Composite Materials*, Elsevier Science, Oxford, UK (2000).
43) R. Kellogg and A. B. Flatau: Proc. SPIE, **3668**(19), 184 (1999).
44) J. L. Butler: Application Manual for the Design Etrema Terfenol-D Magnetostrictive Transducers, Edge Technologies, Ames, IA (1988).
45) G. P. Carman, K. S. Cheung and D. Wang: J. Intelligent Mater. Systems and Structures, **6**, 691 (1995).
46) T. A. Duenas and G. P. Carman: Proc. Adaptive Struct. & Mater. Systems, ASME, AD-**57**/MD-**83**, p. 63 (1998).
47) K. Uchino and S. Hirose: IEEE UFFC Transactions, **48**, 307-321 (2001).
48) L. E. Kinsler, A. R. Frey, A. B. Coppens and J. V. Sanders: *Fundamental of Acoustics*, John Wiley & Sons, New York (1982).
49) S. Nomura and K. Uchino: Ferroelectrics **41**, 117 (1982).
50) K. Uchino, J. Kuwata, S. Nomura, L. E. Cross and R. E. Newnham: Jpn. J. Appl. Phys. **20**, Suppl. 20-4, 171 (1981).
51) R. W. Basedow and T. D. Cocks: J. Phys. E: Sci. Inst. **13**,840 (1980).
52) Y. Nakajima, T. Hayashi, I. Hayashi and K. Uchino: Jpn. J. Appl. Phys. **24**(2), 235 (1985).
53) S. Nomura, O. Osawa, K. Uchino and I. Hayashi: Abstract Jpn. Appl. Phys., p.764, Spring (1982).
54) H. Cao and A. G. Evans: J. Amer. Ceram. Soc. **76**, 890 (1993).
55) X.–H. Du, Q.–M. Wang, U. Belegundu and Kenji Uchino: J. Ceram. Soc. Jpn. **107** (2), 190 (1999).
56) W. D. Callister, Jr.: *Materials Science and Engineering*, p. 189, Wiley (1984).
57) T. Nishida and E. Yasuda ed.: *Evaluation of Mechanical Characteristics in Ceramics*, p. 68, Nikkan-Kogyo (1986).
58) A. A. Griffith: Phil. Trans. Roy. Soc. (London), **A221**, 163 (1920).
59) A. G. Evans and E. A. Charles: J. Amer. Ceram. Soc. **59**, 371 (1976).

60) K. Niihara, R. Morena and D. P. H. Hasselman: Commun. Amer. Ceram. Soc., C-116, Jul. (1982).
61) K. Uchino and T. Takasu: Inspec **10**, 29 (1986).
62) H. Aburatani, S. Harada, K. Uchino, A. Furuta and Y. Fuda: Jpn. J. Appl. Phys. **33**, Pt.1, No.5B, 3091 (1994).
63) T. Yamamoto, H. Igarashi and K. Okazaki: Ferroelectrics **50**, 273 (1983).
64) H. Wang and R. N. Singh: Ferroelectrics **168**, 281 (1995).
65) H. Aburatani, S. Harada, K. Uchino, A. Furuta and Y. Fuda: Jpn. J. Appl. Phys. **33**, 3091 (1994).
66) H. Aburatani and K. Uchino: Jpn. J. Appl. Phys. **35**, L516 (1996).
67) H. Aburatani, J. P. Witham and K. Uchino: Jpn. J. Appl.Phys. **37**, 602 (1998).
68) K. Uchino, *Piezoelectric/Electrostrictive Actuators*, Morikita Pub. Co., Tokyo (1985).
69) Q. M. Zhang, J. Zhao, K. Uchino and J. Zheng: J. Mater. Res., **12**, 226 (1996).
70) K. H. Hellwege et al.: *Landolt-Bornstein, Group III*, Vol. 11, Springer-Verlag, NY (1979).

4

CERAMIC ACTUATOR STRUCTURES AND FABRICATION METHODS

The production of piezoelectric and electrostrictive ceramics takes place in two stages: (1) the preparation of the ceramic powders and (2) the sintering of shaped structures. Wet chemical methods for preparing the ceramic powders are generally employed to optimize the reproducibility of the actuator characteristics. Actuator designs incorporating these ceramics are commonly fabricated with a bimorph, multilayer, or flextensional structure.

4.1 FABRICATION OF CERAMICS AND SINGLE CRYSTALS

The active materials used in many actuator designs are most readily incorporated into the device structure when they are in ceramic form. The process for producing the ceramic generally occurs in two stages: (1) the preparation of the ceramic powders and (2) the sintering of the assembled structures. Single crystals are occasionally incorporated into structures designed for certain special applications.

(1) Preparation of the Ceramic Powders

Particle shape, particle size distribution and compositional uniformity are key factors to control when producing the ceramic powders in order to optimize the reproducibility of the electromechanical response. A conventional method for producing powders is the *mixed-oxide method*, which involves firing a mixture of oxide powders in a process called *calcination*. The calcined material is then mechanically crushed and milled into fine powders. One major disadvantage of the mixed-oxide method is that it tends to produce materials with pronounced microscale compositional fluctuations. Wet chemical methods (such as the *co-precipitation* and *alkoxide methods*) are thus generally preferred as they produce more compositionally homogeneous ceramics. In this section, these processes for producing barium titanate (BT), lead zirconate titanate (PZT) and lead magnesium niobate (PMN) ceramics are reviewed.[1]

Solid-State Reaction (Mixed-Oxide Method)

Let us first consider the general process involved in producing ceramic powders by the mixed-oxide method as it might occur in the preparation of $Pb(Zr_xTi_{1-x})O_3$. The oxide powders PbO, ZrO_2, and TiO_2 are weighed out in appropriate proportions, mixed, and then calcined at a temperature in the range of 800-900°C (depending on the composition) for 1-2 hours. The calcined powder is subsequently crushed and milled into a fine powder. The milling step often leads to certain undesirable features in the product. First of all particle sizes of less than 1 μm generally cannot be produced by mechanical milling. Furthermore, contamination of the powder by the milling media is unavoidable.

The preparation of $BaTiO_3$ by this method can in principle be carried out in a similar way using equimolar quantities of the oxides BaO and TiO_2. In practice, $BaCO_3$ is generally used in place of BaO, however, because high purity BaO is expensive and chemically less reactive.

The process must be modified to some extent when it is used to prepare $Pb[(Mg_{1/3}Nb_{2/3})_{1-x}Ti_x]O_3$ (PMN-PT) ceramics from the starting oxides PbO, MgO, Nb_2O_5 and TiO_2. If the oxides are simply mixed and calcined a second phase (*pyrochlore*) in addition to the perovskite phase is formed. One effective means of suppressing the formation of this second phase has been to add several mole percent of excess PbO during the final sintering stage.[2] An effective solution to this problem as it applies to the preparation of pure $Pb(Mg_{1/3}Nb_{2/3})O_3$ has been developed, which involves an initial two stage calcination process whereby a *columbite* $MgNb_2O_6$ precursor is first prepared and then reacted with PbO to form the desired perovskite phase according to the following reaction:

$$3PbO + MgNb_2O_6 \rightarrow 3\,Pb(Mg_{1/3}Nb_{2/3})O_3$$

The product prepared in this manner is almost entirely perovkite with only the very slightest traces of the pyrochlore phase present.[3] When this method is used for the preparation of PMN-PT, the MgO, Nb_2O_5, and TiO_2 are first mixed and fired at 1000°C to form the columbite precursor. Then PbO is added to the columbite phase, and the mixture is calcined at 800-900°C. The addition of several mole percent excess MgO has been found to be particularly effective in obtaining the perfect perovskite phase.

The Co-Precipitation Method

Since many of the popular piezoelectric/electrostrictive ceramics are of the complex perovkite type described in Section 3.1(3), compositional homogeneity has become as important an issue as phase purity in the production of these compositions. The mixed-oxide method is especially prone to problems in both these areas and, thus, is not generally the preferred method for preparing the ceramics. The *co-precipitation method* has been found to produce materials with a much higher level of compositional homogeneity. The method basically involves adding a precipitant into a liquid solution of mixed metal salts to generate a homogeneous precipitate, which is then subjected to a thermal dissolution process to produce a homogeneous powder of the desired composition.

As an example, let us consider the preparation of a $BaTiO_3$ sample by this method. Oxalic acid is added to an aqueous solution of $BaCl_2$ and $TiCl_4$ to generate a precipitate of $BaTiO(C_2H_4)_2.4H_2O$ with a perfect 1:1 ratio of Ba to Ti on the atomic scale. Thermal dissolution of this precipitate produces highly stoichiometric $BaTiO_3$ powders with good sintering characteristics.

When this method is used to prepare $(Pb,La)(Zr,Ti)O_3$ (PLZT) ceramics, $Pb(NO_3)_2$, $La(NO_3)_3{\bullet}6H_2O$, $ZrO(NO_3)_2{\bullet}2H_2O$ and $TiO(NO_3)_2$ are used as the starting materials.[4] First, the nitrates are mixed in the desired proportion to produce an aqueous solution, then a half volume of ethanol is added to the mixture. Oxalic acid diluted with ethanol is then dripped slowly into the nitric solution, and a PLZT oxalate is precipitated. The thermal dissolution is carried out at 800°C.

In all the cases described so far, a final thermal dissolution of the precipitate is required to obtain the desired powder. The powder specimen can be obtained without this final step, however, for certain compositions, by what is referred to as *direct precipitation method.* One such composition is $BaTiO_3$. When it is prepared by the direct precipitation method, $Ti(OR)_4$ (R: propyl) is dripped into a $Ba(OH)_2$ water solution to produce high-purity, stoichiometric $BaTiO_3$ powders with an average particle size of 10 nm.[1]

Alkoxide Hydrolysis

When metal alkoxides $M(OR)_n$ (M: metal atom, R: alkyl) are mixed in alcohol in appropriate proportions and water is added, the hydrolytic reaction produces alcohol and a metal oxide or metal hydrate. This process is sometimes referred to as the *sol-gel method.* Some ferroelectric compositions that can be synthesized in this way are listed in Table 4.1. The sol-gel method can produce very fine, high purity powders. Since metal alkoxides tend to be volatile, purification is easily accomplished through distillation. High purity can be sustained throughout the hydrolytic reaction because there is no need to introduce any ions other than those of the desired composition. The mechanisms of hydrolysis and condensation are summarized as follows:

Hydrolysis:

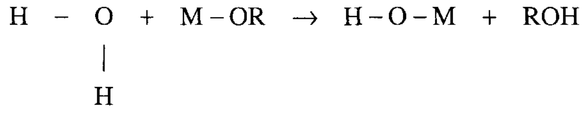

$$\mathrm{H - \underset{\underset{H}{|}}{O} + M-OR \rightarrow H-O-M + ROH}$$

Alkoxylation: (Removal of H as an alcohol)

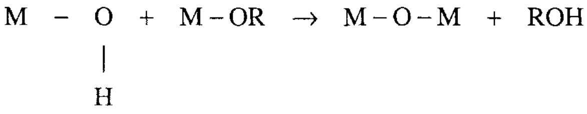

$$\mathrm{M - \underset{\underset{H}{|}}{O} + M-OR \rightarrow M-O-M + ROH}$$

Oxolation: (Removal of H in water)

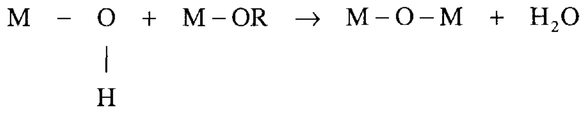

$$\underset{\displaystyle H}{\overset{}{M - \underset{|}{O}}} + M-OR \rightarrow M-O-M + H_2O$$

When this method is employed to produce $BaTiO_3$ powders, the metal alkoxides $Ba(OC_3H_7)_2$ and $Ti(OC_5H_{11})_4$ are diluted with isopropyl alcohol (or benzene). Very fine, stoichiometric $BaTiO_3$ powders with good crystallinity and particle sizes in the range of 10-100 Å (agglomerate size=1 μm) can be obtained by this method. The hydrolytic process produces powder with purity of more than 99.98%, which leads to a significant increase in the permittivity of the sintered ceramic as compared with samples prepared by the mixed-oxide method.[5]

When this method is employed to prepare $Pb(Zr,Ti)O_3$ (PZT) powders, it is found that the lead alkoxide is relatively difficult to obtain as compared to the titanium and zirconium alkoxides. A modified two-stage approach has been developed to synthesize this more challenging composition. In the first stage of the process $(Zr,Ti)O_2$ is prepared by the alkoxide method. The $(Zr,Ti)O_2$ is combined with PbO in the second stage, during which solid-state reaction occurs.[6] A partial sol-gel method such as this, carried out with inexpensive ready-made nanosize powders is an attractive cost-effective alternative for the commercial production of these powders. Another method that has presented some promise involves combining zirconium n-butoxide $Zr[O(CH_2)_3CH_3]_4$ and titanium isopropoxide $Ti[OCH(CH_3)_2]_4$ with lead acetyl acetonate $Pb(CH_3COCHCOCH_3)$ to obtain a PZT precursor phase.[5]

Table 4.1 Some ferroelectric compositions that can be synthesized by the alkoxide hydrolysis method.

Crystalline	$BaTiO_3$ $Ba(Zr,Ti)O_3$ $(Ba,Sr)TiO_3$
Amorphous	$Pb(Mg_{1/3}Nb_{2/3})O_3$ $Ba(Zn_{1/3}Nb_{2/3})O_3$ $Pb(Zr,Ti)O_3$ $(Pb,La)(Zr,Ti)O_3$

(2) The Sintering Process

The calcined powders are generally mixed with an appropriate binder and formed into an appropriate shape by pressing, extrusion, or some other casting method. The green body is subjected to a low temperature "burn-out" process just prior to the final high temperature firing in order to volatilize the binder from the body. This final firing process in which the ceramic attains its optimum density is called *sintering* and is typically carried out at high temperatures (below the melting temperature) and sometimes also at high pressure (*hot pressing*). The process promotes accelerated diffusion of the constituent atoms on the particulate surfaces due to the surface energy (surface tension), which leads to crystal bonding at the interface between adjacent particles as depicted in Figure 4.1. The ceramic body may thus acquire sufficient mechanical strength while retaining its intended shape as it uniformly shrinks. The physical properties of the sintered body will depend not only on the properties of the particulates, but also on features of the microstructure such as the grain boundaries and the configuration of any remaining porosity. The mechanical strength, for example, will depend on the bonding between grains as well as the mechanical strength of the individual particulates. Mechanical failure in ceramics can occur either at the grain boundary (*intergranular fracture*) or across individual grains (*intragranular fracture*). The mechanical strength is thus enhanced for ceramic bodies with mechanically tough crystallites and strong intergranular bonding.

During sintering, the ceramic grains grow and their shape changes significantly. The features of the raw powder have been found to strongly affect the dynamics of the sintering and the characteristics of the final product. In general, the diffusion processes that take place during sintering are accelerated as the particle size of the raw powder is decreased, because the driving force of sintering is related to the surface energy of the particles. Moreover, for fine powders, the diffusion length of the constituent atoms becomes shorter, which accelerates pore diffusion and elimination. This results in high-density ceramics.

There have been many studies on grain growth.[7] The relationship between the grain size, D, and the sintering period, t, is generally defined by:

$$D^{\beta} - D_o^{\beta} \propto t \tag{4.1}$$

where *normal grain growth* is characterized by $\beta=2$, and *abnormal grain growth* by $\beta=3$. The microstructures of PLZT 9/65/35 ceramics fabricated from powders prepared by the oxalic acid/ethanol method and sintered at 1200°C for 1 and 16 hours are pictured in Figure 4.2.[8] These represent cases of normal grain growth characterized by the function shown in Figure 4.3, for which we see a good linear relation between the sintering period and the square of the grain size.

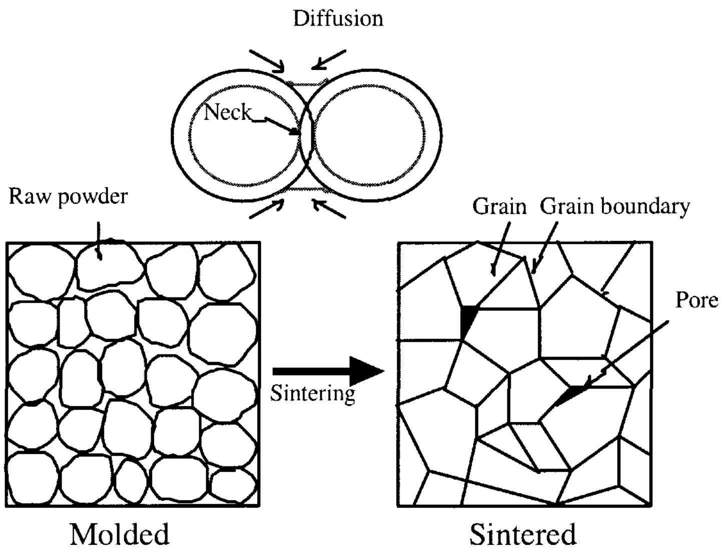

Figure 4.1 Schematic diagrams representing the mechanism for grain growth and the bonding of crystallites during the sintering process.

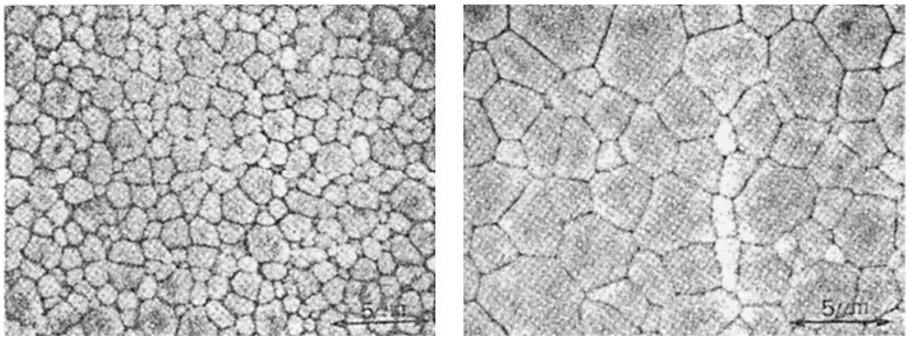

(a) (b)

Figure 4.2 The microstructures of PLZT 9/65/35 ceramics fabricated from powders prepared by the oxalic acid/ethanol method and sintered at 1200°C for (a) 1 hour and (b) 16 hours.[8]

Doping is another method commonly used to regulate sintering conditions and grain growth in certain ceramic compositions. The desired effect of the dopant is to decrease the sintering temperature, and additional effects such as suppression or enhancement of grain growth are sometimes observed. Excess PbO or Bi_2O_3 added to PZT, for example, tends to inhibit grain growth. The addition of 0.8 atom percent of Dy to $BaTiO_3$ ceramics has been found to effectively suppress the grain size to less than 1 μm.[9]

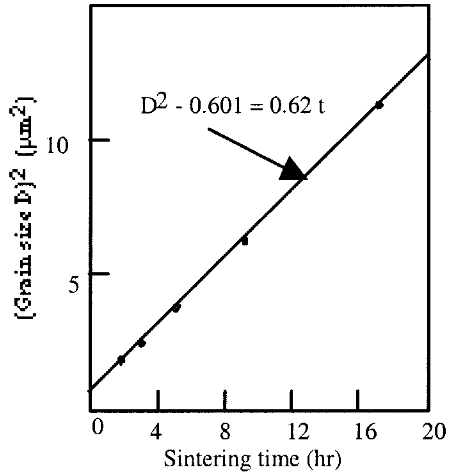

Figure 4.3 Grain growth in PLZT 9/65/35 ceramics plotted as a function of sintering time.[8]

Example Problem 4.1

The cations K^{1+}, Bi^{3+}, Zn^{2+} and Nb^{5+} constitute a disordered complex perovskite crystal, where the first two occupy the A-site and the last two occupy the B-site of the lattice. Determine the possible compositional formulas.

Solution

The perovskite structure is generally described by the following:

$$ABO_3=(K^{1+}{}_{1-x}Bi^{3+}{}_{x})(Zn^{2+}{}_{1-y}\,Nb^{5+}{}_{y})O^{2-}{}_3$$

We begin by accounting for charge neutrality:

$$[1(1-x)] + [3(x)] + [2\,(1-y)] + [5(y)] \;=\; +6 \qquad \text{(P4.1.1)}$$

which yields:

$$2(x) \;+\; 3(y) \;=\; 3 \qquad \text{(P4.1.2)}$$

where $(0 < x < 1,\ 1/3 < y < 1))$

A continuous range of compositions satisfy the conditions for x and y given by Equation (P4.1.2). The composition $(K_{3/4}Bi_{1/4})\ (Zn_{1/6}Nb_{5/6})O_3$ is one possibility within this range.

(3) Single Crystal Growth

Single crystals are not as commonly used in piezoelectric/electrostrictive devices as are ceramics, but there are nevertheless some promising designs under investigation which incorporate single crystals. A few popular piezoelectric single crystals are quartz, grown by hydrothermal methods, and lithium niobate ($LiNbO_3$) and lithium tantalate ($LiTaO_3$), typically grown by the Czochralski method. A unimorph structure fabricated from a thin plate of single crystal $LiNbO_3$ has been reported in which half of the thickness is reverse polarized enabling it to function like a bimorph (see Figure 4.4 for structure).[10] Although this device is fragile and the bending displacement is not large, its linear displacement characteristics coupled with the absence of hysteresis make it attractive for some special applications, such as in scanning tunneling microscopes. Single crystal growth of the morphotropic phase boundary composition of PZT has been actively pursued, but no crystal has yet been grown larger than 1 mm^3. Recently, $Pb(Zn_{1/3}Nb_{2/3})O_3$ (PZN), $Pb(Zn_{1/3}Nb_{2/3})O_3$-$PbTiO_3$ (PZN-PT), and $Pb(Mg_{1/3}Nb_{2/3})O_3$-$PbTiO_3$ (PMN-PT) have become attractive for medical acoustic transducer applications, because it has been found that large single crystals (1 cm^3 and larger) can be easily grown by a simple flux method. They exhibit exceptionally high electromechanical coupling factors (95%) and piezoelectric strain coefficients ($d=1570 \times 10^{-12}$ C/N) when they are poled in a particular direction.[11,12] The crystal growth process involves adding excess PbO to a mixture of ZnO, Nb_2O_5 and TiO_2, and cooling the mixture down from 1150°C to 900°C at a rate of 2.5°C/hr.

4.2 DEVICE DESIGN

A classification of electromechanical ceramic actuators based on structure type is presented in Figure 4.4. Simple devices directly use the longitudinally or transversely induced strain. The simple disk and multilayer types make use of the longitudinal strain, and the cylinder types (the simple cylinder, separated cylinder, and honeycomb designs) utilize the transverse strain. Complex devices do not use the induced strain directly, but rather a magnified displacement, produced through a spatial magnification mechanism (demonstrated by the unimorph, bimorph, moonie, and hinge lever designs) or through a sequential drive mechanism (inchworm). Among the designs shown in Figure 4.4, the multilayer and bimorph types are the most commonly used structures. Although the multilayer type produces only relatively modest displacements (10 μm), it offers a respectable generative force (100 kgf), a quick response speed (10 μsec), long lifetime (10^{11} cycles), and a high electromechanical coupling factor k_{33} (70%). The bimorph type provides large displacements (300 μm), but can only offer a relatively low generative force (100 gf), a much slower response speed (1 msec), a shorter lifetime (10^8 cycles) and a rather low electromechanical coupling factor k_{eff} (10%). We will examine each structure more closely in the sections that follow.

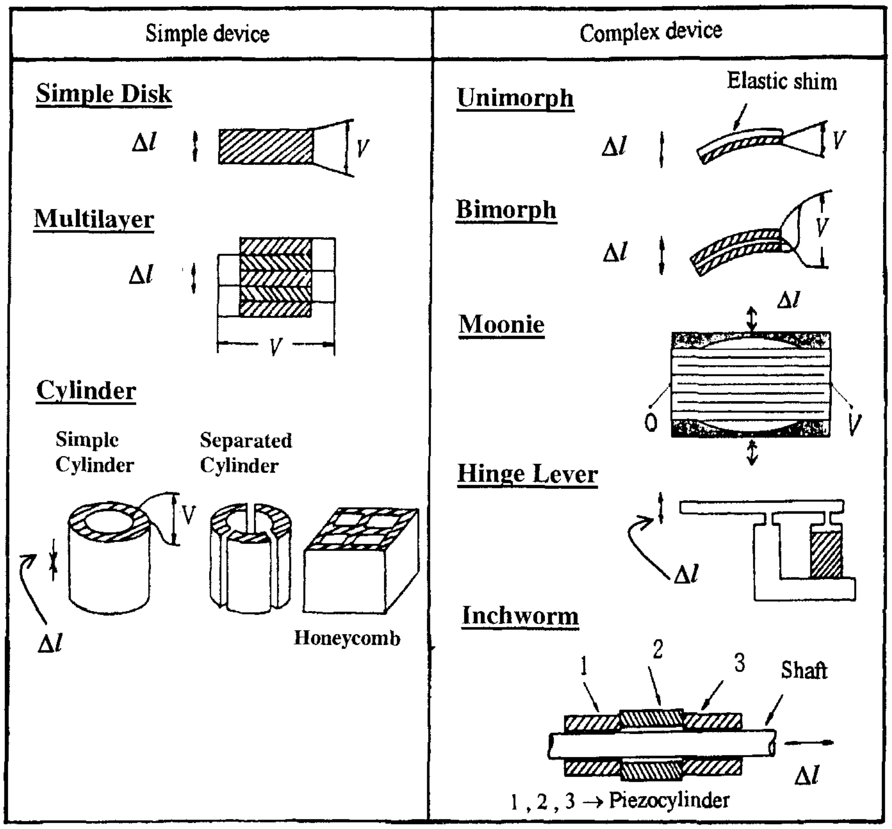
Simple device
Complex device
Simple Disk
Δl
V
Multilayer
Δl
V
Cylinder
Simple Cylinder
Separated Cylinder
V
Δl
Honeycomb
Unimorph
Elastic shim
Δl
V
Bimorph
Δl
V
Moonie
Δl
0
V
Hinge Lever
Δl
Inchworm
1
2
3
Shaft
Δl
1 , 2 , 3 → Piezocylinder

Figure 4.4 A classification of electromechanical ceramic actuators based on structure type.

(1) Disk Actuators

Single disk devices are generally not commercially popular these days because of their low efficiency. They are still considered useful in the laboratory, however, and find their widest application in this setting.

Example Problem 4.2

The apparent dielectric constant of a 1 mm barium titanate-based ceramic disk is measured and found to be 500. Due to a fabrication error, however, a thin air gap of 0.5 μm is discovered between the ceramic and the electrodes that extends over most of the electroded area on both sides of the device. Estimate what the actual dielectric constant of the device should be without this defect.

Solution

The measured capacitance in this case will be the total capacitance of the ceramic and the two air gaps effectively arranged in series within the device. If we denote the capacitor area, thickness and the air gap by A, d and δ, respectively, the total capacitance is given by:

$$\frac{1}{C} = \frac{1}{(\varepsilon_0 K A/d)} + \frac{2}{(\varepsilon_0 A/\delta)} = \left(\frac{1}{\varepsilon_0 A}\right)\left(\frac{d}{K} + 2\delta\right) \quad \text{(P4.2.1)}$$

The apparent dielectric constant was calculated from the measured capacitance according to the relationship:

$$\frac{Cd}{\varepsilon_0 A} = 500 \quad \text{(P4.2.2)}$$

This expression combined with Equation (P4.2.1) allows us to write:

$$\frac{1}{K} + \frac{2\delta}{d} = \frac{1}{500} \quad \text{(P4.2.3)}$$

Substituting $d = 10^{-3}$ m, $\delta = 0.5 \times 10^{-6}$ m into this equation, we determine that the dielectric constant of the defect-free device should be K = 1000.

This kind of fabrication flaw tends to occur when alcohol is used to clean the ceramic disk after polishing and it is not dried completely on a hot plate (above 100°C). This demonstrates well why it is important to take care not to generate even a submicron air gap during the electroding process.

(2) Multilayer Actuators

Ferroelectric ceramic multilayer devices have been investigated intensively for capacitor and actuator applications, because they have low driving voltages and they are highly suitable for miniaturization and integration onto hybrid structures. Miniaturization and hybridization are key concepts in the development of modern micromechatronic systems. The goal for multilayer actuators is to eventually incorporate layers thinner than 10 μm, which is the current standard for multilayer capacitors. The typical layer thickness for multilayer actuators at this time is about 60 μm. A multilayer structure typically exhibits a field-induced strain of 0.1% along its length, *l* (for example, a 1 cm sample will exhibit a 10 μm displacement), and has a fundamental resonance frequency given by:

$$f_r = \frac{1}{2l\sqrt{\rho s_{33}^D}} \quad \text{(4.2)}$$

where ρ is the density and s_{33}^D is the elastic compliance (for example, a 1 cm sample will have a 100 kHz resonance frequency). New multilayer configurations or heterostructures comprised of electromechanical materials and modified electrode patterns are anticipated that will be incorporated into ever more sophisticated smart systems. There are two general methods for fabricating multilayer ceramic devices: (1) the *cut-and-bond method* and (2) the *tape-casting method.*

A schematic diagram of a commercially manufactured piezopile from NTK-NGK is shown in Figure 4.5.[13] It is comprised of one hundred cut and polished PZT ceramic discs, each 1 mm thick, which are stacked and interleaved with metal foils that serve as electrodes within the device. A 100 μm displacement is generated by the pile with an applied voltage of 1.6 kV, and the maximum generative force is about 3 tons. Since the entire device is clamped by bolts and mechanically biased, delamination and mechanical fracture do not readily occur. Although devices such as this offer substantial displacements and generative forces, the cut-and-bond method in general has its disadvantages. One major drawback is the labor-intensive process itself, which is not at all well suited to mass production. The devices also tend to require rather high drive voltages because the minimum layer thickness possible for stacks prepared in this way is only about 0.2 mm.

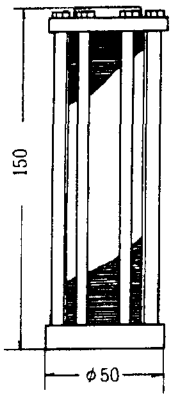

Figure 4.5 Schematic diagram of a piezopile manufactured by NTK-NGK.[13]

The tape-casting method, in which ceramic green sheets with printed electrodes are laminated and co-fired with compatible internal electrodes, is far more conducive to mass production and produces devices with much thinner layers so that low drive voltages may be employed.

The multilayer structure is essentially comprised of alternating ferroelectric and conducting layers which are *co-fired* to produce a dense, cohesive unit as shown in Figure 4.6. A ferroelectric layer sandwiched between a pair of electrodes constitutes a single displacement element. Hundreds of these units may be connected in parallel to the potential difference supplied by the external electrodes, which are connected to the many interleaved internal electrodes of the stack as shown in Figure 4.6. A flowchart for the manufacturing process is shown in Figure 4.7. *Green sheets* are prepared in two steps. First, the ceramic powder is combined with an appropriate liquid solution to form a *slip*. The *slip* mixture generally includes the ceramic powder and a liquid comprised of a *solvent*, a *deflocculant,* a *binder* and a *plasticizer*. During the second part of the process, the slip is cast into a film under a special straight blade, called a "*doctor blade*," whose distance above the carrier determines the film thickness. Once dried, the resulting film, called a *green sheet*, has the elastic flexibility of synthetic leather. The volume fraction of the ceramic in the now polymerized matrix at this point is about 50%. The green sheet is cut into an appropriate size, and internal electrodes are printed using silver, palladium or platinum ink. Several tens to hundreds of these layers are then laminated and pressed using a hot press. After the stacks are cut into small chips, the green bodies are sintered at around 1200°C in a furnace, with special care taken to control the initial binder evaporation at 500°C. The sintered chips are polished, externally electroded, lead wires are attached, and finally the chips are coated with a waterproof spray.

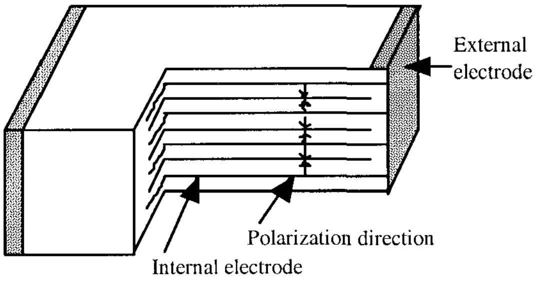

Figure 4.6 The structure of a multilayer actuator.

A cross-sectional view of a conventional *interdigital electrode* configuration is shown in Figure 4.8(a).[14] The area of the internal electrode is slightly smaller than the cross-sectional area of the device. Notice that every two layers of the internal electrodes extend to one side of the device and connect with the external electrode on that side so that all active layers of the device are effectively connected in parallel. The small segments in each layer that are not addressed by the internal electrodes remain inactive, thereby restricting the overall generative displacement and leading to detrimental stress concentrations in the device. A multilayer structure is represented in Figure 4.9(a) and the strain distribution measured in a test device is shown in Figure 4.9(b). The derivative of the displacement distribution provides an estimate of the stress concentration in the device.[15] The internal stress distribution was also predicted using the finite element method. The results of this analysis are summarized in Figure 4.10. The maximum tensile and compressive stresses are 1×10^8 N/m^2 and 1.2×10^8 N/m^2, respectively, which are very close to the critical strength of the ceramic.[15]

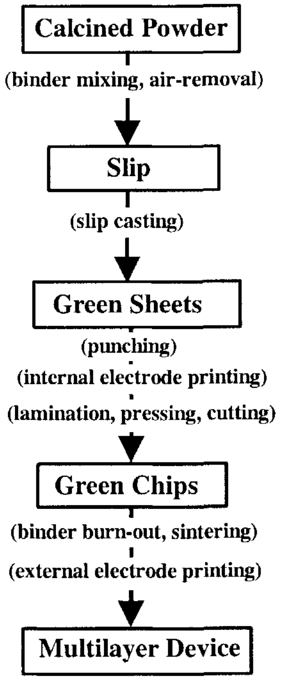
Calcined Powder
(binder mixing, air-removal)
Slip
(slip casting)
Green Sheets
(punching)
(internal electrode printing)
(lamination, pressing, cutting)
Green Chips
(binder burn-out, sintering)
(external electrode printing)
Multilayer Device

Figure 4.7 A flowchart for the fabrication of a multilayer ceramic actuator.

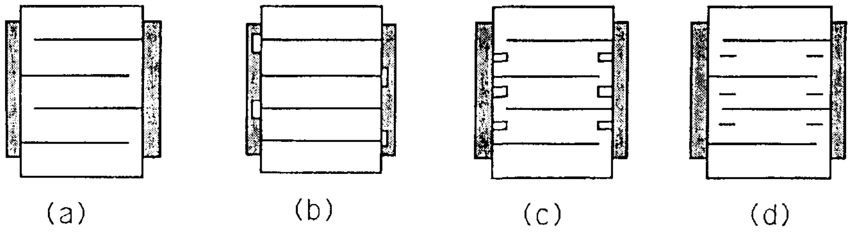

Figure 4.8 Various internal electrode configurations for multilayer actuators: (a) interdigital, (b) plate-through, (c) slit-insert, and (d) interdigital with float electrode.

Crack propagation has been investigated in a variety of multilayer systems.[16] A crack pattern commonly observed in PNNZT piezoelectric actuators under bipolar drive is shown in Figure 4.11(a). It occurs much as predicted in the theoretical treatment of these systems.[15] The crack originates at the edge of an internal electrode and propagates toward the adjacent electrode. Delamination between the electrode and the ceramic occurs simultaneously, leading to a Y-shaped crack. An interesting difference was observed in the case of the antiferroelectric PNZST system shown in Figure 4.11(b). Here a Y-shaped crack is again produced, but it originates in the ceramic between the electrodes.[17] This is probably due to the combination of two distinct induced strains in the ceramic: the anisotropic piezoelectric strain and the more isotropic strain associated with the antiferroelectric response to the applied field.

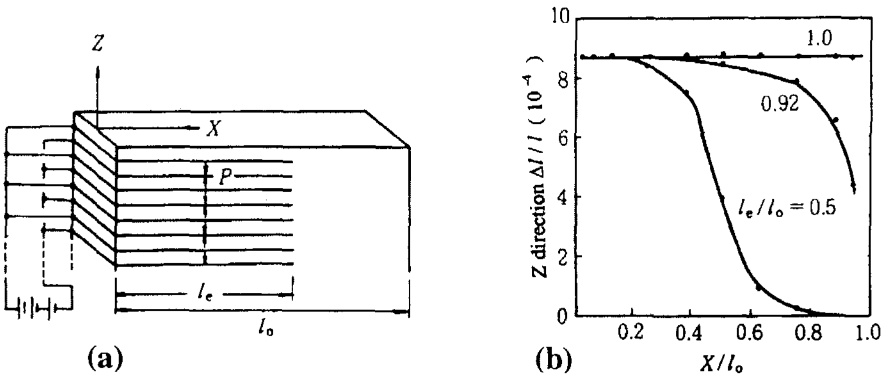

Figure 4.9 A multilayer structure: (a) a schematic depiction and (b) the induced strain distribution measured in a test device.[15]

A modified electrode configuration, called the plate-through design [see Figure 4.8(b)], was developed by NEC as a solution to this particular mechanical problem.[18] The electrode in this modified configuration extends over the entire surface of the ceramic so that the stress concentration cannot develop. This modification requires that an insulating tab terminate every two electrode layers on the sides of the device where the external electrodes are painted. Key issues in producing reliable devices with this alternative electrode design are concerned with the precise application of the insulating terminations and improvement of the adhesion between the ceramic and internal electrode layers. The designers of NEC addressed the first of these issues by developing an electrophoretic technique for applying glass terminators to the device. The problem of adhesion was resolved by making use of a special electrode paste containing powders of both the Ag-Pd electrode material and the ceramic phase. The displacement curve for a (0.65)PMN-(0.35)PT multilayer actuator with ninety-nine layers of 100 μm thick sheets (2x3x10 mm^3) is shown in Figure 4.12(a).[19] We see from these data that a 8.7 μm displacement is generated by an applied voltage of 100 V, accompanied by a slight hysteresis. This curve is consistent with the typical response of a disk device. The transient response of the induced displacement after the application of a rectangular voltage is shown in Figure 4.12(b). Rising and falling responses as quick as 10 μsec are observed.

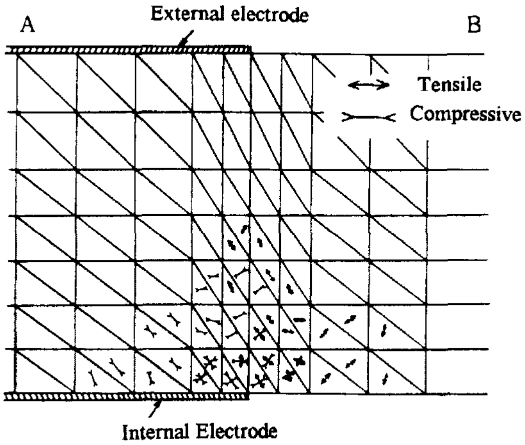

Figure 4.10 The internal stress distribution for a multilayer actuator as predicted by finite element analysis.[15]

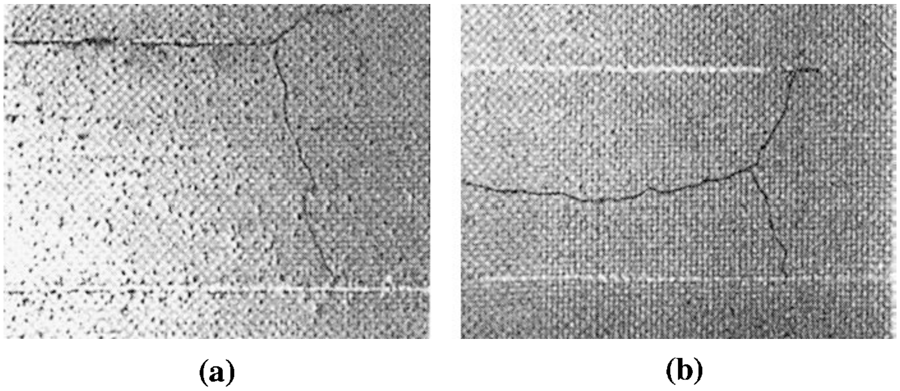
(a) (b)

Figure 4.11 Crack generation in multilayer ceramic actuators under bipolar drive: (a) piezoelectric PNNZT, and (b) antiferroelectric PNZST.[16]

The *slit-insert design* and the *interdigital with float electrode* are shown in Figures 4.8(c) and 4.8(d), respectively. The induced stress concentration is relieved in the slit-insert design while the electric field concentration is avoided with the interdigital with float electrode configuration.[20]

Another common crack pattern is the vertical crack, which will occasionally occur in the layer just adjacent to the top or bottom inactive layer. The inactive layer serves as an interface between the device and the object to which the actuator is attached. A crack occurring in the layer adjacent to the inactive bottom layer of a multilayer device is pictured in Figure 4.13. It originated from a transverse tensile stress produced in this layer due to clamping from the adjacent thick inactive layer.

One solution that has been proposed for this problem is to pre-pole the top and bottom layers of the device.

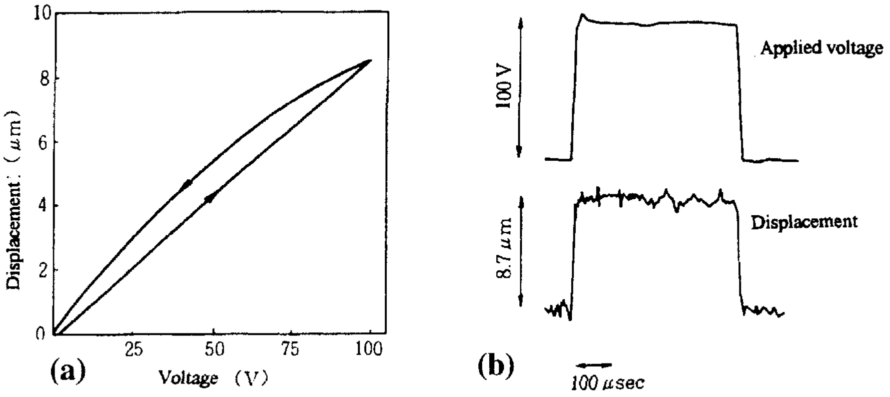

Figure 4.12 The response of a 0.65PMN-0.35PT multilayer actuator: (a) the displacement as a function of applied voltage and (b) the displacement response to a step voltage.[19]

Example Problem 4.3

A piezoelectric multilayer actuator under a certain applied voltage, V, will exhibit an amplified displacement as compared with the displacement generated in a single disk of the active material. An even more pronounced displacement amplification is expected from an electrostrictive device. Verify this using the following equations for the piezoelectric and electrostriction effects: $x = d\,E$ and $x = M\,E^2$.

Solution

Let l, Δl and n be the total thickness, displacement and the number of ceramic layers, respectively. The strain, x, is just equal to $\Delta l / l$. The displacement produced by each type of device is given by the following equations.

(a) The Piezoelectric Actuator:

$$\Delta l = l \text{ x } l \, d \, E = l \, d \, [V / (l / n)] = n \, d \, V \qquad \text{(P4.3.1)}$$

We see from this equation that the displacement is amplified in proportion to the number of layers, n.

(b) The Electrostrictive Actuator:

$$\Delta l = l \, x = l \, M \, E^2 = l \, M \, [V / (l / n)]^2 = n^2 \, (M / l) \, V^2 \qquad \text{(P4.3.2)}$$

We see in this case that the displacement is amplified in proportion to the square of the number of layers, n. The electrostrictive device is thus more effective than the piezoelectric one.

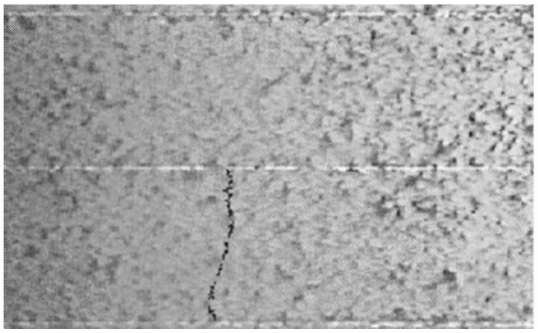

Figure 4.13 A vertical crack observed in the layer just adjacent to the bottom inactive layer in a multilayer actuator.

A multilayer actuator incorporating a new interdigital internal electrode configuration has been developed by Tokin.[21] In contrast to devices with the conventional interdigital electrode configuration, for the modified design line electrodes are printed on the piezoelectric green sheets, which are stacked so that alternate electrode lines are displaced by one-half pitch. This actuator produces displacements normal to the stacking direction through the longitudinal piezoelectric effect. Long ceramic actuators up to 74 mm in length have been manufactured, which can generate longitudinal displacements up to 55 μm.

A three-dimensional positioning actuator with a stacked structure has been proposed by PI Ceramic, in which both transverse and shear strains are induced to generate displacements.[22] As shown in Fig. 4.14(a), this actuator consists of three parts: the top 10 mm long Z-stack generates the displacement along the z direction, while the second and the bottom 10 mm long X and Y stacks provide the x and y displacements through shear deformation, as illustrated in Fig. 4.14(b). The device can produce 10 μm displacements in all three directions when 500 V is applied to the 1 mm thick layers.

Various failure detection techniques have been proposed to implement in smart actuator devices to essentially monitor their own "health."[23] One such "intelligent" actuator system that utilizes acoustic emission (AE) detection is shown in Figure 4.15. The actuator is controlled by two feedback mechanisms: position feedback, which can compensate for positional drift and hysteresis, and breakdown detection feedback, which can shut down the actuator system safely in the event of an imminent failure. As previously described in Section 3.5(3), acoustic emission from a piezoelectric actuator driven by a cyclic electric field is a good indicator of mechanical failure. The emissions are most pronounced when a crack propagates in the ceramic at the maximum speed. A portion of this smart piezoelectric actuator is therefore dedicated to sensing and responding to acoustic emissions. The AE rate in a piezoelectric device can increase by three orders of magnitude just prior to complete failure. During the operation of a typical multilayer piezoelectric actuator, the AE sensing portion of the device will monitor the emissions and respond to any dramatic increase in the emission rate by initiating a complete shut down of the system.

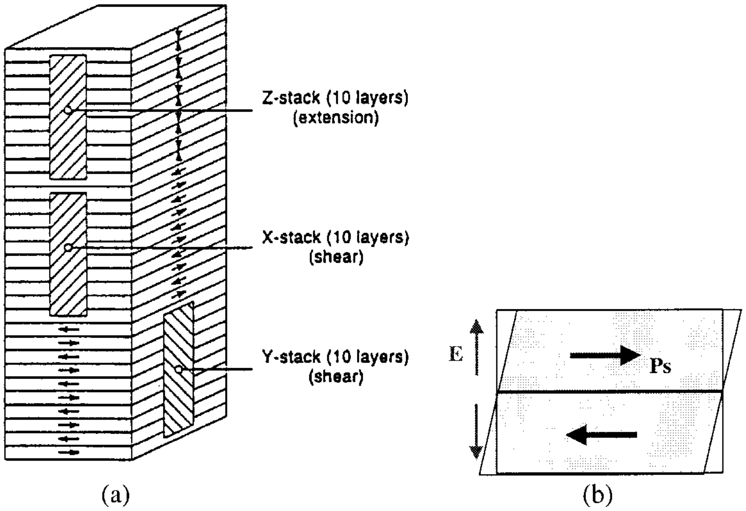

Figure 4.14 A three-dimensional positioning actuator with a stacked structure proposed by PI Ceramic: (a) a schematic diagram of the structure and (b) an illustration of the shear deformation.[22]

Another recent development for device failure self-monitoring is based on a strain gauge type electrode configuration as pictured in Figure 4.16.[24] Both the electric field-induced strain and the occurrence of cracks in the ceramic can be detected by closely monitoring the resistance of a strain gauge shaped electrode embedded in a ceramic actuator. The resistance of such a smart device is plotted as a function of applied electric field in Figure 4.17. The field-induced strain of a "healthy" device is represented by the series of curves depicted in Figure 4.17(a). Each curve corresponds to a distinct number of drive cycles. A sudden decrease in the resistance as shown in Figure 4.17(b) is a typical symptom of device failure.

The effect of aging is manifested clearly by the gradual increase of the resistance with the number of drive cycles as shown for a smart device in Figure 4.17(a). Ceramic aging is an extremely important factor to consider in the design of a reliable actuator device, although there have been relatively few investigations done to better understand and control it. Aging is associated with two types of degradation: (1) depoling and (2) mechanical failure. Creep and zero-point drift in the actuator displacement are caused by depoling of the ceramic. The strain response is also seriously impaired when the device is operated under conditions of very high electric field, elevated temperature, high humidity, and high mechanical stress. The lifetime of a multilayer piezoelectric actuator operated under a DC bias voltage can be described by the empirical relationship:

$$t_{DC} = A\,E^{-n} \exp(W_{DC}/\,kT) \tag{4.3}$$

where W_{DC} is an activation energy ranging from 0.99-1.04 eV.[25]

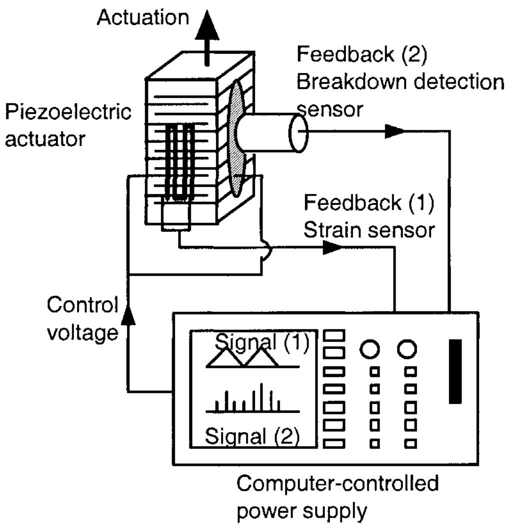
Actuation
Piezoelectric actuator
Feedback (2) Breakdown detection sensor
Feedback (1) Strain sensor
Control voltage
Signal (1)
Signal (2)
Computer-controlled power supply

Figure 4.15 An intelligent actuator system with both position and breakdown detection feedback mechanisms.

Investigations have been conducted on the heat generation from multilayer piezoelectric ceramic actuators of various sizes.[26] The temperature rise, ΔT, monitored in actuators driven at 3 kV/mm and 300 Hz, is plotted as a function of the quantity V_e/A in Figure 4.18, where V_e is the effective actuator volume (corresponding to the electroded portion of the device) and A is its surface area. The linear relationship observed is expected for a ratio of device volume, V_e, to its surface area, A. We see from this trend that a configuration with a small V_e/A will be the most conducive to suppressing heating within the device. Flat and cylindrical shapes, for example, are preferable over cube and solid rod structures, respectively.

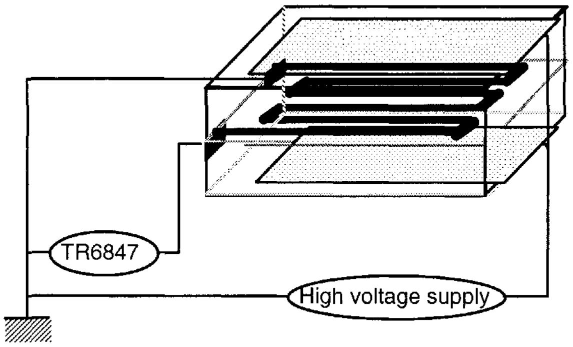

Figure 4.16 Strain gauge configuration of the internal electrode for an intelligent "health monitoring" actuator.[24]

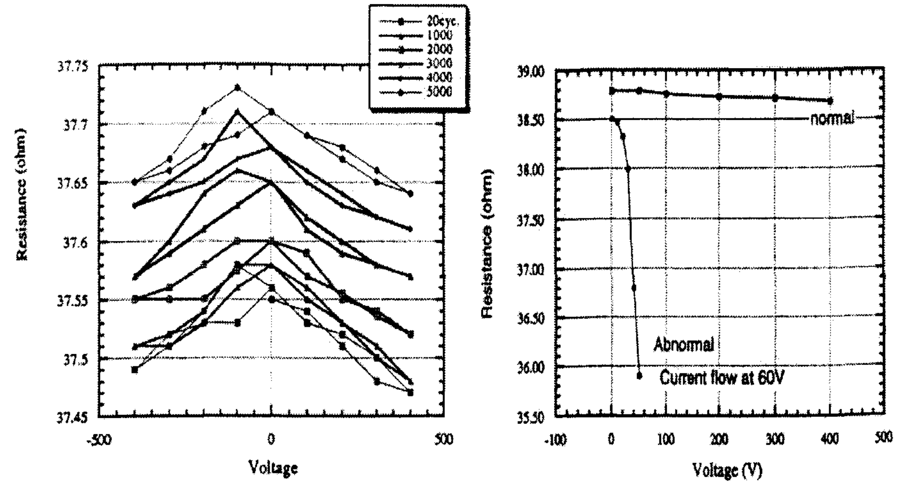

Figure 4.17 Resistance as a function of applied electric field for a smart actuator with a strain gauge type internal electrode for self-monitoring of potential failure: (a) the electric field-induced strain response of a "healthy" device and (b) the response of a failing device.[24]

(3) Cylindrical Devices

In general, the longitudinally induced strain (parallel to the electric field) exhibits less hysteresis than the strain transversely induced in an identical piezoelectric ceramic. The magnitude of the strain induced in either mode, however, does depend on the device configuration. Two cylindrical PZT-5 actuators used for controlling the optical path length in an optical interferometer are pictured schematically in Figure 4.19.[27] Although both designs utilize the displacement along the cylinder axis, the simple cylinder type pictured in Figure 4.19(a) operates through the transverse effect, while the multilayer cylinder design pictured in Figure 4.19(b) operates through the longitudinal effect. The simple cylinder structure tends to exhibit lower hysteresis than the multilayer structure.

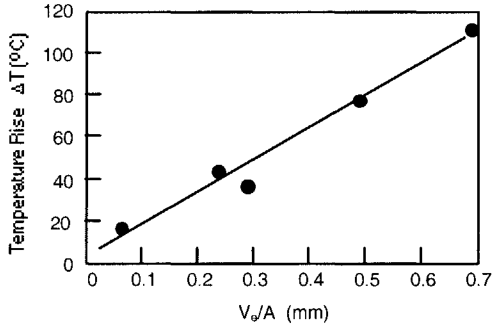

Figure 4.18 The temperature rise, ΔT, monitored in actuators driven at 3 kV/mm and 300 Hz, plotted as a function of the quantity V_e/A, where V_e is the effective actuator volume (corresponding to the electroded portion of the device) and A is its surface area.[26]

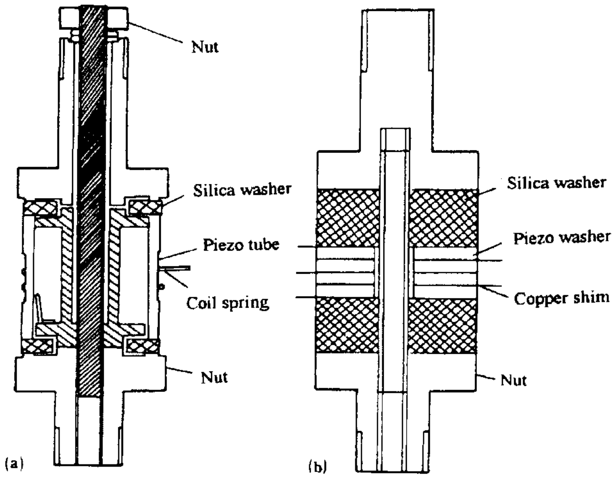

Figure 4.19 Two cylindrical PZT-5 actuators used for controlling the optical path length in an optical interferometer: (a) a simple cylinder type operated through the transverse piezoelectric effect and (b) a multilayer cylinder design operated through the longitudinal effect.[27]

(4) Unimorph/Bimorph

Unimorph and *bimorph* devices are simple structures comprised of ceramic and inactive elastic plates bonded surface to surface. Unimorph devices have one plate and bimorph structures have two ceramic plates bonded onto an elastic *shim*. We will focus on the bimorph structure here.

The bending deformation in a bimorph occurs because the two piezoelectric plates are bonded together and each plate produces its own extension or contraction under the applied electric field. This effect is also employed in piezoelectric speakers. The induced voltage associated with the bending deformation of a bimorph has been used in accelerometers. This is a very popular and widely used structure mainly because it is easily fabricated (the two ceramic plates are just bonded with an appropriate resin) and the devices readily produce a large displacement. The drawbacks of this design include a low response speed (1 kHz) and low generative force due to the bending mode. A metallic sheet shim is occasionally used between the two piezoceramic plates to increase the reliability of the bimorph structure as illustrated in Figure 4.20. When this type of shim is used, the structure will maintain its integrity, even if the ceramic fractures. The bimorph is also generally tapered in order to increase the response frequency while maintaining optimum tip displacement. Anisotropic elastic shims, made from such materials as oriented carbon fiber reinforced plastics, have been used to enhance the displacement magnification rate by a factor of 1.5 as compared to the displacement of a similar device with an isotropic shim.[28]

There have been many studies conducted on these devices which have produced equations describing the tip displacement and the resonance frequency. Two shimless bimorph designs are illustrated in Figure 4.21. Two poled piezoceramic plates of equal thickness and length are bonded together with either their polarization directions opposing each other or parallel to each other. When the devices are operated under an applied voltage, V, with one end clamped (the *cantilever condition*), the tip displacement, δ, is given by:

$$\delta = (3/2)\, d_{31}\, (l^2/\, t^2)\, V \qquad (4.4a)$$

$$\delta = 3\, d_{31}\, (l^2/\, t^2)\, V \qquad (4.4b)$$

where d_{31} is the piezoelectric strain coefficient of the ceramic, t is the combined thickness of the two ceramic plates, and l is the length of the bimorph. Equation 4.4 (a) applies to the antiparallel polarization condition and Equation 4.4 (b) to the parallel polarization condition. Notice that the difference between the two cases arises from the difference in electrode gap. The separation between the electrodes is equal to the combined thickness of the two plates for the antiparallel polarization case [Figure 4.21(a)] and half that thickness for the parallel polarization case [Figure 4.21(b)]. The fundamental resonance frequency in both cases is determined by the combined thickness of the two plates, t, according to the following equation:

$$f_o = 0.161\left[\frac{t}{l^2\sqrt{\rho s_{11}^E}}\right] \tag{4.5}$$

where ρ is the mass density of the ceramic and $s_{11}{}^E$ is its elastic compliance.[29]

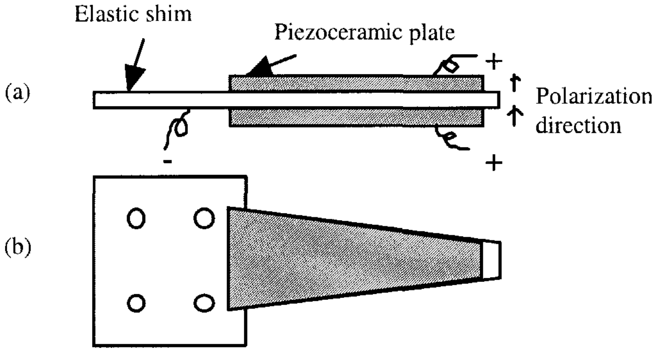

Figure 4.20 The basic structure of a piezoelectric bimorph: (a) side view of the device and (b) top view.

Example Problem 4.4

Using a PZT-based ceramic with a piezoelectric strain coefficient of d_{31}=−300 pC/N, design a shimless bimorph with a total length of 30 mm (where 5 mm is used for cantilever clamping) which can produce a tip displacement of 40 μm under an applied voltage of 20 V. Calculate the response speed of this bimorph. The mass density of the ceramic is ρ=7.9 g/cm^3 and its elastic compliance is $s_{11}{}^E$=16x10^{-12} m^2/N.

Solution

When the device is to be operated under low voltages, the antiparallel polarization type of device pictured in Figure 4.21(a) is preferred over the parallel polarization type pictured in Figure 4.21(b) because it produces a larger displacement under these conditions. Substituting a length of l=25 mm into Equation (4.3b), we obtain the combined piezoelectric plate thickness, t.

$$t = l\sqrt{3(d_{31}V/\delta)}$$

$$= 25\times10^{-3}\,(\mathrm{m})\sqrt{3[300\times10^{-12}(\mathrm{C/N})\;20(\mathrm{V})/40\times10^{-6}\,(\mathrm{m})]} \tag{P4.4.1}$$

$$\rightarrow\rightarrow t = 530\ \mu\mathrm{m}.$$

The ceramic is cut into plates 265 μm in thickness, 30 mm in length, and 4-6 mm in width. The plates are electroded and poled and then bonded together in pairs. The width of the bimorph is usually chosen such that [w/*l* < 1/5] in order to optimize the magnitude of the bending displacement.

The response time is estimated by the resonance period. We can determine the fundamental resonance frequency of the structure from the following equation:

$$f_o = 0.161\left[\frac{t}{l^2\sqrt{\rho s_{11}^E}}\right] \qquad \text{(P4.4.2)}$$

$$= 0.161\left[\frac{530\times10^{-6}(\mathrm{m})}{[25\times10^{-3}(\mathrm{m})]^2\sqrt{7.9\times10^3(\mathrm{kg/m^3})16\times10^{-12}(\mathrm{m^2/N})}}\right] = 378\ (\mathrm{Hz})$$

$$\rightarrow\rightarrow \text{ Response Time} \approx \frac{1}{f_o} = \frac{1}{378(\mathrm{s}^{-1})} = 2.6(\mathrm{ms})$$

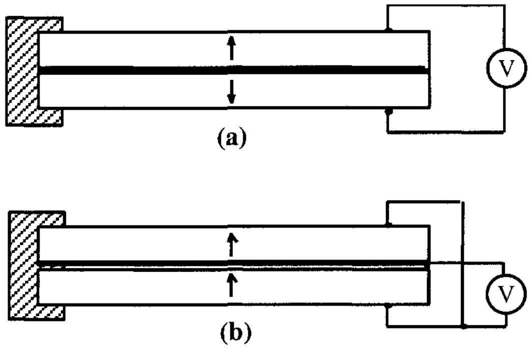

Figure 4.21 Two types of piezoelectric bimorphs: (a) the antiparallel polarization type and (b) the parallel polarization type.

Example Problem 4.5

A unimorph bending actuator can be fabricated by bonding a piezoceramic plate to a metallic shim.[30] The tip deflection, δ, of the unimorph supported in a cantilever configuration is given by:

$$\delta = \frac{d_{31}El^2Y_ct_c}{(Y_m[t_o^2-(t_o-t_m)^2]+Y_c[(t_o+t_c)^2-t_o^2])} \qquad \text{(P4.5.1)}$$

Here E is the electric field applied to the piezoelectric ceramic, d_{31}, the piezoelectric strain coefficient, *l*, the length of the unimorph, Y, Young's modulus for the ceramic or the metal, and t is the thickness of each material. The subscripts c and m denote the ceramic and the metal, respectively. The quantity t_o is the distance between the *strain-free neutral plane* and the bonding surface, and is defined according to the following:

$$t_o = \frac{t_c t_m^2 (3t_c + 4t_m) Y_m + t_c^4 Y_c}{6 t_c t_m (t_c + t_m) Y_m} \qquad \text{(P4.5.2)}$$

Assuming $Y_c = Y_m$, calculate the optimum (t_m/t_c) ratio that will maximize the deflection, δ, under the following conditions:

a) A fixed ceramic thickness, t_c, and
b) a fixed total thickness, $t_c + t_m$.

Solution

Setting $Y_c = Y_m$, the Equations (P4.5.1) and (P.4.5.2) become:

$$\delta = \frac{d_{31} E l^2 t_c}{([t_o^2 - (t_o - t_m)^2] + [(t_o + t_c)^2 - t_o^2])} \qquad \text{(P4.5.3)}$$

$$t_o = \frac{t_c t_m^2 (3t_c + 4t_m) + t_c^4}{6 t_c t_m (t_c + t_m)} \qquad \text{(P4.5.4)}$$

Substituting t_o as it is expressed in Equation (P4.5.4) into Equation (P4.5.3) yields

$$\delta = \frac{d_{31} E l^2 3 t_m t_c}{(t_m + t_c)^3} \qquad \text{(P4.5.5)}$$

The function $f(t_m) = (t_m t_c)/(t_m + t_c)^3$ must be maximized for a fixed ceramic thickness, t_c,and a fixed total thickness, $t_{tot} = t_c + t_m$.

$$\frac{d f(t_m)}{d t_m} = \frac{(t_c - 2t_m) t_c}{(t_m + t_c)^4} = 0 \qquad \text{(P4.5.6a)}$$

The metal plate thickness should be $t_m = t_c/2$ and $t_o = t_c/2$ so that Equation (P4.5.6a) becomes:

$$\frac{d f(t_m)}{d t_m} = \frac{(t_{tot} - 2t_m)}{t_{tot}^3} = 0 \qquad \text{(P4.5.6b)}$$

Thus, it is determined that both the metal and ceramic plate thickness should be $t_m = t_c = t_{tot}/2$ and $t_o = t_{tot}/3$.

The generative displacement of a bimorph is decreased when it is supported at both ends as shown in Figure 4.22(a). When the special shim design pictured in Figure 4.22(b) is used, however, the center displacement of the bimorph is enhanced by a factor of four as compared to the displacement of a conventionally supported device.[31]

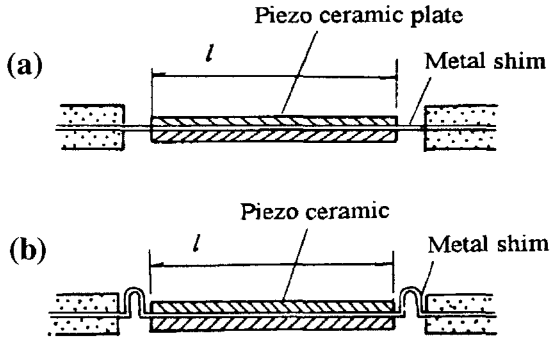

Figure 4.22 Double support mechanisms for a bimorph: (a) conventional design and (b) special shim design.[31]

The bimorph displacement inevitably includes some rotational motion. A special mechanism generally must be employed to eliminate this rotational component of the induced motion. Several such mechanisms are pictured in Figure 4.23.

A twin structure developed by Sony is shown in Figure 4.23(a).[32] It is employed for video tracking control. The design incorporates a flexible head support installed at the tips of two parallel bimorphs. The complex bimorph design pictured in Figure 4.23(b) has been proposed by Ampex. It has electrodes on the top and the bottom of the device that are independently addressed such that any deviation from perfectly parallel motion is compensated for and effectively eliminated. The proposed design also includes a sensor electrode that detects the voltage generated in proportion to the magnitude of the bending displacement. The ring-shaped bimorph design pictured in Figure 4.23(c) has been developed by Matsushita Electric for use in a video tracking control system. The design is compact and provides a large displacement normal to the ring. It also remains firmly supported in operation due to the dual clamp configuration incorporated in the design.

The "Thunder" actuator developed by Face International is essentially a unimorph, but has a curved shape and a tensile stress is maintained on the piezoceramic plate.[33] This actuator is very reliable when operated under both high field and high stress conditions. The device is fabricated at high temperatures and its curved shape occurs due the thermal expansion mismatch between the bonded PZT and metal plates.

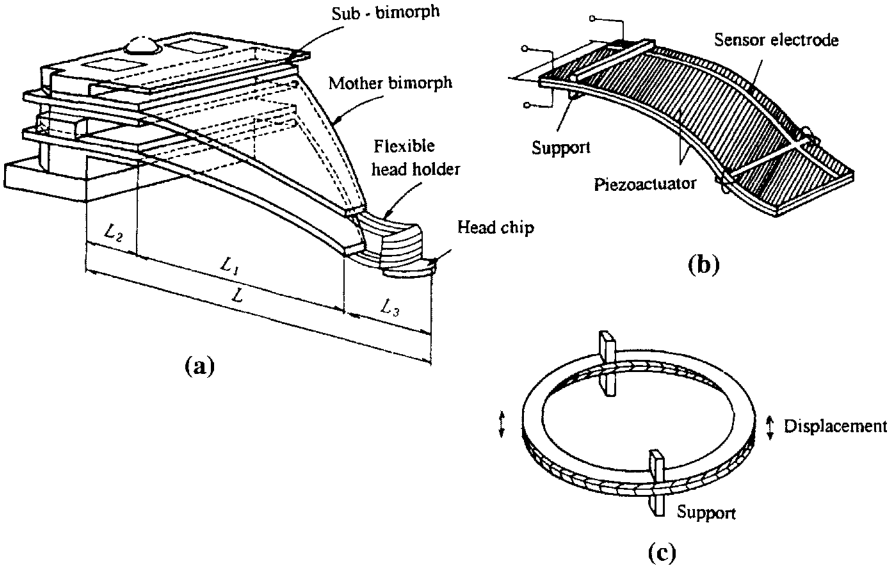

Figure 4.23 Bimorph structures designed to produce perfectly parallel motion: (a) parallel spring (twin), (b) complex bimorph (s-shaped), and (c) ring configurations.

(5) Monomorph/Rainbow

Conventional bimorph bending actuators are composed of two piezoelectric plates, or two piezoelectrics and an elastic shim, bonded together. The bonding layer in the latter, however, causes both an increase in hysteresis and a degradation of the displacement characteristics, as well as delamination problems. Furthermore, the fabrication process for such devices, which involves cutting, polishing, electroding and bonding steps, is rather laborious and costly. Thus, a monolithic bending actuator (*monomorph*) that requires no bonding is a very attractive alternative structure.

Such a monomorph device has been produced from a single ceramic plate.[34] The operating principle is based on the combined action of a semiconductor contact phenomenon and the piezoelectric or electrostrictive effect. When metal electrodes are applied to both surfaces of a semiconductor plate and a voltage is applied as shown in Figure 4.24, the electric field is concentrated on one side (that is, a *Schottky barrier* is formed), thereby generating a non-uniform field within the plate. When the piezoelectric is slightly semiconducting, contraction along the surface occurs through the piezoelectric effect only on the side where the electric field is concentrated. The nonuniform field distribution generated in the ceramic causes an overall bending of the entire plate. The energy of a modified structure including a very thin insulating layer is represented in Figure 4.25(a).[35] The thin insulating layer increases the breakdown voltage.

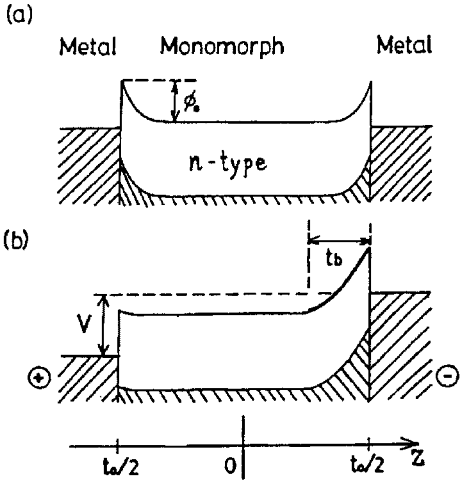

Figure 4.24 Schottky barrier generated at the interface between a semiconductive (n-type) piezoceramic and metal electrodes. Depiction of the energy barrier: (a) before and (b) after the electric field is applied.[34]

Research is underway to develop new compositions of doped barium titanate and lead zirconate titanate piezoelectric ceramics with the semiconducting properties required for use in these monomorph devices. Modified PZT ceramics prepared from a solid solution with the semiconducting perovskite compound $(K_{1/2}Bi_{1/2})ZrO_3$ have the desired electrical properties. When 300 V is applied to a ceramic plate 20 mm in length and 0.4 mm in thickness and fixed at one end, a maximum tip deflection of 200 μm can be obtained [see Figure 4.26(a)]. This is comparable with the optimum deflection of a bimorph device [Figure 4.26 (a)].[36] The *rainbow actuator* by Aura Ceramics is a modification of the basic semiconducting piezoelectric monomorph design, where half of the piezoelectric plate is reduced so as to make a thick semiconducting electrode which enhances the bending action.[37] The energy diagram for the "rainbow" device is shown in Figure 4.25(b).[35]

Another modification of the basic monomorph structure has been reported made from a $LiNbO_3$ single crystal plate which has no bonding layer but instead uses an inversion layer generated in the plate.[38] The 500 mm thick z-cut plates were cut from a single domain lithium niobate crystal. Then the unelectroded samples were heat-treated at 1150°C for 5 hours in flowing Ar gas containing water vapor. After rapid cooling at a rate of 50°C per minute, a two-layer domain configuration structure was created: the spontaneous polarization P_s in the original upward direction in the first layer and an opposing polarization originating from the positive side of the plate in the second. The thickness of the inversion layer depends strongly on the conditions of heat treatment, such as temperature, time and atmosphere. As the annealing temperature or time increases, the inversion layer becomes thicker, and finally reaches the median plane of the plate. After electroding both sides, this single crystal plate will execute a bending deformation with the application of a suitable electric field. Even though the magnitude of the displacement for this device is not as high as a PZT-based bimorph and the actuator is fragile due to crystal cleavage, it has the advantages of a highly linear displacement curve and zero hysteresis.

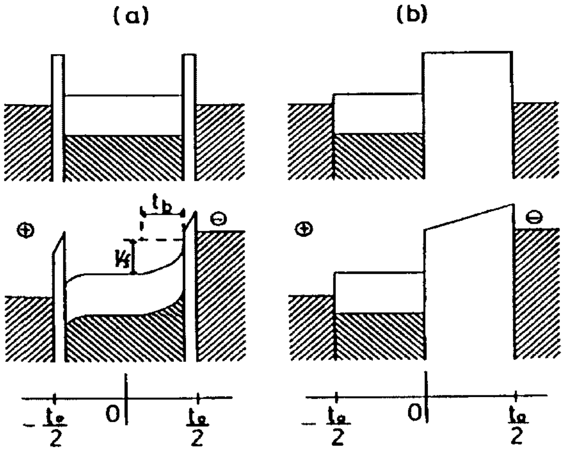

Figure 4.25 Energy diagrams for modified monomorph structures: (a) a device incorporating a very thin insulating layer and (b) the "rainbow" structure.[35]

(6) Moonie/Cymbal

A composite actuator structure called the *moonie* has been developed to amplify the pressure sensitivity and the small displacements induced in a piezoelectric ceramic.[39] The moonie has characteristics intermediate between the conventional multilayer and bimorph actuators; it exhibits an order of magnitude larger displacement (100 μm) than the multilayer, and a much larger generative force (10 kgf) with a quicker response (100 μsec) than the bimorph. This device consists of a thin multilayer ceramic element and two metal plates with a narrow moon-shaped cavity bonded together as pictured in Figure 4.27(a). A moonie with dimensions 5 (mm) x 5 (mm) x 2.5 (mm) can generate a 20 μm displacement under an applied voltage of 60 V, which is 8 times as large as the generative displacement of a multilayer of similar dimensions.[40] A displacement twice that of the moonie can be obtained with the *cymbal* design pictured in Figure 4.27(b). The generative displacement of this device is quite uniform, showing negligible variation for points extending out from the center of the end cap.[41] Another advantage the cymbal has over the moonie is its relatively simple fabrication. The end caps for this device are made in a single-step punching process that is both more simple and more reproducible than the process involved in making the endcaps for the moonie structure.

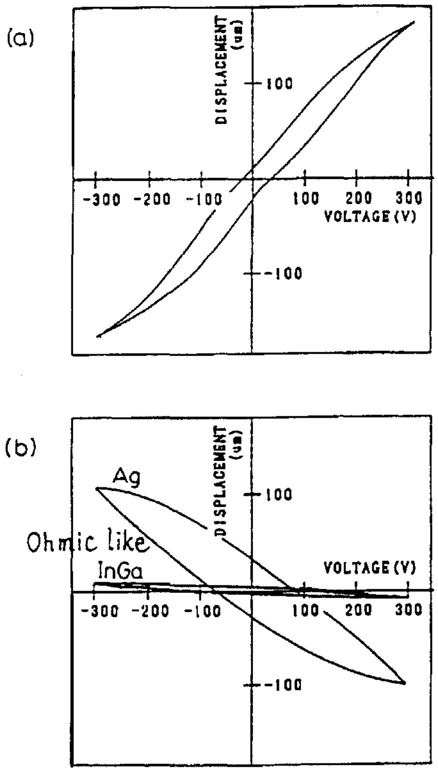

Figure 4.26 Tip displacement curves of (a) PLZT (n-type) and (b) BT (p-type) monomorph structures.[36]

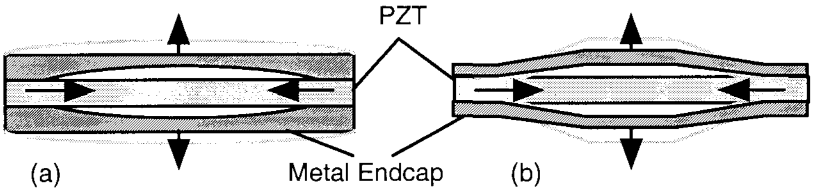

Figure 4.27 Flextensional structures: (a) the moonie[40] and (b) the cymbal[41].

A "ring-morph" has been developed that is made with a metal shim and two PZT rings rather than PZT disks.[42] The bending displacement is amplified by more than 30% when an appropriate inner ring diameter is chosen.

(7) Flexible Composites

Functional composite structures can be formed by embedding oriented needle- or plate-shaped piezoelectric ceramic bodies in a polymer matrix. Such structures have been found to exhibit enhanced sensitivity while maintaining full actuation capabilities. A 1-3 composite structure is pictured in Figure 4.28(a), which is comprised of PZT rods arranged in a two-dimensional array within a polymer matrix.

The simplest composite structure has 0-3 connectivity and is made by dispersing piezoelectric ceramic powders uniformly in a polymer matrix. This structure is pictured schematically in Figure 4.28(b). The two general processes for fabricating this type of composite are the melting and rolling methods outlined in Figure 4.29.[43] The melting method involves mixing the ceramic powders in a molten polymer, while the rolling method makes use of a hot-rolling apparatus to help disperse the powders in a thermosetting polymer matrix prior to their heat treatment.

A 1-3 composite deformable mirror is pictured in Figure 4.30.[55] The glass mirror is attached to the one surface of the composite on which the common electrode is applied, while the individual PZT rods are addressed from the other side of the device. As each rod in the array can be individually addressed, the surface of the deformable mirror can be shaped to any desired contour. A 0-3 composite comprised of PZT powder in a polymer matrix can be used to make flexible bimorphs. Although a large curvature can be obtained with such a bimorph, excessive heat generation during AC drive is a serious problem for these devices. This is due primarily to the highly insulating nature of the polymer matrix. The heat generated through dielectric loss of the piezoelectric ceramic is not readily dissipated.

Active fiber composites (AFC) have been developed at MIT, comprised of PZT needles that are arranged in a polymer matrix.[44] One application for this composite is the helicopter blade vibration control device pictured in Figure 4.31. The fine PZT needles, which are fabricated by an extrusion technique, are arranged in an epoxy resin, and the composite structure is sandwiched between the interdigital electrodes (Ag/Pd), which are coated on a Kepton substrate. The AFC structures are laminated on the helicopter blade such that the PZT fiber axes are oriented 45 degrees with respect to the blade direction in order to produce a torsional deformation of the blade. A major problem with this design is the limitation in the effective applied electric field strength due to the restricted contact area between the flat electrode surface and the rounded contour of the PZT fibers. One remedy for this problem has been to incorporate conducting particles in the epoxy matrix. A more detailed discussion concerning the design and action of the AFC material will be presented in Chapter 8.

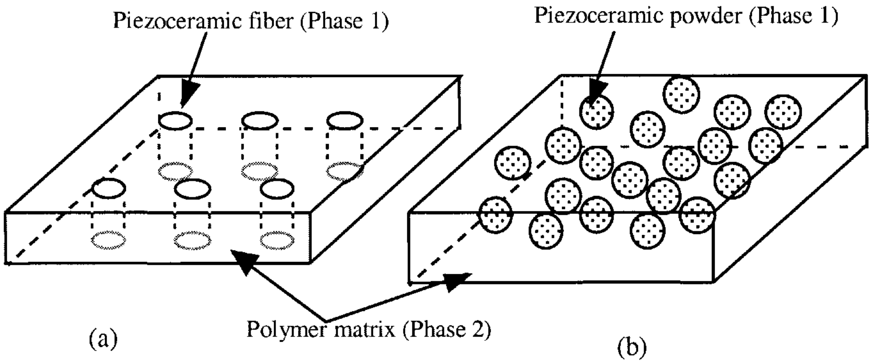
Piezoceramic fiber (Phase 1)
Piezoceramic powder (Phase 1)
(a)
Polymer matrix (Phase 2)
(b)

Figure 4.28 Two PZT/polymer composites: (a) a PZT rod type (1-3) and (b) a PZT powder dispersed in a polymer matrix (0-3). [Connectivity notation: (active (phase 1) – polymer (phase 2)).]

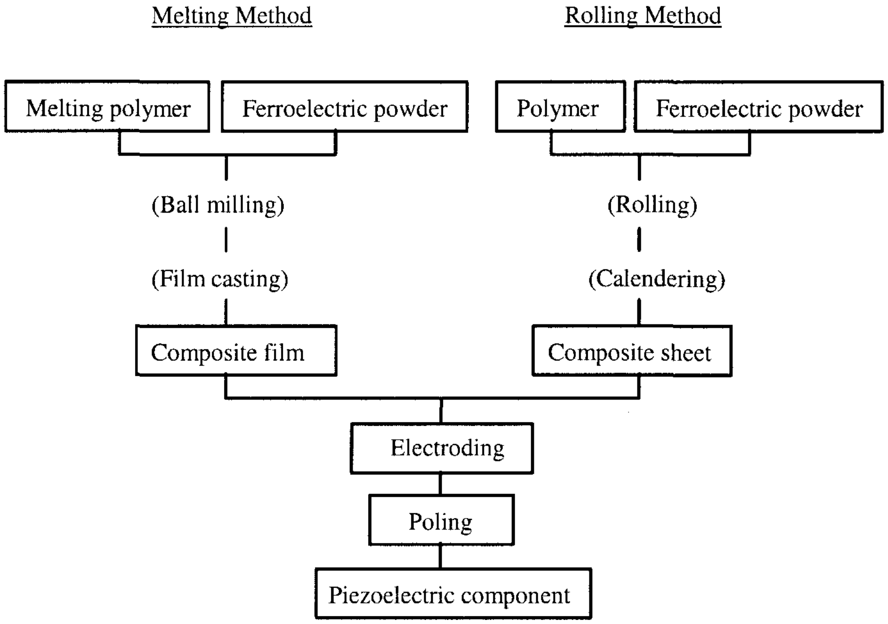
Melting Method
Rolling Method
Melting polymer
Ferroelectric powder
Polymer
Ferroelectric powder
(Ball milling)
(Film casting)
(Rolling)
(Calendering)
Composite film
Composite sheet
Electroding
Poling
Piezoelectric component

Figure 4.29 Flowcharts for the fabrication of PZT: polymer composites.

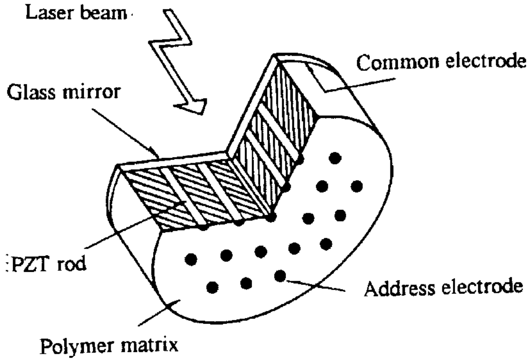

Figure 4.30 A PZT: polymer composite deformable mirror.[55]

(8) Thin Films

The techniques for fabricating oxide thin films fall into two general categories:

1) **Physical Processes:** exemplified by the following commonly used techniques:
   Electron beam evaporation
   RF and DC sputtering
   Ion beam sputtering
   Ion plating

(2) **Chemical Processes:** exemplified by the following commonly used techniques:
   Sol-gel method (dipping, spin coating, etc.)
   Chemical vapor deposition (CVD)
   MOCVD
   Epitaxial methods (liquid phase, melting, capillary, etc.)

Ferroelectric thin films such as $LiNbO_3$, PLZT,[45] and $PbTiO_3$[46] are commonly produced by sputtering.[46] A magnetron sputtering apparatus is shown in Figure 4.32. Heavy argon plasma ions bombard the cathode (target) dislodging its atoms. These atoms are deposited uniformly on the substrate in an evacuated enclosure. The sol-gel technique has also been employed for producing PZT films.[47] Some applications for thin film ferroelectrics are memory devices, surface acoustic wave devices, piezoelectric sensors, and micromechatronic devices.

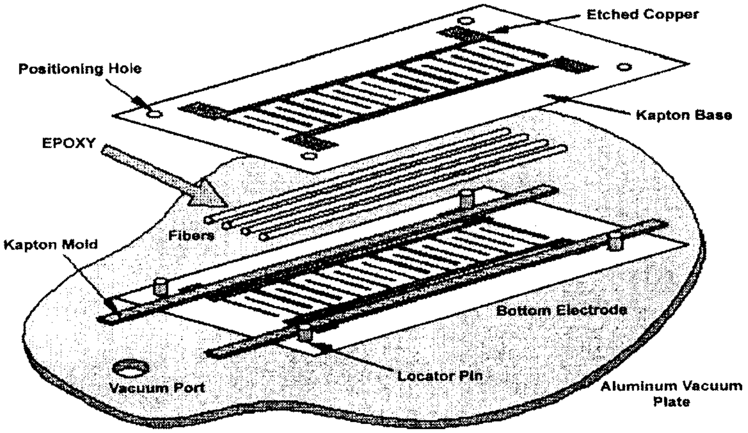
Etched Copper
Positioning Hole
Kapton Base
EPOXY
Kapton Mold
Fibers
Bottom Electrode
Locator Pin
Vacuum Port
Aluminum Vacuum Plate

Figure 4.31 Application of the active fiber composite (AFC), comprised of oriented PZT fibers and epoxy, in a helicopter blade vibration control device.[44]

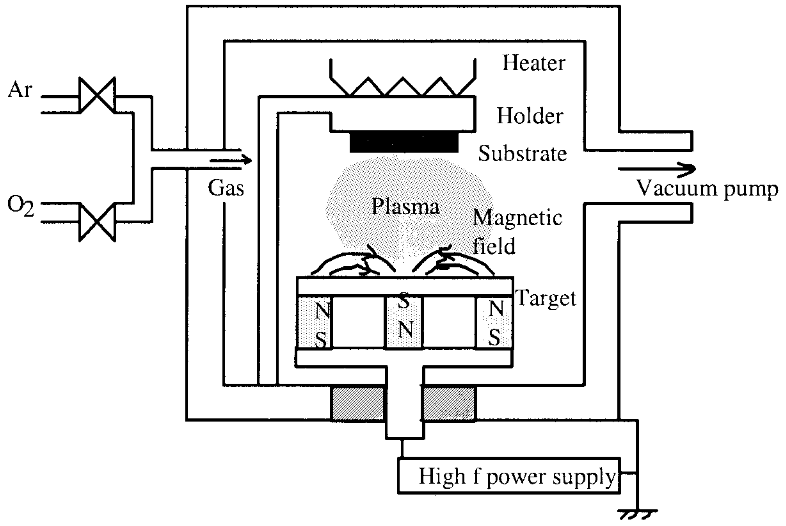
Ar
O_2
Gas
Heater
Holder
Substrate
Vacuum pump
Plasma
Magnetic field
Target
N
S
S
N
N
S
High f power supply

Figure 4.32 Schematic depiction of a magnetron sputtering apparatus.

The *micromachining process* used to fabricate the PZT micropump is illustrated in Figure 4.34. The etching process for the silicon:PZT unit is shown on the left-hand side of the figure and that for the glass plate on the right side. A schematic of the structure of the micropump is pictured in Figure 4.35 and a photograph of an actual device is shown in Figure 4.36. The blood sample and test chemicals enter the system through the two inlets identified in Figure 4.34, are mixed in the central cavity, and finally are passed through the outlet for analysis. The movement of the liquids through the system occurs through the bulk bending of the PZT diaphragm in response to the drive potential provided by the *interdigital surface electrodes*.

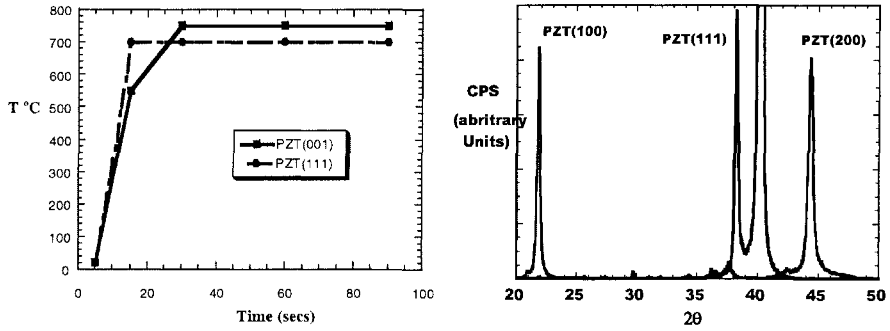

(a) (b)

Figure 4.33 Epitaxially grown rhombohedral (70/30) PZT films with (001) and (111) orientation: (a) optimum rapid thermal annealing profiles and (b) x-ray diffraction patterns for films grown according to these profiles.[48]

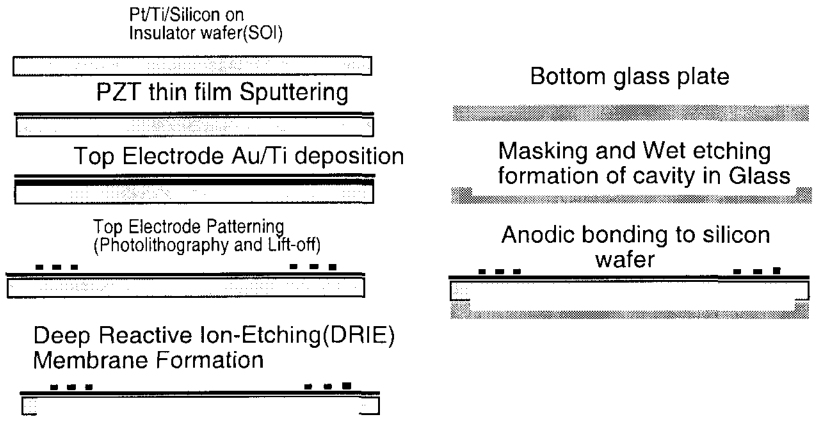
Pt/Ti/Silicon on
Insulator wafer(SOI)
PZT thin film Sputtering
Top Electrode Au/Ti deposition
Top Electrode Patterning
(Photolithography and Lift-off)
Deep Reactive Ion-Etching(DRIE)
Membrane Formation
Bottom glass plate
Masking and Wet etching
formation of cavity in Glass
Anodic bonding to silicon
wafer

Figure 4.34 The micromachining process used to fabricate a PZT micropump.[48]

The properties of the piezoelectric thin film are inevitably affected by three important parameters:

1) Crystallographic Orientation: The P-E hysteresis curves for (111)- and (001)-oriented PZT (70/30) films (thickness =1 μm, x-ray diffraction pattern Figure 4.33(b)) appear in Figure 4.37. The hysteresis curve associated with the (001) film is observed to be more square than that of the (111) film.

2) **Stress from the Substrate:** Tensile or compressive stress is generally present on the piezoelectric film due to thermal expansion mismatch between the film and the substrate. This sometimes results in a higher coercive field.

3) **Size Effects:** Similar to the critical particle size concerns associated with a ferroelectric powder, there may exist a critical film thickness below which ferroelectricity would disappear. This is an issue in ferroelectric thin film research that has yet to be addressed and resolved.

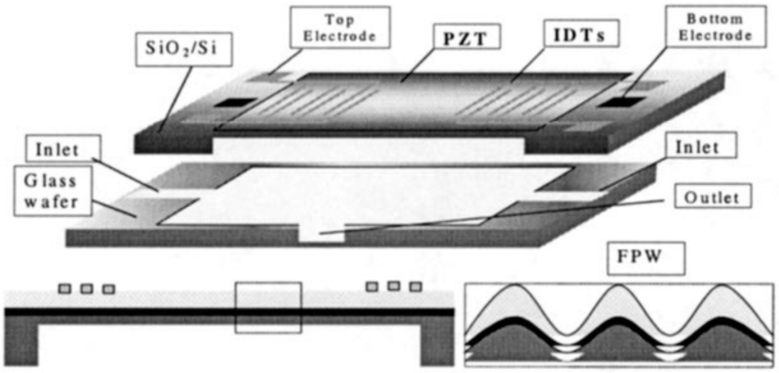
Top Electrode
SiO_2/Si
PZT
IDTs
Bottom Electrode
Inlet
Glass wafer
Inlet
Outlet
FPW

Figure 4.35 A schematic diagram of the structure of a PZT micropump.[48]

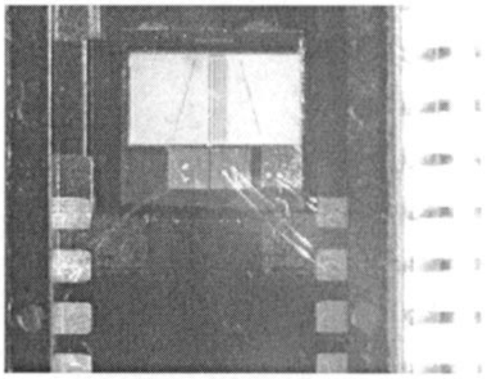

Figure 4.36 Photograph of a PZT micropump (actual size: 4.5 x 4.5 x 2 mm^3).[48]

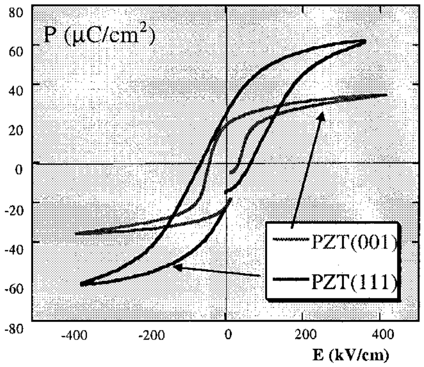

Figure 4.37 Polarization versus electric field curves for (111)- and (001)-oriented rhombohedral (70/30) PZT films.[48]

Example Problem 4.6

Predict on a conceptual basis the polarization and strain curves for epitaxially grown rhombohedral (111)- and (001)-oriented PZT thin films.

Solution

Since the spontaneous polarization is directed along the (111) perovskite axes, there are four equivalent polarization states for the (111) film, while there are only two states for the (001) film, as illustrated schematically in Figure 4.38.[48] The coercive field is, therefore, very well defined for the (001) film, leading to a square P-E curve. Furthermore, since polarization reorientation in this film is more restricted than in the (111) film, one would expect an extended linear portion of the strain curve for field strengths greater than the coercive field as depicted in Figure 4.39.

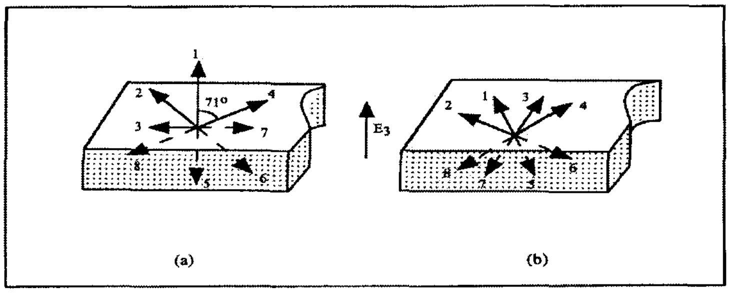

Figure 4.38 Equivalent polarization states for epitaxially grown rhombohedral PZT films: (a) (111)-oriented and (b) (001)-oriented.[48]

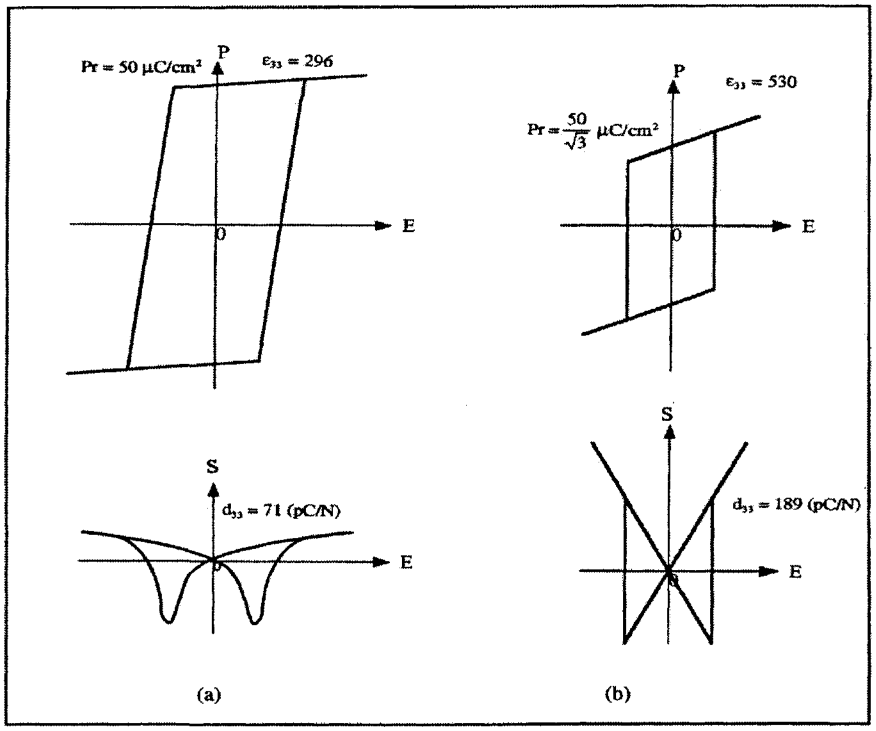

Figure 4.39 Anticipated polarization (top) and strain (bottom) curves for epitaxially grown rhombohedral PZT films: (a) (111)-oriented and (b) (001)-oriented. Note the dramatic increase in the polarization and the strain above the coercive field for the (001) film.[48]

(9) Displacement Amplification Mechanisms

In addition to the flextensional structures, such as bimorphs and cymbals, there are structures that make use of several displacement amplification mechanisms.

A *monolithic hinge structure* is made from a monolithic ceramic body by cutting indented regions in the monolith as shown in Figure 4.40(a). This effectively creates a lever mechanism that may function to either amplify or reduce the displacement. It was initially designed to reduce the displacement (including backlash) produced by a stepper motor, and thus increase its positioning accuracy. Recently, however, monolithic hinge levers have been combined with piezoelectric actuators to amplify their displacement.

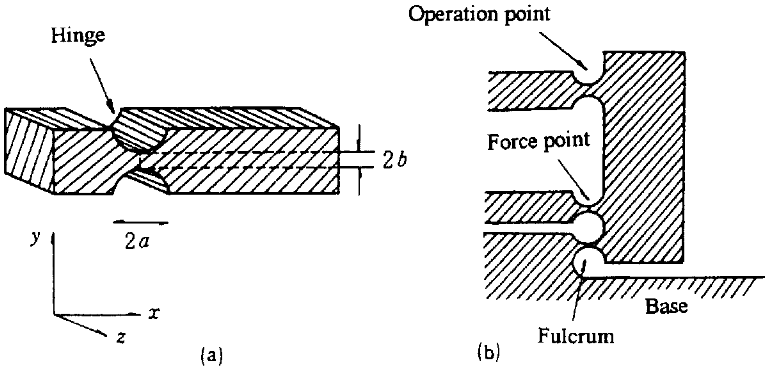

Figure 4.40 Monolithic hinge lever mechanisms: (a) monolithic hinge structure and (b) hinge lever mechanism.

If the indented region of the hinge can be made sufficiently thin to promote optimum bending while maintaining extensional rigidity (ideal case!), a mechanical amplification factor for the lever mechanism close to the apparent geometric lever length ratio is expected. The actual amplification, however, is generally less than this ideal value. If we consider the dynamic response of the device, a somewhat larger hinge thickness [identified as 2b in Figure 4.40(a)] producing an actual amplification of approximately half the apparent geometric ratio is found to be optimum for achieving maximum generative force and response speed. The characteristic response (that is, in terms of the displacement, generative force, and response speed) of an actuator incorporating a hinge lever mechanism is generally intermediate between that of the multilayer and bimorph devices.

When a piezoelectric actuator is to be utilized in a large mechanical control system, the *oil pressure displacement amplification mechanism* shown in Figure 4.41 is often implemented. It is a mechanism especially well suited for oil pressure servo systems. The output displacement Δl_2 is effectively amplified by a 1:2 area ratio according to:

$$\Delta l_2 = (d_1/d_2)^2 \, \Delta l_1 \qquad (4.6)$$

Although the response is slow due to the viscosity of the oil, the overall loss associated with the amplified displacement is very small.

An *inchworm* is a linear motor which advances in small steps over time. An example of an inchworm device designed by Burleigh Instruments is pictured in Figure 4.42.[49] It is comprised of three piezoelectric tubes. Two of the tubes (labeled 1 and 3 in the figure) function to either clamp or release the metal shaft, while the remaining tube (labeled 2 in the figure) actually moves the inchworm along the shaft. When three separate drive voltages of differing phase are applied to the three tubes, the inchworm can translate forward and backward along the metal shaft.

Although this motor is rather slow (0.2 mm/sec), the high resolution per step (1 nm) is a very attractive feature of the device.

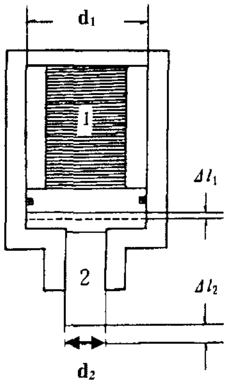

Figure 4.41 An oil pressure displacement amplification mechanism.

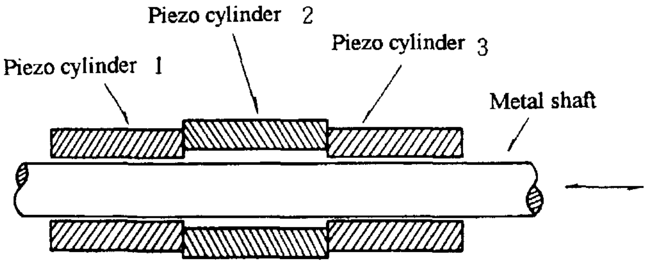

Figure 4.42 An inchworm structure.[49]

4.3 ELECTRODE MATERIALS

(1) Actuator Electrodes: An Overview

The major problem with the most commonly used electrode material, silver (Ag), is that it tends to migrate into ceramics under high electric fields. One solution to this problem has been to use alloys such as silver-palladium (Ag-Pd). Precious metals such as gold (Au), platinum (Pt), and silver-palladium (Ag-Pd) are expensive, however, and thus not very suitable for mass production. As new dielectric materials that can be sintered at low temperature are developed, electrode materials like copper (Cu) and nickel (Ni) become feasible inexpensive alternatives. When the conventional electrode materials must be used, innovative new methods of production can also be employed to reduce the manufacturing cost.

The *bonding method* developed by Ohnishi and Morohashi[50] is one such method. The structure fabricated by this method is a multilayer stack of 22 layers comprised of 0.3 mm thick sintered ceramic disks arranged alternately with 10 μm thick silver (Ag) foils. The multilayer structure is hot-pressed at 900°C for 4 hours. A device of this type with dimensions [5 x 5 x 9 mm^3] demonstrates a bending strength of approximately 100 MPa. The cost of manufacturing multilayer devices by the bonding method is thus significantly cheaper than the conventional methods, because inexpensive metal foils are used for the internal electrodes.

Another innovative fabrication technique has been developed by Morgan Electroceramics which involves incorporating a copper (Cu) internal electrode in a PZT multilayer actuator.[51] The PZT and copper electrode materials are co-fired. Ordinarily the sintering temperature of PZT is too high to allow for co-firing with a copper electrode. The sintering temperature of the PZT used in these structures is reduced to 1015°C by adding excess PbO. Special measures are used to optimize the co-firing process. The oxygen (O_2) pressure is precisely regulated by sintering in a nitrogen (N_2) atmosphere (10^{-10} atm). The pieces are also fired in a special sintering sand, which is essentially a mixture of the Cu and PZT powders. This helps to inhibit the oxidation of the Cu electrode during firing. A four-layer PZT actuator (with layer thickness of 25 μm) fabricated by this method is pictured in Figure 4.43.

Mechanical weakness at the junction between the ceramic and the electrode metal often gives rise to delamination problems. One solution to this problem has been to make a more rigid electrode by mixing ceramic powder of the composition used for the actuator material with the metal electrode paste. We will examine some of the more popular conducting ceramic materials currently used as electrodes in ceramic actuators in the next section.[52]

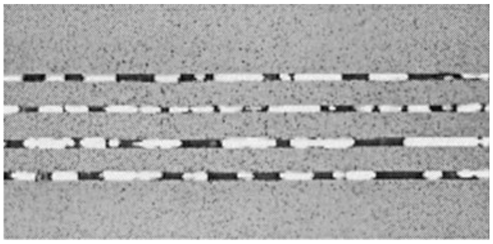

Figure 4.43 A PZT multilayer actuator with Cu internal electrodes co-fired at 1015°C.[51]

(2) Ceramic Electrodes

The most attractive *ceramic electrode materials* are conducting or semiconducting perovskite oxides because of their compatibility with the crystal structure of the actuator ceramics. Among the conducting ceramics $Sr(Fe,Mo)O_3$, $(La,Ca)MnO_3$ and

$Ba(Pb,Bi)O_3$ (which is actually a superconductor) are considered the best, but their conductivity is drastically reduced when they are sandwiched between the lead-based ceramic layers and sintered. One of the few successful structures utilizing a ceramic conductor is a unimorph device comprised of a piezoceramic and a $Ba(Pb,Bi)O_3$ fabricated by hot-pressing. Semiconducting $BaTiO_3$-based ceramics with a *positive temperature coefficient of resistivity* (PTCR) also appear to be promising alternative electrode materials for these structures.

In general, good ceramic electrode materials should possess the following characteristics:

1) a high conductivity,
2) a sintering temperature and shrinkage similar to that of the piezoelectric ceramic,
3) good adhesion with the piezoelectric ceramic,
4) slow diffusion into the piezoelectric ceramic during sintering.

The last characteristic is perhaps the most critical and the ultimate success of the structure will depend on a well-defined interface between the electrode and piezoelectric layers.

Barium Titanate-Based Multilayer Actuator

Barium titanate ($BaTiO_3$), which is a ferroelectric with a Curie temperature of 120°C, is known to become electrically conductive when polycrystalline samples are doped with rare-earth ions.[53,54] The resistivity of some $BaTiO_3$-based ceramics (with 5 mole percent SiO_2 and 2 mole percent Al_2O_3) is plotted in Figure 4.44 as a function of La_2O_3 concentration. We see from these data that relatively small concentrations of La in the range of 0.1 to 0.25 atomic percent lead to a change in the resistivity of more than 10 orders of magnitude. Multilayer actuators comprised of alternating layers of undoped resistive $BaTiO_3$ and the $BaTiO_3$-based semiconducting composition doped with 0.15 atomic percent La have been fabricated by the tape-casting process. The main advantage in using these materials is that atomic diffusion across the interface between layers during the sintering process tends to be suppressed because the layers are compositionally similar, resulting in a well-defined interface between the actuator and electrode layers. Another beneficial feature of this combination is that the sintering temperature and shinkage of both materials are almost the same, so that no residual stress is present in the sample after sintering. The fabrication of this structure is also somewhat simpler since it requires no binder burn-out process, which is a time consuming step required in the fabrication of devices with metal electrodes. A prototype device of this type has been produced with eight 0.5 mm thick actuator layers, sandwiched between 0.25 mm thick electrode layers.[52]

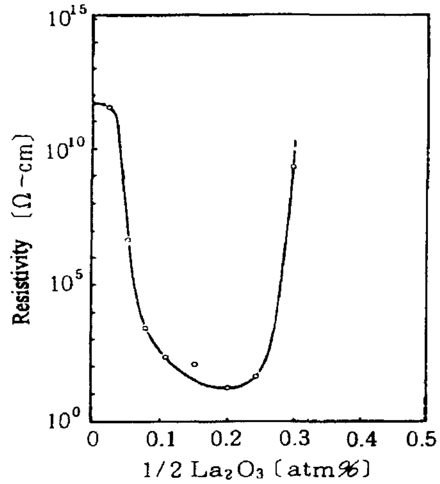

Figure 4.44 The resistivity of $BaTiO_3$-based ceramics (with 5 mole percent SiO_2 and 2 mole percent Al_2O_3) plotted as a function of La_2O_3 concentration.[53,54]

Mechanical Strength of Ceramic Electrode Devices

The mechanical strength of multilayer samples having an overall plate-like shape with their piezoelectric and ceramic electrode layers perpendicular to the plate as shown in Figure 4.45 (a) has been tested by a three-point bend method.[52] Data were also collected for samples of this configuration having the same piezoelectric ceramic as the test specimens and palladium (Pd) electrode layers, which served as a reference. Weibull plots for both are shown in Figure 4.45(b). The mechanical strength of the ceramic electrode device is observed to be about 50 MN/m^2, which is approximately three to four times higher than that observed for the metal electrode actuator. It is also noteworthy that the Weibull coefficient is generally much larger when the ceramics electrodes are used, indicating that the deviation in fracture strength is much smaller. Fracture was observed to occur mainly at the ceramic-electrode interface for the structures with the metal electrodes, while no such tendency was observed for the ceramic electrode device.

The electric field-induced strains measured in the prototype ceramic electrode device are shown in Figure 4.46. It was determined in the study of this structure that the longitudinal strain induced in the actuator layers was $x_3=(5\text{x}10^{-4})$ and the transverse strain $x_1=(-1.2\text{x}10^{-4})$. The measured strains are 30% and 60% smaller than the predicted values for the longitudinal and transverse strains, respectively. The clamping effect associated with this strain anisotropy can be reduced by decreasing the thickness of the electrode layers.

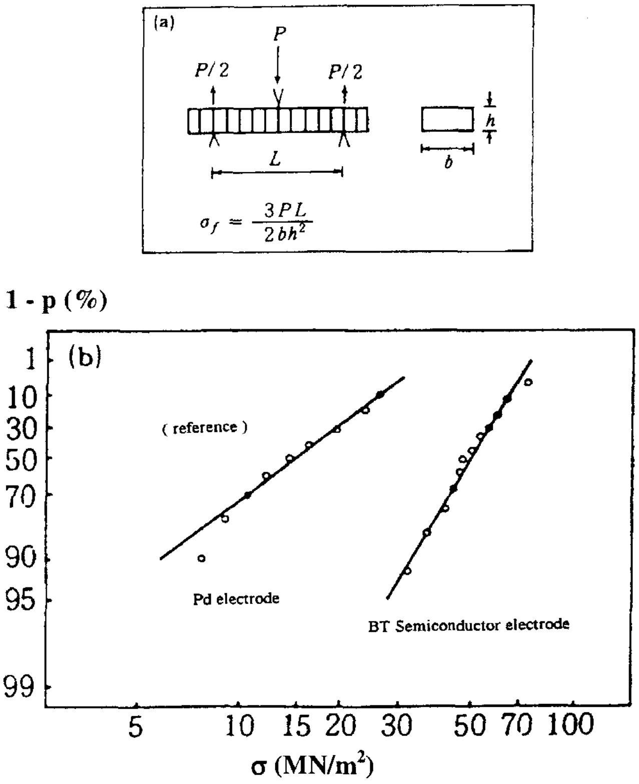

Figure 4.45 Three-point bend testing of multilayer actuators: (a) sample configuration and experimental setup, and (b) the Weibull plots for the ceramic electrode and metal electrode (reference) structures.[52]

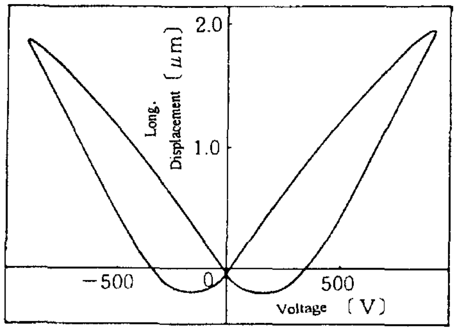

Figure 4.46 Displacement curve for a $BaTiO_3$-based multilayer actuator with ceramic electrodes.[52]

The uniaxial stress dependence of the strain induced in $BaTiO_3$ for several applied electric field strengths is shown in Figure 4.47. The typical strain responses of PZT and PMN-PT specimens are also shown in the figure for comparison. The magnitude of the induced strain in $BaTiO_3$ is not as large as that generated in the lead-based materials, but the generative stress (320 kgf/cm^2) level is comparable with those of the PZT and PMN-PT samples mainly due to the relatively small elastic compliance [$s_{33}=13 \times 10^{-12}$ (m^2/N)] of $BaTiO_3$.

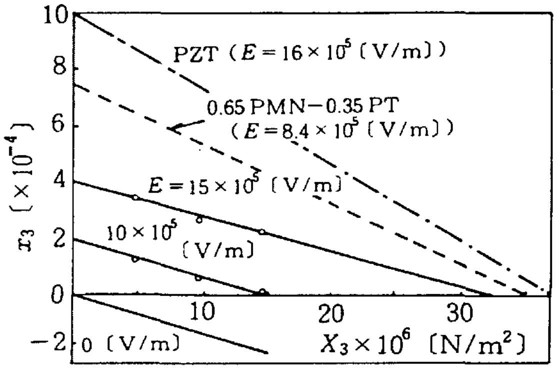

Figure 4.47 The uniaxial stress dependence of the strain induced in $BaTiO_3$ for several applied electric field strengths. The typical strain responses of PZT and PMN-PT specimens are also shown for comparison.

4.4 COMMERCIALLY AVAILABLE PIEZOELECTRIC AND ELECTROSTRICTIVE ACTUATORS

Poled blocks and discs of PZT-based piezoelectric ceramics can be purchased from many companies such as APC International, Aura Ceramics, AVX Kyocera, Burleigh, Channel Products, Edo Corporation, Lockheed-Martin, Morgan Electroceramics, Materials System Inc., Motorola, Piezo Kinetics Inc., Xinξtics (USA), Murata, TDK, Matsushita Electronic Components, Toshiba Ceramic, NGK-NTK, Tokin, Hitachi Metal, Taiheiyo Cement (Japan), Philips, and Siemens (Germany). If the product is not specifically categorized as an actuator, however, it may not have the durability required for actuator applications. Electrostrictive PMN-based materials can be obtained from Lockheed-Martin, AVX-Kyocera, Xinξtics (USA), and Nikki (Japan).

Multilayer and bimorph structures are among the most populuar for use as displacement transducers. Cut-and-bond type multilayer actuators are typically 20-50 layer laminations of 1 mm thick PZT disks, which produce a displacement in the range of 10-100 μm with an applied voltage of 1 kV. Piezo Positioner by OWIS (Germany), Piezo Translator by Physik Instrumente (Germany), PZT Pusher by Burleigh Instruments (USA), Drive Master by Control Technics (USA) and Piezo

Pile by NTK-NGK (Japan) are all commercially available products, which generally cost approximately \$6000 (\$1000 for the actuator and \$5000 for the control system). Low voltage (less than 100 V) multilayer actutators prepared by a tape-casting technology can be obtained from AVX-Kyocera, Morgan Electroceramics (USA), NEC, Tokin, Hitachi Metal, Sumitomo Chemical, Denso (Japan) and Philips (The Netherlands). Bimorph actuators find wide application as video head tracking devices (Sony and Matsushita Electric), swing CCD mechanisms (Toshiba), and big bimorphs (NTK-NGK, Ube Industry and Tokin). Another popular bimorph structure marketed as "Thunders" can be obtained from Face Electronics.

Many actuator devices with other configurations are also currently commercially available including the Inchworm by Burleigh Instruments (USA), the Piezoelectric Pump by Physics International (USA) and Bimor Corp. (Japan), the Piezoelectric Fan by Piezo Electric Products Inc. (USA), Misuzu-Erie and Nippon Denso (Japan), and the Ultrasonic Motor by Shinsei Industry, Fukoku, Nasca, Seiko Instruments and Nikon.

CHAPTER ESSENTIALS

1. Preparation of ceramic powders:
   a. Mixed-oxide technique
   b. Co-precipitation method
   c. Alkoxide hydrolysis

2. Displacement magnification mechanisms:
   a. Multilayer
   b. Unimorph/bimorph
   c. Monolithic hinge lever
   d. Moonie/cymbal
   e. Inchworm

3. Comparison between multilayer and bimorph actuators:
   a. The multilayer type does not exhibit large displacements (10 μm), but has a large generative force (100 kgf), a quick response speed (10 μsec), a long lifetime (10^{11} cycles) and high electromechanical coupling, k_{33} (70 %).
   b. The bimorph type exhibits large displacements (300 μm), but has a relatively low generative force (100 gf), slow response speed (1 ms), a shorter life time (10^8 cycles) and low electromechanical coupling, k_{eff} (10%).

4. Electrode configurations for multilayer actuators:
   a. **Interdigital type** in which internal stresses tend to develop. The following configurations are specifically designed to relieve these stresses.
   b. **Plate-through**
   c. **Slit-insert**
   d. **Float-electrode types**

5. A multilayer structure typically exhibits a field-induced strain of 0.1% along its length, l (for example, a 1 cm sample will exhibit a 10 μm displacement), and has a fundamental resonance frequency given by:

$$f_r = \frac{1}{2l\sqrt{\rho s_{33}^D}}$$

where ρ is the density and $s_{33}{}^D$ is the elastic compliance (for example, a 1 cm sample will have a 100 kHz resonance frequency).

6. Bimorph tip displacement (δ): clamped at one end condition (cantilever):

$$\delta = \frac{3d_{31}l^2 V}{2t^2} \quad \text{or} \quad \delta = \frac{3d_{31}l^2 V}{t^2}$$

depending on the configuration. The fundamental resonance frequency of the bimorph is determined by the total thickness, t, according to:

$$f_r = 0.16\frac{t}{l\sqrt{\rho s_{11}^E}}$$

for both configurations.

CHAPTER PROBLEMS

4.1 Making use of a PZT-based ceramic plate with a piezoelectric strain coefficient, d_{31}=− 300 pC/N, dimensions of 25 mm x 5 mm x 0.5 mm, and a phosphor bronze electrode (a high Q_M material!), design a *unimorph* with a total active length of 25 mm, which will execute its maximum tip displacement under an applied voltage of 100 V. Determine the optimum thickness of the phosphor bronze electrode then calculate the maximum displacement. Here, the density and the elastic compliance of the ceramic are $\rho=7.9$ g/cm^3 and $s_{11}{}^E=16\times10^{-12}$ m^2/N, respectively. You will need to search for the necessary data (Young's modulus etc.) for phosphor bronze. (Refer to Example Problem 4.4.)

4.2 Summarize the problems related to the use of ceramic electrode materials as compare to those associated with conventional metal electrode pastes.

Hint: Due to the limited range of conductivity for the ceramic electrode materials, there will be a cut-off frequency, which presents a fundamental limitation in the response speed.

4.3 Describe the difference between "silver paste" and "silver ink."

Hint: Which includes glass particles?

4.4 The bend curvature (1/R) of a monolithic piezoelectric plate under an electric field E is given by:

$$\frac{1}{R} = \frac{\int_{-(t_o/2)}^{(t_o/2)} Y[d_{31}(Z)][E_3(Z)]Z\,w\,dZ}{\int_{-(t_o/2)}^{(t_o/2)} Y\,Z^2\,w\,dZ}$$

where t_o is the plate thickness, w is the plate width, Y is Young's modulus of the ceramic, and d_{31} is the piezoelectric strain coefficient of the piezoceramic. The reference coordinate system Z is placed such that its origin is at the center of the plate. When Y and w are constant the equation for the bend curvature reduces to:

$$\frac{1}{R} = -\left[\frac{12}{t_o^3}\right]\int_{-(t_o/2)}^{(t_o/2)} [d_{31}(Z)][E_3(Z)]Z\,dZ$$

Given a monomorph plate for which the field distribution E(Z) and the barrier thickness t_b are given by:

$$E(Z) = \left[\frac{q N_d}{\varepsilon_o K}\right][Z - (t_o/2) + t_b]$$

where ($[(t_o/2)-t_b] < Z < [t_o/2]$) and

$$t_b = \sqrt{\left(\frac{2\varepsilon_o K}{q N_d}\right)(\phi_o + V)}$$

where ε_o is the vacuum permittivity, K is the relative permittivity of the monomorph, q is the electron charge, N_d is the donor density, and ϕ_o is the work function. Verify that the curvature is given by:

$$\frac{1}{R} = \frac{-\beta\, d_{31}\, t_b^2\,(3t_o - t_b)}{t_o^3}$$

or

$$\frac{1}{R} = \frac{-\beta\, d_{31}\, t_b^2\,(2t_o - t_b)}{t_o^3}$$

corresponding to the completely poled case [$d_{31}(Z) = d_{31}$(constant)] or the gradually poled case [$d_{31}(Z) = d_{31}(Z - (t_o/2) + t_b) / t_b)$].[34]

4.5 Referring to the Ellingham diagram for Ni and Cu that follows, discuss the higher stability of Cu with PZT when they are co-fired.

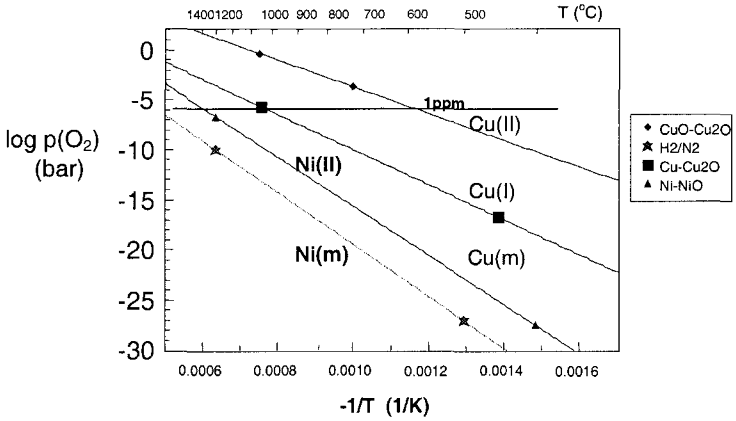

REFERENCES

1) Kato: *Fine Ceramics Technology*, Vol. 3 Fabrication Technology of Ceramic Powder and Its Future, p.166, Industry Research Center, Japan (1983).
2) M. Lejeune and J. P. Boilot: Ferroelectrics **54**, 191 (1984).
3) S. L. Swartz, T. R. Shrout, W. A. Schulze and L. E. Cross: J. Amer. Ceram. Soc. **67**, 311 (1984).
4) Tanada, Yamamura, Shirasaki: Abstract 22nd Jpn. Ceram. Soc. Fundamental Div. 3B5, p.81 (1984).
5) Ozaki: Electronic Ceramics **13**, Summer, p.26 (1982).
6) Kakegawa, Mohri, Imai, Shirasaki and Tekahashi: Abstract 21st Jpn. Ceram. Soc. Fundamental Div. 2C6, p.100 (1983).
7) H. Abe: *Recrystallization*, Mater. Sci. Series 2, Kyoritsu Pub., Tokyo (1969).
8) K. Uchino and T. Takasu: Inspec. **10**, 29 (1986).
9) A. Yamaji, Y. Enomoto, E. Kinoshita and T. Tanaka: Proc. 1st Mtg. Ferroelectric Mater. & Appl. p.269, Kyoto (1977).
10) K. Nakamura, H. Ando and H. Shimizu: Jpn. J. Appl. Phys. **26**, Suppl. 26-2, 198 (1987).
11) J. Kuwata, K. Uchino and S. Nomura: Ferroelectrics **37**, 579 (1981).
12) J. Kuwata, K. Uchino and S. Nomura: Jpn. J. Appl. Phys. **21**(9), 1298 (1982).
13) S. Yamashita: Jpn. J. Appl. Phys. **20**, Suppl. 20-4, 93 (1981).
14) K. Uchino, S. Nomura, L. E. Cross, R. E. Newnham and S. J. Jang: J. Mater. Sci. **16**, 569 (1981).
15) S. Takahashi, A. Ochi, M. Yonezawa, T. Yano, T. Hamatsuki and I. Fukui: Jpn. J. Appl. Phys. **22**, Suppl. 22-2, 157 (1983).
16) A. Furuta and K. Uchino: J. Amer. Ceram. Soc. **76**, 1615 (1993).
17) A. Furuta and K. Uchino: Ferroelectrics **160**, 277 (1994).
18) S. Takahashi: *Fabrication and Application of Piezoelectric Materials* (Edit. Shiosaki), Chap. 14, Actuators, CMC Pub. (1984).
19) S. Takahashi: Sensor Technology **3**, No.12, 31 (1983).

20) H. Aburatani, K. Uchino, A. Furuta and Y. Fuda: Proc. 9th Int'l. Symp. Appl. Ferroelectrics p. 750 (1995).
21) J. Ohashi, Y. Fuda and T. Ohno: Jpn. J. Appl. Phys., **32**, 2412 (1993).
22) A. Banner and F. Moller: Proc. 4th. Int'l. Conf. New Actuators, AXON Tech. Consult. GmbH, p.128 (1995).
23) K. Uchino and H. Aburatani: Proc. 2nd Int'l. Conf. Intelligent Mater., p.1248 (1994).
24) H. Aburatani and K. Uchino: Amer. Ceram. Soc. Annual Mtg. Proc., SXIX-37-96, Indianapolis, April (1996).
25) K. Nagata: Proc. 49th Solid State Actuator Study Committee, JTTAS, Japan (1995).
26) J. Zheng, S. Takahashi, S. Yoshikawa, K. Uchino and J. W. C. de Vries: J. Amer. Ceram. Soc. **79**, 3193 (1996).
27) R. W. Basedow and T. D. Cocks: J. Phys. E: Sci. Inst. **13**, 840 (1980).
28) T. Kitamura, Y. Kodera, K. Miyahara and H. Tamura: Jpn. J. Appl. Phys. **20**, Suppl. 20-4, 97 (1981).
29) K. Nagai and T. Konno Edit.: *Electromechanical Vibrators and Their Applications*, Corona Pub. (1974).
30) K. Abe, K. Uchino and S. Nomura: Jpn. J. Appl. Phys. **21**, L408 (1982).
31) C. Tanuma, Y. Suda, S. Yoshida and K. Yokoyama: Jpn. J. Appl. Phys. **22**, Suppl. 22-2, 154 (1983).
32) Okamoto et al.: Broadcast Technology No.7, p.144 (1982).
33) www.faceco.com
34) K. Uchino, M. Yoshizaki, K. Kasai, H. Yamamura, N. Sakai and H. Asakura: Jpn. J. Appl. Phys. **26** 1046 (1987).
35) K. Uchino, M. Yoshizaki and A. Nagao: Jpn. J. Appl. Phys. **26**, Suppl. 26-2, 201 (1987).
36) K. Uchino, M. Yoshizaki and A. Nagao: Ferroelectrics **95**, 161 (1989).
37) Aura Ceramics, Inc., USA, Catalogue "Rainbow".
38) K. Nakamura, H. Ando and H. Shimizu: Appl. Phys. Lett. **50**, 1413 (1987).
39) Y. Sugawara, K. Onitsuka, S. Yoshikawa, Q. C. Xu, R. E. Newnham and K. Uchino: J. Amer. Ceram. Soc. **75**, 996 (1992).
40) H. Goto, K. Imanaka and K. Uchino: Ultrasonic Techno **5**, 48 (1992).
41) A. Dogan: Ph.D. Thesis, Penn State University (1994).
42) S. Dong and K. Uchino: IEEE UFFC-Trans. (2002). [in press]
43) Kitayama: Ceramics **14**, 209 (1979).
44) B. Z. Janos and N. W. Hagood: Proc. 6th Conf. New Actuators, Actuator '98, Bremen, Germany, p.193 (1998).
45) M. Ishida et al.: Appl. Phys. Lett. **31**, 433 (1977).
46) M. Okuyama et al.: Ferroelectrics **33**, 235 (1981).
47) S. K. Dey and R. Zuleeg: Ferroelectrics **108**, 37 (1990).
48) S. Kalpat, X. Du, I. R. Abothu, A. Akiba, H. Goto and K. Uchino: Jpn. J. Appl. Phys. **40**, 158-162 (2001).
49) Burleigh Instruments Inc., East Rochester, NY, Catalog.
50) K. Ohnishi and T. Morohashi: J. Jpn. Ceram. Soc. **98**, 895 (1990).
51) W. A. Groen, D. Hennings and M. Thomas: Proc. 33rd Int'l. Smart Actuator Symp., State College, PA, April (2001).
52) K. Abe, K. Uchino and S. Nomura: Ferroelectrics **68**, 215 (1986).
53) O. Saburi: J. Phys. Soc. Jpn. **14**, 1159 (1959).
54) Matsuo, M. Fujimura, H. Sakaki, K. Nagase and S. Hayakawa: Amer. Ceram. Soc. Bull. **47**, 292 (1968).
55) J. W. Hardy, J. E. Lefebre and C. L. Koliopoulos: J. Opt. Soc. Amer. **67**, 360 (1977).

5

DRIVE/CONTROL TECHNIQUES FOR PIEZOELECTRIC ACTUATORS

There are three general methods for actuator drive/control that are most commonly employed: DC drive, pulse drive, and AC drive. These methods are typically used for displacement transducers, pulse drive motors and ultrasonic motors, respectively. Displacement transducers are usually controlled in a closed-loop mode. Open-loop control can also be employed, but only when strain hysteresis is negligible and temperature fluctuation during operation is very small. Closed-loop control is a feedback method whereby the electric field-induced displacement of a ceramic actuator is monitored, deviation from the desired displacement is detected, and an electric signal proportional to this deviation is fed back to the ceramic actuator through an amplifier to effectively correct the deviation. Feedback is generally used for these devices to alleviate problems associated with the non-linearity and hysteresis commonly encountered in piezoelectric materials. The pulse drive motor is typically operated in the open-loop mode, but special care must be taken to suppress overshoot and mechanical ringing that can occur after the pulse voltage is applied. The AC voltage applied to ultrasonic motors is not very large, but the drive frequency must be precisely matched with the mechanical resonance frequency of the device for optimum performance. Heat generation, which is a potentially significant problem with this design, can be effectively minimized with the proper selection of operating parameters.

5.1 CLASSIFICATION OF PIEZOELECTRIC ACTUATORS

Piezoelectric and electrostrictive actuators may be classified into two major categories, based on the type of drive voltage applied to the device and the nature of the strain induced by the voltage as depicted in Figure 5.1. They are: (1) *rigid displacement devices,* for which the strain is induced unidirectionally, aligned with the applied DC field, and (2) *resonant displacement devices,* for which an alternating strain is excited by an AC field at the mechanical resonance frequency (*ultrasonic motors*). The first category can be further divided into two general types: *servo displacement transducers* (*positioners*), which are controlled by a feedback system through a position detection signal, and *pulse drive motors*, which are operated in a simple on/off switching mode. The drive/control techniques presented in this chapter will be discussed in terms of this classification scheme.

The response of the resonant displacement devices is not directly proportional to the applied voltage, but is dependent on the drive frequency. Although the positioning accuracy of this class of devices is not as high as that of the rigid displacement devices, ultrasonic motors are able to produce very rapid motion due to their high frequency operation. Servo displacement transducers, which are controlled by a feedback voltage superimposed on a DC bias, are used as positioners for optical and precision machinery systems. In contrast, a pulse drive motor generates only on/off strains, suitable for the impact elements of dot matrix or inkjet printers. An impact actuator can be created with a pulse driven piezoelectric element. A simple flight actuator design is depicted schematically in Figure 5.2. The 2 mm steel ball can be launched as high as 20 mm by this device when a rapid 5 μm displacement is induced in the multilayer actuator.[1]

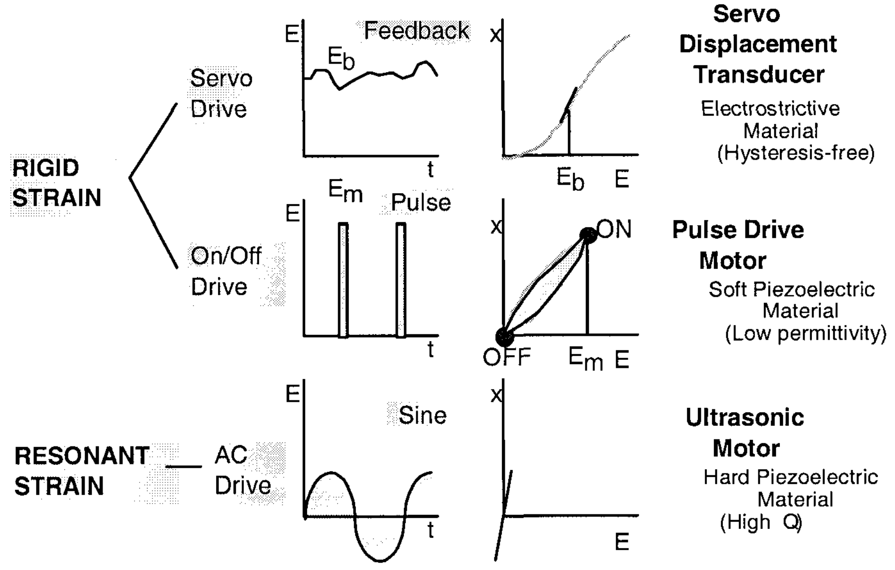
RIGID STRAIN
Servo Drive
On/Off Drive
RESONANT STRAIN
AC Drive
E
Feedback
Eb
t
E
Em
Pulse
t
E
Sine
t
x
Eb
E
x
ON
OFF
Em
E
x
E
Servo Displacement Transducer
Electrostrictive Material (Hysteresis-free)
Pulse Drive Motor
Soft Piezoelectric Material (Low permittivity)
Ultrasonic Motor
Hard Piezoelectric Material (High Q)

Figure 5.1 Classification of piezoelectric/electrostrictive actuators according to the type of drive voltage and the nature of the induced strain.

The material requirements for each class of devices will be different, and certain compositions will be better suited for particular applications. The servo displacement transducer suffers most from strain hysteresis and, therefore, a $Pb(Mg_{1/3}Nb_{2/3})O_3$-$PbTiO_3$ (PMN) electrostrictive material is preferred for this application. It should be noted that even when a feedback system is employed, the presence of a pronounced strain hysteresis general results in a much slower response speed. The pulse drive motor, for which a quick response rather than a small hysteresis is desired, requires a low permittivity material. Soft $Pb(Zr,Ti)O_3$ (PZT) piezoelectrics are preferred over the high permittivity PMN for this application. The ultrasonic motor, on the other hand, requires a very hard piezoelectric with a high mechanical quality factor, Q_m, in order to maximize the AC strain and to minimize heat generation. Note that the figure of merit for the resonant strain is characterized by dE/Q_m (d: the piezoelectric strain coefficient, E: the applied electric field, *l*: the sample length, Q_m: the mechanical quality factor). Although hard PZT materials have smaller d coefficients, they also have significantly larger Q_m values, thus providing the high resonant strains needed for these devices.

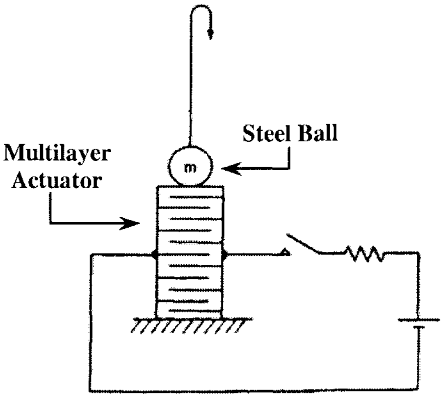

Figure 5.2 A simple flight actuator design.

5.2 FEEDBACK CONTROL

We will consider in this section the design of a microdisplacement control unit functioning as a *servo* (*mechanical feedback*) *system*. An example of use in a precision lathe machine, which can cut a rod with an accuracy of ± 0.01 μm.[2] The positioning system is comprised of a multilayer electrostrictive actuator, a potentiometer position sensor (magnetoresistive type) and a feedback circuit as shown in Figure 5.3. The feedback circuit for this compact positioner is pictured schematically in Figure 5.4. We will begin by reviewing the fundamental principles of the Laplace transform and then determine the *transfer function* for this actuator system. We will conclude our examination of the system by evaluating its stability in terms of steady state deviations induced by external disturbances. The reader is referred to the texts of Amemiya[3] and Davis[4] for a more advanced treatment of feedback systems.

(1) The Laplace Transform

Let us first review an important mathematical tool, the *Laplace transform*. The Laplace transform is generally employed for treating the *transient response* to a pulse input. The *Fourier transform* is preferred for cases where a continuous sinusoidal input is applied, such as for resonance type actuators.

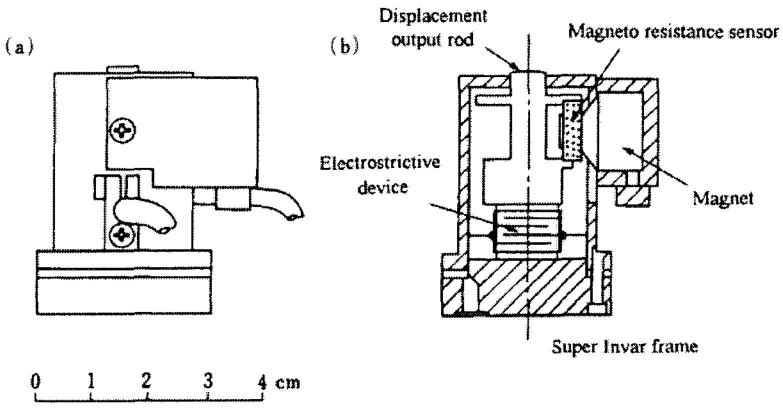
(a)
(b)
Displacement output rod
Magneto resistance sensor
Electrostrictive device
Magnet
Super Invar frame
0 1 2 3 4 cm

Figure 5.3 A smart piezoelectric actuator used as a micropositioner: (a) an external view and (b) a cross-sectional view.

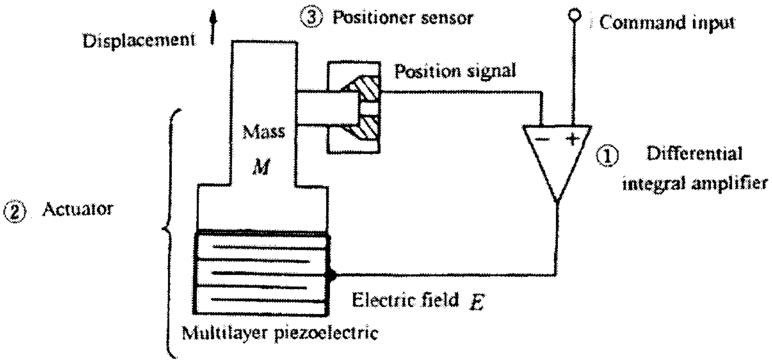
Displacement
③ Positioner sensor
Command input
Position signal
Mass
M
① Differential integral amplifier
② Actuator
Electric field E
Multilayer piezoelectric

Figure 5.4 Schematic representation of the feedback system for the smart micropositioner.

Fundamental Principles of the Laplace Transform

We consider a function u(t) which is defined for $t \geq 0$ [$u(t) = 0$ for $t < 0$], and satisfies $|u(t)| \leq ke^{\delta t}$ for all δ not less than a certain positive real number δ_o. When these conditions are satisfied, $e^{-st}u(t)$ is absolutely integrable for $\mathrm{Re}(s) \geq \delta_o$. We define the Laplace transform:

$$U(s) = L[u(t)] = \int_0^\infty e^{-st}\,u(t)\,dt \tag{5.1}$$

The inverse Laplace transform is represented as $L^{-1}[U(s)]$. Application of the useful theorems for the Laplace transform that are listed ahead reduce the work of solving certain differential equations by reducing them to simpler algebraic forms. The procedure is applied as follows:

1) Transform the differential equation to the s-domain by means of the appropriate Laplace transform.
2) Manipulate the transformed algebraic equation and solve for the output variable.
3) Obtain the inverse Laplace transform from Table 5.1.

Some Useful Theorems for the Laplace Transform:

(a) **Linearity:**

$$L\,[\mathbf{a}\,u_1(t) + \mathbf{b}\,u_2(t)] = \mathbf{a}\,U_1(s) + \mathbf{b}\,U_2(s) \tag{5.2}$$

$$L^{-1}[\mathbf{a}\,U_1(s) + \mathbf{b}\,U_2(s)] = \mathbf{a}\,u_1(t) + \mathbf{b}\,u_2(t) \tag{5.3}$$

(b) **Differentiation with respect to t:**

$$L\left[\frac{d\,u(t)}{dt}\right] = s\,U(s) - u(0) \tag{5.4}$$

$$L\left[\frac{d^n\,u(t)}{d\,t^n}\right] = s^n\,U(s) - \sum s^{n-k}\,u^{k-1}(0) \tag{5.5}$$

(c) **Integration:**

$$L\left[\int u(t)\,dt\right] = U(s)/s + (1/s)\left[\int u(t)\,dt\right]_{t=0} \tag{5.6}$$

(d) **Scaling formula:**

$$L[u(t/a)] = a\,U(sa) \qquad (a > 0) \tag{5.7}$$

(e) **Shift formula with respect to t**: $u(t-k)=0$ for $t < k$
[k: positive real number] This represents the u(t) curve shifted by k along the positive t axis.

$$L[u(t-k)] = e^{-ks}\,U(s) \tag{5.8}$$

(f) **Differentiation with respect to an independent parameter:**

$$L\left[\frac{\partial u(t,x)}{\partial x}\right] = \frac{\partial U(s,x)}{\partial x} \tag{5.9}$$

(g) **Initial and final values**

$$\lim_{t\to 0}[u(t)] = \lim_{|s|\to\infty}[U(s)] \tag{5.10}$$

$$\lim_{t\to\infty}[u(t)] = \lim_{|s|\to 0}[U(s)] \tag{5.11}$$

Table 5.1 Some common forms of the Laplace transform.[5]

	H(t)	G(s)
1	1(t) Step $1(t)=1,\ t>0\ ;\ 1(t)=0,\ t<0$	$1/s$
2	$\delta(t)$ Impulse function $\delta(t)=\infty,\ t=0\ ;\ \delta(t)=0,\ t\neq 0$	1
3	$t^n/n!$ (n: positivcinteger)	$1/s^{n+1}$
4	e^{-at} (a: complex)	$1/(s+a)$
5	$\cos(at)$	$s/(s^2+a^2)$
6	$\sin(at)$	$a/(s^2+a^2)$
7	$\cosh(at)$	$s/(s^2-a^2)$
8	$\sinh(at)$	$a/(s^2-a^2)$
9	$e^{-bt}\cos(at)\quad a^2>0$	$\frac{s+b}{(s+b)^2+a^2}$
10	$e^{-bt}\sin(at)\quad a^2>0$	$\frac{a}{(s+b)^2+a^2}$
11	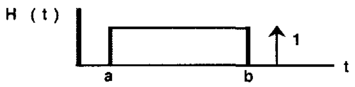	$\frac{1}{s}(e^{-as}-e^{-bs})$
12	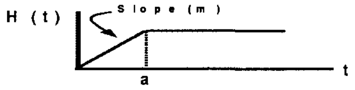	$\frac{m}{s^2}(1-e^{-as})$
13	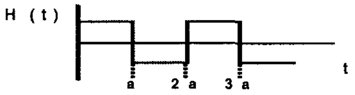	$\frac{1}{s}\tanh\left(\frac{as}{2}\right)$
14	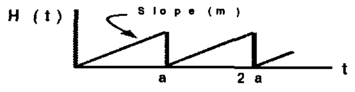	$\frac{m}{s^2}-\frac{ma}{2s}\left[\coth\left(\frac{as}{2}\right)-1\right]$

Example Problem 5.1

Compute the Laplace transform of the Heaviside function (*step function*) H(t)=0 when $t < 0$ and H(t)=1 when $t \geq 0$.

Solution

$$L[H(t)] = \int_0^\infty e^{-st}\, H(t)\, dt = \int_0^\infty e^{-st} dt = (1/s)\, e^{-st}\Big|_0^\infty = 1/s \qquad \text{(P5.1.1)}$$

Example Problem 5.2

Using the result from the previous problem, L[H(t)] = 1/s, obtain the Laplace transform for a *pulse function* defined by the following:

$P(t) = 0$ when $t < a$ and $t > b$ (here, $0 < a < b$)
$P(t) = 1$ when $a < t < b$

Solution

P(t) is obtained by superimposing the two step functions, H(t–a) and –H(t–b). Using the shift formula, we obtain the Laplace transform of P(t):

$$L[P(t)] = e^{-as}\,(1/s) - e^{-bs}\,(1/s) = (1/s)\,(e^{-as} - e^{-bs}) \qquad \text{(P5.2.1)}$$

---

(2) The Transfer Function

A Piezoelectric Actuator / Position Sensor / Differential Amplifier System

First, let's consider the displacement, u, in a piezoelectric actuator by an applied electric field, E, in terms of the simple model depicted in Figure 5.5. Let us assume a mass, M, is applied to the piezoelectric actuator spring, which has an elastic stiffness, c, a piezoelectric strain coefficient, d, a length, *l*, and a cross-sectional area, A. The oscillation of the mass is sustained by the piezoelectric force, which is generated by the applied electric field and described by (Acd)E. The dynamic equation is written as follows:

$$M\frac{d^2u}{dt^2} + \zeta\frac{du}{dt} + \left(\frac{ac}{l}\right)u = (Acd)E \qquad (5.12)$$

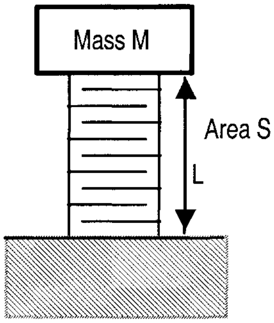

Figure 5.5 A simple piezoelectric actuator and mass model.

where ζ represents the *damping effect*. The Laplace transform of Equation (5.12) is represented as:

$$M s^2 U + \zeta s U + (Ac/l) U = AcdE^{\sim} \qquad (5.13)$$

Here, U and $E^{\sim}$ are the Laplace transforms of u and E, respectively. We may now define the following:

$$U(s) = G_2(s) E^{\sim}(s) \qquad (5.14)$$

where the function G_2 is given by:

$$G_2(s) = Acd / (M s^2 + \zeta s + Ac/l) \qquad (5.15)$$

This function, which essentially relates the input $E^{\sim}(s)$ to the output U, is called the *transfer function*.

We now can consider the position sensor used in this system, which generates a signal voltage e_o proportional to the input displacement u. The transfer function G_3 for the sensor is simply:

$$G_3(s) = K_2 \qquad (5.16)$$

Finally, we consider the differential integral amplifier of the system. The command voltage e_i is at the input, and the differential voltage from the position signal voltage e_o is generated. When the command voltage e_i is larger than the position signal e_o, the voltage difference $(e_i - e_o)$ becomes positive and after being amplified is applied to the piezoelectric actuator so as to increase the displacement. If $e_i < e_o$, the applied electric field is decreased. When we use an integral amplifier, this amplification is described by:

$$E = K_I \int (e_i - e_o)\,dt \qquad (5.17)$$

Thus,

$$E^{\sim} = G_I(s)\,(e_i^{\sim} - e_o^{\sim}) \qquad (5.18)$$

$$G_I(s) = K_I / s \qquad (5.19)$$

There are three types of amplifiers commonly utilized in a system such as this one: *proportional*, *integral*, and *derivative* (*PID controller*) with transfer functions K_I, K_I/s, and $K_I s$, respectively. Any one of these or a combination of these may be used in a given system. In general, system stability will increase with increasing integral components, but only at the expense of the response speed. On the other hand, the responsivity of the system is enhanced significantly with increasing derivative components, but, in this case, there is often some loss in stability.

Example Problem 5.3

The transfer function of a piezoelectric actuator is given by:

$$U(s) = G(s)\,E^{\sim}(s), \qquad (P5.3.1)$$

$$G(s) = Acd / (Ms^2 + \zeta s + Ac/l) \qquad (P5.3.2)$$

Calculate the displacement response to an impulse voltage with $E^{\sim}(s) = 1$.

Solution

In the case of an impulse input, $E^{\sim}(s) = 1$. Thus, *the output displacement U(s) is provided directly by the transfer function G(s)*:

$$U(s) = (Acd/M\omega)\,(\,\omega / [(s + \zeta / 2M)^2 + \omega^2]) \qquad (P5.3.3)$$

where:

$$\omega^2 = (A\,c / Ml) - (\zeta^2 / 4M^2) \qquad (P5.3.4)$$

If the relationship can be expressed in the form of one of the common Laplace transforms found in Table 5.1, we can obtain the solution easily without using complex mathematics. Fortunately, we are able to take this more simple approach here (see #10 in Table 5.1) and the displacement response is found to be of the form:

$$u(t) = (Acd/M\omega)\,\exp[-(\zeta / 2M)t]\,\sin(\omega t) \qquad (P.5.3.5)$$

We see that the sinusoidal vibration is damped according to the magnitude of ζ and that the resonance frequency is also affected by the damping factor ζ.

Block Diagram

Let us describe this servo system in terms of the block diagram pictured in Figure 5.6(a) using the three transfer functions just defined. It should be noted at this point that an amplifier of rather low output impedance (less than 1 Ω) is typically employed a system of this kind. This is necessary because the actuator possesses a relatively large electrostatic capacitance, which can lead to a significant delay in system response if the amplifier output impedance is too high. (Note that the cut-off frequency is determined by the time constant, RC).

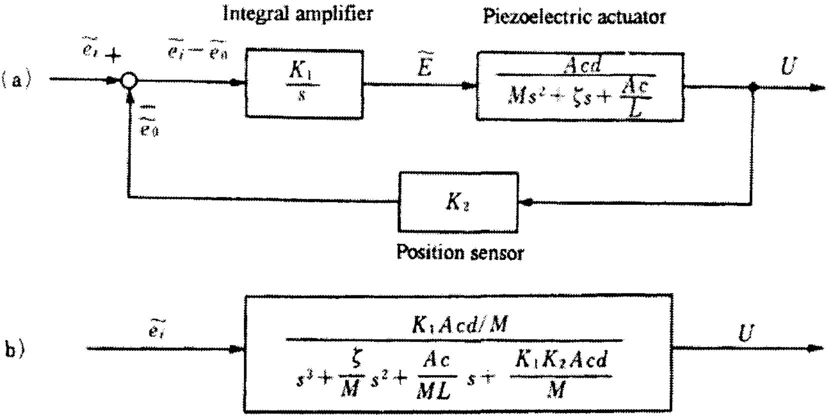
Integral amplifier
Piezoelectric actuator
(a)
$\tilde{e}_i$ +
$\tilde{e}_i - \tilde{e}_0$
$\frac{K_1}{s}$
$\tilde{E}$
$\frac{Acd}{Ms^2+\zeta s+\frac{Ac}{L}}$
U
−
$\tilde{e}_0$
K_2
Position sensor
(b)
$\tilde{e}_i$
$\frac{K_1Acd/M}{s^3+\frac{\zeta}{M}s^2+\frac{Ac}{ML}s+\frac{K_1K_2Acd}{M}}$
U

Figure 5.6 Block diagrams for a piezoelectric actuator servo system representing the function of: (a) the individual system elements and (b) the entire system.

There are generally two ways to unify the block diagram with a feedback loop: open- and closed-loop transfer functions. The *open-loop transfer function* is defined as

$$W_o = G_1G_2G_3\left[\frac{K_1K_2}{s}\right]\frac{Ac\,d}{Ms^2+\zeta s+(Ac/l)} \tag{5.20}$$

The *closed-loop transfer function* is calculated by completing the feedback function:

$$W_c = G_1G_2 - G_1G_2\,(G_1G_2G_3) + G_1G_2\,(G_1G_2G_3)^2 - G_1G_2\,(G_1G_2G_3)^3 + \cdots$$

$$= \frac{G_1G_2}{(1+G_1G_2G_3)}$$

$$= \frac{K_1 Acd/M}{s^3 + (\zeta/M)s^2 + (Ac/Ml)s + (K_1 K_2 Acd/Ml)} \qquad (5.21)$$

This function applies to the entire system as depicted in Figure 5.6(b).

Control Stability

In an ideal situation, where the input command voltage, e_i, changes stepwise as illustrated in Figure 5.7(a), it is expected that the displacement, u, will also change in a stepwise fashion. However, in real situations, the actual displacement that occurs is quite different from the ideal response. A divergent case is depicted in Figure 5.7(d). This is an undesirable response from a practical point of view and, in general, is referred to as *unstable control.*

Even if a more converging response is achieved by the system, this in itself does not guarantee that the difference between the actual displacement voltage, e_o, and the input command voltage, e_i, will be exactly zero after a sufficient time lapse. This displacement deviation, which is called *steady state error*, is an important issue in control engineering. Simply reducing the steady state error to a minimum is not necessarily the objective, however, as too small a displacement deviation can sometimes cause too long a decay time for the transient vibration, which is also not good control. So we see that the decay time for the transient vibration is another key factor in evaluating a particular drive/control method.

(3) Defining the Criterion for System Stability

The Characteristic Equation

When the command input, e_i, is a unit step, the displacement response of the actuator system may be described by:

$$U = W_c e_i^{\sim} = \frac{K_1 Acd/sM}{s^3 + (\zeta/M)s^2 + (Ac/Ml)s + (K_1 K_2 Acd/M)} \qquad (5.22)$$

We may simplify this expression by assuming that: $K_1Acd/M=4$, $\zeta/M=4$, $Ac/Ml=6$ and $K_1K_2Acd/M=4$, which yields:

$$U = 4 / s\,(s^3 + 4s^2 + 6s + 4) \qquad (5.23a)$$

Further manipulation of this equation leads to the following:

$$U = \frac{4}{s(s+2)(s+1+j)(s+1-j)} = \frac{1}{s - \left(\frac{1}{s+2}\right) + \left(\frac{j}{s+1-j}\right) - \left(\frac{j}{s+1+j}\right)} \tag{5.23b}$$

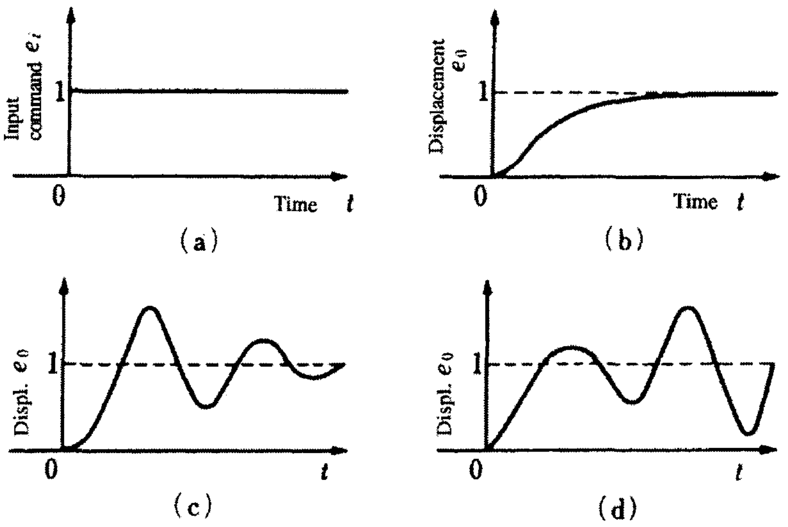

Figure 5.7 Various possible output voltages, e_o, from a step input, e_i.

When we make use of inverse Laplace transform #4 from Table 5.1 leads to the following equation for the displacement u(t):

$$\begin{aligned} u(t) &= [1-e^{-2t} + j\,e^{-(1-j)t} - j\,e^{-(1+j)t}]\ 1(t) \\ &= [1-e^{-2t}-2\,e^{-t}\sin(t)]\ 1(t) \end{aligned} \tag{5.24}$$

With increasing time, the second and third terms approach zero and u(t) becomes more nearly like the step function; therefore, this system is considered to be stable. When the denominator of the closed-loop transfer function is set equal to zero, the resulting equation is called the *characteristic equation*. The system is judged to be stable when the real parts of the characteristic roots are all negative.

The Nyquist Criterion for Stability

The stability of the system can be characterized in terms of the so-called Nyquist criterion. The Nyquist method utilizes the open-loop transfer function W_o:

$$W_o = G_1 G_2 G_3 = \frac{(K_1 K_2 A c d / M)}{s[s^2 + (\zeta / M)s + (Ac / Ml)]} \qquad (5.25)$$

The mathematical verification of this equation is somewhat beyond the scope of this text and, therefore, we will primarily focus our attention on applying the criterion. By substituting $s = j\omega$ (where ω is the angular frequency) into Equation 5.25, the locus of W_0 for ω increasing from 0 to $+\infty$ may be plotted on the complex plane and the resulting curves constitute what is referred to as a *Nyquist diagram*. A set of such curves is shown in Figure 5.8. Considering the tendency of these curves in the direction of the arrow (see K_2=3 curve in Figure 5.8), we can say that *the system is stable if the point (−1 + j 0) is to the left of the locus*. When this point is to the right of the locus, the system is considered unstable and when the Nyquist locus passes through this point, the system is exactly on the critical limit of stability.

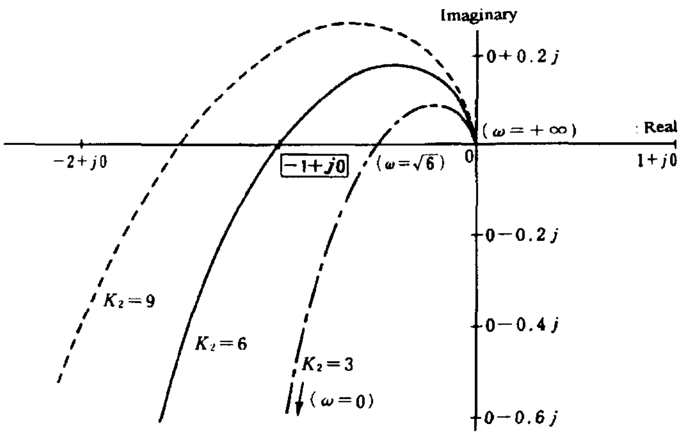

Figure 5.8 A Nyquist diagram for a piezoactuator system.

Let us consider again the case associated with Equation (5.23), for which we assumed $K_1Acd/M=4$, $\zeta/M=4$, $Ac/Ml=6$. The general open-loop transfer function for this system may be written as:

$$W_o = 4\,K_2 / j\omega(-\omega^2 + 4\,j\omega + 6) \qquad (5.26)$$

The curves depicted in Figure 5.8 correspond to this general case for various values of K_2. We see in this situation that if the gain of the displacement sensor K_2 is adjusted to 6, the locus passes precisely through the point (−1 + j 0), exactly at the critical limit of stability. If the gain is reduced to half this value, the point (−1 + j 0) is to the left of the locus (with increasing frequency) and a stable state exists. When the gain is increased by a factor of 1.5, however, K_2 = 9 and the point (−1 + j 0) is to the right side of the locus, resulting in an unstable state. The specific condition described by Equation (5.23) corresponds to $K_2=1$, which by this criterion is found to be a very stable condition.

(4) Steady State Error

When the command voltage, e_i, is changed, the sensor voltage, e_o, which corresponds to the actual position after a sufficient time lapse, will also change such that:

$$e_i^{\sim}-e_o^{\sim} = (1-K_2W_c)\,e_i^{\sim}$$

$$= \frac{e_i^{\sim}\, s\,[s^2 + (\zeta/M)s + (Ac/Ml)]}{s^3 + (\zeta/M)s^2 + (Ac/Ml)s + (K_1 K_2 Acd/M)} \qquad (5.27)$$

When the input is a constant step voltage [that is, $e_i = 1(t)$], we also know that:

$$\lim_{t\to\infty}(e_i - e_o) = \lim_{s\to 0}[s(e_i^{\sim} - e_o^{\sim})] = 0 \qquad (5.28)$$

Thus, the *steady state error* of the position is zero. Considering now an input that is a constantly increasing voltage, such that $e_i = t$, $e_i^{\sim} = 1/s^2$, we find that

$$\lim_{t\to\infty}(e_i - e_o) = \lim_{s\to 0}[s(e_i^{\sim} - e_o^{\sim})] = \frac{1}{K_1 K_2 d l} \qquad (5.29)$$

and the steady state error is no longer equal to zero. If the position sensor gain, K_2, is increased, the steady state deviation decreases. As we have already discussed, however, the system stability also deteriorates with increasing K_2, thus we need to establish some kind of a compromise between the steady state error and the system stability.

The data presented in Figure 5.9 show the experimental data of the position change for our compact actuator system under a step command input. We see in Figure 5.9(b) how the actuator's position gradually drifts without feedback control due to the effects of thermal expansion. The displacement is more effectively regulated when feedback control is employed. Proper choice of the damping constant is also an important factor here in achieving the most stable response. We see in Figure 5.9(b) the effects of choosing a damping constant ζ that is too small; a clear *overshoot* is observed under these conditions at the rise and fall edges of the output signal. When the damping constant is increased by means of a *mechanical damper* such as a plate spring, the overshoot is eliminated as depicted in Figure 5.9(c). It is important to keep in mind, however, in selecting an appropriate ζ that excessively high values will significantly decrease the responsivity of the system.

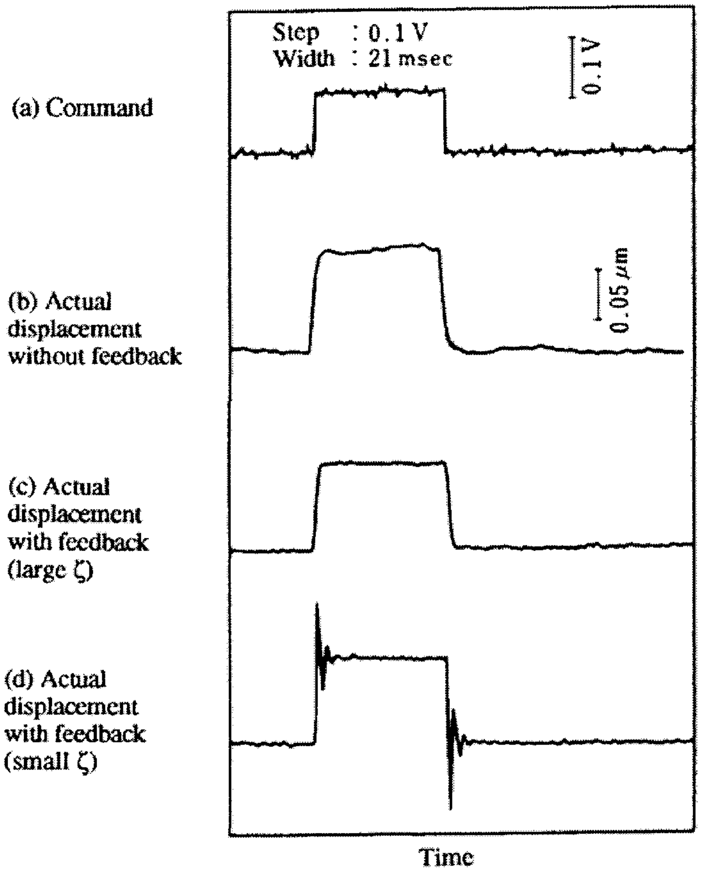

Figure 5.9 Step response of the piezoelectric actuator.

(5) Advantages of Feedback Control

Adding a feedback control system that satisfies the Nyquist stability, generally provides distinct benefits, namely: (1) *a linear relationship between input and output*, (2) *an output response with a flat frequency dependence,* and (3) *minimization of external disturbance effects*. These benefits are described in this section.

Linear Relation Between Input and Output

Let us consider the nonlinear relation depicted in Figure 5.10 between an input voltage, V, as might be applied to an electrostrictive actuator, and the corresponding output response, Y, which in this case would be the position sensor voltage, such that:

$$Y = F(V) = KV^2 \tag{5.30}$$

for an electrostrictive actuator system. Let us add a feedback loop as shown in Figure 5.11(a). We will assume that K and β are constants, and that X, V and Y are variable signals at the points of the system indicated on the block diagram. This system will be in equilibrium for a certain input $X=X_0$ (that is, a command voltage corresponding to a desired position) and corresponding $V=V_0$, $Y=Y_0$. In this state the following equations must be satisfied:

$$V_o = K(X_o - \beta Y_o) \tag{5.31}$$

$$Y_o = F(V_o) \tag{5.32}$$

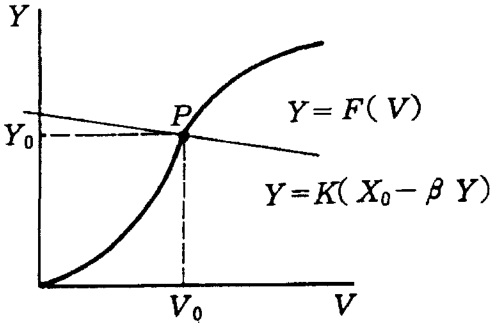

Figure 5.10 A nonlinear relationship between Y (output voltage) and V (input voltage) for an electrostrictive actuator system.

The point (V_o, Y_o) is identified as point P in Figure 5.10. Let's consider a small change in X by an incremental amount, x. The corresponding increments of V and Y are thus given by:

$$v = K(x - \beta y) \tag{5.33}$$

$$y = F'(V_o)\, v \tag{5.34}$$

Substituting and solving for y, we obtain:

$$y = \left[\frac{KF'(V_o)}{1 + \beta KF'(V_o)}\right] x \tag{5.35}$$

If the condition:

$$\beta K F'(V_o) >> 1 \tag{5.36}$$

is satisfied, then:

$$y = (1 / \beta)\, x \tag{5.37}$$

This means that *a linear relation is obtained between the input x and output y* in the feedback control system.

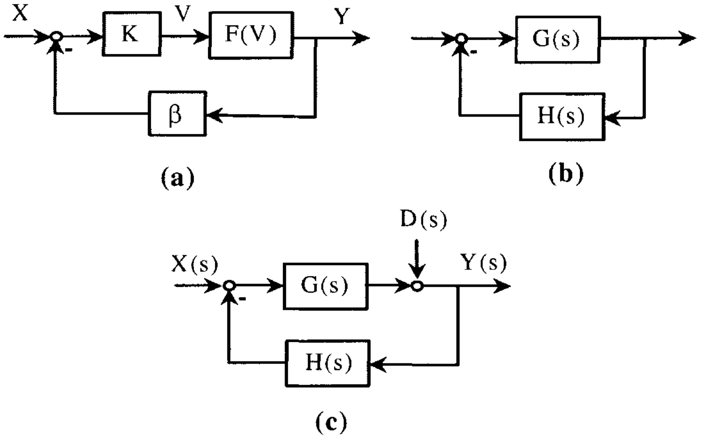

Figure 5.11 Various feedback systems.

Output Response with a Flat Frequency Dependence

Let us now consider a forward transfer function, G(s), and a feedback transfer function, H(s), as depicted in the block diagram of Figure 5.11(b). If we assume this feedback system is stable, its *closed-loop frequency response function, M(jω),* is given by:

$$M(j\omega) = \frac{G(j\omega)}{[1 + G(j\omega)\,H(j\omega)]} \tag{5.38}$$

If the condition:

$$|G(j\omega)\,H(j\omega)| >> 1 \tag{5.39}$$

is satisfied, then:

$$M(j\omega) = 1 / H(j\omega) \tag{5.40}$$

In other words, in the frequency range where the gain of the *open-loop transfer function,* $|G(j\omega)H(j\omega)|$, is sufficiently larger than 1, the closed-loop frequency response function, $M(j\omega)$, depends only on the feedback transfer function, $H(s)$. If $H(j\omega)=\beta$ (constant), $M(j\omega)$ shows a constant characteristic with a gain $(1/\beta)$ and a phase angle of zero in this frequency range.

On the other hand, if the condition

$$|G(j\omega)\,H(j\omega)| << 1 \tag{5.41}$$

is satisfied, then:

$$M(j\omega) = G(j\omega) \tag{5.42}$$

and for the frequency range in which $|G(j\omega)\,H(j\omega)|=1$, $M(j\omega)$ is obtained directly from Equation (5.38). A resonance is occasionally observed around this frequency (near the gain crossing frequency, ω_{cg}).

Minimization of External Disturbance Effects

We may now add an external disturbance (that is, a deviation in position due to *thermal dilatation* or *mechanical noise vibration*) to the system and its associated transfer function, G(s). This is represented as D(s) in the block diagram of Figure 5.11(c). The output, Y(s), for this system will be described by:

$$Y(s) = \left[\frac{1}{[1+G(s)H(s)]}\right]\big(G(s)\,X(s) + D(s)\big) \tag{5.43}$$

The output deviation, $\Delta Y(s)$, due to the external disturbance D(s) is given by:

$$\Delta Y(s) = \frac{D(s)}{[1+G(s)H(s)]} \tag{5.44}$$

Let us consider as an example a step disturbance, $d\cdot 1(t)$ (d: constant, 1(t): unit step function). The saturated output deviation $\Delta y(\infty)$ can be calculated using the Laplace theorem (g) (see page 223):

$$\Delta y(\infty) = \lim_{s\to 0}[s\,\Delta Y(s)] = \lim_{s\to 0}\left[\frac{s}{[1+G(s)H(s)]}(d/s)\right]$$

$$= \frac{d}{[1+G(0)H(0)]} \tag{5.45}$$

The external disturbance can be significantly diminished by a factor of 1/[1+G(0)H(0)], as compared to the case where no feedback is employed. The open-loop transfer function under DC conditions, G(0)H(0), should be sufficiently larger than 1 in order to minimize the output deviation.

If the external disturbance has a frequency spectrum D(jω), the output deviation spectrum is:

$$\Delta Y(j\omega) = \frac{D(j\omega)}{[1+G(j\omega)H(j\omega)]} \tag{5.46}$$

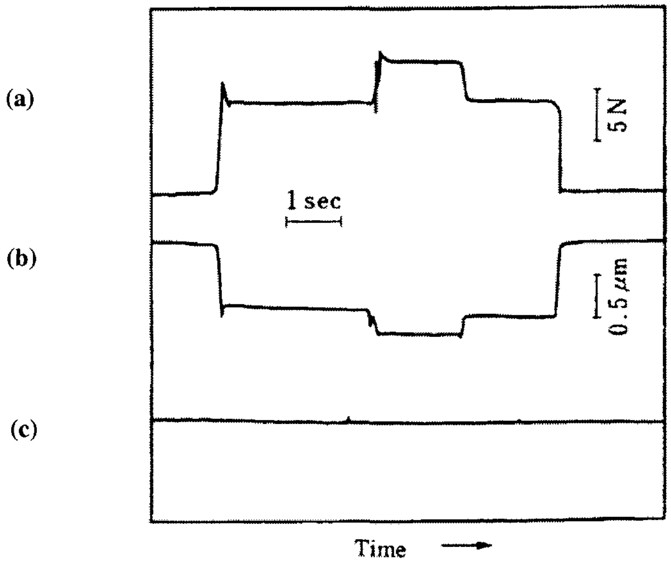

Figure 5.12 Suppression of an external disturbance in a precision lathe machine using feedback: (a) the mechanical load disturbance, (b) the position change of the piezoelectric actuator without feedback, and (c) the position change of the actuator with feedback.

When the condition $|G(j\omega)H(j\omega)|>>1$ is satisfied in the frequency range corresponding to the external disturbance, the feedback control is effective for diminishing the external disturbance. The actuator response in a precision lathe machine to a mechanical step load appears in Figure 5.12. Such a disturbance is generated in the lathe machine when the cutting edge is occasionally caught in a "sticky" material. The remarkable improvement from the 1 μm displacement deviation that occurs without feedback [Figure 5.12(b)] to only 0.2 μm maximum deviation with feedback [Figure 5.12(c)] is clearly demonstrated by these data.

Example Problem 5.4

Describe the *Bode diagram* for the standard second-order system with

$$G(j\omega) = \frac{1}{[(-\omega^2 T^2) + 2\zeta j\omega + 1]} \qquad \text{(P5.4.1)}$$

Solution

The *Bode diagram* is a representation of the transfer function as a function of frequency on a logarithmic scale.

First, let us consider approximate curves for the low and high frequency regions. For $\omega \rightarrow 0$, $|G(j\omega)| = 1$, so that in decibels:

$$dB = 20 \log_{10}(1) = 0 \qquad \text{(P5.4.2)}$$

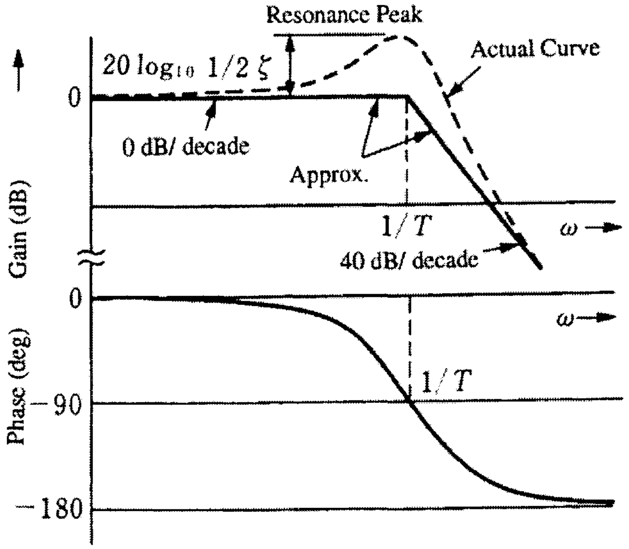

Figure 5.13 The Bode diagram for a standard second-order system.

and the phase is 0° as indicated by the gain and phase curves appearing in Figure 5.13.

For $\omega \rightarrow \infty$:

$$|G(j\omega)| = \left|\frac{1}{(-\omega^2 T^2)}\right| \qquad \text{(P5.4.3a)}$$

so that in decibels:

$$dB = -20 \log_{10}(\omega T)^2 = -40 \log_{10}(\omega T) \qquad \text{(P5.4.3b)}$$

and the phase is -180° as indicated by the gain and phase curves appearing in Figure 5.13.

The low- and high-frequency portions of the gain curve can be approximated with two straight lines as shown in Figure 5.13. The high-frequency portion of the curve is approximated with a straight line having a negative slope of 40 dB/decade (or 12 dB/octave).

Next, we will consider the deviation from these two lines around the bend-point frequency. Substituting $\omega T = 1$ in Equation (P5.4.1) yields:

$$G(j\omega) = \frac{1}{2\zeta j\omega T} = \frac{1}{2\zeta j} \qquad \text{(P5.4.4)}$$

so that the gain and phase become $1/(2\zeta)$ and -90°, respectively. The constant ζ corresponds to the damping constant. If $\zeta=0$, an infinite amplitude will occur at the bend-point frequency (that is, the resonance frequency). When ζ is large ($>1/2$), however, the resonance peak will disappear.

(6) Polarization Control Method

An interesting alternative technique, called *polarization control*, is used to minimize the effect of strain hysteresis in piezoelectric actuators without using a complex closed-loop system. The strain curves for a PZT-based material plotted as a function of applied voltage (proportional to the electric field) and charge (proportional to the polarization) appear in Figure 5.14. Note that the strain curve representing the polarization dependence does not exhibit hysteresis while the curve representing the electric field dependence does.[5] (The reasons for this have already been discussed in Section 2.6.) We see by these trends then that the strain hysteresis that occurs under a voltage control system will be significantly suppressed if polarization control is used instead.

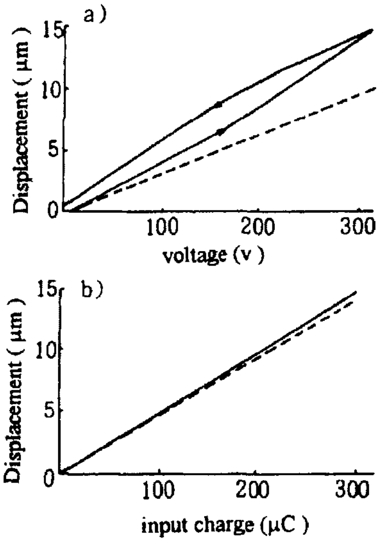

Figure 5.14 The strain curves for a PZT-based material plotted as a function of: (a) applied voltage (proportional to the electric field) and (b) charge (proportional to the polarization). The lack of strain hysteresis in the latter curve demonstrates the usefulness of polarization control for piezoelectric actuators.

An example of a current supply circuit suitable for polarization control is pictured in Figure 5.15. A current proportional to the input voltage, V_{in}, is supplied to the piezoelectric actuator in this circuit. Another noteworthy feature of this current supply is its very high output impedance as compared to the very small output impedance of the conventional voltage supply.

The polarization control technique is effective only for pulse and AC drive methods. When used for DC driving, the resistance of the actuator must be extremely large. Otherwise, charge leakage in the ceramic actuator prevents stable control for quasi-static positioning. A stacked actuator, for example, comprised of 92 layers of PZT ceramic disks (each with a diameter of 20 mm and thickness of 0.5 mm) operated by polarization control is able to maintain its charge only for about 30 minutes.[5]

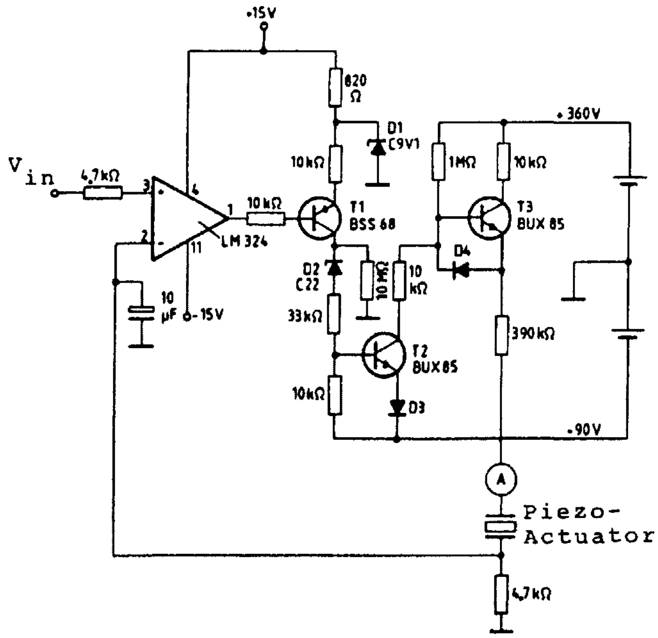
+15V
820 Ω
+360V
D1
C9V1
10kΩ
1MΩ
10kΩ
Vin
4,7kΩ
3
4
1
10kΩ
T1
BSS 68
T3
BUX 85
2
11
LM 324
D2
C22
10MΩ
10 kΩ
D4
10 µF
-15V
33kΩ
390kΩ
T2
BUX85
10kΩ
D3
-90V
A
Piezo-
Actuator
4,7kΩ

Figure 5.15 An example of a drive circuit for polarization control.

5.3 PULSE DRIVE

When a pulsed electric field is applied to a piezoelectric actuator, a mechanical vibration is excited, the characteristics of which depend on the pulse profile. Displacement overshoot and ringing are frequently observed. Quick and precise positioning is difficult to achieve, and moreover can lead to the destruction of the actuator due to the large tensile stress associated with overshoot. We will examine more closely the transient response of a piezoelectric device driven by a pulsed electric field in this section.

(1) The Piezoelectric Equations

If the applied electric field, E, and the stress, X, are small, the strain, x, and the electric displacement, D, induced in a piezoelectric can be represented by the following equations:

$$x_i = s_{ij}^E X_j + d_{mi} E_m \tag{5.47}$$

$$D_m = d_{mi} X_i + K_{mk}^X E_k \tag{5.48}$$

where (i, j = 1, 2, ..., 6; m, k = 1, 2, 3). These are the *piezoelectric equations*. According to the tensor theory presented in Chapter 2, we know that for the lowest symmetry trigonal crystal there are twenty-one independent s_{ij}^E coefficients, eighteen d_{mi} coefficients, and six K_{mk}^X coefficients. We also recognized in that discussion that the number of independent coefficients decreases with increasing crystallographic symmetry. When considering polycrystalline ceramic specimens, the poling direction is typically designated as the *z*-axis. A poled ceramic is isotropic with respect to this *z*-axis and has a Curie group designation $C_{\infty v}$ (∞m). There are 10 non-zero matrix elements (s_{11}^E, s_{12}^E, s_{13}^E, s_{33}^E, s_{44}^E, d_{31}, d_{33}, d_{15}, K_{11}^X, and K_{33}^X) that apply in this case.

When considering the response of an electrostrictive material under DC bias (E_b) the strain is given by:

$$x_i = M_{mi}\,(E_b + E_m)^2 = M_{mi}E_b^2 + 2\,M_{mi}E_bE_m + \delta E_m^2 \tag{5.49}$$

If the alternative definition for d_{mi}:

$$d_{mi} = 2\,M_{mi}\,E_b \tag{5.50}$$

is substituted in Equations (5.47) and (5.48), we can think in terms of an *induced piezoelectric effect* when analyzing the response of an electrostrictive material.

(2) The Transverse and Longitudinal Vibration Modes

The Transverse Vibration Mode

Let's consider a transverse mechanical vibration in the simple piezoelectric ceramic plate with thickness b, width w, and length *l* (b << w << *l*), pictured in Figure 5.16 (and as case (a) in Table 5.2). If the polarization is in the *z* direction and the *x-y* planes are the planes of the electrodes, the extentional vibration in the *x* direction is represented by the following dynamic equation:

$$\rho\frac{\partial^2 u}{\partial t^2} = F = \frac{\partial X_{11}}{\partial x} + \frac{\partial X_{12}}{\partial y} + \frac{\partial X_{13}}{\partial z} \tag{5.51}$$

where u is the displacement in the *x* direction of a small volume element in the ceramic plate. The relationship between the stress, the electric field (only E_z exists) and the induced strain is described by the following set of equations:

$$\begin{aligned} x_1 &= s_{11}^E\,X_1 + s_{12}^E\,X_2 + s_{13}^E\,X_3 + d_{31}\,E_z \\ x_2 &= s_{12}^E\,X_1 + s_{11}^E\,X_2 + s_{13}^E\,X_3 + d_{31}\,E_z \\ x_3 &= s_{13}^E\,X_1 + s_{13}^E\,X_2 + s_{33}^E\,X_3 + d_{33}\,E_z \end{aligned} \tag{5.52}$$

$x_4 = s_{44}{}^E X_4$
$x_5 = s_{44}{}^E X_5$
$x_6 = 2\,(s_{11}{}^E - s_{12}{}^E)\,X_6$

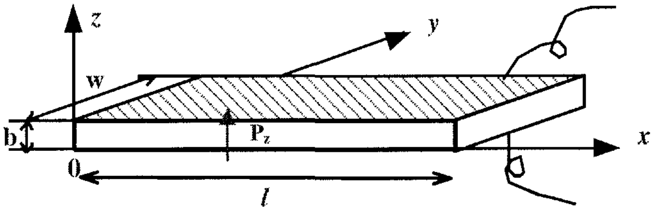

Figure 5.16 Transverse vibration of a rectangular piezoelectric plate.

It is important to note at this point that when an AC electric field of increasing frequency is applied to this piezoelectric plate, length, width and thickness extensional resonance vibrations are excited. If we consider a typical PZT plate with dimensions 100 mm x 10 mm x 1 mm, these resonance frequencies correspond roughly to 10 kHz, 100 kHz and 1 MHz, respectively. We will consider here the fundamental mode for this configuration, the length extensional mode. When the frequency of the applied field is well below 10 kHz, the induced displacement follows the AC field cycle, and the displacement magnitude is given by $d_{31}E_3l$. As we approach the fundamental resonance frequency, a delay in the length displacement with respect to the applied field begins to develop, and the amplitude of the displacement becomes enhanced. At frequencies above 10 kHz, the length displacement no longer follows the applied field and the amplitude of the displacement is significantly reduced.

When a very long, thin plate is driven in the vicinity of this fundamental resonance, X_2 and X_3 may be considered zero throughout the plate. Since shear stress will not be generated by the applied electric field E_z, only the following single equation applies:

$$X_1 = x_1 / s_{11}{}^E - (d_{31} / s_{11}{}^E)\,E_z \qquad (5.53)$$

Substituting Equation (5.53) into Equation (5.51), and assuming that $x_1 = \partial u/\partial x$ and $\partial E_z/\partial x = 0$ (since each electrode is at the same potentials), we obtain the following dynamic equation:

$$\rho \frac{\partial^2 u}{\partial t^2} = \frac{1}{s_{11}^E} \frac{\partial^2 u}{\partial x^2} \qquad (5.54)$$

The Longitudinal Vibration Mode

Let us consider next the longitudinal vibration mode. When the resonator is long in the *z* direction and the electrodes are deposited on each end of the rod as depicted for case (b) in Table 5.2, the following conditions are satisfied:

$$X_1 = X_2 = X_4 = X_5 = X_6 = 0 \text{ and } X_3 \neq 0 \tag{5.55}$$

So that,

$$X_3 = (x_3 - d_{33} E_z) / s_{33}{}^E \tag{5.56}$$

for this configuration. Assuming a local displacement v in the *z* direction, the dynamic equation is given by:

$$\rho \frac{\partial^2 v}{\partial t^2} = \frac{1}{s_{33}^E}\left[\frac{\partial^2 v}{\partial z^2} - d_{33}\frac{\partial E_z}{\partial z}\right] \tag{5.57}$$

The electrical condition for the longitudinal vibration is not $\partial E_z/\partial z = 0$, but rather $\partial D_z/\partial z = 0$, such that:

$$K_3 \frac{\partial E_z}{\partial z} + \frac{d_{33}}{s_{33}^E}\frac{\partial^2 v}{\partial z^2} = 0 \tag{5.58}$$

Substituting Equation (5.58) into Equation (5.57), we obtain:

$$\rho \frac{\partial^2 v}{\partial t^2} = \frac{1}{s_{33}^D}\frac{\partial^2 v}{\partial z^2} \tag{5.59}$$

where:

$$s_{33}^D = \frac{s_{33}^E}{1 + (d_{33}^2 / s_{33}^E K_{33}^X)} = \frac{s_{33}^E}{1 + k_{33}^E} \tag{5.60}$$

The dynamic equations for other vibration modes can be obtained in a similar fashion using the elastic boundary conditions in Table 5.2.

Table 5.2 Characteristics of various resonators with different modes of vibration.[9]

	Factor	Boundary Conditions	Resonator Shape	Definition
a	k_{31}	$X_1 \neq 0,\ X_2 = X_3 = 0$ $x_1 \neq 0,\ x_2 \neq 0,\ x_3 \neq 0$	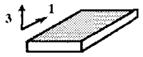	$\dfrac{d_{31}}{\sqrt{s^E_{11} K^X_{33}}}$
b	k_{33}	$X_1 = X_2 = 0,\ X_3 \neq 0$ $x_1 = x_2 \neq 0,\ x_3 \neq 0$	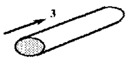 Fundamental Mode	$\dfrac{d_{33}}{\sqrt{s^E_{33} K^X_{33}}}$
c	k_p	$X_1 = X_2 \neq 0,\ X_3 = 0$ $x_1 = x_2 \neq 0,\ x_3 \neq 0$	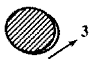 Fundamental Mode	$k_{31}\sqrt{\dfrac{2}{1-\sigma}}$
d	k_t	$X_1 = X_2 \neq 0,\ X_3 \neq 0$ $x_1 = x_2 = 0,\ x_3 \neq 0$	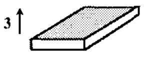 Thickness Mode	$k_{33}\sqrt{\dfrac{K_{33}}{c^D_{33}}}$
e	k_p'	$X_1 = X_2 \neq 0,\ X_3 \neq 0$ $x_1 = x_2 \neq 0,\ x_3 = 0$	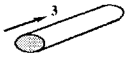 Radial Mode	$\dfrac{k_p - A k_{33}}{\sqrt{1-A^2}\sqrt{1-k^2_{33}}}$
f	k_{31}'	$X_1 \neq 0,\ X_2 \neq 0, X_3 = 0$ $x_1 \neq 0,\ x_2 = 0,\ x_3 \neq 0$	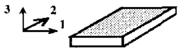 Width Mode	$\dfrac{k_{31}}{\sqrt{1-k^2_{31}}}\sqrt{\dfrac{1+\sigma}{1-\sigma}}$
g	k_{31}''	$X_1 \neq 0,\ X_2 = 0,\ X_3 \neq 0$ $x_1 \neq 0,\ x_2 \neq 0,\ x_3 \neq 0$	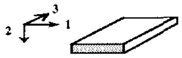 Width Mode	$\dfrac{k_{31} - B k_{33}}{\sqrt{1-k^2_{33}}}$
h	k_{33}'''	$X_1 \neq 0,\ X_2 \neq 0,\ X_3 \neq 0$ $x_1 \neq 0,\ x_2 = 0,\ x_3 = 0$	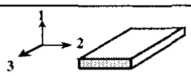 Thickness Mode	$\dfrac{\sqrt{\dfrac{(k_p - A k_{33})^2}{1-A^2} - (k_{31} - B k_{33})^2}}{1 - k^2_{33} - (k_{31} - B k_{33})^2}$
i	k_{33}'	$X_1 \neq 0,\ X_2 = 0,\ X_3 \neq 0$ $x_1 = 0,\ x_2 \neq 0,\ x_3 \neq 0$	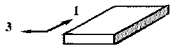 Width Mode	$\dfrac{k_{33} - B k_{31}}{\sqrt{(1-B^2)(1-k^2_{31})}}$
j	$k_{24}=k_{15}$	$X_1 = X_2 = X_3 = 0, X_4 \neq 0$ $x_1 = x_2 = x_3 = 0,\ x_4 \neq 0$		$\dfrac{d_{31}}{\sqrt{K^X_{11}\ s^E_{44}}}$

Here : $A = \dfrac{\sqrt{2}\, s^E_{13}}{\sqrt{s^E_{33}\,(s^E_{11} + s^E_{12})}}, \quad B = \dfrac{s^E_{13}}{\sqrt{s^E_{11}\, s^E_{33}}}$

Consideration of the Loss

When we consider the mechanical loss of the piezoelectric material, which is viscoelastic and proportional to the strain, the dynamic equations (5.54) and (5.59) must be modified.[6]

The transverse vibration mode is now described by:

$$\rho \frac{\partial^2 u}{\partial t^2} = \frac{1}{s_{11}^E}\left[\frac{\partial^2[u + \delta(\partial u / \partial t)]}{\partial x^2}\right] \tag{5.61}$$

and the longitudinal vibration mode by:

$$\rho \frac{\partial^2 v}{\partial t^2} = \frac{1}{s_{33}^D}\left[\frac{\partial^2[v + \delta(\partial v / \partial t)]}{\partial z^2}\right] \tag{5.62}$$

Since Equations (5.54) and (5.59) [and, therefore, Equations (5.61) and (5.62)]) have very similar forms, we will consider just the transverse vibration mode here as an example of how both cases might be treated.

Solution for Transverse Vibration Mode

Let us solve Equation (5.54) using the Laplace transform. Denoting the Laplace transforms of $u(t,x)$ and $E_z(t)$ as $U(s,x)$ and $E^{\sim}(s)$, respectively, Equation (5.54) is transformed by Theorem (f) to:

$$\rho s_{11}^E s^2 U(s,x) = \frac{\partial^2 U(s,x)}{\partial x^2} \tag{5.63}$$

We will assume the following *initial conditions*:

$$u(0,x) = 0 \quad \text{and} \quad \frac{\partial[u(0,x)]}{\partial t} = 0 \tag{5.64}$$

We may also make use of the fact that:

$$\rho\, s_{11}^E = 1/v^2 \tag{5.65}$$

where v is the speed of sound in the piezoelectric ceramic, to obtain a general solution:

$$U(s,x) = A\, e^{(sx/v)} + B\, e^{-(sx/v)} \tag{5.66}$$

The constants A and B can be determined by applying the *boundary conditions* at x= 0 and l:

$$X_1 = \frac{(x_1 - d_{31}E_z)}{s_{11}^E} = 0 \qquad (5.67)$$

We may also make use of the fact that:

$$L[x_1] = (\partial U/\partial x) = A(s/v)e^{(sx/v} - B(s/v)e^{-(sx/v)} \qquad (5.68)$$

In conjunction with the boundary conditions at x= 0 and l to yield:

$$A(s/v) - B(s/v) = d_{31}E^{\sim} \qquad (5.69a)$$
$$A(s/v)e^{(sl/v)} - B(s/v)e^{-(sl/v)} = d_{31}E^{\sim} \qquad (5.69b)$$

Thus, we obtain:

$$A = \frac{d_{31}E^{\sim}(1 - e^{-sl/v})}{(s/v)(e^{sl/v} - e^{-sl/v})} \qquad (5.70)$$

$$B = \frac{d_{31}E^{\sim}(1 - e^{sl/v})}{(s/v)(e^{sl/v} - e^{-sl/v})} \qquad (5.71)$$

and, consequently, Equations (5.66) and (5.68) become:

$$U(s,x) = \frac{d_{31}E^{\sim}(v/s)[e^{-s(l-x)/v} + e^{-s(l+x)/v} - e^{-sx/v} - e^{-s(2l-x)/v}]}{(1 - e^{-2sl/v})} \qquad (5.72)$$

$$L[x_1] = \frac{d_{31}E^{\sim}[e^{-s(l-x)/v} + e^{-s(l+x)/v} - e^{-sx/v} - e^{-s(2l-x)/v}]}{(1 - e^{-2sl/v})} \qquad (5.73)$$

The inverse Laplace transforms of Equations (5.72) and (5.73) now provide the displacement u(t,x) and strain x_1(t,x). Making use of the expansion series

$$1/(1 - e^{-2sl/v}) = 1 + e^{-2sl/v} + e^{-4sl/v} + e^{-6sl/v} + \cdots \qquad (5.74)$$

The strain, x_1(t,x), can now be obtained by shifting the $d_{31}E_z$(t) curves with respect to t according to Theorem (e). We may also consider that since u(t, l/2) = 0 [from U(s, l/2) = 0] and u(t,0)=-u(t, l) [from U(s, 0)=–U(s, l)], the total displacement of the plate device Δl becomes equal to 2u(t, l). We finally arrive at the following:

$$U(s,l) = \frac{d_{31}E^{\sim}(v/s)(1 - e^{-sl/v})}{(1 + e^{-sl/v})} = d_{31}E^{\sim}(v/s)[\tanh(sl/2v)] \qquad (5.75)$$

(i) *Response to a Rectangular Pulse Voltage*

We will now consider the response to a rectangular pulse voltage such as is pictured in the lower left-hand corner of Figure 5.17. We begin by substituting:

$$E^{\sim}(s) = (E_o/s)\,(1 - e^{-(nls)/v}) \tag{5.76}$$

into Equation (5.75), which will allow us to obtain the displacement Δl for n = 1, 2 and 3. The quantity n is a time scale based on half the resonance period of the piezoelectric plate.

For n=1,

$$U(s,l) = \frac{d_{31}\,E_o\,(v/s^2)(1-e^{-sl/v})^2}{(1+e^{-sl/v})}$$

$$= d_{31}\,E_o\,(v/s^2)[1 - 3e^{-sl/v} + 4e^{-2sl/v} - 4e^{-3sl/v} + \cdots] \tag{5.77}$$

Notice that the base function of U(s,l), $1/s^2$, gives the base function of u(t, l) in terms of t. The inverse Laplace transform of Equation (5.77) yields:

$$\begin{array}{ll}
u(t,l) = d_{31}\,E_o\,v\ t & 0 < t < l/v \\
u(t,l) = d_{31}\,E_o\,v\,[t - 3(t - l/v)] & l < t < 2l/v \\
u(t,l) = d_{31}\,E_o\,v\,[t - 3(t - l/v) + 4(t - 2l/v)] & 2l/v < t < 3l/v \\
 & \cdots
\end{array} \tag{5.78}$$

The transient displacement, Δl, produced by the rectangular pulse voltage is pictured in Figure 5.17(a) for n=1. The resonance period of this piezoelectric plate corresponds to ($2l$/v). Notice how under these conditions continuous ringing occurs.

For n=2,

$$U(s,l) = d_{31}E_o\,(v/s^2)\,(1 - 2e^{-sl/v} + e^{-2sl/v}) \tag{5.79}$$

Thus,

$$\begin{array}{ll}
u(t,l) = d_{31}E_o\,v\ t & 0 < t < l/v \\
u(t,l) = d_{31}\,E_o\,v\,[t - 2(t - l/v)] & l < t < 2l/v \\
u(t,l) = d_{31}\,E_o\,v\,[t - 2(t - l/v) + (t - 2l/v)] = 0. & 2l/v < t
\end{array} \tag{5.80}$$

In this case, the displacement, Δl, occurs in a single pulse and does not exhibit ringing as depicted in Figure 5.17(b).

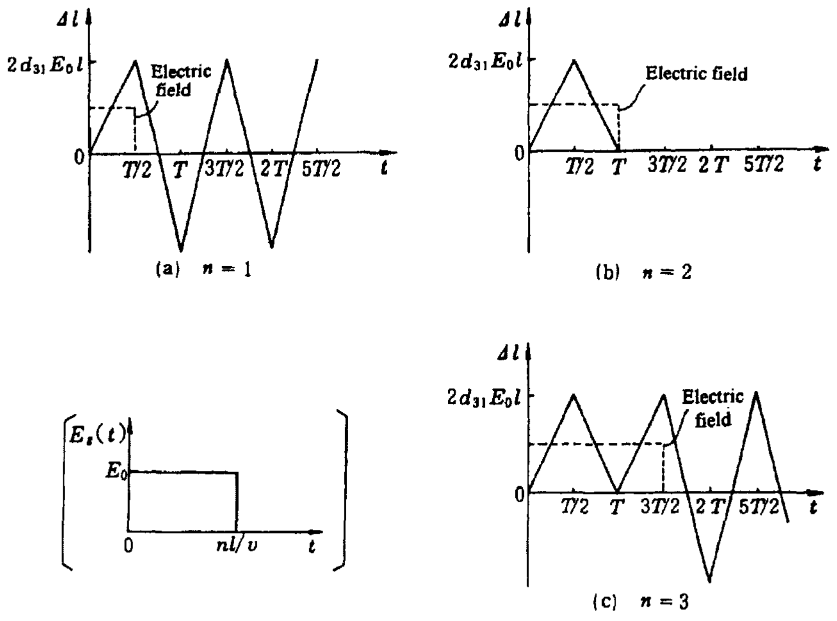

Figure 5.17 Transient displacement Δl produced by a rectangular pulse voltage. (Note that the time interval, T=(2l/v), corresponds to the resonance period of the piezoelectric plate.)

For n=3, U(s, l) is again expanded as an infinite series:

$$U(s,l) = \frac{d_{31}E_0(v/s^2)(1-e^{-3sl/v})(1-e^{-sl/v})}{(1+e^{-sl/v})}$$
$$= d_{31}E_0(v/s^2)[1-2e^{-sl/v}+2e^{-2sl/v}-3e^{-3sl/v}+4e^{-4sl/v}-4e^{-5sl/v}+\cdots] \quad (5.81)$$

The displacement response for this case is pictured in Figure 5.17(c).

So we see from this example that *when a piezoelectric actuator is driven by a rectangular pulse, the mechanical ringing is completely suppressed when the pulse width is adjusted exactly to the resonance period* of the sample (that is, T=2l/v, or integral multiples of the resonance period).

How precisely does the pulse width need to be adjusted? The calculated transient vibration for n=1.9 appears in Figure 5.18. Notice the small amount of ringing that occurs after the main pulse. The actual choice of n, then, will depend on the amount of ringing that can be tolerated for a given application.

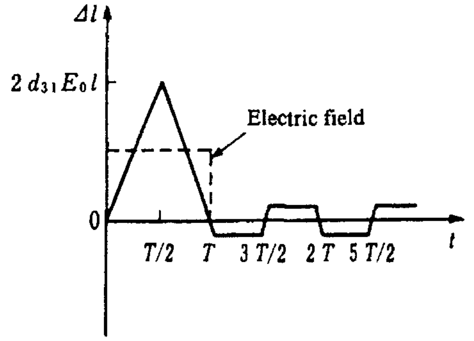

Figure 5.18 Transient displacement, Δl, produced by a rectangular pulse voltage (n = 1.9).

(ii) *Response to a pseudo step voltage*

We can take our discussion one step further by considering the response to a pseudo step voltage such as is pictured in the upper left-hand corner of Figure 5.19. We begin this time by substituting:

$$E^{\tilde{}}(s) = (E_o v/n\, l s^2)\,(1-e^{-nls/v}) \tag{5.82}$$

into Equation (5.75). Let us again obtain the displacement Δl for n=1, 2 and 3.

For n=1,

$$\begin{aligned} U(s,l) &= \frac{(d_{31}E_o/l)(v^2/s^3)(1-e^{-sl/v})^2}{(1+e^{-sl/v})} \\ &= (d_{31}E_o/l)(v^2/s^3)[1-3e^{-sl/v}+4e^{-2sl/v}-4e^{-3sl/v}+\cdots] \end{aligned} \tag{5.83}$$

Notice that the base function of U(s, l), $1/s^3$, will lead to a base function of u(t, l) in the form $t^2/2$ (parabolic curve) such that:

$$\begin{aligned} u(t,l) &= (d_{31}E_o v^2/2l)\, t^2 && 0 < t < l/v \\ u(t,l) &= (d_{31}E_o v^2/2l)\, [t^2 - 3(t-l/v)^2] && l < t < 2l/v \\ u(t,l) &= (d_{31}E_o v^2/2L)\, [t^2 - 3(t-l/v)^2 + 4(t-2l/v)^2] && 2l/v < t < 3l/v \end{aligned} \tag{5.84}$$

The transient displacement for an actuator driven by the pseudo step voltage pictured in Figure 5.19(a) is seen to exhibit continuous ringing. Notice that this curve is actually a sequence of parabolic curves. It is not sinusoidal.

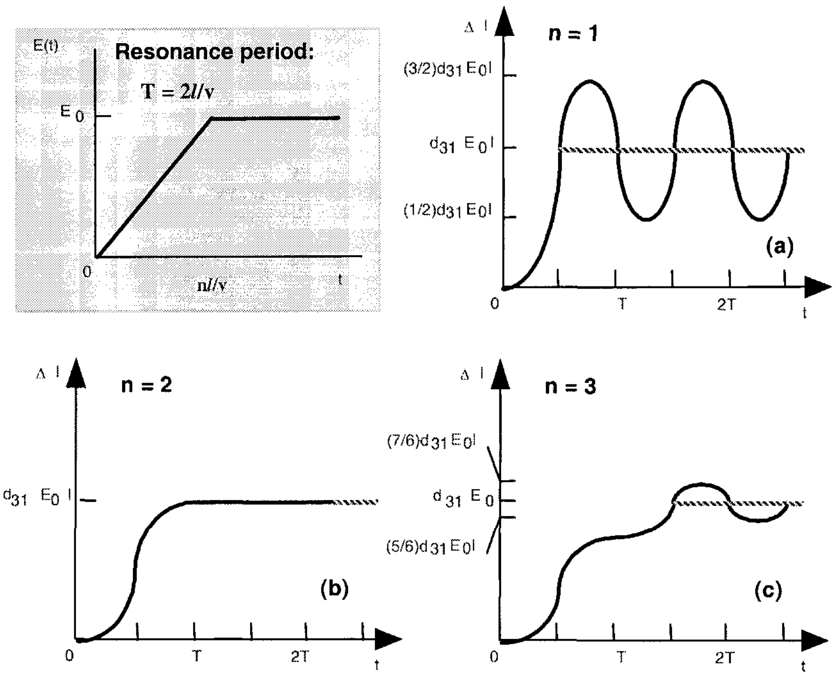

Figure 5.19 Transient displacement Δl produced by a pseudo step voltage.

For n = 2,

$$U(s, l) = (d_{31}E_o/2\,l)\,(v^2/s^3)\,[1 - 2e^{-sl/v} + e^{-2sl/v}] \tag{5.85}$$

Thus,

$$\begin{aligned}
u(t, l) &= (d_{31}E_o v^2/4l)\,t^2 && 0 < t < l/v \\
u(t, l) &= (d_{31}E_o v^2/4l)\,[t^2 - 2\,(t - l/v)^2] && l < t < 2l/v \\
u(t, l) &= (d_{31}E_o v^2/4l)\,[t^2 - 2\,(t - l/v)^2 + (t - 2l/v)^2] && \\
&= (d_{31}E_o l/2) && 2l/v < t
\end{aligned} \tag{5.86}$$

No ringing is apparent in the response for this case represented in Figure 5.19(b). *When the applied field E^{-} includes the term $(1+e^{-sl/v})$, the expansion series terminates in finite terms, leading to a complete suppression of mechanical ringing.*

For n = 3, U(s, l) is again expanded as an infinite series:

$$U(s, l) = (d_{31}E_o/3l)(v^2/s^3)[1 - 2e^{-sl/v} + 2e^{-2sl/v} - 3e^{-3sl/v} + 4e^{-4sl/v} - 4e^{-5sl/v} + \ldots] \tag{5.87}$$

The displacement response for this condition is represented by the curve appearing in Figure 5.19(c).

Experimental Observations of Transient Vibrations

Experimental results are presented here for the transient displacement response of a piezoelectric actuator. A PZT-based bimorph actuator with a mechanical quality factor $Q_m=1000$ (low loss!) was used for the experiments.[7] The bimorph tip displacement was monitored with an eddy current type non-contact sensor. The resonance frequency of this bimorph is about 100 Hz. The response of the bimorph to a rectangular pulse and a pseudo step voltage are shown in Figures 5.20(a) and 5.20(b), respectively. Notice how ringing is completely eliminated in the both cases when the pulse width or the rise time of the pseudo step is adjusted exactly to the resonance period of the bimorph. It should be noted as well how the displacement response is essentially a sequence of triangular or parabolic curves, for the rectangular pulse or the pseudo step inputs, respectively.

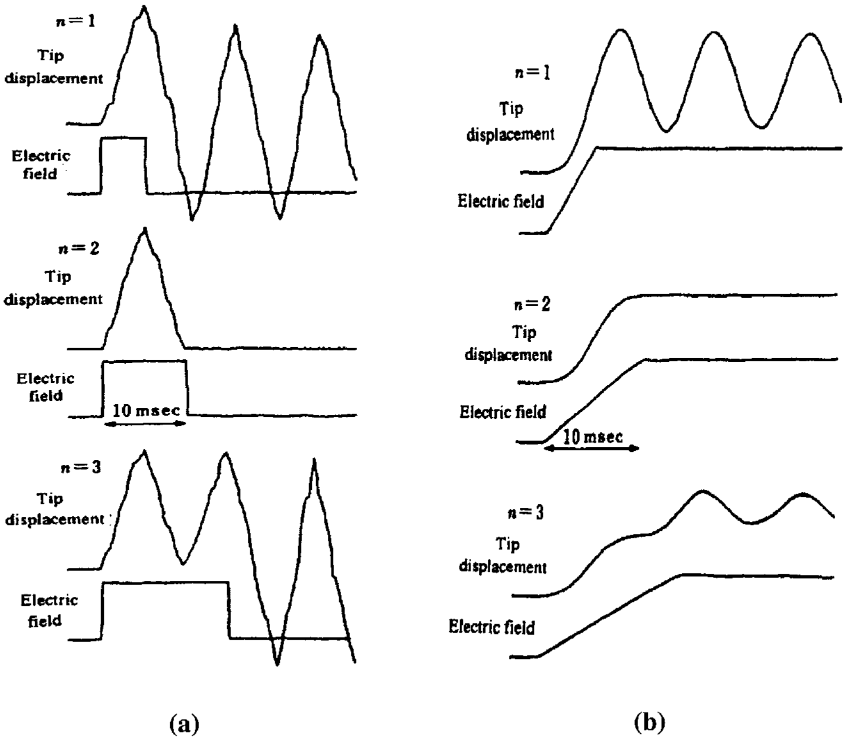

Figure 5.20 Bimorph tip displacement produced by: (a) a rectangular pulse voltage and (b) a pseudo step voltage.[7]

Consideration of the Loss

Recall that in order to properly account for loss effects Equation (5.61) must be used for the transverse vibration rather than Equation (5.54). The displacement U(s,*l*) can then be obtained by making the substitution:

$$s \to \frac{s}{\sqrt{1+\delta s}} \tag{5.88}$$

in Equation (5.75). This solution has not yet been obtained in an explicit form. Approximate solutions for the piezoelectric resonance state have been determined by Ogawa.[6]

Experimental results appear in Figure 5.21.[8] The displacement Δl produced by a rectangular pulse voltage observed in this investigation are similar to the results shown in Figure 5.20, except for the vibrational damping. Once again we see that when the pulse width of this rectangular voltage is adjusted to the piezoelectric resonance period, T, or integral multiples of it, the vibrational ringing is eliminated.

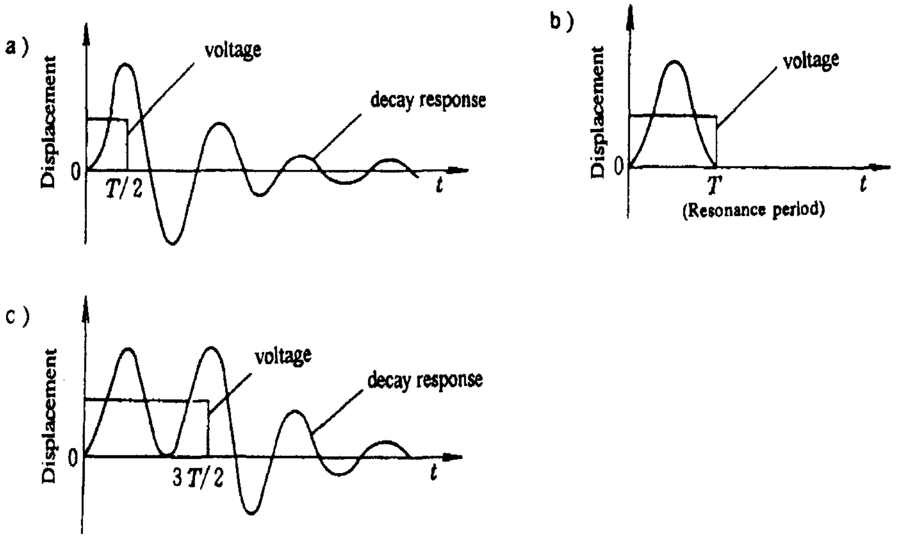

Figure 5.21 Displacement response of a lossy piezoelectric actuator under a rectangular pulse voltage.[8]

(3) Pulse Width Modulation Method

The *pulse width modulation* (*PWM*) method has been used to control an oil pressure servo valve (see Section 8.4).[9] The principle of the PWM method is illustrated in Figure 5.22. A rectangular wave (RW) is generated, with a pulse width determined by the intersection of the standard saw wave (SW) and the command voltage wave (CW), and then amplified and applied to a PZT bimorph flapper. When the bimorph flapper is driven by a rectangular wave ($\pm V_{max}$) of about 1 kHz, the oil pressure outside the nozzle maintains a constant value (as if the flapper were located at some average position) proportional to the *duty factor* (the ratio of the period during which a pulse is sustained over the repetition period), because the response of the oil flow is much slower (about 50 Hz). The oil pressure outside the nozzle, and consequently the spool position, can be controlled in a linear fashion by the command signal (CS), thus diminishing the nonlinearity and hysteresis associated with the piezoelectric response of the PZT (see Figure 5.23).

Engineering control theory guarantees that the time averaged PWM output is proportional to the command input, if the following conditions are satisfied:

1) The ratio of the carrier frequency, f_c, to the input command frequency, f_e, should be greater than 7.
2) The carrier frequency must be high enough compared to the system response to eliminate all ripple in the system output.

As an example, let's consider an oil pressure valve like the one just described, which has a carrier wave frequency (RW) of 1250 Hz. Then the command frequency must not exceed 1250 Hz/7=180 Hz. Where the carrier frequency is much higher than the oil flow response (50 Hz) of the valve, the second condition is also satisfied.

The PWM is very attractive from an engineering control point of view, in particular for eliminating the hysteresis problems that will occur in an open-loop method. However, in general, special care must be taken when utilizing a bimorph actuator. First, the lifetime of the bimorph is limited to 10^8 cycles when it is driven at maximum voltage. Delamination of the bonding layer may occur after only 10 hours when it is operated continuously at the 1 kHz carrier frequency. Second, since the bimorph motion is associated with a large hysteresis, it tends to generate a considerable amount of heat, accelerating the piezoelectric aging effect.

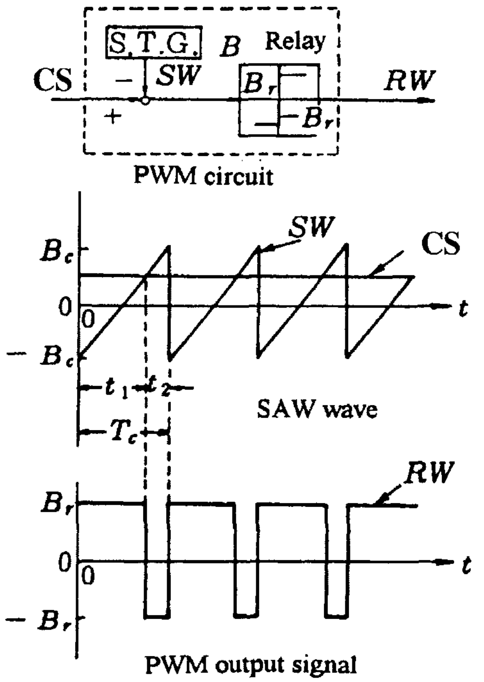
S.T.G.
B
Relay
CS
−
SW
+
B_r
$-B_r$
RW
PWM circuit
B_c
0
$-B_c$
SW
CS
t
0
t_1
t_2
T_c
SAW wave
RW
B_r
0
$-B_r$
0
t
PWM output signal

Figure 5.22 Demonstration of the pulse width modulation (PWM) method used to control an oil pressure servo valve. The duty factor of the rectangular wave (RW) is controlled by the command signal (CS).[9]

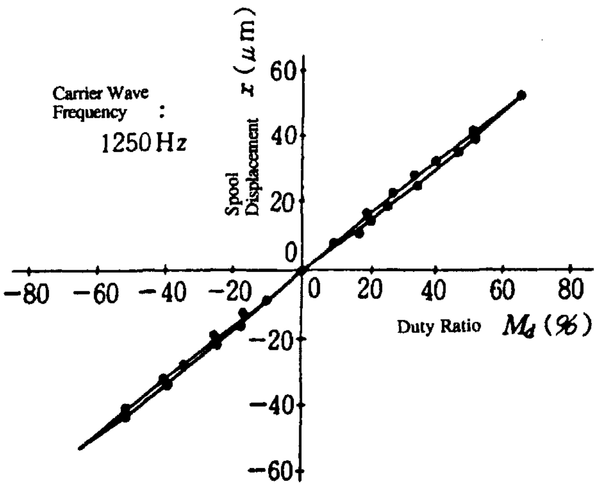

Figure 5.23 Static characteristics of the oil pressure servo valve.[9]

5.4 RESONANCE DRIVE

When an alternating electric field is applied to a piezoelectric ceramic, mechanical vibration is excited, and if the drive frequency is adjusted to the mechanical resonance frequency of the device, a large resonant strain is generated. This phenomenon is called *piezoelectric resonance* and is very useful for applications such as energy trap devices and actuators. We will consider in this section the steady state response of such a device to a sinusoidally varying electric field.

(1) The Electromechanical Coupling Factor

Let us consider first the *electromechanical coupling factor, k,* which represents the energy transduction rate in an electromechanical transducer. (Please refer to Section 3.5 and Reference 10). When an external field is applied on a piezoelectric device to generate a mechanical deformation, a formal definition of k may be written in terms of the stored and input energies as:

$$k^2 = \frac{\text{Mechanical Stored Energy}}{\text{Electrical Input Energy}} \qquad (5.89a)$$

Alternatively, it can also be defined by:

$$k^2 = \frac{\text{Electrical Stored Energy}}{\text{Mechanical Input Energy}} \qquad (5.89b)$$

The internal energy of a piezoelectric vibrator is given by the summation of mechanical energy U_M ($=\int x dX$) and electrical energy U_E ($=\int D dE$). The total energy, U, is calculated as follows, when the linear piezoelectric equations [Equations (5.47) and (5.48)] apply:

$$\begin{aligned} U &= U_M + U_E \\ &= [(1/2)s_{ij}{}^E X_j X_i + (1/2) d_{mi} E_m X_i] + [(1/2) d_{mi} X_i E_m + (1/2)\varepsilon_0 K_{mk}{}^X E_k E_m] \qquad (5.90) \end{aligned}$$

Here, the terms including the elastic compliance, s, and the dielectric constant, K, represent the purely mechanical and electrical energies (U_{MM} and U_{EE}), respectively, The terms including the piezoelectric strain coefficient, d, represent the energy transduction from electrical to mechanical energy and vice versa through the piezoelectric effect. Thus, the electromechanical coupling factor, k, can also be defined by:

$$k = \frac{U_{ME}}{\sqrt{U_{MM}\, U_{EE}}} \qquad (5.91)$$

The value of k will depend on the vibration mode (that is, several values could be obtained from a single ceramic sample corresponding to the different modes of vibration), and can be positive or negative. (The absolute value |k| can be used in the discussion of energy.) Some typical vibration modes appear in Table 5.2 with their associated coupling factors.[9]

It is important to note that the electromechanical coupling factor can also be expressed in the general form:

$$k^2 = d^2 / (K^X s^E) \tag{5.92}$$

which better reflects how the value of k will depend on the mode of vibration and the anisotropic dielectric and elastic properties of the material. It should not be surprising then to find that different values of the electromechanical coupling factor can be obtained for a single specimen.

As an example, let's examine the following data measured for a typical PZT-based piezoelectric ceramic sample. If we first compare the magnitudes of k_{33} and k_{31}, it is generally observed that k_{33} (69%) > k_{31} (39%) because the transverse piezoelectric strain is about 1/3 the longitudinal strain for a given applied electric field strength. Comparing k_{31} and k_p (the planar coupling factor), we general find that k_{31} (39%) < k_p (57%) because k_p is a measure of the material's response that includes the contribution of the (2-dimensional) planar mode, which effectively leads to a higher energy conversion. When we compare k_{33} and k_t (the thickness coupling factor), it is found in most cases that k_{33} (69%) > k_t (48%). This is because the thickness mode is 2-dimensionally clamped, which leads to a lower energy conversion. When we characterize the action of a bimorph, the effective electromechanical coupling factor k_{eff} can be defined for the bending vibration mode. We find in this case that k_{eff} is much smaller (10%) than k_{31} (39%), even though the bending action occurs through the d_{31} piezoelectric strain coefficient. It should be noted as well that k_{15} (61%) tends to be very large in perovskite type piezoelectric ceramics, due to their relatively large shear strain coefficient, d_{15}.

The electromechanical coupling factor is not related to the efficiency of the actuator, which is defined by the ratio of the output mechanical energy to the consumed electrical energy. When the ceramic is deformed by an external electric field, the input electrical energy is, of course, larger than the output mechanical energy. However, the ineffective electrical energy is stored as electrostatic energy in the actuator (the ceramic actuator is also a capacitor!), and reverts to the power supply in the final process of an operating cycle. The efficiency is determined only by the losses manifested as hystereses in the polarization versus electric field, strain versus stress, and strain versus electric field curves (see Chapter 6). Thus, the efficiency of a piezoelectric device is usually more than 97%.

Example Problem 5.5

Calculate the electromechanical coupling factor k_{ij} of a piezoelectric ceramic vibrator for the following vibration modes (see Figure 5.24):

(a) Longitudinal length extension mode ($\parallel$ E): k_{33}
(b) Planar extension mode of the circular plate: k_p

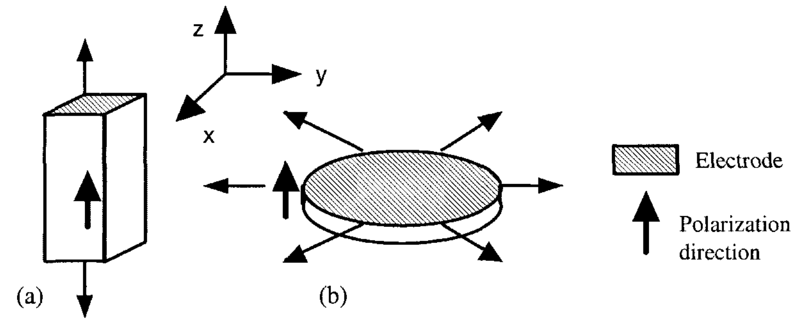

Figure 5.24 Two vibration modes of a piezoelectric device: (a) the longitudinal length extension and (b) the planar extensional modes.

Solution

We will start with the expression:

$$\begin{aligned} U &= (1/2)\, s_{ij}^E X_j X_i + 2\,(1/2)\, d_{mi} E_m X_i + (1/2)\, K_{mk}^X E_k E_m \\ &= U_{MM} + 2\, U_{ME} + U_{EE} \end{aligned} \tag{P5.5.1}$$

and make use of the following definition of the electromechanical coupling factor:

$$k = \frac{U_{ME}}{\sqrt{U_{MM}\, U_{EE}}} = \frac{d^2}{\sqrt{K^X s^E}} \tag{P5.5.2}$$

(a) The piezoelectric equations corresponding to the longitudinal extension are:

$$x_3 = s_{33}^E X_3 + d_{33} E_3$$
$$D_3 = d_{33} X_3 + K_{33}^X E_3$$

So that:

$$\rightarrow\rightarrow \quad k_{33} = \frac{d_{33}}{\sqrt{s_{33}^E K_{33}^X}} \tag{P5.5.3}$$

(b) The piezoelectric equations corresponding to the planar extension are:

$$x_1 = s_{11}^E X_1 + s_{12}^E X_2 + d_{31} E_3$$
$$x_2 = s_{12}^E X_1 + s_{22}^E X_2 + d_{32} E_3$$
$$D_3 = d_{31} X_1 + d_{32} X_2 + K_{33}^X E_3$$

Assuming axial symmetry, $s_{11}^E = s_{22}^E$, $d_{31} = d_{32}$ and $X_1 = X_2$ (= X_p), which allows us to further simplify these equations to:

$$x_1 + x_2 = 2\,(s_{11}^E + s_{12}^E)\,X_p + 2\,d_{31}\,E$$
$$D_3 = 2\,d_{31}\,X_p + K_{33}^X E_3$$

So that:

$$\rightarrow\rightarrow \quad k_p = \frac{2d_{31}}{\sqrt{2(s_{11}^E + s_{12}^E)K_3^X}} = \frac{d_{31}\sqrt{2/(1-\sigma)}}{\sqrt{s_{11}^E K_{33}^X}} = k_{31}\sqrt{2/(1-\sigma)} \qquad \text{(P5.5.4)}$$

where σ is Poisson's ratio given by:

$$\sigma = -s_{12}^E / s_{11}^E \qquad \text{(P5.5.5)}$$

---

(2) Piezoelectric Resonance

Let us consider once again a piezoelectric rectangular plate in which the transverse piezoelectric effect excites the length extensional mode as depicted in Figure 5.16. We will apply a sinusoidal electric field ($E_z=E_0 e^{j\omega t}$) to the plate and consider the *standing transverse vibration mode* for t >> 0. The following expression for the strain coefficient, $x_1(t, x)$, can be obtained by means of Equation (5.73):

$$\begin{aligned} x_1(t,x) &= d_{31} E_o e^{j\omega t}\left[\frac{(e^{-j\omega(l-x)/v} - e^{-j\omega(l+x)/v} + e^{-j\omega x/v} - e^{-j\omega(2l-x)/v})}{(1 - e^{-2j\omega l/v})}\right] \\ &= d_{31} E_o e^{j\omega t}\left[\frac{\sin[\omega(l-x)/v] + \sin[\omega x/v]}{\sin[\omega l/v]}\right] \end{aligned} \qquad (5.93)$$

where s = jω.

Here, the speed of sound, v, is given by:

$$v = \frac{1}{\sqrt{\rho s_{11}^E}} \qquad (5.94)$$

Electrical Impedance

The piezoelectric actuator is an electronic component from the viewpoint of the driving power supply, thus its *electrical impedance* [=*v*(applied)/*i*(induced)] plays an important role. The induced current is just the rate change of the electric displacement D_z, which can be calculated by making use of the definition for D given by Equation (5.48):

$$i = w\left[\frac{\partial}{\partial t}\left(\int_0^l D_z dx\right)\right] = j\omega w \int_0^l \left[\left(K_{33}^X - \left(\frac{d_{31}^2}{s_{11}^E}\right)\right)E_z + \left(\frac{d_{31}\, x_1}{s_{11}^E}\right)\right]dx \qquad (5.95)$$

Substituting the expression given by Equation (5.93) for x_1 in this last equation and this expression for current into the defining equation for the admittance, Y, yields:

$$\begin{aligned} Y &= \frac{1}{Z} = \frac{i}{v} = \frac{i}{E_z b} \\ &= \left(\frac{j\omega w l}{b}\right)K_{33}^{LC}\left[1 + \left(\frac{d_{31}^2}{K_{33}^{LC} s_{11}^E}\right)\left(\frac{\tan(\omega l/2v)}{(\omega l/2v)}\right)\right] \end{aligned} \qquad (5.96)$$

This describes the admittance of a mechanically free (unclamped) sample. Here, the width of the plate is w, its length *l*, and its thickness, b. The applied voltage is *v*, the induced current is *i*, and the speed of sound is v. The quantity K_{33}^{LC} is called the *longitudinally clamped dielectric constant*, which is given by:

$$K_{33}^{LC} = K_{33}^{X} - (d_{31}^2/s_{11}^E) \qquad (5.97)$$

The resonance state is defined when the admittance becomes infinite (or the impedance becomes zero). It is described by Equation (5.96) when: $\tan(\omega l/2v)=\infty$ and $\omega l/2v = \pi/2$. The resonance frequency, f_R, can thus be defined as:

$$f_R = \frac{v}{2l} = \frac{1}{2l\sqrt{\rho\, s_{11}^E}} \qquad (5.98)$$

In contrast, the antiresonance state is realized when the admittance becomes zero (and the impedance infinite). Under these conditions:

$$\left(\frac{\omega_A l}{2v}\right)\cot\left(\frac{\omega_A l}{2v}\right) = \frac{-d_{31}^2}{K_{33}^{LC} s_{11}^E} = \frac{-k_{31}^2}{(1-k_{31}^2)} \qquad (5.99)$$

where ω_A is the angular antiresonance frequency and, according to Table 5.2, the electromechanical coupling factor, k_{31}, is given by:

$$k_{31} = \frac{d_{31}}{\sqrt{s_{11}^{E} K_{33}^{X}}} \tag{5.100}$$

Strain Distribution in the Sample

The position dependence of x_1 may be described by the following expression derived from Equation (5.93):

$$x_1(x) = d_{31} E_o \left[\frac{\cos[\omega(l - 2x)/2v]}{\cos(\omega l/2v)} \right] \tag{5.101}$$

The resonance and antiresonance states may be interpreted in terms of the following conceptual model. In a material with high electromechanical coupling (k close to 1), the resonance or antiresonance states appear for $\tan(\omega l/2v)=\infty$ or 0 (that is, when $\omega l/2v=(m-1/2)\pi$ or $m\pi$, where m is an integer), respectively. The strain distribution, $x_1(x)$, as given by Equation (5.101) for each state is illustrated in Figure 5.25. In the resonance state, large strains and large changes in the "motional" capacitance are induced, and current can flow easily. This is manifested in a large *motional admittance*. On the other hand, at antiresonance, the strains induced in the device exactly cancel, leading to no change in the capacitance and a high impedance. This condition is manifested by a motional admittance of zero.

When we consider a typical case of $k_{31}=0.3$, we find that the antiresonance frequency is closer to the resonance frequency. A material with low coupling coefficients exhibits an antiresonance mode where the capacitance change due to the size change is compensated completely by the charging current. In other words, the total admittance is the sum of the motional admittance and the damped admittance.

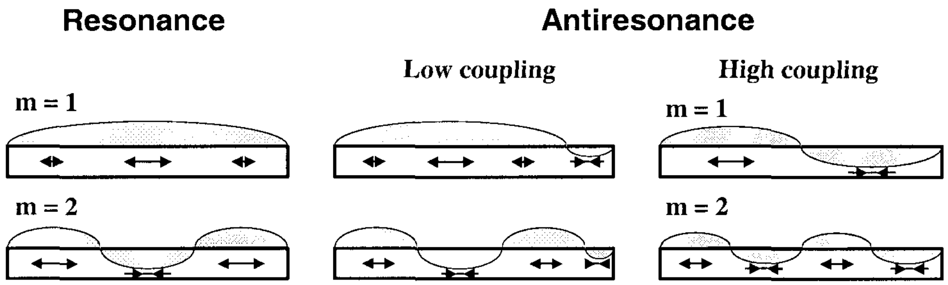

Figure 5.25 The strain distribution, $x_1(x)$, for the resonance and antiresonance states of a piezoelectric actuator.

The general procedure for determining the electromechanical parameters k_{31}, d_{31}, s_{11}^E, and K_{33}^X is described below:

1) The speed of sound in the specimen, v, is obtained from the resonance frequency f_R (see Figure 5.26) using Equation (5.98).
2) The elastic compliance, s_{11}^E, can be calculated using this speed and the density of the specimen, ρ, in Equation (5.94).
3) The electromechanical coupling factor k_{31} can be calculated using the calculated v and the measured antiresonance frequency, f_A, in Equation (5.99). When characterizing low coupling piezoelectric materials, the following approximate equation is also applicable:

$$\frac{k_{31}^2}{(1-k_{31}^2)} = \left(\frac{\pi^2}{4}\right)\frac{\Delta f}{f_R} \tag{5.102}$$

where: $\Delta f = f_A - f_R$.

4) The strain piezoelectric coefficient, d_{31}, is calculated using Equation (5.100) and the measured dielectric constant, K_{33}^X.

Measured impedance curves for two common, relatively high k materials appear in Figure 5.26.[11] Note the large separation between the resonance and antiresonance peaks for the higher k material [Figure 5.26(b)]. In this case: $f_A = 2f_R$.

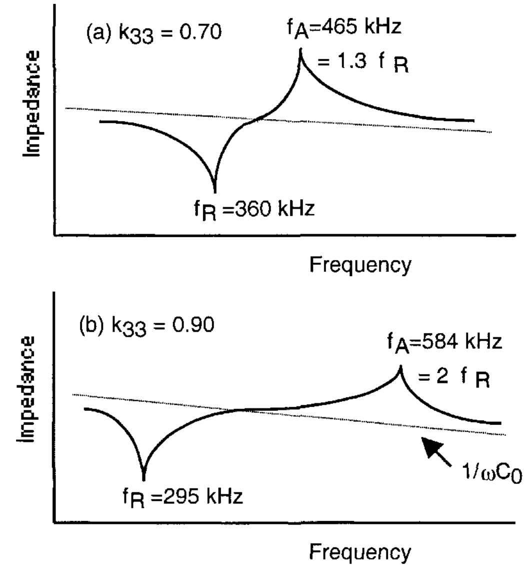

Figure 5.26 Impedance curves for: (a) a PZT 5H ceramic with $k_{33}=0.70$ and (b) a PZN-PT single crystal with $k_{33}=0.90$.[11]

Equivalent Circuits for Piezoelectric Vibrators

The equivalent circuit for a piezoelectric actuator is typically represented by a network comprised of inductive (L), capacitive (C), and resistive (R) components. The equivalent circuit for the resonance state, which has very high admittance (or low impedance), is pictured in Figure 5.27(a). The electrostatic capacitance (*damped capacitance*) is labeled C_d in the diagram and the components L_A and C_A in this series resonance circuit represent the piezoelectric response of the actuator. In the case of the transverse piezoelectric vibration of a rectangular plate, for example, these quantities are defined by the following equations:

$$L_A = \left[\frac{\rho}{8}\right]\left[\frac{l\,b}{w}\right]\left[\frac{(s_{11}^E)^2}{d_{31}^2}\right] \tag{5.103}$$

$$C_A = \left[\frac{8}{\pi^2}\right]\left[\frac{l\,w}{b}\right]\left[\frac{d_{31}^2}{s_{11}^E}\right] \tag{5.104}$$

The resistance, R_A, is associated with the mechanical loss (in particular, the intensive elastic loss $\tan\phi'$ described in Chapter 6). In contrast, the equivalent circuit for the antiresonance state of the same actuator is shown in Figure 5.27(b), which has high impedance as compared to that of the network pictured in Figure 5.27(a).

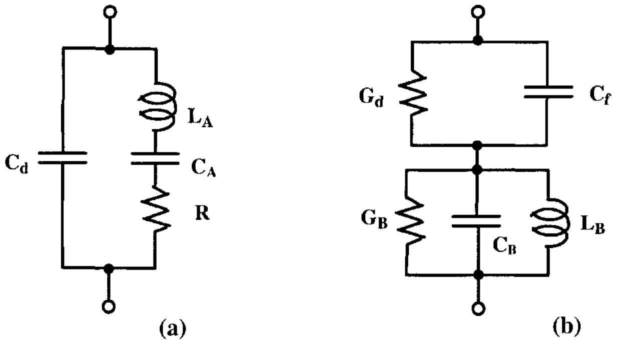

Figure 5.27 Equivalent circuits for a piezoelectric device at: (a) resonance and (b) antiresonance.

Vibration at Antiresonance

Driving piezoelectric transducers and ultrasonic motors in the antiresonant mode, rather than in the resonant state, is an effective method for reducing the load the piezoelectric ceramic presents to the power supply. In terms of the strain distribution that occurs for the antiresonant case (as depicted in Figure 5.25) and its associated integrated u(*x*) curves, if the electromechanical coupling k_{31} is close to 100%, the edge displacement of the plate is almost zero. However, the edge displacement becomes similar to that achieved in the resonant state, if k_{31} is not very large.

The mechanical quality factor, Q_m, and temperature rise, ΔT, of a longitudinally vibrating PZT ceramic bar transducer are plotted as a function of the vibration rate for the resonance (B) and antiresonance (A) modes of operation in Figure 5.28.[12] It is apparent from these data that the quality factor at antiresonance, Q_B, is higher than that at resonance, Q_A, over the entire range of vibration rate investigated. Operation in the antiresonance mode is thus advantageous, because it leads to the same mechanical vibration level without generating heat. Ultrasonic motors are conventionally operated at the resonance frequency; however, these results make it clear that antiresonance operation is actually a more favorable mode in terms of these benefits.

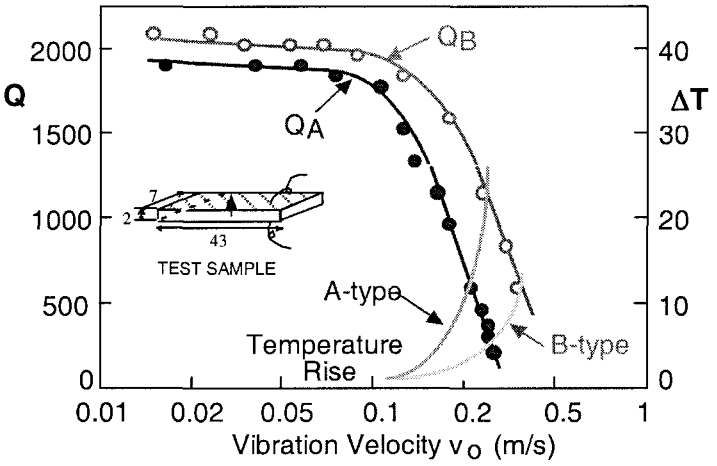

Figure 5.28 The mechanical quality factor, Q, and temperature rise, ΔT, of a longitudinally vibrating PZT ceramic bar transducer plotted as a function of the vibration rate, v_o, for the resonance (B) and antiresonance (A) modes of operation. The longitudinal vibration is produced by the transverse piezoelectric effect acting through d_{31}.[12]

The frequency dependence of the electromechanical conversion efficiency for this device is shown in Figure 5.29 for various applied loads.[13] The difference between the resonance (A-type) and antiresonance (B-type) frequencies is also highlighted on this graph. When the load is not large, a significant variation in the efficiency with frequency is observed. As the load increases, the efficiency curve becomes flatter. When we consider the driving conditions that apply for each state, that is, a constant electric field, E, for the resonance mode and a constant electric displacement, D, for the antiresonance mode, the lower loss in the antiresonance mode makes sense. Recall that the strain hysteresis is significantly less when the strain is considered as a function of the electric displacement as compared with its electric field dependence. Moreover, antiresonance operation requires a low driving current and a high driving voltage, in contrast to the high current and low voltage required for resonance mode operation, thus allowing for the use of a conventional, inexpensive low current power supply.

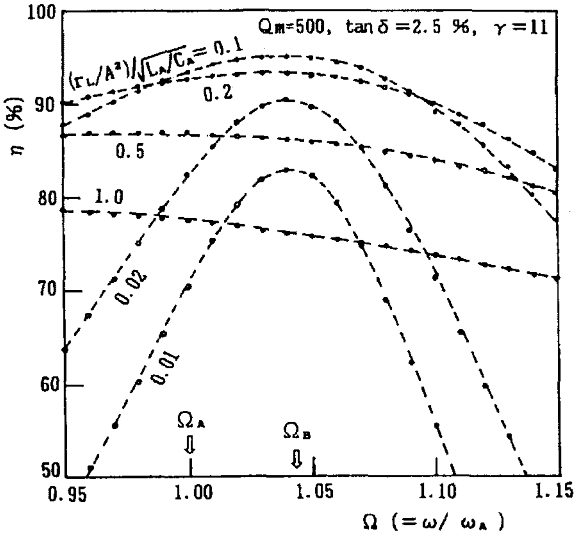

Figure 5.29 Frequency dependence of the electromechanical conversion efficiency of a longitudinally vibrating PZT ceramic bar transducer under various loads. [$\Omega = \omega/\omega_A$; A: resonance; B: antiresonance]

5.5 SENSORS AND SPECIALIZED COMPONENTS FOR MICROMECHATRONIC SYSTEMS

Solid-state actuators are often used in conjunction with displacement sensors or stress sensors in micropositioning systems. We will examine some of the most commonly used position and stress sensors in the first part of this section. We will then consider in some detail the designs of the piezoelectric damper and the piezoelectric transformer and their function in modern micromechatronic systems.

(1) Position and Stress Sensors

We will consider first various methods for measuring microscale displacements. Precise displacement detection at this level is an important part of many drive/control systems, in particular for servo displacement systems. Remarkable advances have been made with microscale position sensors and currently attainable displacement resolutions are $\Delta l=10^{-10}$ m (1 Å) using DC methods and $\Delta l=10^{-13}$ m (10^{-3} Å) using AC methods. The techniques are classified the into two general categories: electrical (resistance, electromagnetic induction and capacitance methods) and optical (optical lever, optical grid, interferometric and optical sensor) methods.[14] A summary of the sensitivity and response of these methods appears in Table 5.3 after the brief descriptions of each that follow.

Resistance Methods

Metal wire *strain gauges*, which are often used to measure the piezoelectric strain ($\Delta l/l$), typically have a resolution of 10^{-6}. The basic structure of this device is pictured schematically in Figure 5.30(a). The strain gauge is usually attached to the sample with an appropriate resin. The resistance of the gauge wire changes when the sample deforms. A Wheatstone bridge is used to precisely measure the resistance change, from which the strain can then be determined. The change in resistance is actually due to two effects: the change in specimen size and the *piezoresistive effect*. In a metal wire gauge the magnitudes of these two effects are comparable, while for a gauge made from a semiconductor the piezoresistive effect is greater by 2 orders of magnitude than the size effect. The frequency response of the strain gauge is generally quite broad. Measurements at frequencies as high as 10 MHz are possible.

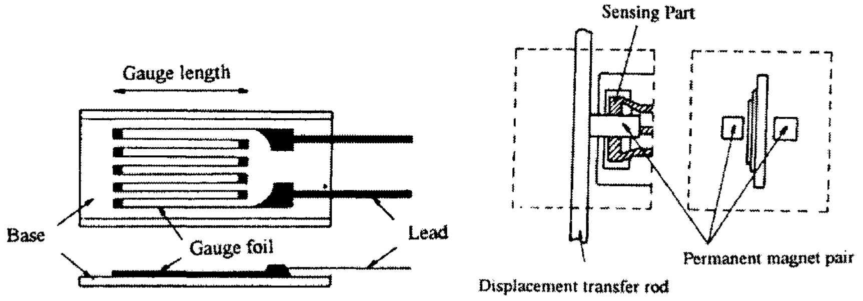

Figure 5.30 The basic structures of: (a) a strain gauge, and (b) a magneto-resistive potentiometer.

Contact potentiometers are similar to helical variable resistors. The contact position can be monitored according to the resistance. There are two general types of potentiometer sensors: the *angle detector* and the *linear position detector*. The resolution of a potentiometer device is limited by the thickness of the resistive helical wire, which is typically about 10 μm. The resolution is quite a bit better, however, for a newer variety, which makes use of a continuous conductive polymer. This type has a resolution to 0.1 μm, and a response of 100 kHz.[15] *Non-contact potentiometers* operate through the *magnetoresistive effect*, by which certain semiconducting materials exhibit a large resistance change with the application of a magnetic field. The basic structure of a typical non-contact potentiometer, comprised of a magnetoresistive sensor and a tiny permanent magnet, is pictured schematically in Figure 5.30(b). This structure tends to have a long lifetime because the lack of contact eliminates problems of wear. It also offers an excellent resolution of 10^{-3} μm.

Electromagnetic Induction Methods

A schematic representation of a *differential transformer* is pictured in Figure 5.31(a). It is comprised of two identical electromagnetic coils and a magnetic core, to which the monitor rod is attached. Any change in the position of the magnetic core will result in a change in the mutual inductance of the two coils. The difference in the voltages induced in the two coils is electronically processed and the resulting signal translated into the corresponding displacement. This is why the device is called a differential transformer. The typical resolution for this sensor is 1 μm, but resolutions on the order of 10^{-2} μm can also be achieved when a lock-in amplifier is incorporated into the system. The response speed is limited to about 100 Hz by both the frequency of the AC input voltage and the mechanical resonance, which is determined by the mass of the core.

Another method uses the *eddy current* in a non-contact device as illustrated in Figure 5.31(b). When a metal plate approaches a coil conducting an AC current, an eddy current (with a ring shaped flow) is induced in the metal plate. The magnetic flux from the eddy current interacts with that of the coil, effectively decreasing the inductance of the coil. There are two types of eddy current sensors: the single-coil sensor, in which the single coil detects the change in inductance, and the triple-coil sensor, in which two secondary coils detect the eddy current generated by a primary coil. A small metal plate (Al foil) is attached to the sample. Since the mechanical load is small, the resonance of the sample can be also measured. The limits of resolution and response for this method are 0.1 μm and 50 kHz, respectively.

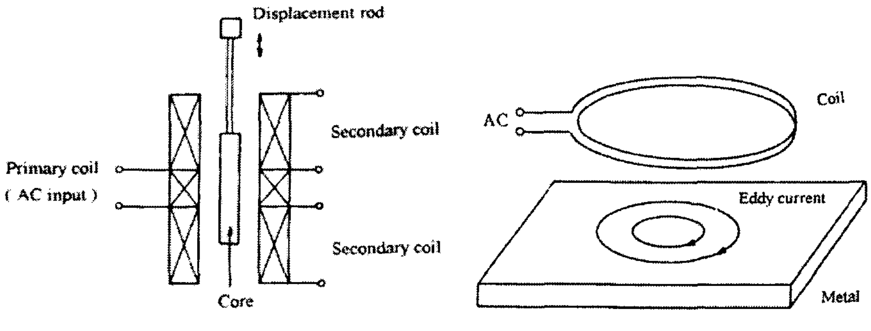

Figure 5.31 Schematic depictions of: (a) the structure of a differential transformer, and (b) an eddy current sensor.

Capacitance Methods

The capacitance of an air-filled parallel-plate capacitor changes linearly with the distance between the two plates. A very sensitive dilatometer, based on this principle and utilizing a very precise capacitance bridge, can achieve AC displacement resolution of up to 10^{-3} Å.[16]

Optical Methods

The *optical lever*, which essentially consists of a laser source and a mirror, has been another popular apparatus for measuring the small displacements produced by such effects as thermal expansion. The sample displacement is transformed to mirror rotation, which is detected by the deflection of the reflected laser beam. The deflection can be measured by means as simple as a ruler on a screen or as sophisticated as a linear optical sensor, which produces an electrical signal directly proportional to the beam position. The resolution is ultimately determined by the laser beam path length and the overall response of the system depends on the mechanical resonance of the mirror mechanism.

Interferometers can be used in conjunction with an optical fiber sensor or on an optical bench. When two or more monochromatic, coherent light beams with the same wavelength are superposed, an interference or "fringe" pattern is formed which depends on the phase difference and the optical path difference between the "arms" of the interferometric system. Double-beam sytems, such as the *Michelson* configuration depicted in Figure 5.32(a), and multiple beam systems, such as the *Fabrey-Perot* configuration depicted in Figure 5.32(b), can be employed for detecting microscale displacements.[17,18] When the optical path length difference between the two beams of a system like the Michelson interferometer changes, the resulting fringe shift will occur in integral multiples of $\lambda/2$. Precise measurement of the changes in light intensity make it possible to detect displacements of less than 1 nm by this method.

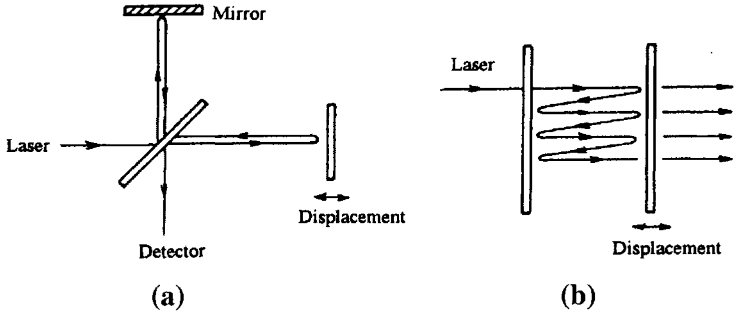

Figure 5.32 Two interferometric systems for measuring displacement: (a) the Michelson interferometer (two beam method) and (b) the Fabrey-Perot interferometer (multiple beam method).

Table 5.3 A summary of microdisplacement measurement techniques.

Principle	Method	Sensitivity	Response
Resistance	**Strain Gauge**		
	Metal	$\Delta l/l = 10^{-6}$	10 MHz
	Semiconductor	$\Delta l/l = 10^{-8}$	10 MHz
	Potentiometer		
	Contact	$\Delta l = 10^{-1}$ μm	100 kHz
	Non-Contact	$\Delta l = 10^{-3}$ μm	1 kHz
Electromagnetic Induction	**Differential Transformer**		
	AC	$\Delta l = 10^{-2}$ μm	100 Hz
	DC	$\Delta l = 10^{-1}$ μm	100 Hz
	Eddy Current	$\Delta l = 10^{-1}$ μm	50 kHz
Optical	**Optical Lever**	$\Delta l = 10^{-1}$ μm	1 kHz
	Optical Fiber	$\Delta l = 10^{-2}$ μm	100 kHz

Stress Sensors

Piezoelectric ceramics activated through the direct piezoelectric effect can function as stress and acceleration sensors. One such piezoelectric stress sensor, designed by Kistler, consists of a stack of quartz crystal plates (extensional and shear types) and can detect three-dimensional stresses.[19] Similar multilayer PZT structures have been proposed for use as three-dimensional actuators and sensors by PI Ceramics of Germany.[20]

A *cylindrical gyroscope* produced by Tokin of Japan is depicted in Figure 5.33.[21] The cylinder has six divided electrodes, one pair of which is used to excite the fundamental bending mode of vibration, while the other two pairs are used to detect the acceleration. When rotational acceleration occurs about the axis of the gyro, the voltage generated on the electrodes is modulated by the *Coriolis force.* By subtracting the signals generated between the two pairs of sensor electrodes, a voltage that is directly proportional to the acceleration can be obtained.

The *converse electrostrictive effect,* which essentially reflects the stress dependence of the dielectric constant, is also used in the design of stress sensors.[22] The *bimorph structure,* which utilizes the difference between the static capacitances of two laminated dielectric ceramic plates, provides superior stress sensitivity and temperature stability. The change in capacitance of the top and bottom plates will be opposite in sign for a uniaxial stress and of the same sign for when a deviation in temperature occurs. The response speed is limited by the capacitance measurement frequency to about 1 kHz. Unlike piezoelectric sensors, electrostrictive sensors are effective in the low frequency range, especially for DC applications.

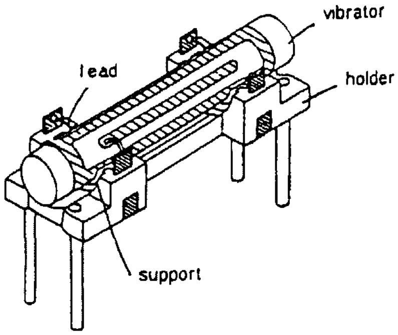

Figure 5.33 A piezoelectric cylindrical gyroscope (Tokin, Japan).[21]

(2) Piezoelectric Damper

The mechanical damper is another important component in a mechatronic system. In addition to electro- and magnetorheological fluids, piezoelectric materials can also be used in mechanical damping devices. Consider a piezoelectric material attached to an object whose vibration is to be damped. When the vibration is transmitted to the piezoelectric material, the mechanical energy of the vibration is converted into electrical energy through the piezoelectric effect, and an AC voltage is generated. If the piezoelectric material is in an open- or short-circuit condition, the generated electrical energy is converted back into vibration energy without loss. This cycle is repeated continuously producing a sustained vibration. If a proper resistance is connected, however, the electrical energy is consumed through Joule heating, leaving less energy to be converted into mechanical energy, and the vibration is rapidly damped. The damping takes place most rapidly when the series combination of the resistance, R, and capacitance, C, of the piezoelectric material is selected such that *impedance matching* occurs. The optimum choice will satisfy the condition: $R=1/(2\pi fC)$, where f is the vibration frequency.[23] A collaborative effort between ACX Company and K2 has led to the production of the new "smart ski" pictured in Figure 5.34 that makes use of this principle. The blade design incorporates PZT patches that effectively suppress excess vibration in the ski as it slides over the snow.[24]

The electric energy, U_E, generated in the first part of the cycle can be expressed in terms of the electromechanical coupling factor, k, and the mechanical energy, U_M, as:

$$U_E = U_M\,(k^2) \tag{5.105}$$

Making use of a suitable series resistance to transform the electrical energy into heat, transforming efficiency as high as 50% can be achieved with the piezoelectric damper. Accordingly, the vibration energy is decreased at a rate of $1-k^2/2$ times per vibration cycle, since energy amounting to $k^2/2$ multiplied by the mechanical vibration energy is dissipated as heat energy. As the square of the amplitude is equivalent to the amount of vibration energy, the amplitude will decrease at a rate of $(1-k^2/2)^{1/2}$ times per vibration cycle. Assuming a resonance period of T_o, the number of vibrations occurring over a time interval, t, will just be $2t/T_o$ and the amplitude of the vibration after t seconds has passed will be:

$$\left[1-\frac{k^2}{2}\right]^{t/T_0} = e^{-t/\tau} \tag{5.106}$$

or

$$\tau = -T_o \ln\left[1-\frac{k^2}{2}\right] \tag{5.107}$$

where τ is the time constant of the exponential decay in the vibration amplitude. So we see from this analysis that the vibration will be more quickly damped when a material with a higher k is used.

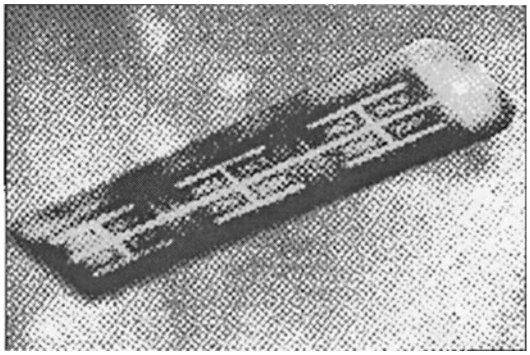

Fig. 5.34 Piezoelectric damper for skis developed by ACX and K2.[24]

Where ceramics tend to be rather brittle and hard, they can be difficult to incorporate directly into a mechanical system. Hence, a flexible piezoelectric composite is a practical alternative. A composite material comprised of a piezoceramic powder and carbon black suspended in a suitable polymer, as pictured schematically in Figure 5.35, can be fabricated with an electrical conductivity that is highly sensitive to small changes in the concentration of carbon black.[25] The conductivity of the composite changes by more than 10 orders of magnitude around a certain fraction of carbon black called the percolation threshold, where links between the carbon particles begin to form. The conducting pathways that form become essentially internal resistances within the material. A concentration of carbon black can thus be established that effectively leads to the formation of a series resistance favorable for significant dissipation of the vibrational energy.

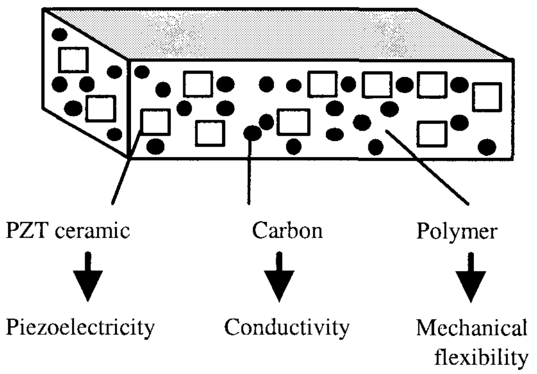

Figure 5.35 A piezoceramic:carbon black:polymer composite for vibration damping.

The dependence of the damping time constant, τ, on the volume percent of carbon black in PLZT:PVDF and PZT:PVDF composites is shown in Figure 5.36. The minimum time constant and therefore the most rapid vibration damping is seen to occur with a volume percent of about 7% carbon black for both composites. Note that the PLZT:PVDF material, with a higher electromechanical coupling, k, exhibits the larger dip in τ and thus more effective damping.

(3) Piezoelectric Transformer

Operating Principle

One of the bulkiest and most expensive components in solid-state actuator systems is the power supply, especially the electromagnetic transformer used in the power supply. Electromagnetic transformer loss occurring through the skin effect, thin wire loss, and core loss all increase dramatically as the size of the transformer is reduced. Therefore, it is difficult to realize miniature low profile electromagnetic transformers with high efficiency. The piezoelectric transformer (PT) is an attractive alternative for such systems due to its high efficiency, small size, and lack of electromagnetic noise. They are highly suitable as miniaturized power inverter components, which might find application in lighting up the cold cathode fluorescent lamp behind a color liquid crystal display or in generating the high voltage needed for air cleaners.

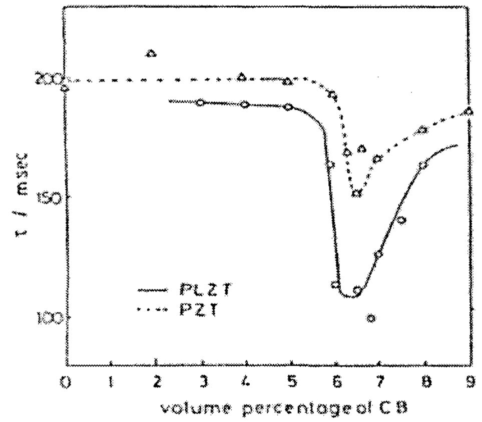

Figure 5.36 Damping time constant, τ, as a function of volume percent of carbon black in PZT:PVDF and PLZT:PVDF composites. [Note that the minimum time constant (quickest damping) occurs at the percolation threshold for both composites, and the higher k material (PLZT:PVDF) is the more effective damper.]

The original design to step up or step down an input AC voltage using the converse and direct piezoelectric properties of ceramic materials was proposed by Rosen.[26] This type of transformer operates by exciting a piezoelectric element like the one pictured at the top of Figure 5.37 at its mechanical resonance frequency. An electrical input is applied to one part of the piezoelectric element (for the element depicted in Figure 5.37, at the top left electrode), which produces a mechanical vibration. This mechanical vibration is then converted back into an electrical voltage at the other end (right edge electrode) of the piezoelectric plate. The voltage step-up ratio, r, without load (open-circuit conditions) is given by:

$$r \propto k_{31}k_{33}\, Q_m\, (l/t) \tag{5.108}$$

where l and t are the electrode gap distances for the input and output portions of the transformer, respectively. Note from this relationship how the length to thickness ratio, the electromechanical coupling factors, and/or the mechanical quality factor are the primary means of increasing the step-up ratio. This transformer was utilized on a trial basis in some color televisions during the 1970's.

In spite of its many attractive features, the original Rosen transformer design had a serious reliability problem. Mechanical failure tends to occur at the center of the device where residual stresses from poling are the most highly concentrated. This happens to also be coincident with the nodal point of the vibration where the highest induced stresses occur. The two more recently developed transformers pictured in Figure 5.37 are designed to avoid this problem and are currently commercially produced for use as back-light inverters in liquid crystal displays. Both of the newer designs make use of more mechanically tough ceramic materials. The Philips Components transformer shown in Figure 5.37(b) further alleviates the problem by using a multilayer structure to avoid the development of residual poling stress in the device.[27] The NEC design pictured in Figure 5.37(c) makes use of an alternative electrode configuration to excite a third resonance excitation (longitudinal) in the rectangular plate to further redistribute the stress concentrations in a more favorable manner.[28]

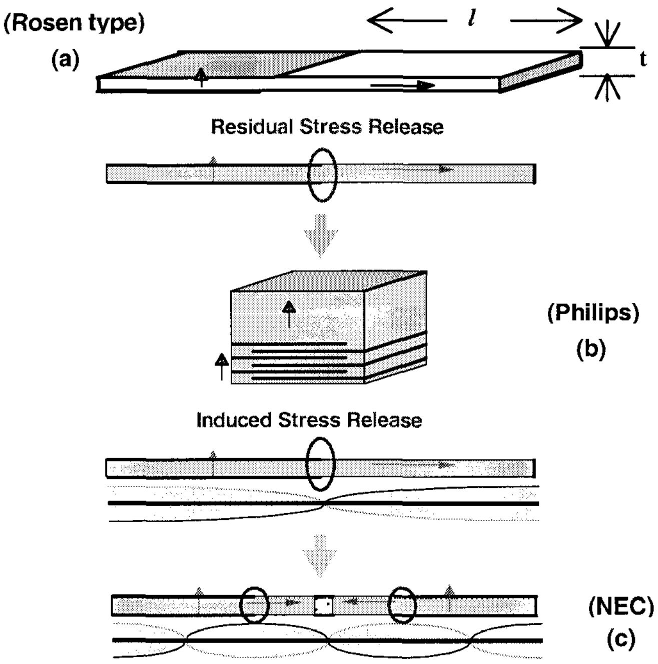

Figure 5.37 Piezoelectric transformer designs: (a) the original Rosen design,[26] (b) a multilayer design developed by Philips,[27] and (c) a triple resonant mode type developed by NEC.[28]

Power Supplies for Piezoelectric Actuators

A variety of new methods for driving piezoelectric actuators has emerged in recent years. We will consider the basic design of these power supplies and a few of the most promising designs here.

A typical system is illustrated in Figure 5.38.[29] If we tune the transformer's frequency to precisely match the resonance frequency of an ultrasonic motor, it can be used as a driver for the system, thus creating a transformer-integrated motor.[30] Such a configuration might, for example, take the form of a ring transformer having the same dimensions as the ultrasonic motor. A transformer coupled with a rectifier can be used to drive a multilayer or bimorph piezoelectric actuator.[29]

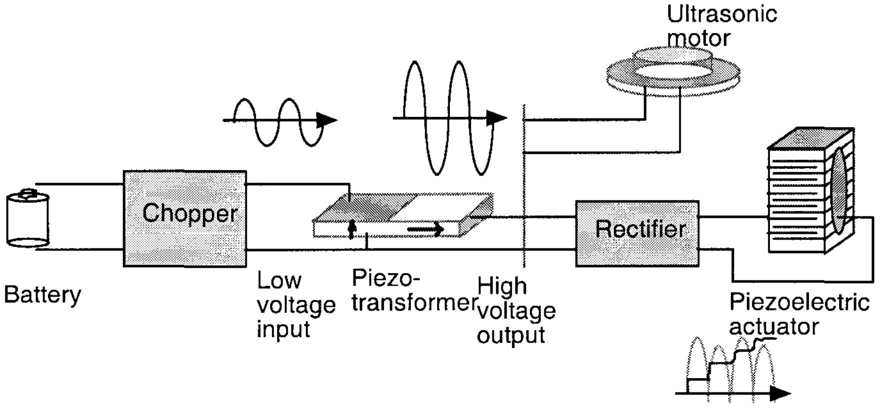

Figure 5.38 The basic configuration of a typical piezoelectric actuator drive system (AC or pseudo DC) incorporating a piezoelectric transformer.[29]

A compact drive system designed for a piezoelectric vibration control device for a helicopter is shown schematically in Figure 5.39. It includes a multilayer piezoelectric actuator to suppress the vibration and a piezoelectric transformer to drive it.

Two kinds of power supplies utilizing piezoelectric transformers powered by a 24 V_{DC} helicopter battery have been developed. One serves as a high voltage DC power supply (100-1000 V, 90 W) for driving a piezoelectric actuator, and the other is an AC adapter (±15 V_{DC}, 0.1-0.5 W) for driving the supporting circuitry. Large and small multi-stacked piezoelectric transformer elements, both with an insulating glass layer between the input and output parts to ensure a completely floating condition, were used for the high voltage supply and the adapter, respectively. An actuator manufactured by Tokin Corporation with dimensions of 10x10x20 mm^3 and capable of generating a 16 μm displacement under the maximum operating voltage of 100 V was used in this system.

Chopped 24 V AC voltage is applied to the piezoelectric transformer with a step-up ratio of about 10. This high voltage AC signal is converted to high voltage DC (300 V) through a rectifier, and the charge is collected on a capacitor (at point A in Figure 5.40). A power amplifier is used to regulate the voltage that is finally applied to the actuator. A Class-D switching amplifier is used rather than a conventional switching or linear amplifier, because it allows more precise control of the amplitude and frequency of the drive signal and a higher actuator response rate due to the chopped DC input voltage. The signal from a pulse width modulation (PWM) driving circuit is applied to the two power MOSFETs of the half bridge, as shown in Figure 5.40, to chop the constant 300 V_{DC} voltage from the piezoelectric transformer and to maintain the desired level of amplitude and frequency control.

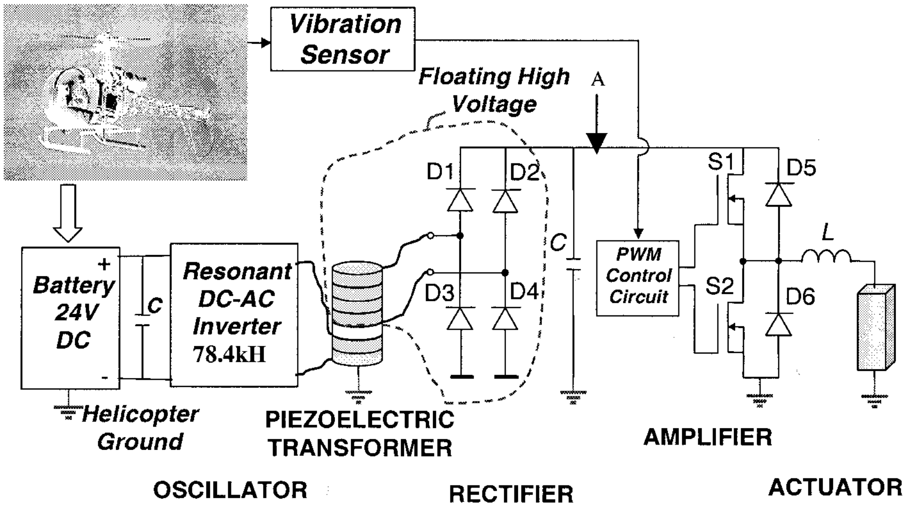
Vibration Sensor
Floating High Voltage
A
D1
D2
D3
D4
C
PWM Control Circuit
S1
S2
D5
D6
L
+
Battery 24V DC
-
C
Resonant DC-AC Inverter 78.4kH
Helicopter Ground
PIEZOELECTRIC TRANSFORMER
AMPLIFIER
OSCILLATOR
RECTIFIER
ACTUATOR

Figure 5.39 Compact drive system for piezoelectric actuator control.[29]

The output voltage is applied to the piezoelectric actuator through a filtering inductance of 100 mH. The PWM carrier frequency is maintained at 40 kHz, which is below the mechanical resonance frequency of the piezoelectric actuator (~60 kHz). The displacement curves of an actuator driven by this newly developed power amplifier are shown in Figure 5.41. The displacement was directly measured with an eddy current sensor. As seen in this figure, a displacement of ±1.5 μm was controlled with an applied voltage of ±20 V. This drive system can be operated at frequencies up to 500 Hz, which is sufficient to maintain active vibration control on a helicopter.

In summary, the piezoelectric transformer can be used as part of the drive circuitry for a piezoelectric actuator. It has the advantages over conventional electromagnetic transformers of being lightweight, compact in size, highly efficient, and free of electromagnetic noise.

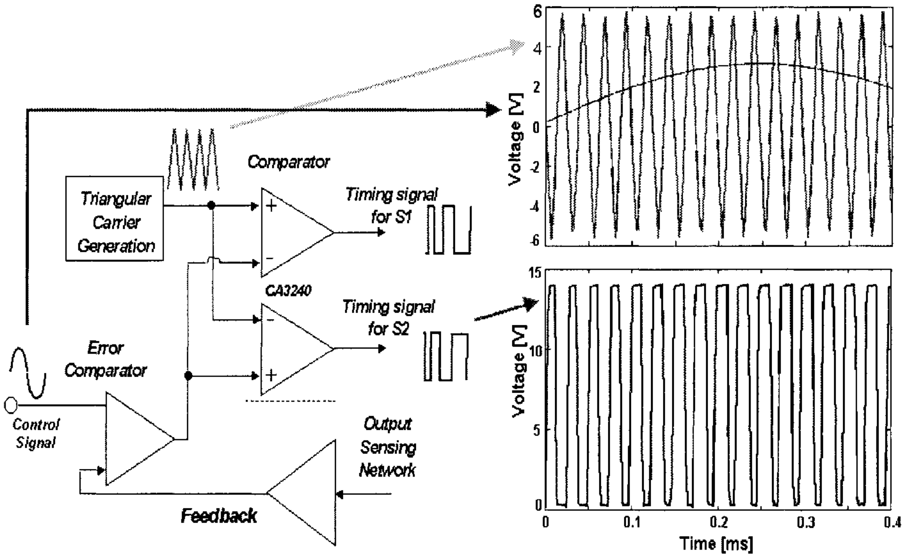
Triangular Carrier Generation
Comparator
Timing signal for S1
CA3240
Timing signal for S2
Error Comparator
Control Signal
Output Sensing Network
Feedback
Voltage [V]
6
4
2
0
-2
-4
-6
Voltage [V]
15
10
5
0
0
0.1
0.2
0.3
0.4
Time [ms]

Figure 5.40 Pulse width modulation circuit for driving the power amplifier.[29]

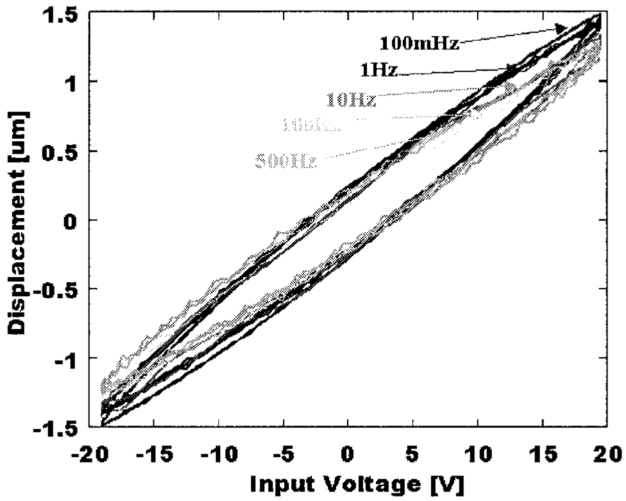

Figure 5.41 The displacement curves of a piezoelectric actuator driven by the newly developed power amplifier.

Example Problem 5.6

Determine the specifications a ceramic actuator drive system with the following characteristics:

(a) The multilayer actuator has 100 ceramic layers, each 100 μm thick with an area of 5 x 5 mm^2. The relative permittivity is 10,000. Calculate the capacitance of the actuator.

(b) Assuming it has a density ρ=7.9 g/cm^3 and elastic compliance $s_{33}{}^{D}=13\text{x}10^{-12}$ m^2/N, calculate the resonance frequency of the actuator. The electrode may be ignored for this calculation.

(c) Determine the current needed if 60 V is to be applied to the actuator as quickly as possible.

(d) The cut-off frequency (1/RC) must be less than the mechanical resonance frequency. Determine the output impedance of the power supply.

Solution

(a)
$$C = n\,\varepsilon_o K\,(A/t) \qquad \text{(P5.6.1)}$$

$$= (100)[8.854 \text{ x } 10^{-12}\,(\text{F/m})](10{,}000)\,[5\text{x}5\text{x}10^{-6}\,(\text{m}^2)/100 \text{ x } 10^{-6}\,(\text{m})]$$

$$\rightarrow C = 2.21 \text{ x } 10^{-6}\,(\text{F})$$

Note: Multilayer actuators have a capacitance of more than 1 μF.

(b) The resonance frequency for the thickness vibration (neglecting the coupling with width vibrations) is given by:

$$f_R = \frac{1}{2l\sqrt{\rho s_{33}^{D}}} \qquad \text{(P5.6.2)}$$

$$= \frac{1}{2(100)[100\text{x}10^{-6}\,(\text{m})]\sqrt{[7.9\text{x}10^{3}\,(\text{kg/m}^3)][13\text{x}10^{-12}\,(\text{m}^2/\text{N})]}}$$

$$\rightarrow f_R = 156\,(\text{kHz})$$

Note: The response speed of the power supply must be greater than the actuator's resonance frequency.

(c) The relationship between the actuator voltage and the charging current is given by:

$$I = Q/\tau_R = C\,V\,f_R \qquad \text{(P5.6.3)}$$

$= [2.21 \times 10^{-6}\ (F)]\ [60\ (V)]\ [156 \times 10^{3}\ (Hz)]$

$\rightarrow I = 21\ (A)$

Note: Ideally a significant current is required by the power supply, even if just for a relatively short period (6 μs). The power is estimated to be 60 (V) x 21 (A). So we see that more than 1 kW is needed for the resonance drive. A power of 12 W is needed for the 2 kHz drive in a dot matrix printer.

(d) Assuming $\omega_R = 2\pi f_R = 1/RC$:

$$R = 1/[2\pi f_R C] \quad \text{(P5.6.4)}$$

$$= 1/(2\pi\,[156 \times 10^{3}\ (Hz)][2.21 \times 10^{-6}\ (F)])$$

$\rightarrow R = 0.46\ (\Omega)$

The output impedance of the power supply should be less than 1 Ω.

The power supply specifications are:

Maximum Voltage: 200 (V), Maximum Current: 10 (A), Frequency Range: 0-500 (kHz), Output Impedance: < 1 (Ω).

CHAPTER ESSENTIALS

1. **Classification of ceramic actuators:**

Actuator Type	Drive	Device	Material Type
Rigid Displacement	Servo	Servo-Displacement Transducer	Electrostrictive
	On/Off	Pulse Drive Motor	Soft Piezoelectric
Resonant Displacement	AC	Ultrasonic Motor	Hard Piezoelectric

2. **Control:** **Open loop** On/off drive
Pulse width modulation (PWM)
Polarization control

Closed loop Servo drive

3. **PWM criteria:**

   a. The ratio of the carrier frequency, f_c, to the input command frequency, f_e, should be greater than 7.
   b. The carrier frequency, f_c, must be high enough (compared to the system response) to eliminate ripple in the system output.

4. **The Laplace transform**: a powerful tool for transient analysis has the general form:

$$U(s) = \int_0^{\infty} e^{-st}\, u(t)\, dt$$

   Among the theorems that apply to the Laplace transform, the following are especially useful:

   a. **Differentiation with respect to t:**

$$L\left[\frac{d\,u(t)}{dt}\right] = s\,U(s) - u(0)$$

$$L\left[\frac{d^n\,u(t)}{d\,t^n}\right] = s^n\,U(s) - \sum s^{n-k}\,u^{k-1}(0)$$

   b. **Shift formula with respect to t**: u(t−k)=0 for t < k
   [k: positive real number] This represents the u(t) curve shifted by k along the positive t axis.

$$L[u(t-k)] = e^{-ks}\,U(s)$$

   c. **Differentiation with respect to an independent parameter:**

$$L\left[\frac{\partial u(t,x)}{\partial x}\right] = \frac{\partial U(s,x)}{\partial x}$$

   d. **Initial and final values**

$$\lim_{t\to 0}[u(t)] = \lim_{|s|\to\infty}[U(s)]$$

$$\lim_{t\to\infty}[u(t)] = \lim_{|s|\to 0}[U(s)]$$

5. **The transfer function:** $G(s) = U(s) / E^{\sim}(s)$ [where: $E^{\sim}(s)$: the input, U (s): the output] G(s) can be obtained by inputting a unit impulse function.
6. **The transfer function of a piezoelectric actuator with a mass of M:**
   $U(s) = G(s)\,E^{\sim}(s)$
   $G(s) = [A\,c\,d / (M\,s^2 + \zeta\,s + Ac/l)]$
7. **The Nyquist criterion of stability:** When the point (−1+j0) is to the left of the Nyquist diagram (increasing ω), the system is stable.

8. **Pulse drive:** The pulse width or rise time must be adjusted to exactly match the resonance period of the actuator system to eliminate vibrational ringing.
9. **Resonance drive:** A high Q_m material is essential in order to optimize the vibration amplitude and to suppress heat generation.
10. **Measuring techniques for microdisplacements:**
    Resistance method: strain gauge, potentiometer
    Electromagnetic induction methods: differential transformer, eddy-current type
    Optical methods: optical lever, optical fiber
11. **Piezoelectric transformers** are promising alternatives to use in the drive circuitry for solid-state actuators.

CHAPTER PROBLEMS

5.1 Using a rectangular piezoelectric plate and the transverse d_{31} mode, consider the design of a flight actuator.

a. Assuming a rectangular negative pulse ($-E_o$) is applied to the plate, which is installed normally and rigidly fixed at one end, verify that the velocity of sound, v, at the other end is given by $[2|d_{31}|E_o v]$, which is independent of the length.

b. Suppose this velocity is acquired by a small steel ball of mass M with no loss in energy. Calculate the maximum height the steel ball will attain when the impulse is applied entirely in the upward direction.

5.2 Considering the strain distribution $x_1(x)$ as depicted in Figure 5.26 for a material with a low electromechanical coupling material, draw the displacement distribution $u(x)$ for both the resonance and antiresonance states, and discuss the difference between the two states.

5.3 Using the equivalent circuit for a piezoelectric transducer in the antiresonance state [see Figure 5.28(b)], derive the equations that define L and C with respect to the intrinsic physical parameters, ρ, d, s^E, and the dimensions of the transducer.

5.4 The transfer function for a piezoelectric actuator is given by:

$$U(s) = G(s)\, E^{\sim}(s)$$

$$G(s) = A\, c\, d \,/\, (M s^2 + \zeta s + Ac/l)$$

Calculate the displacement response to the step voltage: $E^{\sim}(s) = 1/s$.

5.5 Let us consider open-loop and closed-loop transfer functions of the form:
$W_o = 4 / s\,(s^2 + 4\,s + 6)$
$W_c = 4 / (s^3 + 4s^2 + 6s + 4)$
for a ceramic actuator system.

a. Using the Nyquist criterion, check the stability of this feedback control system.

b. Describe the Bode diagram for $W_c(j\omega)$, and discuss the frequency dependence.

5.6 Explain how the type of servo mechanism can be determined from the Bode diagram shown below:

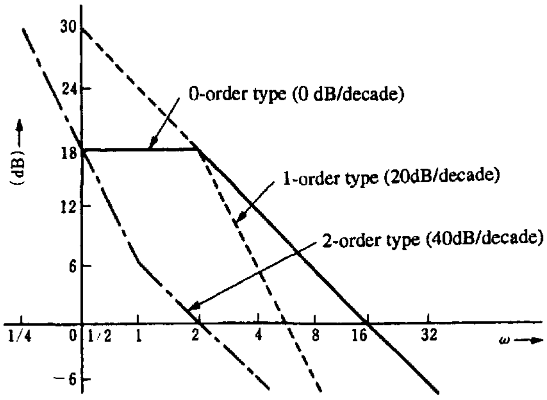

Hint

The slope of the low frequency (ω→0) portion of the Bode diagram identifies the type of the servo mechanism. When the open-loop transfer function has a pole at the origin, the Bode diagram will have a slope of −20 dB/decade in the low frequency region.

Slope (dB/decade)	Type of Servo Mechanism
0	Type 0
−20	Type 1
−40	Type 2

5.7 Using a rectangular piezoceramic plate (length: l, width: w, and thickness: b, poled along the thickness), we have found the following parameters: k_{31}, d_{31}, and Q_m. *Explain the fundamental principles for both the resonance and pulse* drive methods.

The density, ρ, and dielectric constant, K_{33}^X, of the ceramic must be known prior to the following experiments.

a. Using an impedance analyzer, the admittance for the mechanically free sample (that is, one that is supported at the nodal point at the center of the plate) is measured as a function of the drive frequency, f, and the admittance curve shown in Figure 5.27 is obtained. Explain how to determine the k_{31}, d_{31}, and Q_m values from these data. Also verify that the following approximate equation can be used for a low coupling piezoelectric material:

$$k_{31}^2/(1-k_{31}^2) = (\pi^2/4)\,(\Delta f\,/\,f_R)$$

where $\Delta f = f_A - f_R$.

b. Using a pulse drive technique, the transient displacement change was measured as a function of time, and the displacement curve pictured below was obtained. Explain how to determine the the k_{31}, d_{31}, and Q_m values from these data. Use the relationship: $Q_m=(1/2)\omega_0\tau$.

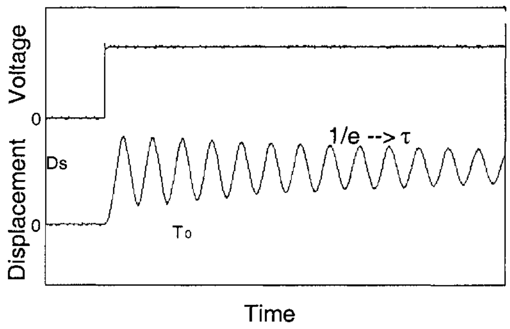

REFERENCES

1) T. Ota, T. Uchikawa and T. Mizutani: Jpn. J. Appl. Phys. **24**, Suppl. 24-3, 193 (1985).
2) K. Uchino: J. Industrial Education Soc. Jpn. **40**(2), 28 (1992).
3) Y. Amemiya Edit.: *Introduction to Mechatronics*, Japan Industrial Tech. Center, Tokyo (1984).
4) S. A. Davis: *Feedback and Control Systems*, Simon & Schuster, Inc., New York (1974).
5) C. V. Newcomb and I. Flinn: Electronics Lett. **18**, 442 (1982).
6) T. Ogawa: *Crystal Physical Engineering*, Shoka-bo Pub., Tokyo (1976).

7) Sugiyama and K. Uchino: Proc. 6th IEEE Int'l. Symp. Appl. Ferroelectrics, p.637 (1986).
8) S. Smiley: US Patent, No. 3614486 (1971).
9) Ikebe and Nakata: J. Oil and Air Pressure **3**, 78 (1972).
10) T. Ikeda: *Fundamentals of Piezoelectric Materials*, Ohm Publication, Tokyo (1984).
11) J. Kuwata, K. Uchino and S. Nomura: Ferroelectrics **37**, 579 (1981).
12) K. Uchino, J. Zheng, A. Joshi, Y. H. Chen, S. Yoshikawa, S. Hirose, S. Takahashi and J. W. C. de Vries: J. Electroceramics, **2**, 33 (1998).
13) S. Hirose, S. Takahashi, K. Uchino, M Aoyagi and Y. Tomikawa: Proc. MRS '94 Fall Mtg., Vol. **360**, p.15 (1995).
14) P. H. Sydenham: J. Phys. E: Sci. Inst. **5**, 721 (1972).
15) Midori-Sokki, Potentiometer, Production Catalog, Japan.
16) K. Uchino and L. E. Cross: Ferroelectrics **27**, 35 (1980).
17) Tanida, Gomi and Nomura: Abstract 44th Jpn. Appl. Phys. Mtg., Fall, p.27 (1983).
18) Evick Engineering, Photonic Sensor, Production Catalog.
19) Kistler, Stress Sensor, Production Catalog, Switzerland.
20) A. Bauer and F. Moller: Proc. 4th Int'l. Conf. New Actuators, Germany, p.128 (1994).
21) Tokin, Gyroscope, Production Catalog, Japan.
22) K. Uchino, S. Nomura, L. E. Cross, S. J. Jang and R. E. Newham: Jpn. J. Appl. Phys. **20**, L367 (1981); K. Uchino: Proc. Study Committee on Barium Titanate, XXXI-171-1067 (1983).
23) K. Uchino and T. Ishii: J. Ceram. Soc. Jpn. **96**, 963 (1988).
24) ACX Company catalogue: Passive Damping Ski.
25) Y. Suzuki, K. Uchino, H. Gouda, M. Sumita, R. E. Newnham and A. R. Ramachandran: J. Ceram. Soc. Jpn., Int'l. Edition **99**, 1096 (1991).
26) C. A. Rosen: "Ceramic Transformers and Filters," Proc. Electronic Component Symp., p. 205-211 (1956).
27) NEC: "Thickness Mode Piezoelectric Transformer," US Patent No. 5,118,982 (1992).
28) S. Kawashima, O. Ohnishi, H. Hakamata, S. Tagami, A. Fukuoka, T. Inoue and S. Hirose: "Third order longitudinal mode piezoelectric ceramic transformer and its application to high-voltage power inverter," IEEE Int'l. Ultrasonic Symp. Proc., Nov. (1994).
29) K. Uchino, B. Koc, P. Laoratanakul and A. Vazquez Carazo: Proc. 3rd Asian Mtg. on Ferroelectrics, Dec. (2000).
30) H.–W. Kim, S. Dong, P. Laoratanakul, K. Uchino and T. Park: IEEE-UFFC Trans. (2002) [in press].

6

LOSS MECHANISMS AND HEAT GENERATION

The loss mechanisms in piezoelectric materials are of three fundamental types: dielectric, mechanical and electromechanical. We will consider first the phenomenology of losses and then examine the methods by which the individual losses are measured. It is generally observed that the generation of heat in a piezoelectric material is due mainly to the intensive dielectric loss, $\tan\delta'$, (that associated with dielectric hysteresis) when driven off-resonance, while the heating is due primarily to the intensive mechanical loss, $\tan\phi'$, (that associated with elastic hysteresis) when the component is driven at resonance. Further, a significant decrease in the mechanical quality factor, Q_m, accompanied by an increase in vibration is observed for piezoelectric ceramic devices driven at resonance. This effect is due entirely to an increase in the extensive dielectric loss. When subjected to a pulse drive, both off-resonance and resonance effects are manifested simultaneously, and the combined action of the dielectric and mechanical loss mechanisms is observed.

6.1 HYSTERESIS AND LOSS IN PIEZOELECTRICS

As the industrial demand for piezoelectric actuators has increased in recent years, fundamental research in this area has become more focused on issues related to reliability. Especially for high power applications, the heat generated by these dielectric and mechanical loss mechanisms is a significant problem.

The loss or hysteresis associated with a piezoelectric can be both detrimental and beneficial. When the material is used in a positioning device, hysteresis in the field-induced strain presents a serious problem in reproducibility of the motion. When the material is driven in a resonance mode, as is the case for ultrasonic motor applications, the losses generate excessive heat in the device. Also because the resonant strain amplification is proportional to the mechanical quality factor, Q_m, low (intensive) mechanical loss materials are generally preferred for ultrasonic motors. On the other hand, a high mechanical loss, which corresponds to a low mechanical quality factor Q_m, is actually used for piezoelectric force sensors and acoustic transducers because it enables a broader range of operating frequencies.

Systematic studies of the loss mechanisms in piezoelectrics operated under high voltage and high power conditions have been limited and, to date, little has been reported in the literature on the subject. A partial theoretical treatment of loss mechanisms can be found, such as that presented in the text by T. Ikeda[1]; however, these descriptions tend to neglect piezoelectric losses, which have become more important in the context of recent investigations. A phenomenological description of the loss mechanisms associated with piezoelectrics will be presented in this chapter.[2] Processes leading to the generation of heat under off-resonance operating conditions and the high power characteristics of devices operated under resonance conditions will be considered. The resonance and anti-resonance vibration modes will be examined with respect to the mechanical quality factor, Q_m. Finally, the mechanisms for heat generation in devices operated under pulse drive conditions will be treated.

(1) Microscopic Origins of the Loss Mechanisms: An Overview

The mechanisms for the electromechanical loss fall into four general categories, defined in terms of fundamental characteristics of the material, namely in relation to: (1) domain wall motion, (2) the lattice type, (3) the microstructure (polycrystalline samples), and (4) the conductivity of the material (highly ohmic samples).[3] When the material is a ceramic piezoelectric, it is the first category that most strongly characterizes the loss.

Some interesting experimental results have been reported concerned with the relationship between dielectric and mechanical losses in piezoceramics.[4] These results are represented in Figure 6.1, in which mechanical loss, $\tan\phi$, is plotted with respect to the dielectric loss, $\tan\delta$, for a series of piezoelectric ceramics with compositions, $Pb_{0.9}La_{0.1}(Zr_{0.5}Ti_{0.5})_{1-x}Me_xO_3$, where Me represents the dopant ions Mn, Fe, or Al, and x covers a range between 0 and 0.09. The mechanical losses were measured on poled ceramic disks 0.4 mm thick and 5 mm in diameter, at their respective radial resonance frequencies (around 520 kHz). Since it is not possible to measure the dielectric losses on poled ceramics at the resonance frequency, due to the occurrence of very strong electromechanical interactions, the measurements were made on depoled specimens at approximately the same frequencies. The Mn-doped ceramics showed dielectric losses below 1%, while Fe doping produced losses of 1-2%, and Al doping increased the loss to over 3%. The linear relationship:

$$\tan\phi = 0.32 \tan\delta \qquad (6.1)$$

was found to apply to these nominal compositions.

Assuming that 90° domain wall movements constitute the primary loss mechanism for these materials, the proportionality constant was defined in terms of the relevant physical parameters, such that:

$$\tan\phi = [m\, x_s^2\, \varepsilon_o\, K^X / P_s^2\, s^E] \tan\delta \qquad (6.2)$$

where m is a constant assigned a value between 0.7-0.8, dependent on the crystalline structure, x_s the spontaneous strain, K^X the dielectric constant at constant stress, P_s the spontaneous polarization, and s^E the elastic compliance at constant electric field. Taking into account the relationship:

$$x_s = Q\, P_s^2 \qquad (6.3)$$

$$d = 2\,Q\,\varepsilon_o\,K^X\,P_S, \tag{6.4}$$

where Q is the electrostrictive coefficient, the proportionality constant in Equation (6.2) is found to be also proportional to the square of the electromechanical coupling factor, k^2. However, note that since the experiments were carried out on samples with different polarization states (that is, unpoled and poled), the correlation is not significant from a theoretical viewpoint. In principle, only the dielectric loss associated with poled samples should be considered.

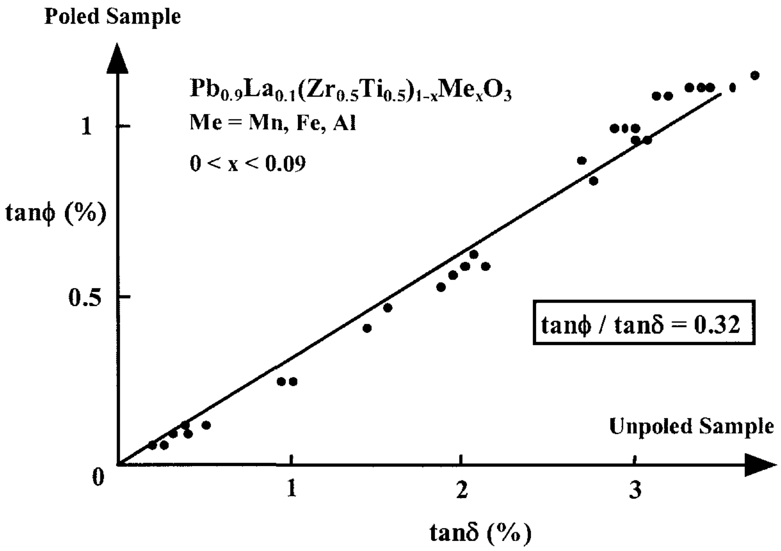

Figure 6.1 The correlation between mechanical loss, tanϕ, and dielectric loss, tanδ, for a series of piezoelectric ceramics with composition $Pb_{0.9}La_{0.1}(Zr_{0.5}Ti_{0.5})_{1-x}Me_xO_3$, where Me represents the dopant ions Mn, Fe, or Al, and x covers a range between 0 and 0.09.[4] [f=520 kHz]

(2) Dielectric Loss and Hysteresis and the Polarization [P(E)]Curve

The Relationship Between Dielectric Hysteresis and the Dissipation Factor

Let us consider first the dielectric loss and hysteresis associated with the electric displacement, D, (which is proportional and almost equal to the polarization, P) versus electric field, E, curve pictured in Figure 6.2, neglecting the electromechanical coupling. When the electric displacement, D, (or polarization, P) traces a different curve with increasing applied electric field, E, than it does when the applied electric field is decreasing, the material is said to be exhibiting *dielectric hysteresis*.

When the dielectric hysteresis is not very large, the observed variation in electric displacement, D, can be represented as if it had a slight phase lag with respect to the applied electric field. If the alternating electric field, E^*, associated with such a phase lagging electric displacement has an angular frequency, $\omega=2\pi f$, it can be expressed as:

$$E^* = E_o\, e^{j\omega t} \qquad (6.5)$$

and the induced electric displacement, D^*, will oscillate at the same frequency but lag in phase by δ, such that:

$$D^* = D_o\, e^{j(\omega t-\delta)} \qquad (6.6)$$

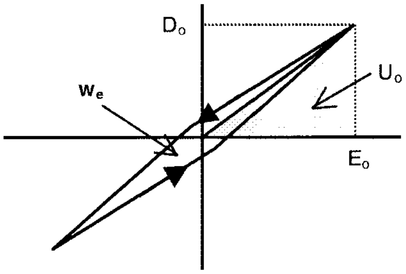

Figure 6.2 A plot of electric displacement, D, as a function of applied electric field, E, characteristic of dielectric hysteresis.

If we express the relationship between D^* and E^* as:

$$D^* = K^* \varepsilon_o E^* \qquad (6.7)$$

where the *complex dielectric constant*, K^*, is:

$$K^* = K' - j\,K'' \qquad (6.8)$$

and where:

$$K''/\,K' = \tan\delta \qquad (6.9)$$

Note that the negative sign preceding the imaginary part of Eq. (6.8) is associated with the phase lag of the electric displacement and that $K'\varepsilon_o= (D_o/E_o)\cos\delta$ and $K''\varepsilon_o= (D_o/E_o)\sin\delta$. In terms of this complex description, the hysteresis loop should be elliptical in shape, which is not what is actually observed.

The integrated area inside the hysteresis loop, labeled w_e in Figure 6.2, is equivalent to the energy loss per cycle per unit volume of the dielectric. It is defined for an isotropic dielectric as:

$$w_e = -\int D\, dE = -\int_0^{2\pi/\omega} D \frac{dE}{dt}\, dt \qquad (6.10)$$

Substituting the real parts of the Electric Field, E^*, and Electric Displacement, D^*, into Equation (6.10) yields:

$$w_e = \int_0^{2\pi/\omega} D_o \cos(\omega t - \delta)[E_o\, \omega \sin(\omega t)]\, dt$$

$$= E_o D_o \omega \sin(\delta) \int_0^{2\pi/\omega} \sin^2(\omega t) dt = \pi E_o D_o \sin(\delta) \qquad (6.11)$$

so that:

$$w_e = \pi K'' \varepsilon_o E_o^2 = \pi K' \varepsilon_o E_o^2 \tan\delta \qquad (6.12)$$

When there is no phase lag (δ=0), the energy loss will be zero (w_e=0) and the electrostatic energy stored in the dielectric will be recovered completely after a full cycle (100% efficiency). However, when there is a phase lag, an energy loss (or non-zero w_e) will occur for every cycle of the applied electric field resulting in the generation of heat in the dielectric material. In this context, the quantity $\tan\delta$ is referred to as the *dissipation factor*.

The electrostatic energy stored during a half cycle of the applied electric field will be just $2U_e$, where U_e, the integrated area so labeled in Figure 6.2, represents the energy stored during a quarter cycle. This can be expressed as:

$$(1/2)w_e = 2\, U_e = 2\, [(1/2)\, (E_o D_o \cos\delta)] = (E_o D_o)\cos\delta \qquad (6.13a)$$

Recognizing that $K'\varepsilon_o = (D_o/E_o)\cos\delta$, Eq. (6.13a) may be rewritten in the form:

$$(1/2)w_e = 2\, U_e = K'\, \varepsilon_o\, E_o^2 \qquad (6.13b)$$

Combining this equation with Equation (6.12) yields an alternative expression for the dissipation factor:

$$\tan\delta = (1/2\pi)\, (w_e / U_e) \qquad (6.14)$$

which highlights the significance of tanδ in terms of the electrostatic energy efficiency.

The Temperature, Electric Field, and Frequency Dependences of the Intensive Dielectric Loss

The temperature, frequency, and electric field dependences of the intensive dielectric loss, tanδ', as determined from dielectric hysteresis data collected under stress-free conditions for a PZT-based ceramic are shown in Figures 6.3, 6.4 and 6.5, respectively.[5] We see from these data that the intensive dielectric loss, tanδ', decreases gradually with increasing temperature (Figure 6.3), but is rather insensitive to frequency in this low frequency range (Figure 6.4). It is also observed in Figure 6.5 that tanδ' initially increases in proportion to the applied electric field and then essentially levels off beyond 1.5 (kV/mm). The complex representation described in the previous section no longer applies for this range of applied electric field.

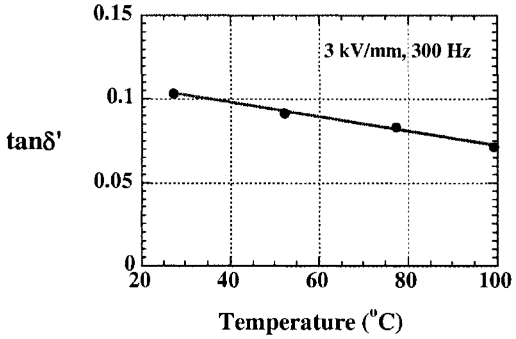

Figure 6.3 The intensive dielectric loss, tanδ', as a function of sample temperature (3 kV/mm, 300 Hz).[5]

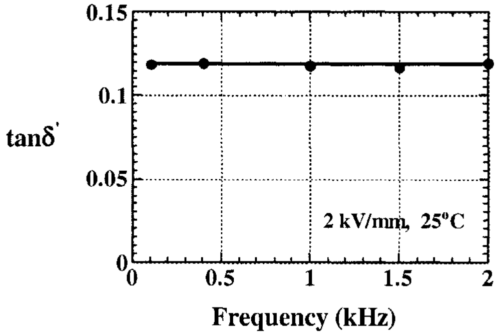

Figure 6.4 The intensive dielectric loss, tanδ', as a function of frequency (T=25°C, E=2 kV/mm).[5]

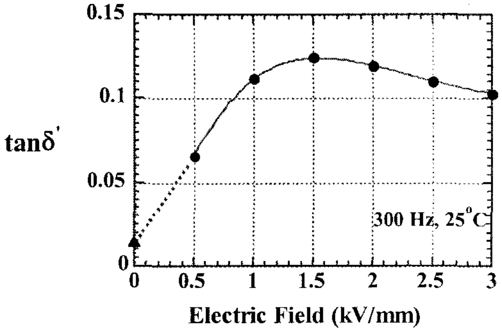

Figure 6.5 The intensive dielectric loss, tanδ', as a function of electric field (T=25°C, f=300 Hz).[5] [The value for E=0 (marked by a solid triangle on the plot) was obtained with an impedance analyzer under a very low electric field.]

(3) Electromechanical Loss and Hysteresis: General Considerations

A Theoretical Description

Let us expand the treatment presented in the previous section to include loss mechanisms associated with piezoelectric materials. We will start with the Gibbs free energy, G, which in this case is expressed as:

$$G = -(1/2)\, s^E X^2 - d\, X\, E - (1/2)\, K^X \varepsilon_0\, E^2 \tag{6.15}$$

and in general differential form as:

$$dG = -x\, dX - D\, dE - S\, dT \tag{6.16}$$

where x is the strain, X is the stress, D is the electric displacement, E is the electric field, S is the entropy, and T is the temperature. Equation (6.16) is the energy expression in terms of the externally controllable (which is denoted as "*intensive*") physical parameters X and E. The temperature dependence of the function is associated with the elastic compliance, s^E, the dielectric constant, K^X, and the piezoelectric charge coefficient, d. We obtain from the Gibbs energy function the following two piezoelectric equations:

$$x = -\frac{\partial G}{\partial X} = s^E X + d\, E \tag{6.17}$$

$$D = -\frac{\partial G}{\partial E} = d\, X + K^X \varepsilon_0\, E \tag{6.18}$$

Note that the Gibbs energy function and the piezoelectric equations derived from it cannot lead to a phase-lagging dielectric loss without invoking irreversible thermodynamic equations and dissipation functions. One can achieve a satisfactory description, however, by introducing complex physical constants into the phenomenological equations; in this way, the loss is treated as a perturbation. The theoretical equations so derived are accurate for cases where the dielectric and mechanical losses, tanδ', tanϕ', and tanθ', are not very large (≈ 0.1).

Therefore, we will introduce the complex parameters K^{X*}, s^{E*}, and d^* in order to account for the hysteretic losses associated with the electric, elastic, and piezoelectric coupling energy:

$$K^{X*} = K^X (1-j \tan\delta') \tag{6.19}$$

$$s^{E*} = s^E (1-j \tan\phi') \tag{6.20}$$

$$d^* = d\ (1-j \tan\theta') \tag{6.21}$$

where θ' is the phase delay of the strain under an applied electric field, or the phase delay of the electric displacement under an applied stress. They will be exactly the same if we use the same complex piezoelectric constant d^* in Equations (6.17) and (6.18). Here, the angle δ' represents the phase delay of the electric displacement in response to an applied electric field under a constant stress (that is, zero stress) condition. Finally, the angle ϕ' is the phase delay of the strain in response to an applied stress under a constant electric field (that is, a short-circuit) condition. We will view these phase delays as "intensive" losses.

Samples of experimentally determined D-E (stress-free conditions), x-X (short-circuit conditions), x-E (stress-free conditions), and D-X (open-circuit conditions) hysteresis curves appear in Figure 6.6. These measurements are standard for the characterization of piezoelectric materials and simple to conduct.

The purely electrical and purely mechanical stored energies and hysteretic losses may be expressed in terms of the dielectric and mechanical hysteresis curves depicted in Figures 6.6(a) and 6.6(b) as:

$$U_e = (1/2)\, K^X \varepsilon_o E_o^2 \tag{6.22}$$

$$w_e = \pi K^X \varepsilon_o E_o^2 \tan\delta' \tag{6.23}$$

$$U_m = (1/2)\, s^E X_o^2 \tag{6.24}$$

$$w_m = \pi s^E X_o^2 \tan\phi' \tag{6.25}$$

according to the analysis carried out in the previous section.

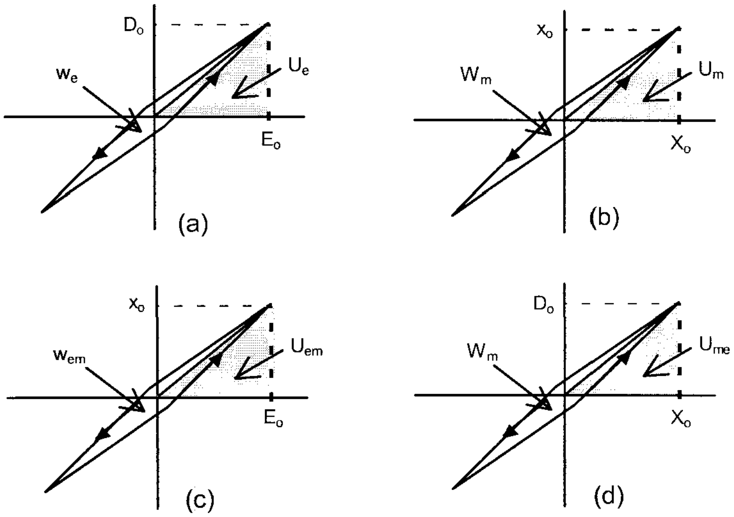

Figure 6.6 Samples of experimentally determined hysteresis curves: (a) D-E (stress-free conditions), (b) x-X (short-circuit conditions), (c) x-E (stress-free conditions), and (d) D-X (open-circuit conditions).

It is not possible to determine the more complicated electromechanical loss by applying a similar analysis to the x-E curve, however, because it does not adequately account for all the elastic energy expended. Let us consider the electromechanical energy, U_{em}, stored during a quarter cycle of the applied electric field cycle (that is, from $E=0$ to $E=E_o$) in terms of our previous analysis:

$$U_{em} = -\int x\,dX = \frac{1}{2}\left[\frac{x_o^2}{s^E}\right] = \frac{1}{2}\left[\frac{(E\,d)^2}{s^E}\right] \tag{6.26}$$

Replacing d and s^E by $d^*=d(1-j\tan\theta')$ and $s^{E*} = s^E(1-j\tan\phi')$, we obtain:

$$U_{em} = \frac{1}{2}\left[\frac{d^2}{s^E}\right]E_o^2 \tag{6.27}$$

and

$$w_{em} = \pi\left[\frac{d^2}{s^E}\right]E_o^2\left(2\tan\theta' - \tan\phi'\right) \tag{6.28}$$

So we see that the x-E hysteresis data analyzed in this manner does not lead to a relationship that involves only the piezoelectric loss, $\tan\theta'$; instead we find that the observed loss involves contributions from both the piezoelectric, tanθ', and the elastic loss, tanϕ'.

Similarly, when we consider the D-X hysteresis data in this manner, the electromechanical energy U_{me} stored during a quarter cycle of the applied stress and the hysteresis loss, w_{me}, that occurs during a full stress cycle, are found to be:

$$U_{me} = \frac{1}{2}\left[\frac{d^2}{K^X \varepsilon_o}\right] X_o^2 \tag{6.29}$$

and

$$w_{me} = \pi \left[\frac{d^2}{K^X \varepsilon_o}\right] X_o^2 \left(2\tan\theta' - \tan\delta'\right) \tag{6.30}$$

Hence, from the D-E and x-X data, we can obtain the contributions of the dielectric loss, tanδ', and the mechanical loss, tanϕ', respectively, we may evaluate finally the electromechanical loss, tan θ'.

Our discussion so far has been concerned with the so-called "intensive" electric, mechanical, and piezoelectric losses, which are defined in terms of the "intensive" (that is, externally controllable) parameters of applied stress, X, and electric field, E. In order to further define the physical significance of the electromechanical losses, we will need to also consider the free energy in terms of the "extensive" (that is, material-related) parameters of strain, x, and electric displacement, D.[1] We will start once again with the differential form of the free energy equation, which in this case is the Helmholtz free energy designated by A, such that:

$$dA = X\,dx + E\,dD - S\,dT, \tag{6.31}$$

We obtain from this energy function the following two piezoelectric equations:

$$X = \frac{\partial A}{\partial x} = c^D x - h D \tag{6.32}$$

$$E = \frac{\partial A}{\partial D} = -h x + \frac{\kappa^x}{\varepsilon_o} D \tag{6.33}$$

where c^D is the elastic stiffness at constant electric displacement (open-circuit conditions), h is the inverse piezoelectric charge coefficient, and κ^x is the inverse dielectric constant at constant strain (mechanically clamped conditions). The extensive dielectric loss (tanδ), mechanical loss (tanϕ), and piezoelectric loss (tanθ) are thus defined in terms of the these quantities expressed in complex form as:

$$\kappa^{x*} = \kappa^{x}(1 + j\tan\delta) \qquad (6.34)$$

$$c^{D*} = c^{D}(1 + j\tan\phi) \qquad (6.35)$$

$$h^{*} = h(1 + j\tan\theta) \qquad (6.36)$$

It should be noted that the dielectric constant under a constant strain (i.e., zero strain or completely clamped) condition, K^{x*}(not K^{X*}), and the elastic compliance under a constant electric displacement (i.e., open-circuit) condition, s^{D*}(not s^{E*}), can simply be provided as the inverses of κ^{x*} and c^{D*}, respectively. Thus, using the same loss quantities represented by Equations (6.34) and (6.35), we can express their corresponding inverse complex quantities as:

$$K^{x*} = K^{x}(1 - j\tan\delta) \qquad (6.37)$$

$$s^{D*} = s^{D}(1 - j\tan\phi) \qquad (6.38)$$

and consider the phase delays associated with them in terms of extensive losses.

Example Problem 6.1

Verify the relationship:

$$\frac{d^2}{s^E K^X \varepsilon_0} = \frac{h^2}{c^D(\kappa^x/\varepsilon_0)} \qquad (P6.1.1)$$

This value is defined as the square of an electromechanical coupling factor (k^2), which should be the same even for different energy description systems.

Solution

When the following equations [Equations (6.17) and (6.18)]:

$$x = s^E X + d E \qquad (P\ 6.1.2)$$

$$D = d X + K^X \varepsilon_0 E \qquad (P6.1.3)$$

are combined with the following [Equations (6.32) and (6.33)]:

$$X = c^D x - h D \qquad (P6.1.4)$$

$$E = -h x + (\kappa^x/\varepsilon_0) D \qquad (P6.1.5)$$

we obtain:

$$X = c^D(s^E X + d E) - h(d X + K^X \varepsilon_0 E) \qquad (P6.1.6)$$
$$E = -h(s^E X + d E) + (\kappa^x/\varepsilon_0)(d X + K^X \varepsilon_0 E) \qquad (P6.1.7)$$

or upon rearranging:

$$(1 - c^D s^E + h\, d)\, X + (h\, K^X \varepsilon_o - c^D d)\, E = 0 \tag{P6.1.8}$$

$$[h\, s^E - (\kappa^x / \varepsilon_o)\, d]\, X + [1 - (\kappa^x / \varepsilon_o)\, K^X \varepsilon_o + h\, d]\, E = 0 \tag{P6.1.9}$$

Combining the latter two equations yields:

$$(1-c^D s^E+hd)[1-(\kappa^x/\varepsilon_o)\, K^X \varepsilon_o + hd] - (h\, K^X \varepsilon_o - c^D d)[hs^E-(\kappa^x/\varepsilon_o)d] = 0 \tag{P6.1.10}$$

which, when simplified, produces the desired relationship:

$$\frac{d^2}{s^E K^X \varepsilon_o} = \frac{h^2}{c^D (\kappa^x / \varepsilon_o)} \tag{P6.1.11}$$

It is important to consider the conditions under which a material will be operated when characterizing the dielectric constant and elastic compliance of that material. When a constant electric field is applied to a piezoelectric sample as illustrated in Figure 6.7(a), the total output energy will be a combination of the energies associated with two distinct mechanical conditions that may be applied to the material: (1) the *mechanically clamped state*, where a constant strain is maintained and the specimen cannot deform, and (2) the *mechanically free state*, in which the material is not constrained and is free to deform. We expect then that during the time interval over which the total input electrical energy is applied the total output energy will just be the sum of the energies associated with these two states, and, under ideal conditions, equivalent to the total input energy. This can be expressed by:

$$\frac{1}{2} K^X \varepsilon_o E_o^2 = \frac{1}{2} K^x \varepsilon_o E_o^2 + \frac{1}{2} \frac{d^2}{s^E} E_o^2 \tag{6.39a}$$

such that:

$$K^X \varepsilon_o = K^x \varepsilon_o + \frac{d^2}{s^E} \tag{6.39b}$$

When a constant stress is applied to the piezoelectric as illustrated in Figure 6.7(b), the total output energy will be a combination of the energies associated with two distinct electrical conditions that may be applied to the material: (1) the *open-circuit state*, where a constant electric displacement is maintained, and (2) the *short-circuit state*, in which the material is subject to a constant electric field. We expect in this case that during the time interval over which the total input mechanical energy is applied, once again the total output energy will just be the sum of the energies associated with these two states, and, under ideal conditions, equivalent to the total input energy. This can be expressed as:

$$\frac{1}{2} s^E X_o^2 = \frac{1}{2} s^D X_o^2 + \frac{1}{2} \frac{d^2}{K^X \varepsilon_o} X_o^2 \tag{6.40a}$$

which leads to:

$$s^E = s^D + \frac{d^2}{K^X \varepsilon_o} \tag{6.40b}$$

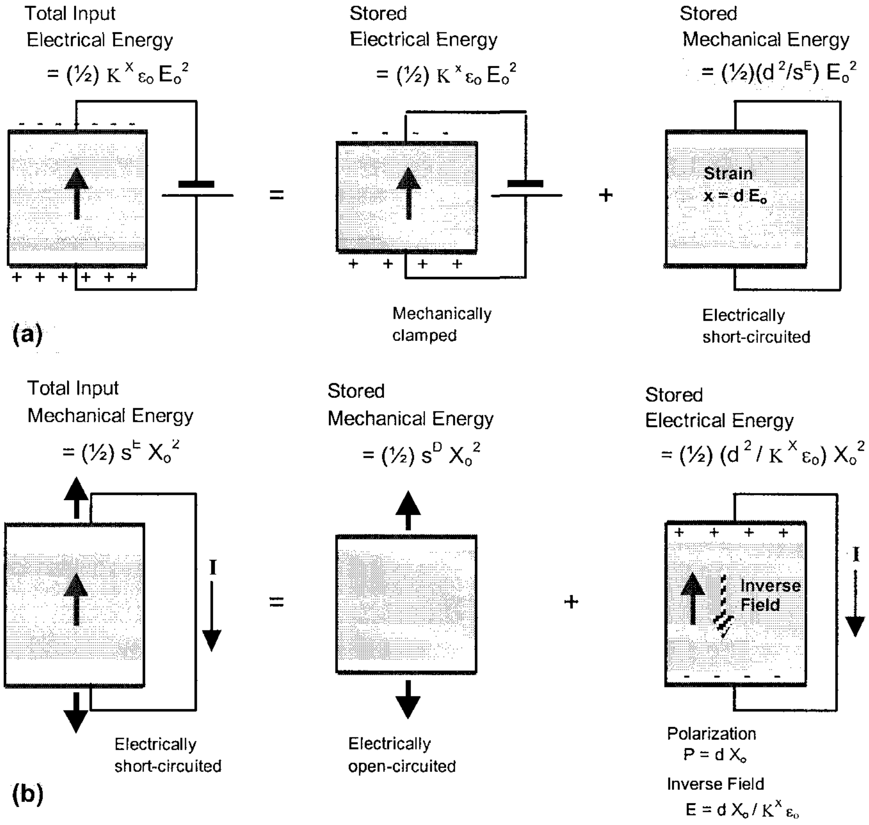
Total Input
Electrical Energy
= (½) $K^X \varepsilon_o E_o^2$
Stored
Electrical Energy
= (½) $K^x \varepsilon_o E_o^2$
Stored
Mechanical Energy
= (½)(d^2/s^E) E_o^2
=
+
Strain
$x = d E_o$
Mechanically
clamped
Electrically
short-circuited
(a)
Total Input
Mechanical Energy
= (½) $s^E X_o^2$
Stored
Mechanical Energy
= (½) $s^D X_o^2$
Stored
Electrical Energy
= (½) ($d^2 / K^X \varepsilon_o$) X_o^2
I
=
+
Inverse
Field
I
Electrically
short-circuited
Electrically
open-circuited
Polarization
$P = d X_o$
Inverse Field
$E = d X_o / K^X \varepsilon_o$
(b)

Figure 6.7 Schematic representation of the response of a piezoelectric material under: (a) constant applied electric field and (b) constant applied stress conditions.

Hence, we obtain the following equations:

$$K^x / K^X = (1 - k^2) \tag{6.41}$$

$$s^D / s^E = (1 - k^2) \tag{6.42}$$

where:

$$k^2 = \frac{d^2}{s^E K^X \varepsilon_o} \tag{6.43}$$

We may also write equations of similar form for the corresponding reciprocal quantities:

$$\kappa^X / \kappa^x = (1 - k^2), \tag{6.44}$$

$$c^E / c^D = (1 - k^2), \tag{6.45}$$

where, in this context,

$$k^2 = \frac{h^2}{c^D (\kappa^X / \varepsilon_o)} \tag{6.46}$$

This new parameter k is the *electromechanical coupling factor*, and identical to the k in Equation (6.43). It will be regarded as a real quantity for the cases we examine in this text (see Example Problem 6.1).

In order to establish relationships between the intensive and extensive losses, we will need to employ the following three equations, which describe the dielectric permittivity under constant stress ($K^X \varepsilon_o$), the elastic compliance under constant electric field (s^E), and the piezoelectric charge coefficient (d) in terms of their corresponding reciprocal quantities:

$$K^X \varepsilon_o = \frac{1}{(\kappa^x / \varepsilon_o)[1 - h^2 / (c^D \kappa^x / \varepsilon_o)]} \tag{6.47}$$

$$s^E = \frac{1}{c^D [1 - h^2 / (c^D \kappa^x / \varepsilon_o)]} \tag{6.48}$$

$$d = \frac{h^2 / (c^D \kappa^x / \varepsilon_o)}{h [1 - h^2 / (c^D \kappa^x / \varepsilon_o)]} \tag{6.49}$$

Replacing the parameters in the three equations above with the complex parameters defined in Equations (6.19)-(6.21) and (6.34)-(6.36), and making use of Equations (6.43) and (6.46) to incorporate the electromechanical coupling factor, k, we obtain the following useful expressions that relate the intensive and extensive losses:

$$\tan\delta' = \left(\frac{1}{1-k^2}\right)\left[\tan\delta + k^2(\tan\phi - 2\tan\theta)\right] \tag{6.50}$$

$$\tan\phi' = \left(\frac{1}{1-k^2}\right)\left[\tan\phi + k^2(\tan\delta - 2\tan\theta)\right] \tag{6.51}$$

$$\tan\theta' = \left(\frac{1}{1-k^2}\right)\left[\tan\delta + \tan\phi - (1+k^2)\tan\theta\right] \tag{6.52}$$

A significant feature of this result is that the intensive dielectric, elastic, and piezoelectric losses are found to be correlated with their extensive counterparts through the real electromechanical coupling factor. The denominator, $(1-k^2)$, appearing in each of the equations above comes essentially from the ratios K^x/K^X and s^D/s^E, which are equivalent to this factor as defined in Equations (6.41) and (6.42). The electromechanical coupling is thus reflected in our description of the dissipation factor, which by definition is just the imaginary part of the relevant complex parameter divided by the real part. It should also be noted that the precise definition of the electromechanical coupling factor for a given piezoelectric material will depend on the mode of vibration at which the sample is driven.

Measurement Techniques

The intensive losses of a PZT-based ceramic actuator manufactured by Philips Components determined from dielectric and mechanical hysteresis data appear in Figure 6.8. The intensive piezoelectric loss for this device is shown in Figure 6.9. An average correlation between the electric field and the compressive stress given by $X=E(K^X\varepsilon_o/s^E)^{1/2}$ was used. The hysteresis measurements were conducted under quasi-static conditions using the experimental apparatus depicted in Figure 6.10. The extensive losses depicted in Figure 6.11 for the PZT ceramic actuator were calculated from the intensive loss data recorded in Figures 6.8 and 6.9.

Note that the piezoelectric losses, $\tan\theta'$ and $\tan\theta$, are not as small as previously believed,[1] but are, in fact, comparable to the dielectric and elastic losses, and increase gradually with the applied field or stress. It is also noteworthy that the extensive dielectric loss, $\tan\delta$, increases significantly with an increase of the intensive parameter (the applied electric field), while the extensive elastic loss, $\tan\phi$, is rather insensitive to changes in the intensive parameter (the applied compressive stress).

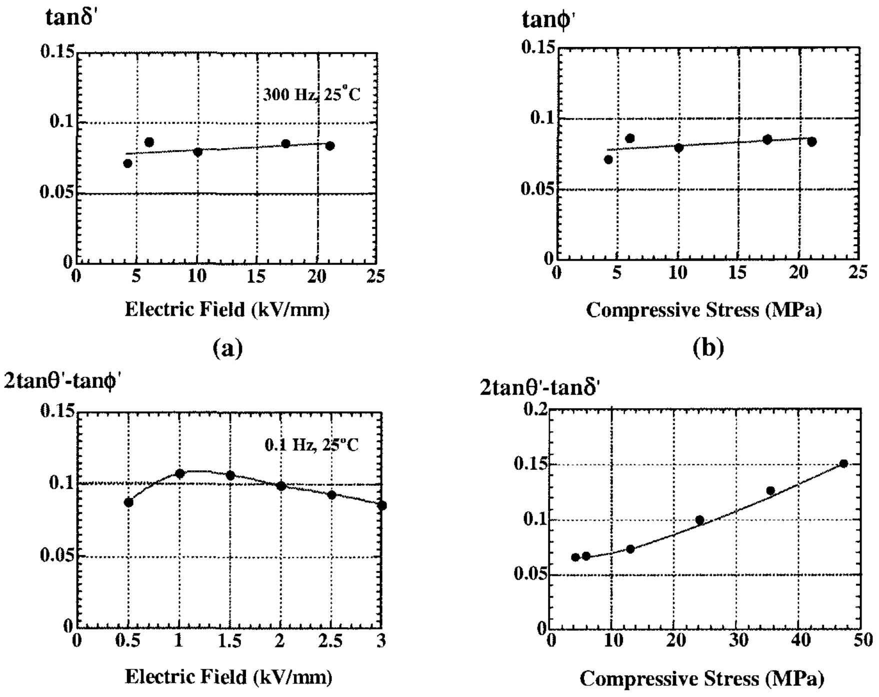

(a) (b) (c) (d)

Figure 6.8 Intensive losses determined from: (a) D-E (mechanically free), (b) x-X (short-circuit), (c) x-E (mechanically free) and (d) D-X (open-circuit) hysteresis data for a PZT-based actuator.

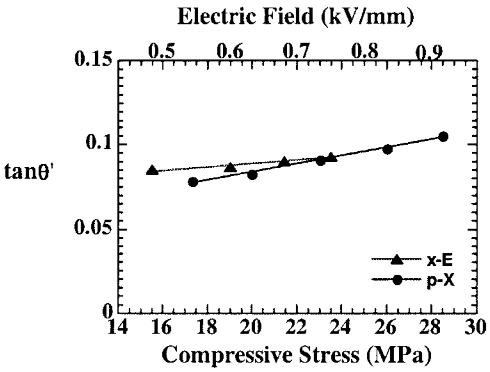

Figure 6.9 The intensive piezoelectric loss, tanθ', as a function of electric field and compressive stress, for a PZT-based actuator.

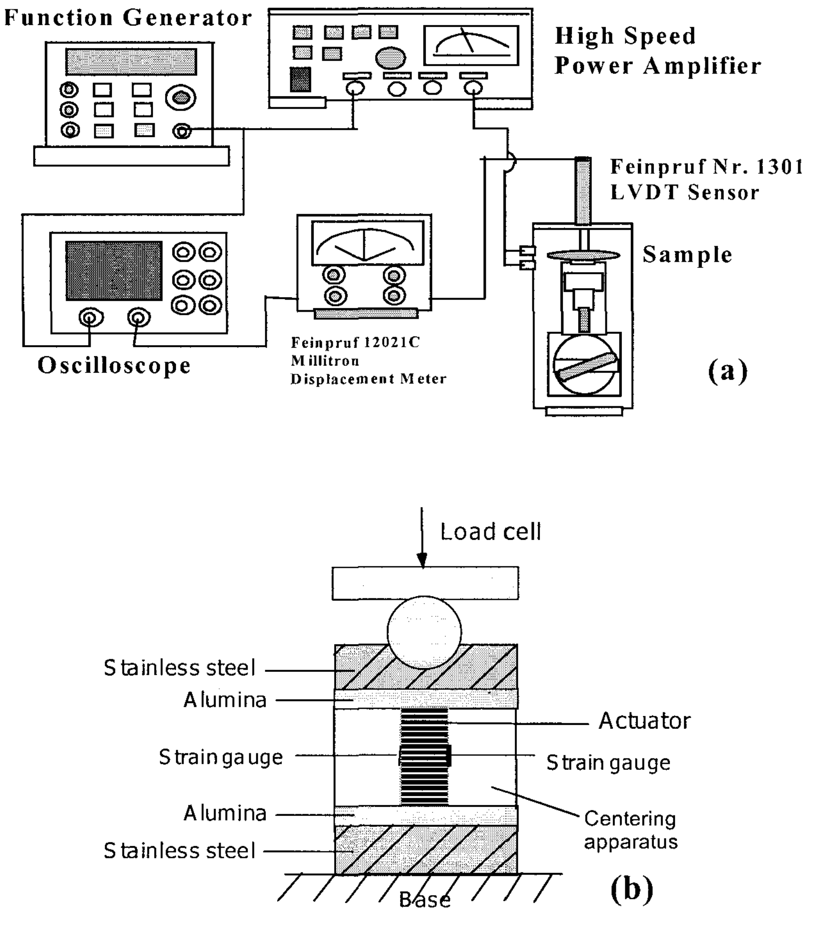
Function Generator
High Speed
Power Amplifier
Feinpruf Nr. 1301
LVDT Sensor
Sample
Oscilloscope
Feinpruf 12021C
Millitron
Displacement Meter
(a)
Load cell
Stainless steel
Alumina
Strain gauge
Alumina
Stainless steel
Actuator
Strain gauge
Centering
apparatus
Base
(b)

Figure 6.10 Experimental apparatus for collecting the hysteresis data: (a) D-E and x-E, and (b) x-X and D-X.

When hysteresis data corresponding to Figures 6.6(a) (D-E) and 6.6(b) (x-X) are collected under constrained conditions, that is, D-E is measured from a material that is mechanically clamped and x-X is measured under open-circuit conditions, the observed hysteresis will be smaller as will be the extensive losses, tanδ and tanϕ. This alternative route for obtaining the three losses independently, however, presents some practical difficulties; it is almost impossible to achieve a completely clamped state for an elastically stiff piezoelectric ceramic, and charge leakage can be significant during an x-X measurement under these conditions.

(4) Losses at Piezoelectric Resonance

So far, we have considered the losses for a quasi-static or off-resonance state. A variety of problems arises when ultrasonic motors are driven at a resonance frequency. Among the most detrimental effects to occur are a significant distortion of the admittance spectrum due to the nonlinear response of the elastic compliance for high amplitude vibrations and the generation of heat, which leads to a serious degradation of motor performance due to depoling of the piezoelectric ceramic. While a high Q_m is desirable for reducing the amount of heat generated in the device, it should be noted that the amplitude of the vibration at resonance is directly proportional to the magnitude of the quality factor.

The Admittance and Displacement at a Piezoelectric Resonance

First, we will consider the admittance spectrum of the piezoelectric ceramic. Similar to what was done in Section 6.1(3), we will make use of the complex parameters $K_{33}{}^{X*}=K_{33}{}^{X}(1-j\tan\delta')$, $s_{11}{}^{E*}= s_{11}{}^{E}(1-j\tan\phi')$, and $d_{31}{}^{*}=d(1-j\tan\theta')$, substituting them this time into Equation (5.96) such that:

$$\begin{aligned}
Y = Y_d + Y_m &= (1-k_{31}^2)\,\frac{j\omega w l K_{33}^X \varepsilon_o}{t}\left[1 - \frac{j}{1-k_{31}^2}\left[\tan\delta' - k_{31}^2(2\tan\theta' - \tan\phi')\right]\right] \\
&\quad + \frac{j\omega w l K_{33}^2 \varepsilon_o}{t}\, k_{31}^2\left[\left(1 - j(2\tan\theta' - \tan\phi')\right)\frac{\tan(\omega l/2v*)}{\omega l/2v*}\right] \\
&= j\omega C_d\left[1 - \frac{j}{(1-k_{31}^2)}\left[\tan\delta' - k_{31}^2(2\tan\theta' - \tan\phi')\right]\right] \\
&\quad + j\omega C_0\, k_{31}^2\left[\left(1 - j(2\tan\theta' - \tan\phi')\right)\frac{\tan(\omega l/2v*)}{\omega l/2v*}\right] \\
&= j\omega C_d(1 - j\tan\delta) + j\omega C_o k_{31}^2\left[\left(1 - j(2\tan\theta' - \tan\phi')\right)\frac{\tan(\omega l/2v*)}{\omega l/2v*}\right] \qquad (6.53)
\end{aligned}$$

where the following additional substitutions are made:

$$C_o = \frac{w l K_{33}^X \varepsilon_o}{t} \qquad (6.54)$$

$$C_d = (1 - k_{31}^2)C_o \qquad (6.55)$$

Note that the loss appearing in the first term of Equation (6.53) (the damped admittance) includes the extensive dielectric loss, tanδ, not the intensive loss, tanδ'.

Making use of the following expression for the complex velocity:

$$v^* = \frac{1}{\sqrt{\rho s_{11}^E (1 - j\tan\phi')}} = v\,(1 + (1/2)\,j\tan\phi') \qquad (6.56)$$

we may define the quantity $1/(\tan(\omega l/2v^*)$ with an expansion-series approximation over a range of frequencies around $\omega l/2v^* = \pi/2$. The resonance state will be defined with respect to a finite admittance maximum, rather than an infinite Y in a loss-free material. We may now make use of two new frequency parameters, Ω, and $\Delta\Omega$, defined as:

$$\Omega = \omega l / 2v \qquad (6.57a)$$

and

$$\Delta\Omega = \Omega - \pi/2\ (<<1) \qquad (6.57b)$$

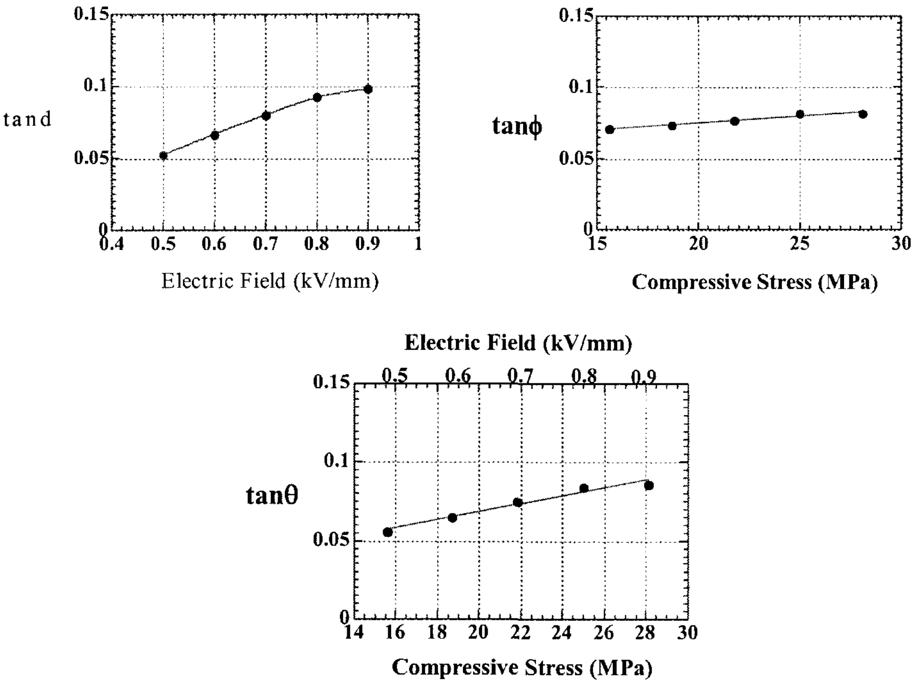

Figure 6.11 The extensive loss factors, tanδ, tanϕ, and tanθ, as a function of electric field or compressive stress, measured for a PZT-based actuator.

Since we know that $\omega\, l/2\, v^* = (\pi/2 + \Delta\Omega)\,[1-(1/2)\, j \tan \phi']$, we may now express:

$$\frac{1}{\tan(\omega\, l/2v^*)} = -\Delta\Omega + j(\pi/4)\tan\phi' \qquad (6.58)$$

Thus, assuming that $\Gamma_{31} = k_{31}^2/(1-k_{31}^2)$, an approximate expression for Y_m over a range of frequencies around the first resonance may be written as follows:

$$\begin{aligned} Y_m &= j\omega C_d \Gamma_{31}\, [(1-j(2\tan\theta - \tan\phi')][(\tan(\omega l/2v^*)/(\omega\, l/2v^*)] \\ &= j\omega_o C_d \Gamma_{31}\left[\frac{1 - j(2\tan\theta - \tan\phi')}{(-\Delta\Omega + j(\pi/4)\tan\phi')(\pi/2)(1-(1/2)\, j\tan\phi')}\right] \\ &= j(8/\pi^2)\,\omega_o\, C_d\, \Gamma_{31}\left[\frac{1 + j[(3/2)\tan\phi' - 2\tan\theta]}{-(4/\pi)\Delta\Omega + j\tan\phi'}\right] \qquad (6.59) \end{aligned}$$

The maximum admittance, Y_m^{max}, is obtained at $\Delta\Omega = 0$:

$$Y_m^{max} = (8/\pi^2)\,\omega_o\, C_d\, \Gamma_{31}\, (\tan\phi')^{-1} \qquad (6.60)$$

In order to obtain the mechanical quality factor, we will need to consider a value of $\Delta\Omega$, which corresponds to the half-power point or an admittance level of $Y_m^{max}/\sqrt{2}$. This condition is met when $\Delta\Omega = (\pi/4)\tan\phi'$, such that:

$$Q_m = \Omega_o/2\,\Delta\Omega = (\pi/2)/2(\pi/4)\tan\phi' = (\tan\phi')^{-1} \qquad (6.61)$$

This verifies the inverse relationship between the mechanical quality factor and the mechanical loss, $Q_m = (\tan\phi')^{-1}$.

Example Problem 6.2

Starting with the following equation for the motional admittance:

$$Y_m = j(8/\pi^2)\,\omega_o\, C_d\, \Gamma_{31}\left[\frac{1 + j\,[(3/2)\tan\phi' - 2\tan\theta]}{-(4/\pi)\Delta\Omega + j\tan\phi'}\right] \qquad (P6.2.1)$$

obtain expressions for the mechanical quality factor, Q_m, and the maximum admittance, Y_m^{max}.

Solution

Focusing on the dependence of this equation on $\Delta\Omega$, we see that it will exhibit its maximum when $\Delta\Omega = 0$, and be at the half-power point (that is, $(1/\ \ 2)Y_m^{max}$) when $(4/\pi)\Delta\Omega = \tan\phi'$.

Since $Q_m=\Omega_0/2\Delta\Omega$ at the half-power point, where $\Omega_0= \pi/2$, we can write:

$$Q_m = \frac{(\pi/2)}{2(\pi/4)\tan\phi'} = \frac{1}{\tan\phi'} \qquad \text{(P6.2.2)}$$

So that,

$$Y_m^{max} = j(8/\pi^2)\omega_o C_d \Gamma_{31}\left[\frac{1+j\,[(3/2)\tan\phi' - 2\tan\theta]}{-(4/\pi)\Delta\Omega + j\tan\phi'}\right] = \frac{(8/\pi^2)\omega_o C_d \Gamma_{31}}{\tan\phi'} \qquad \text{(P6.2.3)}$$

We will next consider the displacement amplification. Once again we may make substitutions of the appropriate complex parameters, this time into Equation (5.101), to yield:

$$u(l) = d_{31}^{*} E_Z l\left[\frac{2v^*}{\omega l}\right]\tan\left(\frac{\omega l}{2v^*}\right)$$

$$= 2d_{31}(1 - j\tan\theta)E_Z l\left[\frac{v[1 + (1/2)j\tan\phi']}{\omega l}\right]\left[\tan\left(\frac{\omega l}{2v^*}\right)\right]$$

$$= 2d_{31}(1 - j\tan\theta)E_Z\ l\left[\frac{v[1 + (1/2)j\tan\phi'}{\omega_o\ l\,[-\Delta\Omega + j(\pi/4)\tan\phi']}\right] \qquad (6.62)$$

The maximum displacement u_{max} is obtained at $\Delta\Omega = 0$:

$$u_{max} = (8/\pi^2)\ d_{31}\ E_z\, l\ (\tan\phi')^{-1} \qquad (6.63)$$

and we see that the maximum displacement at the resonance frequency is $(8/\pi^2)Q_m$ times larger than that occurring at a non-resonance frequency, $(d_{31}E_z\, l)$.

In summary, when we measure the admittance or displacement as a function of drive frequency, we can obtain the mechanical quality factor, Q_m, which is estimated from $Q_m=\omega_o/2\Delta\omega$, where $2\Delta\omega$ is the full width at half maximum as depicted in Figure 6.12. We will also be able to obtain from these data, the intensive mechanical loss, $\tan\phi'$, which has been shown to be just the inverse of the mechanical quality factor.

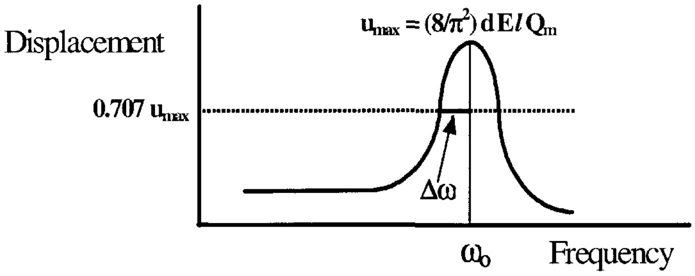

Figure 6.12 Frequency dependence of the induced displacement in a piezoelectric ceramic around the fundamental resonance frequency (k_{31} mode).

The Equivalent Circuit

The equivalent circuit for a piezoelectric actuator is generally represented with a network of inductive (L), capacitive (C0, and resistive ® components. An equivalent circuit representative of the resonant state of the piezoelectric is depicted schematically in Figure 6.13(a). It represents a condition of very low impedance. According to the expression for the admittance previously presented as Equation (6.53), we recognize that C_d corresponds to the electrostatic capacitance (of the longitudinally clamped sample considered in the development of this equation) and that the components L_A and C_A in the RCL series portion of the circuit represent the piezoelectric response. Let's consider as an example the case of a vibration setup in a rectangular plate through the piezoelectric tensor component d_{31}. The reactive equivalent circuit components corresponding to this vibrational state in the material are defined by the following equations:

$$L_A = \left[\frac{\rho}{8}\right]\left[\frac{lb}{w}\right]\left[\frac{s_{11}^{E^2}}{d_{31}^2}\right] \tag{6.64}$$

$$C_A = \left[\frac{8}{\pi^2}\right]\left[\frac{lw}{b}\right]\left[\frac{d_{31}^2}{s_{11}^E}\right] \tag{6.65}$$

where l is the length of the bar sample and w its width. The total resistance, R_A, appearing in the circuit depicted in Figure 6.13(a) represents the combined effect of resistances associated with the dielectric loss, R_d, (damped) and the extensive mechanical loss, R_m (motional). Thus, the effective resistance, R_A, will correspond essentially to the intensive mechanical loss, tanφ', which we found in Equation (6.51) depends on the extensive mechanical loss factor, tanφ, and the coupled dielectric and piezoelectric losses (tanδ–2tanθ). The equivalent circuit corresponding to the antiresonance state of the same actuator is depicted in Figure 6.13(b). In contrast to the low impedance network representing the resonance condition, this equivalent circuit is characterized by a relatively high impedance.

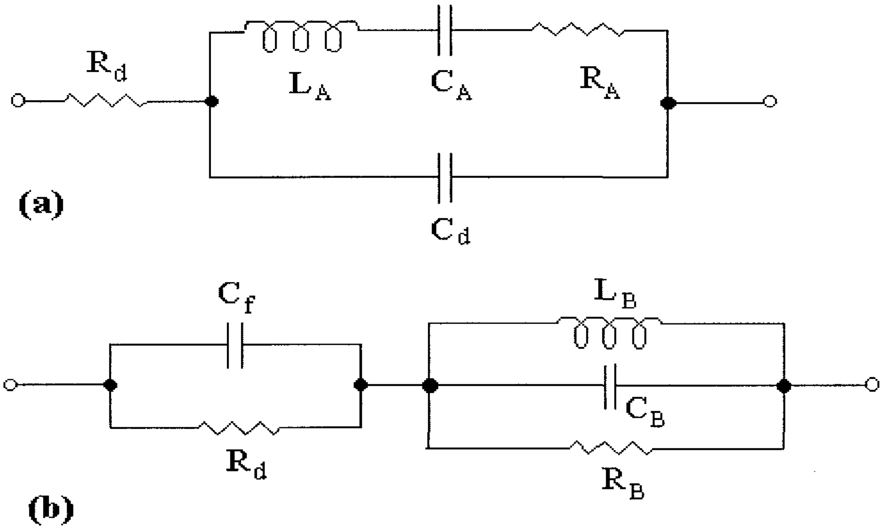

Figure 6.13 Equivalent circuits representing the response of a piezoelectric device: (a) at resonance and (b) at antiresonance.

Electromechanical Loss as a Function of Vibration Velocity

The mechanical quality factor Q_m can be obtained from the admittance data or the AC displacement spectrum at the half-power frequencies. When the data are collected under conventional constant voltage conditions, however, a significant asymmetry in the admittance spectrum is observed with increasing applied voltage (that is, as the vibration velocity is increased). Examples of this distorted response are depicted in Figure 6.14(a), where we see increasing asymmetry in the curves beyond a displacement velocity of 0.063 (m/s) and ultimately a discontinuity in the curve for the sample vibrating at 0.085 (m/s). This asymmetric and hysteretic response at high applied voltages makes this method unsuitable for the precise determination of the electromechanical coupling parameters of a piezoelectric device.

The asymmetry observed in the admittance spectrum under constant voltage conditions originates from the nonlinear elastic properties of the piezoelectric ceramic, which promote a significant increase in the strain around the resonance frequency. The induced AC displacement and vibration velocity are, hence, not directly proportional to the applied voltage and the asymmetric response is observed. The displacement and velocity are proportional to the motional current, however, and, therefore, a resonance method utilizing a constant motional current, where the minimum applied voltage corresponds to the resonance state, was developed to more precisely determine the electromechanical constants of piezoelectrics.[8] Note that the displacement at the end of the rectangular piezoelectric plate is a function of the sample size *l*, but that the vibration velocity at the tip is not size dependent. Thus, it is preferable to refer to the mechanical output with respect to the vibration velocity, rather than the applied electric field. Also note that the vibration velocity generally varies with frequency, and the values indicated near each curve in Figure 6.14 correspond to off-resonance conditions.

A schematic of the high power system used for this method is depicted in Figure 6.15.[10] The sample in this case is formed in a simple block configuration and electroded as appropriate for the desired vibrational mode to be excited. The impedance response of specimens examined with this system is shown in Figure 6.14(b). These data were collected under constant current conditions (that correspond in this case to constant AC displacement and vibration velocity). We see under these conditions almost perfectly symmetrical curves maintained up to relatively high vibration velocities. The mechanical quality factor, Q_m, is precisely determined from the bandwidth of the resonance impedance response measured under these conditions.[10]

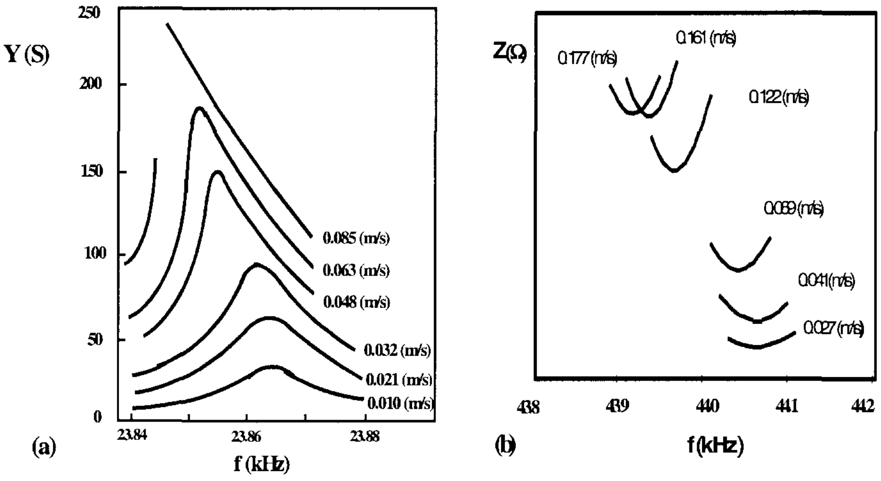

Figure 6.14 Admittance and impedance curves measured for a piezoelectric device under: (a) constant voltage and (b) constant current conditions.[8] [Note the asymmetrical curves obtained under constant voltage conditions and the more symmetric curve shapes obtained under constant current conditions.]

The mechanical quality factor, Q_m, is plotted in Figure 6.16 as a function of composition, x, for a $Pb(Zr_xTi_{1-x})O_3$ ceramic (doped with 2.1 atom percent Fe) at two effective vibration velocities, v_o=0.05 m/s and 0.5 m/s.[6] A trend that is noticeable in Figure 6.16 is the significant overall decrease in the mechanical quality factor with increasing vibration velocity. We also see from the curves shown in the figure complementary trends between the two vibration rates at the morphotropic phase boundary composition (x=0.52); a minimum in the Q_m at the lower vibration velocity corresponds to a maximum Q_m at the higher rate. It should be noted as well the data collected by conventional methods employing an impedance analyzer under low voltage (power) conditions will not reflect the high power performance of these materials.

Let us consider at this point the fundamental mechanism for the observed degradation of the mechanical quality factor, Q_m, with increasing vibration velocity. The effective resistances, R_m, R_d, and R_A, are shown in Figure 6.17 plotted as a function of vibration velocity of a PZT-based hard piezoelectric plate actuator.[8] Note that R_m, which we have indicated is primarily associated with the extensive mechanical loss, is largely insensitive to the vibration velocity, while R_d, which is associated with the extensive dielectric loss, is seen to increase significantly around a certain critical vibration velocity. Thus, the primary loss mechanism at smaller vibration velocities is considered to be the extensive mechanical loss, which provides a high mechanical quality factor, Q_m, under these conditions. As the vibration velocity increases, the contribution of the extensive dielectric loss increases significantly, and the Q_m (inverse of intensive mechanical loss) decreases as the sum of R_m and R_d. Heat is generated in the material beyond that critical vibration velocity where the extensive dielectric loss becomes the dominant factor.

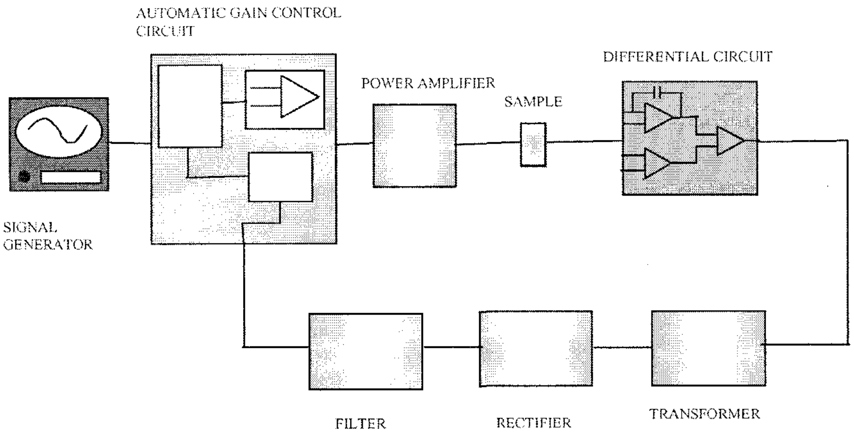

Figure 6.15 Block diagram of the constant current measurement system for determining the mechanical quality factor of piezoelectric ceramics.

It has been proposed that in general the extensive dielectric loss is mainly attributed to 180 degree domain reversal, and the mechanical loss is attributed to non-180 degree domain reorientation.[11] The domain reorientation will depend on the magnitude of the applied electric field; in particular, it has been suggested that the onset of 180 degree domain reversal occurs suddenly at a relatively high electric field, and that this is likely the primary mechanism for the generation of heat in these piezoelectric specimens. Further investigation is required to more precisely identify and model the microscale phenomena associated with the losses that appear to lead to the significant heat generation that occurs in the operation of piezoelectric actuator devices at resonance.

6.2 HEAT GENERATION IN PIEZOELECTRICS

(1) Heat Generation Under Off-Resonance Conditions

Heat generation in various types of PZT-based actuators operated under a relatively large applied electric field (equal to or greater than 1 kV/mm) at an off-resonance frequency has been studied, and a simple analytical method has been established to evaluate the temperature rise. Such an analysis is useful for designing high-power piezoelectric actuators.

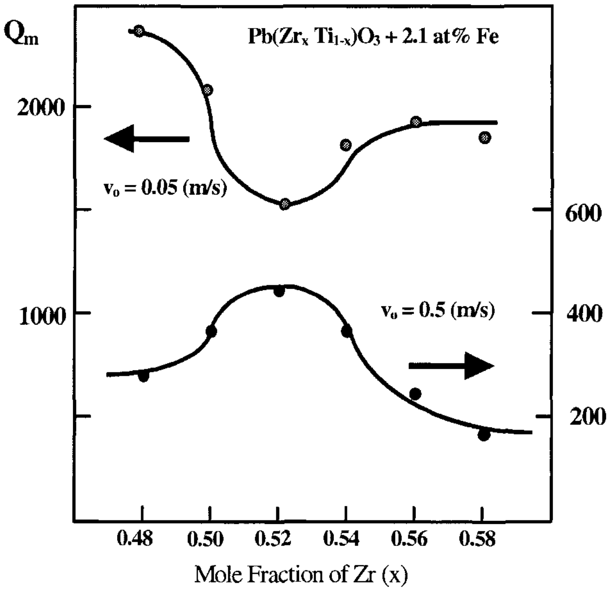

Figure 6.16 Mechanical quality factor, Q_m, plotted as a function of composition, x, at two effective vibration velocities v_o=0.05 m/s and 0.5 m/s for $Pb(Zr_xTi_{1-x})O_3$ doped with 2.1 atom percent Fe.[6]

The heat generated in multilayer piezoelectric ceramic (PZT-based) actuators of various sizes has been investigated and the mechanisms for the heating have been examined.[5] The device temperature of several PZT-based actuators manufactured by Philips driven at 3 kV/mm and 300 Hz is shown in Figure 6.18. A uniform temperature rise throughout the entire device was observed for all actuators tested. The temperature rise is plotted as a function of the ratio V_e/A in Figure 6.19, where V_e is the effective volume (between the electrodes of the device) and A is the surface area. The observed linear relationship is expected for the dissipation of heat through an area enclosing a volume of active material in which the heat is generated. Thus, we see that in designing an actuator that will experience only a small rise in temperature in operation, a small V_e/A is desired.

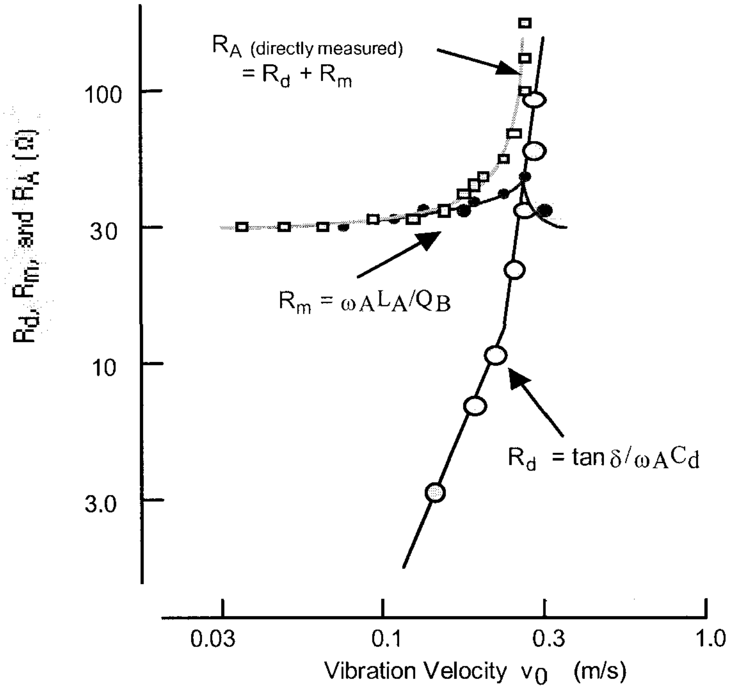

Figure 6.17 Vibration velocity dependence of the effective resistances R_m, R_d, and R_A for a PZT-based hard piezoelectric plate specimen operated in the k_{31} mode.[8]

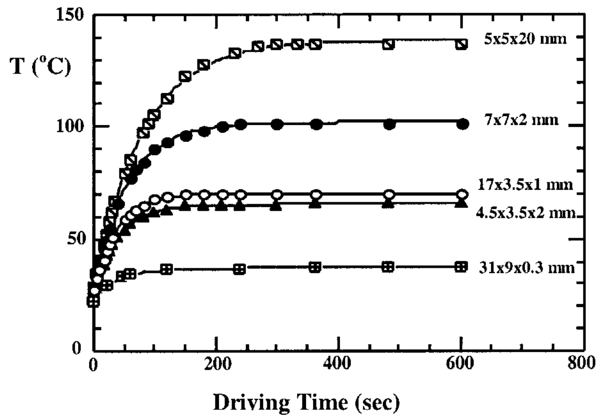

Figure 6.18 Device temperature as a function of driving time for multilayer actuators of various sizes operated at 300 Hz and 3 kV/mm.[5]

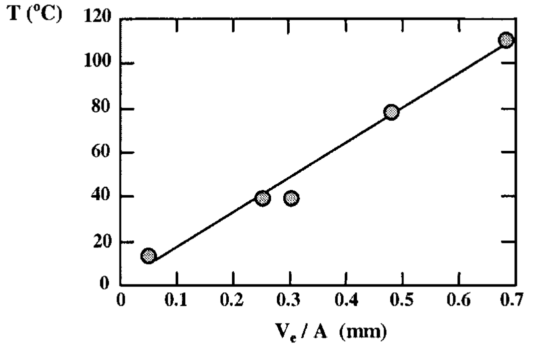

Figure 6.19 Temperature rise plotted as a function of the ratio V_e/A, where V_e is the effective volume in which the heat is generated and A is the surface area through which the heat is dissipated, for PZT multilayer actuators operated at 3 kv/mm and 300 Hz.[5]

According to the law of energy conservation, the amount of heat stored in the piezoelectric, which is just the difference between the rate at which heat is generated, q_g, and that at which the heat is dissipated, q_d, can be expressed as

$$q_g - q_d = V \rho C (dT/dt) \tag{6.66}$$

where it is assumed a uniform temperature distribution exists throughout the sample and V is the total volume, ρ is the mass density, and C is the specific heat of the specimen. The heat generation in the piezoelectric is attributed to losses. Thus, the rate of heat generation, q_g, can be expressed as:

$$q_g = w\,f\,V_e \qquad (6.67)$$

where w is the loss per driving cycle per unit volume, f is the driving frequency, and V_e is the effective volume of active ceramic. According to the measurement conditions, this w corresponds to the dielectric hysteresis loss, w_e, which was previously defined by Equation 6.23 in terms of the intensive dielectric loss tanδ' as:

$$w = w_e = \pi K^X \varepsilon_o E_o^2 \tan\delta'$$

Substituting for tanδ' by using the relationship defined by Equation (6.50), we arrive at an expression for the dielectric hysteresis loss written in terms of the extensive dielectric loss, tanδ, and the electromechanical loss, (tanϕ−2 tanθ):

$$w_e = [1/(1-k^2)][\tan\delta + k^2(\tan\phi - 2\tan\theta)]\,\pi K^X \varepsilon_o E_o^2 \qquad (6.68)$$

Note that we do not need to account for w_{em} explicitly [as defined by Equation (6.28)], because the electromechanical loss is already included implicitly in our current expression for w_e. If we neglect the transfer of heat through conduction, the rate of heat dissipation (q_d) from the sample is the sum of the rates of heat flow by radiation (q_r) and by convection (q_c):

$$q_d = q_r + q_c = e\,A\,\sigma\,(T^4 - T_o^4) + h_c A\,(T - T_o) \qquad (6.69)$$

where e is the emissivity of the sample, A is the sample surface area, σ is the Stefan-Boltzmann constant, T_o is the initial sample temperature, h_c is the average convective heat transfer coefficient.

Thus, Equation (6.66) can be written in the form:

$$w\,f\,V_e - A\,k(T)\,(T - T_o) = V\,\rho\,C\,(dT/dt) \qquad (6.70)$$

where the quantity

$$k(T) = \sigma\,e\,(T^2 + T_o^2)(T + T_o) + h_c \qquad (6.71)$$

is the overall heat transfer coefficient. If we assume that k(T) is relatively insensitive to temperature change, solving Equation (6.70) for the rise in temperature of the piezoelectric sample yields:

$$T - T_o = [w\,f\,V_e / k(T)\,A]\,(1 - e^{-t/\tau}) \qquad (6.72)$$

where the time constant τ is expressed as:

$$\tau = \rho\,C\,V / k(T)\,A \qquad (6.73)$$

As t → ∞, the maximum temperature rise in the sample becomes:

$$\Delta T = w f V_e / k(T) A \tag{6.74}$$

As t → 0, the initial rate of temperature rise is given by

$$dT/dt = (w_T f V_e / \rho C V) = \Delta T / \tau \tag{6.75}$$

where w_T can be regarded under these conditions as a measure of the total loss of the piezoelectric. The dependences of k(T) on applied electric field and frequency are shown in Figures 6.20 and 6.21, respectively. The total loss, w_T, as calculated from Equation (6.75) is given for three multilayer specimens in Table 6.1. The experimentally determined P-E hysteresis losses measured under stress-free conditions are also listed in the table for comparison. It is seen that the extrinsic P-E hysteresis loss agrees well with the calculated total loss associated with the heat generated in the driven piezoelectric.

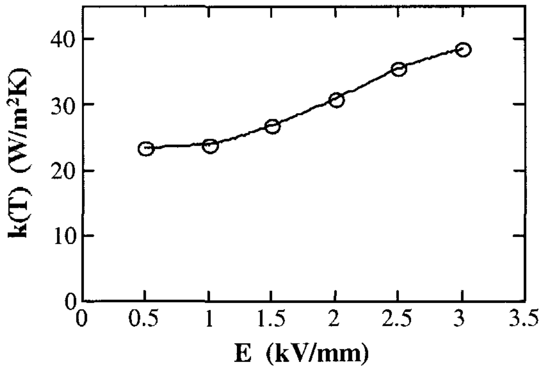

Figure 6.20 The overall heat transfer coefficient, k(T), plotted as a function of applied electric field for a PZT multilayer actuator with dimensions of 7 x 7 x 2 mm^3 driven at 400 Hz.[5]

(2) Heat Generation Under Resonance Conditions

The generation of heat has been observed in rectangular piezoelectric plates when driven at resonance.[9] Although the maximum electric field is not very large, heat is generated due to the large strain/stress induced at resonance. The maximum heat generation was observed in the nodal regions for the resonance vibration, which correspond to the locations where the maximum strains/stresses are generated.

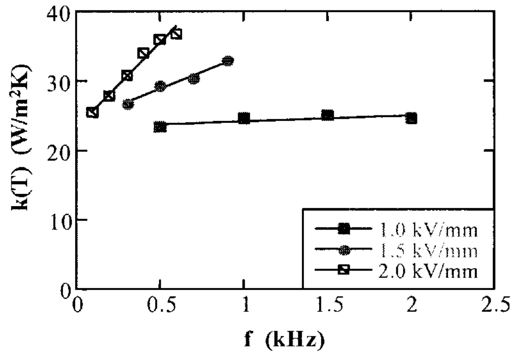

Figure 6.21 The overall heat transfer coefficient, k(T), plotted as a function of frequency for a PZT multilayer actuator with dimensions of 7 x 7 x 2 mm^3 under three different applied electric field strengths.[5]

Table 6.1 Loss and overall heat transfer coefficient for PZT multilayer samples (E = 3 kV/mm, f = 300 Hz).[5]

Actuator	4.5 x 3.5 x 2.0 mm^3	7.0 x 7.0 x 2.0 mm^3	17 x 3.5 x 1.0 mm^3
w_T (kJ/m^3)	19.2	19.9	19.7
P-E hysteresis loss (kJ/m^3)	18.5	17.8	17.4
k(T) (W/m^{2}K)	38.4	39.2	34.1

The temperature variation in a PZT-based plate sample as observed with a pyroelectric infrared camera is shown in Figure 6.22. The images in Figures 6.22(a) and 6.22(b) depict the temperature variations in samples driven at the first (28.9 kHz) and second resonance (89.7 kHz) modes, respectively. The highest temperature (dark spot) is evident at the nodal areas for the specimen in Figures 6.22(a) and 6.22(b). This observation supports the claims described in the previous section that the heat generated in a resonating sample is associated with the intensive elastic loss, tanϕ', which has been shown to be related to the coupled action of the extensive mechanical, dielectric, and electromechanical losses as defined by Equation (6.51). According to that discussion, we determined that the resonance loss at small vibration velocities is mainly determined by the intensive mechanical loss, which provides a high mechanical quality factor, Q_m, and with increasing vibration velocity, the contribution of the extensive dielectric loss significantly increases and heat is generated in the sample, as we observe for the samples depicted in Figure 6.22.

This is also in agreement with the result presented in Section 6.2(1), where a high voltage was applied to the specimen at an off-resonance frequency. We concluded there that the heat is generated largely through the intensive dielectric loss, tanδ'. Where both the "intensive" dielectric and mechanical losses are closely related to the "extensive" dielectric and mechanical losses as expressed by Equations (6.50) and (6.51), and the extensive dielectric loss tanδ is known to change significantly with both the externally applied electric field and stress, it appears that the major contribution to the heat generation in both cases is from the "extensive" dielectric loss.

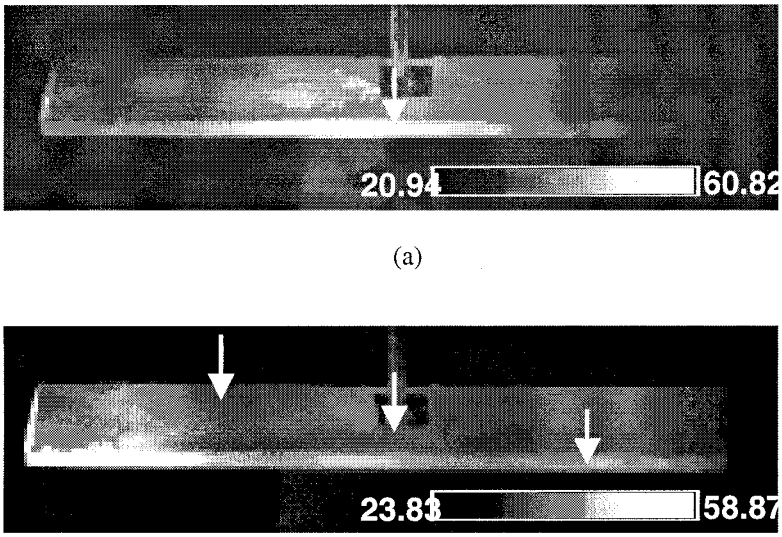

(a)

(b)

Figure 6.22 Temperature variations in a PZT-based plate sample observed with a pyroelectric infrared camera. The specimens are driven at two different resonance frequencies: (a) the first resonance mode (28.9 kHz) and (b) the second resonance mode (89.7 kHz). The arrows indicate the highest temperature areas (dark areas).

(3) Heat Generation Under Pulse Drive

We consider here the situation where a piezoelectric actuator is operated under a high, pulsed electric field. Heat generation is expected when the actuator is driven cyclically. We will consider the temperature rise of a PZT multilayer actuator operated under a pulse drive signal with a trapezoidal waveform, such as is typically applied to diesel engine injection systems. The trapezoidal waveform has a maximum voltage of 100 V, a frequency of 60 Hz, and a duty cycle of 50%. The dependence of the heat generated in the device, as manifested by an increase in temperature of the actuator, on the rise time of the driving pulse are summarized in Table 6.2 and Figure 6.23. The temperature rise is observed to be rather strongly dependent on the rise time, and can be attributed largely to the vibrational overshoot and ringing effects occurring in the driven actuator. A series of waveforms are depicted in Figure 6.24, which shows the actuator response to driving pulses with increasing rise times. A significant ringing effect is observed for the shorter rise time, which leads to the generation of additional heat in the device through the mechanical resonance response that is occurring under these conditions. Depending on the magnitude of the overshoot and ringing effects that are induced, the temperature rise can be increased by more than 50% as compared with the temperature of the device when no ringing occurs (corresponding roughly to the off-resonance condition).

Table 6.2 Heat generation in a PZT multilayer actuator driven by trapezoidal waveforms with various rise times [100V (maximum voltage, unipolar), 60 Hz, 50% duty cycle].

Rise time (μsec)	72	85	97	102	146	240	800
Temperature rise (°C)	23.7	21.6	20.5	20.2	20.3	18.6	16.6
V_{rms} (V)	72.9	72.8	72.7	72.7	72.6	72.1	71.3

In conclusion, when a piezoelectric actuator is operated under pulse drive conditions, heat will be generated in the device due to both the intensive dielectric and mechanical losses occurring via the mechanical resonance of the device (that is, the ringing effect). In order to minimize the generation of heat in the device when operated under these conditions, care must be taken to reduce the vibrational overshoot and ringing effects by changing the rise time of the driving pulse. As described in Section 5.3, the optimum rise time in this case will be one that is equal to the resonance period of the actuator.

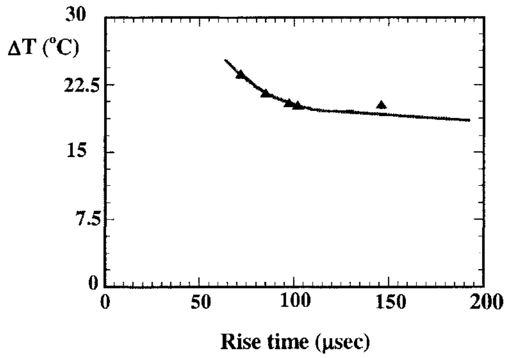

Figure 6.23 Temperature rise plotted as a function of rise time for a PZT multilayer actuator driven by a pulse with a trapezoidal waveform [100 V (maximum voltage, unipolar), 60 Hz, 50% duty cycle].

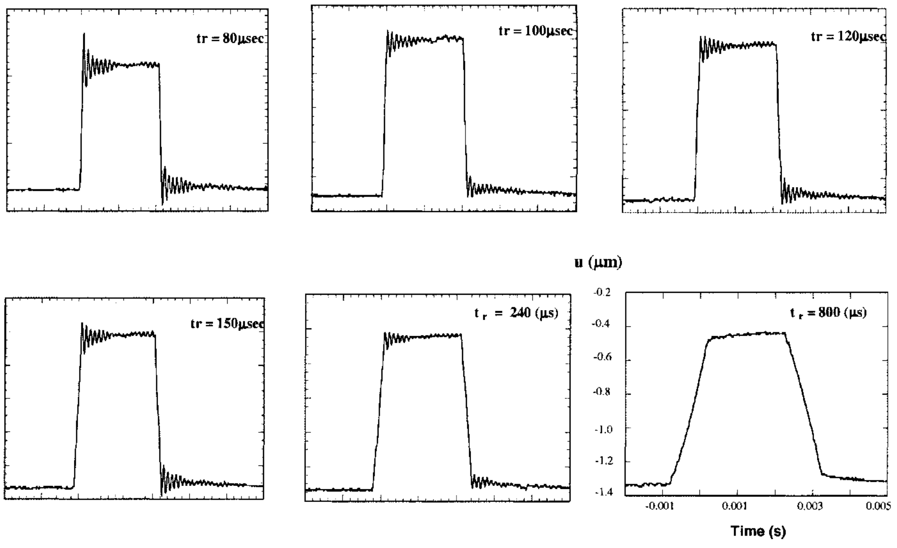

Figure 6.24 Rise time dependence of the vibrational ringing in a PZT multilayer actuator driven by a pulse with a trapezoidal waveform [100 V (maximum voltage, unipolar), 60 Hz, 50% duty cycle].

6.3 HARD AND SOFT PIEZOELECTRICS

Small amounts of dopants sometimes drastically change the dielectric and electromechanical properties of ceramics. Donor doping tends to facilitate domain wall motion, leading to enhanced piezoelectric charge coefficients, d, and electromechanical coupling factors, k, producing what is referred to as a "soft piezoelectric." Acceptor doping, on the other hand, tends to pin domain walls and impeding their motion, leading to an enhanced mechanical quality factor, Q_m, producing what is called a "hard piezoelectric." Table 6.3 summarizes the advantages and disadvantages of soft and hard piezoelectrics and compares their characteristics with a leading electrostrictive material, $Pb(Mg_{1/3}Nb_{2/3})O_3$ (PMN). The electrostrictive ceramic is commonly used for positioning devices where hysteresis-free performance is a primary concern. However, due to their high permittivity, the electrostrictive devices are generally used only for applications that require slower response times.

Table 6.3 Advantages (+) and disadvantages (–) of soft and hard piezoelectrics, compared with the features of a leading electrostrictive material, $Pb(Mg_{1/3}Nb_{2/3})O_3$ (PMN).

Material	**d**	**k**	**Q_m**	**Off-Resonance Applications**	**Resonance Applications**
PMN	High^{+} (DC Bias)$^{-}$	High^{+} (DC Bias)$^{-}$	Low^{-} (DC Bias)$^{-}$	High Displacement^{+} No Hysteresis^{+}	Broad Bandwidth^{+}
Soft PZT-5H	High^{+}	High^{+}	Low^{-}	High Displacement^{+}	Heat Generation^{-}
Hard PZT-8	Low^{-}	Low^{-}	High^{+}	Low Strain^{-}	High AC Displacement^{+}

On the other hand, the soft piezoelectric materials with their relatively low permittivity and high piezoelectric charge coefficients, d, can be used for applications requiring a quick response time, such as pulse driven devices like inkjet printers. Soft piezoelectrics generate a significant amount of heat when driven at resonance, however, due to their small mechanical quality factor, Q_m. Thus, for ultrasonic motor applications, hard piezoelectrics with a larger mechanical quality factor are preferred despite the slight sacrifices incurred with respect to their smaller piezoelectric strain coefficients, d, and the electromechanical coupling factors, k.

(1) Dopant Effects on Piezoelectric Response

Let us consider the crystallographic defects produced on the perovskite lattice due to doping. Acceptor ions, such as Fe^{3+}, lead to the formation of oxygen deficiencies ($\square$) in the PZT lattice, and the resulting defect structure is described by:

$$Pb(Zr_yTi_{1-y-x}Fe_x)(O_{3-x/2}\square_{x/2})$$

Acceptor doping allows for the easy reorientation of deficiency-related dipoles. These dipoles are comprised of an Fe^{3+} ion (effectively the negative charge) and an oxygen vacancy (effectively the positive charge). The oxygen deficiencies are produced at high temperature (>1000°C) during sintering, but the oxygen ions are still able to migrate at temperatures well below the Curie temperature (even at room temperature), because the oxygen and its associated vacancy are only 2.8 Å apart and the oxygen can readily move into the vacant site as depicted in Figure 6.25(a).

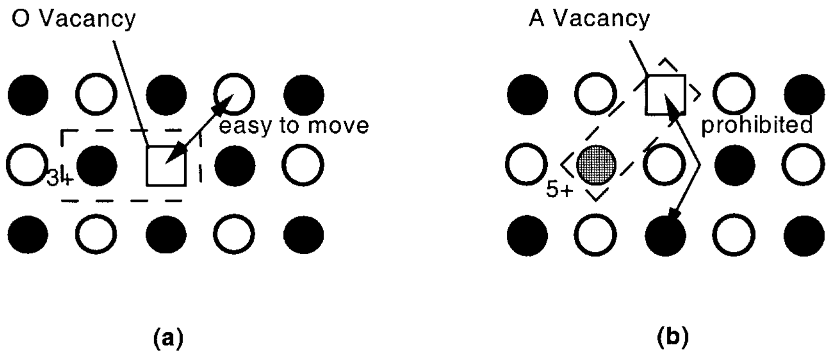

Figure 6.25 Lattice vacancies in PZT containing: (a) acceptor and (b) donor dopants.

In the case of donor dopant ions, such as Nb^{5+}, a Pb deficiency is produced and the resulting defect structure is designated by the following:

$$(Pb_{1-x/2}\square_{x/2})(Zr_yTi_{1-y-x}Nb_x)O_3$$

Donor doping is not very effective in generating movable dipoles, since the Pb ion cannot easily move to an adjacent A-site vacancy due to the proximity of the surrounding oxygen ions as depicted in Figure 6.25(b).

These simple defect models help us to understand and explain various changes in the properties of a perovskite ferroelectric of this type that occur with doping. The effect of donor doping in PZT on the field-induced strain response of the material was examined for the soft piezoelectric composition $(Pb_{0.73}Ba_{0.27})(Zr_{0.75}Ti_{0.25})O_3$.[12] The parameters *maximum strain*, x_{max}, and the *degree of hysteresis*, $\Delta x/x_{max}$, are defined in terms of the hysteresis response depicted in Figure 6.26(a). The maximum strain, x_{max}, is induced under the maximum applied electric field. The degree of hysteresis, $\Delta x/x_{max}$, is just the ratio of the strain induced by half the maximum applied electric field to the maximum strain, x_{max}. The effect of acceptor and donor dopants (2 atom percent concentration) on the induced strain and degree of hysteresis is shown in Figure 6.26(b). It is seen that materials incorporating high valence donor-type ions on the B-site (such as Ta^{5+}, Nb^{5+}, W^{6+}) exhibit excellent characteristics as positioning actuators, namely, enhanced induced strains and reduced hysteresis. On the other hand, the low valence acceptor-type ions (+1, +2, +3) tend to suppress the strain and increase the hysteresis and the coercive field. Although acceptor-type dopants are not desirable when designing actuator ceramics for positioner applications, acceptor doping is important in producing "hard" piezoelectric ceramics, which are preferred for ultrasonic motor applications. In this case, the acceptor dopant acts to pin domain walls, resulting in the high mechanical quality factor characteristic of a hard piezoelectric.

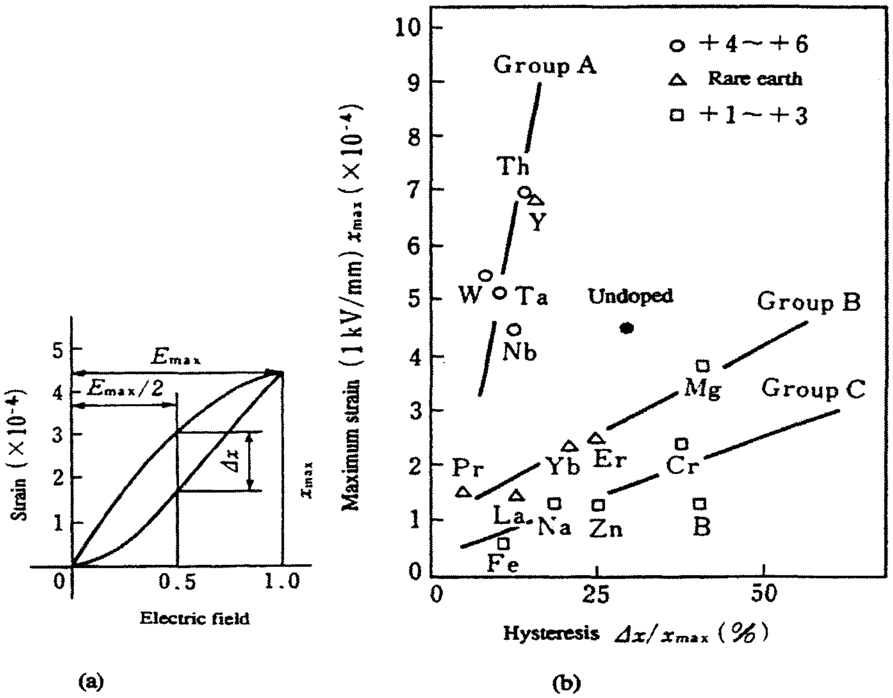

Figure 6.26 Maximum strain and hysteresis in $Pb_{0.73}Ba_{0.27}(Zr_{0.75}Ti_{0.25})O_3$-based ceramics: (a) hysteresis curve showing the parameters needed for defining the maximum strain, x_{max}, and the degree of hysteresis, $\Delta x/x_{max}$, and (b) the dopant effect on actuator parameters.[12]

Example Problem 6.3

The coercive electric field, E_c, of a ferroelectric material is defined to be the minimum field strength required to reorient the polarization direction of a polar domain by 180°. It is also affected by the presence of dopants on the crystalline lattice. Explain the effect of dopants on the "soft" and "hard" characteristics of PZT piezoelectric materials in terms of the simple defect model described in Section 6.3(1).

Solution

The "soft" and "hard" characteristics are reflected in the coercive field E_c, or more precisely in the stability of the domain walls. A piezoelectric is classified as "hard" if it has a coercive field greater than 1 kV/mm, and "soft" if the coercive field is equal to or less than 1 kV/mm.

Consider the transient state of a 180° domain reversal that occurs at a domain wall associated with a configuration of head-to-head polar domains. We know from Gauss' law that:

$$\operatorname{div} D = \rho \tag{P6.3.1}$$

where D is the electric displacement and ρ is the charge density. The domain wall is very unstable in a highly insulating material and therefore readily reoriented and the coercive field for such a material is found to be low. However, this head-to-head configuration is stabilized in a more conductive material and thus a higher coercive field is required for polarization reversal and the associated domain wall movement to occur. These two cases are illustrated schematically in Figure 6.27.

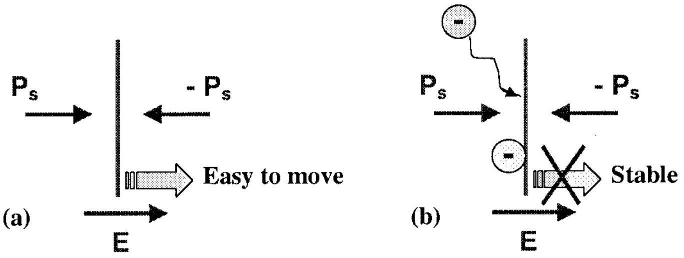

Figure 6.27 Stability of 180° domain wall motion in: (a) an insulating material and (b) a material with free charges.

Next, let us consider the free charges associated with defect structures present in a doped PZT material. The presence of acceptor dopants, such as Fe^{3+}, in the perovskite structure is found to produce oxygen deficiencies, while donor dopants, such as Nb^{5+}, produce A-site deficiencies. Acceptor doping allows for the easy reorientation of deficiency-related dipoles. These dipoles are comprised of a Fe^{3+} ion (effectively the negative charge) and an oxygen vacancy (effectively the positive charge). The oxygen ions are able to migrate at temperatures well below the Curie temperature (even at room temperature), because the oxygen and its associated vacancy are only 2.8 Å apart and the oxygen can readily move into the vacant site. Thus, acceptor doping effectively pins domain walls and "hard" characteristics are observed. On the other hand, donor doping is not very effective in generating movable dipoles, since the Pb ion cannot easily move to an adjacent A-site vacancy due to the proximity of the surrounding oxygen ions. “Soft” characteristics are, therefore, observed for donor-doped materials. Another factor that should be considered here is that lead-based perovskites, such as PZT, tend to be p-type semiconductors due to the evaporation of lead during sintering and are thus already “softened” to some extent by the lead vacancies that are produced. Hence, donor-doped materials will exhibit large piezoelectric charge coefficients, d, but will also exhibit pronounced aging due to their soft characteristics.

(2) High Power Characteristics

Let us now consider high power piezoelectric ceramics for ultrasonic (AC drive) applications. When the ceramic is driven at a high vibration rate (that is, under a relatively large AC electric field) heat will be generated in the material resulting in significant degradation of its piezoelectric properties. A high power device such as an ultrasonic motor therefore requires a very "hard" piezoelectric with a high mechanical quality factor, Q_m, to reduce the amount of heat generated.

The temperature rise in undoped, Nb-doped, and Fe-doped PZT samples is plotted as a function of vibration velocity in Figure 6.28.[10] A significant reduction in the generation of heat is apparent for the Fe-doped (acceptor-doped) ceramic. Commercially available hard PZT ceramic plates tend to generate the maximum vibration velocity around 0.3 m/s when operated in a k_{31} mode. Even when operated at higher applied electric field strengths, the vibration velocity will not increase for these devices; the additional energy is just converted into heat.

Higher maximum vibration velocities have been realized in PZT-based materials modified by dopants that effectively reduce the amount of heat generated in the material and thus allow for the higher rates of vibration. The vibration velocity for devices with the $(1-z)Pb(Zr_xTi_{1-x})O_3$-$(z)Pb(Mn_{1/3}Sb_{2/3})O_3$ composition developed by NEC[13] is shown as a function of Zr concentration, x, in Figure 6.29. The maximum vibration velocity of 0.62 m/s occurs at the x=0.47, z=0.05 composition and is accompanied by a 20°C temperature rise with respect to room temperature. The incorporation of additional rare earth dopants to this optimum base composition results in an increase in the maximum vibration velocity to 0.9 m/s (Figure 6.30).[14] This increased vibration rate represents a threefold enhancement over that typically achieved by commercially produced hard PZT devices and corresponds to an increase in the vibration energy density by an order of magnitude with minimal heat generated in the device.

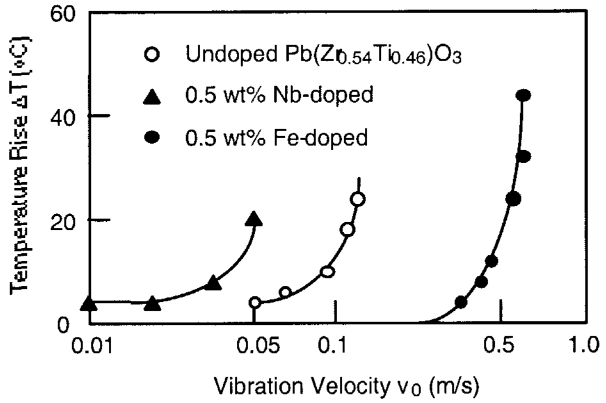

Figure 6.28 Temperature rise, ΔT, plotted as a function of effective vibration velocity, v_o, for undoped, Nb-doped, and Fe-doped PZT samples.[10]

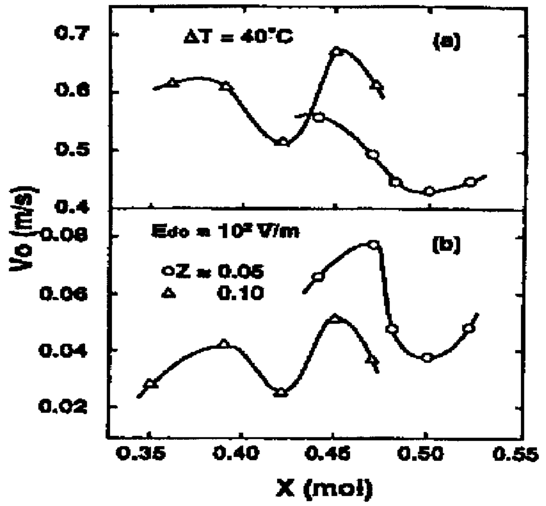

Figure 6.29 Maximum vibration velocity plotted as a function of Zr content, x, for PZT-based devices from the system $(1-z)Pb(Zr_xTi_{1-x})O_3$-$(z)Pb(Mn_{1/3}Sb_{2/3})O_3$. The maximum vibration velocity of 0.62 m/s occurs at the x=0.47, z=0.05 composition and is accompanied by a 20°C temperature rise with respect to room temperature.[13]

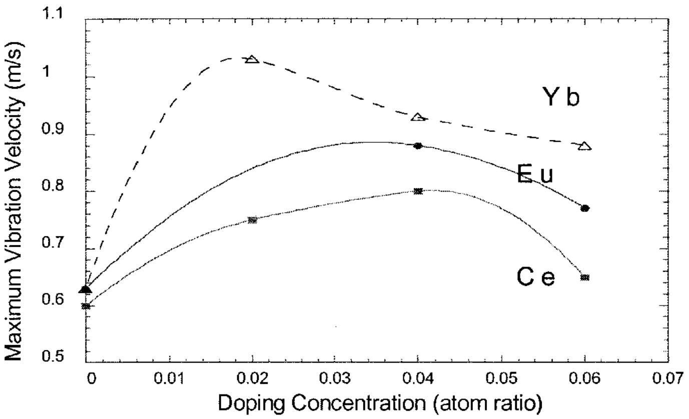

Figure 6.30 Maximum vibration velocity versus rare earth ion doping concentration in the base system of $(0.95)Pb(Zr_{0.47}Ti_{0.53})O_3$-$(0.05)Pb(Mn_{1/3}Sb_{2/3})O_3$.[14]

CHAPTER ESSENTIALS

1. Various techniques for measuring the dielectric, mechanical and piezoelectric losses separately:

   a. Data from D-E, x-X, x-E, and D-X hysteresis curves for determining the dielectric, mechanical, and piezoelectric losses.

   b. Examination of the heat generated under resonance and off-resonance conditions for determining the intensive mechanical and dielectric losses.

   c. Resonance/antiresonance measurement techniques for determining the intensive and extensive mechanical losses, respectively.

2. Concerning the electromechanical losses:

   Piezoelectric Losses ($\tan\theta'$ and $\tan\theta$) are not as small as previously believed.

   Extensive Dielectric Loss ($\tan\delta$) increases with the applied electric field.

   Extensive Mechanical Loss ($\tan\phi$) is insensitive to changes in the applied compressive stress.

3. Heat generation in piezoelectrics:

   a. Off-Resonance Drive occurs primarily through the intensive dielectric loss, tanδ'.

   b. Resonance Drive occurs primarily through the intensive mechanical loss, tanϕ'.

   c. Pulse Drive occurs through the combined effects of the intensive dielectric and mechanical losses.

   The fundamental mechanism acting in all cases is the extensive dielectric loss, tanδ, which is enhanced by a large applied electric field or stress.

4. A significant decrease in mechanical quality factor, Q_m, occurs with increasing vibration level in a piezoelectric ceramic driven at resonance. Data collected by conventional methods employing an impedance analyzer under low voltage (power) conditions will not reflect the high power performance of these materials. A general depiction of the variation of Q_m with vibration rate for a typical piezoelectric actuator appears in Figure 6.31.

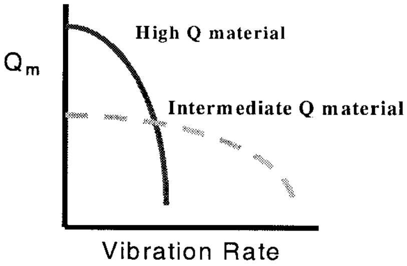

Figure 6.31 A general depiction of the variation of Q_m with vibration rate for a typical piezoelectric actuator.

CHAPTER PROBLEMS

6.1 Substituting the complex parameters: $K^{X*}=K^{X}(1-j\tan\delta')$, $\kappa^{x*}=\kappa^{x}(1+j\tan\delta)$, $s^{E*}=s^{E}(1-j\tan\phi')$, $c^{D*}=c^{D}(1+j\tan\phi)$, $d^{*}=d(1-j\tan\theta')$, $h^{*}=h(1+j\tan\theta)$ into the equations:

$$K^{X}\varepsilon_o = \frac{c^{D}(\kappa^{x}/\varepsilon_o)}{(1-h^2)(\kappa^{x}/\varepsilon_o)}$$

$$s^{E} = \frac{(\kappa^{x}/\varepsilon_o)c^{D}}{(1-h^2)\ c^{D}}$$

$$d = \frac{h}{(1-h^2)}\left[\frac{c^{D}(\kappa^{x}/\varepsilon_o)}{c^{D}(\kappa^{x}/\varepsilon_o)}\right]$$

verify the relationships between the intensive and extensive losses:

$$\tan\delta' = \left(\frac{1}{1-k^2}\right)\left[\tan\delta + k^2(\tan\phi - 2\tan\theta)\right]$$

$$\tan\phi' = \left(\frac{1}{1-k^2}\right)\left[\tan\phi + k^2(\tan\delta - 2\tan\theta)\right]$$

$$\tan\theta' = \left(\frac{1}{1-k^2}\right)\left[\tan\delta + \tan\phi - (1+k^2)\tan\theta\right]$$

where k is the real electromechanical coupling factor.

REFERENCES

1) T. Ikeda: *Fundamentals of Piezoelectric Materials Science*, Ohm Publication Company, Tokyo, p.83 (1984).
2) K. Uchino and S. Hirose: IEEE-UFFC Trans. **48**, 307-321 (2001).
3) K. H. Haerdtl: Ceram. Int'l. **8**, 121-127 (1982).
4) P. Gerthsen, K. H. Haerdtl and N. A. Schmidt: J. Appl. Phys. **51**, 1131-1134 (1980).
5) J. Zheng, S. Takahashi, S. Yoshikawa, K. Uchino and J. W. C. de Vries: J. Amer. Ceram. Soc., **79**, 3193-3198 (1996).
6) K. Uchino: *Piezoelectric Actuators and Ultrasonic Motors*, Kluwer Academic Publishers, Boston, p.197 (1997).
7) S. Takahashi and S. Hirose: Jpn. J. Appl. Phys., **32**, 2422-2425 (1993).
8) S. Hirose, M. Aoyagi, Y. Tomikawa, S. Takahashi and K. Uchino: Proc. Ultrasonics Int'l. '95, Edinburgh, pp.184-187 (1995).
9) S. Tashiro, M. Ikehiro and H. Igarashi: Jpn. J. Appl. Phys., **36**, 3004-3009 (9197).
10) K. Uchino, J. Zheng, A. Joshi, Y. H. Chen, S. Yoshikawa, S. Hirose, S. Takahashi and J. W. C. de Vries: J. Electroceramics, **2**, 33-40 (1998).
11) K. Uchino and S. Hirose: IEEE Trans. UFFC, **48**, 307-321 (2001).
12) A. Hagimura and K. Uchino: Ferroelectrics, **93**, 373 (1989).
13) S. Takahashi, Y. Sasaki, S. Hirose and K. Uchino: Proc. Mater. Res. Soc. Symp. Vol. 360, p.305 (1995).
14) Y. Gao, Y. H. Chen, J. Ryu, K. Uchino and D. Viehland: Jpn. J. Appl. Phys. **40**, 79-85 (2001).

7

INTRODUCTION TO THE FINITE ELEMENT METHOD FOR PIEZOELECTRIC STRUCTURES

The finite element method and its application to the piezoelectric system are introduced in this chapter.

7.1 BACKGROUND INFORMATION

Consider the piezoelectric domain Ω pictured in Figure 7.1, within which the displacement field, $\mathbf{u}$, and electric potential field, ϕ, are to be determined. The $\mathbf{u}$ and ϕ fields satisfy a set of differential equations that represent the physics of the continuum problem considered. Boundary conditions are usually imposed on the domain's boundary, Γ, to complete the definition of the problem.

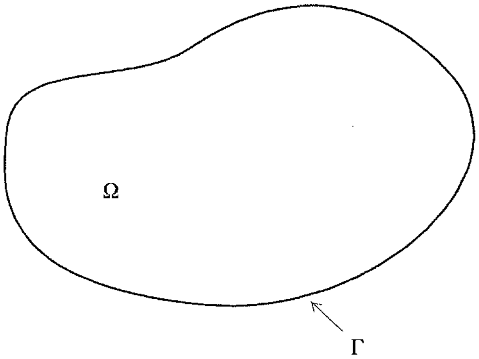

Figure 7.1 Schematic representation of the problem domain Ω with boundary Γ.

The finite element method is an approximation technique for finding solution functions.[1] The method consists of subdividing the domain Ω into sub-domains, or *finite elements*, as illustrated in Figure 2. These finite elements are interconnected at a finite number of points, or *nodes*, along their peripheries. The ensemble of finite elements defines the *problem mesh.* Note that because the subdivision of Ω into finite elements is arbitrary, there is not a unique mesh for a given problem.

Within each finite element, the displacement and electric potential fields are uniquely defined by the values they assume at the element nodes. This is achieved by a process of *interpolation* or *weighing* in which *shape functions* are associated with the element. By combining, or *assembling*, these local definitions throughout the whole mesh, we obtain a trial function for Ω that depends only on the nodal values of **u** and ϕ and that is "piecewise" defined over all the interconnected elementary domains. Unlike the domain Ω, these elementary domains may have a simple geometric shape and homogeneous composition.

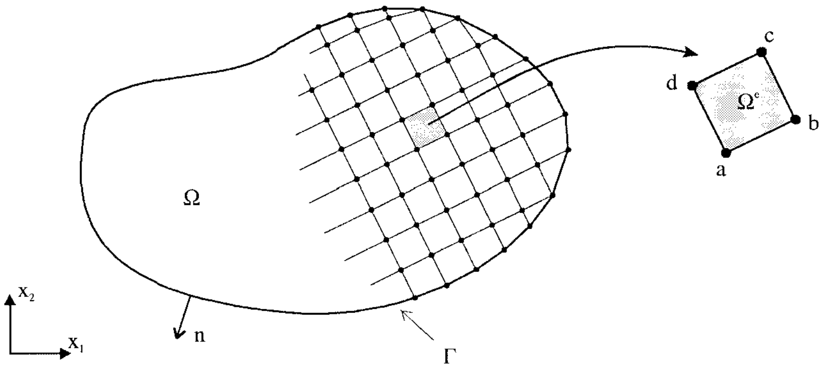

Figure 7.2 Discretization of the domain Ω.

We will show in the following sections how this trial function is evaluated in terms of the variation principle to produce a system of linear equations whose unknowns are the nodal values of **u** and ϕ.[2]

7.2 DEFINING THE EQUATIONS FOR THE PROBLEM

(1) The Constitutive and Equilibrium Equations

The constitutive relations for piezoelectric media may be derived in terms of their associated thermodynamic potentials.[3] Assuming the strain, x, and electric field, E, are independent variables, the basic equations of state for the converse and direct piezoelectric effects are written:

$$\begin{cases} X_{ij} = c^{E}_{ijkl} x_{kl} - e_{kij} E_k \\ D_i = e_{ikl} x_{kl} + \chi^{x}_{ij} E_j \end{cases} \tag{7.1}$$

The quantities c^E (elastic stiffness at constant electric field), e (piezoelectric stress coefficients), and χ^x (dielectric susceptibility at constant strain) are assumed to be constant, which is reasonable for piezoelectric materials subjected to small deformations and moderate electric fields. Furthermore, no distinction is made between isothermal and adiabatic constants.

On the domain, Ω, and its boundary, Γ, (where the normal is directed outward from the domain) the fundamental dynamic relation must be verified:

$$\rho \frac{\partial^2 \mathbf{u}_i}{\partial t^2} = \frac{\partial T_{ij}}{\partial r_j} \tag{7.2}$$

where **u** is the displacement vector, ρ the mass density of the material, t the time, **X** is the stress tensor, and $\mathbf{r} = \langle r_1\ r_2\ r_3 \rangle$ is a unit vector in the Cartesian coordinate system.

When no macroscopic charges are present in the medium, Gauss's theorem imposes for the electric displacement vector, **D**:

$$\frac{\partial D_i}{\partial r_i} = 0 \tag{7.3}$$

Considering small deformations, the strain tensor, **x,** is written as:

$$\mathbf{x}_{kl} = \frac{1}{2}\left(\frac{\partial \mathbf{u}_k}{\partial r_l} + \frac{\partial \mathbf{u}_l}{\partial r_k}\right) \tag{7.4}$$

Assuming electrostatic conditions, the electrostatic potential, ϕ, is related to the electric field **E** by:

$$\mathbf{E} = -\operatorname{grad} \phi \tag{7.5}$$

or, equivalently,

$$E_i = -\frac{\partial \phi}{\partial r_i} \tag{7.6}$$

Using Equations (7.2), (7.3) and (7.6) in combination with (7.1) yields:

$$\begin{cases} -\rho\omega^2 u_i = \dfrac{\partial}{\partial r_j}\left(c^E_{ijkl} x_{kl} - e_{kij} E_k\right) \\ \dfrac{\partial}{\partial r_j}\left(e_{ikl} x_{kl} + \chi^x_{ij} E_j\right) = 0 \end{cases} \tag{7.7}$$

(2) Boundary Conditions

Mechanical and electrical boundary conditions complete the definition of the problem.

The mechanical conditions are as follows:

- The Dirichlet condition on the displacement field, u, is given by:

  $$\mathbf{u}_i = \mathbf{u}_i^o \tag{7.8}$$

  where $\mathbf{u}^o$ is a known vector. For convenience, we name the ensemble of surface elements subjected to this condition S_u.
- The Neumann condition on the stress field, **X**, is given by:

  $$\mathbf{X}_{ij} \cdot \mathbf{n}_j = \mathbf{f}_i^o \tag{7.9}$$

  where **n** is the vector normal to Γ, directed outward, and $\mathbf{f}^o$ is a known vector. For convenience, we name the ensemble of surface elements subjected to this condition S_X.

The electrical conditions are as follows:

- The conditions for the excitation of the electric field between those surfaces of the piezoelectric material that are not covered with an electrode and are, therefore, free of surface charges are given by:

  $$\mathbf{D}_i \cdot \mathbf{n}_i = 0 \tag{7.10}$$

  where **n** is the vector normal to the surface. For convenience, we name the ensemble of surface elements subjected to this condition S_σ. Note that with condition (7.9), we assume that the electric field outside Ω is negligible, which is easily verified for piezoelectric ceramics.
- When considering the conditions for the potential and excitation of the electric field between those surfaces of the piezoelectric material that are covered with electrodes, we assume that there are p electrodes in the system. The potential on the whole surface of the p^{th} electrode is:

$$\phi = \phi_p \tag{7.11}$$

The charge on that electrode is:

$$-\iint_{S_p} D_i n_i dS_p = Q_p \tag{7.12}$$

In some cases, the potential is used, and in others it is the charge. In the former case, ϕ_p is known and Equation (7.11) is used to determine Q_p. In the latter case, Q_p is known and Equation (7.10) is used to determine ϕ. Finally, in order to define the origin of the potentials, it is necessary to impose the condition that the potential at one of the electrodes be zero ($\phi_0 = 0$).

(3) The Variational Principle

The variational principle identifies a scalar quantity Π, typically named the *functional*, which is defined by an integral expression involving the unknown function, w, and its derivatives over the domain Ω and its boundary Γ. The solution to the continuum problem is a function w such that

$$\delta\Pi = 0 \tag{7.13}$$

Π is said to be stationary with respect to small changes in w, δw. When the variational principle is applied, the solution can be approximated in an integral form that is suitable for finite element analysis. In general, the matrices derived from the variational principle are always symmetric.

Equation (7.7) and the boundary conditions expressed by Equations (7.8) to (7.12) allow us to define the so-called Euler equations to which the variational principle is applied such that a functional of the following form is defined that is stationary with respect to small variations in w.

$$\begin{aligned}\Pi = {} & \iiint_{\Omega}\frac{1}{2}(x_{ij}\, c^E_{ijkl}\, x_{kl} - \rho\omega^2 u_i^2)\, d\Omega - \iint_{S_u}(u_i - u_i^o) n_j (c^E_{ijkl} x_{kl} - e_{kij} E_k) dS_u \\ & - \iiint_{\Omega}\frac{1}{2}(2x_{kl} e_{ikl} E_i + E_i \chi^x_{ij} E_j) d\Omega - \iint_{S_X} f_i u_i dS_X \\ & - \sum_{p=0}^{M} \iint_{S_p} (\phi - \phi_p) n_i (e_{ikl} x_{kl} + \chi^x_{ij} E_j) dS_p + \sum_{p=0}^{p} \phi_p Q_p \end{aligned} \tag{7.14}$$

Note that the first term of this expression for Π represents the Lagrangian of the mechanical state. Satisfying the stationary condition for Π implies that all the conditions described by Equations (7.7) through (7.12) are satisfied.

7.3 APPLICATION OF THE FINITE ELEMENT METHOD

(1) Discretization of the Domain

The domain Ω is divided into sub-domains Ω^e, or finite elements (Figure 7.2), such that:

$$\Omega = \sum_e \Omega^e \tag{7.15}$$

Common finite elements available for discretizing the domain are shown in Figure 7.3. As a result of the discretization, the functional Π can then be written as:

$$\Pi = \sum_e \Pi^e \tag{7.16}$$

Note that the term Π^e contains only volume integral terms if the element Ω^e is inside the domain Ω. Elements having a boundary coincident with Γ will have a term Π^e that contains both volume and surface integrals.

(2) Shape Functions

The finite element method, being an approximation process, will result in the determination of an approximate solution of the form:

$$\mathbf{w} \approx \hat{\mathbf{w}} = \sum \mathbf{N}_i \mathbf{a}_i \tag{7.17}$$

where the N_i are shape functions prescribed in terms of independent variables (such as coordinates) and the a_i are nodal parameters, known or unknown. The shape functions must guarantee the continuity of the geometry between elements. Moreover, to ensure convergence, it is necessary that the shape functions be at least C^m continuous if derivatives of the m^{th} degree exist in the integral form. This condition is automatically met if the shape functions are polynomials complete to the m^{th} order.

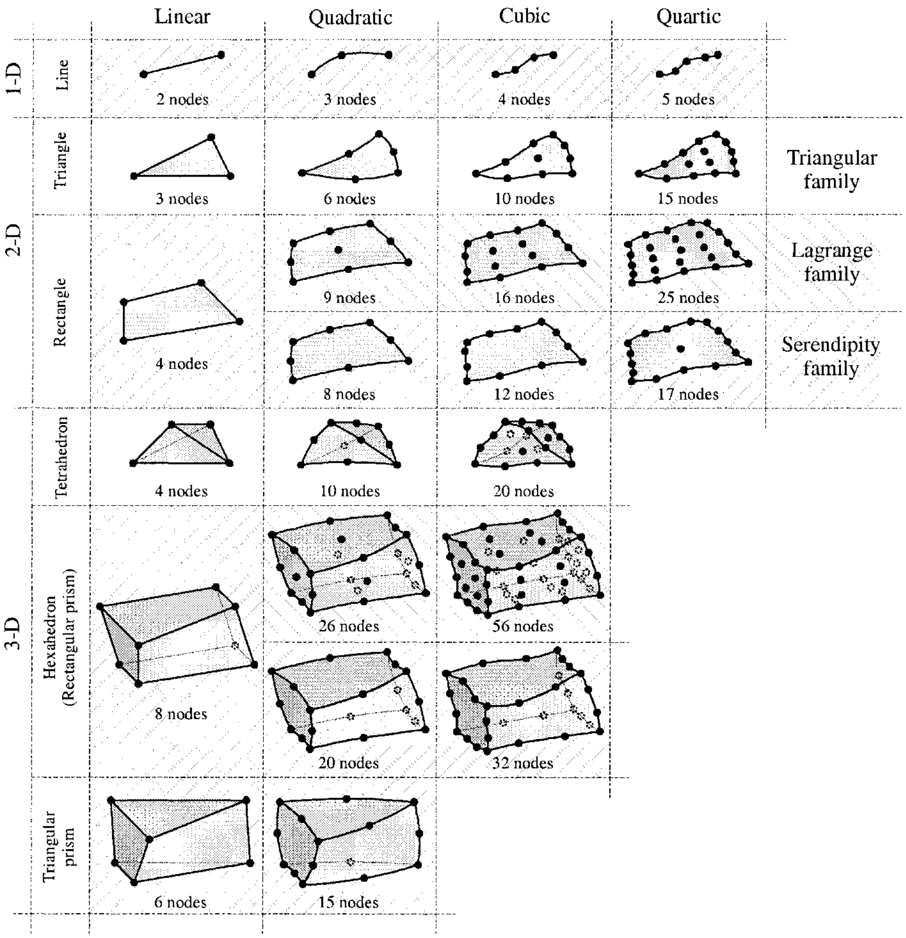
Linear
Quadratic
Cubic
Quartic
1-D
Line
2 nodes
3 nodes
4 nodes
5 nodes
2-D
Triangle
3 nodes
6 nodes
10 nodes
15 nodes
Triangular family
Rectangle
4 nodes
9 nodes
16 nodes
25 nodes
Lagrange family
8 nodes
12 nodes
17 nodes
Serendipity family
3-D
Tetrahedron
4 nodes
10 nodes
20 nodes
Hexahedron (Rectangular prism)
8 nodes
26 nodes
56 nodes
20 nodes
32 nodes
Triangular prism
6 nodes
15 nodes

Figure 7.3 Common finite elements.

The construction of shape functions for an element Ω^e, defined by n nodes, usually requires that if N_i is the shape function for node i, then $N_i=1$ at node i, and $N_i=0$ at the other nodes. Also, for any point p in Ω^e we must have:

$$\sum_1^n N_i(p) = 1 \tag{7.18}$$

Polynomials are commonly used to construct shape functions. For instance a Lagrange polynomial:

$$N_i(\xi) = \prod_{\substack{k=1 \\ k \neq i}}^{n} \frac{\xi_k - \xi}{\xi_k - \xi_i} \tag{7.19}$$

can be used at node i of a one-dimensional element containing n nodes (see Figure 7.4). It verifies the following conditions.

$$\begin{cases} N_i(\xi_i) = 1 \\ N_i(\xi_{k \neq i}) = 0 \\ \sum_{1}^{n} N_i(\xi) = 1 \end{cases} \tag{7.20}$$

For the 4-node rectangular element of Figure 7.5, we can write the four shape functions as:

$$N(\xi, \eta) = N_i(\xi) N_j(\eta) \tag{7.21}$$

where i and j indicate the row and column of the node in the element and i,j=1,2. The conditions described by Equation (7.20) can be verified for these functions. Finally, the position of any point p with coordinates (ξ, η) in the element is given by:

$$\begin{bmatrix} \xi \\ \eta \end{bmatrix} = \left\langle \left(\frac{1}{4}\right)[(-1)+\xi][(-1)+\eta] \left(-\frac{1}{4}\right)[(1)+\xi][(-1)+\eta] \left(-\frac{1}{4}\right)[(-1)+\xi][(1)+\eta] \left(\frac{1}{4}\right)[(1)+\xi][(1)+\eta] \right\rangle \begin{bmatrix} -1 & -1 \\ 1 & -1 \\ -1 & 1 \\ 1 & 1 \end{bmatrix} \tag{7.22}$$

In most cases, the same shape functions are used to describe the element geometry and to represent the solution $\hat{\mathbf{w}}$.

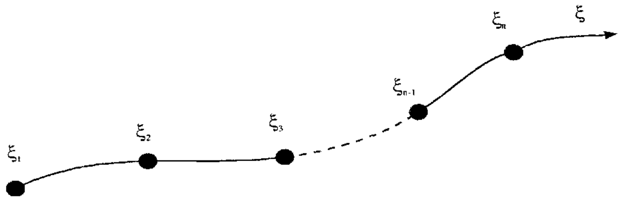

Figure 7.4 A generalized n-node linear element.

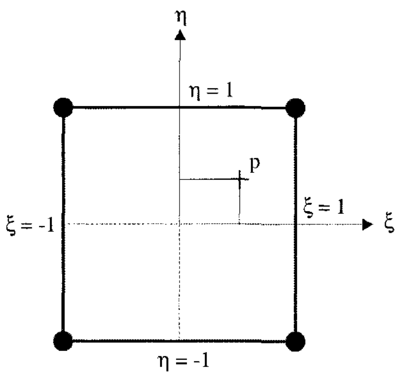

Figure 7.5 An example of a four-node quadrilateral element.

(3) Parent Elements

In order to better represent the actual geometry, it is generally useful to use curvilinear finite elements for the discretization of Ω. These elements are then mapped into parent finite elements (Figure 7.6) in order to facilitate the computation of Π^e.

An isoparametric representation is commonly used to perform the mapping of the actual elements into the reference elements. Consider a volume element Ω^e of the domain Ω defined by n nodes. The position vector **R** of a point p of Ω^e can be written as a function of parameters ξ, η, and ζ:

$$\xi \to R = R(\xi) \tag{7.23}$$

which is the same as:

$$R = \begin{Bmatrix} x \\ y \\ z \end{Bmatrix} = \begin{Bmatrix} x(\xi,\eta,\zeta) \\ y(\xi,\eta,\zeta) \\ z(\xi,\eta,\zeta) \end{Bmatrix} \tag{7.24}$$

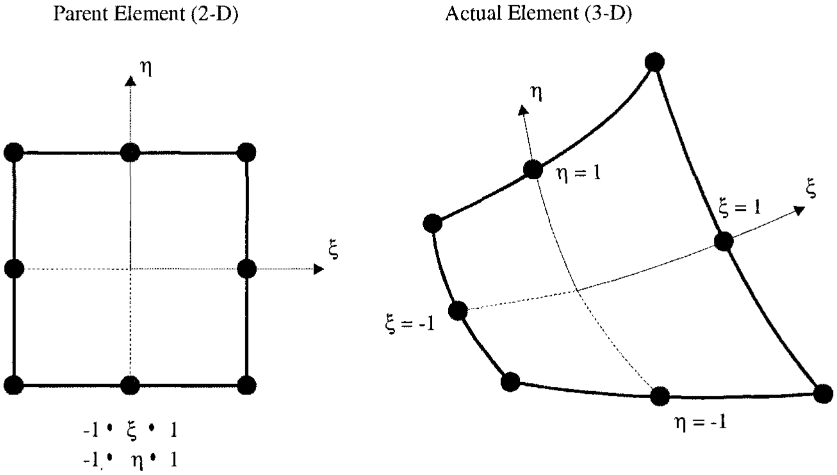

Figure 7.6 An example of a parent element for an 8-node quadrilateral element.

The finite element representation can be written in the following form:

$$\begin{aligned} x &= \mathbf{N}(\xi,\eta,\zeta)\mathbf{x}_n \\ y &= \mathbf{N}(\xi,\eta,\zeta)\mathbf{y}_n \\ z &= \mathbf{N}(\xi,\eta,\zeta)\mathbf{z}_n \end{aligned} \tag{7.25}$$

where:

$$\begin{aligned} \mathbf{x}_n &= \langle x_1 \quad x_2 \quad \dots \quad x_n \rangle \\ \mathbf{y}_n &= \langle y_1 \quad y_2 \quad \dots \quad y_n \rangle \\ \mathbf{z}_n &= \langle z_1 \quad z_2 \quad \dots \quad z_n \rangle \\ \mathbf{N} &= \langle N_1 \quad N_2 \quad \dots \quad N_n \rangle \end{aligned} \tag{7.26}$$

The scalars x_i, y_i, and z_i represent the Cartesian coordinates at node i and N_i is the shape function at node i. A differential element at point p is thus defined by:

$$dR = F_\xi d\xi \tag{7.27}$$

and

$$\frac{\partial}{\partial \xi} = F_\xi^{\,x} \frac{\partial}{\partial R} = J \frac{\partial}{\partial R} \tag{7.28}$$

where:

$$\mathbf{F}_\xi = \begin{bmatrix} x_{,\xi} & x_{,\eta} & x_{,\zeta} \\ y_{,\xi} & y_{,\eta} & y_{,\zeta} \\ z_{,\xi} & z_{,\eta} & z_{,\zeta} \end{bmatrix} = [\mathbf{a}_1 \quad \mathbf{a}_2 \quad \mathbf{a}_3] \tag{7.29}$$

and

$$d\mathbf{R} = \mathbf{a}_1 d\xi + \mathbf{a}_2 d\eta + \mathbf{a}_3 d\zeta \tag{7.30}$$

Vectors $\mathbf{a}_1$, $\mathbf{a}_2$, and $\mathbf{a}_3$ are the base vectors associated with the parametric space, $\mathbf{J}$ is the Jacobian matrix of the transformation, and $\mathbf{F}_\xi$ is the transformation matrix from the parametric space to the Cartesian space.

From Equations (7.27) and (7.28), we obtain:

$$d\xi = \mathbf{F}_\xi^{-1} d\mathbf{R} \tag{7.31}$$

and

$$\frac{\partial}{\partial \mathbf{R}} = \mathbf{J}^{-1} \frac{\partial}{\partial \xi} = \mathbf{j} \frac{\partial}{\partial \xi} \tag{7.32}$$

A volume element is defined by:

$$dV = \left|(\mathbf{dx} \wedge \mathbf{dy}) \cdot \mathbf{dz}\right| \tag{7.33}$$

which, in Cartesian space, is dV = dx dy dz, and in parametric space:

$$dV = \left|(\mathbf{a}_1 d\xi \wedge \mathbf{a}_2 d\eta) \cdot \mathbf{a}_3 d\zeta\right| \tag{7.34}$$

which is the same as:

$$dV = J d\xi d\eta d\zeta \qquad \text{where } J = \left|\det \mathbf{J}\right| \tag{7.35}$$

Therefore, the quantity Π^e can be expressed in parametric space as:

$$\int_{\Omega^e} (\ldots) dx\, dy\, dz = \int_{\Omega^{\text{parent}}} (\ldots) J\, d\xi\, d\eta\, d\zeta \tag{7.36}$$

which allows the computation of each element to be performed on the parent element rather than on the real element.

(4) Discretization of the Variational Form

We now write the solution functions for the piezoelectric problem in terms of the shape functions. For each element Ω^e defined by n nodes, the electric field is obtained from Equation (7.6) and can be written in the form:

$$\mathbf{E} = -\mathbf{B}_\phi^e \mathbf{\Phi} \tag{7.37}$$

where $\mathbf{\Phi}$ is the vector associated with the nodal values of the electrostatic potential:

$$\mathbf{B}_\phi^e = \begin{bmatrix} \mathbf{B}_{\phi 1}^e & \mathbf{B}_{\phi 2}^e & \cdots & \mathbf{B}_{\phi n}^e \end{bmatrix} \tag{7.38}$$

and

$$\mathbf{B}^e_{\phi i} = \begin{bmatrix} \dfrac{\partial N^e_i}{\partial x} \\ \dfrac{\partial N^e_i}{\partial y} \\ \dfrac{\partial N^e_i}{\partial z} \end{bmatrix} \tag{7.39}$$

The terms $\mathbf{B}^e{}_{\phi i}$ are the first spatial derivatives of the shape functions. Similarly, for each Ω^e the strain tensor defined by Equation (7.4) becomes:

$$\mathbf{x} = -\mathbf{B}^e_u\mathbf{U} \tag{7.40}$$

where **U** is the vector of the nodal values of the displacement:

$$\mathbf{B}^e_u = \begin{bmatrix}\mathbf{B}^e_{u1} & \mathbf{B}^e_{u2} & \cdots & \mathbf{B}^e_{un}\end{bmatrix} \tag{7.41}$$

and

$$\mathbf{B}^e_{ui} = \begin{bmatrix} \dfrac{\partial N^e_i}{\partial x} & 0 & 0 \\ 0 & \dfrac{\partial N^e_i}{\partial y} & 0 \\ 0 & 0 & \dfrac{\partial N^e_i}{\partial z} \\ 0 & \dfrac{\partial N^e_i}{\partial z} & \dfrac{\partial N^e_i}{\partial y} \\ \dfrac{\partial N^e_i}{\partial z} & 0 & \dfrac{\partial N^e_i}{\partial x} \\ \dfrac{\partial N^e_i}{\partial y} & \dfrac{\partial N^e_i}{\partial x} & 0 \end{bmatrix} \tag{7.42}$$

Consequently, Equation (7.1) becomes:

$$\begin{cases} \mathbf{X} = c^E\mathbf{B}^e_u\mathbf{U} + e^X\,\mathbf{B}^e_\phi\,\mathbf{\Phi} \\ \mathrm{D} = e\,\mathbf{B}^e_u\mathrm{U} + \chi^x\mathbf{B}^e_\phi\,\mathbf{\Phi} \end{cases} \tag{7.43}$$

Finally, we can rewrite the functional Π^e on the element as:

$$\begin{aligned}\Pi^e &= \frac{1}{2}\iiint\limits_{\Omega^e} U^{e^X}(B_u^{e^X} c^E B_u^e - \rho\omega^2 N^{e^X} N^e) U^e d\Omega^e \\ &+ \iiint\limits_{\Omega^e} U^{e^X} B_u^{e^X} e B_\phi^e \Phi^e d\Omega^e - \frac{1}{2}\iiint\limits_{\Omega^e} \Phi^{e^X} B_\phi^{e^X} \chi^x B_\phi^e \Phi^e d\Omega^e \\ &- \iint\limits_{S_X^e} U^{e^X} N^{e^X} f\, dS_X^e + \sum_{p=0}^{P} \phi_p Q_p \end{aligned} \tag{7.44}$$

After integrating the shape function matrices and their derivatives, we can write:

$$\Pi^e = \frac{1}{2} U^{e^X}(K_{uu}^e - \omega^2 M^e) U^e + U^{e^X} K_{u\phi}^e \Phi^e + \frac{1}{2}\phi^{e^X} K_{\phi\phi}^e \Phi^e - U^{e^X} F^e + \sum_{p=0}^{P} \phi_p Q_p \tag{7.45}$$

where:

$$\begin{aligned} K_{uu}^e &= \iiint\limits_{\Omega^e} B_u^{e^X} c^E B_u^e d\Omega^e \\ M^e &= \iiint\limits_{\Omega^e} \rho\omega^2 N^{e^X} N^e d\Omega^e \\ K_{\phi u}^e &= \iiint\limits_{\Omega^e} B_u^{e^X} e\, B_\phi^e d\Omega^e \\ K_{\phi\phi}^e &= -\iiint\limits_{\Omega^e} B_\phi^{e^X} \chi^x B_\phi^e d\Omega^e \\ F^e &= \iint\limits_{S_X^e} N^{e^X} f\, dS_X^e \end{aligned} \tag{7.46}$$

and K^e_{uu}, $K^e_{\phi u}$, and $K^e_{\phi\phi}$ are the elastic, piezoelectric, and dielectric susceptibility matrices, and M^e is the consistent mass matrix.

(5) Assembly

The matrices in (7.46) must be rearranged for the whole domain Ω by a process called assembly. From this process, we obtain the following matrices:

$$\begin{aligned}
K_{uu} &= \sum_e K^e_{uu} \\
M &= \sum_e M^e \\
K_{\phi u} &= \sum_e K^e_{\phi u} \\
K_{\phi\phi} &= \sum_e K^e_{\phi\phi} \\
F &= \sum_e F^e
\end{aligned} \tag{7.47}$$

The application of the variational principle implies the minimization of the functional Π with respect to variations of the nodal values **U** and **Φ**. Therefore:

$$\frac{\partial \Pi}{\partial u_i} = 0 \qquad \forall\ i \tag{7.48}$$

and

$$\frac{\partial \Pi}{\partial \phi_j} = 0 \qquad \forall\ j \tag{7.49}$$

Making use of Equations (7.45) and (7.16), and applying the stationary condition to Π, we obtain:

$$\begin{bmatrix} K_{uu} - \omega^2 M & K_{u\phi} \\ K_{u\phi}^{\ X} & K_{\phi\phi} \end{bmatrix} \begin{bmatrix} U \\ \Phi \end{bmatrix} = \begin{bmatrix} F \\ -Q \end{bmatrix} \tag{7.50}$$

The vector for the nodal charges, **Q**, is such that for all nodes i that belong to an electrode p with potential ϕ_p, the sum of the charges Q_i is equal to ϕ_p. For all other nodes j that do not belong to an electrode, $Q_j = 0$.

(6) Computation

Specific integration, diagonalization, and elimination techniques are employed to solve the system (7.50) on a computer. A full description of these techniques is a topic that extends well beyond the scope of this text and thus will not be presented here. The matrix equation (7.50) may be adapted for a variety of different analyses, such as the static, modal, harmonic, and transient types:

- Static Analysis:

$$\begin{bmatrix} K_{uu} & K_{u\phi} \\ K_{u\phi}{}^{X} & K_{\phi\phi} \end{bmatrix} \begin{bmatrix} U \\ \Phi \end{bmatrix} = \begin{bmatrix} F \\ -Q \end{bmatrix} \tag{7.51}$$

- Modal Analysis:

$$\begin{bmatrix} K_{uu} - \omega^2 M & K_{u\phi} \\ K_{u\phi}{}^{X} & K_{\phi\phi} \end{bmatrix} \begin{bmatrix} U \\ \Phi \end{bmatrix} = \begin{bmatrix} 0 \\ -Q \end{bmatrix} \tag{7.52}$$

- Harmonic Analysis

$$\begin{bmatrix} K_{uu} - \omega^2 M & K_{u\phi} \\ K_{u\phi}{}^{X} & K_{\phi\phi} \end{bmatrix} \begin{bmatrix} U \\ \Phi \end{bmatrix} = \begin{bmatrix} F \\ -Q \end{bmatrix} \tag{7.53}$$

- Transient Analysis

$$\begin{bmatrix} M & 0 \\ 0 & 0 \end{bmatrix} \begin{bmatrix} \ddot{U} \\ \ddot{\Phi} \end{bmatrix} + \frac{1}{\omega_o} \begin{bmatrix} K'_{uu} & K'_{u\phi} \\ K'_{u\phi}{}^{X} & K'_{\phi\phi} \end{bmatrix} \begin{bmatrix} \dot{U} \\ \dot{\Phi} \end{bmatrix} + \begin{bmatrix} K_{uu} & K_{u\phi} \\ K_{u\phi}{}^{X} & K_{\phi\phi} \end{bmatrix} \begin{bmatrix} U \\ \Phi \end{bmatrix} = \begin{bmatrix} F \\ -Q \end{bmatrix} \tag{7.54}$$

Each of these cases requires specific conditioning and computation techniques. Some of the techniques used in the commercial program ATILA are demonstrated in the CD supplement to the text.

CHAPTER ESSENTIALS

1. Within each finite element, the displacement and electric potential fields are uniquely defined by the values they assume at the element nodes (*degrees of freedom*). This definition is obtained by *interpolation*, or utilizing *shape functions* associated with the element. By combining, or *assembling*, these local definitions throughout the whole mesh, we obtain a trial function for Ω that depends only on the nodal values of $\mathbf{u}$ and ϕ and that is "piecewise" defined over all the interconnected elementary domains.

2. Mechanical and electrical boundary conditions complete the definition of the problem. The Dirichlet conditions apply to the displacement field $\mathbf{u}$ and the Neumann conditions to the stress field $\mathbf{X}$. Note that with this condition we assume that the electric field outside Ω is negligible, which is easily verified for piezoelectric ceramics.

3. Using the system of equations and the defined boundary, we obtain the functional:

$$
\begin{aligned}
\Pi = & \iiint_{\Omega} \frac{1}{2}(x_{ij}\, c^{E}_{ijkl}\, x_{kl} - \rho\omega^{2} u_{i}^{2})\, d\Omega - \iint_{S_u} (u_i - u_i^{o}) n_j (c^{E}_{ijkl} x_{kl} - e_{kij} E_k)\, dS_u \\
& - \iiint_{\Omega} \frac{1}{2}(2x_{kl} e_{ikl} E_i + E_i \chi^{x}_{ij} E_j)\, d\Omega - \iint_{S_X} f_i u_i\, dS_X \\
& - \sum_{p=0}^{M} \iint_{S_p} (\phi - \phi_p) n_i (e_{ikl} x_{kl} + \chi^{x}_{ij} E_j)\, dS_p + \sum_{p=0}^{P} \phi_p Q_p
\end{aligned}
$$

4. The domain Ω is divided into sub-domains Ω^{e}, or finite elements (*discretization*), and the functional Π can be written as:

$$
\Pi^{e} = \frac{1}{2} U^{e^{X}} (K^{e}_{uu} - \omega^{2} M^{e}) U^{e} + U^{e^{X}} K^{e}_{u\phi} \Phi^{e} + \frac{1}{2} \phi^{e^{X}} K^{e}_{\phi\phi} \Phi^{e} - U^{e^{X}} F^{e} + \sum_{p=0}^{P} \phi_p Q_p
$$

where:

$$
\begin{aligned}
K^{e}_{uu} &= \iiint_{\Omega^{e}} B^{e^{X}}_{u} c^{E} B^{e}_{u}\, d\Omega^{e} \\
M^{e} &= \iiint_{\Omega^{e}} \rho\omega^{2} N^{e^{X}} N^{e}\, d\Omega^{e} \\
K^{e}_{\phi u} &= \iiint_{\Omega^{e}} B^{e^{X}}_{u}\, e\, B^{e}_{\phi}\, d\Omega^{e} \\
K^{e}_{\phi\phi} &= -\iiint_{\Omega^{e}} B^{e^{X}}_{\phi} \chi^{x} B^{e}_{\phi}\, d\Omega^{e} \\
F^{e} &= \iint_{S^{e}_{X}} N^{e^{X}} f\, dS^{e}_{X}
\end{aligned}
$$

and K^{e}_{uu}, $K^{e}_{\phi u}$, and $K^{e}_{\phi\phi}$ are the elastic, piezoelectric, and dielectric susceptibility matrices, and M^{e} is the consistent mass matrix.

5. By applying the stationary condition to Π, the solution is derived from:

$$
\begin{bmatrix} K_{uu} - \omega^{2} M & K_{u\phi} \\ K_{u\phi}^{X} & K_{\phi\phi} \end{bmatrix} \begin{bmatrix} U \\ \Phi \end{bmatrix} = \begin{bmatrix} F \\ -Q \end{bmatrix}
$$

The matrix equation (7.50) may be adapted for a variety of different analyses, such as the static, modal, harmonic, and transient types.

CHAPTER PROBLEMS

7.1 Using the ATILA software code template on the CD supplement, calculate the resonance frequencies and simulate the vibrations for a Π shaped ultrasonic motor with the following design parameters:

   a. leg material: aluminum and brass
   b. leg length: 10, 15 and 20 mm

REFERENCES

1) O. C. Zienkiewicz: *The Finite Element Method* – 3rd ed., expanded and revised, McGraw-Hill, UK (1977).
2) J.-N. Decarpigny: Application de la Méthode des Eléments Finis à l'Etude de Transducteurs Piézoélectriques, Doctoral Thesis, ISEN, Lille, France (1984).
3) T. Ikeda: *Fundamentals of Piezoelectricity*, Oxford University Press, Oxford (1990).
4) B. Dubus, J.-CBertrand, J.-C. Debus and J. Coutte: Modélisation de Matériaux Piézoélectriques et Electrostrictifs par la Méthode des Eléments Finis, Revue Européenne des Eléments Finis, **8** (5-6), pp. 581-606 (1999).

8

SERVO DISPLACEMENT TRANSDUCER APPLICATIONS

Piezoelectric/electrostrictive actuators are classified into three categories, based on the type of driving voltage applied to the device and the nature of the strain induced by the applied voltage: (1) servo displacement transducers, (2) pulse drive devices operated in a simple on/off switching mode, and (3) ultrasonic resonant devices. The fields of application of the ceramic actuators are also classified into three categories: (1) positioning, (2) motor application, and (3) vibration suppression.

This chapter will focus on servo displacement transducers and applications. These devices are used for positioning and vibration suppression in optical control systems (such as those implementing deformable mirrors) and mechanical systems implementing such mechanical devices as microscope stages, linear motion guide mechanisms, oil pressure servo valves and VCR head control mechanisms. Many of the devices for these applications are made from lead magnesium niobate (PMN)-based electrostrictive ceramics because the hysteresis in their strain response is small as compared with that exhibited by other electrostrictive and piezoelectric materials.

8.1 DEFORMABLE MIRRORS

(1) The Monolithic Piezoelectric Deformable Mirror

Precise wave front control with as small a number of parameters as possible and compact construction is a common and basic requirement for *adaptive optical systems*. Continuous surface deformable mirrors, for example, tend to be more desirable than segmented mirrors in terms of controllability. The monolithic piezoelectric deformable mirror pictured in Figure 8.1 has been produced that is comprised of a PZT bulk ceramic (the ceramic monolith) with electrodes arranged in a two-dimensional configuration.[1] Applying suitable voltages to the electrodes causes the mirror to deform, as if pushing the mirror by rods from the backside. One application of this mirror is demonstrated in Figure 8.2 in which the phase of the reflected light is effectively modulated by adjusting the contour of the mirror surface. A deformable mirror can also be used to correct the distortion that occurs in a telescope image due to atmospheric conditions, as illustrated in Figure 8.3. Various electrode configurations have been proposed to produce a variety of mirror contours.[2]

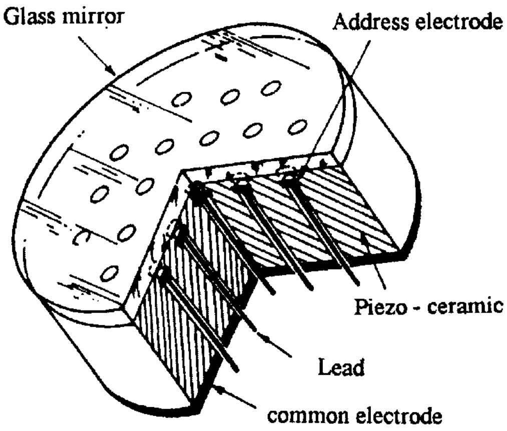
Glass mirror
Address electrode
Piezo - ceramic
Lead
common electrode

Figure 8.1 A deformable mirror made from a piezoelectric monolith.[1]

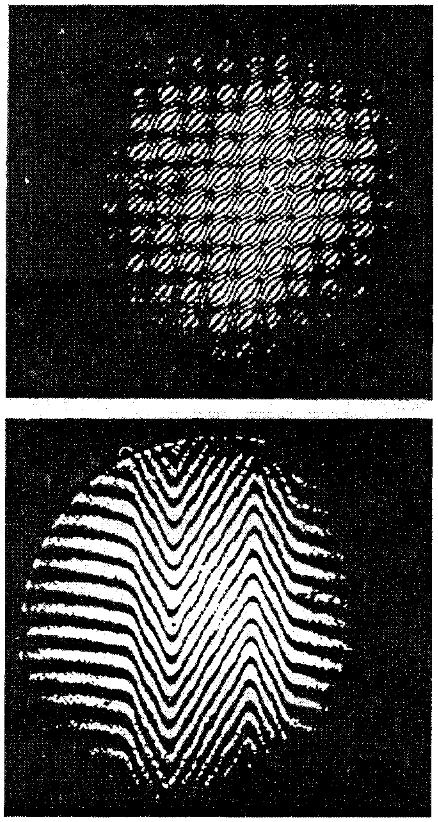

Figure 8.2 Application of the monolithic piezoelectric deformable mirror for phase modulation.[1]

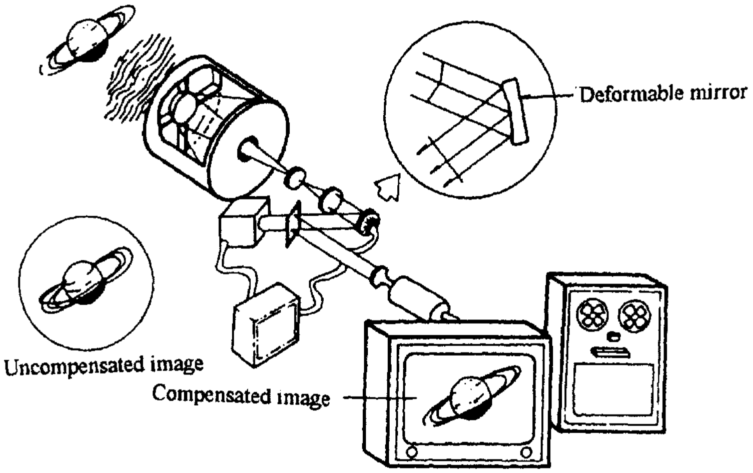

Figure 8.3 A telescope image correction system using a monolithic piezoelectric deformable mirror.[1]

(2) The Multimorph Deformable Mirror

The monolithic piezoelectric deformable mirror requires many electrodes (350 elements) and many electrical leads to the individual electrode elements. Furthermore, since each element does not function independently, a minicomputer is required for its control. A much simpler multimorph deformable mirror has been proposed which can be more simply controlled by means of a microcomputer.[3,4]

In the case of the *two-dimensional multimorph deflector design*, a static deflection along the z axis $f_i(x,y)$ is generated by the voltage distribution on the ith layer $V_i(x,y)$, which can be obtained by solving the following system of differential equations:

$$A\left[\frac{\partial^4 f_i(x,y)}{\partial x^4}+2\frac{\partial^4 f_i(x,y)}{\partial x^2 \partial y^2}+\frac{\partial^4 f_i(x,y)}{\partial y^4}\right]+B_i\left[d_{31}\frac{\partial^2 V_i(x,y)}{\partial x^2}+d_{32}\frac{\partial^2 V_i(x,y)}{\partial y^2}\right]=0 \tag{8.1}$$

where $[i=1,2,\ldots,I]$, A and B_i are constants, d_{31} and d_{32} are piezoelectric strain coefficients, and I is the total number of layers in the multimorph. This equation is derived specifically for piezoelectric layers, but may also be adapted to describe a device comprised of electrostrictive layers, provided the nonlinear relationship between the electric field and the induced strain characteristic of electrostrictive materials is properly taken into account.

When the conditions $d_{31}=d_{32}$ and $f_i(x,y) = 0$ under $V_i(x,y) = 0$ $(i = 1, 2, \ldots, I)$ are assumed, then Equation (8.1) reduces to:

$$\nabla^2 f_i(x,y) + C_i V_i(x,y) = 0 \tag{8.2}$$

where C_i is a constant which is different for each layer and ∇^2 is the Laplacian operator. Thus, we see in general that the contour of the mirror surface can be changed by means of an appropriate electrode configuration and *applied voltage distribution* on each electroactive ceramic layer.

The contour of the mirror surface can be represented by the Zernike aberration polynomials, whereby an arbitrary surface contour modulation g(x,y) can be described as follows:

$$g(x,y) = C_r(x^2+y^2) + C_c^1 x(x^2+y^2) + C_c^2 y(x^2+y^2) + \cdots \tag{8.3}$$

Notice that the Zernike polynomials are orthogonal and therefore completely independent of each other. The C_r and C_c terms represent *refocusing* and the *coma aberration*, respectively. As far as human vision is concerned, correction for aberrations, up to the second order in this series (representing astigmatism), is typically sought to provide an acceptably clear image.

The important parameters for designing the electrode configurations are as follows:

a. **The Effective Optical Area**: Typically, only the central portion of the mirror surface (amounting to about one quarter of the total mirror surface) is used since the outer portions are difficult to deform when the boundary conditions for optimum operation are applied. The electrode covering the active area is divided into J identical elements (typically in an 8x8 array).

b. **The Deflection of Each Unit**: The deflection of a particular unit with the application of unit voltage is given by:

$$u_{ij}(x,y) = \frac{16C_i}{\pi^4}\sum_{p,q}\left[\frac{1}{pq(P^2+Q^2)}\right]\Pi \tag{8.4}$$

where:

$$\Pi \equiv \sin(P\pi\xi_j)\sin(Q\pi\eta_j)\sin(P\pi u/2)\sin(Q\pi v/2)\sin(P\pi x)\sin(Q\pi y)$$

$P = (p/l_x)$ and $Q = (q/l_y)$

and the coordinates (ξ_j, η_j) identify the center of the jth electrode element. All elements have the same area (uv). The suffix i refers to the ith layer.

c. **The Voltage Distribution**: The level of voltage V_{ij}, j = 1, 2, ..., J applied to each element to generate the deflections $f_i(x,y)$ is determined such that the mean-square error between the generated and the required deflections over the effective optical area is minimized.

d. **Electrode Shape**: Certain groups of elements are addressed with the same voltage to effectively establish a desired electrode shape and associated mirror contour.

As examples, let us consider the cases where we wish to refocus and to correct for the coma aberration. A uniform large area electrode can provide a parabolic (or spherical) deformation with the desired focal length. In the case of coma correction, one could employ the electrode pattern shown in Figure 8.4, which consists of only six elements addressed by voltages applied in a fixed ratio.

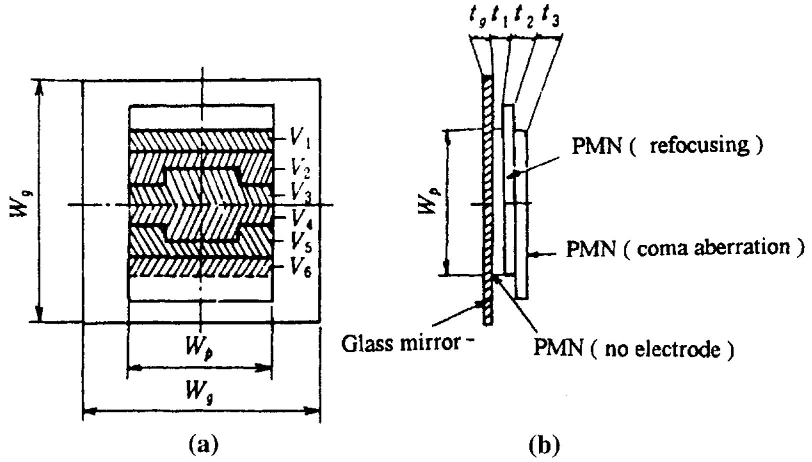

Figure 8.4 A two-dimensional multimorph deformable mirror designed for refocusing and coma aberration correction: (a) front view and (b) cross-sectional view of the structure.[4]

Measurement of the deflection of a deformable mirror has been carried out using the holographic interferometric system pictured schematically in Figure 8.5.[3] The presence of the *hologram* in the system effectively eliminates effects of the initial deformation of the mirror from the final interferogram. Some experimental results characterizing mirror deformations established for the purpose of refocusing, coma correction, and both refocusing and coma correction are shown in Figure 8.6. Good agreement between the desired and generated contours is seen in each case. These results also demonstrate the effectiveness of achieving a superposition of deformations by means of an appropriate configuration of discrete electrodes. The deformable mirror examined in this study was found to have a linear response to sinusoidal input voltages with frequencies up to 500 Hz.

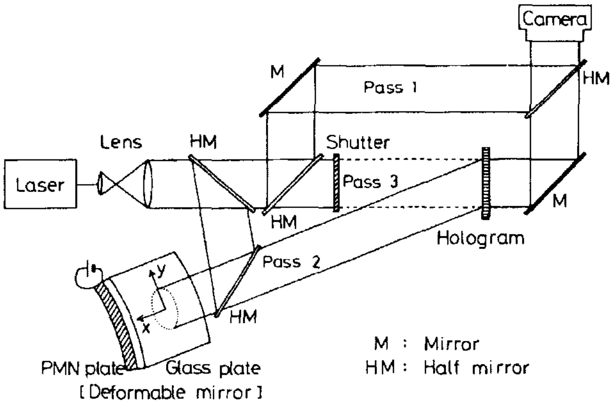

Figure 8.5 Optical system for the deformable mirror.[3]

Interferograms from deformable mirrors incorporating PZT piezoelectric and PMN electrostrictive elements under a series of applied voltages are shown in Figure 8.7.[3] A distinct hysteresis for the PZT mirror is apparent, while no significant hysteretic effect is observed for the PMN mirror.

(3) The Articulating Fold Mirror

An active mirror for use in space imaging systems called the articulating fold mirror has been developed.[5] The system is depicted schematically in Figure 8.8. Three articulating fold mirrors were incorporated into the optical train of the Jet Propulsion Laboratory's Wide Field and Planetary Camera-2, which was installed into the Hubble Space Telescope in 1993. As shown in Figure 8.8, each articulating fold mirror utilizes six PMN electrostrictive multilayer actuators to precisely tip and tilt a mirror in order to correct for the aberration in the Hubble telescope's primary mirror.

Images of the core of M100, a spiral galaxy in the Virgo cluster, before and after the correction of the aberration appear in Figure 8.9. The corrections have helped to restore the Hubble system to its original imaging specifications.

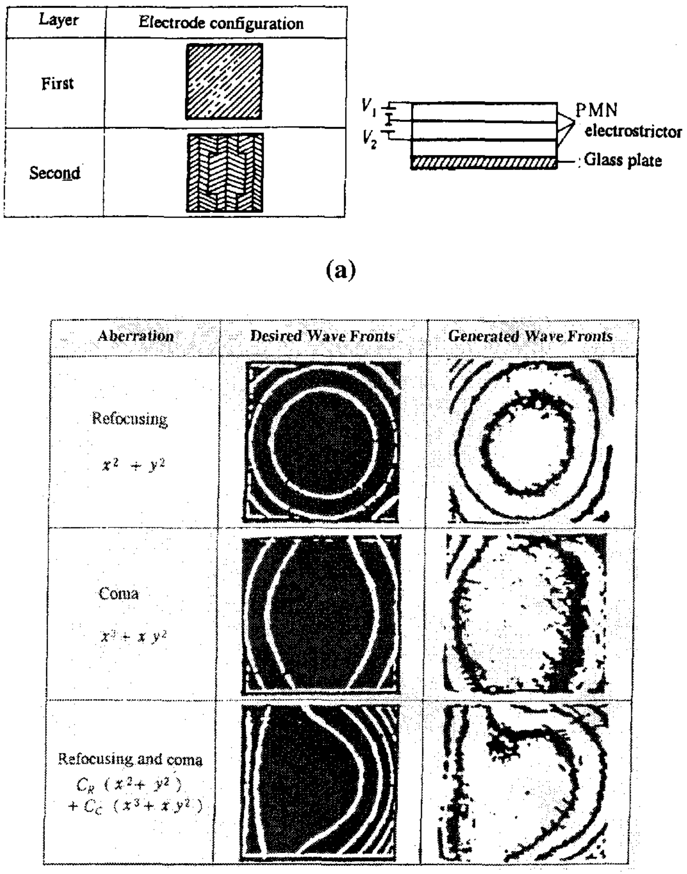
Layer
Electrode configuration
First
Second
V_1
V_2
PMN electrostrictor
Glass plate
(a)
Aberration
Desired Wave Fronts
Generated Wave Fronts
Refocusing
$x^2 + y^2$
Coma
$x^3 + x y^2$
Refocusing and coma
$C_R\ (x^2 + y^2) + C_C\ (x^3 + x y^2)$

(b)

Figure 8.6 A PMN-based multilayer deformable mirror: (a) diagrams of internal electrode configurations and the overall multilayer structure and (b) interferograms revealing the surface contours produced on the mirror.[3]

8.2 MICROSCOPE STAGES

An adjustable sample stage for optical and electron microscopes has been developed that utilizes a monolithic hinge lever mechanism.[6] A schematic depiction of the stage and its components appears in Figure 8.10. The displacement induced in the PZT multilayer actuator under an applied voltage of 1 kV is amplified by a factor of thirty by means of a two-stage lever mechanism, leading to an actual displacement of 30 μm at the center of the stage.

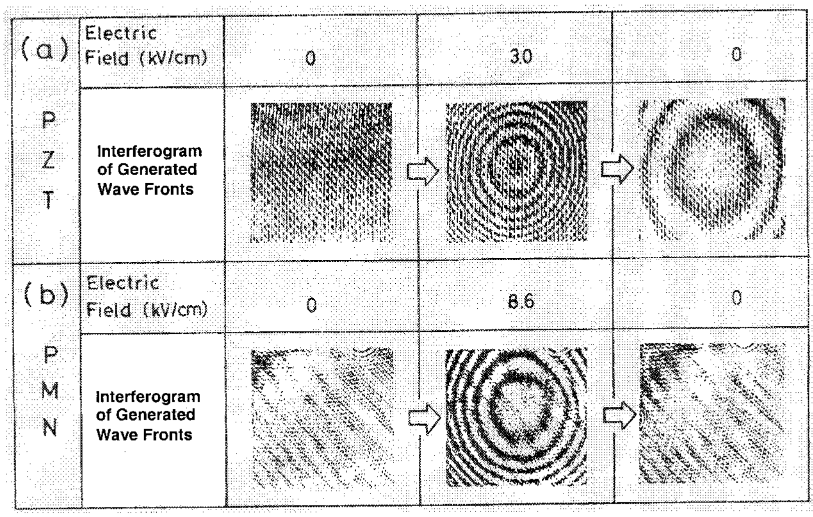
(a)
Electric Field (kV/cm)
0
3.0
0
PZT
Interferogram of Generated Wave Fronts
(b)
Electric Field (kV/cm)
0
8.6
0
PMN
Interferogram of Generated Wave Fronts

Figure 8.7 Interferograms from: (a) PZT and (b) PMN deformable mirrors.[3]

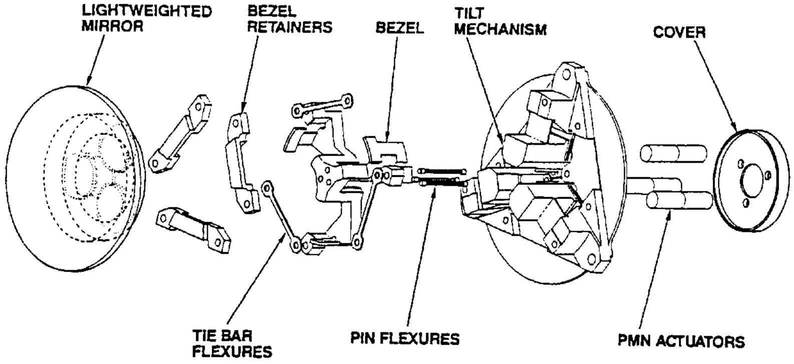
LIGHTWEIGHTED MIRROR
BEZEL RETAINERS
BEZEL
TILT MECHANISM
COVER
TIE BAR FLEXURES
PIN FLEXURES
PMN ACTUATORS

Figure 8.8 Schematic diagram of an articulating fold mirror utilizing PMN actuators.[5]

The sample stage must be compact, especially when it is to be used in the electron microscope, and able to withstand vacuum conditions of about 10^{-9} mmHg. In order to meet the latter condition, a suitable nonvolatile bonding resin should be used between the layers of the multilayer actuator, and electrode materials such as zinc and cadmium, which are highly volatile under these conditions, must be avoided.

A probe scanning actuator for a scanning tunneling microscope (STM) has been proposed that makes use of a PZT tripod structure as illustrated in Figure 8.11.[7] One primary limitation with this design is the displacement hysteresis of the probe actuator, which directly affects the reproducibility and resolution of the STM image. A more reliable PMN-based probe actuator design that is virtually hysteresis free has been developed to overcome this limitation.[8]

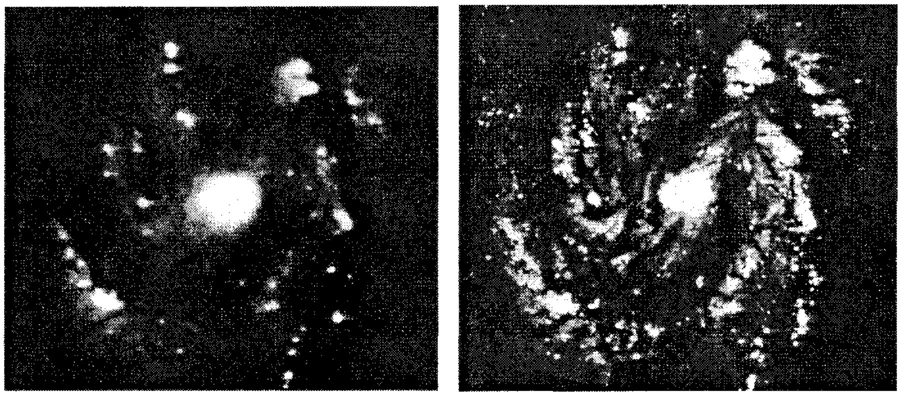

(a) (b)

Figure 8.9 Hubble space telescope images of the M100 galaxy: (a) before and (b) after installation of the articulating fold mirrors to correct for aberration in the system.[5]

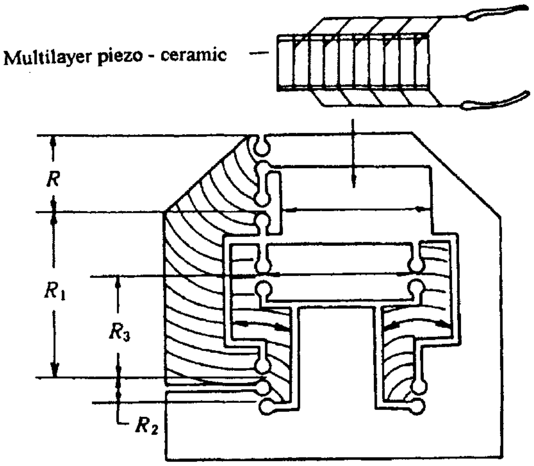

Figure 8.10 An adjustable microscope stage using a monolithic hinge lever mechanism.[6]

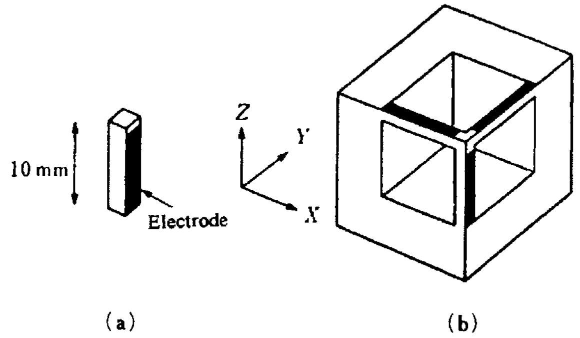

Figure 8.11 A probe control actuator for a scanning tunneling microscope: (a) an individual ceramic unit and (b) the tripod structure.[7]

8.3 HIGH PRECISION LINEAR DISPLACEMENT DEVICES

Recent developments in precision diamond cutting and polishing have been remarkable. The high degree of precision for flatness required of laser interferometric mirrors to adequately satisfy the requirements for most applications to date has been achieved with these machines. The requirements for newly developed applications, however, indicate an even higher precision in the flatness of the laser mirror surfaces (on the order of 0.05 μm), and thus more sophisticated precision linear motion guide mechanisms must be employed on the cutting apparatus. Conventional guide mechanisms, such as air bearings and roller type bearings, produce residual noise vibration (ringing) due to the low friction contact between surfaces, which results in a slow response. An ultrahigh precision linear guide system that makes use of PZT actuators has been developed with a linear motion tolerance of ± 0.06 μm / 200 mm.[9] A similar mechanism can be employed to produce an ultraprecise x-y positioning stage.[10]

(1) An Ultrahigh Precision Linear Motion Guide Mechanism

A block diagram of the linear guide mechanism is shown in Figure 8.12. The linear motion is driven by the transfer screw mechanism pictured in the lower right-hand side of the figure. As the motion occurs, the transverse motion and the pitching and rolling of the moving table relative to the master scale (made of fused quartz) installed on the base is monitored by the three differential transformers installed in the bottom of the movable table as shown in the figure. The three PZT positioners situated at the edges of the table (two of which are shown in the figure) respond to signals processed by the feedback circuit so as to maintain a constant position.

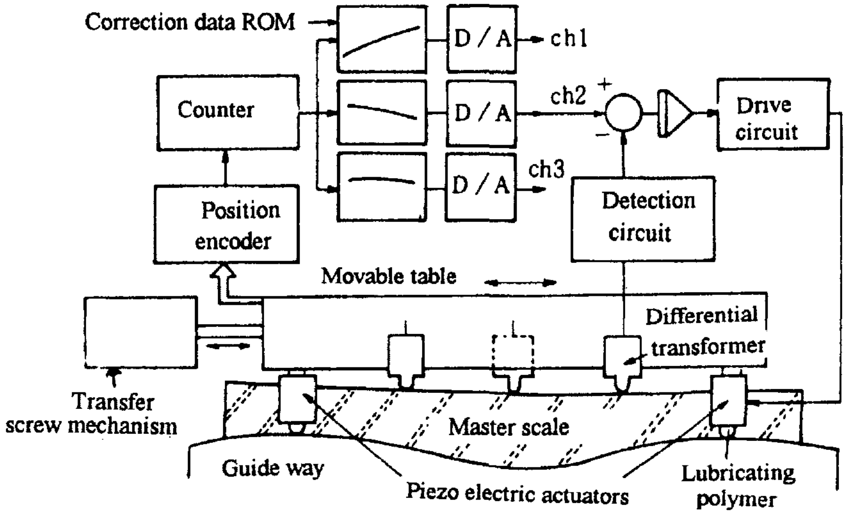
Correction data ROM
Counter
Position encoder
D / A
D / A
D / A
ch1
ch2
ch3
+
−
Drive circuit
Detection circuit
Movable table
Differential transformer
Transfer screw mechanism
Master scale
Guide way
Piezo electric actuators
Lubricating polymer

Figure 8.12 Block diagram of the ultrahigh precision linear motion guide system.[9]

The key component of this mechanism is the feedback circuit. The flatness of the master scale is initially measured as a function of position by a position encoder and the data are recorded as correction data in the *ROM (read only memory)* of the system. The table position at a given time is measured and the correction signal corresponding to that particular table position is combined with the differential transformer signal. The resulting signal is processed and then fed back to the PZT actuators. This process is effective in producing a precision in the linear motion that actually exceeds that of the master scale. The flatness error of the master scale is depicted in Figure 8.13. The correction data collected by the three differential transformers are stored in the ROM of channels 1-3 as reference data for correction by the PZT acuators. Based on the correction data processed by the system the master scale exhibits some concavity with a flatness error amounting to a 0.2 μm deviation.

Some additional features of this system are depicted in Figure 8.14. The movable table is guided on a slider medium, which for this system is a polymer lubricant as shown in Figure 8.14(a). The linear motion of the table is typically accompanied by a ±2 μm transverse displacement. The linear drive system is comprised of an electromagnetic rotary motor and a transfer screw mechanism. The PZT actuators installed between the moving table and the polymer slider have a cylindrical configuration [see Figure 8.14(a)] and can produce a displacement up to ±3 μm depending on the magnitude of the applied voltage. The three differential transformers are installed beneath the table, as shown in Figure 8.14. The transverse motion is monitored after being amplified by a factor of four by means of the lever mechanism.

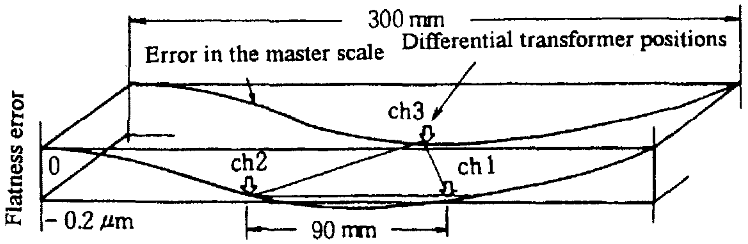
300 mm
Error in the master scale
Differential transformer positions
Flatness error
ch3
ch2
ch1
0
- 0.2 μm
90 mm

Figure 8.13 A depiction of the flatness error of the master scale for the ultrahigh precision linear motion guide system.[9]

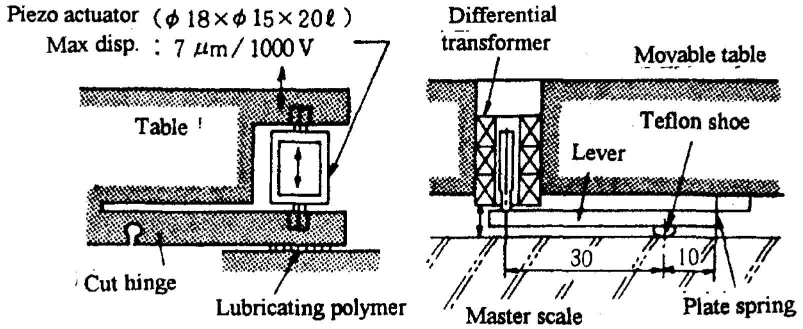
Piezo actuator (ϕ 18×ϕ 15×20ℓ)
Max disp. : 7 μm/1000 V
Table
Cut hinge
Lubricating polymer
Differential transformer
Movable table
Teflon shoe
Lever
30
10
Master scale
Plate spring

(a) (b)

Figure 8.14 Details of the ultrahigh precision linear motion guide system: placement of (a) a piezoelectric actuator and (b) a differential transformer in the system.[9]

The data shown in Figure 8.15 indicate the effectiveness of this high precision linear guide system in maintaining a linear translation with a significantly reduced transverse displacement. The data appearing in Figure 8.15(a) represent the motion of the table without the servo correction. The ±2 μm transverse motion is apparent in these data. The data appearing in Figure 8.15(b) represent the motion of the table when the servo mechanism is coupled with the master scale. These data indicate that transverse displacement has been reduced to ±0.15 μm. The data appearing in Figure 8.15(c) represent the motion of the table when the servo mechanism is employed and some correction of the master scale (reference) data is applied. This results in a transverse displacement that has been further reduced to about ±0.06 µm. Although we have focused here on the transverse displacement correction, it should be noted that this system is also effective in reducing the pitching motion from ±0.8 second without the servo to ± 0.1 second when the feedback mechanism is in operation.

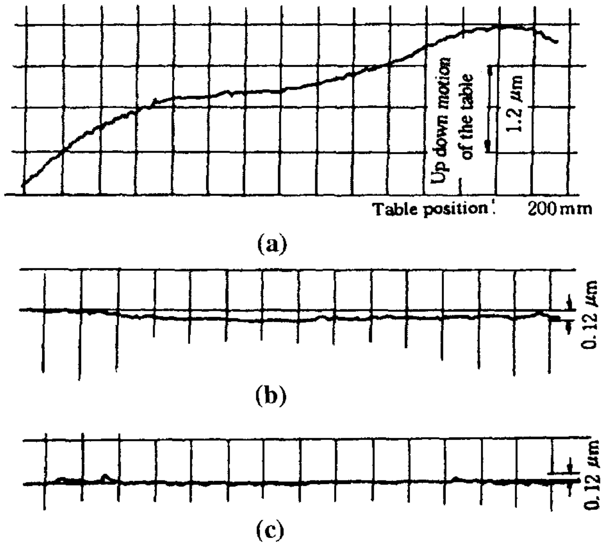

Figure 8.15 Data indicating the reduction of the transverse displacement in a system incorporating the ultrahigh precision linear guide mechanism: transverse movement (a) without the servo mechanism, (b) with the servo mechanism, and (c) with the servo mechanism and scale error correction applied.[9]

(2) An Ultraprecise x-y Stage

An ultraprecise x-y positioning stage based on a similar mechanism has also been developed.[10] A schematic representation of the stage appears in Figure 8.16. Highly precise positioning, on the order of ± 0.05 µm accompanied by only a 1 µrad yaw, is achieved with this stage for manipulations over a relatively broad area of 120 (mm) x 120 (mm). Moreover, movement of this stage can be quite rapid [10 (mm) / 200 (ms)]. The use of ultraprecise x-y stages such as this has become increasingly more important in the photolithographic processing of VLSI semiconductor chips.

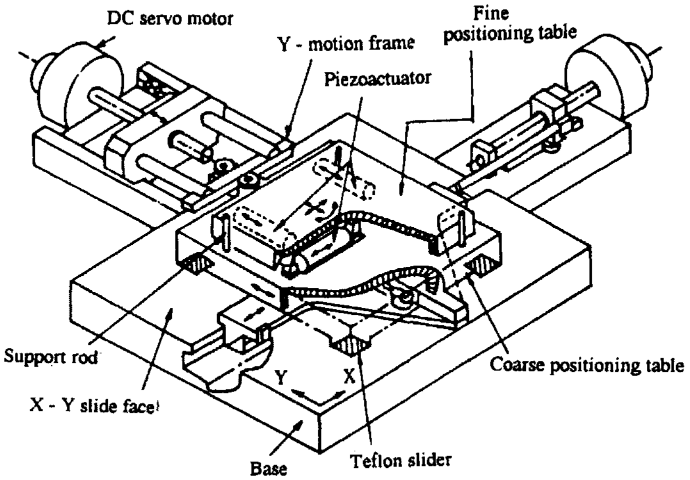

Figure 8.16 An ultrahigh precision x-y positioning stage.[10]

8.4 SERVO SYSTEMS

A classification of servo systems with respect to power and response is shown in Figure 8.17.[11] We see from this layout that a system employing a combination of electric and oil pressure control (that is, an electrohydraulic system) is required to achieve both high power and quick response. An even quicker response, on the order of 1 kHz, is currently desired for the electrohydraulic system. This is actually the maximum and generally least attainable speed indicated in Figure 8.17, however, and has yet to be realized for any of the most commonly employed systems featured in this classification. Among the more recent developments for enhancing the performance of devices in this class is a simplified valve structure that makes use of a piezoelectric PZT flapper.[11,12] This design proves to be limited in its usefulness, however, due to the hysteretic response of the PZT. In order to effectively compensate for the hysteresis, the device is controlled by a pulse width modulated drive voltage, which causes the flapper to constantly vibrate in sympathy with the carrier signal, thus severely limiting the high frequency response and the durability of the servo valve. (The design and operation of this device is presented in more detail in Chapter 5.) A modification of this basic design, incorporating an electrostrictive PMN bimorph for the flapper instead of the problematic piezoelectric PZT, has been developed that effectively overcomes these limitations.[13, 14]

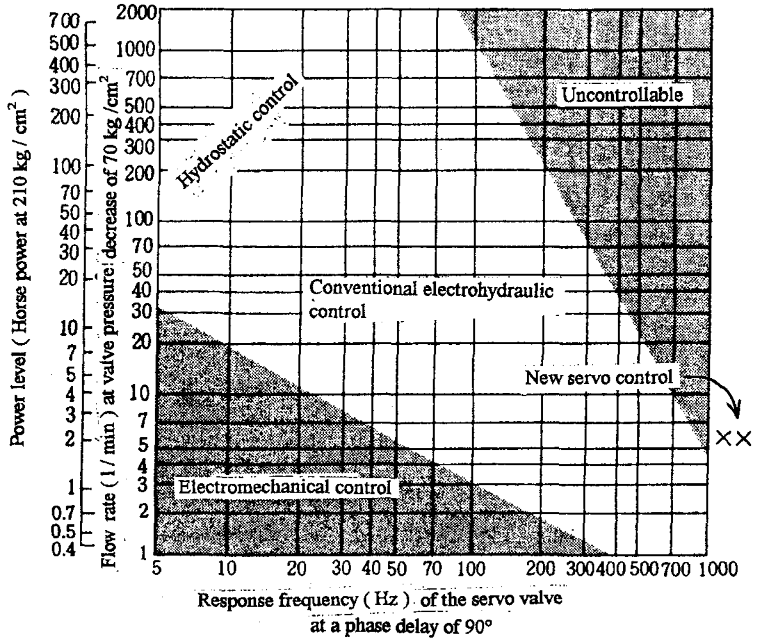

Figure 8.17 Classification of servo valves with respect to power and response.[11]

(1) Oil Pressure Servo Valves

A schematic depiction of a two-stage four-way valve appears in Figure 8.18.[14] The first stage of the valve contains a PMN-based electrostrictive flapper. The second stage spool is the smallest currently available with a diameter of only 4 mm and a nominal flow rate of 6 liter/min.

The electrostrictive composition 0.45PMN-0.36PT-0.19BZN (PMN: lead magnesium niobate, PT: lead titanate, BZN: barium zinc niobate) is used because of its large displacement and small hysteresis. The flapper has a multimorph structure in which two PMN thin plates are bonded on both sides of a phosphor bronze shim as shown in Figure 8.19. The *multimorph* structure is used for its enhanced tip displacement, generative force and response speed. The structure is addressed such that the top and bottom electrodes and the metal shim have a common ground potential as shown in the figure, and a high voltage (designated by V_1 and V_2 in the figure) is applied on the electrodes between the two PMN plates on each side of the shim. The tip deflection exhibits a quadratic dependence on the applied voltage as would be expected for an electrostrictive response, thus, in order to obtain a linear relation, a *push-pull driving* method is adopted in which the applied voltages are controlled such that:

$$V_1 = V_o + v_{app}$$
$$V_2 = V_o - v_{app} \qquad [V_o = 600\ \mathrm{V}] \qquad (8.5)$$

where v_{app} is the applied signal voltage. A plot of v_{app} as a function of displacement x, as shown in Figure 8.20, is seen to be nearly linear. Notice that the displacement hysteresis for the PMN-based ceramic is much smaller than what would occur for a PZT piezoelectric. The resonance frequency of this flapper in oil is about 2 kHz.

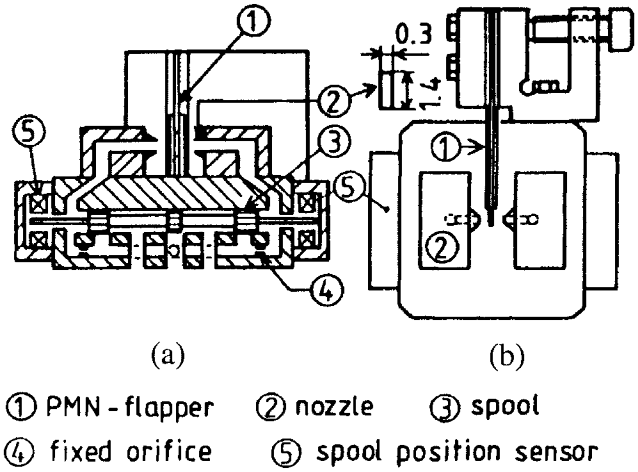
①
②
③
④
⑤
0.3
1.4
(a)
(b)
① PMN - flapper
② nozzle
③ spool
④ fixed orifice
⑤ spool position sensor

Figure 8.18 A schematic depiction of a two-stage four-way valve: (a) front view and (b) top view.[14]

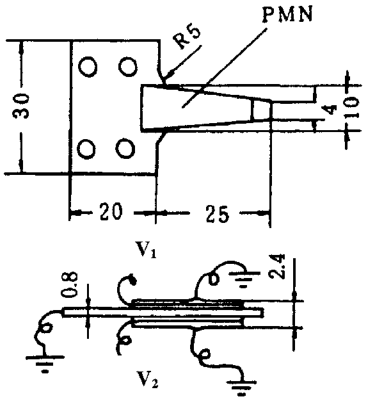
PMN
R5
30
4
10
20
25
V1
0.8
2.4
V2

Figure 8.19 The multimorph electrostrictive flapper.[14]

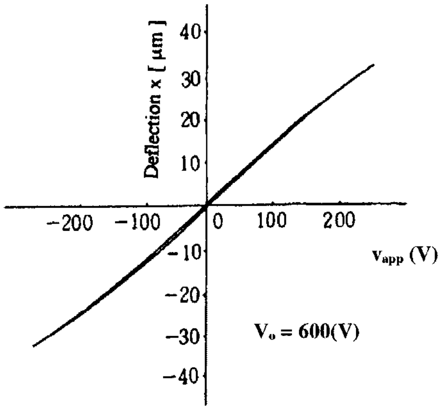

Figure 8.20 Push-pull drive characteristics of the electrostrictive flapper.[14]

The conventional force feedback method makes use of a structure in which the flapper tip and the spool are connected by a spring, which limits the responsivity of the system. In order to overcome this limitation, an alternative electric feedback method, for which a signal associated with the spool position is used, has been developed.[13,14] A compact differential transformer (50 kHz) is employed to detect the spool position. This method has various merits including a readily variable feedback gain and the option of a *speed feedback* mode of operation.

A block diagram of the oil pressure servo valve from reference input to spool displacement is shown in Figure 8.21. Several approximations are adopted for the frequency range below 1 kHz:

1) The power supply is represented by $K_a / (T_a s + 1)$.
2) The transfer function of the flapper has a second-order form.
3) The compressibility of the oil is neglected.
4) The visco-resistance between the spool and sleeve is also neglected.

It is assumed in the following analyses that the speed feedback mode of operation has not been employed. When the input-output relation for the system depicted in Figure 8.21 is expressed in a simple *second-order form*, the following transfer function is obtained:

$$\frac{Y(s)}{R(s)} = \left[\frac{1}{K_p}\right] \frac{1}{a_0 s^2 + a_1 s + 1} \tag{8.6}$$

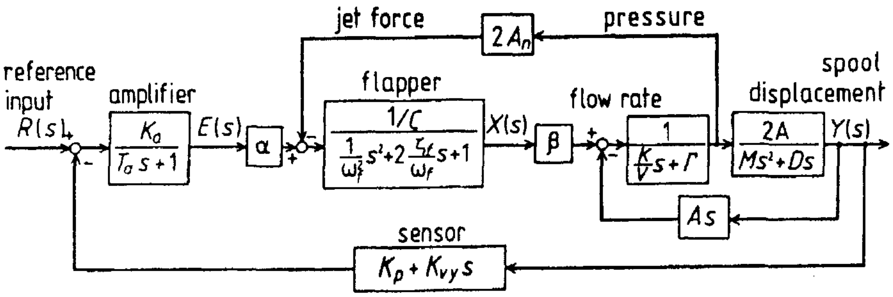
jet force
2A_n
pressure
reference input
R(s)
amplifier
K_a / (T_a s + 1)
E(s)
α
flapper
1/C / (1/ω_f² s² + 2 ζ_f/ω_f s + 1)
X(s)
β
flow rate
1 / (K/V s + Γ)
spool displacement
2A / (Ms² + Ds)
Y(s)
As
sensor
K_p + K_vy s
+
-

Figure 8.21 Block diagram of the servo valve. [13,14]

where:

$$a_0 = \frac{[1 + (2A_n \beta / C\Gamma)]M + 2[(2\zeta_f / \omega_f) + T_a](A^2/\Gamma)}{a_2}$$

$$a_1 = \frac{2(A^2/\Gamma)}{a_2}$$

$$a_2 = \frac{2A\beta\alpha K_a K_b}{C\Gamma}$$

Example Problem 8.1

Neglecting the higher order terms and K_{vy} and D, derive Equation (8.6) from the block diagram shown in Figure 8.21.

Solution

There are four variables represented in Figure 8.21: R(s), E(s), X(s), and Y(s). We may write the following three equations for the nodes indicated by open circles in the block diagram:

$$\left[\frac{T_a s + 1}{K_a}\right] E(s) = R(s) - [K_p + K_{vy} s] Y(s) \qquad \text{(P8.1.1)}$$

$$C\left[\frac{1}{\omega_f^2} s^2 + 2\frac{\zeta_f}{\omega_f} s + 1\right] X(s) = \alpha E(s) - 2A_n \left[\frac{M s^2 + D s}{2A}\right] Y(s) \qquad \text{(P8.1.2)}$$

$$\left[\frac{K}{V}s + \Gamma\right]\left[\frac{M\,s^2 + D\,s}{2A}\right]Y(s) = \beta X(s) - A\,s\,Y(s) \qquad \text{(P8.1.3)}$$

Solving Equation (P8.1.1) for E(s), substituting this expression into Equation (P8.1.2), and solving for X(s) yields:

$$X(s) = \frac{\left[\left(\frac{\alpha K_a}{T_a s+1}\right)R(s) - \left(\frac{\alpha K_a(K_p + K_{vy}\,s)}{T_a s+1}\right)Y(s) - \left(\frac{A_n(M s^2 + D\,s)}{A}\right)Y(s)\right]}{C\left[\frac{1}{\omega_f^2}s^2 + \frac{2\zeta_F}{\omega_F}s + 1\right]} \qquad \text{(P8.1.4)}$$

Combining Equation (P8.1.4) with Equation (P8.1.3) allows us to write:

$$\left[\frac{((K/v)s + \Gamma)(M s^2 + D s)}{2A} + A s\right]Y(s) = \beta X(s) \qquad \text{(P8.1.5)}$$

where:

$$\beta X(s) = \frac{\beta\left[\left(\frac{\alpha K_a}{T_a s+1}\right)R(s) - \left(\frac{\alpha K_a(K_p + K_{vy}\,s)}{T_a s+1}\right)Y(s) - \left(\frac{A_n(M s^2 + D\,s)}{A}\right)Y(s)\right]}{C\left[\frac{1}{\omega_f^2}s^2 + \frac{2\zeta_F}{\omega_F}s + 1\right]}$$

We can now obtain the inverse transfer function in the initial form:

$$\frac{R_s}{Y_s} = \Sigma\left(T_a s + 1\right) + \left(K_p + K_{vy} s\right) \qquad \text{(P8.1.6)}$$

where:

$$\Sigma \equiv \frac{C}{2\alpha\beta K_a A}\left(\frac{1}{\omega_f^2}s^2 + \frac{2\zeta_f}{\omega_f}s + 1\right)\left[\left(\frac{K}{V}s + \Gamma\right)\left(M s^2 + D s\right) + 2A^2 s\right] + \frac{A_n(M s^2 + D s)}{\alpha K_a A}$$

Neglecting terms of order higher than s^2 results in the somewhat more simplified form of the inverse transverse function:

$$\frac{R(s)}{Y(s)} = K_p + s K_p \boldsymbol{\Phi} + s^2 K_p \boldsymbol{\Psi} \qquad \text{(P8.1.7)}$$

where:

$$\Phi \equiv \frac{K_{vy}}{K_p} + \frac{A_n D}{\alpha K_a A K_p} + \frac{C\Gamma}{2A\alpha\beta K_a K_p}\left(\frac{2A^2}{\Gamma} + D\right)$$

$$\Psi \equiv \left[A_n M + A_n D T_a\right]\frac{1}{\alpha K_a A K_p} + \left[\frac{KD}{V} + \Gamma M\right]\frac{C}{2A\alpha\beta K_a K_p} + \left[\frac{C2\zeta_f}{\omega_f} + CT_a\right]\frac{\left(\Gamma D + 2A^2\right)}{2A\alpha\beta K_a K_p} + \frac{T_a A_n D}{\alpha K_a A K_p}$$

Neglecting the terms containing K_{vy} and D and further simplifying Equation (P8.1.7) produces Equation (8.6).

The static spool displacement of the oil pressure servo valve utilizing the electronic feedback system is shown as a function of reference input in Figure 8.22. The slight hysteresis and nonlinearity manifested in the response curve for the non-regulated valve shown in Figure 8.20 do not appear in the data recorded in Figure 8.22 due to the action of the feedback mechanism implemented in this system. The dynamic characteristic of the spool displacement is shown in Figure 8.23. The 0 dB gain level was adjusted at 10 Hz. A slight peak in the gain curve occurs at 1800 (Hz) and the 90° retardation frequency is about 1200 Hz. The maximum spool displacement at 1 kHz is ± 0.03 mm. In terms of the classification scheme appearing in Figure 8.17, this new servo system is placed in the position of the two x's indicating that it is the fastest servo valve currently available.

(2) Air Pressure Servo Valves

Similar nozzle-flapper mechanisms can be applied for air pressure control.[15] The main difference between the oil and air pressure control systems is the force applied to the flapper. The typical range of diameter for most nozzle-flapper mechanisms utilized in oil and air pressure control systems is d_n=0.3-0.8 mm, and the maximum force on the flapper f_{max} is determined by the following:

$$f_{max} < (1/2)\,\pi\, d_n^2\, p \qquad (8.7)$$

where p is the nozzle pressure. The typical range of p for oil pressure systems is 70-210 kgf/cm^2, and for air pressure systems 3 kgf/cm^2. The nozzle-flapper distance is generally adjusted to less than $d_n/4$.

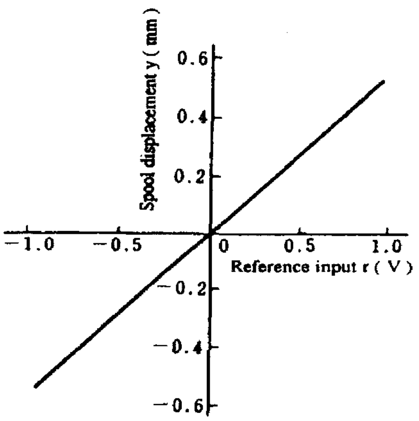

Figure 8.22 The static spool displacement of the oil pressure servo valve utilizing the electronic feedback system plotted as a function of reference input.[13,14]

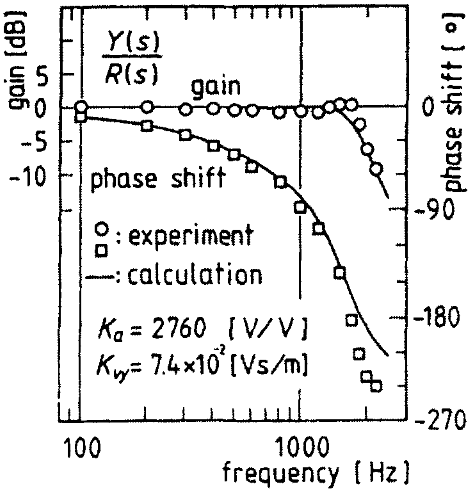

Figure 8.23 Normalized frequency characteristics of the oil pressure servo valve utilizing the electronic feedback system.[13,14]

(3) A Direct Drive Spool Servo Valve

A direct drive spool servo valve has also been developed that uses two multilayer PMN-based actuators coupled with a sophisticated hinge lever mechanism as shown in Figure 8.24.[14] This system exhibits an even quicker response with a 90° phase retardation frequency of about 1400 (Hz).

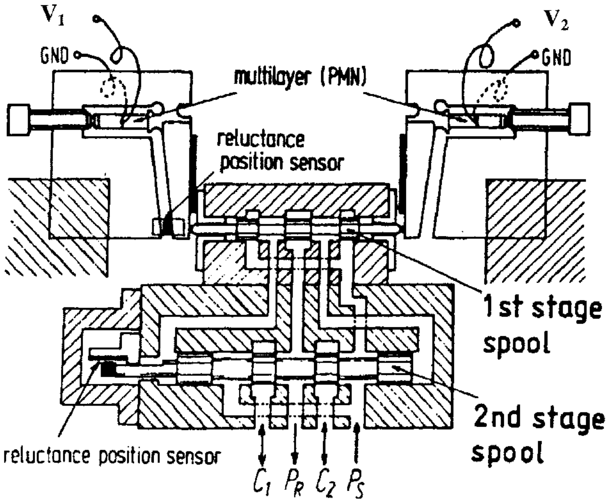

Figure 8.24 Schematic diagram of a direct drive spool servo valve incorporating two PMN-based multilayer actuators.[14]

8.5 VCR HEAD TRACKING ACTUATORS

The requirements for high quality VCR images have become increasingly stringent, especially when the tape is played in still, slow, or quick mode. When the tape is moving at a speed different from the normal speed, the head trace deviates from the recording track in a manner that depends on the velocity difference as illustrated in Figure 8.25. In order to monitor this deviation, the head traces on the guard band, generating *guard band noise.*[16] The auto tracking scan system produced by Ampex makes use of a piezoelectric actuator, which responds to the guard band noise signal to effectively regulate the position of the head so that it continues to follow the recording track. The piezoelectric device generates no magnetic noise.

These actuators typically have a bimorph structure because of the relatively large displacement they can produce. Special care must be taken to not produce a *spacing angle* between the head and the tape when bimorph devices are used for tracking, because a single bimorph tends to undergo a slight rotation as it deflects. Various alternative designs have been proposed to produce a rotation free deflection.

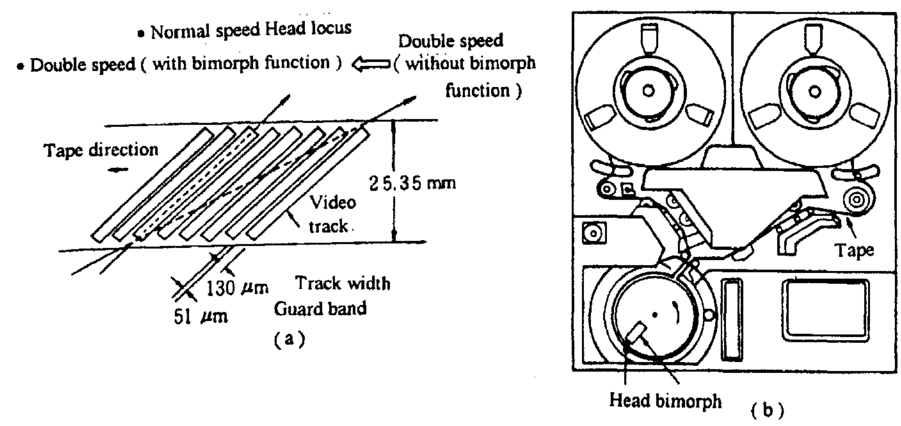
• Normal speed Head locus
• Double speed (with bimorph function)
Double speed (without bimorph function)
Tape direction
25.35 mm
Video track
130 μm Track width
51 μm Guard band
(a)
Tape
Head bimorph
(b)

Figure 8.25 The auto tracking scan system incorporating a bimorph piezoelectric actuator: (a) detail of the videotape and locus of the video head and (b) a schematic of the entire system showing the placement of the head bimorph.[16, 17]

The s-shape mode bimorph developed by Ampex is depicted in Figure 8.26.[16] The tip of the bimorph bends to oppose the rotation. In order to detect the tape track, the head is vibrated at 450 Hz, and this modulation signal is fed back to the actuator. The sensor electrode is for monitoring the head position, as well as for electrical damping.

A parallel spring mechanism developed by Sony is shown in Figure 8.27.[17] This actuator has been installed on a broadcasting VCR, the BVH-1000 [a schematic depiction of this system is shown Figure 8.25(b)]. Since the track width is wide (130 μm) for obtaining high-resolution images, a large displacement is required for the actuator.

A ring bimorph developed for a commercially available VCR by Matsushita Electric is pictured in Figure 8.28.[18,19] This compact movable head allows for noiseless image searching in both the quick scan (up to 8 times) and still/slow modes. An auto tracking system incorporating a piezoelectric actuator has been proposed as a standard device in 8 mm VCRs.[16]

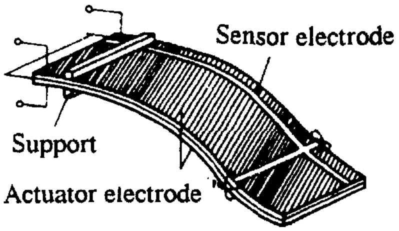
Sensor electrode
Support
Actuator electrode

Figure 8.26 The s-shape mode bimorph developed by Ampex.

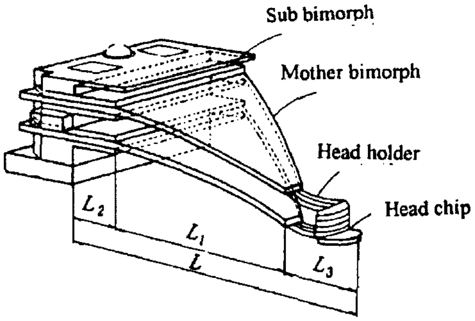
Sub bimorph
Mother bimorph
Head holder
Head chip
L_2
L_1
L
L_3

Figure 8.27 A parallel spring mechanism developed by Sony.[17]

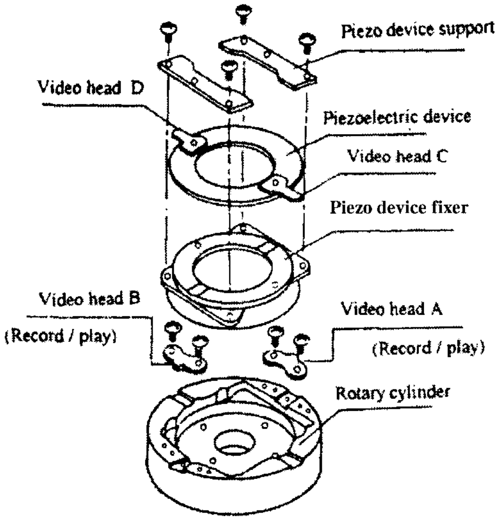
Piezo device support
Video head D
Piezoelectric device
Video head C
Piezo device fixer
Video head B
(Record / play)
Video head A
(Record / play)
Rotary cylinder

Figure 8.28 A ring bimorph by Matsushita Electric.[18,19]

8.6 VIBRATION SUPPRESSION AND NOISE ELIMINATION SYSTEMS

(1) Vibration Damping

The U.S. Army is interested in developing a rotor control system for helicopters. A bearingless rotor flexbeam with integrated piezoelectric strips is pictured in Figure 8.29.[20] An active fiber composite ply has been designed to generate the twisting motion of the helicopter blades.[21] The fibers are aligned transversely as shown in Figure 8.30 in order to sense and actuate in-plane stresses and strains. Semicontinuous 130 μm diameter PZT fibers are currently used. The matrix material is comprised of B-staging epoxy and a fine PZT powder, which is used to increase the dielectric constant of the matrix so that a higher electric field can be established within the high permittivity fibers. Glass fibers, 9 μm in diameter, can also be included to further enhance the strength of the blade. Various types of PZT sandwiched beam structures have been investigated for this and similar flexbeam applications and for active vibration control.[22]

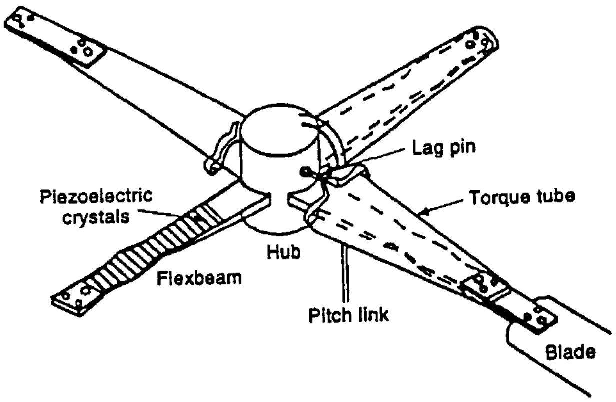

Figure 8.29 A bearingless rotor flexbeam with integrated piezoelectric strips.[20]

(2) Noise Elimination

A block diagram of a system for eliminating acoustic noise is shown in Figure 8.31.[23] The acoustic noise is detected by a piezoelectric microphone, and the signal is fed back to a piezoelectric high-power speaker to generate a conjugate wave (identified as the "antinoise" signal in the figure), which effectively cancels the noise signal as shown.

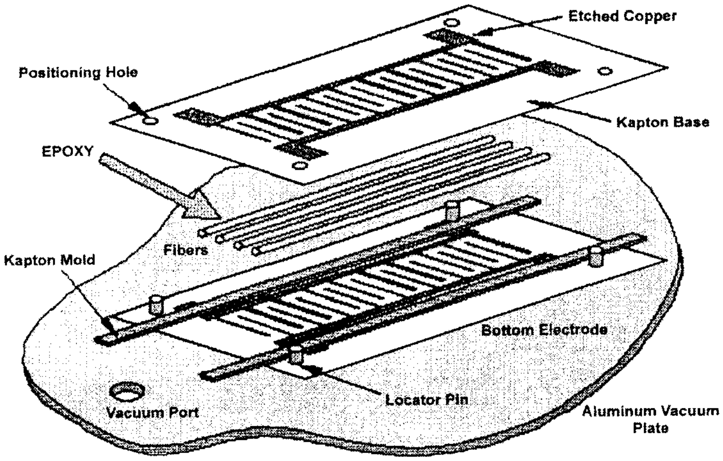
Etched Copper
Positioning Hole
Kapton Base
EPOXY
Fibers
Kapton Mold
Bottom Electrode
Locator Pin
Vacuum Port
Aluminum Vacuum Plate

Figure 8.30 An active fiber composite ply designed for use in the bearingless rotor flexbeam.[21]

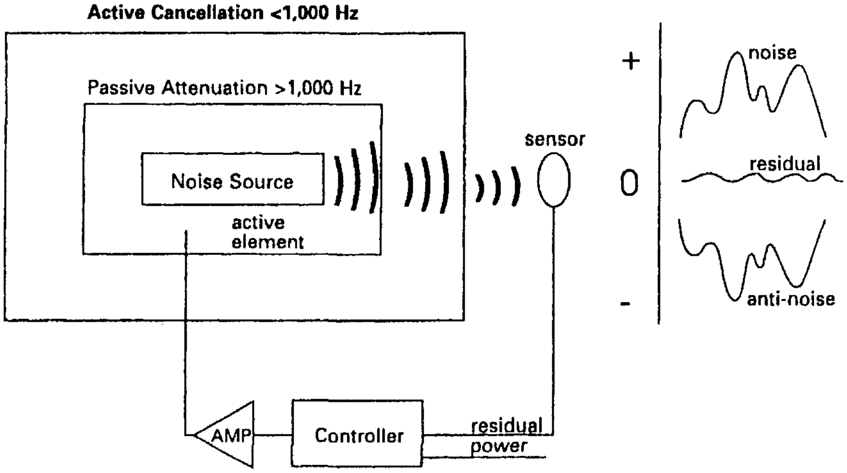
Active Cancellation <1,000 Hz
Passive Attenuation >1,000 Hz
Noise Source
active element
sensor
+
0
-
noise
residual
anti-noise
AMP
Controller
residual
power

Figure 8.31 A block diagram of a system for eliminating acoustic noise.[23]

CHAPTER ESSENTIALS

1. The deformable mirror surface contour can be represented by the *Zernike aberration polynomials*, which can be used to optimize the design of the system.
   a. Each orthogonal term represents the function of individual devices independent of the other elements in the system.
   b. Higher order corrections can be made by increasing number of terms used.
   c. Error evaluation is also possible.

2. An ultrahigh precision linear guide system that makes use of PZT actuators has been developed. The transverse motion and the pitching and rolling of the moving table are monitored by the three differential transformers installed in the bottom of the movable table. Three PZT positioners situated at the edges of the table respond to signals processed by a feedback circuit so as to maintain a constant position. This process is effective in producing precision in the linear motion that actually exceeds that of the master scale.

CHAPTER PROBLEMS

7.1 Describe the merits of implementing the expansion series for designing an actuator device.

7.2 Is the following argument correct?
"Given a servo system with a position sensor and an actuator, the precision of position control will not exceed the specified master scale precision."

7.3 Write a brief definition for each of the following important micropositioning terms.
   a. pitch
   b. roll
   c. yaw

REFERENCES

1) J. W. Hardy, J. E. Lefebre and C. L. Koliopoulos: J. Opt. Soc. Amer. **67**, 360 (1977).
2) J. W. Hardy: Proc. IEEE **66**, 651 (1978).
3) K. Uchino, Y. Tsuchiya, S. Nomura, T. Sato, H. Ishikawa and O. Ikeda: Appl. Optics **20**, 3077 (1981).
4) T. Sato, H. Ishikawa, O. Ikeda, S. Nomura and K. Uchino: Appl. Optics **21**, 3669 (1982).
5) J. L. Fanson and M. A. Ealey: Active and Adaptive Optical Components and Systems II, SPIE **1920**, Albuquerque (1993).
6) F. E. Scire and E. C. Teague: Rev. Sci. Instruments **49**, 1735 (1978).

7) S. Okayama, H. Bando, H. Tokumoto and K. Kajimura: Jpn. J. Appl. Phys. **24**, Suppl. 24-3, 152 (1985).
8) K. Uchino: Ceramic Databook '88 (Chap. Ceramic Actuators), Inst. Industrial Manufacturing Technology, Tokyo (1988).
9) S. Moriyama and F. Uchida: Proc. Jpn. Procision Eng. Soc. **201**, p.61 (Spring, 1984).
10) S. Moriyama, T. Harada and A. Takanashi: Precision Machine, **50**, 718 (1984).
11) Ikebe and Nakada: Proc. Jpn. Measurement and Automation Soc., 7-5, p.480 (1971).
12) Ikebe and Nakada: Oil and Air Pressure, **3**, 78 (1972).
13) H. Ohuchi, K. Nakano, K. Uchino, S. Nomura and H. Endo: Proc. Oil and Air Pressure Soc., **3**, p.9 (Fall, 1983).
14) H. Ohuchi, K. Nakano, K. Uchino, H. Endoh and H. Fukumoto: Proc. Fluid Control & Measurement, Tokyo, Pergamon Press, p.415 (1985).
15) K. Yamamoto, A. Nomoto and Y. Ueda: Proc. SICE, **1408**, p.121 (1982).
16) A. Ohgoshi and S. Nishigaki: Ceramic Data Book '81, p.35 Inst. Industrial Manufacturing Technology, Tokyo (1981).
17) Okamoto et al.: Broadcasting Technology, No.7, p.144 (1982).
18) M. Kobayashi, M. Tomita, K. Yamada and M. Matsumoto: National Technical Report, **28**, 419 (1982).
19) K. Yamada et al.: Abstract Television Soc. Jpn., 8-2 (1982).
20) F. K. Straub: Smart Mater. Struct., **5**, 1 (1996).
21) N. W. Hagood: Introduction to AMSL/MIT, http://amsl.mit.edu/research.
22) P. C. Chen and I. Chopra: Smart Mater. Struct., **5**, 35 (1996).
23) H. B. Strock: Spectrum-Performance Materials, 51-1, Decision Resources (1993).

9

PULSE DRIVE MOTOR APPLICATIONS

Pulse drive motors are used in swing CCD image sensors, microangle goniometer devices, inchworms, dot matrix and inkjet printer heads, piezoelectric relays, and automobile adaptive suspension systems. Low permittivity actuator materials are essential for these applications, due to the low currents typically applied to the devices from the power amplifiers used in these systems. Vibration overshoot and ringing are critical drive/control issues for this class of devices and, thus, effective means for suppressing these detrimental effects will also be considered in this chapter.

9.1 IMAGING SYSTEM APPLICATIONS

The swing CCD image sensor, the swing pyroelectric sensor, and the piezoelectric bimorph camera shutter are presented here as key examples of how the new actuators can be used in state-of-the-art imaging systems. Each offers unique advantages over the conventional devices previously used in these systems.

(1) The Swing CCD Image Sensor

Charge-coupled devices (CCD) have become popular as solid-state image sensors, and are employed widely in video cameras. Although the resolution and sensitivity have recently undergone considerable improvement, there are still problems in image resolution, especially in the horizontal direction.[1] One method for improving the horizontal resolution involves alternately swinging a CCD chip by a half picture unit cell (pixel) as the image data are sampled.[2]

A magnified view of an interline transfer type CCD is shown in Figure 9.1.[2] The sensing part of the optical image system is made up of photodiodes, and the remaining parts, which include vertical CCD registers and transfer lines and overflow drains, are shielded by an aluminum coating. The principle of the swing imaging method is illustrated schematically in Figure 9.2. The CCD chip substrate is shifted alternately in the horizontal direction by half of the horizontal pixel pitch (P_H) with respect to the input image light as shown in Figure 9.2(a). The timing of this swing motion is adjusted to correspond to the frame period as shown in Figure 9.2(b) so as to sample the image data at two spatial points (A and B). The image signals obtained in the A and B fields are combined and processed such that a two-fold improvement in the horizontal resolution is achieved. This method also leads to an effective sensing area twice that obtained by a conventional system. This can significantly reduce the appearance of moire patterns (an interference phenomenon) in the image.

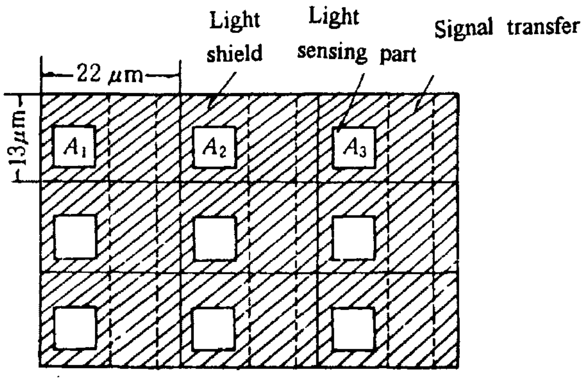
Light shield
Light sensing part
Signal transfer
22 μm
13μm
A_1
A_2
A_3

Figure 9.1 A magnified view of an interline transfer type CCD.[2]

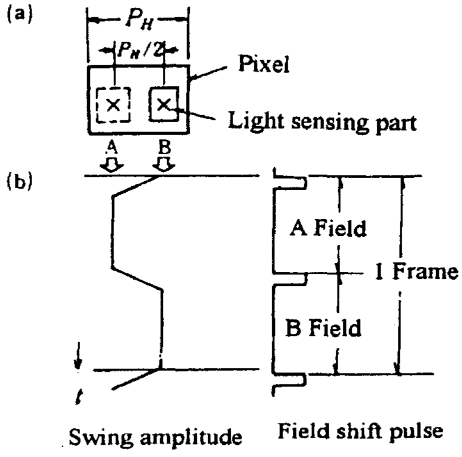
(a)
P_H
$P_H/2$
Pixel
Light sensing part
A
B
(b)
A Field
1 Frame
B Field
t
Swing amplitude
Field shift pulse

Figure 9.2 Operation of the swing CCD image sensor: (a) The CCD chip substrate is shifted alternately in the horizontal direction by half of the horizontal pixel pitch (P_H) and (b) the timing of the swing motion is adjusted to correspond to the frame period.[2]

The structure of the swing CCD sensor developed by Toshiba is shown in Figure 9.3.[2] The CCD substrate is translated by a pair of piezoelectric bimorphs supported at both ends. The supports are needed to protect the bimorph from external noise vibrations. A special brace is used that provides the required support without decreasing the deflection of the bimorph (see Figure 4.22). A drive voltage of only

15 V is required to generate an 11 μm displacement, which corresponds to half of the CCD pixel pitch, so that no high voltage supply is required. In order to suppress the vibration overshoot and ringing that occurs when the system is driven by a step-voltage, a trapezoidal waveform with a rise/fall time of 4 ms, which is almost equal to the resonance period, is used (see Figure 5.19).[2]

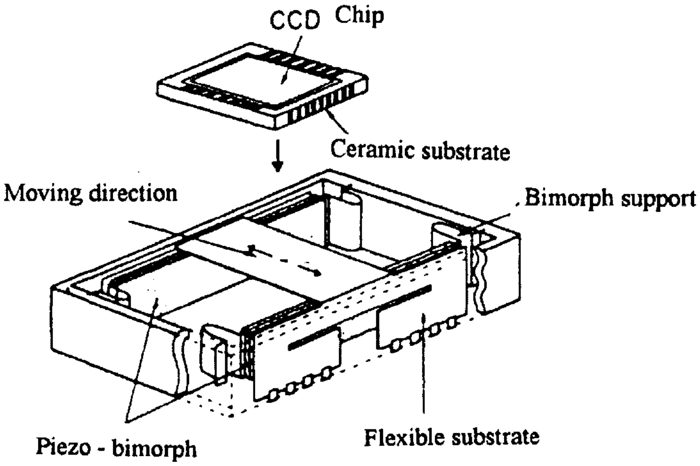

Figure 9.3 The structure of the swing CCD sensor developed by Toshiba.[2]

(2) The Swing Pyroelectric Sensor

The piezoelectric bimorph can also be used in a similar manner with pyroelectric sensors. A large electromagnetic motor has conventionally been used for chopping infrared light to monitor the temperature. A tiny pyroelectric sensor that makes use of a piezoelectric bimorph light chopper developed by Sanyo is shown in Figure 9.4.[3] The compact size, light weight, and low cost of the unit make it a suitable temperature sensor for microwave ovens.

(3) The Piezoelectric Bimorph Camera Shutter

Following the recent introduction of various automatic features in cameras, such as automatic focusing and automatic film winding, many innovative designs for compatible mechanisms for driving systems with dual focus and zoom type lenses were developed. The shutter must also be adjusted in these systems, thus compact and lightweight shutters suitable for quick movement are required. A camera shutter incorporating a piezoelectric bimorph developed by Minolta is pictured in Figure 9.5.[4] The number of components for this system, as compared with conventional spring-charge mechanisms, is reduced by one-third. A tip displacement of 300 μm of the piezoelectric bimorph can provide a shutter opening of 8 mm in diameter. In order to eliminate hysteresis effects and to ensure that the shutter is completely closed after an exposure, a reverse potential is applied to the piezoelectric bimorph at the end of every operation.

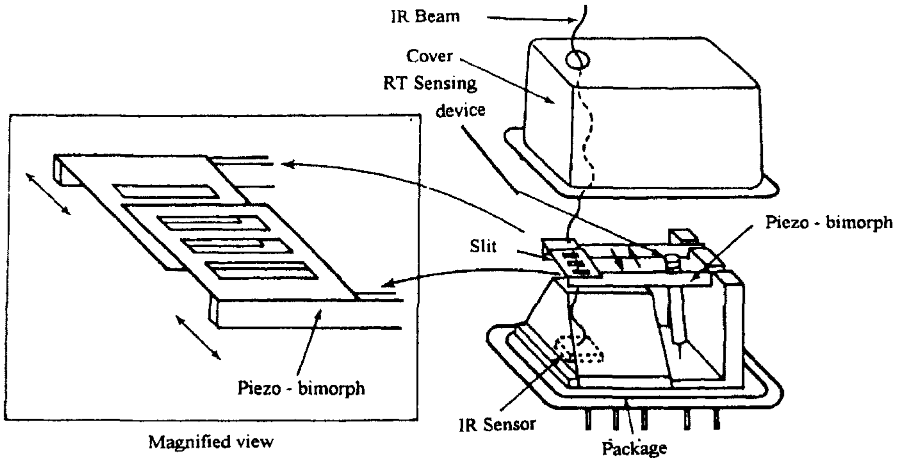
IR Beam
Cover
RT Sensing device
Slit
Piezo - bimorph
Piezo - bimorph
Magnified view
IR Sensor
Package

Figure 9.4 The structure of the swing pyroelectric sensor.[3]

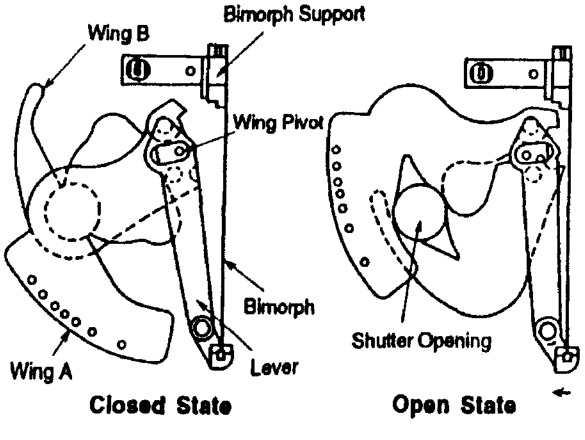
Wing B
Bimorph Support
Wing Pivot
Bimorph
Lever
Wing A
Shutter Opening
Closed State
Open State

Figure 9.5 A camera shutter incorporating a piezoelectric bimorph developed by Minolta.[4]

9.2 INCHWORM DEVICES

The motion produced by an inchworm device is similar to that produced by an ultrasonic motor in terms of the general speed and execution of the motion, but the mechanisms for their operation are completely different. The inchworm is driven by a rectangular signal at a frequency below its resonance frequency, and its movement is intermittent and discrete.

(1) A Microangle Goniometer

A microangle goniometer consisting of a fixed inchworm and a turntable is pictured in Figure 9.6.[5] The inchworm is comprised of an electrostrictive unimorph and two electromagnets. Let us consider the operation of the inchworm with reference to the timing diagram shown in Figure 9.7. The operation cycle is initiated with the movable electromagnet on and the fixed one off. The drive voltage is applied to the electrostrictive unimorph to displace the movable magnet. The angular position of the turntable is thereby advanced. The two electromagnets are then alternately switched on and off, the voltage on the unimorph is removed, and the movable magnet is returned to its initial position with the turntable kept in its displaced position. Repetition of this process drives the turntable sequentially and the rotation angle increases. The rotation direction is reversed by exchanging the clamp timing of the two electromagnets.

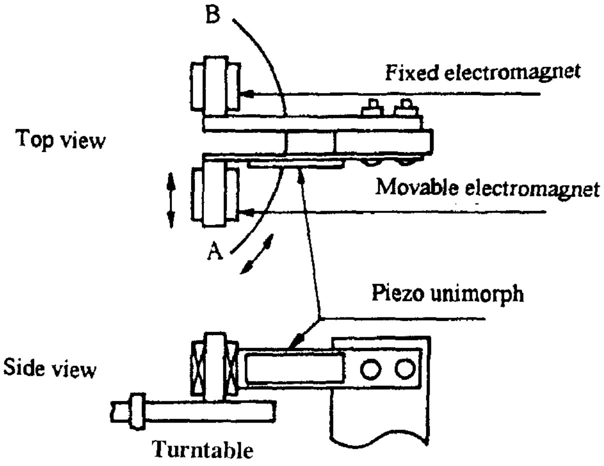

Figure 9.6 A microangle goniometer consisting of a fixed inchworm and a turntable.[5]

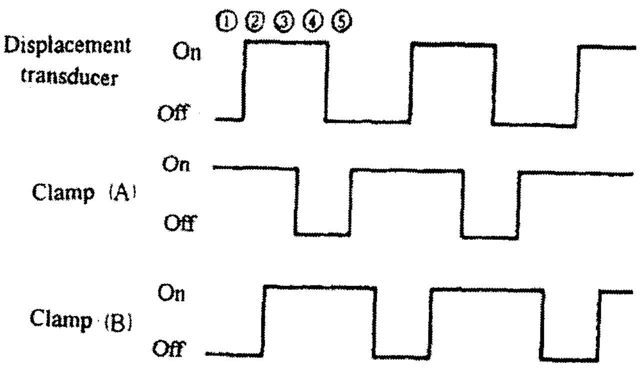

Figure 9.7 Timing diagram for the components of the inchworm microangle goniometer system.[5]

The operation of the microgoniometer at 0.5 Hz is illustrated in Figure 9.8. The angular position as a function of time has a clear triangular form comprised of discrete steps. The angular velocity of the turntable is controlled by the voltage applied to the unimorph, current passing through the electromagnets, and by the drive frequency. The system produces a maximum angular speed of 10^{-2} rad/sec and a maximum shift of 6×10^{-4} rad/step. A modified version of this inchworm microgoniometer, utilizing three PZT actuators for both the clamp and shifting operations, has also been proposed by a group at Hitachi.[6]

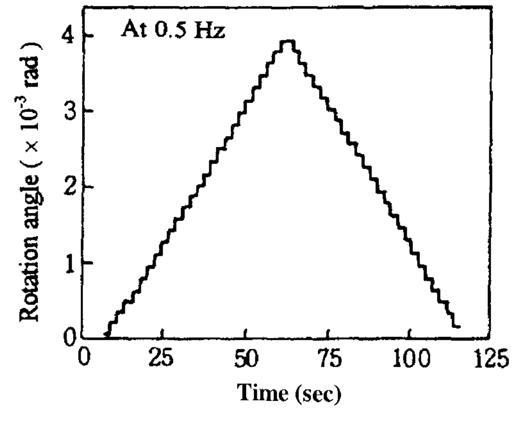

Figure 9.8 The response of the inchworm microangle goniometer system operated at 0.5 Hz.[5]

(2) Linear Walking Machines

Sophisticated linear walking machines have been developed by two German companies. A linear drive inchworm, incorporating two d_{33} (longitudinal mode) and two d_{31} (transverse mode) multilayer actuators, fabricated by Philips is pictured in Figure 9.9.[7] Very precise positioning of less than 1 nm has been reported for this device. There are some problems with this design however, in particular, the rather high level of audible noise in operation, significant heat generation when it is driven at high frequency, and high manufacturing costs due to the use of several multilayer piezoelectric actuators. A two-legged inchworm manufactured by Physik Instrumente appears in Figure 9.10.[8] The motion of a pair of inchworm units, consisting of two multilayer actuators, are coupled such that there is a 90° phase difference between them in order to produce a smoother, more continuous movement of the device.

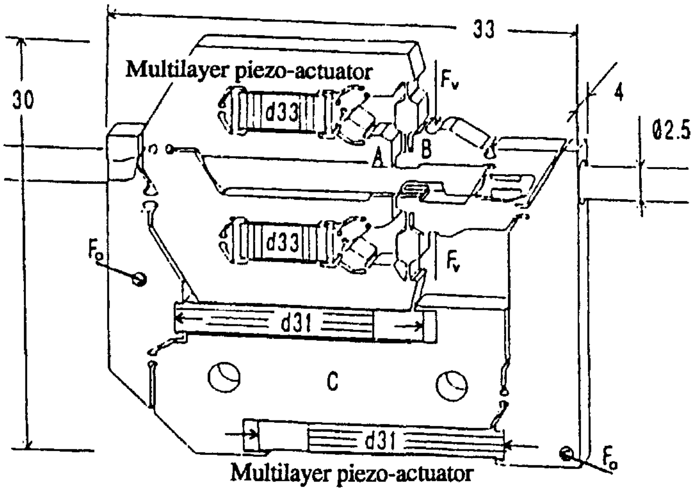

Figure 9.9 A linear drive inchworm, incorporating two d_{33} (longitudinal mode) and two d_{31} (transverse mode) multilayer actuators, fabricated by Philips.[7]

Microwalking vehicles incorporating an inchworm mechanism comprised of two electromagnets and a multilayer piezoelectric actuator are pictured in Figure 9.11.[9] When a diamond cutting edge is installed on this vehicle, it becomes a compact machining tool. The tool can move over any sloped surface provided the surface is magnetic as illustrated in Figure 9.12. Tasks ranging from microgroove cutting to microdust elimination can be achieved by attaching different tools to the vehicle.

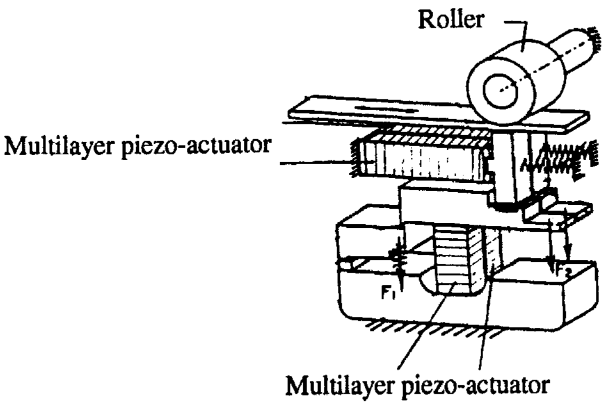
Roller
Multilayer piezo-actuator
F₁
F₂
Multilayer piezo-actuator

The Control Voltage Sequence

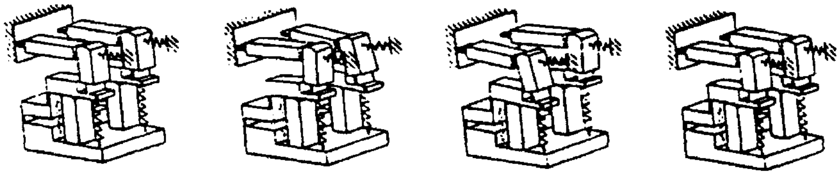

Figure 9.10 A two-legged inchworm smooth walking device manufactured by Physik Instrumente.[8]

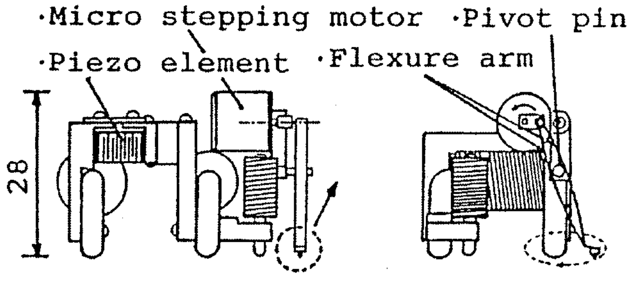
•Micro stepping motor •Pivot pin
•Piezo element •Flexure arm
28

Figure 9.11 Compact microwalking machining vehicles incorporating an inchworm mechanism comprised of two electromagnets and a multilayer piezoelectric actuator.[9]

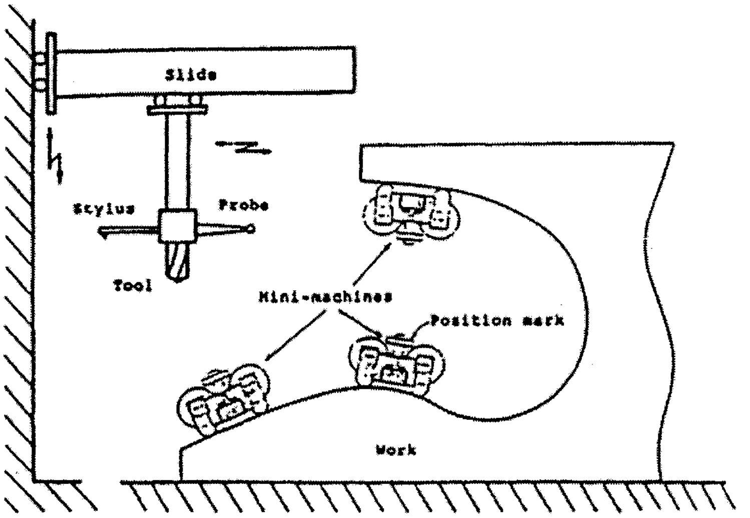
Slide
Stylus
Probe
Tool
Mini-machines
Position mark
Work

Figure 9.12 Illustration of micromachining using multiple compact vehicles. The attractive force between the mini-machine and the work surface is magnetic.[9]

Impact mechanism walking machines have also been proposed.[10] The structure of such a walker is pictured in Figure 9.13. The moving table is attached to a V-shaped guide rail. The weight table is moved by the counterforce of the main weight when an expansion or contraction of the multilayer piezoelectric actuator is induced at an appropriate rate as illustrated in the motion sequence depicted in Figure 9.14. Note that the clamping force of the table is provided by the frictional force, which is determined by the coefficient of friction between the surfaces and the weight of the table.

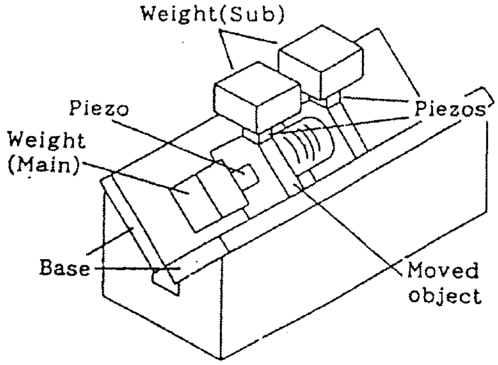
Weight(Sub)
Piezo
Weight
(Main)
Piezos
Base
Moved
object

Figure 9.13 Impact mechanism walking machine utilizing a piezoelectric multilayer actuator.[10]

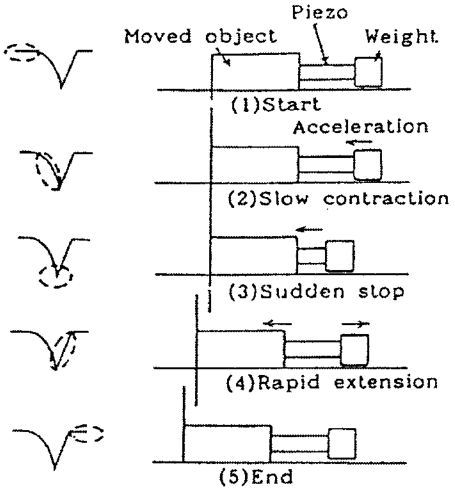

Figure 9.14 Motion sequence for a walker with an impact mechanism. Notice the slow and rapid action of the piezoelectric actuator.[10]

9.3 DOT MATRIX PRINTER HEADS

Although the production of impact dot matrix printers has decreased in recent years, they are still popular in offices and factories. Since the piezoelectric dot matrix printer is the first mass-produced device using multilayer ceramic actuators, and one of the most successful products, it is worthwhile to examine more closely some of the most commonly used designs.

The advantages of the piezoelectric printer head compared to the conventional electromagnetic types are:

1) low energy consumption,
2) low heat generation (electromagnetic solenoids generate significant heat!),
3) fast printing speed.

Both bimorph and multilayer types have been developed, but only the multilayer type has been commercialized, because of its:

1) longer lifetime,
2) faster printing speed,
3) higher impact force,
4) higher efficiency.

A dot matrix printer mechanism incorporating an array of piezoelectric bimorphs proposed by Piezo Electric Products Incorporated is pictured in Figure 9.15. Printing wires are installed at the tip of each of the seven bimorphs supported in a cantilever style. The printing speed at an operating frequency of 1 kHz is 200 cps, when a 5 x 7 character style is used.

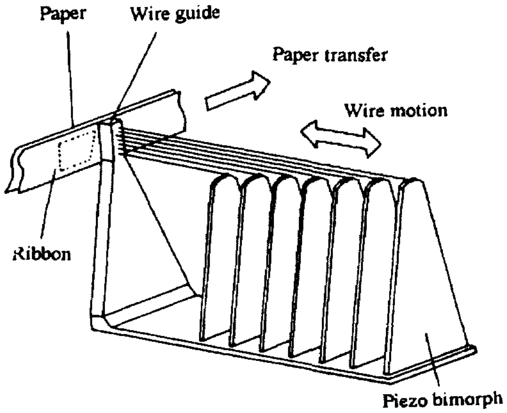

Figure 9.15 A dot matrix printer mechanism incorporating an array of piezoelectric bimorphs proposed by Piezo Electric Products Incorporated.

(1) Printer Head Element Using a Multilayer Actuator

NEC developed a printer head element utilizing a longitudinal multilayer actuator, which provides much superior characteristics to the bimorph type in printing speed and durability.[11,12] Since the longitudinal multilayer actuator does not exhibit a large displacement, a suitable displacement magnification mechanism is essential for this system. A printing wire stroke of 500 μm should be produced from the 10 μm actuator displacement. A high energy transmission efficiency is also desired for this magnification mechanism.

A differential two-stage magnification mechanism is shown in Figure 9.16(a).[11] The displacement induced in a multilayer actuator pushes up the force point and rotates lever 1 and lever 2 around the fulcrum counter-clockwise and clockwise, respectively, so that the tip displacements of levers 1 and 2 are amplified five times. This is the primary displacement magnification mechanism occurring through a monolithic hinge lever. These opposing displacements are transferred to lever 3 in the secondary amplification stage, generating a large wire stroke. This is the *differential magnification mechanism.* Typical characteristics of this design (in a static condition) are an 8 μm displacement of the piezoactuator, a 240 μm wire stroke, and overall displacement magnification of thirty. The displacement magnification can be increased if necessary. The static energy transmission coefficient e is defined as:

$$e \equiv \frac{\text{Output Energy from the Magnification Mechanism}}{\text{Stored Energy in the Piezoactuator}} = \frac{(\zeta_m^2/2\,C_m)}{(\zeta_c^2/2\,C_c)} \qquad (9.1)$$

where ζ_c is the free displacement (m) of the piezoceramic device, C_c is the compliance of the ceramic (m/N), ζ_m is the free displacement (m) of the displacement magnification mechanism, and C_m is the compliance of the mechanism (m/N). The static energy transmission coefficient for this design can be as large as 51%. The printer head is constructed from a stack of these elements arranged in an alternating configuration as shown in Figure 9.16(b).[12] The nine printing wires, each of diameter 0.25 mm, are brought together along the wire guide as shown in the figure.

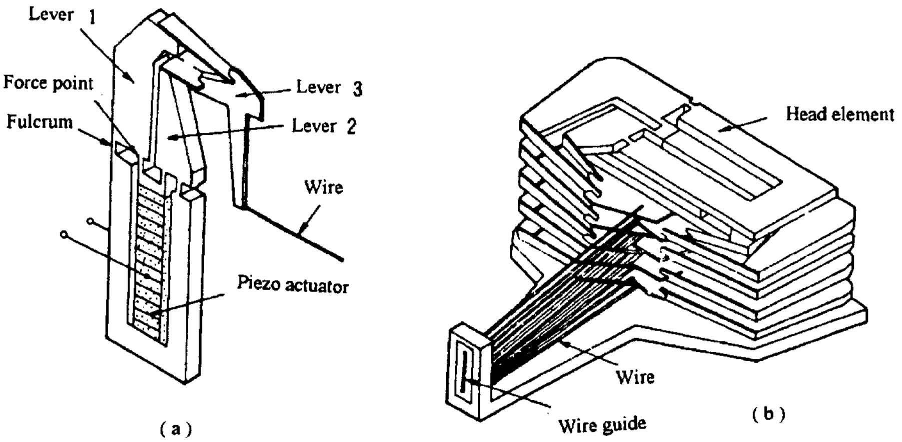

Figure 9.16 An inkjet printer head developed by NEC: (a) the differential two-stage magnification mechanism used in a single element and (b) the entire printer head assembly.[11,12]

(2) The Equivalent Circuit for the Piezoelectric Printer Head

The use of an equivalent electrical circuit for representing the vibrations of an electromechanical system has become a standard method of analysis for designing and characterizing the optimum performance of various piezoelectric vibrators. A schematic of the equivalent circuit for the printer head described in the last section appears in Figure 9.17(b).[13] The analysis helps to characterize the *rigidity, nonlinearity, and hysteresis* of the wire motion as they influence the impact on the paper and the ink ribbon/platen combination.

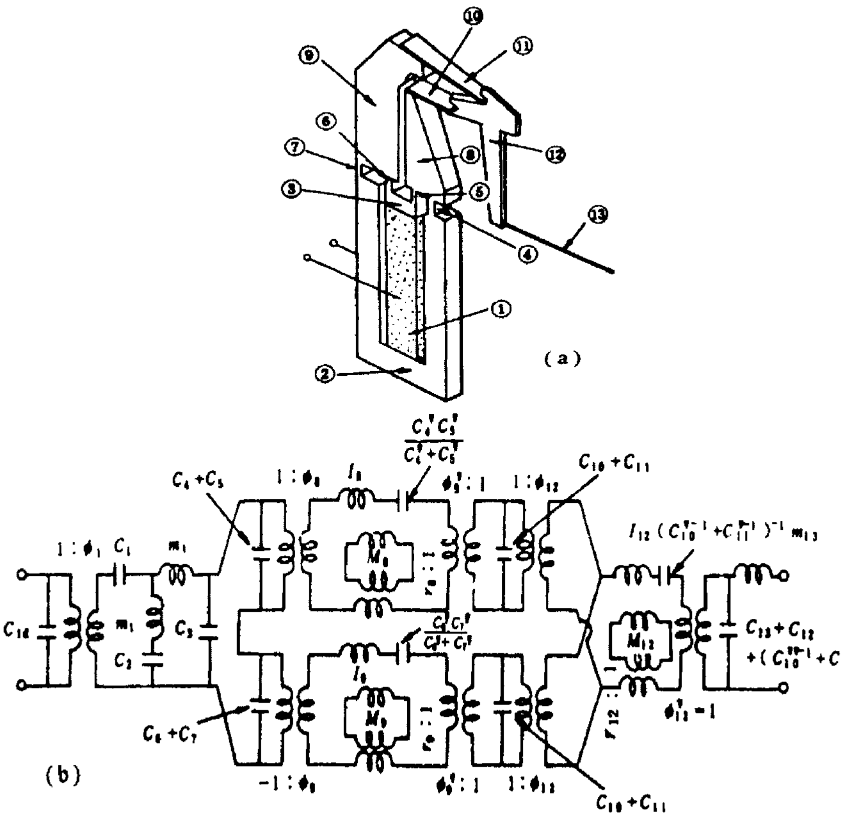

Figure 9.17 A schematic of the equivalent circuit for the dot matrix printer head elements: (a) an individual differential type piezoelectric printer head element and (b) equivalent circuit for the element.[13]

The equivalent circuit components appearing in the schematic for the circuit shown in Figure 9.17(b) are designated by subscripts, which correspond to the numbered features of the individual element pictured in Figure 9.17(a). The lever's moment of inertia is represented by I_i and the lever mass by M_i. The compliances of each part are associated with the capacitances designated by C_i, C_i' and C_i''. The quantity designated by ϕ_1, at the first transformer (left-hand side of the diagram) represents the electromechanical transduction rate and the quantities ϕ_i and ϕ_i', appearing near the other transformers in the circuit represent the transduction of the linear movement into an angular displacement. The transduction rate associated with the movement of the center of mass is represented by the quantities, r_i. The damped capacitance is designated by C_{1d}. The equivalent mass of the actuator is represented by m_1 and the equivalent mass of the wire by m_{13}.

The load of the printer head, consisting of the paper, ink ribbon and platen, has a significant nonlinear stiffness (3rd-6th order) with respect to the impact force as well as a distinct hysteresis. An approximate representation of this nonlinear relationship is shown in Figure 9.18.[13] The decrease in the repulsion coefficient that occurs due to the hysteresis is represented by an equivalent resistance, R_L, connected in parallel to an equivalent capacitance, C_L, where the nonlinear stiffness is associated with the quantity $1/C_L$. A model printer head, with 0.45 mm between the wire tip and the printing media, was fabricated and the experimental data related to the wire head displacement and the impact force collected for the prototype were compared with those generated in a computer simulation carried out on the equivalent circuit. The results summarized in Table 9.1 and Figure 9.19 indicate good agreement between the experimental and theoretical data.

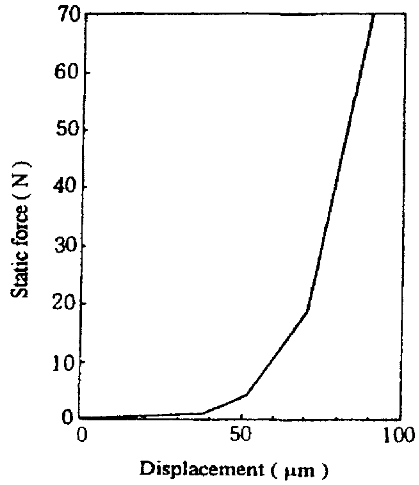

Figure 9.18 An approximate representation of the nonlinear stiffness associated with the printer head load.[13]

Table 9.1 Experimental and equivalent circuit analysis data characterizing the performance of a prototype printer head.[13]

	Experimental	Calculated
Eigenfrequency (Hz)	1740-1840	1785
Free Stroke (μm)	670–710	730
Impact Force (N)	7.5–8.3	7.98

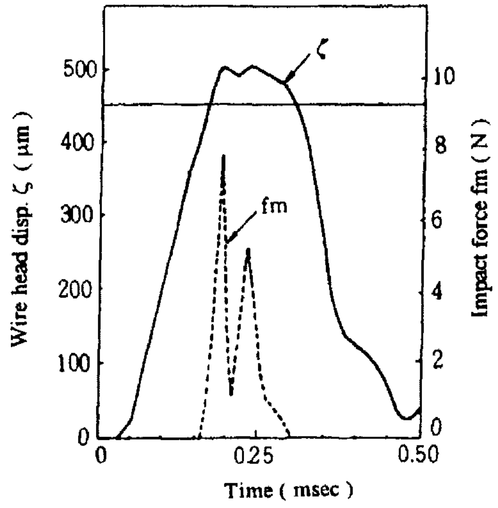

Figure 9.19 Response characteristics of the wire head.[13]

(3) Operation Characteristics of the Multilayer Actuator Printer Head

Specifications for the printer head incorporating multilayer piezoelectric actuators are summarized in Table 9.2.[12] The following features are particularly noteworthy.

Response Frequency: The eigenfrequency of the head element (in free vibration without impacting the platen) is 1.7 kHz. When impact with the platen occurs the response frequency increases to 2.2 kHz. This frequency corresponds to a printing speed of more than 300 cps for characters comprised of 7x6 dots.

Impact Force: The impact force on the ribbon and paper (55 kg type) is 0.9 kgf. Printing pressure of this magnitude allows for triplicate printing when wires of 0.25 mm diameter are used.

Energy Consumption: This print head exhibits an exceptionally low energy consumption of 3 mJ/dot per printing wire.

Drive Voltage: The drive voltage is only 90 V, much smaller than required for the piezoelectric bimorph type.

Heat Generation: The heat generation is about 0.7 mJ/dot per wire, which is an order of magnitude smaller than occurs in conventional electromagnetic types. Thus, the printer head can be covered completely, allowing for nearly noiseless printing.

Table 9.2 Specifications for the multilayer piezoelectric actuator printer head.[12]

Pin Number	9
Wire Diameter (mm)	0.25
Eigenfrequency (kHz)	1.7
Response Frequency (kHz)	2.2
Printing Pressure (kgf)	0.9
Energy Consumption (mJ/dot)	3
Multiple Page Capability	triplicate
Drive Voltage (V)	90

(4) Flight Actuator Printer Head

The flight actuator described Section in 5.1 can be used in impact printers as shown in Figure 9.20.[14] Elimination of mechanical ringing or double strike can be achieved with the proper adjustment of the applied voltage pulse width as shown in Figure 9.21.

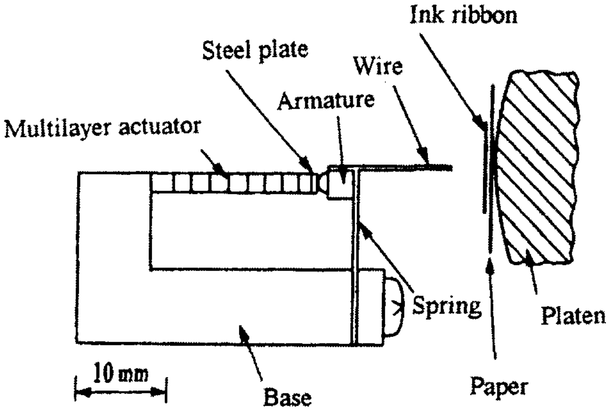

Figure 9.20 A flight actuator printer head.[14]

9.4 INKJET PRINTERS

The current generation of printers, following the impact dot matrix types, includes inkjet and laser printers. These better satisfy the need for better image quality and faster printing.

(1) The Basic Design of the Piezoelectric Inkjet Printer Head

In this section, we will examine the basic design of a piezoelectric inkjet printer head capable of printing intermediate gray scales.[15-17] A drop-on-demand type of piezoelectric printer head is shown in Figure 9.22. The head is comprised of a piezoelectric ceramic cylinder, a micro one-way valve, and a flow resistance component, which together function as a tiny pump. This micropump responds over a broad range of frequencies and can produce a wide range of ink drop sizes.[15] The key component of this printer head is the microvalve. The structure of the microvalve is pictured in Figure 9.23. The valve and base patterns are successively plated onto a substrate using electroforming techniques. They are then removed from the substrate by a delamination process.

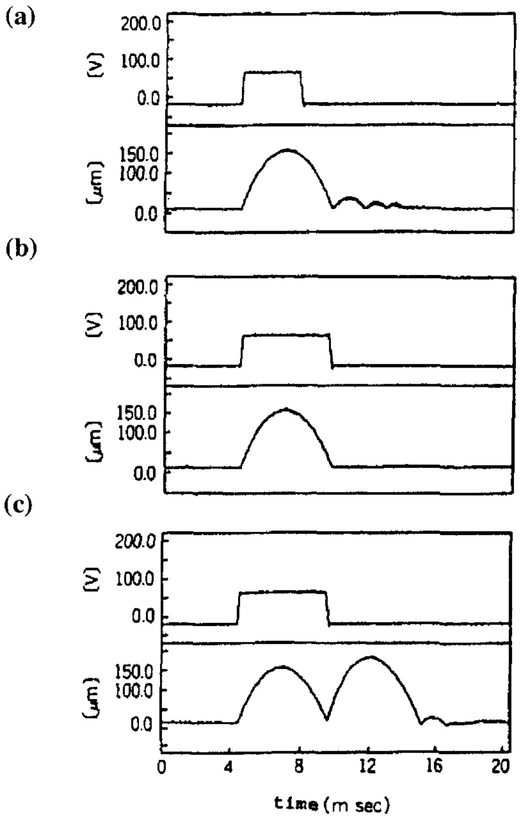

Figure 9.21 Adjustment of the drive voltage pulse width applied to a flight actuator print head leading to conditions of: (a) mechanical ringing, (b) no mechanical ringing, and (c) double strike.[14]

Operation mode	Valve	Operating illustration
(1) Stop ($V_p=0$)	Closed	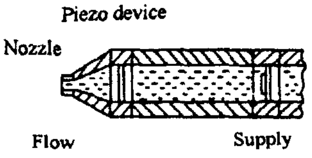
(2) Ink jet ($V_p=V_1$)	Open	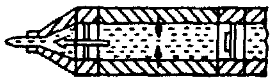
(3) Ink supply ($V_p=-V_2$)	Open	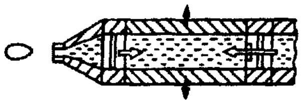
(4) Stop ($V_p=0$)	Closed.	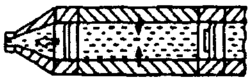

Figure 9.22 Operation of a drop-on-demand type piezoelectric printer head.[15-17]

The area of the printed dot can be adjusted to four distinct levels with the application of an appropriate drive voltage pulse width. The smallest dot diameter possible for this print head is 80 μm. Gray scale printing is achieved by using dot-area modulation. The dot density for a 2x2 matrix created with five gray levels is 8 dots/mm (which corresponds to a pixel density of 4 pel/mm). The reflection density from the gray scale pattern printing of this print head, operated with a drive frequency of 10 kHz, is plotted as a function of gray level in Figure 9.24. A range of seventeen intermediate gray scales is represented. Another piezoelectric inkjet printer head incorporating a piezoelectric bimorph is shown in Figure 9.25.[18]

(2) Integrated Piezo Segment Printer Head

A high speed, high resolution color printer which makes use of integrated piezoelectric segments has been developed by Seiko-Epson.[19] The inkjet head structure incorporating the Multi-Layer Ceramic with Hyper-Integrated Piezoelectric Segments (MLChips) is pictured in Figure 9.26. The inkjet is activated primarily by the bending mode of a piezoelectric unimorph. Layers of zirconia (to form the ink chambers), the vibration plate, and the PZT actuator plate are co-fired in the fabrication process. This produces a stable structure, which allows for adequate vibration isolation between ink chambers as well as some retardation of mechanical aging effects.

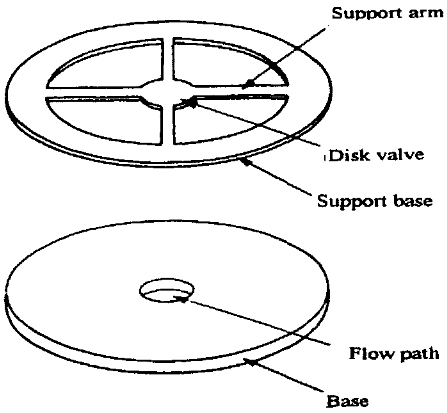
Support arm
Disk valve
Support base
Flow path
Base

Figure 9.23 The structure of the micro one-way valve with a flow path diameter of 1 μm.[15]

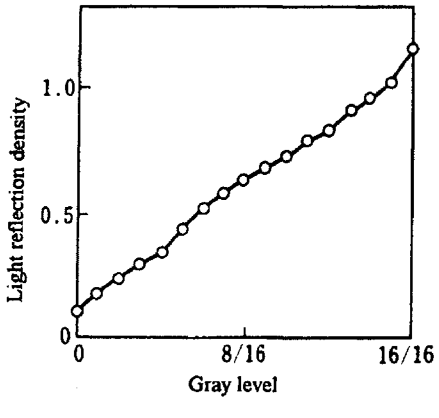

Figure 9.24 The reflection density from the gray scale pattern printing of the drop-on-demand type piezoelectric printer head plotted as a function of gray level. [Drive frequency: 10 kHz.][15]

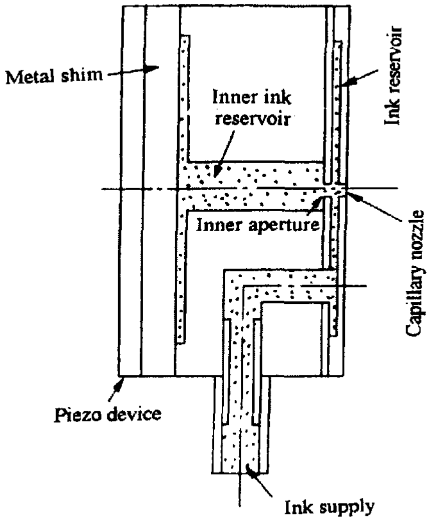
Metal shim
Inner ink reservoir
Ink reservoir
Inner aperture
Capillary nozzle
Piezo device
Ink supply

Figure 9.25 A piezoelectric inkjet printer head incorporating a piezoelectric bimorph.[18]

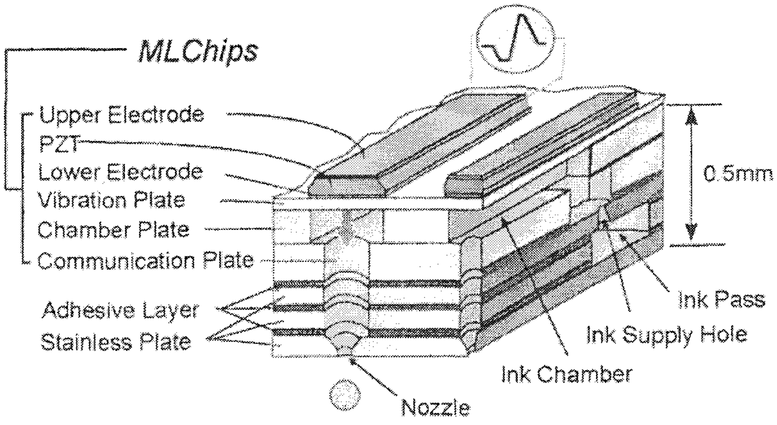
MLChips
Upper Electrode
PZT
Lower Electrode
Vibration Plate
Chamber Plate
Communication Plate
Adhesive Layer
Stainless Plate
0.5mm
Ink Pass
Ink Supply Hole
Ink Chamber
Nozzle

Figure 9.26 The inkjet head structure incorporating the Multi-Layer Ceramic with Hyper-Integrated Piezoelectric Segments (MLChips) developed by Seiko-Epson.[19]

An MLChips unit 10 mm x 10 mm in size is composed of two arrays of 48 ink chambers. High precision nozzle fabrication is essential for proper ink drop generation and ink impact accuracy, and thus two advanced processes are employed: submicrometer precision pressing and microchip water repellency treatment. The so-called face eject back contact structure of the printer head is depicted in Figure 9.27. This laminated structure, which more readily allows for various configurations of the inkjet nozzles in a two-dimensional array, is well suited to mass production at low cost.

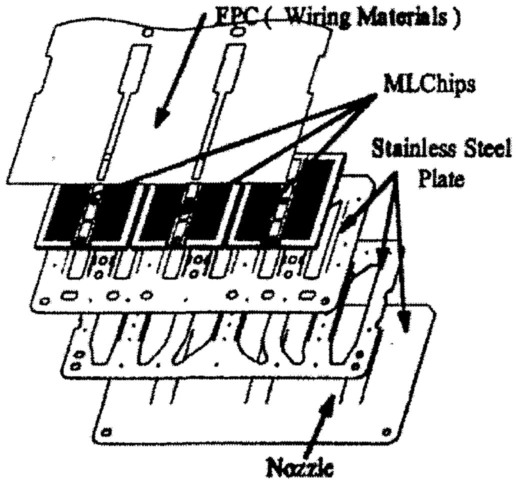

Figure 9.27 The face eject back contact structure of the printer head incorporating the MLChips technology developed by Seiko-Epson.[19]

High speed meniscus control is achieved by implementing the pull-push-pull (PPP) method. The concept is illustrated in Figure 9.28. An intermediate voltage is applied to the PZT actuator in its initial state. The first "pull" stage of the process occurs when the applied voltage is reduced and the ink meniscus is smoothly drawn into the nozzle. The "push" occurs with a rapid step up to the highest voltage thereby exciting a large vibration in the vibration plate that causes ink to be ejected from the nozzle. Finally, in the second "pull" stage the voltage is reduced to an intermediate level at a rate that effectively damps the meniscus vibration quickly. This three-step meniscus control process provides precise and rapid ink drop formation and delivery to the page.

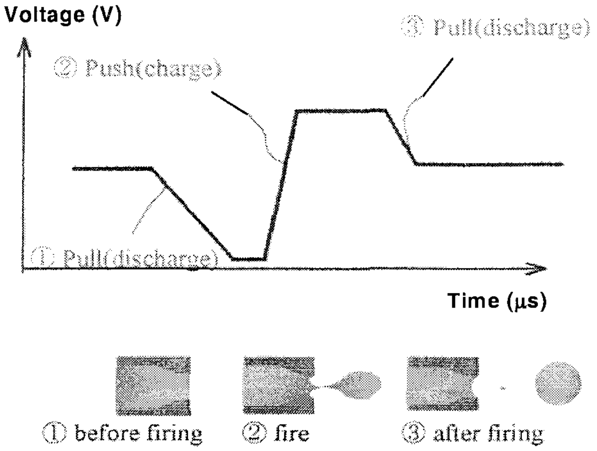

① before firing ② fire ③ after firing

Figure 9.28 The pull-push-pull meniscus control method.[19]

The present integrated piezoelectric printer head characteristics are as follows:

1) Ink Chamber Density: 120 dpi,
2) Number of Nozzles [N]: 48 N x 6 colors,
3) Response: 28.2 kHz,
4) Minimum Ink Drop: 4 pl,
5) High Definition Mode: Multisized Dot Technology 4/7/11 pl,
6) High Speed Mode: MSDT 11/23/39 pl.

9.5 PIEZOELECTRIC RELAYS

The relay is a basic component commonly found in electrical equipment. Most current relays are mechanical switches driven by electromagnetic solenoids. The need for increasingly faster response and more compact size has stimulated the development of new types of relays. The piezoelectric relay is a promising alternative. The basic structure of a piezoelectric relay proposed by Piezo Electro Products, Inc. (PEPI) is pictured in Figure 9.29.[20] The primary advantages of the piezorelay over the electromagnetic type are (1) low energy consumption, (2) no heat generation, (3) no generation of electromagnetic noise, (4) quick response, (5) compact size, and (6) suitability for integration. The structure pictured in Figure 9.29, which utilizes the coupled action of a piezoelectric bimorph and a spring, is readily integrated into relay arrays. Relay cards, 6 mm in thickness and with a density of several pieces per square centimeter, are commercially available.

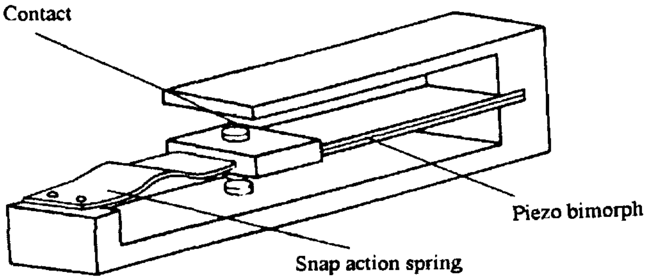
Contact
Piezo bimorph
Snap action spring

Figure 9.29 The basic structure of a piezoelectric relay proposed by Piezo Electro Products, Inc.[20]

Another relay incorporating a piezoelectric bimorph manufactured by Omron is pictured in Figure 9.30.[21] This design includes an especially sensitive snap-action switch, which is activated with only several tens of micron displacement and leads to an overall response speed of less than 5 ms.

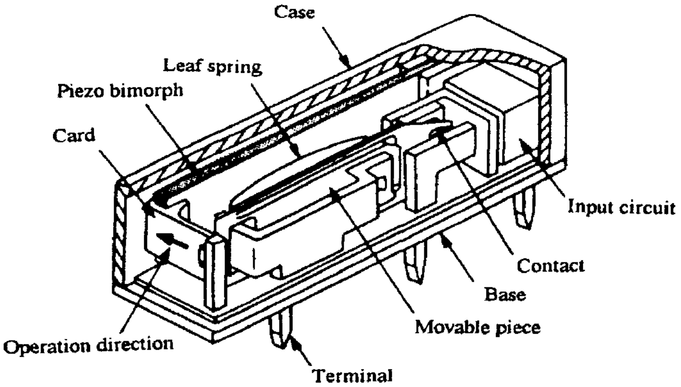
Case
Leaf spring
Piezo bimorph
Card
Input circuit
Contact
Base
Movable piece
Operation direction
Terminal

Figure 9.30 A piezoelectric bimorph relay developed by Omron.[21]

When a piezoelectric bimorph is used as the actuator for a relay of this type, the generative force is decreased with the deflection, thus leading to contact problems. A snap-action spring or a permanent magnet is often used in conjunction with the bimorph to ensure proper contact by producing a system with *mechanical bistability*. Both the on and off states are mechanically stable, and no continuous application of electric field is necessary. This is the fundamental principle of *latching relays*. The piezoelectric bimorph functions in this case only to switch between the two states. The latching function is especially useful for emergency shut-down situations. The relay retains the initial state so that the system is restored to normal operation when restarted. Latching relays typically constitute only 10% of the total relay production, but the unit price is about 10 times higher than non-latching varieties, leading to comparable sales overall.

A multilayer piezoelectric actuator relay has also been introduced by NEC on a trial basis.[22] The schematic diagram of this device pictured in Figure 9.31 illustrates the operation of the monolithic hinge lever mechanism.

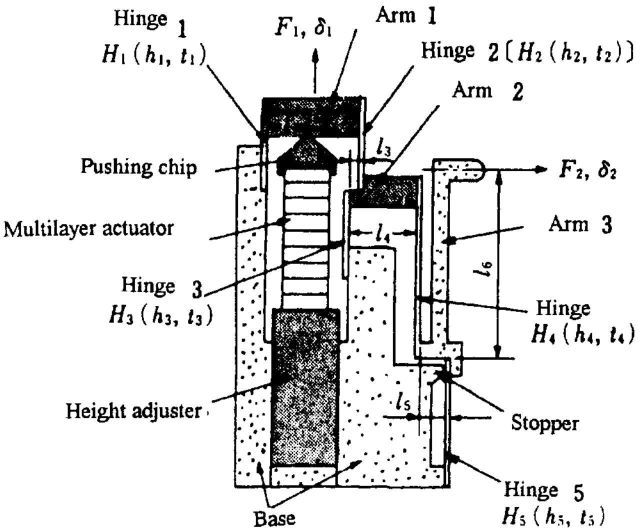

Figure 9.31 A multilayer piezoelectric actuator relay introduced by NEC.[22]

A compact latching relay has been developed utilizing a shape memory ceramic unimorph.[23] The basic structure of the relay is similar to the Omron design pictured in Figure 9.30, with the shape-memory ceramic unimorph (made from an antiferroelectric-ferroelectric phase transition material as described in Section 3.1) replacing the piezoelectric bimorph. Once the bending is induced in the unimorph by applying a pulse voltage, it can be maintained for more than a week. Recovery of the original shape is obtained by applying an inverse bias voltage. The static conditions for switching are shown in Figure 9.32. The dynamic responses of the shape memory latching relay and a conventional electromagnetic coil relay are compared in Figure 9.33. Although some chattering is apparent in the responses of both relays, the shape memory ceramic one exhibits much quicker action (1.8 ms rise) and lower energy consumption (7 mJ) than the electromagnetic relay. Use of a smart material in the design of a relay can thus be effective in reducing the number of components and the total size of the device.

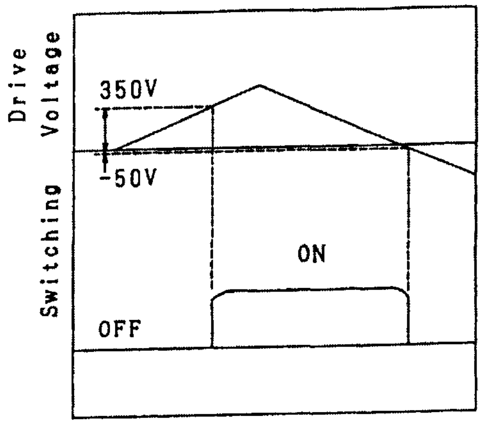

Figure 9.32 The static conditions for switching of a compact latching relay utilizing a shape memory ceramic unimorph.[23]

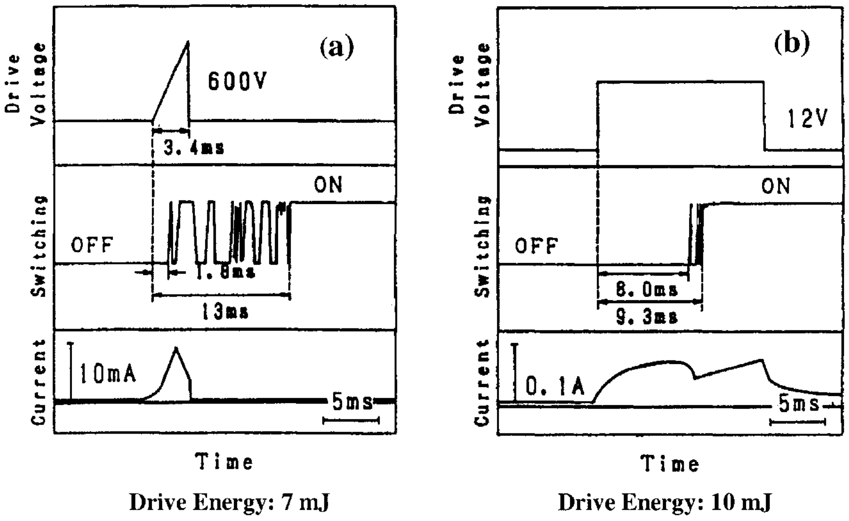

Drive Energy: 7 mJ

Drive Energy: 10 mJ

Figure 9.33 Dynamic response of two latching relays: (a) a shape memory ceramic relay and (b) an electromagnetic coil relay.[23]

9.6 ADAPTIVE SUSPENSION SYSTEMS

In general, when a shock absorber of an automobile provides a higher damping force (referred to as a "hard" damper), the controllability and stability of the vehicle are improved. Driving comfort is diminished, however, because the road roughness is easily transferred to the passengers. The purpose of the electronically controlled shock absorber is to provide both controllability and comfort simultaneously. When normal, relatively smooth road conditions exist, the system is set to provide a low damping force ("soft" damping) so as to optimize passenger comfort, and when rougher terrain is encountered the damping force is increased accordingly to improve the controllability while still maintaining a reasonable level of comfort. In order to effectively respond to variations in the road surface, a highly responsive sensor/actuator combination is required for the shock absorbing system.

The piezoelectric TEMS (Toyota Electronic Modulated Suspension) system, which is designed to adapt its dampening action to each change in road surface texture encountered was installed on the "Celcio" in 1989.[24] The structure of this electronically controlled shock absorber is pictured in Figure 9.34. The sensor is comprised of 5 layers of 0.5 mm thick PZT disks. It has a sensing speed of 2 ms and roughness resolution is about 2 mm. The actuator in this system is comprised of 88 layers of 0.5 mm thick disks. A 50 µm displacement is induced with an applied voltage of 500 V, and this is magnified forty times by means of a piston/plunger pin combination. The stroke of the piston pushes the change valve regulating the damping force down, thereby opening the bypass oil route and effectively decreasing the flow resistance ("softening" the damping effect). This adjustable damper is basically a binary (hard or soft) control system.

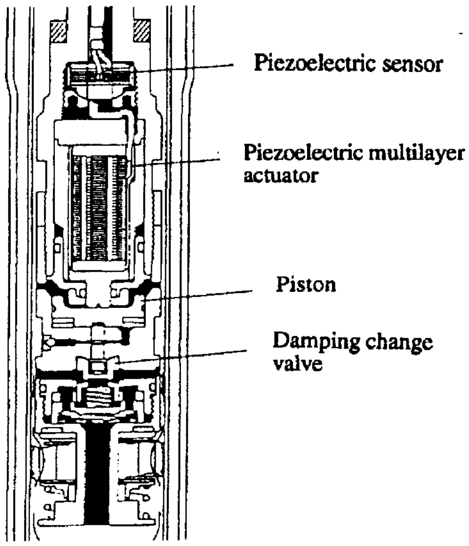

Figure 9.34 The piezoelectric TEMS (Toyota Electronic Modulated Suspension) system.[24]

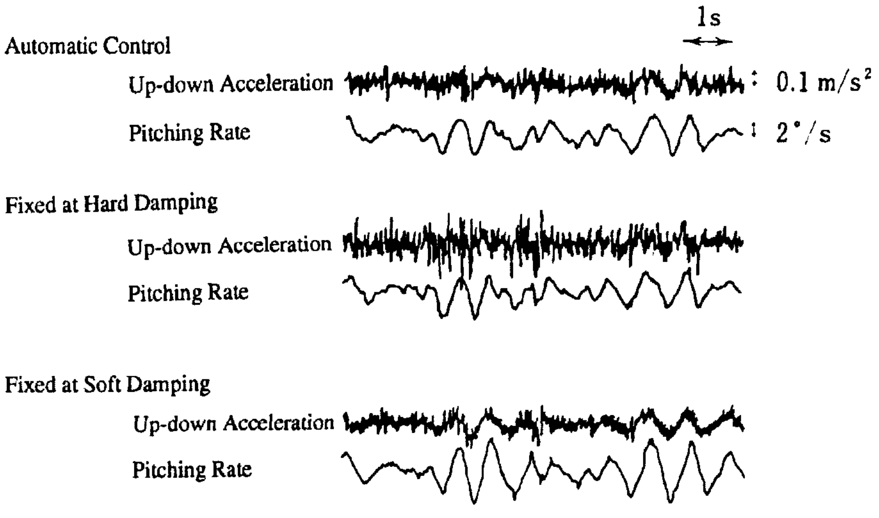

Figure 9.35 The response of the adaptive TEMS system as compared to two conditions of fixed damping.[24]

The response of the adaptive system as compared to two conditions of fixed damping is shown in Figure 9.35. The up-down acceleration and pitching rate were monitored when the vehicle was driven on a rough road. When the TEMS system was used (top set of curves), the up-down acceleration was suppressed to a level comparable with that obtained with fixed soft damping, providing comfortable driving conditions. At the same time, the pitching rate was also suppressed to a level comparable with that obtained with fixed hard damping, allowing for better controllability.

CHAPTER ESSENTIALS

1. Advantages of the Piezoelectric Printer Head: to a conventional electromagnetic type:
   a. low energy consumption,
   b. low heat generation (electromagnetic solenoids generate significant heat!),
   c. fast printing speed.
2. Merits of the Multilayer Actuator: for the impact printer application as compared to the bimorph type:
   a. longer lifetime,
   b. faster printing speed,
   c. higher impact force,
   d. higher efficiency.
3. The Co-Fired Integrated Multilayer Printer Head Structure: allows for successful mass production of the inkjet printer.

4. Latching Relays: typically constitute only 10% of the total relay production, but the unit price is about 10 times higher than non-latching varieties, leading to comparable sales overall. It is thus considered a highly functional and valuable device!
5. Shape Memory Ceramic Latching: use of a smart material such as this in the design of a relay can be effective in reducing the number of components and the total size of the device.

CHAPTER PROBLEMS

9.1 Piezoelectric actuators can be employed in laser and inkjet printers. Survey the recent literature on this issue.

9.2 List and briefly describe the major problems of using a piezoelectric ceramic in a pulse drive device (in terms of the tensile stress, heat generation etc.).

REFERENCES

1) Y. Endo, Y. Egawa, N. Harada and G. Yoshida: Proc. Jpn. Television Soc., 3-19 (1983).
2) K. Yokoyama and C. Tanuma: Electronic Ceramics **15**, Spring, p.45 (1984).
3) K. Shibata, K. Takeuchi, T. Tanaka, T. Yokoo, S. Nakano and Y. Kuwano: Jpn. J. Appl. Phys. **24**, Suppl. 24-3, 181 (1985).
4) Minolta Camera, Product Catalog "Mac Dual I, II."
5) M. Aizawa, K. Uchino and S. Nomura: Jpn. J. Appl. Phys., **22**, 1925 (1983).
6) Tojo and Sugihara: Proc. Jpn. Precision Eng., p.423 (Fall, 1983).
7) M. P. Coster: Proc. 4th Int'l. Conf. on New Actuators, 2.6, p.144, Germany (1994).
8) R. Gloess: Proc. 4th Int'l. Conf. on New Actuators, P26, p.190, Germany (1994).
9) N. Aoyama et al.: Proc. J. Precision Engr. Soc. P.897 (1992).
10) T. Higuchi, Watanabe and Kudo: J. Precision Engr. **54** (11), 2107 (1988).
11) K. Yano, T. Hamatsuki, I. Fukui and E. Sato: Proc. Jpn. Electr. Commun. Soc., 1-157 (Spring, 1984).
12) K. Yano, I. Fukui, E. Sato, O. Inui and Y. Miyazaki: Proc. Jpn. Electr. Commun. Soc., 1-156 (Spring, 1984).
13) K. Yano, T. Inoue, S. Takahashi and I. Fukui: Proc. Jpn. Electr. Commun. Soc., 1-159 (Spring, 1984).
14) T. Ota, T. Uchikawa and T. Mizutani: Jpn. J. Appl. Phys. **24**, Suppl. 24-3, 193 (1985).
15) M. Tsuzuki, M. Suga and Banno: Symp. Jpn. Electr. Commun. Soc., IE 83-59 (1983).
16) M. Suga, M. Tsuzuki and Banno: Symp. Jpn. Electr. Commun. Soc., EMC 84-46 (1984).
17) M. Suga and M. Tsuzuki: Jpn. J. Appl. Phys. **23**, 765 (1984).
18) Nikkei Electronics, Oct. 3, p.72 (1979).
19) N. Kurashima: Proc. Machine Tech. Inst. Seminar, MITI, Tsukuba, Japan (1999).
20) Piezo Electric Products Inc., Product Catalog.
21) Sato, Taniguchi and Ohba: OMRON Technics, No. 70, p.52 (1983).
22) S. Mitsuhashi, K. Wakamatsu, Y. Aihara and N. Okihara: Jpn. J. Appl. Phys., **24**, Suppl. 24-3, 190 (1985).
23) A. Furuta, K. Y. Oh and K. Uchino: Sensor and Mater., **3** (4), 205 (1992).
24) Y. Yokoya: Electronic Ceramics, **22**, No. 111, p.55 (1991).

10

ULTRASONIC MOTOR APPLICATIONS

The pulse drive motors described in the previous chapter are driven by an applied voltage with a *rectangular waveform* at a frequency less than the resonance frequency, while ultrasonic devices are driven by a *sinusoidal AC voltage* at the *resonance frequency*. Ultrasonic devices are divided into three general categories. The first type is operated in a mode that produces a simple ultrasonic vibration for uses such as the ultrasonic scalpel. The second type is designed to transmit energy to air or a liquid for applications such as the piezoelectric fan, the piezoelectric pump, and the ultrasonic microscope. *Ultrasonic motors* constitute the final category, which will be the primary focus of this chapter. The ceramic materials typically used in the fabrication of high power ultrasonic motors are similar to the conventional piezoelectric PZT-based materials used for vibrator/resonator applications, but a high mechanical quality factor, Q_m, is generally required for the motors, as described in Section 6.1. This and other design parameters will be examined further throughout the chapter.

10.1 GENERAL DESCRIPTION AND CLASSIFICATION OF ULTRASONIC MOTORS

(1) Historical Background

Electromagnetic motors have actually existed for more than a hundred years. While these motors still dominate the industry, further improvement of the current designs is limited. These improvements await the development of suitable new magnetic and superconducting materials. Efficient motors of this type smaller than 1 cm are difficult to produce. An electromagnetic motor with a submillimeter rotor used in a wristwatch, for example, requires a permanent magnet about 1 cm in diameter. The efficiency of piezoelectric ultrasonic motors is independent of their size and therefore they have gained much attention for minimotor applications.

The basic structure of an ultrasonic motor is depicted in Figure 10.1. It consists essentially of a high frequency power supply, a stator, and a slider/rotor piece. The stator is composed of a piezoelectric driver and an elastic vibrator. The slider has an elastic moving component with a friction coat on the side facing the stator. The motor is driven by a compact and inexpensive drive circuit, which, in conjunction with its simple design, makes it especially suitable for mass production.

The first practical ultrasonic motor was proposed by H. V. Barth of IBM in 1973.[1] The rotor in this design is in contact with two horns placed on either side of it as shown in Figure 10.2. When one of the horns is driven by its piezoelectric vibrator, the rotor is driven in one direction, and rotation in the opposite direction occurs when the other horn is driven. Various mechanisms based on virtually the same principle have been subsequently proposed.[2,3] The motors of this design were ultimately not very useful, however, due to changes in the vibration amplitude that tend to occur at higher temperatures and as a consequence of mechanical degradation. In the 1980's, more precise and sophisticated positioners, which do not generate magnetic field noise, were required by integrated circuit manufacturers as the pattern density on chips continued to increase. This trend helped to accelerate the development of new ultrasonic motors. The merits and demerits of modern ultrasonic motors are summarized in Table 10.1.

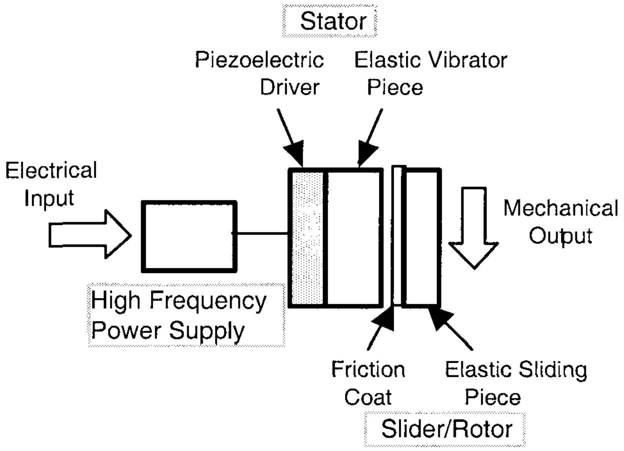
Stator
Piezoelectric Driver
Elastic Vibrator Piece
Electrical Input
Mechanical Output
High Frequency Power Supply
Friction Coat
Elastic Sliding Piece
Slider/Rotor

Figure 10.1 The basic structure of an ultrasonic motor.

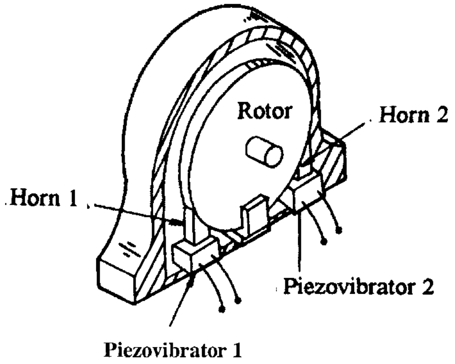
Rotor
Horn 2
Horn 1
Piezovibrator 2
Piezovibrator 1

Figure 10.2 The first practical ultrasonic motor proposed by H. V. Barth of IBM in 1973.[1]

Table 10.1 The merits and demerits of modern ultrasonic motors.

Merits	Demerits
➢ Low Speed and High Torque	➢ High Frequency Power Supply Required
➢ Direct Drive	➢ Torque vs. Speed Droop
➢ Quick Response	➢ Low Durability
➢ Wide Range of Speeds	
➢ Hard Brake with No Backlash	
➢ Excellent Controllability	
➢ Fine Position Resolution	
➢ High Power-to-Weight Ratio	
➢ Quiet Drive	
➢ Compact Size and Light Weight	
➢ Simple Structure and Easy Production	
➢ No Generation of Electromagnetic Radiation	
➢ Unaffected by External Electric or Magnetic Fields	

Example Problem 10.1

Write expressions for the input current density, the induced strain, and the stored electric and elastic energies and any related quantities for a longitudinal piezoelectric actuator under DC, AC off-resonance, and AC resonance drive conditions.

Solution

I. DC Drive

Electric Field: $E_3 = V / l$
Polarization: $P_3 = K_3 E_3$
Generative Strain: $x_3 = d_{33} E_3$
Generative Stress: $X_3 = x_3 / s_{33}^E = (d_{33}/s_{33}^E) E_3$
Stored Electric Energy: $U_{EE} = (P_3 E_3)/2 = (K_3 E_3^2)/2$
Stored Piezoelectric Energy: $U_{ME} = (x_3 X_3)/2 = (d_{33}^2 E_3^2)/2\, s_{33}^E$
Electromechanical Coupling Factor: $k_{33}^2 = U_{ME}/U_{EE} = d_{33}^2 / K_3\, s_{33}^E$

II. AC Drive (off-resonance)

Electric Field: $E_3 = [V_o \sin(\omega t)]/l$
Current Density: $J_3 = Y_o E_3 = \omega K_3 E_3$
Vibration Amplitude: $x_3 = d_{33} E_3$

Vibration Velocity: $v = \omega\, d_{33}\, E_3$

Input Electric Energy Density: $u_{EE} = J_3\, E_3 = \omega K_3 E_3^2$

Mechanical Energy Density: $u_{ME} = \omega\, (d_{33}^2/s_{33}^E) E_3^2 = \omega\, k_{33}^2\, K_3\, E_3^2$

III. AC Drive (resonance)

Electric Field: $E_3 = [V_o \sin(\omega_o t)]/l$

Current Density: $J_3 = Y_m\, E_3 = \omega\alpha\, K_3 E_3$

Vibration Velocity: $v = 1/\sqrt{\rho\, s_{33}^E}$

Resonance Frequency: $f_o = v/2\, l$

Resonance Amplification: $\alpha = Y_m/Y_o$

Vibration Amplitude: $x_3 = \alpha d_{33} E_3\, l$

Maximum Vibration Velocity: $v_m = \omega_o \alpha d_{33} E_3\, l = \pi\, \alpha\, v\, d_{33}\, E_3$

Sound Pressure: $p = \rho v (v_m) = \pi\alpha\rho v^2 d_{33} E_3 = \pi\alpha (d_{33}/s_{33}^E) E_3$

Input Electric Power: $P = IV = J_3 S\, E_3\, l\ = \omega_o \alpha\, K_3 E_3^2 V_m$

Mechanical Energy Density: $u_{ME} = \omega_o \alpha E_3\, l\, (d_{33}^2/s_{33}^E) E_3 S$

$= \omega_o \alpha\, (d_{33}^2/s_{33}^E) E_3 V_m$

where ρ is the mass density.

Note: Some of these parameters are α times larger than those defined for the off-resonance mode.

(2) Classification of Ultrasonic Motors

There are two general types of ultrasonic motors: the *rotary type* and the *linear type*. They can be further distinguished by their shape. The rod, π-shaped, ring, and cylinder types are depicted in Figure 10.3.

The vibration induced in the motor is either in the form of a standing wave or a traveling wave. Recall that a *standing wave* is described by:

$$u_s(x,t) = A\, [\cos(kx)]\, [\cos(\omega t)] \tag{10.1}$$

while the equation for a *traveling wave* is:

$$u_t(x,t) = A \cos(kx - \omega t) \tag{10.2}$$

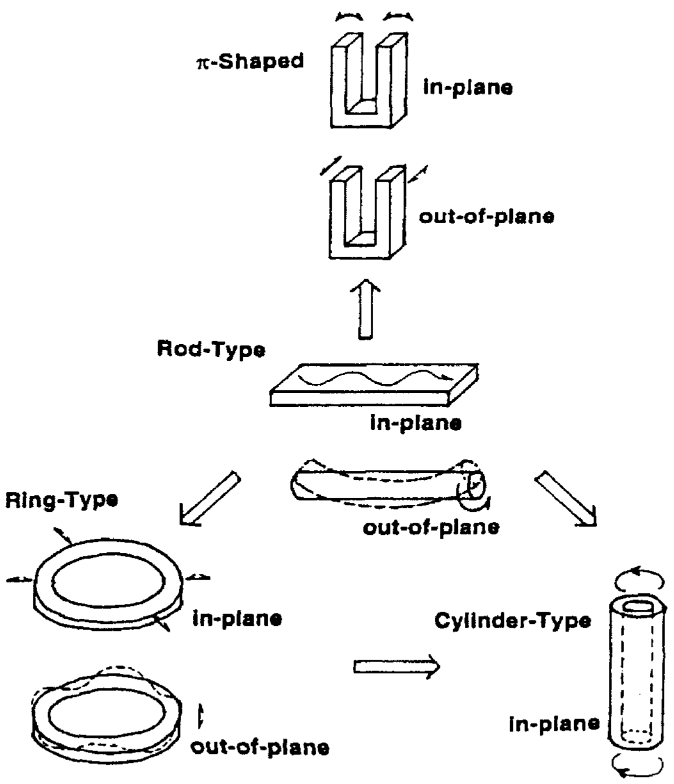
π-Shaped
In-plane
out-of-plane
Rod-Type
In-plane
Ring-Type
out-of-plane
In-plane
Cylinder-Type
out-of-plane
In-plane

Figure 10.3 Various ultrasonic motor configurations.

Equation (10.2) can be rewritten as:

$$u_t(x,t) = A\,[\cos(kx)][\cos(\omega t)] + A\,[\cos(kx - \pi/2)][\cos(\omega t - \pi/2)] \qquad (10.3)$$

This leads to an important result. *A traveling wave can be generated by superposing two standing waves with a phase difference of 90 degrees between them.* This is the only feasible way to generate a stable traveling wave in a structure of finite size and volume.

The Standing Wave Motor

The standing wave motor is sometimes referred to as a *vibratory coupler* or a *"woodpecker" motor.* A vibratory piece is connected to the piezoelectric driver and the tip portion executes an elliptical displacement as shown in Figure 10.4.[4] Orienting an x-y coordinate system such that the x-axis is normal to the rotor face, we see in Figure 10.4(a) that the vibratory piece is in contact with the rotor or slider at a slight angle, θ. When a displacement:

$$u_x = u_o \sin(\omega t + \alpha) \qquad (10.4)$$

is excited in the piezoelectric vibrator, the vibratory piece will bend due to its contact with the rotor, causing the tip of the vibrator to move along the rotor face between points A and B as shown in Figure 10.4(b). The tip then moves freely from point B to point A. When the resonance frequency of the vibratory piece, f_1, is adjusted to the resonance frequency of the piezovibrator, f_o, and the bending deformation is sufficiently small compared with the length of the piece, the displacement of the tip from point B to point A is described by:

$$x(t) = u_o \sin(\omega t + \alpha) \quad \textit{and} \quad y(t) = u_1 \sin(\omega t + \beta) \qquad (10.5)$$

which produces an *elliptical locus*. The torque is thus applied only as the vibrator tip moves from A to B. Some slight rotation speed ripple is observed, however, due to the inertia of the rotor.

The standing wave motor has the advantages of low production cost and high efficiency (theoretically up to 98%). The fundamental disadvantages of this design are related to some variability of the locus and a certain degree of asymmetry between the clockwise and counterclockwise rotations.

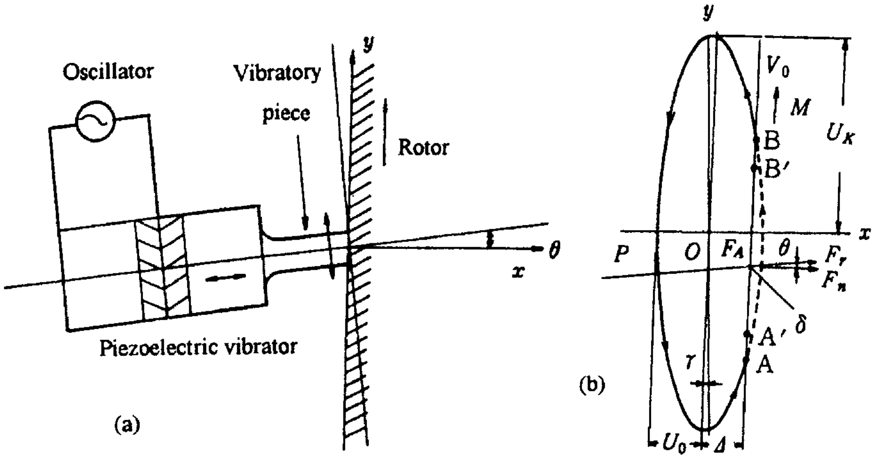

Figure 10.4 The vibratory coupler type of motor: (a) system configuration and (b) locus of vibrator tip locus.[4]

The Traveling Wave Motor

The superposition of two standing waves with a 90-degree phase difference produces a traveling wave in the type of motor that bears this name (also known as the *surface wave* or *"surfing" motor*). A particle on the surface of the elastic body executes a displacement with an *elliptical locus* due to the coupling of longitudinal and transverse waves as shown in Figure 10.5. This motor requires two vibration sources to generate the traveling wave, leading to a rather low efficiency (not more than 50%). The rotation direction is readily changed, however, by switching the phase difference from 90 to –90 degrees.

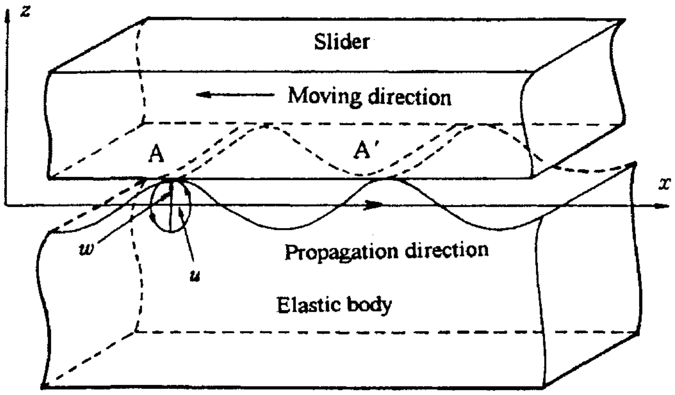

Figure 10.5 The traveling wave type of motor.

The following classification will be employed for presenting and comparing the essential features of the most popular and widely used ultrasonic motors currently available. Four principal categories constitute this classification scheme:

1. Standing Wave Motors: in which one major vibrational mode is induced by means of one actuator component. [Note that we will include the vibratory coupler motor in this category even though it is technically not a purely standing wave device, but rather exhibits a coupling of the standing wave and bending mode vibrations. The operation of the device can still be adequately described in terms of the conventional standing wave model if appropriate allowances are made for the bending mode.]

2. Mixed-Mode Motors: in which two vibrational modes are induced by means of two actuators. (This type is, in a sense, a variation of the standing wave motor, but in this case two standing waves are induced and combined.)

3. Traveling Wave Motors: in which two vibrational modes with a phase difference of 90 degrees between them are excited by two actuators and combine to produce the traveling wave.

4. Mode Rotation Motors: in which one vibrational mode is excited through the action of several actuators. This is, in a sense, a variation of the traveling wave type, but in this case multiple actuators are used to induce the individual vibrations with an appropriate phase difference to generate the desired displacement when combined.

10.2 STANDING WAVE MOTORS

(1) Rotary Motors

The fundamental structure of the rotary motor is pictured in Figure 10.6. The design developed by Sashida has four vibratory pieces, which are installed on the end of a cylindrical vibrator and are pressed onto the rotor.[4] It can attain a rotation speed of 1500 rpm, a torque of 0.8 kg-cm, and an output of 12 W (with 40% efficiency) from an input of 30 W applied at 35 kHz. This type of ultrasonic motor can achieve a much higher speed than is possible for the inchworm (described in Chapter 9) because it is operated at a higher frequency corresponding to its resonance frequency where an amplified displacement occurs ($\Delta l = \alpha \text{ d E } l$). The characteristic power-related features measured for this motor are plotted as a function of torque in Figure 10.7. The production of prototypes such as this one in the early 1980's motivated the surge of research that has occurred in the last two decades concerned with the development and application of ultrasonic motors.

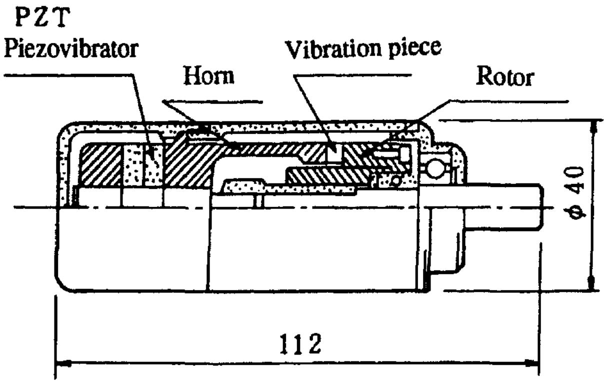

Figure 10.6 A typical rotary motor structure.[4]

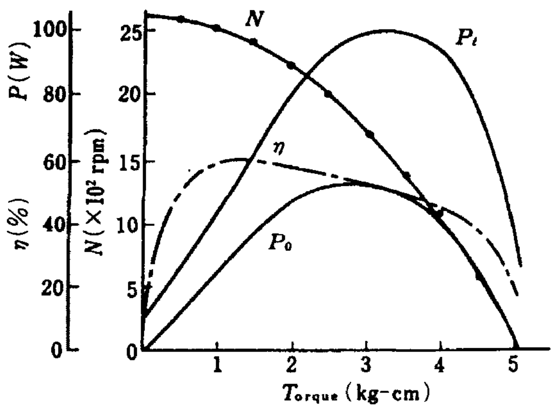

Figure 10.7 Power-related characteristics of the Sashida rotary motor.[4]

Another variation on this basic design which makes use of a hollow piezoelectric ceramic cylinder as a torsional vibrator appears in Figure 10.8.[5] An interdigital type electrode pattern is printed at a 45° angle on the cylinder surface as shown in Figure 10.8(b) so that the torsional vibration can be induced in the structure. A rotor attached to the end of the cylinder is thus rotated in response to this vibration.

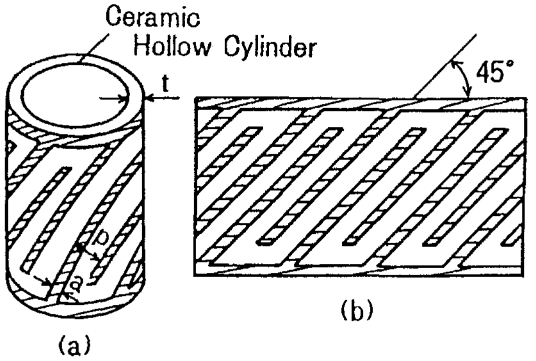

Figure 10.8 A piezoelectric hollow cylinder torsional vibrator developed by Tokin Corporation: (a) the basic structure and (b) the interdigital electrode configuration for inducing the torsional vibration.[5]

A simpler and more compact motor has been designed that makes use of a metal tube rather than a piezoelectric PZT.[6] The basic structure of the stator is shown in Figure 10.9(a). Two rectangular poled PZT pieces are bonded to the metal tube as shown in the figure. When Plate X is driven, a bending vibration is excited along the x-axis. Due to the non-uniform mass distribution of Plate Y, a second bending vibration is also induced along the y-axis that lags in phase the bending vibration established in the x direction. This results in an elliptical clockwise displacement. When Plate Y is driven, a counterclockwise wobble motion is excited. The rotor is a cylindrical rod with a pair of stainless ferrules separated with a spring as shown in the diagram of the entire motor assembly appearing in Figure 10.9(b). The cost for the materials and simple construction of this motor is quite low as compared with some of the more elaborate designs. Another advantage lies in the fact that only a single-phase power supply is required to drive the motor.

The power-related characteristics of a metal cylinder motor 2.4 mm in diameter and 12 mm in length with no load applied are plotted as a function of torque in Figure 10.10. The motor was driven at 62.1 kHz in both rotation directions. A no-load speed of 1800 rpm and an output torque up to 1.8 mNm were obtained for rotation in both directions under an applied rms voltage of 80 V. The very high level of torque produced by this motor is due to the dual stator configuration and the high contact force between the metal stator and rotors. The rather high maximum efficiency of about 28% for this relatively small motor is a noteworthy feature of the data presented in Figure 10.10. One of the world's smallest ultrasonic motors to date is pictured in Figure 10.11.[6] It is 1.8 mm in diameter and 4 mm in length. The rotor is a thin hollow tube, through which an optical fiber can pass.

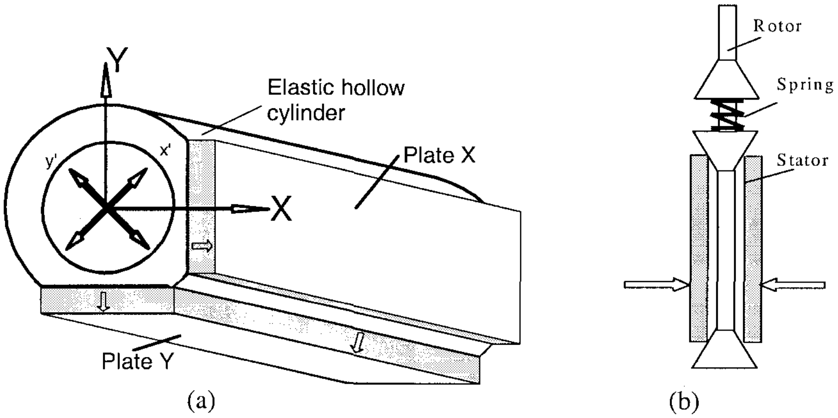

Figure 10.9 A metal tube rotary motor: (a) structure of the metal tube stator and (b) assembly of the entire motor.[6]

(2) Linear Motors

A *π-shaped linear motor* comprised of a multilayer piezoelectric actuator and fork-shaped metallic legs is pictured in Figure 10.12.[7] Due to the slight difference in mechanical resonance between the two legs, there will be a phase difference of 90 or −90 degrees (depending on the drive frequency) between the bending vibrations set up in the legs. The walking slider moves similarly to the way a horse uses its fore and hind legs to trot. A test motor with dimensions 20x20x5 mm^3 exhibits a maximum speed of 15 cm/s and a maximum thrust of 0.2 kgf with an efficiency of 20%, when driven by a 6 V, 98 kHz (actual power = 0.7 W) input signal as indicated by the data appearing in Figure 10.13. This motor has been employed in a precision x-y stage.

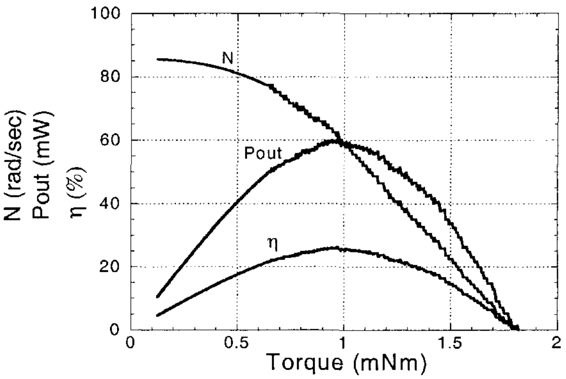

Figure 10.10 The power-related characteristics of a metal cylinder rotary motor plotted as a function of torque.[6] [Diameter: 2.4 mm, length: 12 mm, operating frequency: 62.1 kHz, load: none]

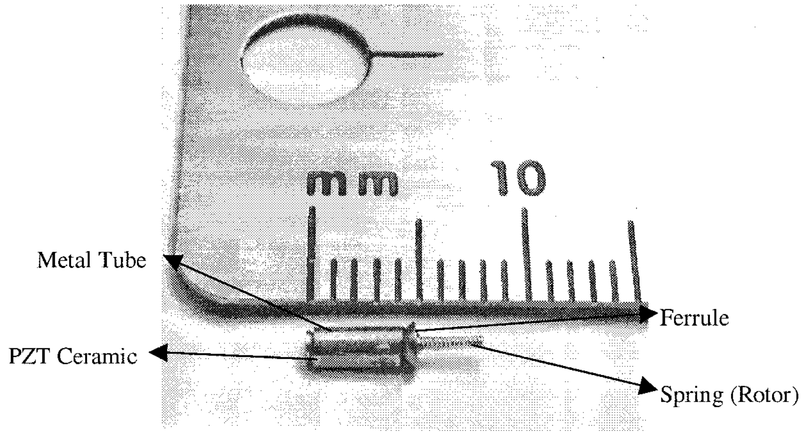

Figure 10.11 One of the world's smallest ultrasonic motors to date.[6] [Diameter: 1.8 mm, length: 4 mm]

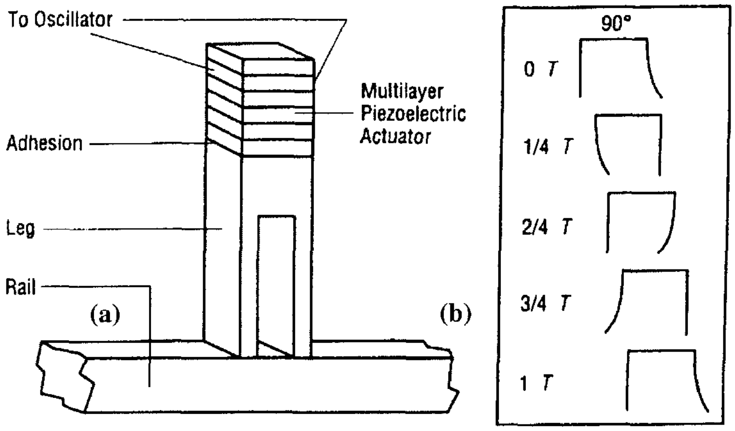

Figure 10.12 A π-shaped linear ultrasonic (walking) motor: (a) the basic structure and (b) a motion sequence showing the walking action of the legs in operation.[7] (Note how the 90-degree phase difference between the legs enables the device to walk.)

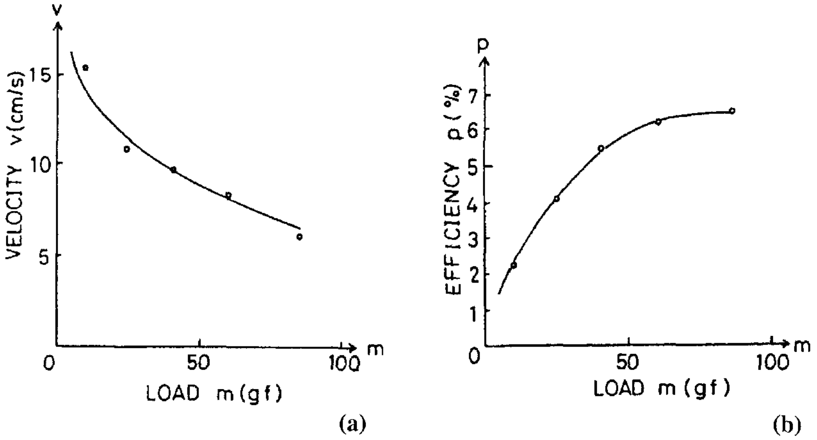

(a) (b)

Figure 10.13 Performance characteristics of a π-shaped test motor: (a) velocity and (b) efficiency as a function of load.[7] [Dimensions: 20x20x5 mm^3, drive voltage: 6 V, 98 kHz]

10.3 MIXED-MODE MOTORS

A significantly improved rotary motor has been developed by Hitachi Maxel that makes use of a torsional coupler instead of the vibratory pieces used in the conventional design.[8] The torsional coupler transforms the longitudinal vibration generated by the Langevin vibrator to a transverse vibration, producing an elliptical rotation of the tip. The modified motor pictured in Figure 10.14 exhibits higher torque and efficiency due to the action of the torsional coupler and an enhanced contact force with the rotor. A motor 30 mm x 60 mm in size with a 20-30° cant angle between the leg and vibratory pieces provides a torque as high as 13 kg cm with an efficiency of 80%. However, this type produces only unidirectional rotation. Even though this motor is driven by a pulsed input, the output rotation is quite smooth due to the inertia of the rotor.

The *Windmill motor* pictured in Figure 10.15 has a flat and wide configuration that is driven by a metal-ceramic composite structure.[9] The motor is comprised of four basic components: a stator, a rotor, a ball bearing, and the housing structure as shown in Figure 10.15(a). The piezoelectric part is simply a ring with a diameter of 3.0 mm electroded on its top and bottom surfaces that has been transversely poled (that is, across its thickness). The metal rings are fabricated by *electric discharge machining* and have four arms placed 90° apart on the inner circumference of the ring as shown in Figure 10.15(b). The metal and piezoelectric rings are bonded together, but the arms remain free, allowing them to move like cantilever beams. The length and cross-sectional area of each arm are selected such that the resonance frequency of the secondary bending mode of the arms is close to the resonance frequency of the radial mode of the stator. The rotor is placed at the center of the stator and rotates when an electric field is applied having a frequency between the radial and bending resonance modes. The truncated cone shape at the rotor end ensures constant contact with the tips of the arms.

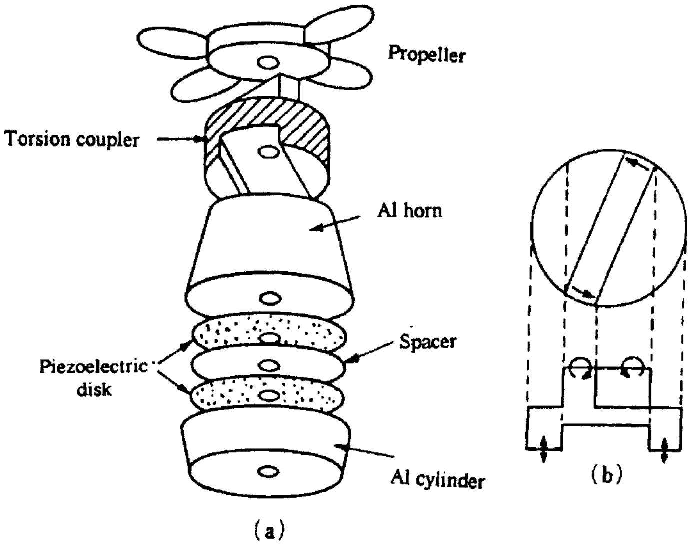

Figure 10.14 A mixed-mode ultrasonic motor incorporating a torsional coupler: (a) the structure of the entire motor and (b) motion of the torsional coupler.[8]

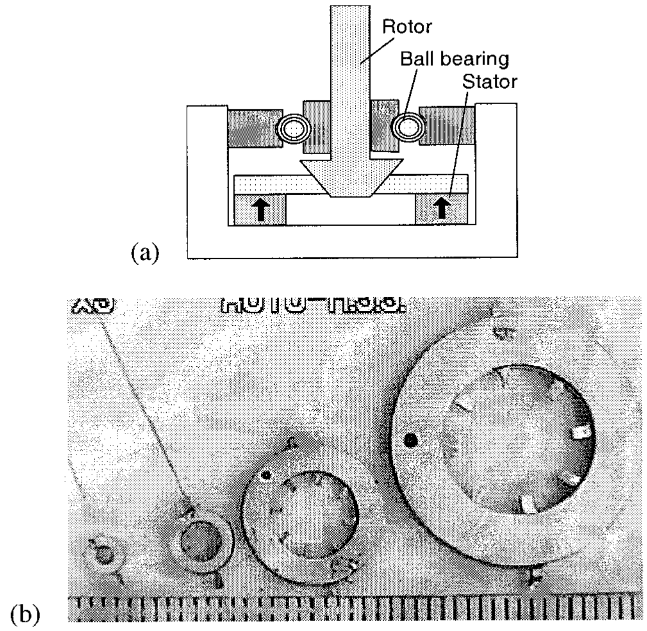

Figure 10.15 The "windmill" motor: (a) cross-sectional view and (b) various stators.[9] [Diameter: 3-20 mm][9]

Rotation is produced by the alternate contraction and expansion of the stator. During the contraction portion of the cycle, the four arms at the center of the metal ring clamp the rotor and apply a tangential force to it. Since the radial mode frequency of the stator is close to the secondary bending mode frequency of the arms, the deformations add and the tips of the arms bend down. During the expansion portion of the cycle, the arms release the rotor at a different position. The resulting motion is similar to the action produced by a human hand as it grasps and twists an object.

The radial mode resonance frequency, no-load speed, and maximum torque are plotted as a function of motor size in Figure 10.16. When a motor with a 5 mm diameter is driven at 160 kHz, a maximum speed of 2000 rpm and a maximum torque of 0.8 mNm is attained. The speed, efficiency, and output power of a 3 mm diameter motor are plotted as a function of load torque in Figure 10.17. The starting torque of 17 μNm for this motor is one order of magnitude higher than that of a thin film motor of a similar size.

A dual vibration coupler motor is pictured in Figure 10.18.[10] A torsional Langevin vibrator acts in conjunction with three multilayer actuators to generate larger transverse and longitudinal surface displacements of the stator, as well as to control their phase difference between them. The rotation direction is switched by changing the phase difference. Since it is quite difficult to match the torsional and longitudinal resonance frequencies, the motor is generally operated at a frequency corresponding to the torsional resonance frequency.

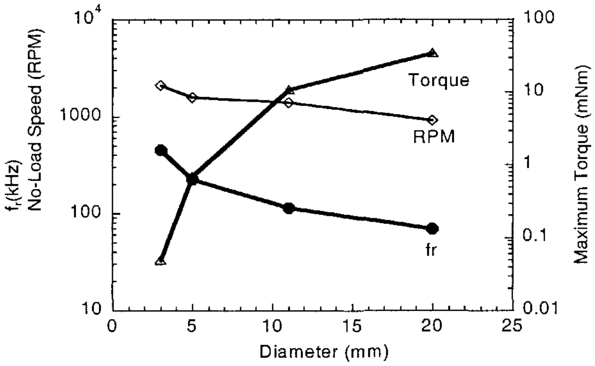

Figure 10.16 Radial mode resonance frequency, no-load speed, and starting torque as a function of stator diameter.[9] [Drive: 15.7 V, 160 kHz]

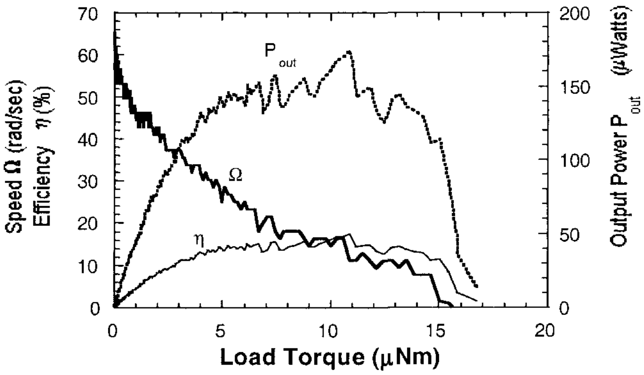

Figure 10.17 Speed, efficiency, and output power as a function of load torque for a 3 mm diameter motor.[9]

10.4 TRAVELING WAVE MOTORS

(1) Linear Motors

A linear motor driven by two bending vibrations is pictured in Figure 10.19.[11,12] The two piezoelectric vibrators installed at both ends of a transmittance steel rod excite and receive the traveling transverse wave, which is an antisymmetric fundamental lambda wave. Adjustment of the load resistance of the receiving vibrator produces a perfect traveling wave. Movement in the reverse direction is induced by exchanging the exciting and receiving roles of the piezoelectric vibrators.

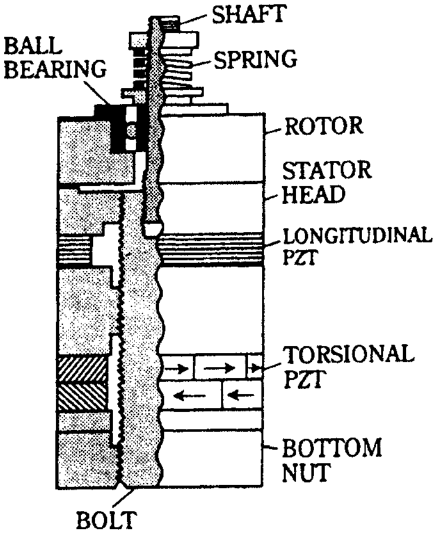
SHAFT
BALL BEARING
SPRING
ROTOR
STATOR HEAD
LONGITUDINAL PZT
TORSIONAL PZT
BOTTOM NUT
BOLT

Figure 10.18 A dual vibration (longitudinal and torsional) vibration coupler motor.[10]

The bending vibration transmitted via the rail rod is represented by the following differential equation:

$$\frac{\partial^2 w(x,t)}{\partial t^2} + \left(\frac{YI}{\rho A}\right)\frac{\partial^2 w(x,t)}{\partial x^2} = 0 \tag{10.6}$$

where w(x,t) is the transverse displacement (see Figure 10.5), x is the coordinate along the rod axis, Y is Young's modulus of the rod, A is its cross-sectional area, ρ is its density, and I is its moment of inertia. Assuming a general solution of the form:

$$w(x,t) = W(x)\,[A \sin(\omega t) + B \cos(\omega t)] \tag{10.7}$$

the wave transmission velocity, v, and the wavelength, λ, are given by:

$$v = \left(\frac{YI}{\rho A}\right)^{1/4} \sqrt{\omega} \tag{10.8}$$

$$\lambda = 2\pi\left(\frac{YI}{\rho A}\right)^{1/4}\frac{1}{\sqrt{\omega}} \tag{10.9}$$

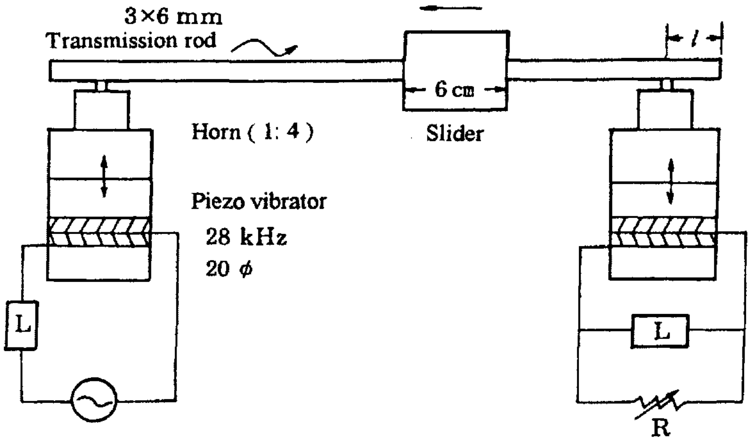
3×6 mm
Transmission rod
l
6 cm
Horn (1: 4)
Slider
Piezo vibrator
28 kHz
20 ϕ
L
L
R

Figure 10.19 A linear motor driven by two bending vibrations.[11,12]

When the motor is driven in this manner, a wavelength as short as several millimeters can be readily produced by adjusting either the cross-sectional area, A, or the moment of inertia, I, of the rod thereby ensuring adequate surface contact with the slider. A typical wavelength is about 26.8 mm.

The structure of the slider, clamped to the transmission rod with an appropriate force is pictured in Figure 10.20. The contact face is coated with rubber or a vinyl resin.

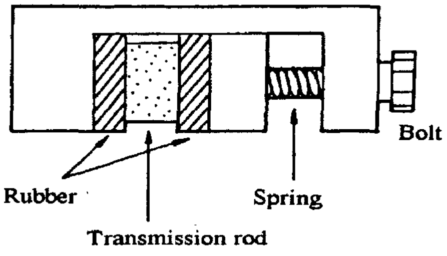
Bolt
Rubber
Spring
Transmission rod

Figure 10.20 End view of the slider clamped to the transmission rod.[11,12]

The transmission efficiency is strongly affected by the contact position of the vibration sources on the rod. The periodic variation of the transmission efficiency with the position of the piezoelectric driver with respect to the free end of the rod (this length is labeled *l* in Figure 10.19) is shown in Figure 10.21. The optimum position for the vibration source is at a distance *l* from the end of the rod that corresponds to exactly one wavelength, 26.8 mm.

The slider is 60 mm long clamp, where its length is selected to be approximately two wavelengths of the vibration. It is driven at a speed of 20 cm/s and produces a thrust of 5 kgf at 28 kHz. A serious problem with this type of linear motor lies in its low efficiency (around 3%) since the entire rod must be excited, while only a relatively small portion of it is utilized for the output. The ring type motors described in Section 10.4 generally have a higher efficiency because the stator and the rotor have the same length and the entire rod can be utilized.

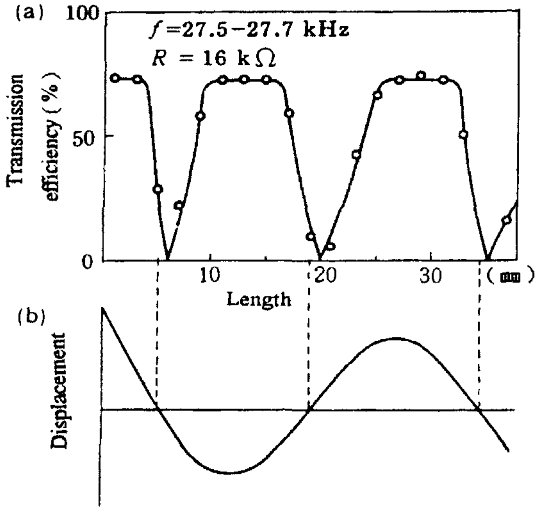

Figure 10.21 Characteristics of the linear motor as a function of position of the piezoelectric driver with respect to the end of the rod: (a) the transmission efficiency and (b) the displacement.[11,12]

A $LiNbO_3$ surface acoustic wave motor is pictured in Figure 10.22.[13] Rayleigh waves are excited in two mutually perpendicular directions on the surface of a Y-cut $LiNbO_3$ crystal plate (127.8°-rotation) via two pairs of interdigital surface electrodes arranged as shown in Fig. 10.22(a). The slider structure with three balls as legs appears in Figure 10.22(b). The driving vibration amplitude and the wave velocity of the Rayleigh waves are adjusted to 6.1 nm and 22 cm/s, respectively, in both the x and y directions. It is important to note that even though the vibration amplitude is much smaller ($<$ 1/10) than the surface roughness of the $LiNbO_3$, the slider moves smoothly. The mechanisms for this have not yet been fully identified, but one possibility may be related to a local enhancement of the frictional force through the ball contact.

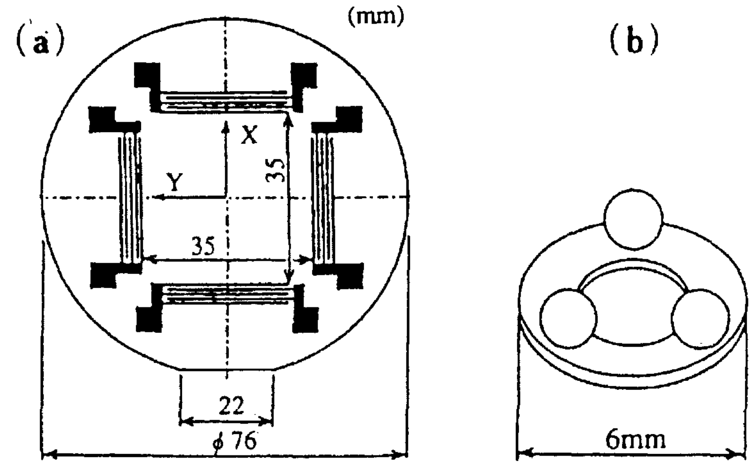
(a)
(mm)
X
Y
35
35
22
ϕ76
(b)
6mm

Figure 10.22 A $LiNbO_3$ surface acoustic wave motor: (a) the stator structure and (b) the slider structure.

A rectangular plate dual-mode vibrator motor is pictured in Figure 10.23.[14] The fundamental longitudinal (L_1) mode and eight harmonic bending (B_8) mode vibrations, which have practically the same resonance frequency, are utilized in the operation of this device. When input signals with a phase difference of 90 degrees are applied to the L-mode and B-mode electrodes, identical elliptical displacements are generated at both ends of the plate, causing the rollers in contact with these areas to rotate. Such a system is well suited for the task of conveying paper and cards.

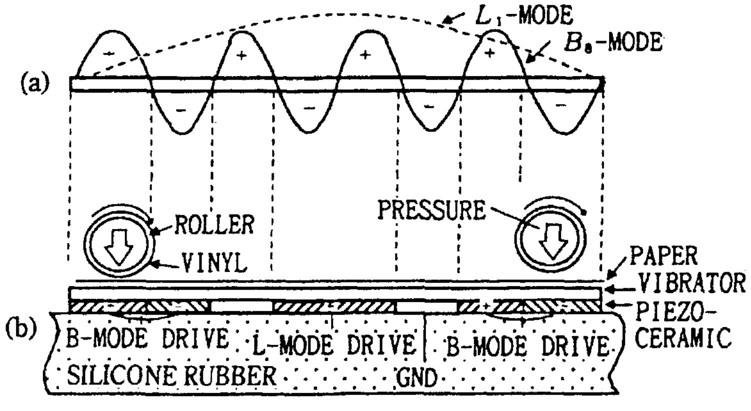
(a)
L1-MODE
B8-MODE
+
-
ROLLER
VINYL
PRESSURE
PAPER
VIBRATOR
PIEZO-CERAMIC
(b)
B-MODE DRIVE
L-MODE DRIVE
B-MODE DRIVE
SILICONE RUBBER
GND

Figure 10.23 A rectangular plate dual-mode vibrator motor: (a) the fundamental longitudinal L_1 mode and the eighth harmonic bending B_8 mode vibrations and (b) schematic diagram of the motor.[14]

The π-shaped device described in Section 10.2(2) can be modified to operate as a traveling wave motor.[15] Two multilayer actuators are installed at the two corners of the π-shaped frame as shown in Figure 10.24. When input signals with a 90-degree phase difference are applied to the actuators, a "trotting" motion is induced in the legs of the device.

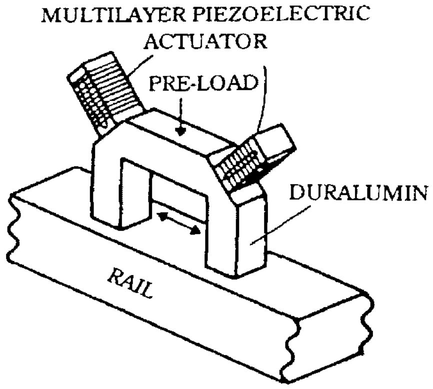
MULTILAYER PIEZOELECTRIC ACTUATOR
PRE-LOAD
DURALUMIN
RAIL

Figure 10.24 A π-shaped ultrasonic linear motor of the traveling wave type.[15]

(2) Rotary Motors

When the rod discussed in the previous section is bent to form a ring, it can be operated as a rotary motor. Two types of ring motors are pictured in Figure 10.25, one operates via a bending mode and the other via an extensional mode of vibration.[16] Although the basic principle of operation for these motors is similar to that for the linear type, more sophisticated methods of ceramic poling must be applied and somewhat more complex mechanical support structures are needed.

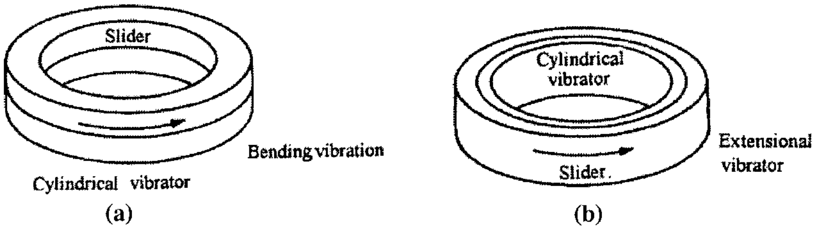
Slider
Bending vibration
Cylindrical vibrator
(a)
Cylindrical vibrator
Slider.
Extensional vibrator
(b)

Figure 10.25 Two types of ring ultrasonic motors utilizing (a) a bending mode and (b) an extensional mode vibration.[16]

Operation of "Surfing" Rotary Motors

When a source of vibration is acting at a given position on a closed ring (either circular or square) at the resonance frequency of the ring, a standing wave is excited, due to the interference of the two disturbances that proceed from the source around the ring in opposite directions. When more than one vibrator is applied, the superposition of the disturbances generated by the sources (two from each source) can produce a traveling wave around the ring.

Assuming a vibration of the form $A\cos(\omega t)$ is applied at position $\theta=0$ on an elastic ring, the n-th mode standing wave established in the ring is described by:

$$u(\theta,t) = A\,[\cos(n\theta)][\cos(\omega t)] \tag{10.10}$$

A general expression for a traveling wave is:

$$u(\theta,t) = A\cos(n\theta - \omega t) \tag{10.11}$$

Alternatively, a traveling wave can be represented as the superposition of two standing waves in an equation of the form:

$$u(\theta,t) = A[\cos(n\theta)][\cos(\omega t)] + A[\cos(n\theta - \pi/2)][\cos(\omega t - \pi/2)] \tag{10.12}$$

from which we see that *a traveling wave can be generated by superposing two standing waves whose phases differ by 90 degrees with respect to both position and time.* In more general terms we can say that the superposition of standing waves with any constant phase difference except π can result in a traveling wave. In principle, excitation at only two positions on the ring is sufficient to generate a traveling wave. Some commonly used vibration source configurations are illustrated in Figure 10.26. In practice, the largest number of vibration sources possible is preferred in order to increase the mechanical output. When deciding upon the total number and placement of the vibration sources the symmetry of the electrode pattern must be carefully considered.

The displacements produced in ring motors of the bending and extensional mode types are depicted in Figure 10.27.[16] The displacement locus becomes an elongated ellipse normal to the surface for the thin ring motor operated in the bending mode, while the locus is a flat ellipse independent of the thickness for the device operated in the extensional mode. The thrust direction on the top and bottom surfaces is the same for the bending mode motor, but they are in opposite directions for the extensional mode motor. The main advantage of the extensional mode over the bending mode is its higher speed due to its relatively high resonance frequency.

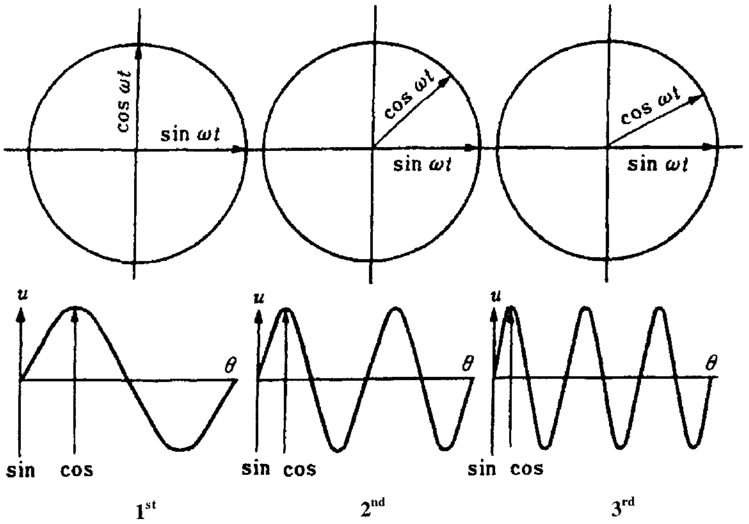
cos ωt
sin ωt
cos ωt
sin ωt
cos ωt
sin ωt
u
θ
sin
cos
1st
u
θ
sin
cos
2nd
u
θ
sin
cos
3rd

Figure 10.26 Some commonly used vibration source configurations for generating a traveling wave in a ring motor.[16]

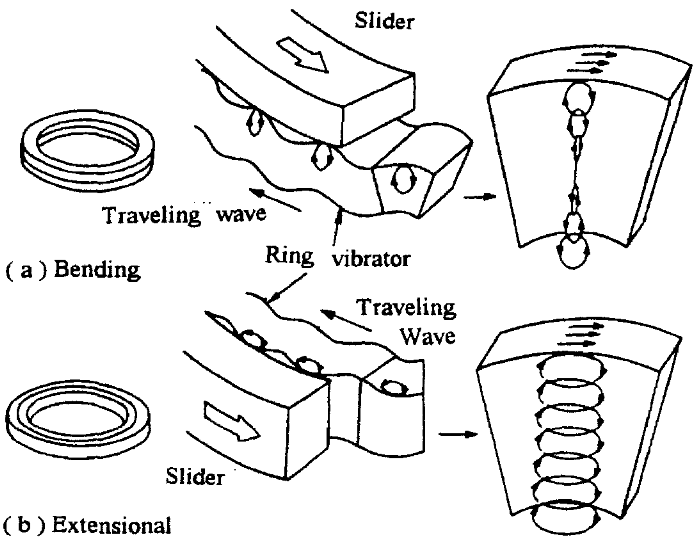
Slider
Traveling wave
(a) Bending
Ring vibrator
Traveling Wave
Slider
(b) Extensional

Figure 10.27 Ring motor displacements for: (a) the bending mode and (b) extensional mode types.[16]

Examples of "Surfing" Rotary Motors

The first successful "surfing" rotory motor was developed by Sashida.[17] The stator structure for this device is pictured schematically in Figure 10.28. A traveling wave is induced in the elastic body by the thin piezoelectric ring to which it is bonded. A ring-shaped slider in contact with the "rippled" surface of the elastic ring can be driven in either the clockwise or counterclockwise direction depending on the phase of the input voltage applied to the piezoelectric. The motor's thin design makes it suitable for installation in a camera as part of the automatic focusing system. Eighty percent of the exchange lenses in Canon's EOS camera series have already been replaced by the ultrasonic motor mechanism. Most of the newer versions of the surfing rotary motor developed in the United States and Japan generally have been variants of this original design.

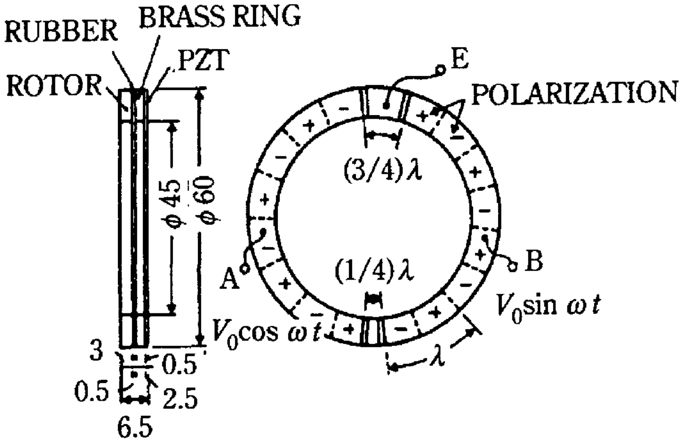

Figure 10.28 Stator structure of the original "surfing" rotary motor developed by Sashida.[17]

The PZT piezoelectric ring is divided into 16 positively and negatively poled regions and two asymmetric electrode gap regions so as to generate a 9th mode traveling wave at 44 kHz. The electrode configuration for this design is asymmetric and requires more complex lead connections than the simple basic structure described in the previous section.

A photograph and a side view schematic of the motor appear in Figures 10.29 and 10.30, respectively. It is comprised of a 2.5 mm thick brass ring with a 60 mm outer diameter and a 45 mm inner diameter bonded onto a 5 mm thick PZT ceramic ring with divided electrodes printed on the back side. The rotor is a polymer ring that has been coated with a hard rubber or polyurethane. The motor speed is plotted as a function of torque for several levels of applied voltage in Figure 10.31.

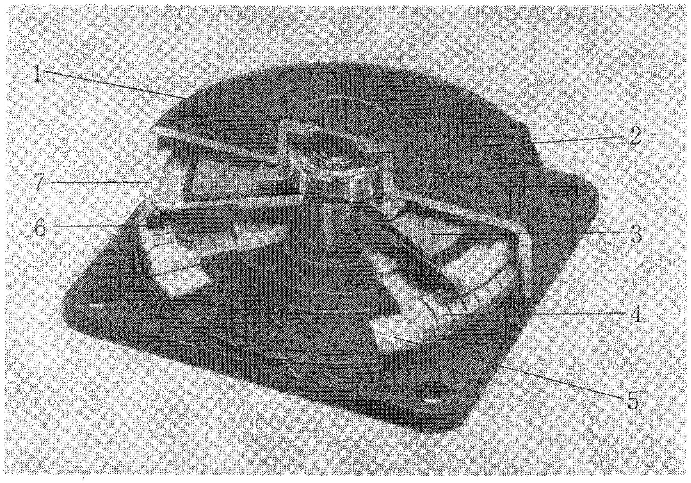

Figure 10.29 Photograph of the Sashida's surfing rotary motor (Shinsei Industry).[17] [1. housing, 2. bearing, 3. spring, 4. stator, 5. PZT ring, 6. contact material, 7. rotor]

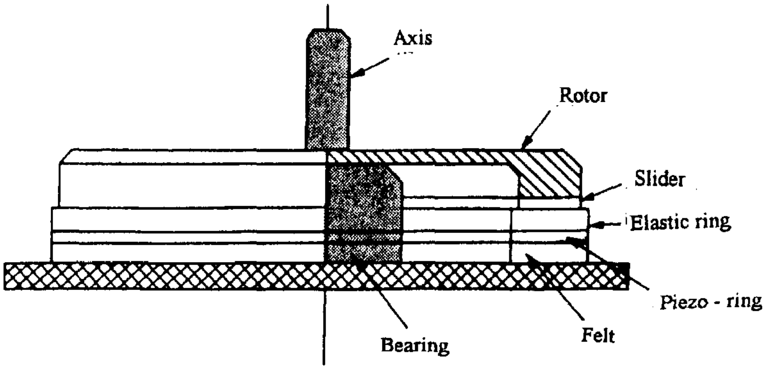

Figure 10.30 A side view schematic of Sashida's surfing rotary motor.[17]

The automatic focusing mechanism incorporating this rotary motor that was developed for the Canon camera is pictured in Figure 10.32.[17] The placement of two motors in the system is shown in Figure 10.32(a). The compact size of the device allows it to fit nicely above and beneath the lens array. A more detailed view of the motor's contact with the lens components appears in Figure 10.32(b). The stator actually has a ring of teeth, positioned on an antinode circle as pictured in Figure 10.33(a), which effectively amplifies the transverse elliptical displacement and increase the speed. The lens position is shifted by means of the screw mechanism shown in Figure 10.32(b).

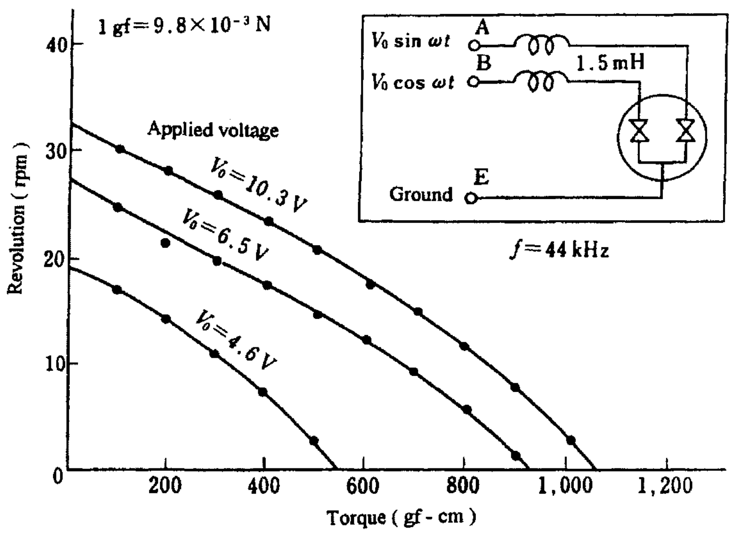

Figure 10.31 The surfing motor speed plotted as a function of torque for several levels of applied voltage.[17]

The advantages of this motor over a conventional electromagnetic motor are:

1. Silent Drive: due to the ultrasonic operating frequency and the absence of a gear mechanism. This makes the system especially suitable for video cameras with microphones.
2. Compact Size: allowing it to be incorporated in a space efficient manner in systems such as the automatic focusing camera.
3. High Speed: since the motor requires no gear mechanism, it can operate at higher speeds than its electromagnetic counterpart.
4. Energy Saving: this compact, self-contained motor unit is highly efficient.

One important consideration in the design of these traveling wave motors concerns the support of the stator. The nodal points or lines of a standing wave motor are stationary and thus serve as ideal contact points for the support structure. A traveling wave device will not have this feature and care must be taken in selecting and making contact with the support points such that the bending vibration is not significantly suppressed. The stator for this motor is supported along an axial direction with a felt interface to establish a "gentle" frictional contact as shown in Figure 10.32(b). The rotation of the stator is stopped by means of pins, which latch onto the stator teeth when engaged. An alternative means of support for a traveling wave stator has been proposed by Matsushita Electric. It is essentially a nodal line support method applied to a higher order vibration mode as illustrated in Figure 10.33(b).[18] Note the relative position of the nodal circle used for support with respect to the placement of the stator teeth on an adjacent antinodal circle as depicted in Figure 10.33(a).

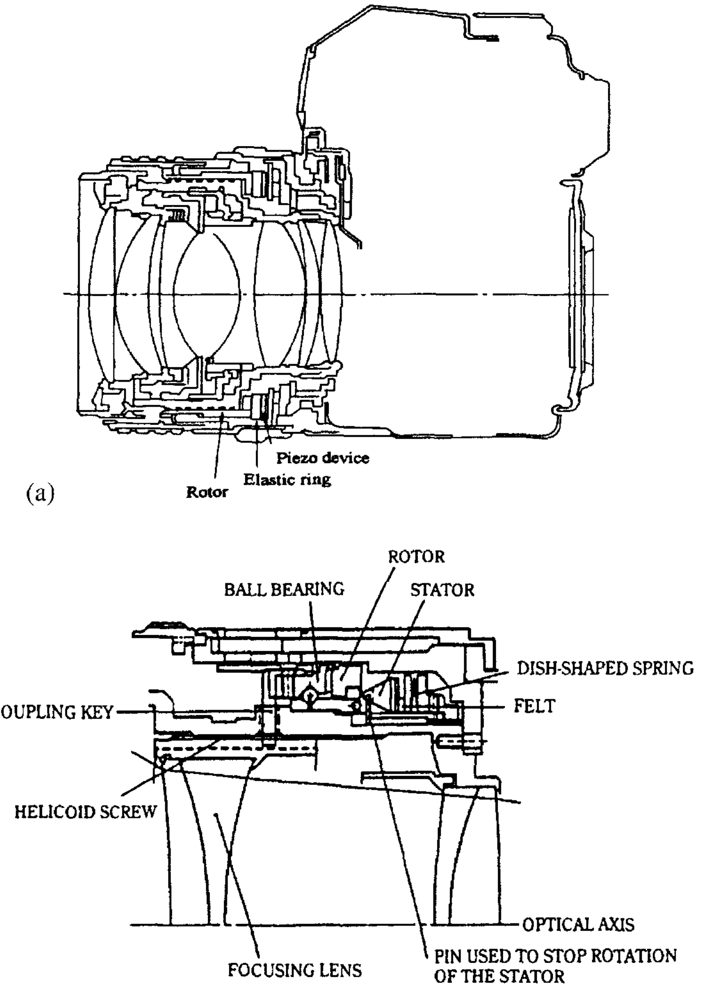
Piezo device
Elastic ring
Rotor
(a)
ROTOR
BALL BEARING
STATOR
DISH-SHAPED SPRING
FELT
COUPLING KEY
HELICOID SCREW
OPTICAL AXIS
PIN USED TO STOP ROTATION OF THE STATOR
FOCUSING LENS
(b)

Figure 10.32 The automatic focusing mechanism, developed by Canon, incorporating the surfing rotary motor: (a) placement of two motors in the system and (b) detail showing the motor's contact with the lens components.[17]

A much smaller version of this basic surfing motor design, measuring only 10 mm in diameter and 4.5 mm in thickness, has been produced by Seiko Instruments.[19]

The structure of this miniature motor is pictured in Figure 10.34. When it is driven with a driving voltage of 3 V and a current of 60 mA a no-load speed of 6000 rev/min with a torque of 0.1 mN.m is generated. Smaller motors similar to these have also been developed by Allied Signal to be used as mechanical switches for launching missiles.[20]

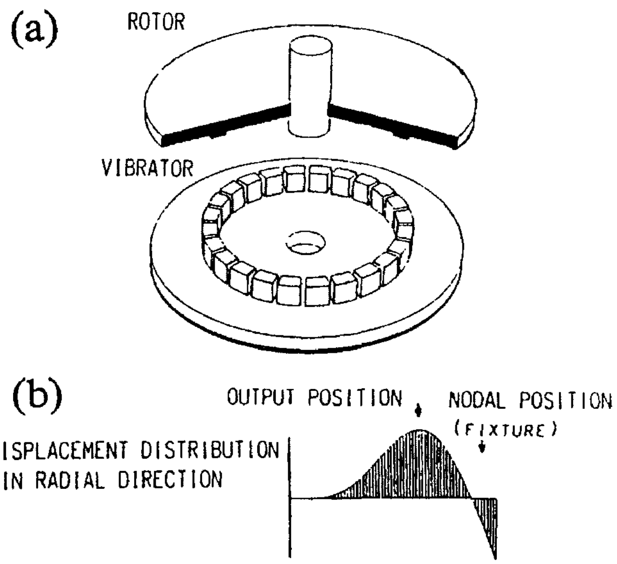

Figure 10.33 Support mechanism for the surfing rotary motor stator: (a) a ring of teeth is placed on an antinodal circle and (b) the support is placed on a nodal circle associated with a higher order vibration mode.[18]

Simple disk structures are preferable over unimorphs for motors because the bending action of the unimorph cannot generate sufficient mechanical power and its electromechanical coupling factor is generally less than 10%.[21,22] Therefore, instead of the unimorph structure, a simple disk is generally used in these motors. The (1,1), (2,1) and (3,1) vibration modes of a simple disk, which are axial-asymmetric modes, are depicted in Figure 10.35. Excitation of these modes can produce a rotation of the inner and outer circumferences, resulting in "hula hoop" action.

An interesting design referred to as the "spinning plate" motor is pictured in Figure 10.36.[23] A combination rotary/bending vibration is excited in a PZT rod when sine and cosine voltages are applied to the divided electrodes. The inner surface of a cup-like rotor is brought in contact with the "spinning" rod to produce the rotation.

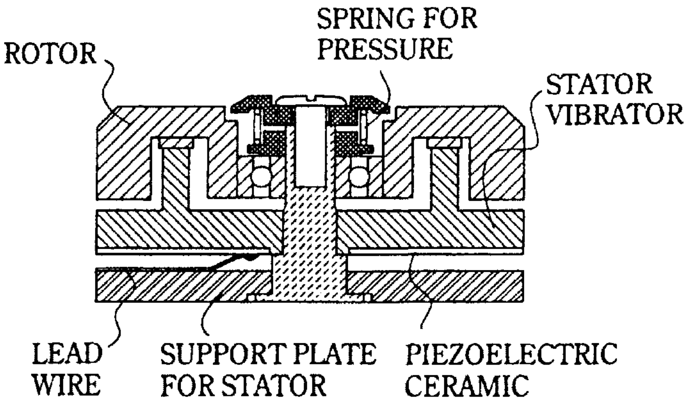
SPRING FOR PRESSURE
ROTOR
STATOR VIBRATOR
LEAD WIRE
SUPPORT PLATE FOR STATOR
PIEZOELECTRIC CERAMIC

Figure 10.34 A miniature version of the surfing rotary motor design produced by Seiko Instruments.[19] [Diameter: 10 mm, thickness: 4.5 mm]

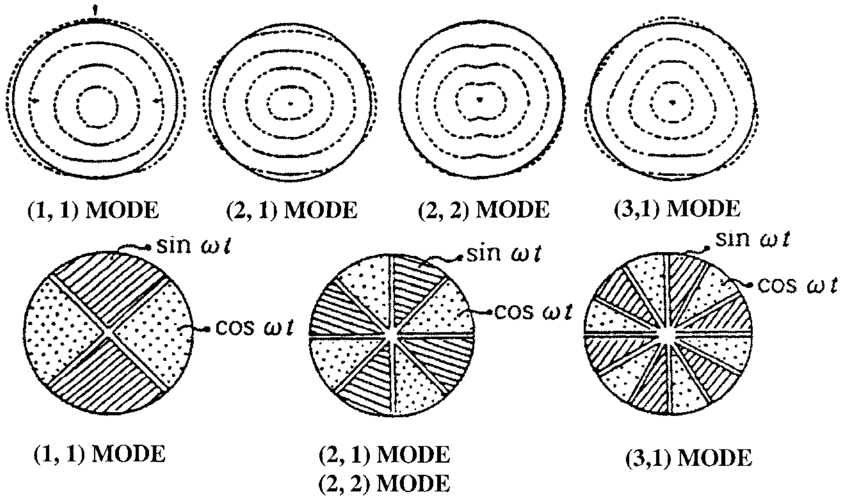
(1, 1) MODE
(2, 1) MODE
(2, 2) MODE
(3,1) MODE
sin ωt
cos ωt
(1, 1) MODE
sin ωt
cos ωt
(2, 1) MODE
(2, 2) MODE
sin ωt
cos ωt
(3,1) MODE

Figure 10.35 A disk-shaped "hula hoop" rotary motor.[21, 22]

10.5 MODE ROTATION MOTORS

The PZT tube motor pictured in Figure 10.37, which was developed jointly by researchers at the Pennsylvania State University and the Institute of Materials Research and Engineering in Singapore, has a long, thin configuration.[24] It is similar to the Tokin motor[23] in appearance, but the mechanism for its operation is quite different. Four segmented electrodes are applied to the PZT tube (having an outer diameter of either 1.5 mm or 2.2 mm) and it is uniformly poled along the radial direction. A rotary bending mode of vibration is excited in the PZT cylinder when sine and cosine voltages are applied to the segmented electrodes as shown in Figure 10.37. The vibrating PZT stator thus simultaneously drives the two rotors in contact with each end of the wobbling cylinder. The motion is analogous to that produced by the "spinning plate" motor operated by a four-phase drive voltage.

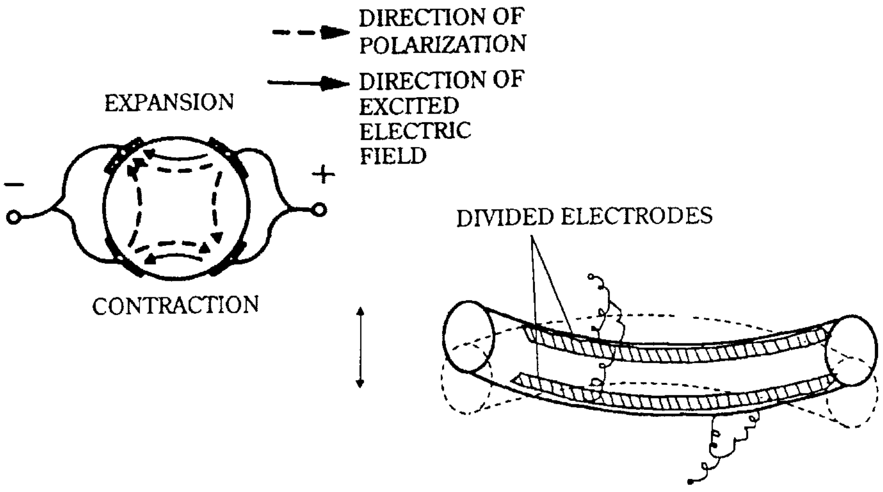
DIRECTION OF POLARIZATION
DIRECTION OF EXCITED ELECTRIC FIELD
EXPANSION
−
+
CONTRACTION
DIVIDED ELECTRODES

Figure 10.36 The "spinning plate" rotary motor.[23]

A PZT tube motor of this type with inner and outer diameters of 1.5 mm and 2.2 mm, respectively, 7 mm in length, and having a mass of 0.3 g generates a torque of 0.1 mNm and has a no-load speed of 1000-2000 rpm. The specifications for the PZT tube motor with those of two other commercially available motors appear in Table 10.2. A tube motor of this size generally has an efficiency of more than 20%, which is about one order of magnitude higher than that exhibited by the electromagnetic motors. The power density of the PZT tube motor exceeds that of the Seiko motor by about one order of magnitude which is due primarily to the utilization of the rotary bending mode of vibration in the operation of the device. The tube motor is highly suitable for a variety of precision micromechanical applications, such as intravascular medical microsurgery. The primary disadvantage of this design lies with the difficulty in manufacturing the delicate PZT tubes with the required degree of uniformity in wall thickness and cylinder symmetry, which leads to a rather high manufacturing cost. The metal tube motor is thus a less expensive alternative for these types of applications.

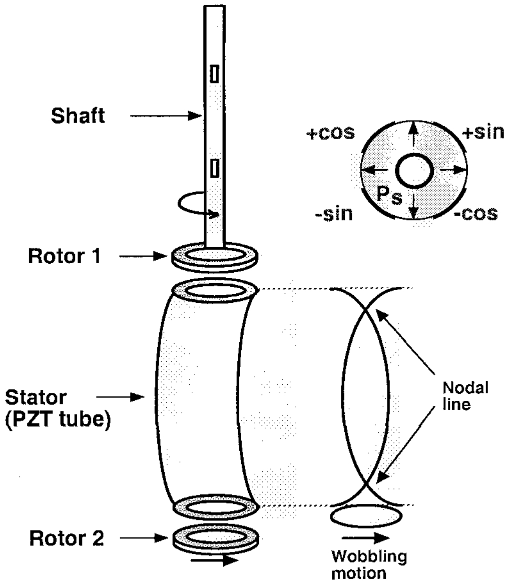
Shaft
Rotor 1
Stator
(PZT tube)
Rotor 2
+cos
+sin
-sin
-cos
Ps
Nodal line
Wobbling motion

Figure 10.37 The PZT tube motor developed by researchers at Penn State and the Institute of Materials Research and Engineering in Singapore.[24]

Table 10.2 The specifications for the PSU/IMRE tube motor and two other commercially available motors.

	Motorola Electromagnetic Micromotor	Sieko Ultrasonic Micromotor	PSU/IMRE Ultrasonic Micromotor
Outer Diameter (mm)	7	8	2.2
Length (mm)	16	4.5	8
Input Power (V)	1.5	1.5-3.5*	3-6*
(mA)	126	60-12	2-5
No-Load Speed (rpm)	5000	1200	1000-2000
Starting Torque (mNm)	0.075	0.05-0.1	0.1

* A booster circuit is required.

10.6 PERFORMANCE COMPARISON AMONG VARIOUS ULTRASONIC MOTORS

The standing wave motors are generally among the least expensive, primarily because they require only a single vibration source. This type also offers an exceptionally high efficiency (as high as 98% theoretically), but the motion in both the clockwise and counterclockwise directions is generally not well controlled. Traveling wave type motors require more than one vibration source to generate the propagating wave, leading to a much lower efficiency (typically not more than 50%), but its rotational motion is generally far more controllable. The performance characteristics of three motors representing the standing wave type (vibratory coupler), a hybrid type ("compromise teeth vibrator"), and the traveling wave type are summarized in Table 10.3.[25]

Table 10.3 The performance characteristics of three motors representing the standing wave type (a vibratory coupler by Hitachi Maxel), a hybrid type (the "compromise teeth vibrator" by Matsushita), and the traveling wave type (by Shinsei Industry).[25]

CHARACTERISTICS TYPES	Rotation	Rotation Speed [rpm]	Rotation Torque [kgf·cm]	Efficiency [%]	Size	Analogy
Vibratory Coupler Type 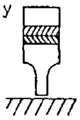	Uni-Direction	600	13	80	Slim & Long	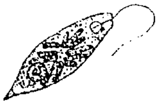 Euglena
Compromise Type 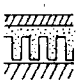	Reversible	600	1	45	⋮	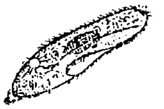 Paramecium
Surface Wave Type 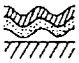	Reversible	600	0.5	30	Wide & Thin	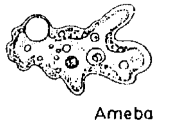 Ameba

The traveling wave motor does not lend itself well to miniaturization. A sufficient gap between adjacent electrodes is required to ensure proper insulation between them. During electrical poling, which involves alternating the polarity across adjacent poled regions in the ceramic, cracks readily develop in the electrode gap regions where residual stresses tend to concentrate. This problem ultimately precludes any further miniaturization of the traveling wave type of motor. Standing wave motors, on the other hand, with their much simpler structures, are much better suited for miniaturization. They simply require a uniformly poled piezoelectric element, a few lead wires, and a single power supply.

Another problem associated with the traveling wave motor concerns the support of the stator. In the case of a standing wave motor, the nodal points or lines are generally supported, which has a minimum effect on the resonance vibration. A traveling wave does not have stable nodal points or lines and therefore relatively elaborate support structures must be designed that will not significantly suppress the bending vibration. One of the simplest means is the method previously described that is depicted in Figure 10.28, whereby the stator is supported along an axial direction with a layer of felt between the pieces to minimize the damping effects on the vibration.

In general, the following design concepts must be optimized in the development of new microscale ultrasonic motors:

1. A *simple structure* for which the number of components is as small as possible is desirable.
2. A *simple poling configuration* should be utilized.
3. It is best to *minimize the number of vibration sources* and drive circuit components required for operation. (Standing wave motors meet this requirement nicely.)

10.7 MICROSCALE WALKING MACHINES

Current advances in biomedical research and ultraprecise surgical techniques require sophisticated tiny actuators for manipulation of such tools as optical fibers, catheters, and microscale surgical blades. Microscale walking devices are especially attractive for applications such as these and thus much research related to the development of the tiny walkers has been underway in recent years.

(1) PVDF Walker

Two early designs for PVDF bimorph walking machines are pictured in Figure 10.38.[26] The devices were fabricated from two PVDF films, each with a thickness of 30 μm, bonded together and bent with a curvature of 1 cm^{-1}. The legs of the walker are of slightly different widths so that there will be a difference between their resonance frequencies so that the leg movement required for both clockwise and counterclockwise rotations of the device will be possible.

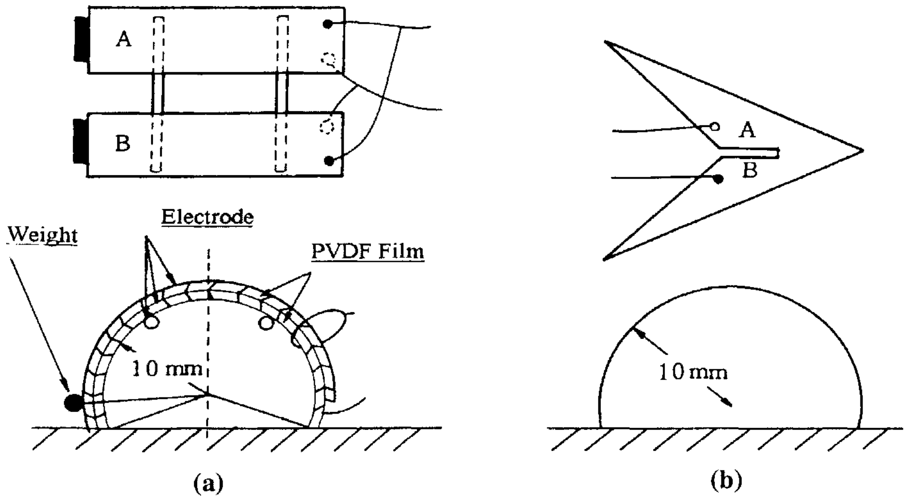
A
B
Electrode
Weight
PVDF Film
10 mm
(a)
A
B
10 mm
(b)

Figure 10.38 Two early designs for PVDF bimorph walking machines: (a) the arch and (b) the triangular configurations.[26]

(2) A Ceramic Multilayer Ultrasonic Motor

Schematic diagrams of a ceramic multilayer motor and its electrode pattern are pictured in Figure 10.39.[27] Longitudinal (L_1) and bending (B_2) modes are simultaneously excited in the device when the appropriate input signals are applied to the external electrodes. The speed and efficiency of the motor is shown as a function of load in Figure 10.40.

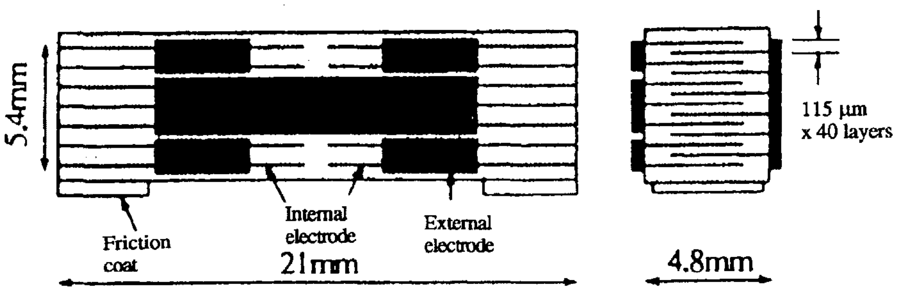
5.4mm
Friction coat
Internal electrode
External electrode
21mm
115 μm x 40 layers
4.8mm

Figure 10.39 A simple ceramic multilayer linear ultrasonic motor.[27]

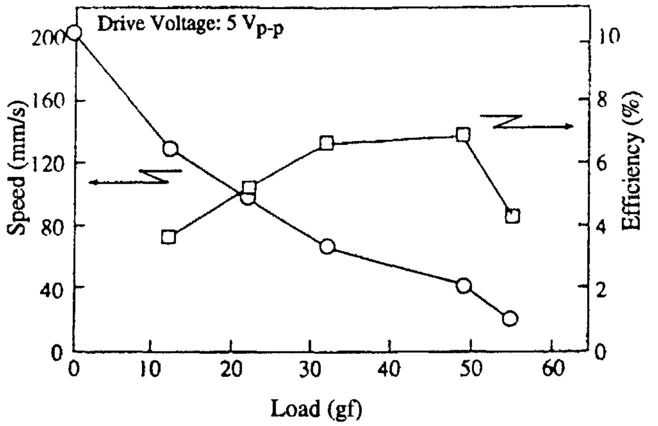

Figure 10.40 The speed and efficiency of the ceramic multilayer linear ultrasonic motor as a function of load.[27]

(3) Ultrasonic Motor Vehicles

The Mussierkun toy developed by Seiko Instruments is a tiny vehicle with dimensions 10x10x10 mm^3 incorporating ultrasonic motors 8 mm in diameter. The toy is activated by illuminating an optical sensor in Mussierkun's eye.[28]

A four-wheel vehicle (7 x 7 x 7 mm^3) produced by researchers at the Pennsylvania State University is pictured in Figure 10.41.[29] It is driven by two metal tube motors (4 mm in length). The forward, backward, and sideways motions of the vehicle are controlled by a joystick remote control device.

10.8 CALCULATIONS FOR THE SPEED AND THRUST OF ULTRASONIC MOTORS

Calculations for the speed and thrust of an ultrasonic motor include parameters associated with both the type of motor and the contact conditions between the slider and the stator portions of the device. The contact models typically employed represent the following conditions: (1) rigid slider and rigid stator, (2) compliant slider and rigid stator, and (3) compliant slider and compliant stator. Further, the pulsed drive for the vibratory coupler type motor and the continuous drive of a surface wave type must be incorporated into the calculation.

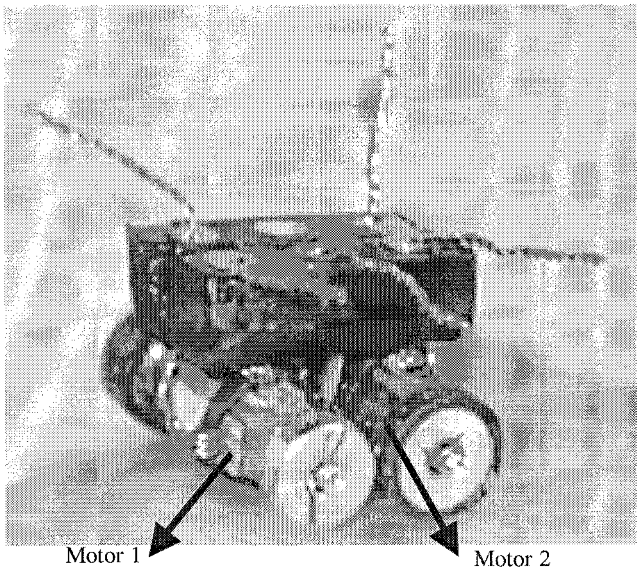

Figure 10.41 A four-wheel vehicle (7 x 7 x 7 mm^3) produced by researchers at the Pennsylvania State University, utilizing two metal tube motors.[29]

(1) Surface Wave Motor Calculations

The rigid slider and rigid stator contact model is employed in the analysis of surface wave motors. The slider speed can be obtained from the horizontal velocity of the stator surface portion of the stator as it undergoes the displacement depicted in Figure 10.42. The phase velocity of the vibration, v_{sw}, is simply given by:

$$v_{sw} = f\lambda \tag{10.13}$$

where f is the frequency and λ the wavelength of the stator vibration. The speed of the slider, v, is described by:

$$v = \frac{(4\pi^2)Ze_o f}{\lambda} \tag{10.14}$$

where Z is the transverse vibration amplitude and e_o is the distance between the surface and the neutral plane as shown in Figure 10.42.

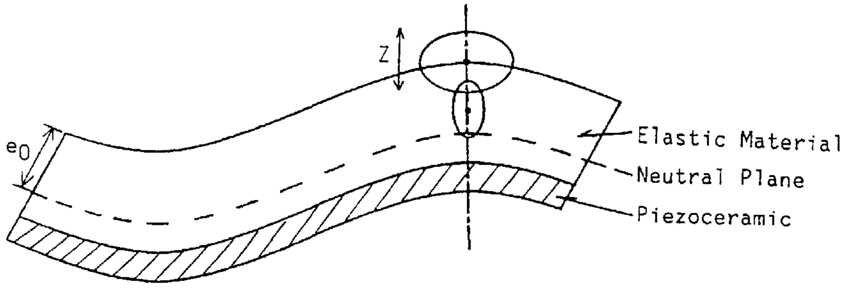

Figure 10.42 Stator displacement of a surface wave type motor.

Example Problem 10.2

Calculate the phase velocity of the surface vibration, v_{sw}, and the slider speed, v, for a surface wave type motor, using the following typical measured values: bulk vibration velocity: 5050 (m/s), vibration frequency: 30 (kHz), vibration wavelength: $\lambda = 28$ (mm), distance e_0: 3.5 (mm), and transverse surface vibration amplitude: 1 (μm).

Solution

Using the known values of vibration frequency and wavelength the phase velocity of the surface vibration is calculated as follows:

$$v_{sw} = f\lambda = [30\text{x}10^{3}\,(\text{Hz})]\,[28\text{x}10^{-3}\,(\text{m})] \qquad \text{(P10.2.1)}$$

$$\rightarrow\rightarrow \quad v_{sw} = 850\,(\text{m/s})$$

which is found to be much slower than the bulk vibration velocity.

The slider speed may be determined from the given data according to the following:

$$v = \frac{(4\pi^2)Ze_0 f}{\lambda} \qquad \text{(P10.2.2)}$$

$$= \frac{(4\pi^2)[1\text{x}10^{-6}\,(\text{m})][3.5\text{x}10^{-3}\,(\text{m})][30\text{x}10^{3}\,(\text{Hz})]}{[28\text{x}10^{-3}\,(\text{m})]}$$

$$\rightarrow\rightarrow \quad v = 150\,(\text{mm/s})$$

which is considerably slower than the bulk vibration velocity!

(2) Vibration Coupler Motor Calculations

The compliant slider and rigid stator contact model is employed in the analysis of vibration coupler motors. The horizontal and vertical displacements of the rigid stator shown as a and b, respectively, in Fig. 10.43, are described by:

$$a = a_o\,[\cos(\omega t)] \quad \text{and} \quad b = b_o\,[\sin(\omega t)] \tag{10.15}$$

The horizontal speed of the stator may thus be expressed as:

$$v_h = \frac{\partial a}{\partial t} = -a_o\omega[\sin(\omega t)] \tag{10.16}$$

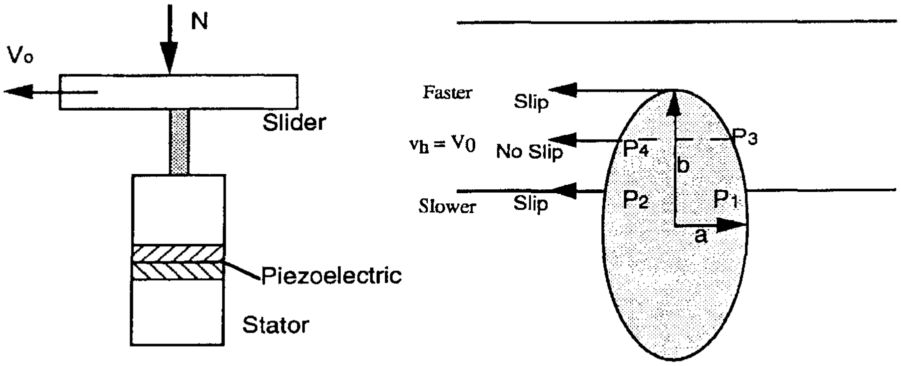

Figure 10.43 The vibration coupler motor: (a) schematic depiction of the motor structure and (b) the displacement of the stator.

The normal force, n, is plotted as a function of phase, ωt, in Figure 10.44. The curve shown is defined as:

Slider and Stator in Contact: $(\pi/2-\phi/2) < \omega t < (\pi/2+\phi/2)$

$$n = \beta[\sin(\omega t) - \cos(\phi/2)] \tag{10.17a}$$

Slider and Stator Not in Contact: $0 < \omega t < (\pi/2-\phi/2)$ and $(\pi/2-\phi/2) < \omega t < (2\pi)$

$$n = 0 \tag{10.17b}$$

where ϕ is a measure of the contact period as shown in Figure 10.44 and β is a parameter defined in the analysis that follows.

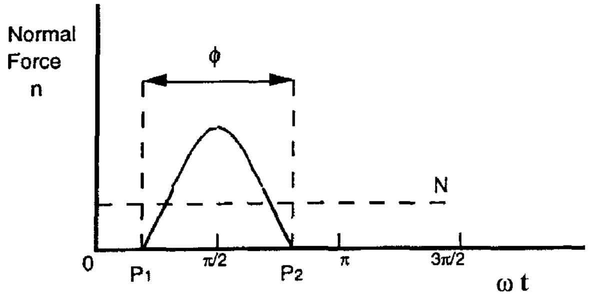

Figure 10.44 The normal force acting for a vibratory coupler motor plotted as a function of phase.

The integrated normal force, N, is given by:

$$N = \int n\, d(\omega t)$$

$$= \left(\frac{1}{2\pi}\right) \int_{\pi/2-\phi/2}^{\pi/2+\phi/2} \beta[\sin(\omega t) - \cos(\phi/2)]\, d(\omega t)$$

$$N = \left(\frac{\beta}{\pi}\right)[\sin(\phi/2) - (\phi/2)\cos(\phi/2)] \tag{10.18}$$

from which we may define the parameter, β, as:

$$\beta = \frac{\pi N}{[\sin(\phi/2) - (\phi/2)\cos(\phi/2)]} \tag{10.19}$$

The no-load slider speed corresponds to the average horizontal stator speed (v_h), and is identified as v_o in the plot of v_h as a function of phase (ωt) in Figure 10.45. It is thus evaluated over the phase interval between P_1 and P_2 by:

$$v_o = \int v_h\, d(\omega t)$$

$$= \left(\frac{1}{\phi}\right) \int_{\pi/2-\phi/2}^{\pi/2+\phi/2} -a_o\omega\, [\sin(\omega t)]\, d(\omega t)$$

$$v_o = \frac{-a_o\omega[\sin(\phi/2)]}{(\phi/2)} \tag{10.20}$$

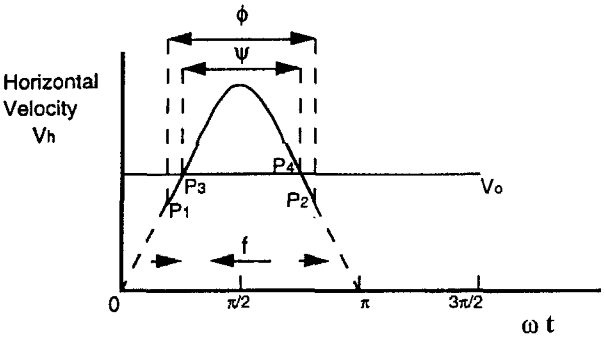

Figure 10.45 The horizontal stator speed of a vibratory coupler motor plotted as a function of phase.

When the phase conditions identified by P_3 and P_4 in Figure 10.45 exist, no slip is observed and

$$v_h = v_o = -a_o\omega[\cos(\psi/2)] \tag{10.21}$$

Comparison of Equations (10.20) and (10.21) indicates that:

$$\cos(\psi/2) = \frac{\sin(\phi/2)}{(\phi/2)} \tag{10.22}$$

The frictional force, **f**, is defined in terms of the kinetic coefficient of friction between the slider and the stator, μ_k, and under conditions where it acts as an accelerating force or a drag force it is expressed as follows:

Accelerating Force: $(\pi/2-\psi/2) < \omega t < (\pi/2+\psi/2)$

$$\mathbf{f} = \mu_k n \tag{10.23a}$$

Dragging Force: $(\pi/2-\phi/2) < \omega t < (\pi/2-\psi/2)$ and $(\pi/2-\psi/2) < \omega t < (\pi/2 + \phi/2)$

$$\mathbf{f} = -\mu_k n \tag{10.23b}$$

The magnitude of the maximum thrust, F, is given by the integrated frictional force as:

$$F = \int f\, d(\omega t)$$

$$= \left(\frac{1}{2\pi}\right) \int_{\pi/2-\phi/2}^{\pi/2+\phi/2} \mu_k \beta[\Gamma(\omega t)]d(\omega t)$$

$$= \left(\frac{\mu_k \beta}{2\pi}\right) \left[\int_{\pi/2-\phi/2}^{\pi/2-\psi/2} [\Gamma(\omega t)]d(\omega t) - \int_{\pi/2-\psi/2}^{\pi/2+\psi/2} [\Gamma(\omega t)]d(\omega t) + \int_{\pi/2+\psi/2}^{\pi/2+\phi/2} [\Gamma(\omega t)]d(\omega t) \right]$$

where $\Gamma(\omega t) \equiv \sin(\omega t) - \cos(\phi / 2)$.

Integrating yields:

$$F = \mu_k N \left[1 - \frac{[\sin(\psi/2) - (\psi/2)\cos(\phi/2)]}{[\sin(\phi/2) - (\phi/2)\cos(\phi/2)]} \right] \qquad (10.24)$$

When $\psi < \phi << 1$:

$$F \approx \mu_k N[1 - 2(\psi/\phi)] \approx \mu_k N[1 - 2(1/\sqrt{3})] \qquad (10.25)$$

When $\phi=0$ and $\psi=0$, $v_o= -a_o\omega$ and $F= -0.155\mu_k N$. When $\phi=\pi$ and $\cos(\psi/2)= 2/\pi$, $v_o=-(2/\pi)a_o\omega$ and $F= -0.542\mu_k N$. So we see, in general, that as the contact period, ϕ, is increased, the thrust, F, increases at the expense of the slider speed.

In summary, if the contact period, ϕ, under a certain normal force, N, can be determined experimentally or theoretically, the no-load speed, v_o, can be calculated from Equation (10.20) and the no-slip position angle, ψ, from Equation (10.22). The thrust, F, can then be obtained from Equation (10.24).

10.9 ELEMENTS OF DESIGNING AN ULTRASONIC MOTOR

The process for designing an ultrasonic motor will be demonstrated for the π-shaped linear motors pictured in Figure 10.46. A multilayer type is depicted in Figure 10.46(a)[30] and a bimorph type in Figure 10.46(b). We will follow the process outlined in the design flowchart presented in Figure 10.47.

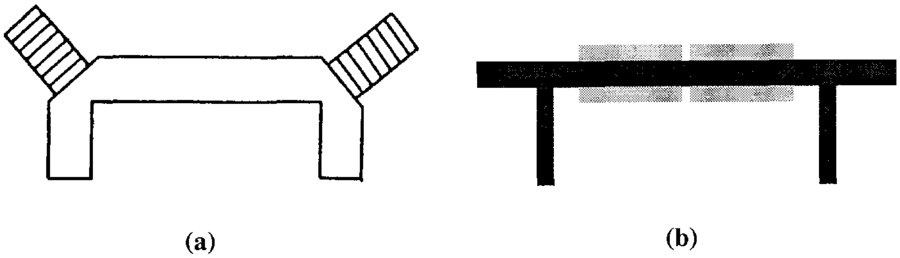

Figure 10.46 Two π-shaped linear motors: (a) a multilayer type[30] and (b) a bimorph type.

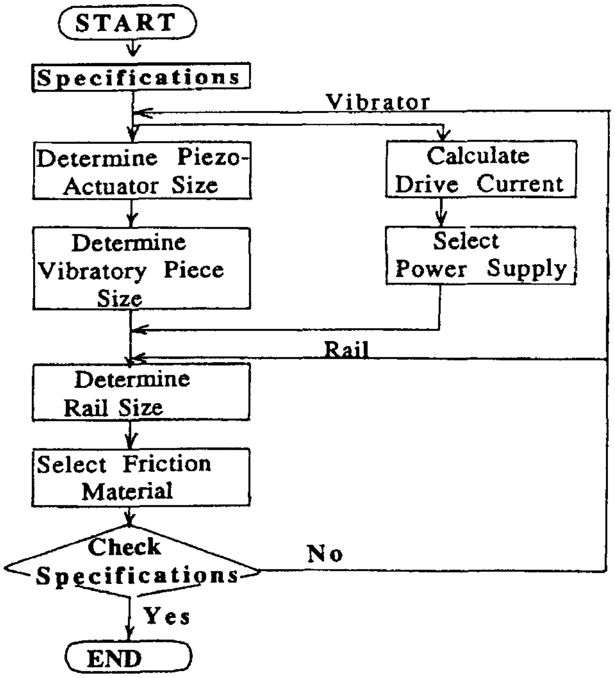
START
Specifications
Vibrator
Determine Piezo-Actuator Size
Calculate Drive Current
Determine Vibratory Piece Size
Select Power Supply
Rail
Determine Rail Size
Select Friction Material
Check Specifications
No
Yes
END

Figure 10.47 A flowchart for the design of an ultrasonic motor.

(1) Defining the Specifications of the Device

Let us assume that the customer has provided the following required specifications for a π-shaped linear motor:

Table 10.4 Desired Specifications for a π-shaped linear motor.

Thrust (gf)	200
Speed (cm/s)	20
Size (mm^3)	20 x 40 x 5
Drive Frequency (kHz)	90

(2) Determining the Size of the Piezoelectric Actuator

The size of the piezoelectric actuator is determined largely by the resonance frequency at which it will be operated. The π-shaped multilayer motor requires an actuator that will be operated in a thickness longitudinal mode of vibration. The resonance frequency for the desired vibrational mode is given by:

$$f_r = \left(\frac{1}{2l}\right)\sqrt{\frac{1}{\rho s_{33}^D}} \tag{10.26}$$

Assuming a mass density for the ceramic of $\rho=7.8\text{x}10^3$ (kg/m^3), a compliance of $s_{33}^D=25\text{x}10^{-12}$ (m^2/N), and a length $l=9$ (mm), the resonance frequency for the thickness longitudinal mode will be:

$$f_r = \left(\frac{1}{2[9\text{x}10^{-3}\,(\text{m})]}\right)\sqrt{\frac{1}{[7.8\text{x}10^3\,(\text{kg}/\text{m}^3)][25\text{x}10^{-12}\,(\text{m}^2/\text{N})]}}$$

$$\to\to\ f_r = 1.25\text{x}10^5\,(\text{Hz})$$

The resonance frequency of the piezoelectric actuator should actually be selected slightly higher than the drive frequency to allow for the presence of the vibratory piece, which will be installed later. The size of the multilayer actuator produced by NEC/Tokin is about 5x5x9 (mm^3).

(3) Determing the Size of the Vibratory Piece

The two legs and cross bar of the π-shaped structure are referred to as the "cantilevers" and the "free bar," respectively. The resonance frequency for both is described by a general equation of the form:

$$f = \left(\frac{\alpha_m^2}{2\sqrt{3}\,(2\pi)}\right)\left(\frac{t}{l^2}\right)\sqrt{\frac{Y}{\rho}} \tag{10.27}$$

where l is the length of the element, t is its thickness, Y is Young's modulus, ρ is the mass density, and α_m is a parameter determined by the vibration mode. Values for α_m are given in Figure 10.48 for the first three resonance modes of the cantilever and free bar elements. The second mode resonance frequencies for the cantilevers (c) and the free bar (b) are thus defined as follows:

$$f_{2c} = 1.01\left(\frac{t}{l_c^2}\right)\sqrt{\frac{Y}{\rho}} \tag{10.28a}$$

$$f_{2b} = 2.83\left(\frac{t}{l_b^2}\right)\sqrt{\frac{Y}{\rho}} \tag{10.28b}$$

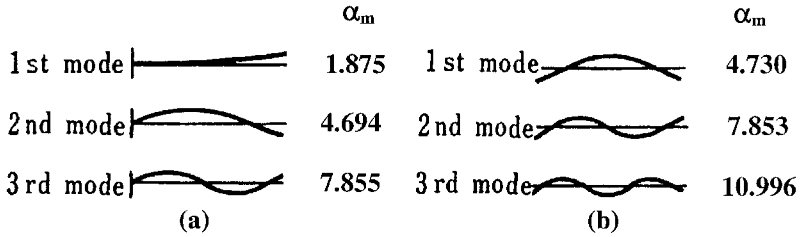

Figure 10.48 Values of the parameter α_m corresponding to the first three resonance modes for the elements of a π-shaped linear motor: (a) the cantilevers and (b) the free bar.

Using the mass density [ρ=2.76x10^3 (kg/m^3)] and Young's modulus [Y=7.03x10^{10} (N/m^2)] for aluminum, and the dimensions determined by finite element analysis indicated in Figure 10.49, the cantilever and free bar second mode resonance frequencies are found to be f_{2c}=255 (kHz) and f_{2b}=106 (kHz).

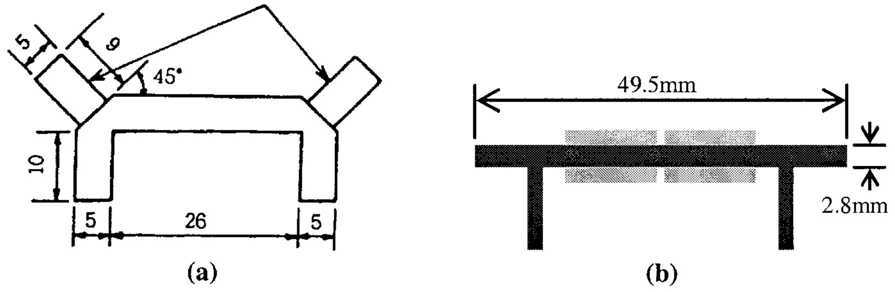

(a) (b)

Figure 10.49 Dimensions of two π-shaped linear motors determined by finite element analysis (FEM): (a) the multilayer type[30] and (b) the bimorph type.

Free vibration analysis is performed using a finite element analysis (FEM) program on the structures. Some results are presented in Figure 10.50. In order to achieve high speed both the longitudinal and flexural modes must be excited at an intermediate drive frequency. Theoretically and experimentally determined resonance frequencies for the bending (L1) and transverse (up and down) vibrational (B4) modes of the cantilever element on a bimorph type π-shaped linear motor are plotted as a function of thickness of the element in Figure 10.51. The data obtained by finite analysis [Figure 10.51(a)] and the experimental results are in good agreement with a discrepancy of less than 4% for both resonance frequencies. It is important for the proper operation of this device that these two resonances are adjusted to the same frequency. We see from the data of Figure 10.51 that this condition is satisfied when the element has a thickness of about 2.8 (mm).

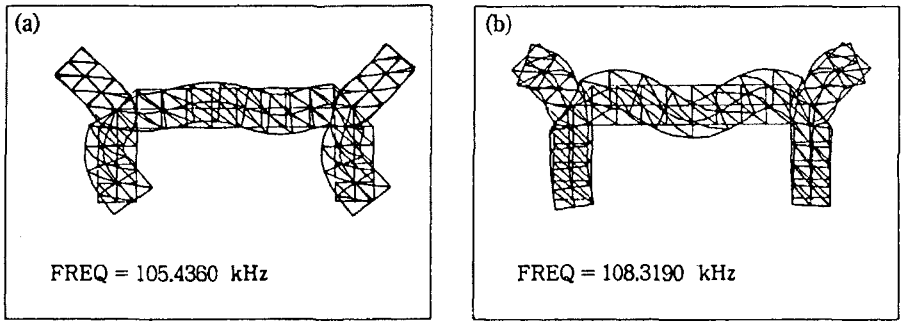

Figure 10.50 Some results of the free vibration finite element analysis on a bimorph type π-shaped linear motor: (a) leg bending is excited at 105 kHz, and (b) transverse leg motion is excited at 108 kHz.

Next, driven vibrational analysis is performed on the device. The trace of the leg movement when a sinusoidal drive is applied to one actuator and a cosine drive on the other as shown in Figure 10.52 is determined. Both actuators are driven at 90 (kHz) with a force of 6 (N). The elliptical loci of the legs' displacement for various positions on the legs are shown at the bottom of Figure 10.52. The counterclockwise rotation of all points produces an efficient drive force against the rail.

(4) Determining the Rail Size

The rail size depends primarily on the motor size. Once this has been decided upon according to the preceding considerations, an appropriate rail configuration can be selected. In the case of the π-shaped motor discussed here, a rail with a cross-section of 5x5 (mm^2) is used.

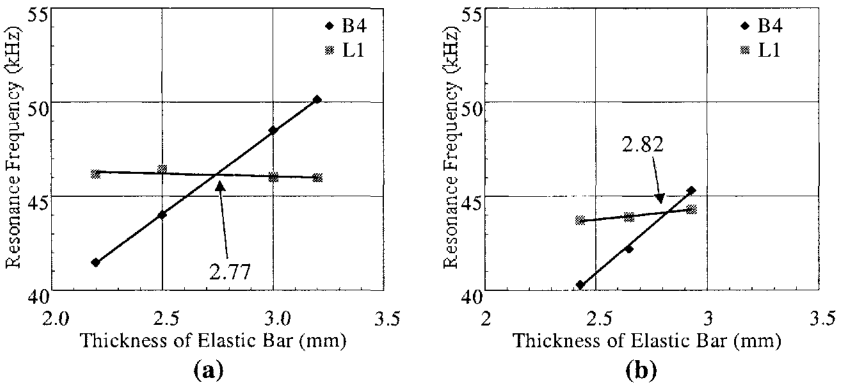

Figure 10.51 Resonance frequencies for the bending (L1) and transverse vibrational (B4) modes of the cantilever element on a bimorph type π-shaped linear motor plotted as a function of thickness determined by: (a) finite element analysis and (b) experiment.

(5) Selecting the Proper Drive Conditions

The resonance frequencies of the ultrasonic motor are measured with an impedance analyzer. Two actuators are connected together with the same polarity for the symmetric modes (a 180° phase difference between the legs), and with the opposite polarity for the antisymmetric modes (a zero phase difference between the legs). Some typical spectra for the π-shaped motor are shown in Figure 10.53.

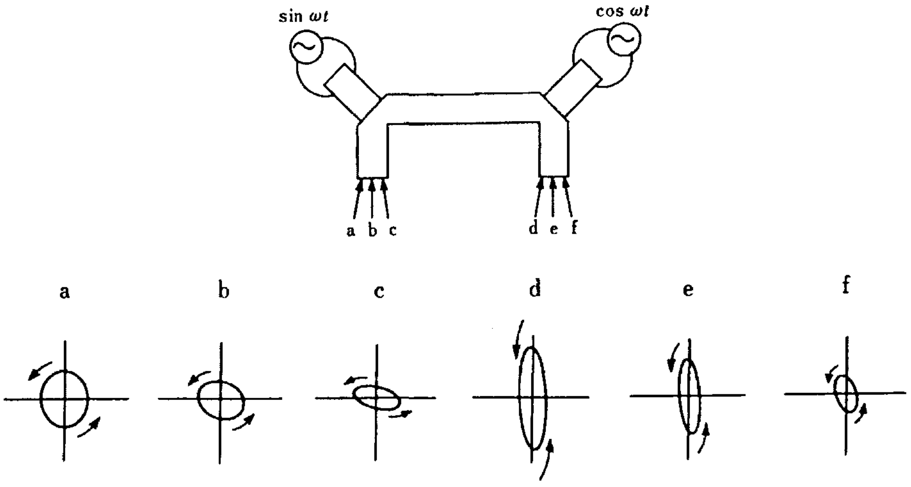

Figure 10.52 Driven vibrational analysis of the π-shaped linear motor.

The motor will be driven most efficiently over the frequency range that extends from a resonance mode that produces a large longitudinal displacement to one corresponding to a large bending displacement. The drive frequency should also fall between the frequencies form symmetric and antisymmetric leg motion, ideally such that there is either a 90° or a –90° phase difference between the legs conducive for the "trotting" motion of the device.

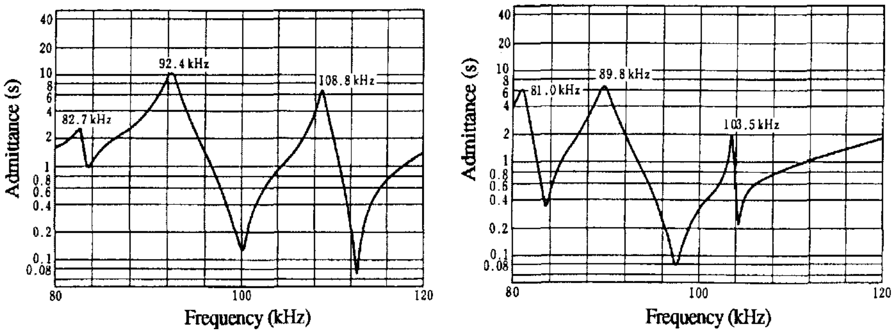

(a) (b)

Figure 10.53 Admittance spectra for a π-shaped ultrasonic motor: (a) the symmetric and (b) and antisymmetric vibration modes.

Driven vibration analysis by FEM typically indicates the same counterclockwise elliptical vibration of both legs. The displacement of the legs can also be examined using a laser Doppler method. Typical data collected by this method for a π-shaped linear ultrasonic motor are summarized in Figure 10.54. We see from these data that there exists a frequency range over which the same rotation direction is produced in both legs. This agrees well with FEM predictions.

(6) Checking the Motor Specifications

The dependence of the motor propagation direction on drive frequency for a π-shaped motor is shown in Figure 10.55, and the speed of the motor as a function of drive voltage and load are shown in Figures 10.56(a) and 10.56(b), respectively. The maximum no-load speed and maximum load are approximately 20 cm/s and 200 gf (20 N), respectively. The propagation direction of the motor is reversed by exchanging the drive signals applied to the two multilayer actuators. Tests of the motor's action in both directions result in similar speed versus drive voltage curves. The measured parameters for the motor thus meet the original device specifications requested by the customer.

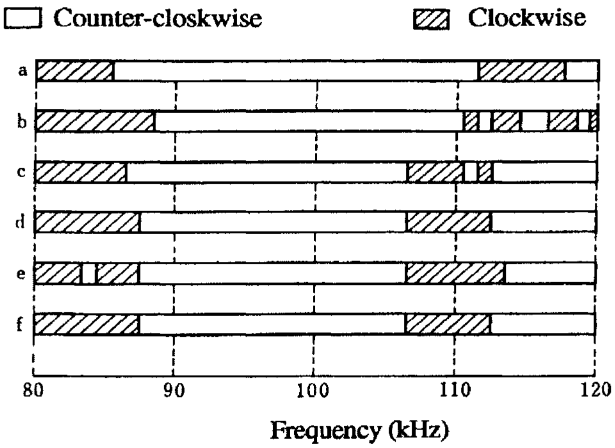

Figure 10.54 Rotation direction of the elliptical vibration of the two legs of a π-shaped ultrasonic linear motor as determined by the laser Doppler method. [a, b, c: first leg, d, e, f: second leg]

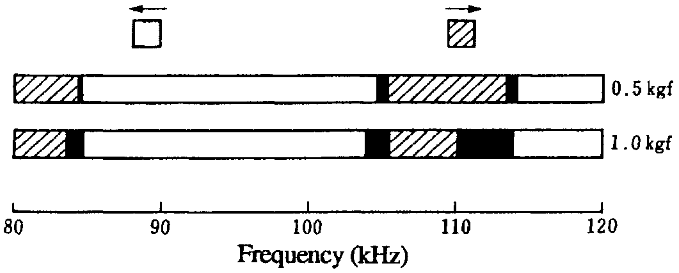

Figure 10.55 The dependence of the motor propagation direction on drive frequency for a π-shaped ultrasonic linear motor.

10.10 OTHER ULTRASONIC MOTOR APPLICATIONS

(1) The Ultrasonic Surgical Knife

The blades of conventional surgical knives tend to become coated with clotted blood during an operation thus impeding the cutting of tissue. Ultrasonic vibration of the knife is an effective means of maintaining a clear blade for longer periods of time during the procedure.[31] The ultrasonic vibration in the vicinity of the cut also helps to accelerate the rate of blood clotting near the wound after the incision is made. A very thin ultrasonic tube-shaped knife has been proposed for fine procedures such as cataract surgery.[32]

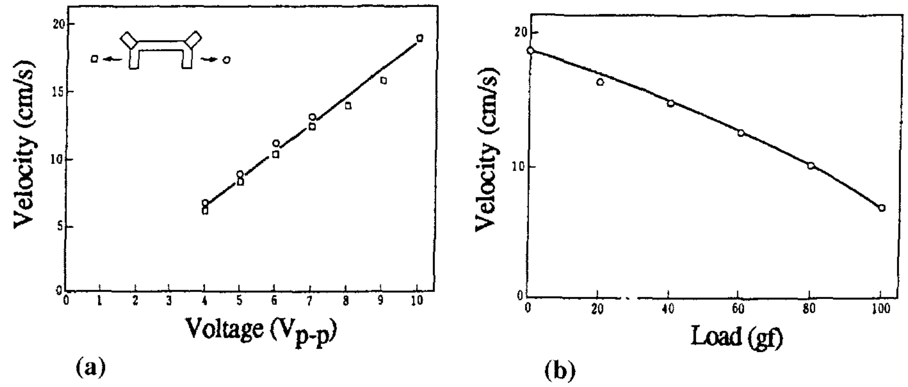

Figure 10.56 Speed of the π-shaped ultrasonic linear motor plotted as a function of: (a) the drive voltage and (b) the load.

(2) The Piezoelectric Fan/Pump

An ultrasonic device designed to displace air is the piezoelectric fan, which has been used for cooling electronic circuits[33] and for suspending particulate substances.[34] Devices designed to displace liquids include piezoelectric pumps, ink jets, and evaporators.[35,36]

Piezoelectric Fans

Some electronic components such as high power transistors generate heat and, therefore, require a local compact cooling system which does not generate electromagnetic noise. A compact piezoelectric fan developed by Piezo Electric Products, Incorporated (PEPI) is shown in Figure 10.57.[37] The device includes a pair of piezoelectric bimorphs which are driven out of phase in order to optimize the fan action. A flexible blade attached to a weight is installed at the tip of each bimorph. This configuration causes the bottom and the top of the blade to have a phase difference of 90° when driven by the bimorph so that it executes a motion similar to a swimming fish. A piezoelectric fan unit with dimensions 4 x 2 x 1.2 cm^3 is capable of decreasing the heat generated from a 30 W heater to several mW. Compact piezoelectric fans with a similar design are also fabricated by Misuzu-Erie and Nippon Denso[38] of Japan.

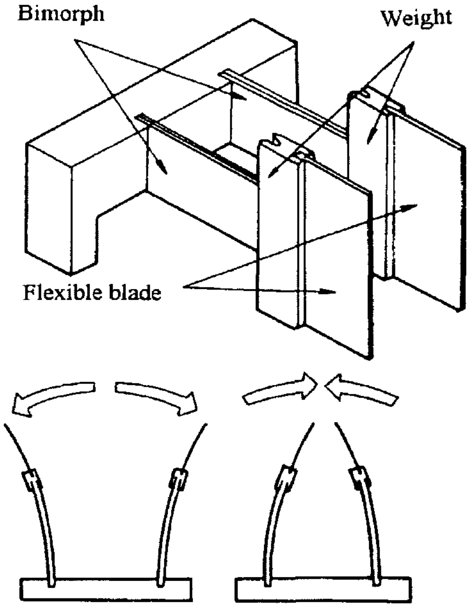

Figure 10.57 A compact piezoelectric fan developed by Piezo Electric Products, Incorporated (PEPI).[37]

Piezoelectric Pumps

Piezoelectric pumps are generally comprised of a dual bimorph structure coupled to two one-way valves as shown in Figure 10.58, which depicts a pump produced by Bimor, Incorporated, of Japan.[39] This device can be driven directly by the commercial line voltage (50-60 Hz and 100 V) because the bimorph resonance frequency has been tuned to approximately 50-60 Hz. The flow characteristics of piezoelectric pumps operated in air and water are shown in Figure 10.59. These pumps are most extensively used for injection of intravenous drip in hospitals and for automatic seasoning equipment in hotels.

Evaporators

The general structure of a piezoelectric evaporated is quite similar to that of the inkjet. The major differences between the two devices are primarily related to the drive resonance and the maximum evaporation rate of the liquid. One significant application for the piezoelectric evaporated has been in cool vapor humidifiers, which are preferred in homes with small children for safety reasons. A more recent application that has attracted considerable attention is its use as part of a system for evaporating heavy oil in diesel engines to increase the combustion efficiency of the fuel.

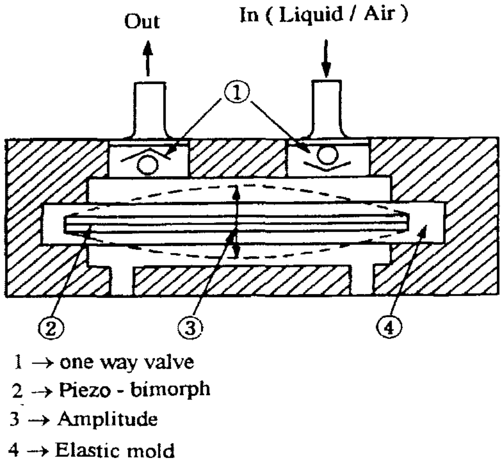
Out
In (Liquid / Air)
①
②
③
④
1 → one way valve
2 → Piezo - bimorph
3 → Amplitude
4 → Elastic mold

Figure 10.58 A piezoelectric pump produced by Bimor, Incorporated.[39]

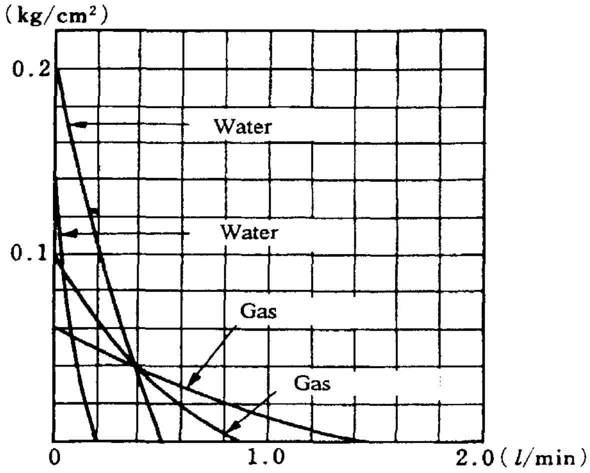

Figure 10.59 The flow characteristics of piezoelectric pumps operated in air and water.

Example Problem 10.3

Describe the role of the "horn" in ultrasonic motors.

Solution

A "horn" is an AC resonance displacement amplification mechanism. *It effectively produces an amplification of the resonance displacement that is inversely proportional to the diameter of the vibrator.* Three commonly used types are depicted in Figure 10.60. The *exponential cut horn* (a) exhibits the highest energy transmission efficiency, but the fabrication procedure needed to produce a precisely cut horn of this shape is not simple and thus not cost efficient from a production point of view. The *linear taper horn* (b) exhibits an intermediate efficiency and is somewhat easier to fabricate. The *step contoured horn* (c) is the easiest to fabricate, but is the least efficient due to reflection of a portion of the vibration energy at the neck of the structure.

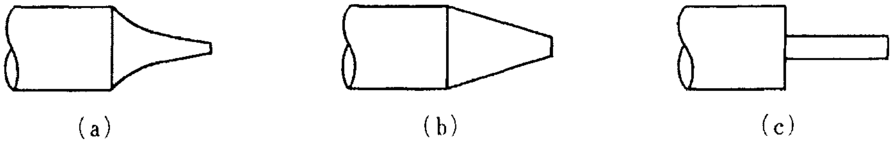

Figure 10.60 Three commonly used horn types: (a) the exponential cut horn, (b) the linear taper horn, and (c) the step contoured horn.

10.11 MAGNETIC MOTORS

Motors activated by magnetic actuators have the capability of operating by remote control. Prototype micromagnetic devices have been demonstrated that can fly, walk, swim and drill.[40] One intriguing design has the shape of a tiny butterfly, which can actually fly between a pair of magnetic poles when it is magnetically driven at a frequency corresponding to the resonance frequency of the butterfly's wings. Another interesting and potentially useful device is the magnetic screw motor pictured in Figure 10.61. The photos depict the device drilling through a piece of beef as it is driven by a cyclic magnetic field. The rate of rotation of the magnetic drill is thus synchronized with the frequency of the applied field and in this demonstration the rate of drilling occurred at approximately 1 mm/s.

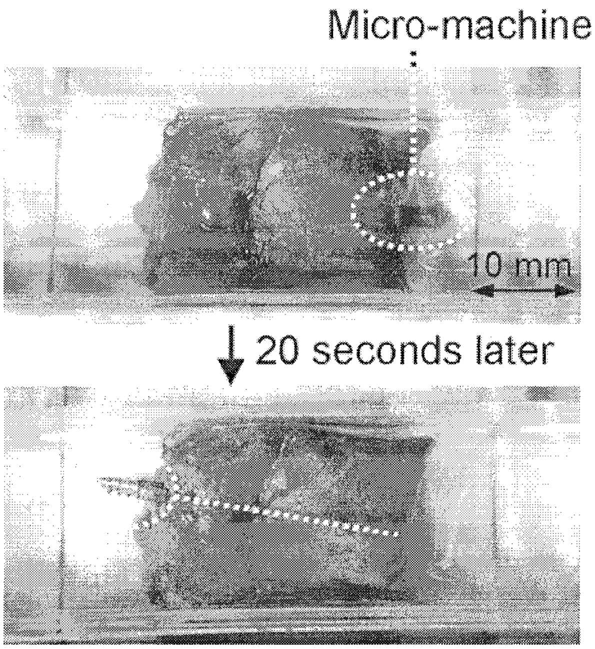

Figure 10.61 A magnetic screw motor.[40]

10.12 RELIABILITY OF ULTRASONIC MOTORS

We have considered in some detail in this chapter the essential elements involved in the development of ultrasonic motors. In particular, we examined the following key concepts:

1) Basic Materials Development: identifying materials with low loss that are able to sustain high vibration rates

2) Methods for Measuring High Field Electromechanical Couplings

3) Fundamental Ultrasonic Motor Design Considerations:
   a) Displacement Magnification Mechanisms: such as the horn and hinge lever mechanisms
   b) Basic Ultrasonic Motor Types: classified according to their mode of operation, such as the standing wave type and the traveling wave type
   c) Frictional Contact: between the stator and moving parts of the motor

4) Drive and Control of the Ultrasonic Motor:
    a) High Frequency/High Power Supplies
    b) Resonance/Antiresonance Modes of Operation

Important in the consideration of all these relevant areas is the matter of reliability. We will consider here the reliability of an ultrasonic motor in terms of three critical issues: (1) *heat generation* within the device, (2) the *friction materials* used, and (3) the *drive/control techniques* employed.

(1) Heat Generation

The primary factor affecting the reliability of an ultrasonic motor is heat generation within the device. The heat generated during operation can be great enough to cause the temperature to increase as high as 120°C and cause serious degradation in the performance of the motor due to depoling of the piezoelectric ceramic. A hard piezoelectric with a high mechanical quality factor, Q_m, is thus required to inhibit the excessive generation of heat and the detrimental effects of thermal depoling. Selection of an appropriate material is also influenced by the fact that the amplitude of the mechanical vibration at resonance is directly proportional to the magnitude of Q_m. Materials from the solid-solution system PZT-Pb(Mn,Sb)O_3 described in Chapter 6 are excellent choices in this regard as motors in which they are contained have been found to operate at input/output power levels an order of magnitude higher than those incorporating conventionally used hard PZT materials. No significant heating was observed for these devices when operated at these higher power levels.[41,42]

(2) Frictional Coating and Lifetime

The efficiency of the Shinsei ultrasonic motor incorporating various friction materials with respect to maximum output is shown in Figure 10.62.[43] The highest ranking materials among those represented in the figure are those in the A group, PTFE (polytetrafluoroethylene, Teflon), PPS (Ryton), PBT (polybutylterephthalate), and PEEK (polyethylethyl ketone). Some of the more popular materials used in commercially available motors include Econol (Sumitomo Chemical), CFRP (carbon fiber reinforced plastic, Japan Carbon), PPS (Sumitomo Bakelite), and polyimide. The wear for an ultrasonic motor incorporating CFRP friction material is plotted as a function of driving period in Figure 10.63. The data indicate that a 0.5 mm thick coat of this material will last approximately 600-800 hours.[44]

Until recently, the lifetime of an ultrasonic motor was largely determined by the durability of the friction material used in the device. The emergence of new, more durable friction materials has led to considerably longer lifetimes for some of the more recently developed motors. As one example, let us consider the performance of the Shinsei motor USR 30.[43] The motor is driven continuously for 2000 hours such that there is alternately a clockwise rotation for one minute and then counterclockwise for the next minute, a rotation rate of 250 rpm, and a load of 0.5 kg-cm. The change in the rate of rotation after this drive period was less than 10%. A second test examines the deterioration of motor characteristics under intermittent drive conditions whereby the motor rotates clockwise for one revolution and then counterclockwise for the next revolution with no load applied. After 250 million revolutions under these conditions, no significant degradation in motor characteristics was observed. Considering the lifetime requirements for motors such as this used in a VCR, about 2000-3000 hours, we see that the lifetime of the ultrasonic motor will quite adequately meet the required specifications.

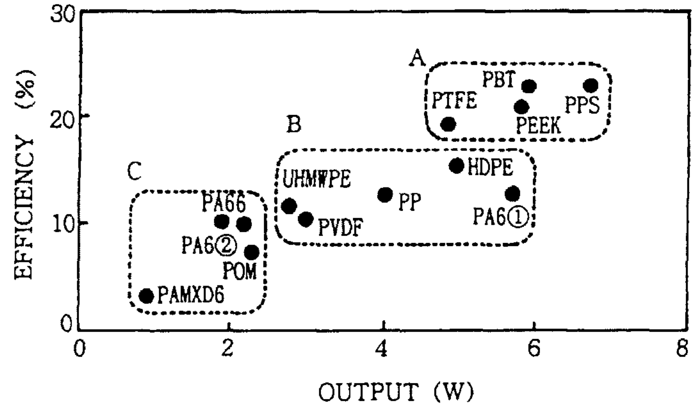

Figure 10.62 The efficiency of the Shinsei ultrasonic motor incorporating various friction materials with respect to maximum output.[43]

(3) Drive and Control of the Ultrasonic Motor

The four principal methods for controlling an ultrasonic motor are summarized in Figure 10.64. Pulse width modulation is the best of the four in terms of the high degree of controllability and efficiency that can be achieved.

When the motor is driven at the antiresonant frequency, rather than at the resonance frequency, the load on the piezoelectric ceramic and the power supply are reduced. The mechanical quality factor Q_m and temperature rise of a PZT ceramic bar sample driven at its fundamental resonance (A-type) and antiresonance (B-type) frequencies are plotted as a function of vibration velocity in Figure 10.65.[45] The data show that that Q_B is higher than Q_A over the entire vibration velocity range indicating that the same level of mechanical vibration can be achieved in the antiresonance mode as attained in the resonance mode, but without excessive heat generation. Moreover, when it is operated in the antiresonance mode the admittance is very low and therefore it can be powered by a conventional inexpensive low current, high voltage source, in contrast to the high current, low voltage source required for driving the piece at resonance.

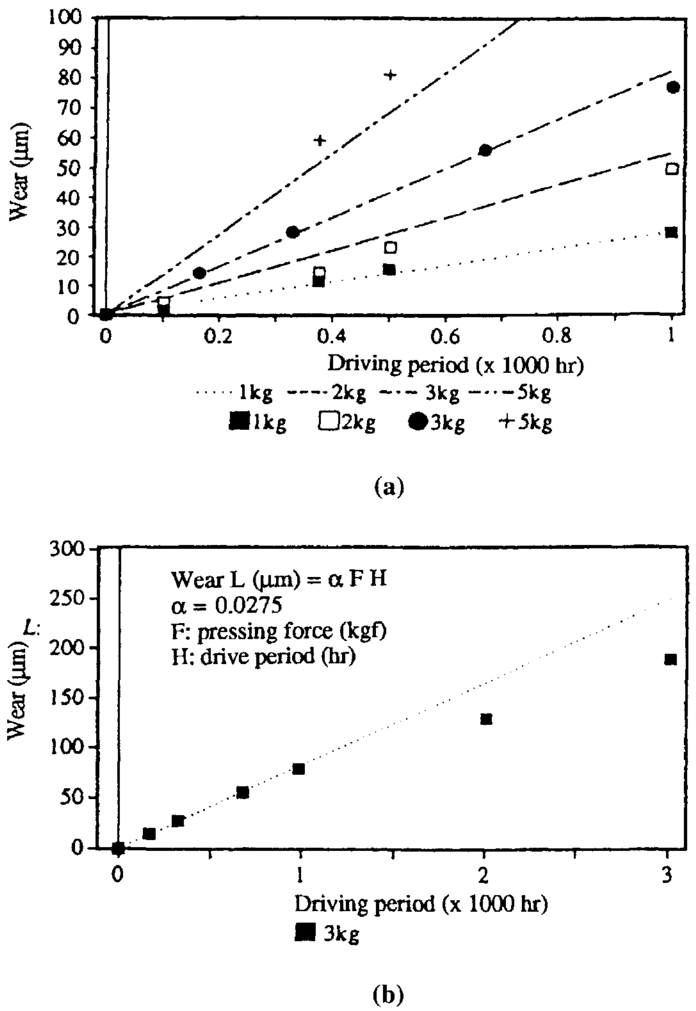

Figure 10.63 Wear as a function of driving period for an ultrasonic motor incorporating CFRP friction material: (a) over a range of contact forces and (b) with a contact force of 3 kgf.[44]

One final feature of ultrasonic motors should be highlighted before we close our discussion on this class of devices. They are generally characterized by low speed and high torque, in contrast to the high speed and low torque characteristic of conventional motors. Thus, ultrasonic motors do not require gear mechanisms, which allows for their very *quiet operation* and their *compact size*. The relative simplicity of their design is also favorable from a reliability point of view as there are fewer components that will be subject to wear and failure over the lifetime of the motor.

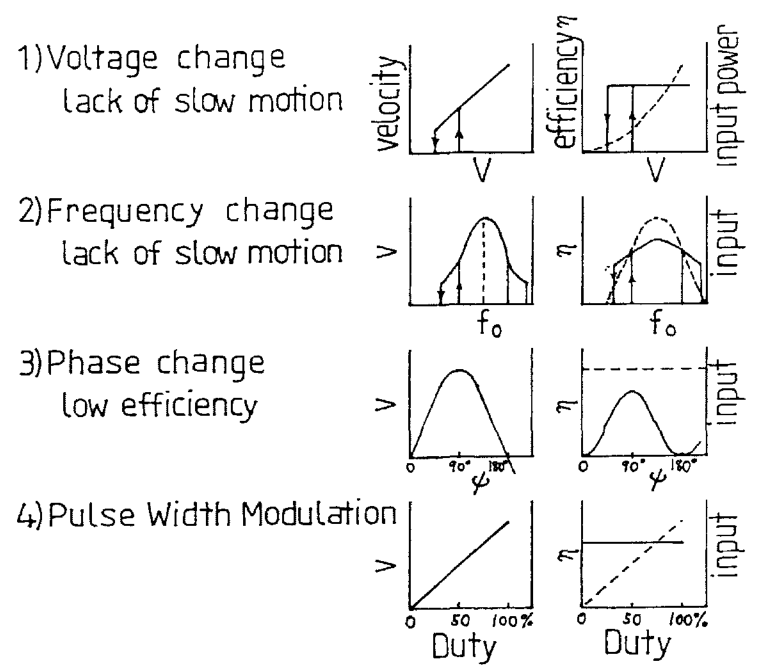
1) Voltage change
lack of slow motion
velocity
efficiency η
input power
V
2) Frequency change
lack of slow motion
v
η
input
f0
3) Phase change
low efficiency
v
η
input
0 90° 180°
φ
4) Pulse Width Modulation
v
η
input
0 50 100%
Duty

Figure 10.64 The four principal methods for controlling an ultrasonic motor.

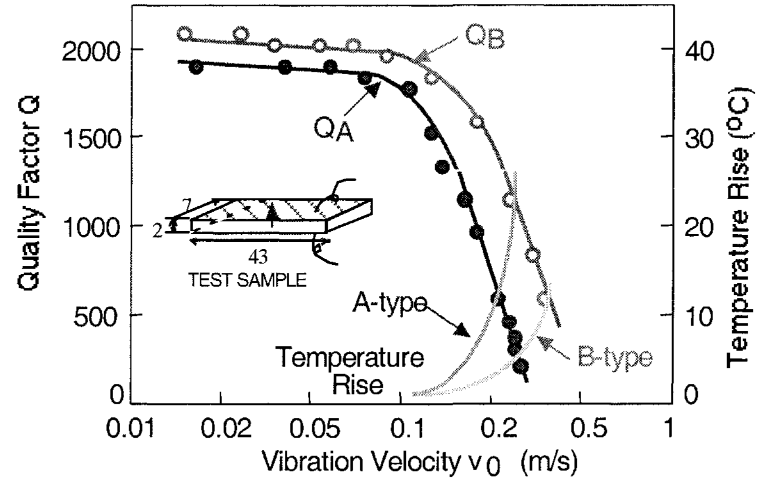

Figure 10.65 The quality factor Q and temperature rise for a PZT bar driven at a fundamental resonance (A) and antiresonance (B) frequency plotted with respect to vibration velocity.[45] [Longitudinal vibration]

CHAPTER ESSENTIALS

1. Merits and Demerits of Ultrasonic Motors:

Merits	Demerits
➢ Low Speed and High Torque ➢ Direct Drive ➢ Quick Response ➢ Wide Range of Speeds ➢ Hard Brake with No Backlash ➢ Excellent Controllability ➢ Fine Position Resolution ➢ High Power-to-Weight Ratio ➢ Quiet Drive ➢ Compact Size and Light Weight ➢ Simple Structure and Easy Production ➢ No Generation of Electromagnetic Radiation ➢ Unaffected by External Electric or Magnetic Fields	➢ High Frequency Power Supply Required ➢ Torque vs. Speed Droop ➢ Low Durability

2. Classification of Ultrasonic Motors:
   a. Rotary Type
   b. Linear Type
   c. Rod Type
   d. π-Shaped
   e. Ring (square) and Cylinder Types
   f. Standing Wave Type
   g. Mixed-Mode Type
   h. Traveling Wave Type
   i. Mode Rotation Type

3. Principle of Operation for the Traveling Wave Type: A traveling wave can be generated by superposing two standing waves with a 90-degree phase difference between them.

4. Contact Models for Speed/Thrust Calculations:
   a. Rigid Slider and Rigid Stator
   b. Compliant Slider and Rigid Stator
   c. Compliant Slider and Compliant Stator

5. Essential Elements Involved in the Development of Ultrasonic Motors:
    a. Basic Materials Development
    b. Methods for Measuring High-Field Electromechanical Couplings
    c. Fundamental Ultrasonic Motor Design Considerations:
        i. Displacement Magnification Mechanisms
        ii. Basic Ultrasonic Motor Types
        iii. Frictional Contact
    d. Drive and Control of the Ultrasonic Motor:
        i. High Frequency/High Power Supplies
        ii. Resonance/Antiresonance Modes of Operation

CHAPTER PROBLEMS

10.1 Describe the general principle for generating a traveling wave on an elastic ring using a unimorph structure. Then, assuming a displacement produced by the second order vibration mode of the form $u(\theta,t)=A\cos(2\theta-\omega t)$, describe two possible electrode and poling configurations that can be applied to the piezoelectric ceramic ring to produce the traveling wave.

10.2 Verify Equations (10.18) to (10.25) for the compliant slider and rigid stator model. Evaluate the average speed, v_o, and the maximum thrust, F, for the cases of $\phi = 0$ and $\phi = \pi$.

10.3 Survey the recent literature (that is, from the last five years) and prepare a brief report on the research that has been done on piezoelectric ultrasonic motors during this period. Be sure to include the following in your report:

a. Include a list of papers (at least five) which report on ultrasonic motors.

b. Prepare a classification of the motors reported using the categories described in this chapter (that is, standing wave type or traveling wave type, rotary or linear type, etc.).

c. Provide a brief explanation of the basic operating principles of the motors included in your report.

d. Summarize and briefly describe any intended applications for the motors included in your report.

REFERENCES

1) H. V. Barth: IBM Technical Disclosure Bull. **16**, 2263 (1973).
2) V. V. Lavrinenko, S. S. Vishnevski and I. K. Kartashev: Izvestiya Vysshikh Uchebnykh Zavedenii, Radioelektronica **13**, 57 (1976).
3) P. E. Vasiliev et al.: UK Patent Application GB 2020857 A (1979).
4) T. Sashida: Oyo Butsuri **51**, 713 (1982).
5) Y. Fuda and T. Yoshida: Ferroelectrics, **160**, 323 (1994).
6) B. Koc, J. F. Tressler and K. Uchino, Proc. Actuator 2000 (7th Int'l. Conf. New Actuators, June 19-21, 2000), p.242-245 (2000).
7) K. Uchino, K. Kato and M. Tohda: Ferroelectrics **87**, 331 (1988).
8) A. Kumada: Jpn. J. Appl. Phys., **24**, Suppl. 24-2, 739 (1985).
9) B. Koc, P. Bouchilloux, and K. Uchino: IEEE Trans.-UFFC, **47**, 836 (2000).
10) K. Nakamura, M. Kurosawa and S. Ueha: Proc. Jpn. Acoustic Soc., No.1-1-18, p.917 (Oct., 1993).
11) Nikkei Mechanical, Feb. 28 issue, p.44 (1983).
12) M. Kurosawa, S. Ueha and E. Mori: J. Acoust. Soc. Amer., **77**, 1431 (1985).
13) M. Takahashi, M. Kurosawa and T. Higuchi: Proc. 6th Symp. Electro-Magnetic Dynamics '94, No. 940-26 II, D718, p.349 (July, 1994).
14) Y. Tomikawa, T. Nishituka, T. Ogasawara and T. Takano: Sonsors & Mater., **1**, 359 (1989).
15) K. Ohnishi, K. Naito, T. Nakazawa and K. Yamakoshi: J. Acoust. Soc. Jpn., **47**, 27 (1991).
16) S. Ueha and M. Kuribayashi: Ceramics **21**, No.1, p.9 (1986).
17) T. Sashida: Mech. Automation of Jpn., **15** (2), 31 (1983).
18) K. Ise: J. Acoust. Soc. Jpn., **43**, 184 (1987).
19) M. Kasuga, T. Satoh, N. Tsukada, T. Yamazaki, F. Ogawa, M. Suzuki, I. Horikoshi and T. Itoh: J. Soc. Precision Eng., **57**, 63 (1991).
20) J. Cummings and D. Stutts: Amer. Ceram. Soc. Trans. "Design for Manufacturability of Ceramic Components", p.147 (1994).
21) A. Kumada: Ultrasonic Technology **1** (2), 51 (1989).
22) Y. Tomikawa and T. Takano: Nikkei Mechanical , Suppl., p.194 (1990).
23) T. Yoshida: Proc. 2nd Memorial Symp. Solid Actuators of Japan: Ultra-precise Positioning Techniques and Solid Actuators for Them, p.1 (1989).
24) S. Dong, L. C. Lim and K. Uchino: IEEE Trans.-UFFC [in press] (2001).
25) K. Uchino: Solid State Phys., Special Issue "Ferroelectrics" **23** (8), 632 (1988).
26) T. Hayashi: Proc. Jpn. Electr. Commun. Soc., US84-8, p.25 (June, 1984).
27) H. Saigo: 15th Symp. Ultrasonic Electronics (USE 94), No. PB-46, p.253 (Nov. 1994).
28) Seiko Instruments: Product Catalogue "Mussier" (1997).
29) B. Akbiyik: Undergraduate Thesis, Electr. Engr., Kirikkale University, Turkey (2001).
30) K. Onishi: Ph.D. Thesis, Tokyo Institute of Technology, Japan (1991).
31) Y. Tsuda, E. Mori and S. Ucha: Jpn. J. Appl. Phys., **22**, Suppl., 3 (1983).
32) Y. Kuwahara: *Cataract Surgery*, Igaku-Shoin, Tokyo (1970).
33) E. Kolm and H. Kolm: Chemtech **3**, 180 (1983).
34) H. Hatano, Y. Kanai, Y. Ikegami, T. Fujii and K. Saito: Jpn. J. Appl. Phys., **21**, 202 (1982).
35) R. Aoyagi and H. Shimizu: Proc. Jpn. Acoust. Soc., p.251 (1981).
36) K. Asai and A. Takeuchi: Jpn. J. Appl. Phys., **20**, Suppl. 20-3, 169 (1981).
37) Piezo Electric Product Inc.: Produsts Catalog.

38) M. Yorinaga, D. Makino, K. Kawaguchi and M. Naito: Jpn. J. Appl. Phys., **24**, Suppl. 24-3, 203 (1985)
39) T. Narasaki: Proc. 13th Intersoc. Energy Conversion Eng. Conf., Soc. Automotive Eng., p.2005 (1978).
40) K. Arai: www.riec.tohoku.ac.jp/Lab/Arai (2001).
41) S. Takahashi, Y. Sasaki, S. Hirose and K. Uchino: Proc. MRS '94 Fall Mtg. Vol.**360**, p.2-5 (1995).
42) Y. Gao, Y. H. Chen, J. Ryu, K. Uchino and D. Viehland: Jpn. J. Appl. Phys., **40**, 79-85 (2001).
43) Y. Tada, M. Ishikawa and N. Sagara: Polymer Preprints **40**, 4-17-23, 1408 (1991).
44) K. Ohnishi et al.: SAW Device 150 Committee, Jpn. Acad. Promotion Inst., Abstract 36th Mtg., p.5 (Aug., 1993).
45) S. Hirose, S. Takahashi, K. Uchino, M. Aoyagi and Y. Tomikawa: Proc. Mater. for Smart Systems, Mater. Res. Soc., Vol. **360**, p.15 (1995).

11

THE FUTURE OF CERAMIC ACTUATORS IN MICROMECHATRONIC SYSTEMS

After twenty-five years of intensive research and development of solid-state actuators, the focus has gradually shifted to applications. Piezoelectric shutters (Minolta Camera); automatic focusing mechanisms (Canon) in cameras, dot matrix printers (NEC), and inkjet printers (Epson); and piezoelectric part-feeders (Sanki) have been commercialized and mass produced on a scale of several tens of thousands of pieces per month. Throughout this period of commercialization, especially over the last decade, new actuator designs and methods of drive and control have been developed to meet the requirements of the latest applications. At a somewhat slower pace advances in device reliability and strength have likewise occurred, although some considerable work is yet to be done in further extending the lifetime of devices and ensuring consistent performance over that period. An overview of these recent trends in development followed by a projected view of future trends and design concepts will be presented in this chapter.

11.1 DEVELOPMENT TRENDS AS VIEWED FROM PATENT STATISTICS

A chart depicting the breakdown of 508 patent disclosures filed in Japan from 1972 to 1984 with respect to technical content appears in Figure 11.1(a) and a chart representing the breakdown for 550 patents disclosed from 1988 to 1990 is shown in Figure 11.1(b).[1] Four major categories characterize the technical content: (1) materials development, (2) device design, (3) drive/control systems, and (4) applications. Specific areas within these major categories include new compositions, fabrication processes, multilayer actuators, bimorph structures, displacement magnification mechanisms, drive methods, control methods, servo displacement transducers, and pulse drive and ultrasonic motor applications. Note that device application concepts constitute most of the patents summarized in Figure 11.1(a), while only about one-quarter of the patents classified in Figure 11.1(b) are related to this area. This tendency is generally observed in the development of any device. Once the basic design is proposed, various prototype devices are fabricated and application patents are filed. However, as the actual commercialization is promoted, the focus shifts to the optimization of the designs, cheap and efficient manufacturing processes, and new drive/control methods.

The application patents filed from 1972 to 1984 were primarily concerned with pulse drive motors (43%) and servo displacement transducers (40%), while ultrasonic motor applications (5%) were of only marginal interest at this time. The proportions shift quite noticeably during the 1988 to 1990 time frame, however, when, in general, application patents decreased to about 27%, but more than a third of that group was dedicated to ultrasonic motor applications (11%), while the servo displacement and pulse motor applications constituted the rest in equal portion (8%).

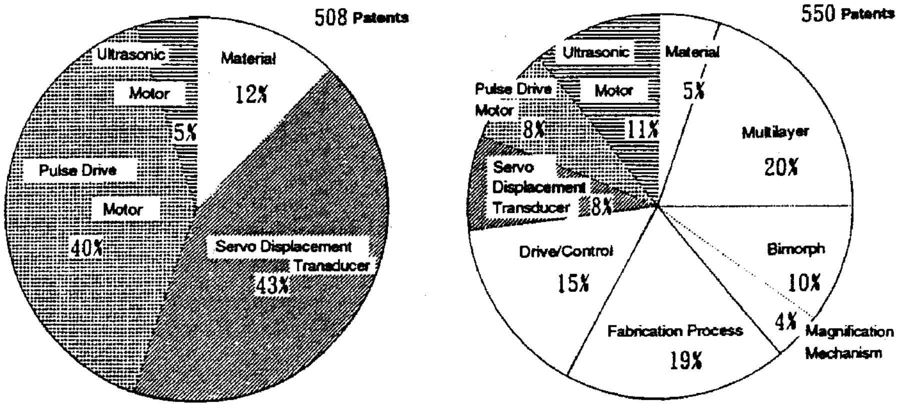

(a) (b)

Figure 11.1 Breakdown of patent disclosures filed in Japan between 1972 and 1990 with respect to technical content: (a) 1972 to 1984 (508 patents) and (b) 1988 to 1990 (550 patents).[1]

The first stage in the development of piezoelectric actuators was focused primarily on the inexpensive mass production of devices such as computer hardware, imaging devices, and sensors and was pursued largely by electronic manufacturing companies. Some examples are the dot matrix printers produced by NEC, the swing CCD image devices produced by Toshiba, the VCR tracking heads produced by Sony and Matsushita Electric, and the piezoelectric relays produced by OMRON. More recently, in the second stage of development, chemical companies, including organic/petrochemical industries such as TOTO Corporation, Tokin, Hitachi Metal, Murata Manufacturing Co., Ube Industry, Tosoh, NTK, Sumitomo Special Metal, Toshiba Ceramics, Taiheiyo Cement, Mitsui Chemical, and NGK, have become involved. Their aim is to extend their domain by producing specialized ceramic powders in collaborative ventures with optical and mechanical industries. In these industries, where precision cutting and polishing machines are used extensively, the quality and reliability of the actuator is more important than low cost and the investment in high quality materials is essential.

11.2 THE PIEZOELECTRIC ACTUATOR/ULTRASONIC MOTOR MARKET

(1) Comparison of U.S., Japanese, and European Industries

Recent production and applications of ceramic actuators in the United States, Japan, and Europe are summarized in Table 11.1. The developments in the United States are generally supported by the military-related government institutions and are mainly focused on active vibration control using relatively large actuators (>30 cm). In contrast, piezoelectric actuators and ultrasonic motors have been developed by private industries in Japan for applications requiring precision positioners and compact motors made with tiny actuators (<1 cm). Most of the products and applications are too consumer-oriented to be supported by the Japanese government. The only major government sponsored research in this area in Japan concerns "micromechanisms," which is primarily focused on small motors for the micromachining of silicon. European developments are a little behind Japan and the United States, but target a broad range of applications. The typical device size produced by European industries at this time is on the order of about 10 cm.

Table 11.1 Summary of ceramic actuator production and applications in the United States, Japan, and Europe.

	United States	Japan	Europe
FOCUS	Military Products	Consumer Products	Laboratory Equipment
DEVICES	Vibration Dampeners	Mini-Motors Positioners Vibration Dampeners	Mini-Motors Positioners
APPLICATIONS	Space Structures Military Vehicles	Office Equipment Cameras Precision Machining Automobiles	Stepper Motors Airplane Components Automobiles Hydraulic Systems
ACTUATOR SIZE	Larger Scale (>30 cm)	Miniature Scale (<1 cm)	Intermediate Scale (10 cm)
MAJOR PRODUCERS	AVX/Kyocera Morgan Matroc Itek Optical Systems Burleigh Allied Signal	Tokin Corporation NEC Hitachi Metal Mitsui Chemical Canon Seiko Instruments	Philips Siemens Hoechst Ceramic Tec. Ferroperm Physik Instrumente

(2) The Ceramic Actuator Market

The major markets for ceramic actuators in Japan and the United States are summarized in Table 11.2. Several years ago Mr. Sekimoto, Former President of NEC, made a prediction for the piezoelectric actuator market in his New Year's speech for 1987, stating that the market for the devices would reach $10 billion in the near future. The actuator market in the United States has been dominated by the military until recently and, therefore, is more difficult to estimate in terms of production and profit. An overview of recent activity in the Japanese market related to ceramic actuators is presented briefly here to provide some perspective on the growth that has occurred lately in this area.

Table 11.2 Major markets for piezoelectric actuators in Japan (1994) and the United States (1996).

Market	Production (pieces / year)
JAPAN (1994)	
Ink Jet Printers (Epson)	5×10^5
Dot Matrix Printers (NEC)	3×10^5
Camera Shutters (Minolta)	1×10^5
Camera Autofocus Systems (Canon)	3×10^4
Parts Feeders (Sanki)	1×10^4
Piezoelectric Transformers (NEC, Tokin, Mitsui Chemical)	5×10^5
UNITED STATES (1996)	
Smart Submarine Skins (Navy)	
Hydrophones (Navy)	
Propeller Noise Eliminators (Navy)	
Smart Aircraft Skins (Air Force)	
Helicopter Rotor Motors (Army)	
Aeroservoelastic Control Systems (Army)	
Motor Mounts (Army)	
Cabin Noise Eliminators (Army)	
Seat Vibration Dampeners (Army)	

Production of Ceramic Actuator Elements in Japan

Tokin and other companies are producing multilayer actuators at a rate of roughly two million pieces per year. They are sold at an average rate of $50 per piece, bringing the total market value to about $100 million. Predictions for the next five years indicate that the production rate will increase by a factor of ten while production costs will decrease by a quarter, leading to a total market growth of up to $250 million.

If multilayer actuators are incorporated into the design of certain electronic devices, the anticipated market growth for these products could increase by about a factor of ten. For example, the original dot-matrix printer produced by NEC cost on average about $3000, while the later design incorporating multilayer actuators costs only about $100. NEC produced about 100,000 dot matrix printers in 1986, making them the leader with total sales of $300 million. Epson has started to produce piezoelectric ink jet printers (unit price about $300) at a rate of 1 million units per year, bringing total sales for this product to about $5 billion.

Camera-Related Devices Produced by Japanese Companies

Piezoelectric bimorph type camera shutters have been widely commercialized by Minolta Camera. The "Mac Dual" series is produced at a rate of about 300,000 units per year. The camera costs about $350 (the actuator costs less than $1) and total sales exceed $100 million per year.

Canon's automatic focusing systems incorporating an ultrasonic motor are very popular. About 80% of the exchange lenses in the "EOS" series produced in 1992 had ultrasonic motors and the trends indicate that the automatic focusing systems for all cameras of this type will include ultrasonic motors in the near future. This series is produced at a rate of about 300,000 pieces per year, and with unit cost at about $700 per unit, total sales are current about $210 million per year.

The Ultrasonic Motor Market in Japan

Ultrasonic motors appeared as a new product in June of 1986 when Shinsei Industry introduced a propagation wave type version of the motor on a trial basis. The first production batch (about 1500 pieces) was used for automatic curtain drawers in the New Tokyo Municipal Building in 1990. The motors have been widely commercialized since that time and continue to show tremendous growth potential. Shinsei Industry has developed and promoted a variety of new products and systems over the last twenty years or so including an extremely successful series of nuclear magnetic resonance (NMR) medical instruments.

There have been several key applications of the ultrasonic motor promoted by various companies that have been vital to the surge of growth that has occurred in the marketing of these devices over the last few decades. One of the first large scale applications of the ultrasonic motor occurred in 1991 when the motors were incorporated into the headrest control unit of the Toyota New Crown sedan. The automatic focusing units of Canon’s EOS series of cameras has been another major application for the motors. Canon is also promoting the development of smaller motors for use in the automatic film winding system of their cameras. This will likely become another important area of application for the motors that will contribute significantly to their market growth. Seiko Instruments currently produces a line of wristwatches which utilize two miniature ultrasonic motors for the silent alarm and perpetual date change functions. One million watches are produced per year and they sell for \$200 per watch. Ultrasonic motors are also important components in Sanki's part feeders, which are currently sold at a cost of \$500 per unit, generating about \$10 million per year in total sales.

One of the most promising future applications for ultrasonic motors is in an automated window shutter system. The proposed system will sell for about \$2000 per unit and they will be produced initially at a rate of 100,000 per year, generating about \$200 million per year. It is anticipated as well that ultrasonic motors will find greater application in computer hardware, such as disk drives (such as floppy and CD drives), and significant production and sale of the motors for these applications will occur over the next few years.

It is the proposed goal of Matsushita Electric to replace all the conventional miniaturized electromagnetic motors currently used, most of which are now produced by Mabuchi at a production rate of 1 billion pieces per year. Even when the relatively low cost of the ultrasonic motors (about \$3 per unit) is taken into account the anticipated total sales of the motors is significant (about \$3 billion per year). It is projected that even if only 10% of the conventional electromagnetic motors are replaced by ultrasonic motors, about \$300 million from the sale of the motors can be generated per year, which translates to approximately \$3 billion from the sale of the devices in which the motors have been incorporated.

In conclusion, summing up the estimated annual sales from these prospective markets alone, approximately \$500 million from the sale of individual ceramic actuator elements, about \$300 million from camera-related applications, and roughly \$150 million related to the sale of ultrasonic motors, a total of near \$1 billion is anticipated. Mr. Sekimoto's prediction of ceramic actuator sales amounting to near \$10 million in the near future may in fact be realized! At the very least, the current trends suggest a bright financial future for the ceramic actuator industry.

11.3 FUTURE TRENDS IN ACTUATOR DESIGN

(1) Concepts Related to the Design of Smart Actuators

The performance of smart actuators is dependent on a combination of several factors which can be classified into three general categories: (1) material properties, (2) device design, and (3) drive technique. We will now consider the development of new devices with respect to these matters as both a summary of the key ideas presented in the text and a means to predict to some extent the course of future trends in the marketing of ceramic actuator devices.

Optimizing Material Properties

Achieving a higher induced strain or stress is a primary objective in the development of new actuator/transducer materials. The most commonly implemented sample geometry for *lead zirconate titanate (PZT)* has been one in which the electric field is applied parallel to the spontaneous polarization (poling) direction, mainly because PZT has traditionally been available only in polycrystalline form. As we saw in Chapter 3, among piezoelectric ceramics the maximum induced strain ($\approx 0.1\%$) is generated in lanthanum-doped PZT (PLZT) and electrostrictive lead magnesium niobate-lead titanate, $Pb(Mg_{1/3}Nb_{2/3})O_3$-$PbTiO_3$ (PMN-PT).

Subsequent work on lead zinc niobate-lead titanate, $Pb(Zn_{1/3}Nb_{2/3})O_3$-$PbTiO_3$ (PZN-PT) single crystals, which included detailed studies of the optimum crystal orientations for the maximum piezoelectric response, indicated that even higher strain levels of up to 1.3% were possible for these materials. Furthermore, materials from this system in thin film [100] form are expected to exhibit more ideal (square) polarization and strain versus electric field hysteresis loops due to a more simple process of domain reversal. As we saw in Chapter 3, this characteristic is especially important in the design of MEMS devices.

Reproducibility of the strain characteristics depends in general on the *grain size, porosity,* and *impurity content* of the material. Increasing the grain size enhances the magnitude of the field-induced strain, but degrades the *fracture toughness* and increases the *hysteresis*. Thus, the grain size should be optimized for each application. On the other hand, porosity does not affect the strain behavior significantly. The tip deflection of unimorphs made from a $Pb(Mg_{1/3}Nb_{2/3})O_3$-based material is not affected by porosity, if it is kept below 8% as shown by the data appearing in Figure 11.2.[2] Hence, fine powders made by wet chemical processes such as *co-precipitation* and *sol-gel* are desirable, and suitable ceramic preparation processes are sought (as discussed in Chapter 4) to optimize grain size and porosity.

The *impurity level* (donor- or acceptor-doped) is another key material design parameter, which can lead to significant enhancements in the strain and hysteresis/loss characteristics of the material as described in Section 6.3. Studies on the effect of dopants on the quasi-static field-induced strain in $(Pb_{0.73}Ba_{0.27})(Zr_{0.75}Ti_{0.25})O_3$ indicate that since donor-doping produces "*soft*" characteristics, a sample with a donor dopant will exhibit larger strains and less hysteresis when driven under a high pseudo DC electric field (1 kV/mm). On the other hand, acceptor doping produces "*hard*" characteristics, leading to small hysteresis losses and a large mechanical quality factor when the sample is driven under a small AC electric field. Such materials are suitable for ultrasonic motor and piezotransformer applications. Data reported for the temperature rise as a function of vibration velocity of undoped, Nb-doped, and Fe-doped $Pb(Zr,Ti)O_3$ samples driven at resonance indicate that heat generation in the Fe-doped (acceptor) specimen is especially low (see Figure 6.28). The maximum temperature rise is observed at the nodal points in the specimen where maximum stress and strain occur when the sample is driven in this mode (see Figure 6.22). The major loss factor associated with this temperature rise is apparently the (intensive) mechanical loss of the PZT. We considered the mechanisms for heat generation and the suppression of this effect in piezoelectric materials in Chapter 6.

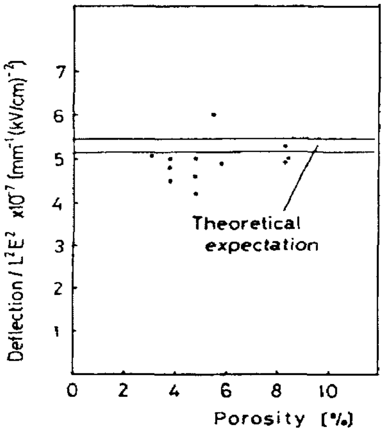

Figure 11.2 Tip deflection of a $Pb(Mg_{1/3}Nb_{2/3})O_3$-based unimorph plotted as a function of the sample porosity.[2]

The practical limit for the maximum vibration velocity (v_{max}) of conventional piezoceramics has already been attained. Once this maximum velocity is exceeded, any additionally input electrical energy is converted into heat, rather than into mechanical energy. The typical root-mean-square value of v_{max} for the commercially available materials (for specimens exhibiting a temperature rise $\approx 20^{\circ}C$ above room temperature) is around 0.3 m/sec for a rectangular k_{31} sample. Ceramics from the $Pb(Mn,Sb)O_3$-$Pb(Zr,Ti)O_3$ (PMS-PZT) system typically exhibit a v_{max} of 0.62 m/sec, while specimens from this system doped with Yb, Eu, and Ce have achieved maximum velocities of up to 0.9 m/sec (see Figure 6.30). These are considered the "champions" at present. Input electrical energy and output mechanical energy one order of magnitude higher than what are generally characteristic levels for conventional commercially available piezoelectrics are anticipated for these materials, without significant heat generation. This is an excellent demonstration of the important role ion doping can play in the design of new materials and the tailoring material properties for specific applications.

The material's strain characteristics may be stabilized with respect to temperature variations by developing suitable solid solutions or composite structures. New trends focused on these concerns involve such applications as high temperature actuators for engines and cryogenic actuators for laboratory equipment and space structures. Ceramic actuators are best used under compressive stress conditions, because the ceramic is, in general, relatively weak under an applied tensile stress. Data reported for the compressive uniaxial stress dependence of the weak-field piezoelectric strain coefficients (d) for various PZT ceramics indicate that hard piezoelectric compositions have the highest d coefficients. The details of this study and the implications for new applications were examined in Section 3.5.

Optimizing Device Design

One significant drawback of using piezoelectrics in actuators is their small induced strains (only about 0.1%). Thus, much effort has been made to find new ways to amplify the displacement. The methods employed fall into two general categories: (1) amplification with respect to space and (2) amplification with respect to time. The first type is demonstrated by bimorphs and moonie/cymbal devices, and the latter is exemplified by inchworms and ultrasonic motors.

(i) *Moonies/Cymbals*

Two of the most popular actuator designs are the multilayers and bimorph structures. The multilayer device, in which roughly 100 thin piezoelectric or electrostrictive ceramic sheets are stacked together, has the advantages of low drive voltage (100 V), quick response (10 μsec), high generative force (1000 N), and high electromechanical coupling. The displacement produced by these devices, however, is only on the order of 10 μm and, therefore, not sufficient for some applications. On the other hand, the bimorph, which consists of a series of only relatively few piezoelectric and elastic plates bonded together, generates a considerably larger bending displacement of several hundred μm, but has a rather low response time (1 msec) and generative force (1 N). Two popular composite flextensional actuator structures, called the "moonie" and the "cymbal," were designed to have characteristics intermediate between those associated with multilayer and bimorph actuators. This type of transducer typically exhibits displacements an order of magnitude larger than those produced by multilayer devices, and has a much larger generative force and quicker response than the bimorph structure. The composite device consists of a thin multilayer piezoelectric element (or a single ceramic disk) sandwiched between two metal plates bent and bonded together such that, in the case of the moonie, narrow moon-shaped cavities are created within the device. We examined the structure and performance of these actuators in Chapter 4.

(ii) *Compact Ultrasonic Motors*

These devices, which function by means of high power ultrasonic vibrations, were first commercially demonstrated by Sashida (see Figures 10.28-10.30). When two phase-shifted sinusoidal voltages are alternately applied to the thin piezoelectric ring within this device the surface of an elastic layer bonded to the piezoelectric becomes "rippled." A ring-shaped slider in contact with the induced surface waves thus undergoes a rotation by effectively "surfing" over the dynamically deformed surface. Even though this ripple displacement is not particularly large, when operated at a relatively high frequency (15-200 kHz) the slider is able to attain quite high rotational speeds. Canon has installed this compact rotary motor in the lens assembly of a camera as part of the automatic focusing mechanism (see Figure 10.32). Using essentially the same principle, Seiko Instruments has further miniaturized the ultrasonic motor to a diameter as small as 10 mm and installed this tiny motor in a wristwatch to function as a silent alarm (see Figure 10.34). The primary limiting factor in miniaturizing this type of motor lies in the ceramic manufacturing process. Standing wave-type motors, the structure of which is less complicated, are more suitable for miniaturization. The *windmill* and *metal tube-type motors*, developed at Penn State and described in Chapter 10, are inexpensive and advanced performance micromotors that show much promise for a variety of applications. *Finite element analysis* (FEM) has emerged as a powerful tool for predicting vibration modes in a stator. An introduction to the method as it is applied to actuator design was presented in Chapter 7 and a demonstration of the ATILA software (Magsoft Corporation) is provided on the CD-ROM supplement to this textbook.

(iii) *MEMS Devices*

Thin films of PZT can be deposited onto a silicon membrane and microactuators and sensors can then be micromachined from the film. Such a system is referred to as a microelectromechanical system (MEMS). A MEMS blood tester based on such a structure has been developed recently by Omron Corporation of Japan (Figure 4.36). Surface waves are induced in the PZT layer of the device when the appropriate input signal is applied to two surface interdigital electrodes. The blood sample is drawn inside the device and mixed with a test chemical that is introduced into the system through two inlets. The blood and the chemical agent are mixed in a cavity at the center of the device and then transferred via an outlet to a monitor. The finite element method was employed in the design of this system to evaluate the flow rate of the fluid as a function of parameters such as the thickness of the PZT film, the thickness of the silicon membrane, the inlet and outlet nozzle size, and the cavity size (see Chapter 4).

(iv) *New Electrode Materials and Configurations*

Silver electrodes are popular and desirable from a manufacturing point of view, but they present serious problems, especially when used with lead-based materials under high electric field and high humidity conditions. The silver tends to migrate into the active material under these conditions, thus degrading the performance of the device. This problem can be avoided by making use of a silver-palladium alloy or more expensive, platinum electrodes. Where the aim is to produce inexpensive reliable ceramic actuators, copper (Cu) and nickel (Ni) electrodes, which may be fired at temperatures as low as 900°C, are attractive (see Section 4.3). The development of ceramic compositions that can be sintered at lower temperatures (and thus co-fired with the alternative electrode materials just described) is another very active area of research at this time. Delamination of the electrode layer is yet another serious problem that occurs for multilayer-type actuators as well as bimorph structures. Composite electrode materials prepared as metal and ceramic powder colloids, ceramic electrodes, and electrode configurations with via holes are some of the more promising solutions to this problem. The internal stress concentrations that can develop with the application of an electric field sometimes initiate cracks in the device. Large tensile stress concentrations associated with the production of such defects are readily observed at the edge of the internal electrode (see Figure 4.11). One strategy for overcoming this problem is to design an electrode that generates a maximum tensile stress that is never greater than the critical mechanical strength of the ceramic. Several electrode configurations have been proposed that meet this basic criterion: the *plate-through type*, the *slit-insert type*, and the *float-electrode-insert type* (see Figure 4.8). Each has features that can effectively extend the lifetime of the actuator. The reasons why the lifetime is extended with decreasing layer thickness as described in Chapter 4, however, have not yet been identified. There are still some processing related dilemmas associated with these designs that limit their practical implementation at this time. The plate-through type, for example, requires a specialized, expensive processing step to generate the external insulating coating, while the consistent production of very thin slits is a major drawback of the slit-insert type.

(v) Controlling Heat Generation

Heat generation is another important concern in designing multilayer actuators. Measurements of the heat generated in multilayer piezoelectric ceramic actuators of various sizes have been reported (see Figure 4.18). In order to suppress the heat generated in such a structure, a design conducive to a small V_e/A is preferred; a hollow cylinder, for example, is preferred to a solid rod configuration. When an actuator is to be driven off-resonance, it is also important to consider that the heat is generated largely through the intensive dielectric loss, rather than through the intensive mechanical loss, as is the case for resonance mode operation. We addressed these and other design considerations related to the suppression of heat generation in Chapter 6.

(vi) Reducing Aging Effects and Extending Device Lifetime

The aging of a device arises primarily from two factors: depoling and destruction. Creep and zero-point drift of the displacement are manifested when the ceramic has become depoled. The induced strain can be significantly degraded when the actuator is operated under very high electric fields, at elevated temperature, in high humidity conditions, and under excessive mechanical stress. The effects of temperature and DC bias field on the lifetime of a multilayer piezoelectric actuator have been reported by Nagata [see Section 4.2(2)].[3] The lifetime of an actuator, t_{DC}, operated under a DC bias field, E, is described by the following empirical equation:

$$t_{DC} = A\, E^{-n} \exp(W_{DC} / kT) \qquad (11.1)$$

where n has a value of about 3 and W_{DC} is an activation energy, which extends over a range of 0.99-1.04 eV (see Figure 11.3). Device "health" monitoring systems have been proposed which utilize a variety of failure detection techniques. An "intelligent" actuator system that makes use of acoustic emission (AE) monitoring has been proposed (see Figures 4.15 and 11.4).[4] In this system, the actuator is controlled by two feedback mechanisms: (1) *position feedback*, which can compensate for positional drift and hysteresis, and (2) *breakdown detection feedback*, which can stop the actuator system safely before any serious damage to the work occurs (such as in a lathe machine). Among the systems presented in Chapter 4 is a new electrode configuration, similar to that used for a strain gauge, which has been proposed as another innovative device for health monitoring (see Figure 4.16).

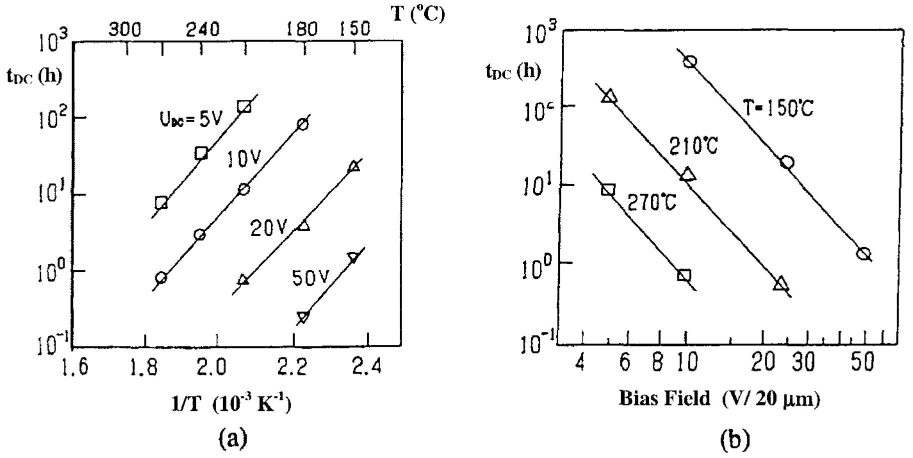

Figure 11.3 Lifetime, t_{DC}, of a multilayer piezoelectric actuator plotted as a function of: (a) temperature and (b) DC bias voltage.[3]

Development of New Drive/Control Techniques

Piezoelectric and electrostrictive actuators may be classified into two general categories: (1) *rigid displacement devices*, for which the strain is induced along the direction of the applied DC field, and (2) *resonating displacement devices*, for which the alternating strain is excited by an AC field at the mechanical resonance frequency (see Figure 5.1). The first can be further divided into two types: (1a) *servo displacement transducers*, which are controlled by a feedback system through a position-detection signal and often employed as positioners, and (1b) *pulse drive motors*, which are operated in a simple on/off switching mode and are used in systems such as dot matrix printers. The material requirements for these classes of devices are somewhat different, and certain compounds will be better suited to particular applications. The ultrasonic motor, for instance, requires a very hard piezoelectric with a high mechanical quality factor, Q_m, to inhibit heat generation. The performance of servo displacement transducer tends to be adversely affected by strain hysteresis and, therefore, electrostrictive PMN is generally used for these devices. A good pulse drive motor requires a low permittivity material exhibiting a quick and optimum response at a specific operating power more than small hysteresis, so soft PZT piezoelectrics are preferred over the high permittivity PMN materials for this application. Issues related to the characterization of piezoelectric and electrostrictive materials for actuator applications were presented in Chapter 5.

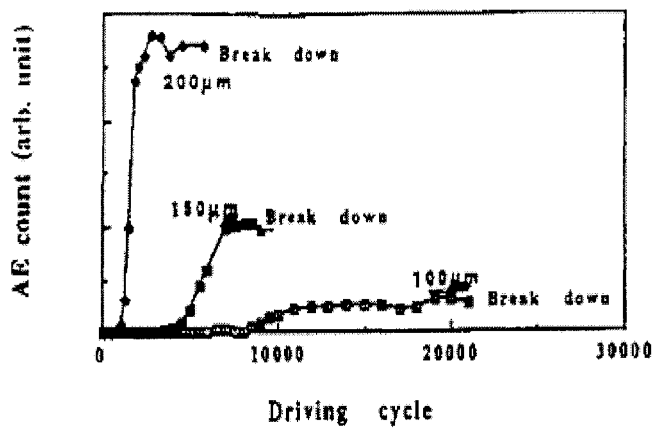

Figure 11.4 Acoustic emission (AE) count from piezoelectric PZT-PNN multilayer actuators with the various layer thicknesses (100, 150, and 200 μm) as a function of number of drive cycles.[4]

A new application for piezoelectrics has recently been proposed: the *piezoelectric transformer*. The piezoelectric transformer offers a variety of advantages over conventional electromagnetic types, namely: (1) it is small and lightweight, (2) it is highly efficient, (3) it generates no magnetic noise, and (4) it is made of nonflammable components. The piezoelectric transformer is expected to find a wide range of application, one of which is in driving piezoelectric actuators. Since most piezoelectric actuators are driven by voltages in the range of 100-1000 V, a transformer is required when battery driven circuitry is employed. The compact piezoelectric device is an attractive alternative to the conventional electromagnetic transformers currently used for this purpose. We discussed a variety of new applications for the piezoelectric transformer in some detail in Chapter 5.

(i) *Pulse Drive*

Pulse drive of the piezoelectric/electrostrictive actuator tends to lead to the generation of very large tensile stresses in the device, sometimes large enough to initiate cracks. In such cases, a compressive bias stress should be applied by means of a clamping mechanism such as a helical spring or a plate spring. Another way to inhibit these stresses is by suppressing the transient vibrations of the piezoelectric by applying an appropriate pseudostep voltage. As we considered in Section 5.3, the overshoot and ringing of the tip displacement is completely suppressed when the rise time is precisely adjusted to the resonance period of the piezoelectric device. A rise in temperature is occasionally observed, particularly when the actuator is driven repeatedly in pulse drive. Suitable adjustment of the pulse rise time is another important factor in controlling the generation of heat in the device. Depending on the degree of the overshoot, the temperature of the piezoelectric actuator can increase by more than 50% as compared to the case where there is no vibrational ringing (which corresponds roughly to the off-resonance condition). When the piezoelectric actuator is operated under pulse drive, a resonance-related heating mechanism due to the intensive mechanical loss is superposed with the off-resonance heat generation that is associated largely with the intensive dielectric (PE hysteresis) loss. Thus, care must be taken to reduce the mechanical vibration overshoot and ringing by adjusting the step rise time in order to maintain minimal heat generation in the device (see Figures 6.23 and 6.24).

(ii) *Antiresonance Drive*

It has been proposed that ultrasonic motors be driven in the antiresonance mode as opposed to the resonance mode of operation conventionally used. The quality factor, Q_m, and the temperature rise of a rectangular PZT ceramic bar have been investigated when the bar is driven at both fundamental resonance (A mode) and antiresonance (B mode). It was found in this study that the quality factor at antiresonance, Q_B, is higher than that at resonance, Q_A, over the entire range of vibration velocity investigated (see Figure 10.65). These findings indicate that operation of the motor in the antiresonance mode can provide the same mechanical vibration level without generating heat. Ultrasonic motors have conventionally been operated in the resonance mode, at the fundamental resonance frequency; however, we now see that operating at the antiresonance frequency results in a higher mechanical quality factor, Q_m, and higher efficiency than possible at resonance. Moreover, at antiresonance, the admittance of the material is very low, and the motor can be operated at a lower current and a higher voltage, in contrast to the high current and low voltage drive conditions required for resonance operation. This means that a conventional inexpensive power supply may be used to drive the motor. We considered the practical aspects of ultrasonic motor design and operation in Chapter 10.

(2) Future Trends for Smart Actuators

Higher Function

Much of the current interest in solid-state actuators stems from the development of smart materials and structures. The evolution of this family of materials is gradually progressing through stages ranging from *trivial functionality* to *smart* to *intelligent* and finally to a more "*wise*" mode of operation. As already discussed, the off-diagonal couplings listed in Table 1.2 all have corresponding converse effects (such as the piezoelectric and converse piezoelectric effects) so that both "*sensing*" and "*actuating*" functions can be realized in the same material. One example is the material used in the electronic modulated automobile shock absorber developed by Toyota Motors pictured in Figure 9.34. The sensor detects the road roughness and the actuator responds by modifying the valve position to change the rate of shock absorption. Both the sensor and the actuator are multilayer piezoelectric devices.

Miniaturization

Future research trends will follow two general courses, the development of *large scale devices* for application in larger systems such as space structures and *miniature devices* for use in systems such as office and medical equipment. The smallest devices will be required for medical diagnostic equipment such as blood test kits and surgical catheters. The development of piezoelectric thin films compatible with silicon technology for microelectromechanical systems (MEMS) will become increasingly important. The structure depicted in Figure 11.5 is a good example. A tiny PZT ultrasonic rotary motor (with a 2.0 mm outer diameter) is mounted on a silicon membrane.[5] The eight electrodes are addressed in a four-phase sequence (sine, cosine, −sine, −cosine). The torque obtained is three orders of magnitude higher than that of a silicon MEMS motor of equivalent size.

As the size of these miniature devices decreases, the weight of the electric lead wire from the power supply becomes significant. Remote control will be required for submillimeter devices. A photodriven actuator is thus a promising candidate for microscale displacement applications. The photostriction effect was discussed in Section 1.3(9), and a fully remote control microwalking machine of this type is pictured in Figure 11.6.

Integration

Achieving higher functionality and enhanced performance sometimes requires additional components (for example, the addition of a position sensor to a smart structure) and therefore increasing complexity of the system. The development of these rather complex systems generally requires the combined expertise of interdisciplinary research teams. As the size of the team increases and the contributions of individual segments of the team become more compartmentalized, the cost of development and production of the product tends to increase, and the efficiency of the process tends to deteriorate. This is sometimes referred to as the "*spaghetti syndrome.*"

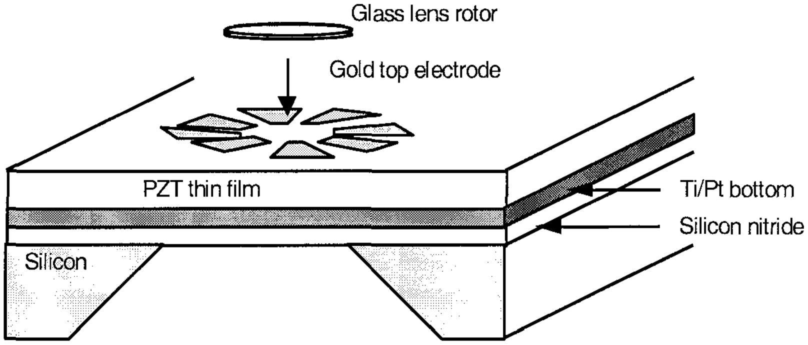

Figure 11.5 Schematic depiction of a PZT MEMS motor, with an eight-pole stator (Inner diameter: 1.2 mm, outer diameter: 2.0 mm), mounted on a silicon membrane.[5]

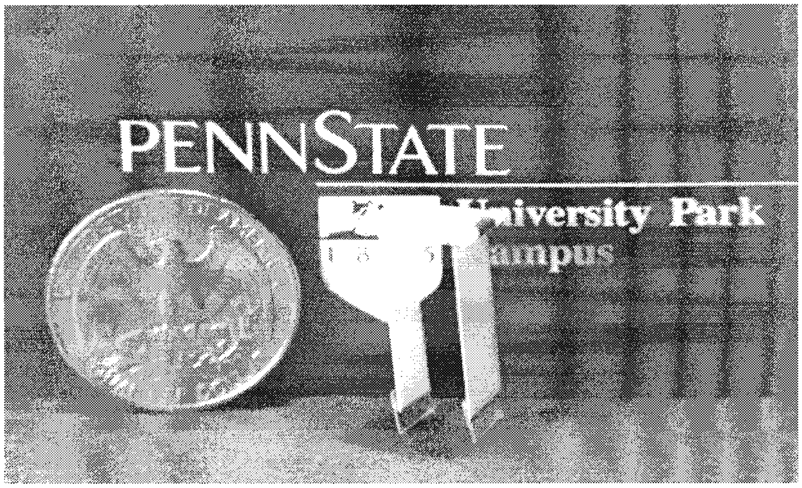

Figure 11.6 Photostrictive walking device. Note the fully remote control.

On the other hand, miniaturization also requires, in addition to smaller components, fewer elements overall. In order to satisfy the requirements of both higher functionality and miniaturization, a very smart material is needed. Smarter devices allow for fewer components in the system. The performance of a miniature system is thus better rated in terms of *performance/volume* or *performance/volume cost* as opposed to simply the overall performance of the unit.

As the degree of integration is increased, the reliability of the unit becomes an increasingly important issue. Thus, the development of systems with more sophisticated and responsive "health monitoring" capabilities will be necessary.

Target Markets and Applications

We will conclude with a brief introduction to the research and development activities of the International Center for Actuators and Transducers at the Pennsylvania State University.

The Japanese Technology Transfer Association conducted market research in 1991 focused on the goals of eighty Japanese electronic components companies in developing new actuator devices. The results of the study are summarized as follows:

1) Motors, approximately *5-8 mm diameter*, are the most commonly needed for office equipment applications, such as personal computers, printers, and copy machines.

2) The optimum specifications for displacement transducers are: displacement 100 μm, force 100 N, and response speed 100 μsec.

Since the design of conventional electromagnetic motors is not conducive to miniaturization, piezoelectric ultrasonic motors are currently the only practical alternative devices to satisfy the 5-8 mm size requirement. The "cymbal" transducer was developed to meet the specifications for displacement transducers, since no other electromechanical actuator configuration at that time satisfied these requirements.

The center has identified three primary long-term target areas of application for new micromechatronic systems: information, biological, and ecological technologies. Compact ultrasonic motors are important for the information technology applications. In addition to the development of suitable ultrasonic motors for these purposes, compact piezoelectric transformers (no magnetic noise) and photostrictive actuators are also being developed to meet the needs of this industry. A new keyword has been coined for the "integration of transducers for information technology, *transinforgration*. The biological applications are focused primarily on simple actuators and sensors for daily medical checks. The design of these devices generally involves the use of a suitable thin or thick piezoelectric film, which ideally should be manufactured inexpensively and be disposable. Microsurgical instruments incorporating miniature ultrasonic motors are also attractive for minimally invasive surgical procedures, such as the removal of kidney stones. The ecological applications for this class of devices will initially involve primarily the sensing capabilities of these smart systems for monitoring the presence of pollutants in a given environment. Future applications will likely make fuller use of the actuating elements of the system to also respond to an unacceptably high level of pollutants to initiate an appropriate action.

One ecological concern that directly impacts the development of lead-based devices is the increasing concern in both the United States, Japan, and Europe to more strictly regulate the handling of lead-based products to ensure minimal public exposure to this toxic element. The development of new policies in this area could lead to serious restrictions on the use of PZT and other popular lead-based compositions as early as the year 2020. It is clear that the time has come to initiate serious research in search of new materials that do not contain lead to replace the lead-based compositions that are currently the mainstay of the electromechanical device industry.

The number of patents related to lead-free piezoelectric materials filed worldwide from 1986 to 2001 is shown in Figure 11.7. The number of patents in this area has increased dramatically since 1999, largely in response to the increased regulation of lead-containing products throughout the world. Lead-free piezoelectric materials can be classified into five general categories: (1) piezoelectric single crystals [such as langasite ($La_3Ga_5SiO_{14}$) and lithium tetraborate ($Li_2B_4O_7$)], (2) tungsten-bronze ferroelectric ceramics, (3) bismuth layer structure ferroelectric ceramics, (4) compositions based on the potassium-sodium niobate, $KNbO_3$-$NaNbO_3$ system, and (5) perovskite ferroelectric ceramics. A breakdown of the relative development of these classes of materials in terms of the number of related patents filed and papers published is depicted in Figure 11.8. The development of bismuth compounds [bismuth layered and $(Bi,Na)TiO_3$] is clearly an important area at this time as indicated in the figure, where we see the number of patents filed related to these materials is about 61% of the total number surveyed. This is mainly because bismuth compounds are easily prepared as compared to the other categories of materials. Dramatic development of these materials is anticipated over the next decade.

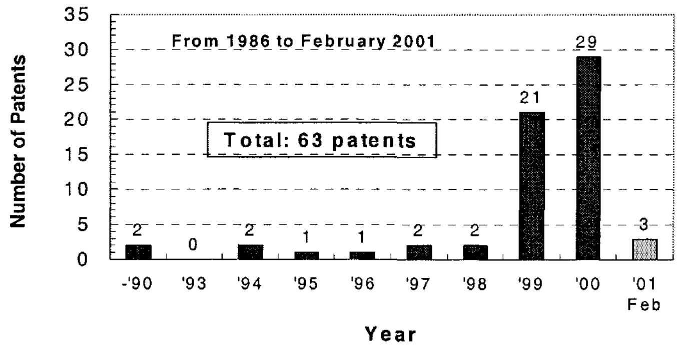

Figure 11.7 The number of patents related to the development of lead-free piezoelectric ceramics filed worldwide from 1986 to 2001.

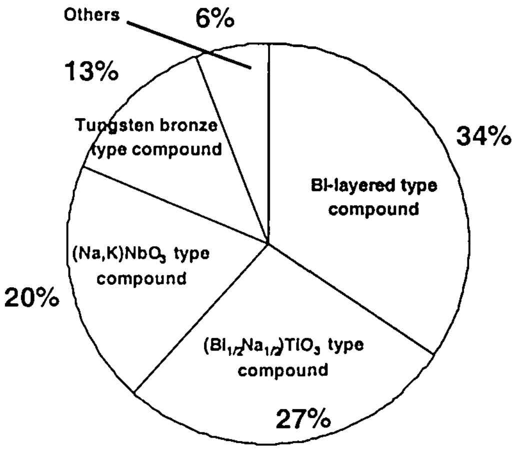

Figure 11.8 A breakdown of the relative development of lead-free materials in terms of the number of related patents and papers. (Total number in survey: 102)

CHAPTER ESSENTIALS

1. **Current Markets:** for piezoelectric actuators and ultrasonic motors:
   a. Computer-related
   b. Camera-related
2. **Reliability of ceramic actuators:**
   a. Ceramics: depends on reproducibility of batches, temperature characteristics of the material, the applied stress, the level of induced strain, and aging effects.
   b. Devices: depends on the electrode material and configuration electrode designs, layer thickness, the presence of "health monitoring" mechanisms.
   c. Drive Systems: depends on the drive mode (pulse or continuous), the control of heat generation mechanisms, and the power level.
3. **Future Directions:**
   a. Large-Scale Devices: for vehicles and space structures.
   b. Miniature Devices: for office equipment.
   c. Ultra-miniaturization: for medical applications.
   d. Remote Control: will become increasingly important, especially for miniature and ultra-miniature devices.
4. **Key Goals:**
   a. Avoid the "Spaghetti Syndrome."
   b. Increase the performance/volume cost rating of the device
   c. Desired motor specifications: size: 5-8 mm, desired features: high speed, torque, efficiency.

CHAPTER PROBLEMS

1.1 Based on a literature survey from the past five years, discuss and summarize recent research related to the reliability of piezoelectric actuators. The papers should deal with issues such as actuator design, low hysteresis/high power piezoelectrics, manufacturing reproducibility, and high temperature characteristics. Your survey should include at least five papers.

   a. Classify the reliability issues addressed in the papers in terms of materials-, design-, and drive/control-related issues.

   b. Summarize the problems addressed in the papers and their possible solutions.

   c. Provide a complete list of the papers used for your report.

REFERENCES

1) K. Uchino: Proc. 9th Int'l. Symp. Appl. Ferroelectrics, p.319 (1995).
2) K. Abe, K. Uchino and S. Nomura: Jpn. J. Appl. Phys., **21**, L408 (1982).
3) K. Nagata: Proc. 49th Solid State Actuator Study Committee, JTTAS (1995).
4) K. Uchino and H. Aburatani: Proc. 2nd Int'l. Conf. Intelligent Materials, p.1248 (1994).
5) A. M. Flyn, L. S. Tavrow, S. F. Bart, R. A. Brooks, D. J. Ehrlich, K. R. Udayakumar and L. E. Cross: J. Microelectromechanical Systems, **1**, 44 (1992).

INDEX

Abnormal grain growth, 173
Acoustic emission, 156–63, 185–87
  Kaiser effect, 159–60
Active fiber composites (AFC), 199–201, 371
Actuators
  bimorph, 190-95, 254
  device design, 176–208
    bimorph, 190–95
    composites, 199–202
    cylindrical devices, 188–89
    cymbal, 197–99
    disk actuators, 177–78
    displacement amplification mechanisms, 206–8, 385–86
      inchworm, 207–8
      monolithic hinge structure, 206–7, 353–56, 398-99
      oil pressure, 207–8
    monomorph, 195–97
    moonie, 197–99
    multilayer actuators, 178–88
    rainbow, 195–97
    thin films, 201–6
    unimorph, 190–95
  elastomer actuator, 24–26
  electrodes, 208–13
    internal, 180–88
      interdigital with float electrode, 183
      plate-through design, 182–84
      slit-insert design, 183
  electrorheological fluid actuator, 27–31
  electrostrictive actuator, 22–24, 31
    commercialized, 213–14
    resonant displacement devices, 219–21
    response speed, 143–45
[Actuators]
    rigid displacement devices, 219–21
  magnetorheological fluid actuator, 27–31
  magnetostrictive actuator, 18–22, 31
  mechanical properties, 145–63
  multilayer actuators, 178–88
    fabrication
      cut-and-bond method, 179
      tape-casting method, 179–81
  new actuators, 8–10
  photostrictive actuator, 26–27
  piezoelectric actuator, 22–24, 31, 219–21
    commercialized, 213–14
    electrical impedance, 260–61
    equivalent circuits, 263
    resonant displacement devices, 219–21
    response speed, 143–45
    rigid displacement devices, 219–21
  polymer actuator, 24–26
  polymer film actuator, artificial muscle, 13–14
  shape memory actuator, 14–18, 31, 398–99
  smart actuator, 7–8
    future trends, 33–34
    health monitoring, 185–89
      acoustic emission, 185–87
      strain gauge electrode, 186–88
  solid-state actuator, 7–32
Adaptive optical systems, 347
Aging, 143, 186–87
Antiferroelectric materials, physical properties, 46–48

Antiferroelectricity, phenomenological theory, 77–80
Artificial muscle. *See* Actuators, polymer film actuator, artificial muscle

Barium titanate ($BaTiO_3$), 42–46, 106
  ceramic processing
    alkoxide hydrolysis (sol-gel method), 172
    co-precipitation method, 170-71
    direct precipitation method, 171
    mixed-oxide method, 170
    sintering, 174
  domain reorientation, 82–91
  domain structure, 85–86
  grain size effects, 92–97
  history, 103
  multilayer actuator, 210–13
  piezoelectric effect in ceramics, 106
  piezoelectric effect in single crystal, 55
  spontaneous polarization, 67–68

Calcination, 169
Ceramic powder processing methods, 169–72
  alkoxide hydrolysis (sol-gel method), 171–72
  co-precipitation method, 170–71
  mixed-oxide method, 169–70
Ceramic processing
  hot pressing, 173
  sintering, 173–75
    doping, 174–75
Coercive field, 82, 83
  crystal structure effects, 91–92
  dopant effects, 322–23
  hard and soft piezoelectrics, 118
Columbite, 170
Composites
  active fiber composites (AFC), 371
  electro/magnetorheological fluids, 27–31
  electrostrictive, 139
  magnetostrictive Terfenol-D/epoxy, 128–29
  piezoelectric, 103, 122–25, 197–202
    active fiber composites (AFC), 199–201
    piezoceramic/carbon black/polymer, 271–73
Contact potentiometers, 266
Cracks
  lateral crack, 152
  median crack, 152
  Palmqvist crack, 151
Critical particle size (D_{crit}), 93, 204
Curie constant, 44
Curie temperature, 42
Curie-Weiss law, 44
Curie-Weiss temperature, 44

Deformable mirror, 199
Dielectric constant
  complex, 288
  longitudinally clamped dielectric constant, 260
Dielectric materials, 37
Dielectric relaxation, 93
Differential transformer, 267
Digital displacement, 120
Dipole moment, 41
Dipole orientation polarization, 37
Displacement amplification mechanisms, 207–8
Displacement reduction mechanisms, 3–7
Dissipation factor, 287–90
Dot matrix printer head, 22
Drive techniques
  mechanical ringing, 248–52
  off-resonance drive, heat generation, 310–14
  piezoelectric transformer, 272–77
  position sensors, 265–70
    capacitance methods, 268
    electromagnetic induction methods, 267
    optical methods, 268–69
    resistance methods, 266–67
  pulse drive, 241–55
    heat generation, 317–18
    longitudinal vibration mode, 244, 246
    pseudo step voltage, 250–53
    pulse width modulation, 254–55
    rectangular pulse, 252–53
    rectangular pulse voltage, 248–50
    transverse vibration mode, 242–43, 246–51
  resonance drive, 256–65
    antiresonance state, 260–65

[Drive techniques]
        equivalent circuit, antiresonance, 306–7
        equivalent circuit, resonance, 306–7
        heat generation, 314–16
        motional admittance, 261
        piezoelectric resonance, 256, 259–65
            equivalent circuit, 263
        resonance state, 260–65
    stress sensors, 269–70
Duty factor, 254

Efficiency (η), 134
Elastic deformation, 48
Electric displacement, 37
Electric field-induced strain, 48–49
Electric polarization, 37
Electric poling, 110
    mechanical strength, 156–59
Electrodes
    application
        bonding method, 209
        co-firing with ceramic, 209
    materials, 208–13
        ceramic, 209–13
Electromechanical coupling factor (k), 70, 131–36, 298–99
Electronic polarization, 37
Electrostriction, 22, 37, 49
    converse electrostriction effect, 69, 269
    direct electrostriction effect, 69
    electrostriction coefficient (M)
        definition, 49
        tensor form, 50–52
    electrostriction coefficient (Q)
        matrix form, 60–61
        measurement, 71
        tensor form, 50–52
    phenomenological description, 64–67
    stress dependence, 145–48
    temperature coefficient (TCE), 139–42
    temperature dependence, 71–72, 138–42
        macroscopic composite method, 139
        microscopic approach, 139–42
[Electrostriction]
    tensor representation, 50–52
Electrostrictive materials
    ceramics, compared with piezoelectric materials, 116–17
    mechanical properties, 145–63

Feedback control, 221–41
    polarization control, 239–41
    system design
        characteristic equation, 229–30
        closed loop frequency response function, 235
        Fourier transform, 221
        Laplace transform, 221–25
        Nyquist criterion, 230–32
        steady state error, 229, 232–33
        transfer function, 225–29
            Bode diagram, 238–39
            closed loop, 228
            open loop, 228
Ferroelectric materials, 49
    domain reorientation, 82–92
        Uchida-Ikeda model, 86–91
    physical properties, 42–46
    relaxor ferroelectrics, 113–19
    thin films, 201–6
Ferroelectricity, 37–39
    first-order phase transition, 44, 63–64
    phenomenological theory, 62–64
    second-order phase transition, 62–63, 68–69
Finite element method (FEM), 329–46
    assembly, 342–43
    boundary conditions, 332–33
    computation techniques, 343–44
    constitutive equations, 330–32
    discretization
        piezoelectric domain, 334
        variational form, 340–42
    finite elements, 329
    mesh, 329
    nodes, 329
    parent elements, 337–40
    piezoelectric domain, 329
    shape functions, 330, 334–37
    variational principle, 333–34
Fracture mechanics, 149–51

Fracture toughness, 149, 151–56
  grain size effects, 156–57

Giant magnetostriction, 19, 127–29
Giant magnetostrictive materials, 127–29
Grain size effects, ferroelectricity, 92–98

Heat generation, 310–18
  off-resonance drive, 310–14
  pulse drive, 317–18
  resonance drive, 314–16
Hydrostatic pressure model, 93–97
Hysteresis, 285–310
  dielectric, 287–91
  electromechanical measurement, 299–301
  theoretical description, 291–99

Inchworm. *See* Motors, linear, inchworm
Ionic polarizability, 41
Ionic polarization, 37

Kanzig region, 113

Landau theory, 62
Laplace transform. *See* Feedback control, system design, Laplace transform
Lead lanthanum zirconate titanate. *See* PLZT
Lead magnesium niobate. *See* PMN
Lead magnesium niobate-lead titanate. *See* PMN-PT
Lead titanate ($PbTiO_3$), 109
Lead zinc niobate-lead titanate. *See* PZN-PT
Lead zirconate titanate. *See* PZT
Lithium niobate ($LiNbO_3$), 106
  monomorph, 196–97
  single crystal growth, 176
  surface acoustic wave motor, 420–21
Lithium tantalate ($LiTaO_3$), 106
  single crystal growth, 176
Lorentz factor, 41
Loss, dielectric, 287–91
  extensive, 285
  intensive, 285, 290-91
Loss, electromechanical, 285–310
  domain reorientation, 309
  extensive, 294–96
[Loss, electromechanical]
  intensive, 291–94
  measurement, 299–301
  mechanisms, 286–87
  resonance conditions, 302–10
  theoretical description, 291–99
Loss, mechanical, intensive, 285

Magnetostriction, 9, 18, 127–29
  phenomenological theory, 80–81
Magnetostrictive materials, 127–29
Matrix notation, piezoelectric (d and g) and electrostriction (M and Q) tensors, 52–61
Mechanical quality factor (Q_m), 136
  measurement, 307–10
Mechanical strength
  electric poling, 156–59
  field-induced strain, 156–59
MEMS (microelectromechanical systems), 10–12
Micromachining
  bulk, 10
  surface, 10
  PZT micropump, 202–4
Micropositioning, 3
Microscopic composition fluctuation model, 113
Morphotropic phase boundary, 107
Motors
  linear, inchworm, 207–8, 379–84
  pulse drive motors, 219, 375–402
  ultrasonic motors, 219, 264, 403–60
    designing, 442–49
    historical background, 403–6
    horn, 453
    magnetic, 453–54
    mixed-mode, 409, 414–17
      dual vibration coupler, 416–17
      rotary, 414–15
      windmill, 415–16
    mode rotation, 410, 430–32
    piezoelectric fans and pumps, 450–53
    reliability, 454–58
    speed and thrust calculations, 436–42
    standing wave, 407–8, 409, 410–14
      linear, 412–14

- [Motors]
    - - rotary, 410–12
    - surgical knife, 449
    - traveling wave, 409, 410, 417–30
        - linear, 417–22
            - LiNbO$_3$ surface acoustic wave motor, 420–21
            - rectangular plate dual-mode vibrator, 421
            - π-shaped, 422
        - rotary, 422–31
            - spinning plate, 429–31
            - surfing, 423–29
    - walking machines, 434–36

- Néel temperature, antiferroelectric material, 78
- Nitinol, 126–27. *See* Actuators, shape memory actuator
- Normal grain growth, 173

- One-dimensional two-sublattice model, 77–80
- Optical lever, 268

- Particle size effects. *See* Grain size effects
- PbTiO$_3$. *See* Lead titanate (PbTiO$_3$)
- Phase-change materials, 120
- Photostriction, 26–27
- Photovoltaic effect, 26
- Piezoelectric devices
    - damper, 270–73
    - piezoelectric transformer, 272–77
- Piezoelectric effect, 22, 39, 241–42
    - converse piezoelectric effect, 22, 37, 48, 50, 69, 330
    - direct piezoelectric effect, 53, 69, 130, 330
    - efficiency (η), 134
    - electromechanical coupling factor (k), 131–36, 256–59, 298–99
    - energy transmission coefficient (λ_{max}), 131–36
    - history, 103–4
    - induced, 242
    - induced effect in relaxor ferroelectrics, 117
- [Piezoelectric effect]
    - mechanically clamped state, 296
    - mechanically free state, 296
    - open-circuit state, 296
    - piezoelectric strain coefficient (d), 129–30
        - definition, 48
        - matrix form, 52–61
        - tensor form, 50–52
    - piezoelectric voltage coefficient (g), 130
        - tensor form, 50–52
    - resonance, 256, 259–65
    - short-circuit state, 296
    - single crystals, 72–77
    - stress dependence, 145–48
    - tensor representation, 50–52
- Piezoelectric materials, 105–26
    - applications, 45
    - ceramics, 106–13
        - compared with electrostrictive materials, 116–17
    - diphasic composites, 122–25, 199–202
    - dopant effects, 320–23
    - figures of merit, 129–38
    - hard piezoelectric, 108, 118, 319–25
    - hysteresis. *See* Hysteresis
    - loss, electromechanical. *See* Loss, electromechanical
    - mechanical properties, 145–63
    - phenomenological theory, 109
    - polymers, 120–22
    - relaxor ferroelectrics, 113–19
    - single crystals, 106
    - soft piezoelectric, 108, 118, 319–25
    - thin films, 126
        - fabrication techniques, 201–3
        - properties, 203–6
- Piezoresistive effect, 266
- PLZT (lead lanthanum zirconate titanate), 22, 26
    - ceramic processing
        - co-precipitation method, 171
        - sintering, 173–75
    - electric field-induced strain, 88–91
    - electrostriction, 115
        - frequency dependence, 143–44

[PLZT (lead lanthanum zirconate titanate)]
  fracture toughness and mechanical strength, 156–57
  grain size effects, 92–97
  loss, dielectric, 286–87
  piezoelectric effect, 82
  piezoelectric properties, 110–12
  principal strain (S_S) and spontaneous polarization (P_S), 91–92
PMN (lead magnesium niobate), 22
  ceramic, crack propagation, 157–59
  electric field induced strain, 88–91
  electrostriction, temperature dependence, 71
  electrostriction in single crystal form, 56–57
  relaxor behavior, 113–15
PMN-PT (lead magnesium niobate-lead titanate)
  ceramic processing, mixed-oxide method, 170
  electrostriction, 115
    pressure dependence, 145–47
    temperature dependence, 138–39
  multilayer actuator, 182
  single crystal growth, 176
Poisson's ratio, 83, 259
Polarization reversal, 49
Poling. *See* Electric poling
Polyvinylidene difluoride. *See* PVDF
Polyvinylidene difluoride trifluoroethylene. *See* PVDF-TrFE
Positioners, servo displacement transducers, 219
Positioning systems, servo system, 221–41
Potassium dihydrogen phosphate (KDP), 103
Principal strain (S_S), 87
Pseudoplasticity, 15
Pulse drive motor applications
  adaptive suspension systems, 399–401
  dot matrix printer head, 384–91
  imaging systems, 375–78
  inchworm devices, 379-84
    impact mechanism walking machines, 383–84
    linear drive inchworm, 381–84
    microangle goniometer, 379–80
    microwalking vehicles, 381–84
[Pulse drive motor applications]
  inkjet printer head, 390–96
  piezoelectric bimorph camera shutter, 377–78
  piezoelectric relays, 396–99
  swing CCD image sensor, 375–77
  swing pyroelectric sensor, 377
PVDF (polyvinylidene difluoride), 24, 103, 120–22
PVDF-TrFE (polyvinylidene difluoride trifluoroethylene), 24, 122
Pyrochlore, 170
Pyroelectricity, 39
PZN (lead zinc niobate), single crystal growth, 176
PZN-PT (lead zinc niobate-lead titanate), 109–10
  piezoelectric effect, single crystal, 117–19
  single crystal electrical impedance, 262
    growth, 176
PZT (lead zirconate titanate), 32
  bimorph, 252, 254-55
  ceramic
    crack propagation, 157–59
    electrical impedance, 262
    electromechanical losses, 299–301
    heat generation, 314–16
    mechanical quality factor (Q_m), 308–10
  ceramic processing
    alkoxide hydrolysis (sol-gel method), 172
    mixed-oxide method, 169
  co-fired electrodes, 209
  creep characteristic, 143–44
  doping, 320–23
  electric field-induced strain, 88–91
  history, 103
  multilayer actuator
    heat generation, 310–14, 317–18
  phase diagram, 107
  piezoelectric effect
    ceramic, 76–77
    single crystal, 72–77
    stress dependence, 147–48
  piezoelectric properties, 69–71, 107–8
  thin film, 126, 201–6

Quartz, 106

Relaxor ferroelectric. *See* Ferroelectric materials, relaxor ferroelectrics
Ringing. *See* Drive techniques, mechanical ringing
Rochelle salt, 103

Schottky barrier, 195
Sensors
  position, 265–70
  stress sensor, 269–70
Servo displacement transducer applications
  deformable mirrors, 347–53
    articulating fold mirror, 352
    monolithic piezoelectric, 347–49
    multimorph, 349–52
    Zernike aberration polynomials, 350–52
  linear displacement devices, 356–60
    linear motion guide mechanism, 356–59
    ultraprecise x-y positioning stage, 359–60
  microscope stages, 353–56
  noise elimination, 371–72
  servo system devices, 360–68
    air pressure servo valves, 366–67
    direct drive spool servo valve, 368
    oil pressure servo valves, 361–66
  VCR head tracking, 368–70
  vibration suppression, 371–72
Servo systems, 360–68
  air pressure, 366–67
  direct drive spool servo valve, 368
[Servo systems]
  oil pressure, 207, 254–55
  oil pressure servo valves, 361–66
Shape memory actuators. *See* Actuators, shape memory actuator
Shape memory alloys, 126–27
Shape memory effect, 14–18, 120
Single crystal growth, 176
Smart materials, 7–8
Smart ski, 270-71
Smart skins, 2
Soft phonon mode, 40
Spontaneous polarization, 39–42
Strain gauges, 266
Superelasticity, 15–16

Tensor representation, piezoelectric effect and electrostriction, 50–52
Terfenol-D, 19, 127–29
Thermal expansion, 48
Thin films, fabrication techniques, 201–3
Transfer function. *See* Feedback control, system design, transfer function

Uchida-Ikeda model, 86–91
Ultrasonic motors, 2, 403–60

Voice coil motor, 3, 6

Weibull coefficient, 154
Weibull plot, 154

Zero point drift, 143

KOAX03
11/22/06